



US Army Corps  
of Engineers

AD-A215 417



CONTRACT REPORT GL-89-2

(2)

# RE-EVALUATION OF THE LOWER SAN FERNANDO DAM

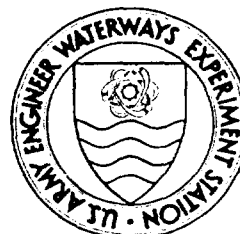
Report 3

THE BEHAVIOR OF UNDRAINED CONTRACTIVE SAND  
AND ITS EFFECT ON SEISMIC LIQUEFACTION  
FLOW FAILURES OF EARTH STRUCTURES

by

Andres Vasquez-Herrera, Ricardo Dobry

Department of Civil Engineering  
Rensselaer Polytechnic Institute  
Troy, New York 12180-3590



DTIC  
ELECTE  
NOV 24 1989  
S B D

September 1989

Report 3 of a Series

Approved For Public Release; Distribution Unlimited

Prepared for DEPARTMENT OF THE ARMY  
US Army Corps of Engineers  
Washington, DC 20314-1000

Under Contract No. DACW39-86-K-0019  
and  
Contract No. 86-003

Monitored by Geotechnical Laboratory  
US Army Engineer Waterways Experiment Station  
3909 Halls Ferry Road, Vicksburg, Mississippi 39180-6199

89 11 21 105

Destroy this report when no longer needed. Do not return  
it to the originator.

The findings in this report are not to be construed as an official  
Department of the Army position unless so designated  
by other authorized documents.

The contents of this report are not to be used for  
advertising, publication, or promotional purposes.  
Citation of trade names does not constitute an  
official endorsement or approval of the use of  
such commercial products.

Cover photograph by the U.S. Geological Survey

Unclassified  
SECURITY CLASSIFICATION OF THIS PAGE

REPORT DOCUMENTATION PAGE				Form Approved OMB No. 0704-0188		
1a. REPORT SECURITY CLASSIFICATION Unclassified			1b. RESTRICTIVE MARKINGS			
2a. SECURITY CLASSIFICATION AUTHORITY			3. DISTRIBUTION/AVAILABILITY OF REPORT Approved for public release; distribution unlimited			
2b. DECLASSIFICATION/DOWNGRADING SCHEDULE						
4. PERFORMING ORGANIZATION REPORT NUMBER(S)			5. MONITORING ORGANIZATION REPORT NUMBER(S) Contract Report GL-89-2			
6a. NAME OF PERFORMING ORGANIZATION See reverse		6b. OFFICE SYMBOL (if applicable)	7a. NAME OF MONITORING ORGANIZATION USAEWES Geotechnical Laboratory			
6c. ADDRESS (City, State, and ZIP Code) See reverse			7b. ADDRESS (City, State, and ZIP Code) 3909 Halls Ferry Road Vicksburg, Mississippi 39180-6199			
8a. NAME OF FUNDING/SPONSORING ORGANIZATION US Army Corps of Engineers		8b. OFFICE SYMBOL (if applicable)	9. PROCUREMENT INSTRUMENT IDENTIFICATION NUMBER Contract No. DACW39-86-K-0019 Contract No. 86-003			
8c. ADDRESS (City, State, and ZIP Code) Washington, DC 20314-1000			10. SOURCE OF FUNDING NUMBERS			
			PROGRAM ELEMENT NO.	PROJECT NO.	TASK NO.	WORK UNIT ACCESSION NO.
11. TITLE (Include Security Classification) Re-Evaluation of the Lower San Fernando Dam; Report 3: The Behavior of Undrained Contractive Sand and Its Effect on Seismic Liquefaction Flow Failures of Earth Structures						
12. PERSONAL AUTHOR(S) Vasquez-Herrera, Andres; Dobry, Ricardo						
13a. TYPE OF REPORT Report 3 of a Series		13b. TIME COVERED FROM _____ TO _____		14. DATE OF REPORT (Year, Month, Day) September 1989		
				15. PAGE COUNT 546		
16. SUPPLEMENTARY NOTATION This report is available from the National Technical Information Service, 5285 Port Royal Road, Springfield, VA 22161.						
17. COSATI CODES			18. SUBJECT TERMS (Continue on reverse if necessary and identify by block number) Earthquakes                      Soils Liquefaction			
FIELD	GROUP	SUB-GROUP				
19. ABSTRACT (Continue on reverse if necessary and identify by block number) <p>A comprehensive experimental testing program (129 tests) was conducted on several silty sands in order to better understand the factors influencing seismically induced liquefaction flow failures, with emphasis on earth dams and slopes. A commercial sand and two sands obtained from engineering projects in Venezuela (Eastern Shore of Lake Maracaibo) and California (San Fernando Dam) were used. Most of the tests were undrained cyclic torsional experiments of the strain-controlled type, performed on solid cylindrical remolded specimens which had been anisotropically consolidated in a triaxial cell (Cyt-CAU tests). In addition, a number of selected CIU, CAU, Cyt-CIU and other types of tests were also conducted, including some experiments on dilative sand. Most of the specimens were compacted using the moist tamping undercompaction method, which produces relatively homogeneous samples. Selected tests on the San Fernando sand prepared using a wet raining sedimentation method were used to verify the influence of a more heterogeneous, layered fabric on soil behavior.</p> <p style="text-align: right;">(Continued)</p>						
20. DISTRIBUTION/AVAILABILITY OF ABSTRACT <input checked="" type="checkbox"/> UNCLASSIFIED/UNLIMITED <input type="checkbox"/> SAME AS RPT. <input type="checkbox"/> DTIC USERS			21. ABSTRACT SECURITY CLASSIFICATION Unclassified			
22a. NAME OF RESPONSIBLE INDIVIDUAL			22b. TELEPHONE (Include Area Code)		22c. OFFICE SYMBOL	

## 6a. NAME OF PERFORMING ORGANIZATION (Continued).

Department of Civil Engineering  
Rensselaer Polytechnic Institute  
Troy, New York 12180-3590

## 19. ABSTRACT (Continued).

*Soil test results*

The results of the Cyt-CAU and other cyclic and monotonic tests are analyzed in detail from ~~two~~ complementary viewpoints: the shear strength behavior of the soil (including steady-state lines, effective stress conditions at triggering of flow failure, and the pore water pressure needed for triggering) for both monotonic and cyclic loading; and the pore water pressure buildup and number of straining cycles needed for triggering during cyclic loading. The influence of ~~a number of~~ <sup>several</sup> parameters is investigated, including: void ratio, minor effective consolidation stress, coefficient of anisotropic consolidation, cyclic torsional shear strain, sand fabric, and sand type.

On the basis of the laboratory results and of a literature review, a conceptual framework is proposed for the evaluation of seismic flow failure of specific engineering projects, including the possibility of undrained and partially drained mechanisms. This procedure is applied to the upstream slope slide induced in the Lower San Fernando Dam by the 1971 earthquake. It is concluded that i) the hydraulic fill sand in the dam was contractive prior to the earthquake, ii) the seismic strains induced by the shaking were much greater than those needed to trigger flow failure in the critical layer, and iii) the local factor of safety of the critical layer in the upstream slope after triggering was significantly lower than one, thus explaining the observed failure. Conclusion i) means that a purely undrained evaluation (also called Mechanism A in the literature) using the techniques proposed here would have predicted the 1971 upstream failure, as well as the good performance of the downstream slope, which had a local factor of safety close to unity after triggering. *Earthquakes, Earth dams.*

(RDC)

Accession For	
NTIS GRA&I	<input checked="" type="checkbox"/>
DTIC TAB	<input type="checkbox"/>
Unannounced	<input type="checkbox"/>
Justification	
By	
Distribution/	
Availability Codes	
Dist	Avail and/or Special
A-1	





## PREFACE

This study was a part of an investigation of the strength of soils that have been weakened by earthquake shaking, and the stability of embankment dams containing or founded on susceptible soils. This report is one of a series which documents the investigation. The project was carried out jointly by Geotechnical Engineers, Inc. (GEI), H. Bolton Seed, Inc., Rensselaer Polytechnic Institute (RPI), and the U.S. Army Engineer Waterways Experiment Station (WES). Principal Investigators were Dr. Gonzalo Castro for GEI, Professor H. Bolton Seed, Professor Ricardo Dobry for RPI, and Dr. A. G. Franklin for WES. Mr. Edward Pritchett, Office of the Chief of Engineers, Washington, DC, was responsible for recognizing the importance and timeliness of this research to the Corps of Engineers, and for generating Corps support for the project. Funding was provided through the US Army Engineer District, Kansas City, for whom oversight was provided by Mr. Francke Walberg.

Essential to the overall investigation was an exploration and records review effort at the Lower San Fernando Dam, in order to obtain crucial data and soil samples for laboratory testing. This effort included an extensive drilling and penetration testing program, excavation of a large-diameter shaft, in-situ testing, collection of samples, and review of historical records. The Los Angeles Department of Water and Power, owner of the Lower San Fernando Dam, provided access to the site and to the historical records, and other assistance. The California Department of Water Resources provided information from their files.

Drilling, Standard Penetration Testing, and undisturbed sampling from borings was performed by WES, under the supervision of Mr. Joseph Gatz. Cone Penetration Test soundings were performed by Earth Technology Corporation (ERTEC). Excavation of the exploratory shaft was done by Zamborelli Drilling Company, under the direction of GEI. Investigations and sampling in the shaft, and the review of historical records, were done by and under the supervision of Mr. Tom Keller of GEI.

The work presented in this report was carried out at RPI under WES Contract No. DACW39-86-K-0019, and with additional funding from INTEVEP, S.A., of Venezuela, under Contract No. 86-003.

The technical monitor and Contracting Officer's Representative at WES was Dr. A. G. Franklin, Chief of the Earthquake Engineering and Geosciences Division, Geotechnical Laboratory. The primary WES reviewer was Dr. Paul F. Hadala, Assistant

Chief of the Geotechnical Laboratory. Chief of the Geotechnical Laboratory was Dr. William F. Marcuson III.

Commander and Director of WES during the preparation of this report was COL Larry B. Fulton, EN. Dr. Robert W. Whalin was Technical Director.

This report is essentially identical to the thesis presented by Andres Vasquez-Herrera to the Civil Engineering Department, Rensselaer Polytechnic Institute (RPI), in partial fulfillment of the requirements for the degree of Doctor of Philosophy.

The authors gratefully acknowledge the contributions and useful discussions throughout the project by Messrs. Heriberto Echezuria, German Febres and Enrique Gajardo of INTEVEP, S.A. and Jacinto Abi-Saab and Juan Murria of MARAVEN; Drs. A. G. Franklin and William F. Marcuson III of WES; Drs. Leslie F. Harder, H. Bolton Seed and Raymond B. Seed of the University of California at Berkeley; and Mr. Thomas O. Keller of Geotechnical Engineers, Inc.

The authors also want to thank Dr. Gonzalo Castro of Geotechnical Engineers, Inc., and Ahmed-W. Elgamal, Apostolos Papageorgiou, and Thomas F. Zimmie of RPI for their fruitful discussions and for their reviewing of this report; and Messrs. Mohamad H. Baziar and Li Liu of RPI for reviewing the report and making useful suggestions.

## TABLE OF CONTENTS

	PAGE
LIST OF TABLES . . . . .	viii
LIST OF FIGURES . . . . .	x
NOTATION . . . . .	xxvii
1. INTRODUCTION . . . . .	1
1.1. General . . . . .	1
1.2. Problem Statement, Scope and Objectives . . . . .	3
1.3. Report Organization . . . . .	7
2. BACKGROUND . . . . .	8
2.1. Fundamentals of Liquefaction . . . . .	8
2.2. The Steady State Concept . . . . .	13
2.3. Liquefaction Mechanisms . . . . .	17
2.4. Flow Failure Evaluation Procedures . . . . .	20
2.5. The Cyclic Strain Approach . . . . .	25
2.6. The CyT-CAU Test . . . . .	29
2.7. Previous Results by Mohamad . . . . .	32

3.	SCOPE AND OBJECTIVES OF THE EXPERIMENTAL STUDY . . .	53
4.	FLOW FAILURE LABORATORY TESTING EQUIPMENT AND PROCEDURES . . . . .	56
4.1.	General . . . . .	56
4.2.	Sands Tested . . . . .	57
4.3.	The Axial/Torsional Triaxial System . . . . .	60
4.4.	Description of Tests . . . . .	68
4.5.	Guidelines for Flow Failure Testing . . . . .	73
4.6.	Moist Tamping and Sedimentation Sample Preparation Procedures. . . . .	81
5.	TESTING PROGRAM . . . . .	97
6.	SHEAR STRENGTH BEHAVIOR: RESULTS OF EXPERIMENTAL PROGRAM . . . . .	107
6.1.	General . . . . .	107
6.2.	The Steady State Lines . . . . .	113
6.2.1.	Results on Ottawa Sand F125 . . . . .	114
6.2.2.	Results on Sand A . . . . .	116
6.2.3.	Results on San Fernando Sand SF7 . . . . .	117
6.2.4.	Discussion . . . . .	119
6.3.	Effective Stress Conditions at Triggering of Flow . . . . .	126
6.3.1.	Results on Ottawa Sand F125 . . . . .	126
6.3.2.	Results on Sand A . . . . .	130
6.3.3.	Results on San Fernando Sand SF7 . . . . .	131
6.3.4.	Discussion . . . . .	132

6.4.	Pore Water Pressure Needed for Triggering . .	137
6.5.	Tests on Dilative Samples . . . . .	138
6.6.	Influence of Testing Procedures . . . . .	143
7.	PORE PRESSURE BUILDUP AND TRIGGERING DUE TO CYCLIC STRAINING: RESULTS OF EXPERIMENTAL PROGRAM . . .	209
7.1.	General . . . . .	209
7.2.	Number of Straining Cycles to Trigger Flow Failure . . . . .	214
7.2.1.	Results on Ottawa Sand Fl25 . . . . .	214
7.2.2.	Results on Sands A, B and C . . . . .	219
7.2.3.	Results on San Fernando Sand SF7 . . . . .	221
7.2.4.	Discussion . . . . .	224
7.3.	Pore Water Pressure Buildup During Cyclic Straining. . . . .	226
7.3.1.	Results on Ottawa Sand Fl25 . . . . .	226
7.3.2.	Results on Sands A, B and C . . . . .	228
7.3.3.	Results on San Fernando Sand SF7 . . . . .	229
7.3.4.	Discussion . . . . .	230
7.4.	Pore Pressure Buildup and Triggering for Different Sands . . . . .	232
7.5.	A Pore Pressure and Triggering Model for Cyclic Straining of Contractive Sands. . . . .	233
7.6.	Accumulated Axial Strain at Triggering . . .	244

8.	CONSIDERATIONS ON LIQUEFACTION FLOW FAILURE EVALUATION . . . . .	315
8.1.	General . . . . .	315
8.2.	Evidence of Liquefaction Flow Failures . . .	318
8.3.	Cases Involving Monotonic Flow Failures . . .	320
	8.3.1 Monotonic Flow Slides in Coastal Deposits	321
	8.3.2 Monotonic Flow Slides in Hydraulic Fill Earth Structures . . . . .	327
8.4.	Cases Involving Seismic Flow Failures . . . .	339
	8.4.1. Flow Slides in Natural Deposits . . . .	340
	8.4.2. Flow Slides in Hydraulic Fill Earth Structures. . . . .	344
8.5.	Cases Involving Physical Model Studies . . .	352
	8.5.1. Shaking Table Tests . . . . .	352
	8.5.2. Centrifuge Tests . . . . .	357
8.6.	Some Important Factors in Liquefaction Flow Failure Evaluation . . . . .	364
8.7.	Proposed Conceptual Framework . . . . .	373
9.	A REANALYSIS OF THE LOWER SAN FERNANDO DAM SLIDE .	408
9.1	General . . . . .	408
9.2	Upper and Lower San Fernando Dams . . . . .	409
9.3	Earthquake Damage to the Upper and Lower San Fernando Dams in 1971 . . . . .	412
9.4	Field Investigation of the Lower San Fernando Dam . . . . .	416

9.5 Determination of Contractive Zone Within the Dam . . . . .	420
9.6 Determination of In-Situ $S_{us}$ . . . . .	423
9.7 Triggering and Flow Failure Evaluation of the Lower San Fernando Dam. . . . .	425
9.8 Earthquake Shaking Before 1971 . . . . .	431
10. SUMMARY AND CONCLUSIONS . . . . .	465
REFERENCES . . . . .	475
APPENDIX I - INDIVIDUAL TEST RESULTS ON OTTAWA SAND F125	496
APPENDIX II - INDIVIDUAL TEST RESULTS ON SANDS A, B AND C . . . . .	501
APPENDIX III - INDIVIDUAL TEST RESULTS ON SAN FERNANDO SAND SF7 . . . . .	506
APPENDIX IV - INDIVIDUAL TEST RESULTS ON UNDISTURBED SPECIMENS OF SANDS A, B OR C . . . . .	509

# LIST OF TABLES

	PAGE
Table 2.1. Steady-State Strength Envelope Angles $\bar{\alpha}_{us}$ for Several Uniform Clean Sands (after Mohamad, 1985) .	35
Table 4.1. Properties of Soils Tested . . . . .	85
Table 4.2. MTS Measurement Capabilities . . . . .	86
Table 5.1. Numbers and Types of Tests Performed on Remolded Samples . . . . .	103
Table 5.2. Parameters Studied for Laboratory Tests Shear Strength Results . . . . .	104
Table 5.3. Parameters Studied for Cyclic Laboratory Test Results for Pore Water Pressure Buildup and Triggering . . . . .	105
Table 5.4. Ranges of Values for Parameters Studied with Cyclic CyT-CAU Tests on Contractive Sands . . . .	106
Table 6.1. Strength Envelopes of Lines of Phase Transformation for Various Sands . . . . .	150
Table 6.2. Steady-State Strength Envelopes for Various Sands . . . . .	151
Table 8.1. Estimated Void Ratios for the Centrifuge Test Shown in Fig. 8.23 (after Habibian et al., 1985)	382
Table 9.1. Sequence of Events in the Flow Slide of the Lower San Fernando Dam (after Seed, 1979) . . . .	438



Table 9.2. Determination of In Situ $S_{us}$ Using the In Situ Void Ratios of the Undisturbed Specimens. The In-Situ $e$ Were Estimated by GEI (1988) . . . . .	439
Table 9.3. Parameters Used in the Static Finite Element Analysis of the Lower San Fernando Dam (after Mohamad, 1985) . . . . .	440
Table 9.4. Estimated Peak Ground Accelerations from Historical Earthquakes Prior to 1971 . . . . .	441
Table 9.5. Triggering Evaluation of the Upstream Slope of the Lower San Fernando Dam . . . . .	442

# LIST OF FIGURES

	PAGE
Fig. 2.1. Schematic Description of the Steady-State Line (SSL) Using Drained Tests . . . . .	36
Fig. 2.2. Comparison of Two Basic Types of Stress-Strain Behavior Found in Soils Under Undrained Monotonic Shear - a) Type I, b) Type II (NRC, 1985) . . . . .	37
Fig. 2.3. Different Representations of the Steady-State Line . . . . .	38
Fig. 2.4. Density and Stress Conditions for Liquefaction Flow Failure and Liquefaction Cyclic Mobility . . .	39
Fig. 2.5. Examples of Flow Failure Mechanism A (NRC, 1985) . . . . .	40
Fig. 2.6. Example of a Potential Situation for Mechanism B Failure. Local Drainage Occurs But It Is Globally Undrained (NRC, 1985) . . . . .	41
Fig. 2.7. Change in the Undrained Stress Path that a Soil Follows as a Result of Becoming Loosened Because of Local Volume Change . . . . Path A Depicts Stress Path Without Loosening. Path B Depicts Stress Path After Loosening (NRC, 1985)	
Fig. 2.8. Examples of a Potential Situation for Mechanism C Failure Resulting from Spreading of Pore Pressures and Global Volume Changes (NRC, 1985) . . . . .	43
Fig. 2.9. Illustration of Procedure for Obtaining Field SSL from Tests on "Undisturbed" and Reconstituted Specimen (after Poulos et al., 1985) . . . . .	44

Fig. 2.10. Tentative Relationship Between Residual Strength and SPT N-Values for Sands (after Seed, 1987) . . . . .	45
Fig. 2.11. Stress-Controlled Cyclic Triaxial Tests of Saturated Crystal Silica Sand (after Dobry et al., 1982) . . . . .	46
Fig. 2.12. Summary of Results from Strain-Controlled Triaxial Tests on Seven Different Sands with Different Specimen Preparation Techniques . . . . .	47
Fig. 2.13. Illustration of Problem of Seismically Induced Liquefaction Flow Failure of an Earth Dam (after Mohamad, 1985) . . . . .	48
Fig. 2.14. Stress Conditions in Strain-Controlled CyT-CAU Test . . . . .	49
Fig. 2.15. Possible Contractive Zone in a Hydraulic-Fill Dam and the Simulation of Conditions by the CvT-CAU Test . . . . .	50
Fig. 2.16. Effective Stress Paths Showing "Elbows" (from Mohamad, 1985) . . . . .	51
Fig. 2.17. SSL for Banding Sand Determined by Mohamad (1985) . . . . .	52
Fig. 4.1. Grain Size Distribution Curves for Ottawa Sand F125 . . . . .	87
Fig. 4.2. Normalized Membrane Penetration for Various Sands (after Baldi and Nova, 1984) . . . . .	88
Fig. 4.3. Grain Size Distribution Curve for Sand A . . . .	89
Fig. 4.4. Grain Size Distribution Curve for Sand B . . . .	90

Fig. 4.5.	Grain Size Distribution Curve for Sand C . . .	91
Fig. 4.6.	Grain Size Distribution Curve for Sand SF7 . .	92
Fig. 4.7.	Schematic Diagram of Cyclic Axial/Torsional Triaxial Cell . . . . .	93
Fig. 4.8.	Schematic Diagram of a Specimen Being Prepared in Compaction Mold Attached to the Triaxial Cell .	94
Fig. 4.9.	Schematic of the Process for Selecting the Undercompaction Water Content . . . . .	95
Fig. 4.10.	Determination of the Undercompaction of the First Layer for a Sample of Sand F125 (data from Baziar, 1987) . . . . .	96
Fig. 6.1.	Monotonic Triaxial $\overline{\text{CIU}}$ Test on Silty Sand A ( $\overline{\sigma}_{1c} = \overline{\sigma}_{3c} = 6.5 \text{ kg/cm}^2$ ) . . . . .	152
Fig. 6.2.	Monotonic Triaxial $\overline{\text{CAU}}$ Test on Silty Sand A ( $\overline{\sigma}_{3c} = 5.1 \text{ kg/cm}^2$ , $\overline{\sigma}_{1c} = 10.2 \text{ kg/cm}^2$ ) . . . . .	153
Fig. 6.3.	Cyclic Torsional Triaxial CyT- $\overline{\text{CAU}}$ Test on Silty Sand A ( $\overline{\sigma}_{3c} = 4.07 \text{ kg/cm}^2$ , $\overline{\sigma}_{1c} = 8.34 \text{ kg/cm}^2$ , $\gamma_{cy} = 0.05\%$ ) . . . . .	154
Fig. 6.4.	Pore Water Pressure Buildup During CyT- $\overline{\text{CAU}}$ Test on Silty Sand A shown in Fig. 6.3 . . . . .	155
Fig. 6.5.	Monotonic Triaxial $\overline{\text{CIU}}$ Test on Ottawa Sand F125 ( $\overline{\sigma}_{3c} = \overline{\sigma}_{1c} = 4.08 \text{ kg/cm}^2$ ) . . . . .	156
Fig. 6.6.	Monotonic Triaxial $\overline{\text{CAU}}$ Test on Ottawa Sand F125 ( $\overline{\sigma}_{3c} = 0.98 \text{ kg/cm}^2$ , $\overline{\sigma}_{1c} = 1.97 \text{ kg/cm}^2$ ) . . . . .	157

Fig. 6.7. Cyclic Torsional Triaxial CyT-CAU Test on Ottawa Sand Fl25 ( $\bar{\sigma}_{3c}=4.07$ kg/cm <sup>2</sup> , $\bar{\sigma}_{1c}=6.20$ kg/cm <sup>2</sup> , $\gamma_{cy}=0.116\%$ ) . . . . .	158
Fig. 6.8. Pore Water Pressure Buildup for the CyT-CAU Test in Figure 6.7 . . . . .	159
Fig. 6.9. Monotonic Triaxial CU Test on Sand SF7 ( $\bar{\sigma}_{3c}=\bar{\sigma}_{1c}=1.98$ kg/cm <sup>2</sup> ) . . . . .	160
Fig. 6.10. Monotonic Triaxial Strain-Controlled CAU Test on Sand SF7 ( $\bar{\sigma}_{3c}=0.98$ kg/cm <sup>2</sup> , $\bar{\sigma}_{1c}=1.67$ kg/cm <sup>2</sup> ) . . . . .	161
Fig. 6.11. Cyclic Torsional Triaxial CyT-CAU Test on Sand SF7 ( $\bar{\sigma}_{3c}=0.98$ kg/cm <sup>2</sup> , $\bar{\sigma}_{1c}=2.17$ kg/cm <sup>2</sup> , $\gamma_{cy}=0.0107\%$ ) . . . . .	162
Fig. 6.12. Pore Water Pressure Buildup Versus Number of Cycles for the CyT-CAU Test in Figure 6.11 . . . . .	163
Fig. 6.13. Steady-State Strength Envelope for Ottawa Sand Fl25 . . . . .	164
Fig. 6.14. Steady-State Lines of Ottawa Sand Fl25 in $e-\bar{p}$ and $e-q$ space . . . . .	165
Fig. 6.15. Steady-State Lines for Ottawa Sand Fl25 in $e-\bar{\sigma}_3$ and $e-q$ space . . . . .	166
Fig. 6.16. Comparison Between Drained and Undrained Tests Defining the SSL of Ottawa Sand Fl25 . . . . .	167
Fig. 6.17. Steady-State Strength Envelope on Silty Sands A, B and C . . . . .	168
Fig. 6.18. Steady-State Strength Envelope on Silty Sand A . . . . .	169

Fig. 6.19. Steady-State Strength Envelope on Silty Sand SF7 . . . . .	170
Fig. 6.20. Steady-State Strength Envelope on Silty Sand SF7 in $e-\bar{\sigma}_3$ Space for Sedimented and Moist Tamped Specimens . . . . .	171
Fig. 6.21. Steady-State Strength Envelope on Silty Sand SF7 in $e-q$ Space for Sedimented and Moist Tamped Specimens . . . . .	172
Fig. 6.22. Steady-State Strength Envelope Points for the Intact Specimens and Comparison with $\bar{a}_{us}$ Obtained from Remolded Specimens . . . . .	173
Fig. 6.23. Comparison of Peak Strength Envelopes Between Load and Strain-Controlled Monotonic CTU Tests on Ottawa Sand Fl25 . . . . .	174
Fig. 6.24. Triggering Envelope for Ottawa Sand Fl25 with Specimens Consolidated Below $\bar{a}_{up}=17^\circ$ . . . . .	175
Fig. 6.25. Triggering Envelope for Ottawa Sand Fl25 Specimens Consolidated with $K_c=2.0$ . . . . .	176
Fig. 6.26. Triggering Envelope for Ottawa Sand Fl25 Specimens Consolidated with $K_c=2.5$ . . . . .	177
Fig. 6.27. Triggering Envelope for Ottawa Sand Fl25 Specimens Consolidated with $K_c=2.9$ . . . . .	178
Fig. 6.28. Comparison Between Triggering Envelopes of Ottawa Sand Fl25 Showing the Influence of $K_c$ . . . . .	179
Fig. 6.29. Influence of $K_c$ on $\bar{a}_{ut}$ for Ottawa Sand Fl25 . . . . .	180
Fig. 6.30. Comparison Between SSL and Triggering Conditions in Ottawa Fl25 Sand . . . . .	181

Fig. 6.31. Triggering of Flow Failure Strength Envelope for Sand A . . . . .	182
Fig. 6.32. Triggering Envelope of Sedimented and Moist Tamped Specimens of Sand SF7 Consolidated with $K_c \leq 1.87$ Using Sedimented Specimens . . . . .	183
Fig. 6.33. Triggering Envelope of Sedimented and Moist Tamped Specimens of Sand SF7 with $K_c = 1.7$ . . . .	184
Fig. 6.34. Triggering Envelope of Sedimented and Moist Tamped Specimens of Sand SF7 with $K_c = 1.87$ . . . .	185
Fig. 6.35. Triggering Envelope of Sedimented and Moist Tamped Specimens of Sand SF7 with $K_c = 2.0$ . . . .	186
Fig. 6.36. Triggering Envelope of Sedimented and Moist Tamped Specimens of Sand SF7 with $K_c = 2.2$ . . . .	187
Fig. 6.37. Variation of $\bar{a}_{ut}$ as a Function of $K_c$ for Sand SF7 . . . . .	188
Fig. 6.38. Comparison Between Brittleness Index and Liquefaction Potential in Ottawa Sand F125 . . . .	189
Fig. 6.39. Variation of Brittleness Index as a Function of $K_c$ for Ottawa Sand F125 . . . . .	190
Fig. 6.40. Variation of $r_{ut}$ with $K_c$ for Ottawa Sand F125 . . . . .	191
Fig. 6.41. Variation of $r_{ut}$ as a Function of $K_c$ for Sand SF7 . . . . .	192
Fig. 6.42. Monotonic Triaxial $\bar{C}IU$ Test on Dilative Specimen of Sand A ( $\bar{\sigma}_{1c} = \bar{\sigma}_{3c} = 6.98 \text{ kg/cm}^2$ ) . . . .	193

Fig. 6.43. Monotonic Triaxial $\overline{CTU}$ Test on Dilative Specimen of Sand A Showing a More Pronounced Elbow ( $\overline{\sigma}_{1c} = \overline{\sigma}_{3c} = 7.1 \text{ kg/cm}^2$ ) . . . . .	194
Fig. 6.44. Cyclic Torsional Triaxial $CyT-\overline{CAU}$ Test on Dilative Sample of Sand SF7 ( $\overline{\sigma}_{3c} = 0.98 \text{ kg/cm}^2$ , ( $\overline{\sigma}_{1c} = 2.63 \text{ kg/cm}^2$ , $\gamma_{cy} = 0.053\%$ ) . . . . .	195
Fig. 6.45. Pore Water Pressure Buildup for the $CyT-\overline{CAU}$ Test in Fig. 6.44 . . . . .	196
Fig. 6.46. Results of a $CyT-\overline{CAU}$ Test on a Dilative Sample of Sand SF7 Carried Out Until It Reached the Strength Envelope $\overline{\alpha} = \overline{\alpha}_{us} - 29^\circ$ followed by Monotonic Loading ( $CyT-\overline{CAU} + \overline{CAU}$ Test) . . . . .	197
Fig. 6.47. Pore Water Pressure Buildup of the $CyT-\overline{CAU} + \overline{CAU}$ Test Shown in Fig. 6.44 . . . . .	198
Fig. 6.48. $CyT-\overline{CAU} + \overline{CAU}$ Test On An Initially Dilative Sample of Sand A Showing Steady-State Conditions at Higher Stresses . . . . .	199
Fig. 6.49. Pore Water Pressure Buildup of the $CyT-\overline{CAU} + \overline{CAU}$ Test Shown in Fig. 6.48 . . . . .	200
Fig. 6.50. $CyT-\overline{CAU} + \overline{CAU}$ Test on a Contractive Specimen of Sand F125 Showing Triggering and Steady-State Conditions . . . . .	201
Fig. 6.51. Pore Water Pressure Buildup of $CyT-\overline{CAU} + \overline{CAU}$ Test Shown in Fig. 6.50 . . . . .	202
Fig. 6.52. Effect of Void Ratio Measurements Before Saturation on the SSL of Ottawa Sand F125 . . . . .	203
Fig. 6.53. Effect of Stone Correction Factor for the Triaxial Ends on the SSL of Ottawa Sand F125 . . . . .	204



Fig. 6.54. Crushing of Sand Grains in a Typical CyT-CAU Test on Ottawa Sand Fl25 Showing Changes in Grain Size Distribution . . . . .	205
Fig. 6.55. SSL for Sand A Showing Cumulative Effects of Incorrect Testing Procedures . . . . .	206
Fig. 6.56. SSL for Sand B Obtained Using Incorrect Testing Procedures . . . . .	207
Fig. 6.57. SSL for Sand C Obtained Using Incorrect Testing Procedures . . . . .	208
Fig. 7.1. Pore Water Pressure Buildup in Strain-Controlled CyT-CIU Tests on Isotropically Consolidated Samples of Ottawa Sand Fl25 . . . . .	246
Fig. 7.2. Pore Water Pressure Buildup in Strain-Controlled CyT-CIU Tests on Anisotropically Consolidated ( $K_c=2.0$ ) Samples of Ottawa Sand Fl25) . . . . .	247
Fig. 7.3. Schematic Diagram of the Triggering Relationship . . . . .	248
Fig. 7.4. Schematic Diagram for the Normalization Procedure to Generate the PWP Buildup Curves . . . . .	249
Fig. 7.5. Triggering Relationship for CyT-CIU Tests on Sand Fl25, $K_c=1.00$ . . . . .	250
Fig. 7.6. Triggering Relationship for CyT-CAU Tests on Sand Fl25, $K_c=1.2$ . . . . .	251
Fig. 7.7. Triggering Relationship for CyT-CAU Tests on Ottawa Sand Fl25, $K_c=1.5$ . . . . .	252
Fig. 7.8. Triggering Relationship for CyT-CAU Tests on Ottawa Sand Fl25, $K_c=2.0$ . . . . .	253

Fig. 7.9. Triggering Relationship for CyT-CAU Tests on Ottawa Sand Fl25, $K_C=2.5$ . . . . .	254
Fig. 7.10. Triggering Relationships for CyT-CAU Tests on Ottawa Sand Fl25, $K_C=2.9$ . . . . .	255
Fig. 7.11. PWP Buildup After 5 Cycles of Constant Shear Strain in Ottawa Sand Fl25 . . . . .	256
Fig. 7.12. Modified Triggering Relationships of Ottawa Sand Fl25, $K_C=1.0$ . . . . .	257
Fig. 7.13. Modified Triggering Relationships of Ottawa Sand Fl25, $K_C=1.2$ . . . . .	258
Fig. 7.14. Modified Triggering Relationships of Ottawa Sand Fl25, $K_C=1.5$ . . . . .	259
Fig. 7.15. Modified Triggering Relationships of Ottawa Sand Fl25, $K_C=2.0$ . . . . .	260
Fig. 7.16. Modified Triggering Relationships of Ottawa Sand Fl25, $K_C=2.5$ . . . . .	261
Fig. 7.17. Modified Triggering Relationships of Ottawa Sand Fl25, $K_C=2.9$ . . . . .	262
Fig. 7.18. Curves of the Function T in Ottawa Sand Fl25 for $K_C=1.0-2.0$ ( $n_t$ in cycles, $\bar{\sigma}_{3C}$ in kg/cm <sup>2</sup> ) . .	263
Fig. 7.19. Curves of the Function T in Ottawa Sand Fl25 for $K_C=2.5-2.9$ ( $n_t$ in cycles, $\bar{\sigma}_{3C}$ in kg/cm <sup>2</sup> ) . .	264
Fig. 7.20. Triggering Relationship Range of Ottawa Sand Fl25 for all Tests with $K_C=1.5-2.9$ , $\bar{\sigma}_{3C}=1$ kg/cm <sup>2</sup> . .	265
Fig. 7.21. Triggering Relationship for CyT-CAU Tests on Sand A, $K_C=1.22$ , $\bar{\sigma}_{3C}=3.72$ kg/cm <sup>2</sup> . . . . .	266

Fig. 7.22. Triggering Relationship for CyT-CAU Tests on Sand A, $K_c=1.5$ , $\bar{\sigma}_{3c}=3.72$ kg/cm <sup>2</sup> . . . . .	267
Fig. 7.23. Triggering Relationship for CyT-CAU Tests on Sand A, $K_c=2.0$ . . . . .	268
Fig. 7.24. Triggering Relationship for CyT-CAU Tests on Sand A, $K_c=2.25$ , $\bar{\sigma}_{3c}=3.72$ kg/cm <sup>2</sup> . . . . .	269
Fig. 7.25. PWP Buildup After 5 Cycles of Constant Shear Strain in Sands A, B, and C . . . . .	270
Fig. 7.26. Modified Triggering Relationship for Sand A, $K_c=2.0$ . . . . .	271
Fig. 7.27. Triggering Relationships for Sand A, $\bar{\sigma}_{3c}=3.72$ kg/cm <sup>2</sup> . . . . .	272
Fig. 7.28. Triggering Relationships for Moist Tamped Specimens of Sand SF7, $\bar{\sigma}_{3c}=1$ kg/cm <sup>2</sup> . . . . .	273
Fig. 7.29. Comparison of Triggering Relationships Between Moist Tamped Specimens and Sedimented Samples of Sand SF7, $K_c=1.7$ , $\bar{\sigma}_{3c}=1$ kg/cm <sup>2</sup> . . . . .	274
Fig. 7.30. Comparison of Triggering Relationships Between Moist Tamped Specimens and Sedimented Samples of Sand SF7, $K_c=1.87$ , $\bar{\sigma}_{3c}=1$ kg/cm <sup>2</sup> . . . . .	275
Fig. 7.31. Comparison of Triggering Relationships Between Moist Tamped Specimens and Sedimented Samples of Sand SF7, $K_c=2.0$ , $\bar{\sigma}_{3c}=1$ kg/cm <sup>2</sup> . . . . .	276
Fig. 7.32. Triggering Relationships for Moist Tamped Specimens of Sand SF7, $K_c=2.2$ , $\bar{\sigma}_{3c}=1$ kg/cm <sup>2</sup> . . . . .	277
Fig. 7.33. PWP Buildup after 5 Cycles of Constant Shear Strain with Different $K_c$ in Sand SF7 . . . . .	278

Fig. 7.34. Modified Triggering Relationships for Sand SF7, $K_C=1.7$ . . . . .	279
Fig. 7.35. Modified Triggering Relationships for Sand SF7, $K_C=1.87$ . . . . .	280
Fig. 7.36. Modified Triggering Relationships for Sand SF7, $K_C=2.0$ . . . . .	281
Fig. 7.37. Curves of the Function T in Sand SF7 ( $n_t$ in cycles, $\bar{\sigma}_{3C}$ in kg/cm <sup>2</sup> ) . . . . .	282
Fig. 7.38. PWP Buildup Curves of Ottawa Sand F125, for $K_C=1.0$ . . . . .	283
Fig. 7.39. PWP Buildup Curves of Ottawa Sand F125, for $K_C=1.2$ . . . . .	284
Fig. 7.40. PWP Buildup Curves of Ottawa Sand F125, for $K_C=1.5$ . . . . .	285
Fig. 7.41(a). PWP Buildup Curves of Ottawa Sand F125, for $K_C=2.0$ (Legend of Points in Fig. 7.41(b)) . . . .	286
Fig. 7.41(b). Legend of Data Points Presented in Fig. 7.41(a) . . . . .	287
Fig. 7.42. PWP Buildup Curves of Ottawa Sand F125, for $K_C=2.5$ . . . . .	288
Fig. 7.43. PWP Buildup Curves of Ottawa Sand F125, for $K_C=2.9$ . . . . .	289
Fig. 7.44. PWP Buildup Curves of Ottawa Sand F125, for $K_C=1.0-2.9$ . . . . .	290
Fig. 7.45. PWP Buildup Curves of Sand A, for $K_C=1.22$ .	291

Fig. 7.46.	PWP Buildup Curves of Sand A, for $K_c=1.5$	292
Fig. 7.47.	PWP Buildup Curves of Sand A, for $K_c=2.0$	293
Fig. 7.48.	PWP Buildup Curves of Sand A, for $K_c=2.25$	294
Fig. 7.49.	PWP Buildup Curves of Sand A, for $K_c=1.22-2.25$	295
Fig. 7.50.	PWP Buildup Curves of Sand SF7, for $K_c=1.4$	296
Fig. 7.51.	PWP Buildup Curves of Sand SF7, for $K_c \approx 1.7$ (Solid Points Represent Sedimented Sample)	297
Fig. 7.52.	PWP Buildup Curves of Sand SF7, for $K_c \approx 1.87$ (Solid Points Represent Sedimented Sample)	298
Fig. 7.53.	PWP Buildup Curves of Sand SF7, for $K_c=2.0$ (Solid Points Represent Sedimented Sample)	299
Fig. 7.54.	PWP Buildup Curves of Ottawa Sand SF7, for $K_c=2.2$	300
Fig. 7.55.	PWP Buildup Curves of Ottawa Sand SF7, for $K_c=1.4-2.2$	301
Fig. 7.56.	Band of Triggering Relationships for all Tests with $K_c=2.0$ , $\bar{\sigma}_{3c}=1 \text{ kg/cm}^2$ in Three Sands	302
Fig. 7.57.	PWP Buildup Bands for All Tested Sands, for $K_c=1.0-3.0$	303
Fig. 7.58.	Schematic Diagram of the 3 Criteria Comprising the PWP Triggering Model	304
Fig. 7.59.	PWP Buildup Curve Approximation for Sand A, for $K_c=2.0$	305

Fig. 7.60. PWP Buildup Curve Approximation for Sand A, (all $K_c$ ) . . . . .	306
Fig. 7.61. Evaluation of Function $h$ for the Modelling of the Triggering Relationships . . . . .	307
Fig. 7.62. Approximation of Triggering Relationships for Sand A ( $\bar{\sigma}_{3c}=3.72$ kg/cm <sup>2</sup> ) . . . . .	308
Fig. 7.63. Comparison Between Predicted and Actual Results of a CyT-CAU Test on Sand A Using the PWP Triggering Model . . . . .	309
Fig. 7.64. Evaluation of the Function $I$ for the Triggering Relationship of Sand SF7 . . . . .	310
Fig. 7.65. Use of the PWP Buildup Curves to Account for the Incorporation of Variable Shear Strains into the PWP Triggering Model . . . . .	311
Fig. 7.66. Cumulative Axial Strain at Failure Compared to PWP at Failure for Ottawa Sand F125 . . . . .	312
Fig. 7.67. Cumulative Axial Strain at Failure Compared to PWP at Failure for Sand A . . . . .	313
Fig. 7.68. Cumulative Axial Strain at Failure Compared to PWP at Failure for Sand SF7 . . . . .	314
Fig. 8.1. Profile of Flow Slide at Vlietepolder, Holland (after Koppejan, et al., 1948) . . . . .	383
Fig. 8.2. Profile of Flow Slide in Mississippi River Bank (after Senour and Turnbull, 1948) . . . . .	384
Fig. 8.3. Profile and Plan of Slide in Helsinki Harbor (after Andersen and Bjerrum, 1968) . . . . .	385

Fig. 8.4. Cross Section of Necaxa Dam No. 2 (after Schuyler, 1907; 1909) . . . . .	386
Fig. 8.5. Cross Section of Calaveras Dam (after Hazen, 1918) . . . . .	387
Fig. 8.6. Cross Section of Saluda Dam (after Engineering News Record, 1930a) . . . . .	388
Fig. 8.7. Cross Section of Alexander Dam (after Engineering News Record, 1930b) . . . . .	389
Fig. 8.8. Cross Section of Fort Peck Dam (after Casagrande, 1965) . . . . .	390
Fig. 8.9. Artist's Concept of Flow Slide at Valdez (after Seed, 1967) . . . . .	391
Fig. 8.10. Approximate Sections Through Large Slide Area Near Lake Rinihue, Chile (after Seed, 1967) . . . .	392
Fig. 8.11. Cross Section of Slide in the Lower San Fernando Dam (after Seed et al., 1973) . . . . .	393
Fig. 8.12. Plan and Profile of the Slide in the Sheffield Dam (after Engineering News Record, 1925; Seed et al., 1969) . . . . .	394
Fig. 8.13. Profile of El Cobre Old Dam (after Dobry and Alvarez, 1967) . . . . .	395
Fig. 8.14. Profile of the No. 1, No. 2 and No. 3 Dykes of Mochikoshi Tailings Dam (after Okusa and Anma, 1980) . . . . .	396
Fig. 8.15. Shaking Table Test of Model Foundation on a Stratified Sand Deposit (after Huishan and Taiping, 1984) . . . . .	397

Fig. 8.16. Centrifuge Model of a Submerged Embankment Subjected to Earthquakes (after Dean and Schofield, 1983) . . . . .	398
Fig. 8.17. Centrifuge Model of a Compacted Silt Embankment Resting on a Sand Foundation Showing Model Geometry . Before Earthquake, and Crack Pattern after Earthquake (after Schofield and Venter, 1984)	
Fig. 8.18. Contours of Excess PWP of Model Shown in Fig. 8.18, 300 ms After First Earthquake and After Fifth Earthquake (after Schofield and Venter, 1984) . .	400
Fig. 8.19. Steady-State Strength Envelopes for Leighton Buzzard Sand Using Drained Simple Shear and Undrained Triaxial Compression . . . . .	401
Fig. 8.20. Determination of SSL for Leighton Buzzard Sand Used in the Centrifuge Model Shown in Fig. 8.23 (data from Atkinson and Bransby, 1978; Succarieh et al., 1987) . . . . .	402
Fig. 8.21. Comparison Between SSL of Leighton Buzzard Sand and Ottawa Sand F125 . . . . .	403
Fig. 8.22. Position of SSL of Leighton Buzzard Sand Compared to Other Sands . . . . .	404
Fig. 8.23. Centrifuge Test of a Well Compacted Dyke Resting on Foundation with Layer of Loose Sand (after Habibian et al., 1985) . . . . .	405
Fig. 8.24. Schematic Representation of a Submerged Sand Embankment Overlaid by a Soft Clay Layer (after Arulanandan et al., 1988) . . . . .	406
Fig. 8.25. Flowchart of Proposed Conceptual Framework for Analyzing Liquefaction Flow Failures . . . . .	407



Fig. 9.1. Cross Section of the Lower and Upper San Fernando Dams . . . . .	443
Fig. 9.2. Maximum Accelerations Recorded on Rock in San Fernando Earthquake, 1971 (after Seed et al., 1973) . . . . .	444
Fig. 9.3. Acceleration Time History Derived from Seismoscope Record on East Abutment of Lower San Fernando Dam, Earthquake of 1971 (after Scott, 1973) . . . . .	445
Fig. 9.4. Location and Changes in Water Level in Piezometers Following the Earthquake - Upper San Fernando Dam (after Seed et al., 1973) . . . . .	446
Fig. 9.5. Location and Changes in Water Level in Piezometers Following the Earthquake - Lower San Fernando Dam (after Seed et al., 1973) . . . . .	447
Fig. 9.6. Contours of $\bar{\sigma}_{3c}$ Within Saturated Hydraulic Fill Sand of Lower San Fernando Dam (after Mohamad, 1985) . . . . .	448
Fig. 9.7. Plan of the Lower San Fernando Dam Showing the Different Cross Sections Studied (after Seed et al., 1973) . . . . .	449
Fig. 9.8. Section E-E of the Lower San Fernando Dam (after Seed et al., 1973) . . . . .	450
Fig. 9.9. Section F-F of the Lower San Fernando Dam (after Seed et al., 1973) . . . . .	451
Fig. 9.10. Cross Section of the Lower San Fernando Dam at the Time of the 1985 Exploration (after GEI, 1988) . . . . .	452
Fig. 9.11. Location of Borings in the 1985 Exploration Study (after GEI, 1988) . . . . .	453

Fig. 9.12. Determination of Contractiveness of the In Situ Materials of the Lower San Fernando Dam . .	454
Fig. 9.13. Determination of In Situ $S_{us}$ Using the GEI Procedure (after GEI, 1988) . . . . .	455
Fig. 9.14. Estimates of the In Situ $S_{us}$ Using the Average Void Ratio and the In Situ SSL . . . . .	456
Fig. 9.15. Critical Failure Surface Through Upstream Slope of the Lower San Fernando Dam (after GEI, 1988) . . . . .	457
Fig. 9.16. Critical Failure Surface Through Downstream Slope of the Lower San Fernando Dam (after GEI, 1988) . . . . .	458
Fig. 9.17. Dynamic Analyses of the Lower San Fernando Dam Showing Magnitude of Cyclic Shear Strains . . . .	459
Fig. 9.18. Peak Cyclic Shear Strain Induced by the Earthquake With $a_p = 0.6 g$ , Predicted Using QUAD-4 .	460
Fig. 9.19. Triggering Band for San Fernando Sand SF7, $K_c = 2$ , $\bar{\sigma}_{3c} = 1 \text{ kg/cm}^2$ (data from Fig. 7.31) . . .	461
Fig. 9.20. Peak Cyclic Shear Strains Induced by the Earthquake with $a_p = 0.1g$ , Predicted Using QUAD-4 .	462
Fig. 9.21. Peak Cyclic Shear Strains Induced by the Earthquake with Different Values of $a_p$ , Predicted Using QUAD-4 . . . . .	463
Fig. 9.22. Peak Cyclic Shear Strains Induced by the Earthquake on the Critical Layer of the Upstream Slope Predicted Using QUAD-4 ( $\gamma_p$ from Fig. 9.21) .	464

## NOTATION

a	acceleration
$a_p$	peak horizontal acceleration at crest of dam
B	pore pressure parameter for isotropic undrained loading
B	bulk modulus in nonlinear static analyses
c	cohesion
$C_u = d_{60}/d_{10}$	uniformity coefficient
$C_{rm}$	membrane penetration correction factor for excess pore pressure
$d_{10}$	diameter at which 10% by weight of the soil is finer
$d_{50}$	median grain size
$d_{60}$	diameter at which 60% by weight of the soil is finer
$D_r$	relative density
$E_i$	initial value of tangent Young's modulus in nonlinear static analyses
$E_t$	tangent Young's modulus in nonlinear static analyses
e	void ratio
$e_{max}$	maximum void ratio
$e_{min}$	minimum void ratio
G	secant shear modulus during dynamic loading

$G_{\max}$	dynamic shear modulus at small strains
$g$	acceleration due to gravity
$I_b$	brittleness index
$K$	modulus number of nonlinear static analyses
$k_b$	bulk modulus number in nonlinear static analyses
$K_c = \bar{\sigma}_{1c} / \bar{\sigma}_{3c}$	ratio of major to minor principal effective stresses at end of consolidation
$(K_1)_{\max}$	dynamic shear modulus parameter
$L_p$	Casagrande's 'Liquefaction Potential'
$m$	bulk modulus exponent in nonlinear static analyses
$m$	mass
$n$	modulus exponent in nonlinear static analyses
$n$	number of cycles of cyclic strain or stress
$n_t$	number of cycles to trigger liquefaction flow failure
PWP	pore water pressure
$p_a$	atmospheric pressure
$p = (\sigma_1 + \sigma_3) / 2$	mean of major and minor total stresses
$\bar{p} = (\bar{\sigma}_1 + \bar{\sigma}_3) / 2$	mean of major and minor effective stresses
$\bar{p}_c$	value of $\bar{p}$ at end of consolidation
$\bar{p}_{ut}$	value of $\bar{p}$ at point of triggering of liquefaction flow failure
$\bar{p}_{us}$	value of $\bar{p}$ during undrained steady-state flow deformation

$q=(\sigma_1-\sigma_3)/2$	minimum shear stress
$q=(\bar{\sigma}_1-\bar{\sigma}_3)/2$	maximum shear stress
$q_c=q_s=r_s$	value of $q$ at end of consolidation
$q_p=r_p$	peak value of $q$ during cyclic triaxial test
$q_{ut}$	value of $q$ at point of triggering of liquefaction flow failure
$q_{us}$	value of $q$ during undrained steady-state flow deformation
$R_f$	failure ratio in nonlinear static analyses
$r_u=u/\bar{\sigma}_{3c}$	residual pore pressure ratio
$r_{ut}$	value of $r_u$ at point of triggering of liquefaction flow failure
$S_u$	undrained shear strength
$S_{us}$	steady state shear strength on the failure plane
$T_n$	peak torque in $n$ th cycle during strain-controlled CyT-CAU test
$T_1$	peak torque in first cycle during strain-controlled CyT-CAU test
$u$	excess pore pressure
$u_t$	excess pore pressure at point of triggering of liquefaction flow failure
$\alpha$	angle defining obliquity of strength envelope
$\alpha_d$	angle defining obliquity of drained strength envelope

$\bar{\sigma}_{1us}$	value of $\bar{\sigma}_1$ during undrained steady-state flow deformation
$\sigma_3$	total minor principal stress
$\bar{\sigma}_3$	effective minor principal stress
$\bar{\sigma}_{3c}$	value of $\bar{\sigma}_3$ in test specimen at end of consolidation
$\bar{\sigma}_{3us}$	value of $\bar{\sigma}_3$ during undrained steady-state flow deformation
$\bar{\sigma}_{3fus}$	value of $\bar{\sigma}_3$ during undrained steady-state flow deformation on the failure plane
$\sigma_{cy}$	cyclic deviator stress in cyclic triaxial test
$\sigma_d = (\sigma_1 - \sigma_3)$	deviator stress
$(\sigma_1 - \sigma_3)_f$	deviator stress at failure in nonlinear static analyses
$(\sigma_1 - \sigma_3)_{ult}$	ultimate (asymptotic) value of deviator stress in nonlinear static analyses
$\bar{\sigma}_m$	mean effective stress
$\tau$	shear stress
$\tau_d$	driving shear stresses
$\tau_{cy}$	cyclic shear stress
$\tau_p = q_p$	peak shear stress in cyclic triaxial test
$\tau_s = q_s$	initial static shear stress
$\tau_{xy}$	shear stress on horizontal plane
$\phi$	angle of internal friction

$\bar{\phi}$  angle of internal friction in terms of  
effective stresses

$\bar{\phi}_{us}$  value of  $\bar{\phi}$  during steady-state flow  
deformation

$\bar{a}_{up}$	angle defining obliquity of peak undrained strength envelope in terms of effective stresses using <u>CTU</u> test
$\bar{a}_{us}$	angle defining obliquity of undrained residual or steady state-strength envelope in terms of effective stresses
$\bar{a}_{ut}$	angle defining obliquity of undrained triggering of flow strength envelope in terms of effective stresses
$\gamma_{cy}$	cyclic shear strain
$\gamma_{cp}$	peripheral cyclic shear strain in CyT- <u>CAU</u> test
$\gamma_t$	threshold cyclic shear strain
$\gamma_{xy}$	shear strain on horizontal plane
$\epsilon_{ut}$	axial strain
$\epsilon_{dil}$	axial strain at which dilation tendency begins in <u>CTU</u> test
$\epsilon_t$	axial strain at point of triggering of liquefaction flow failure
$(\rho g)_b$	buoyant unit weight
$(\rho g)_t$	total unit weight
$\sigma_1$	total major principal stress
$\bar{\sigma}_1$	effective major principal stress
$\bar{\sigma}_{1c}$	value of $\bar{\sigma}_1$ in test specimen at end of consolidation



## CHAPTER 1

### INTRODUCTION

#### 1.1 General

One of nature's most incredible displays of force is the amount of destruction caused by earthquakes. These have repeatedly caused severe devastation to both man made structures and natural terrains. One of the major causes of this destruction is what is known as liquefaction.

Throughout the years the term liquefaction has been loosely used to describe the condition achieved by a saturated cohesionless (usually sandy) soil which is associated with high pore water pressures (pwp) and a decrease in the capacity of the soil to carry load. Although the word liquefaction was originally coined for failures triggered by static loads, it was later extended to include triggerin, by seismic ground motions and other dynamic phenomena. Liquefaction flow failure occurs when a mass of granular soil loses its ability to carry its current load due to a reduction in the shear strength of the soils involved; the material loses its strength and flows like a heavy liquid producing very large deformations.

Many cases of seismic liquefaction flow failure have been reported for centuries throughout the world. They are typically associated, either with naturally deposited loose

saturated sands or with artificial hydraulic fills deposited without compaction, as in mine tailings dams (Dobry and Alvarez, 1967; Marcuson et al., 1979) and hydraulic fill dams (Seed et al., 1973). Natural loose sandy formations most susceptible to liquefaction flow failure are recently deposited lacustrine deposits, river banks and alluvial plains (Yamada, 1966; Seed, 1968; Yoshimi, 1970; Hamada, 1986).

One of the most widely known liquefaction flow failure case histories, is the slide of the upstream slope of the Lower San Fernando Dam due to the 1971 earthquake near Los Angeles, California. This slide carried a large portion of the dam, leaving only 4 to 5 feet of freeboard and a severely cracked downstream slope. A total catastrophic failure was narrowly avoided, but the possibility of breaching of the dam and flooding of the densely populated downstream area, with 80,000 residents, caused a growing concern among government agencies, researchers and the general public. The dam had been analyzed 4 years earlier using the existing design criteria and had been found to be safe against seismic failure (Seed, 1975). The 1971 incident led to a reappraisal of the existing methodology because of its inability to predict such a failure. Since then, an increase in research has greatly advanced our state

of knowledge on the subject; however, some key questions remain unanswered. The work presented herein attempts to answer some of these questions and improve our understanding of others on the basis of laboratory tests specifically designed for that purpose. These tests are performed on several sands to verify their generality. Using the test results, as well as a review of case histories and model laboratory experiments, a pwp and triggering model is proposed, and a conceptual framework is developed for the analysis of earth dams susceptible to seismic liquefaction from failure. The Lower San Fernando Dam is reanalyzed using this proposed methodology in order to test its validity. We should not forget that as geotechnical engineers our goal should always be to understand and predict what happens in the field by using all possible means available to us.

## 1.2 Problem Statement, Scope and Objectives

When an earth structure composed of liquefiable sand is shaken by an earthquake, the seismically induced shear stresses and strains cause the soil elements to undergo changes from their static state of stress. These stress changes typically happen so fast (a few seconds to a few minutes) that it seems reasonable to assume, in first

approximation, that they occur in undrained condition for a wide variety of soil types and field situations. The tendency of the soil skeleton to densify causes the undrained loaded sand to build up an excess pore water pressure (pwp) and a corresponding decrease in normal effective stress. As shown by Castro (1969) and discussed extensively in this work, this pwp may trigger a significant decrease in shear strength if the sand is so loose as to be contractive under shear. If enough soil elements experience this shear strength decrease, a liquefaction flow slide with the failure surface going through those elements can occur.

The magnitudes of seismically induced stresses and strains in an earth structure depend mainly on the characteristics of the earthquake, the shear stiffness of the soils present, and the geometric conditions of the problem. In this work, extensive cyclic laboratory tests of a special type have been conducted to better understand the basic behavior of contractive sands, such as may have been present in the cases involving liquefaction flow failures. These are cyclic torsional triaxial on anisotropically consolidated samples, to be called here CyT-CAU tests. This type of test was originally developed by Mohamad (1985); however, the emphasis of his work was the steady-state strength, whereas the focus of this work will also include

the conditions necessary to initiate or trigger liquefaction flow failure. This type of test was systematically used herein to evaluate the influence of various parameters on the buildup of pore water pressure (pwp), the triggering of flow failure, and the steady-state of deformation. The CyT-CAU test borrows ideas from the cyclic strain approach (Dobry, 1982) and the steady-state concept (Castro, 1969; Poulos, 1981), and uses recent advances in laboratory test equipment to simulate more realistically what happens in the field. Although extensive experimental work including cyclic undrained tests on sands has been carried out in the past, for the most part it has focussed on denser, dilative sands that are not susceptible to flow failure (Seed and Lee, 1966; Lee and Seed, 1967). Also, most of the cyclic tests have been stress-controlled rather than strain-controlled as used herein. Of the more limited body of experimental work dealing specifically with liquefaction flow failure, not much has been done with the conditions necessary to trigger it seismically. On the other hand, the issues of overall stability after all liquefiable elements have reached the steady-state of deformation have been studied in more detail and are better understood (Castro, 1969, 1982; Kramer and Seed, 1988). New results will be shown herein that will identify and explain better the role

of different factors involved in the triggering of this destructive phenomenon.

The results produced herein are used to develop a pwp and triggering model and a proposed conceptual framework for analysis and evaluation of earth structures that are susceptible to liquefaction flow failure. This procedure is based on the characteristics of the soils susceptible to liquefaction flow failure, as obtained from the laboratory test results presented herein, and from the examination of available case studies and model experiments. The analyses of case histories are very important in understanding the behavior of large masses of soils susceptible to liquefaction flow failure.

It is understood that not all natural sand deposits or earth structures in the field are susceptible to liquefaction flow failure when subjected to seismic loading. However, during strong ground motions, earth structures that do not exhibit flow failure have often suffered large permanent deformations. Even though these permanent deformations of an earth structure that does not experience liquefaction flow failure is a very important issue, this subject lies beyond the scope of this work. However, it should not be forgotten that the amount of deformations caused by flow failures are much larger.

### 1.3 Report Organization

A brief description of and the underlying motivation for this work has been explained in the previous two sections. In order to better understand the rest of this report the current state of knowledge relevant to the subject of liquefaction flow failures is discussed in Chapter 2. Since a great portion of this work is based on laboratory tests, the scope and objectives of the experimental investigation are discussed in Chapter 3. Chapter 4 describes the laboratory testing equipment, the testing procedures and the reasons for choosing the type of sands used for this investigation. A description of the experimental program is presented in Chapter 5. The main experimental results are shown and discussed in Chapters 6 and 7 for the shear strength behavior and pore water pressure buildup, respectively. A conceptual framework is developed and a method is proposed in Chapter 8 to evaluate seismic liquefaction flow failures, by using the laboratory results and the insight developed by case histories. Chapter 9 applies the proposed methodology to the Lower San Fernando Dam. Finally, Chapter 10 presents the conclusions reached in this work and suggests some topics for future work.

## CHAPTER 2

### BACKGROUND

#### 2.1 Fundamentals of Liquefaction

Some of the controversies that have surrounded the topic of seismically induced liquefaction stem from a confusion of terminology, as two different phenomena have been called liquefaction. This definition problem has been identified and the two phenomena have been named cyclic mobility (or cyclic liquefaction) and liquefaction flow failure (or actual liquefaction), see Casagrande (1975), Castro (1975), Seed (1976), and NRC (1985). The original confusion arose because the appearance of both phenomena require the prior development of significant values of pore water pressure (pwp) due to the seismic stresses and strains, and also because both phenomena involve large deformations of the soil.

Cyclic mobility was first studied by Seed and his coworkers (Seed and Lee, 1966; Lee and Seed, 1967; Lee et al., 1975; Seed et al., 1969, 1975; and Seed, 1983). They introduced the use of undrained stress-controlled cyclic triaxial tests for evaluating the seismic liquefaction resistance of saturated sands. The initial cyclic triaxial tests were on isotropically consolidated specimens (CCIU), but later they extended their cyclic triaxial investigation



to anisotropically consolidated specimens (CCAU).

Liquefaction flow failure was originally studied by Casagrande and continued by Castro and Poulos (Casagrande, 1936; Castro, 1969, 1975; Poulos, 1981; Castro et al., 1982). These authors investigated the liquefaction of isotropically and anisotropically consolidated sands in both monotonic and cyclic triaxial tests. In addition, they developed the steady-state concept that explains the undrained behavior of sands in cyclic or monotonic loading.

Although both Seed and Castro have used cyclic triaxial tests to study liquefaction in their research, a major difference lies in their respective definitions of failure and the effect of anisotropic consolidation on liquefaction resistance. Seed and his coworkers define failure as the development of a specified value of cyclic strain under conditions of high pwp during cyclic stress-controlled loading. The progressive softening of the sand is accompanied by high values of pwp, but it does not necessarily lead to a loss in shear strength. They concluded that static shear due to anisotropic consolidation always increases the liquefaction resistance or cyclic strength, which they define as the amplitude of the cyclic deviator stress needed to cause a specific accumulated axial strain in a given number of cycles.

On the other hand, Castro and his collaborators define failure as complete liquefaction, characterized by the sudden loss of strength of the specimen causing it to flow under steady-state conditions until the shear stresses acting on the mass are as low as the reduced shear resistance (Castro et al., 1982). Steady state conditions refer to the continuous state of deformation of a soil mass at constant volume, constant normal effective stress, constant shear stress and constant velocity (Poulos, 1981). They later showed that the steady-state concept first developed for monotonic loading, applies also to cyclic loading. This phenomenon is the one that will be referred when talking of liquefaction flow failure.

Any cohesionless soil such as sand has a tendency to change volume when monotonically sheared in drained condition; loose soils decrease in volume (contractive soil) whereas dense soils increase in volume (dilative soil). Both types of sand will tend to a critical density value that has been called the critical void ratio (Casagrande, 1936) and has been found to be a function of the minor effective confining stress  $\bar{\sigma}_3$ . The critical void ratio is the density marking the boundary between contractive and dilative soils; a soil element that is denser than the critical void ratio will be dilative and one that is looser

will be contractive. The locus of all critical void ratios is called the steady-state line, (Castro, 1975; Poulos, 1981). When a soil reaches the steady-state line (SSL) it keeps deforming at constant shear stress and void ratio, and this is called the steady-state condition, as shown in Fig. 2.1 (Poulos, 1981).

If the loading situation and/or soil conditions are such as to restrict drainage, then the contractive soil will create positive pwp ( $u > 0$ ) and a decrease in strength, whereas the dilative soil will create negative pwp ( $u < 0$ ) and an increase in strength relative to the drained strength. On the other hand, undrained cyclic test results show that both loose and dense sands accumulate positive pwp once the static and/or cyclic shear stress acting on the soil is released.

The behavior of undrained anisotropically consolidated sands under cyclic loading is a combination of the above mentioned two apparently conflicting facts. For relatively small cyclic and accumulated strains, both contractive and dilative sands develop net positive pwp. On the other hand, at large strains contractive sands can have large positive pwp, while in dilative sands the opposite is true, the pwp are decreased and can even become negative. Since undrained flow failures consist essentially of large unidirectional

shear deformations, they are controlled by the undrained monotonic behavior at large strains. The steady-state concept provides a good framework for understanding and predicting this monotonic behavior of sands at large strains.

Two distinct types of monotonically loaded undrained cohesionless soil stress-strain behavior can be identified depending on whether the soil is contractive or dilative; these have been called Type I and Type II respectively (NRC, 1985).

Type I Stress-Strain Behavior. - A typical stress-strain relationship for an anisotropically consolidated undrained contractive sand can be seen in Fig. 2.2. A soil sample is consolidated anisotropically to point (c) and then loaded monotonically in compression. It is characterized by having a peak shear strength (point p) followed by a decrease to a constant steady-state shear strength (point s) which is less than the consolidation shear stress. During loading, the soil experiences a constant increase of pwp ( $u$ ) and corresponding decrease in effective stress  $\bar{\sigma}_3 = \bar{\sigma}_{3c} - u$  until the steady-state is reached; however, the pore pressure ratio  $r_u = u/\bar{\sigma}_{3c}$  is never equal to 1.0.

Type II Stress-Strain Behavior. - A dilative soil sample

that is consolidated to the same loading conditions (point c) as in the above case will exhibit a totally different behavior. As the sample is loaded undrained, the resistance will initially rise sharply and then more gradually until a plateau is reached at which the sample is deforming under steady-state conditions (point s). While the pwp may initially increase for small values of axial strain, it will later decrease and become negative at larger values of strain. The fact that pwp becomes negative is the reason for the great increase in shear strength, causing the undrained steady-state shear strength to be much larger than the consolidation shear stress and the drained strength.

## 2.2 The Steady State Concept

The steady-state concept has its inception in the works of Casagrande in the 1930's. Research has shown that for a given soil, as the void ratio decreases the effective normal stresses at steady-state increases. This can be seen in a three dimensional plot of void ratio  $e$ , effective normal stress  $\bar{p}$  and shear stress  $q$  (Fig. 2.3a). The steady-state line (SSL) is the graphical representation of the locus of all points deforming in steady-state condition. For convenience we usually display the three dimensional representation of the SSL into a pair of two dimensional

plots; that of  $e$  versus steady-state normal stress  $\bar{p}_{us}$  and  $e$  versus steady-state shear stress  $q_{us}$ . Sometimes the strength envelope with inclination  $\bar{\alpha}_{us} = \arctan q_{us}/\bar{p}_{us}$  is also shown along the two SSL (see Fig. 2.3a). The two SSL of  $\bar{p}_{us}$  and  $q_{us}$  versus  $e$  are uniquely related through the value of  $\bar{\alpha}_{us}$ , which in turn is a measure of the friction angle at steady-state,  $\sin \bar{\phi}_{us} = \tan \bar{\alpha}_{us}$ . Any normal stress, shear stress and density parameters can be used for these SSL; however, very often  $\bar{\sigma}_{3us}$  and  $\bar{q}_{us}$  are utilized instead of  $\bar{p}_{us}$  and  $q_{us}$  (see Fig. 2.3b). In this case both SSL are parallel and uniquely related by

$$\frac{q_{us}}{\bar{\sigma}_{3us}} = \frac{\tan \bar{\alpha}_{us}}{(1 - \tan \bar{\alpha}_{us})} \quad (2.1)$$

Sometimes the values at steady-state corresponding to the failure plane are used; then the steady-state shear strength on the failure plane is  $S_{us}$  and the minor principal stress on the failure plane becomes  $\sigma_{fus}$ , so that  $S_{us} = \bar{\sigma}_{fus} \tan \bar{\phi}_{us}$ . They are related to  $\bar{\sigma}_{3us}$  and  $q_{us}$  through the undrained steady-state friction angle  $\bar{\phi}_{us}$  as follows:

$$S_{us} = q_{us} \cos \bar{\phi}_{us} \quad (2.2)$$

$$\bar{\sigma}_{fus} = \left( \frac{\cos^2 \bar{\phi}_{us}}{1 - \sin \bar{\phi}_{us}} \right) \bar{\sigma}_{3us} \quad (2.3)$$

Based on the discussion in the previous section we can state that for a soil to be deforming in steady-state conditions the  $e$  vs  $\bar{\sigma}_{3US}$  point must be on the SSL, the plot of  $e$  vs  $q_{US}$  must be on the SSL, and the soil is deforming continuously with no tendency for changes of stresses, volume and velocity. Only if all the above criteria are met, can we say that the steady-state of deformation has been reached (Castro et al., 1982). A soil element that is to the right of the  $e$  vs  $\bar{\sigma}_{3US}$  SSL is defined as contractive and a soil element to the left is dilative. If the SSL is plotted in semilog paper it will represent a straight line for many sands.

Another issue of great importance in liquefaction flow failure is that concerning driving shear stresses. They are defined as the shear stresses resulting from the geometry and loading conditions on the soil, in the same manner as the shear stresses defined in a slope stability analysis. They are not the shear stresses resulting from geologic deposition in level homogenous ground where the soil exists in a condition of  $K_0 \neq 1$ , because these stresses are not needed for equilibrium. Only those shear stresses needed for equilibrium and stability are considered driving shear stresses ( $\tau_d$ ).

If the soil loading is sufficiently fast, or the boundary conditions are appropriate, the loading is essentially undrained, and therefore the strength governing the soil stability is the undrained shear strength at large strains,  $S_{us}$ . When a condition arises such that  $\tau_d > S_{us}$ , then it is possible for large changes in geometry and loading to take place in order to reduce the driving shear stresses to  $q_{us}$ .

It has been shown (Castro, 1969; 1975) that in order for liquefaction flow failure to occur in a monotonic undrained triaxial test, the  $e$  vs  $\bar{\sigma}_{3us}$  point has to be in the contractive side of the SSL at the beginning of undrained shear. Furthermore; it has also been shown (Castro et al., 1982; Mohamad, 1985) that for liquefaction flow failure to occur during cyclic loading, both the  $e$  vs  $\bar{\sigma}_{3us}$  and  $e$  vs  $q_{us}$  points have to be to the right of the SSL at the beginning of undrained shear. In other words, the soil element must both be contractive and subjected to driving shear stresses greater than  $S_{us}$ . If the soil is dilative or contractive with  $\tau_d < S_{us}$ , then cyclic loading will produce cyclic mobility instead of liquefaction flow failure (see Fig. 2.4).

The steady-state line is a unique property of a granular soil and is independent of stress history and



loading path. Therefore various types of tests, monotonic or cyclic, can be used to define the SSL (Castro, 1982; Mohamad, 1985).

The critical state concept that has been successfully applied to the behavior of clays (Schofield and Wroth, 1968), has also been applied to sands with more limited success. In general in soils, the critical state line is not identical to the SSL. In dilative sands tested undrained, they are also different due to localization problems. The critical state line is defined by Atkinson and Bransby (1978) by using drained simple shear tests with dilation. More information on the relationship between critical state and steady state will be given in Section 6.2.4.

### 2.3 Liquefaction Mechanisms

In 1985 a national workshop on liquefaction was held with the participation of the leading researchers on the subject (NRC, 1985). Three types of possible flow failure mechanisms were identified which are relevant to slopes and embankments. These are illustrated in Figs. 2.5 through 2.8.

Mechanism A (Fig. 2.5) corresponds to the saturated soil having constant volume behavior locally and globally

(completely undrained), at all times before and during the flow failure. Flow failure can occur only if the soil exhibits the Type I stress-strain behavior already discussed and shown in Fig. 2.1, in which a substantial reduction of shear strength occurs until the steady-state strength is reached.

Mechanism B (Figs. 2.6 and 2.7) assumes that the total mass of sand remains in constant volume (globally undrained), but with local density redistributions occurring, with some zones in the sand loosening while others densify. As a result, a zone within the sand which had a type II dilative behavior in Fig. 2.2 (stress path A in Fig. 2.7) is loosened enough so that it becomes contractive (stress path B in Fig. 2.7), loses its strength and flows. This process of local density redistribution may cause enough sand to switch from dilative to a contractive behavior to induce a full-fledged flow failure of the slope or embankment.

Finally, in Mechanism C (Fig. 2.8), the high pore water pressures developed within the sand will tend to spread into the surrounding soils and reduce their shear strength. This upward flow may also induce cracking in overlying cohesive soils, allowing the sand to be carried upwards into the cracks. One manifestation of this cracking (upward flow of

water and soil) is the appearance of sand boils at the ground surface during and after many earthquakes. One additional consequence of this loss of sand by upward flow could be the loosening of part of the sand, which again, similarly to Mechanism B, may locally switch from dilative to contractive, drop its shear strength and help trigger a flow failure.

Therefore, while Mechanism A is totally undrained, Mechanisms B and C include partial drainage, pwp and void redistribution and even loss of solids. Some field and lab evidence about the possible occurrence of these partial drainage phenomena and the creation of conditions of Mechanisms B and C is presented in Chapter 8.

Liquefaction flow failure is then a phenomena where a sandy soil skeleton loses its capacity to carry the load to which it is subjected due to the decrease in shear strength of the sandy soils.

Much discussion has occurred with respect to the relative importance of the mechanisms among themselves, because most researchers have overlooked Mechanisms B and C due to the fact that they have not been reproduced in laboratory tests. However, case histories and model tests are begining to shed new light on these two mechanisms. The incorporation of drainage and density redistribution into an

already complicated problem could probably represent the solution to most engineering problems in liquefaction flow failure evaluation.

#### 2.4 Flow Failure Evaluation Procedures

Although various researchers have proposed different methods for liquefaction evaluation (NRC, 1985), only one procedure really exists for evaluating liquefaction flow failure. There appears to be general consensus on the general guidelines, but there is still considerable discussion concerning the way to perform each step in the methodology (NRC, 1985).

The main steps of the procedure are as follows:

- 1) Determine the geometry of the problem and the soil profile, with particular emphasis on identifying loose zones of saturated cohesionless soils that might be susceptible to flow failure.

- 2) Determine the shear strength of all the soils present. For contractive sands this implies calculating the steady-state or residual shear strength corresponding to the liquefied zone after triggering has occurred. The way to do this has become a hotly debated issue between two methods. The method proposed by Poulos (1985) is based on laboratory

tests of undisturbed specimens sampled using special techniques, and correcting the obtained steady-state shear strength to represent the in-situ value (Fig. 2.9). The method by Seed (1987) bypasses the need for laboratory tests by using a correlation between Standard Penetration Test (SPT) and residual strength (Fig. 2.10).

3) After assigning the steady-state strength or residual strength values to the liquefied sands, a static limit analysis is performed to determine if the factor of safety (FS) is less than one. If this is the case, liquefaction flow failure can occur as long as an earthquake is strong and/or long enough to trigger it.

4) A study of the amount of seismic loading is performed to see if the assumed earthquake can trigger the flow failure.

As can be observed in the above mentioned steps, the two biggest issues are how to measure the undrained steady-state shear strength (or residual strength) for the sands, and to decide if a specific earthquake ground shaking can trigger liquefaction flow failure. Let us look at these in more detail.

Since the undrained steady-state strength is sensitive to changes in void ratio such as those occurring during sampling, transportation, handling and testing; Poulos et

al. (1985) have suggested the following procedure to estimate the in-situ steady-state strength.

Step 1. - Determination of the in-situ void ratio of the undisturbed samples that will be tested in the laboratory. There are many ways to do this but the recommended procedures are fixed piston sampling, ground freezing and coring or hand carving in test pits. Whichever method is used, the goal is to minimize the volume changes and to be able to record them.

Step 2. - Perform an undrained loading test to induce flow failure in an undisturbed specimen. Since the sample has probably densified, high consolidation stresses might be needed to make it contractive. Monotonic tests in isotropically consolidated samples (CTU) are the best for this, since it avoids additional volume changes due to anisotropic consolidation.

Step 3.- Perform a series of undrained loading tests to induce flow failure of remolded specimens using the exact material of the undisturbed sample to define a SSL. The slope of the SSL for remolded specimens will be used to define the SSL for the undisturbed sample, by noting that SSL's for similar materials having different gradations are parallel. This comes out of the fact that the slope of a SSL is a function of the angularity of the grains, which are

the same for remolded and undisturbed specimens (Poulos et al., 1985).

Step 4. - Correct the steady-state strength measured in the undisturbed sample using the procedure sketched in Fig. 2.9. This strength is corrected by backtracking the shear strength along a line parallel to the remolded SSL to the in-situ void ratio. This will be the in-situ value of steady-state strength to be used in the stability analysis.

Of paramount importance in this procedure is the accuracy with which in-situ void ratios are measured. This is due to the fact that the SSL is quite flat and small changes in density could lead to large changes in steady-state strength. For example, results on a typical sand show that an uncertainty in 3 pcf could lead to sixfold changes in  $S_{us}$  (Poulos et al., 1985).

Although the above procedure has been used to evaluate a number of dams, Seed (1985) indicated that this method yields somewhat higher values compared to what he calls residual strength. (Seed notes that this residual strength is synonymous with undrained steady-state strength provided the soil is sheared at truly constant volume. There is no certainty that this undrained condition actually has existed in the field in the cases studied by Seed to develop the chart shown in Fig. 2.10. Thus, the results shown would

account in an empirical way for possible deviations from constant volume conditions in the field during flow (NRC, 1985). This explanation given by Seed contradicts the key assumption in the procedure developed by Poulos et al. (1985), that the void ratio of a sand deposit, after it liquefies, is the same it had before it liquefied.

The procedure by Poulos et al. (1985), has other points which have been disputed (Alarcon and Leonards, 1988; Arulanandan and Muraleetharan, 1988; De Alba, 1988; Dennis, 1988; Kutler, 1988; Pilecki, 1988; Pyke, 1988a, 1988b). These include the uniqueness of the steady-state line, the problems associated with measuring in situ densities and, very importantly, the drainage conditions. These issues will be addressed in Chapter 8.

Another important point are the conditions necessary for triggering of flow failure. The current state of the art is the Seed-Lee-Idriss procedure, in which stress-controlled cyclic triaxial tests on both isotropically and anisotropically consolidated specimens are used in conjunction with dynamic finite element analyses to determine if failure has occurred (Seed et al. 1975). For the stress-controlled cyclic test on isotropically consolidated, typically dilative specimens, the conditions



of  $r_u = 1.0$  or cyclic strain of  $\pm 5\%$  are considered triggering (Seed et al., 1975; 1987). For the tests on anisotropically consolidated sands, also typically on dilative sand, he uses as triggering criterium an accumulated axial strain equal to 5% (Seed et al., 1975; 1987). For contractive sands, however, much smaller values of pore pressure ratio  $r_u$  and axial strain are needed to trigger flow failure (Dobry et al., 1985; Vasquez-Herrera et al., 1988; see also Chapter 7) and therefore, the Seed-Lee-Idriss procedure could be unconservative.

## 2.5 The Cyclic Strain Approach

The current state-of-the-art methodology to predict pwp buildup during earthquakes at level sites (as different from slopes) has been developed mainly by Seed and his coworkers (Seed and Idriss, 1971; Seed et al, 1975: Seed, 1979). It is based on the premise that pwp buildup in saturated sands, subjected to a given cyclic shear stress history, is mainly a function of the relative density ( $D_r$ ) and the initial effective stresses acting on the sand. Cyclic tests performed in more recent years have revealed that a number of other factors besides  $D_r$  also influence significantly the results of stress-controlled tests. Some of these are:

fabric, prior straining, aging and overconsolidation. It was shown (Mulilis et al., 1975; Seed, 1979) that the effect of these factors can be even more significant than those caused by large variations in relative density (see Fig. 2.11). The influence of all these factors on the cyclic strength of sands by stress controlled tests certainly complicates the state-of-the-art and makes its practical use more difficult. Because of the problem with stress-controlled tests, Peck (1979) proposed to rely more on empirical correlations based on field SPT measurements rather than using cyclic laboratory tests.

A different method called the cyclic shear strain approach (also known as the strain approach) has been introduced as an alternative to the cyclic stress approach. The cyclic strain approach is based on the premise that pwp buildup during cyclic shear loading is controlled mainly by the magnitude of the cyclic shear strain. This leads to the conclusion that shear modulus ( $G$ ) rather than  $D_r$  is the main parameter controlling pwp buildup in the field (Dobry et al., 1982). A practical consequence is that the in-situ shear modulus at small strains  $G_{max}$  can be obtained from geophysical measurements of shear wave velocity, and used for predicting pwp generation (Dobry et al., 1981; Stokoe and Woods, 1972). This in-situ method gives better results

at measuring  $G_{\max}$  than trying to measure the in-situ  $D_r$ , which very usually is not determined directly but instead is inferred from penetration tests. Therefore, the proposed strain approach, based on seismic shear strains, in-situ measurements of  $G_{\max}$  and cyclic strain-controlled tests, is different from the current practice, which is based on seismic shear stresses, in-situ penetration measurements for  $D_r$  determination and stress-controlled tests.

Silver and Seed (1971) and Youd (1972) showed experimentally that cyclic shear strain ( $\gamma_{cy}$ ) rather than cyclic shear stress ( $\tau_{cy}$ ), is a more fundamental parameter controlling the densification of dry sands. Martin et al. (1975) successfully developed a cyclic strain, effective stress model to predict pwp buildup in saturated sands during undrained stress-controlled tests. All of these findings strongly suggested that ( $\gamma_{cy}$ ) rather than ( $\tau_{cy}$ ), controls both densification and liquefaction in sands.

Other researchers using cyclic test results on dry sand (Drnevich and Richart, 1970; Youd, 1972; Pyke et al., 1974) concluded that there is a threshold cyclic shear strain ( $\gamma_t$ ) of the order of  $10^{-2}\%$  below which no densification occurs and therefore pwp buildup would not be possible. The  $\gamma_t$  has been measured in the laboratory in undrained conditions on isotropically and anisotropically consolidated dilative

samples, and has been found to be unaffected by the coefficient of anisotropic consolidation (Dobry et al., 1981a, 1982; Dyvik et al., 1984; Thomas et al., 1985). These results on dilative sands where cyclic mobility occurs show that a threshold strain exists at which pwp buildup begins. This is obviously very important for liquefaction prediction, thus tying in well with the strain approach to pore water pressure buildup and liquefaction.

In terms of cyclic laboratory tests, there is experimental evidence that the previously discussed factors that increase the cyclic strength of sands also increase the shear modulus of sands (Seed and Idriss, 1971; Drnevich and Richart, 1970; Hardin and Drnevich, 1972; Pyke et al., 1974; Dobry and Ladd, 1980). This helps in explaining why the ratio  $\gamma = r/G$  is less influenced by these factors than  $r$ , by suggesting that both  $r$  and  $G$  are similarly affected. As a result, the pwp buildup in strain-controlled tests is less sensitive to these factors than in stress-controlled tests. Figure 2.12 shows the results of a large number of cyclic triaxial test results on isotropically consolidated samples prepared using different methods, and tested using different relative densities and confining pressures. The figure displays the pore pressure ratio at the end of 10 cycles of constant shear strain. It can be seen the scatter for

strain-controlled tests is much less than that created using stress-controlled tests in Fig. 2.11, especially considering the differences among relative densities, confining stresses and methods of sample preparation. On the basis of results of cyclic strain-controlled tests such as these, a pore pressure model for sands in level ground conditions was developed (Pierce, 1985) and later applied to predict some case histories (Vucetic, 1986).

## 2.6 The CyT-CAU Test

A soil element susceptible to seismic liquefaction flow failure in slopes and embankments has been typically consolidated anisotropically, and thus has a value of  $K_C = \bar{\sigma}_{1c} / \bar{\sigma}_{3c}$  greater than 1. It has a low density which in first approximation is assumed to make it contractive, and it is subjected to driving shear stresses larger than the undrained steady-state shear strength. This situation resembles the case of a seismically induced liquefaction flow failure of an earth dam such as shown in Fig. 2.13. The driving shear stresses usually act on different planes than the seismic stresses and strains, with the earthquake stresses and strains acting predominantly along horizontal planes. Furthermore, the static shear stresses acting along the potential sliding surface remain unchanged during the

earthquake, until failure has occurred. Finally, and as previously discussed, in first approximation the seismic loads causing pwp buildup should be modelled using cyclic strain-controlled loading. It has been very difficult to simulate all these aspects in a laboratory environment, as this requires that the seismic strains causing pwp buildup be modelled in strain control, while the flow failure itself should be driven by the static shear stresses in load control. This problem was resolved by Mohamad (1985) by using the CyT-CAU test shown in Fig. 2.14, which simulates the stress conditions in the field as shown in Fig. 2.15.

Liquefaction flow failure takes place in two different consecutive stages: (1) a first stage of pwp controlled by the level and duration of the cyclic shear strains acting on a horizontal plane, and (2) a second unidirectional flow failure stage, driven by the weight of the structure or sliding mass, which acts on a different plane.

A CyT-CAU test is performed by first consolidating a triaxial specimen anisotropically such that  $K_c > 1$ . The maximum static shear stress acting on a  $45^\circ$  plane is thus:  $\tau_s = (\bar{\sigma}_{1c} - \bar{\sigma}_{3c})/2$ . Next a torsional horizontal cyclic shear strain  $\gamma_{cy}$ , simulating the seismic action, is applied under undrained conditions in the strain-controlled mode. (More

details on the selection and use of  $\tau_{cy}$  in CyT-CAU tests as sketched in Fig. 2.14 and 2.15 are given in Section 4.4). The cyclic shear strain induces a pore pressure buildup which softens the soil; thereby simulating the first stage of pore pressure buildup previously described. If the conditions are such that the soil element is contractive and  $\tau_d = \tau_s > q_{us}$ , then liquefaction flow failure is triggered after a number of cycles ( $n_t$ ). This flow failure is driven by the static driving shear stress and corresponds to the second stage of unidirectional flow failure.

The traditional cyclic triaxial test on anisotropically consolidated specimens was the first to simulate liquefaction conditions. However, there are some major differences between the loading conditions used in this test and those in the field. These are: (1) in the cyclic triaxial test the driving static shear stresses and the seismically induced shear stresses always act on the same plane, whereas in the field they might not; (2) because the maximum static and cyclic shear stresses are applied on the same plane in the cyclic triaxial test, the maximum shear stresses are reduced below the initial static value periodically during cycling, whereas in the field the maximum shear stresses are typically equal to or larger than the static shear stresses; and (3) in the cyclic triaxial

test on anisotropically consolidated samples, the cyclic loading has to be in stress control, while better pwp results would be obtained if it were in strain control. These problems of the cyclic triaxial test are solved in the CyT-CAU test.

For these reasons it is believed that the CyT-CAU is a better test to simulate in situ liquefaction flow failure than the traditional cyclic triaxial test.

## 2.7 Previous Results by Mohamad

In the Ph.D. thesis by Mohamad (1985), the CyT-CAU test was first developed and used to understand the liquefaction flow failures of earth dams. He made a substantial contribution by interpreting the results of cyclic triaxial tests and the effect of static shear on the conventionally defined cyclic triaxial strength of sand.

In his thesis he advanced the notion that seismic liquefaction flow failure occurs in two stages: one of pwp buildup controlled by the magnitude of the seismic strains, followed by a steady-state stage of deformation after the liquefaction has been triggered. The CyT-CAU test was developed by him to simulate in the lab those two stages, following as closely as possible what happens in the field.



The CyT-CAU technique was used to study pwp buildup, triggering of flow failure and the steady-state of deformation.

Some of the other major findings of his thesis were the following. In his cyclic CyT-CAU test results on Banding Sand, liquefaction flow failure triggered when the effective stress path reached the steady-state strength envelope  $\bar{\sigma}_{us}$  (which was unique for CIU, CAU and CyT-CAU). On the other hand, his monotonic CIU and CAU tests triggered at a different envelope, except for one CAU test that was consolidated above the monotonic triggering strength envelope. The magnitude of  $K_c$  was found to have an uncertain and not large effect on pwp buildup. The value of  $\bar{\sigma}_{3c}$  had a strong effect on the normalized pwp buildup,  $r_u$ , but little influence on the non-normalized pwp buildup  $u$ . He also observed that not much cyclic modulus degradation occurred throughout most of the cyclic part of the CyT-CAU test.

He also concluded that the 'line of phase transformation' or 'characteristic line' found by other authors in dilative sands (Ishihara et al., 1975; Luong and Sidaner, 1981) was identical to the steady-state strength envelope, essentially obtained from tests on contractive sands. This conclusion arose by his observing that

monotonic test results on Banding sand coincided with the steady-state failure envelope at the point at which the effective stress path bent sharply to the right (elbow). This elbow was found in both dilative sands without flow failure, as well as in partially contractive sands with limited flow (see Fig. 2.16); in both cases the elbow point was found in Banding sand to correspond to the steady-state conditions. Using this conclusion he compiled information by other researchers showing that the steady-state strength envelope varies as a function of the particle angularity (see Table 2.1).

Mohamad also used the CyT-CAU to determine the steady-state strength parameters; however, the scatter of his results, shown in Fig. 2.17, was quite large. This scatter could present serious problems when using the liquefaction evaluation procedure suggested by Poulos et al., (1985) to determine the insitu  $S_{us}$ ; because the slope and position of the SSL were not well defined. He offered no explanation for this scatter of his steady-state strength results.

Further discussions of Mohamad's findings in the light of the experimental results reported herein are presented in Sections 6.2.4 and 6.6.

Table 2.1. Steady-State Strength Envelope Angles  $\bar{\sigma}_{us}$  for Several Uniform Clean Sands (after Mohamad, 1985)

SAND	$\bar{\sigma}_{us}$	PARTICLE SHAPE	REFERENCE(S)
Fontainebleau Sand	25.1°	Shape unknown	Luong and Sidaner (1981)
Banding Sand	26.5°	Subrounded	Castro (1969); Castro et al. (1982) Authors
Ottawa Sand	26.5°	Rounded	Vaid and Chern (1983)
Reid-Bedford Sand	27.7°	Subrounded with rounded and angular	Durham and Townsend (1972)
Fuji Sand	28.1°	Subangular	Ishihara et al. (1975)
Antelope Valley Sand	28.9°	Subangular to angular	Lade and Hernandez (1977)
Mine Tailings Sand	29.7°	Angular	Castro, et al. (1982)

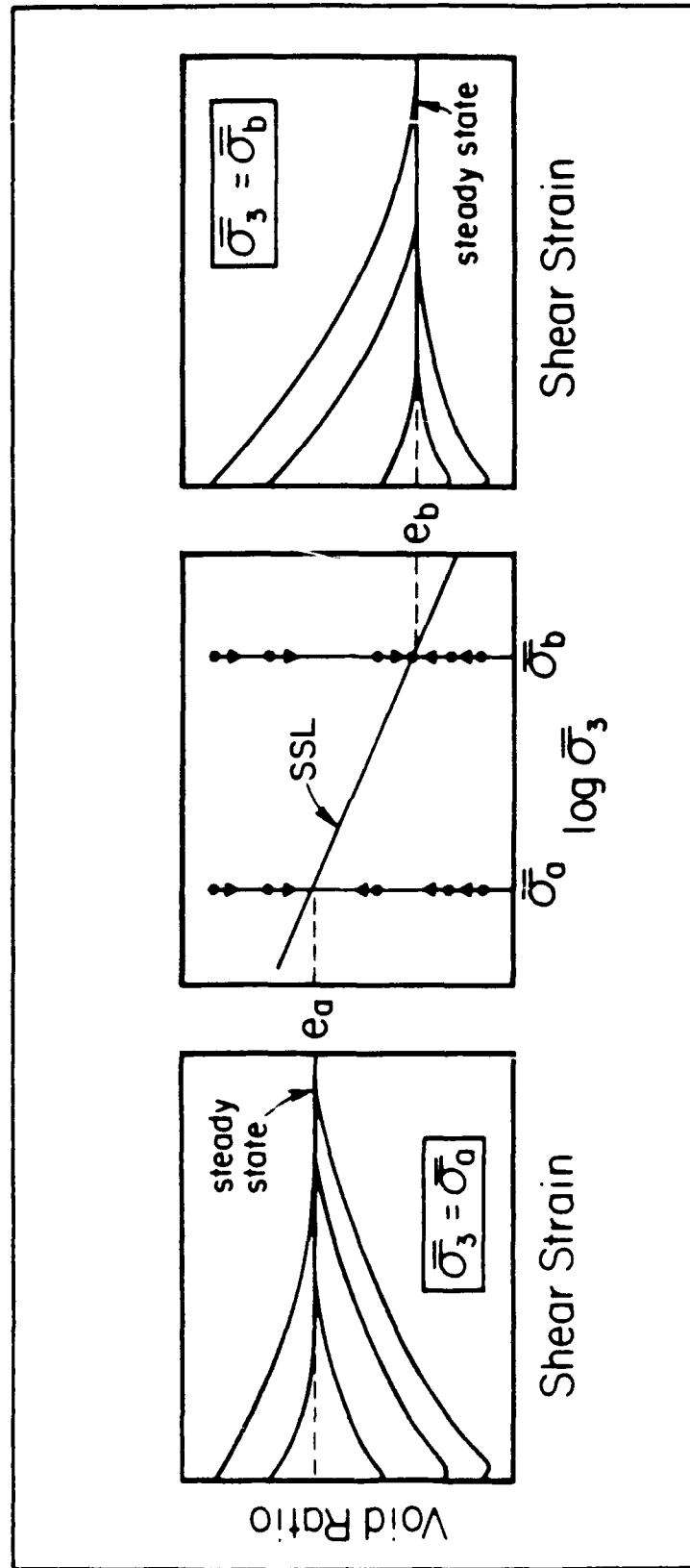
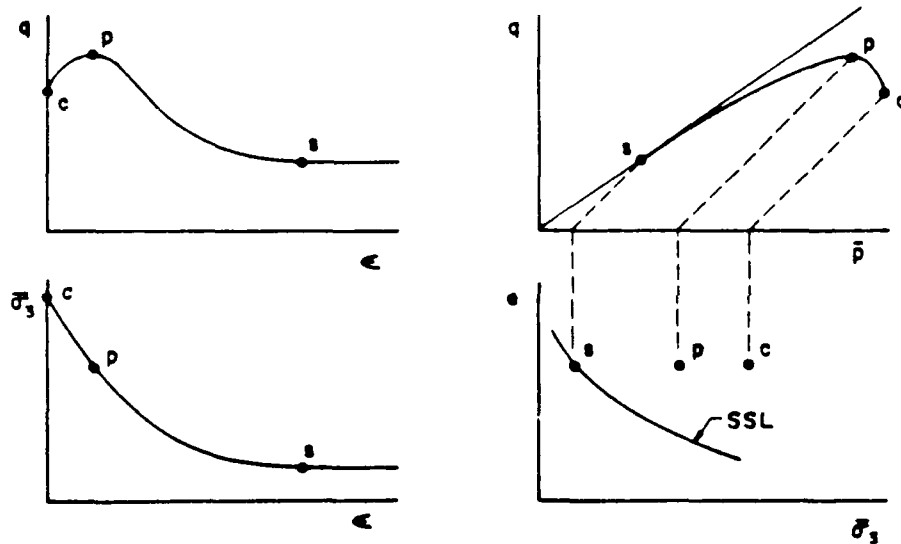
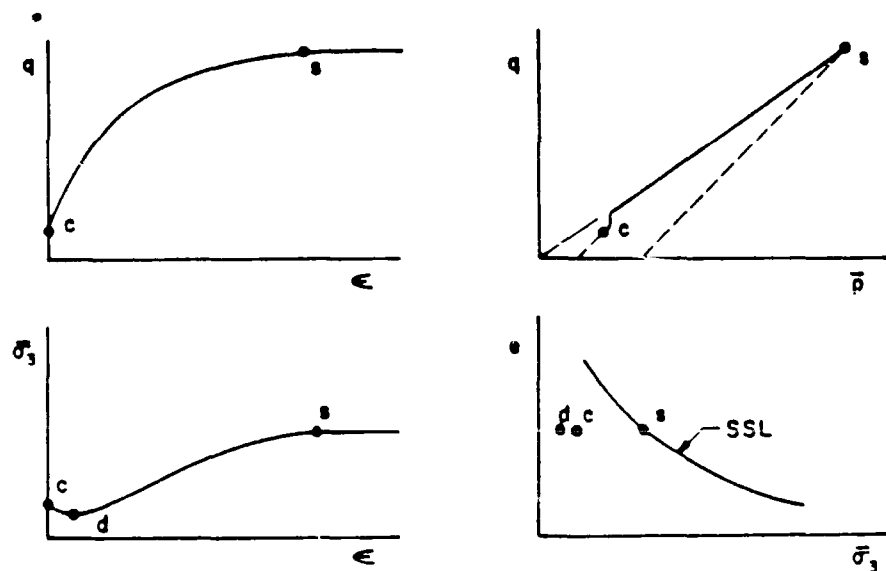


Fig. 2.1.1. Schematic Description of the Steady-State Line (SSL) Using Drained Tests



(a) UNDRAINED STRESS STRAIN BEHAVIOR, Type I



(b) UNDRAINED STRESS STRAIN BEHAVIOR, Type II

Legend: SSL = Steady State Line, s = steady state,  
c = consolidation state, p = peak strength.

Fig. 2.2. Comparison of Two Basic Types of Stress-Strain Behavior Found in Soils Under Undrained Monotonic Shear - a) Type I, b) Type II (NRC, 1985)

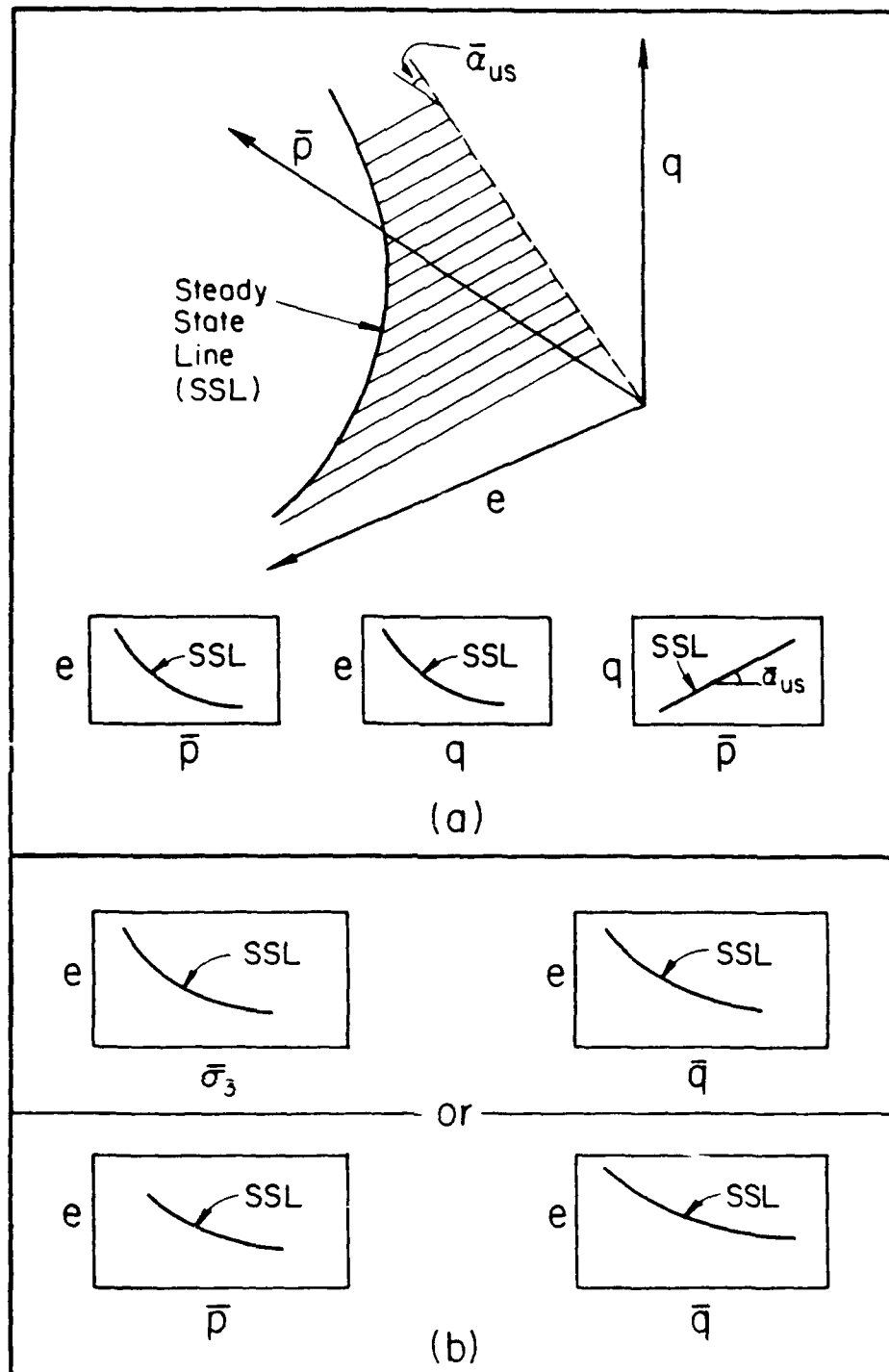


Fig. 2.3. Different Representations of the Steady-State Line

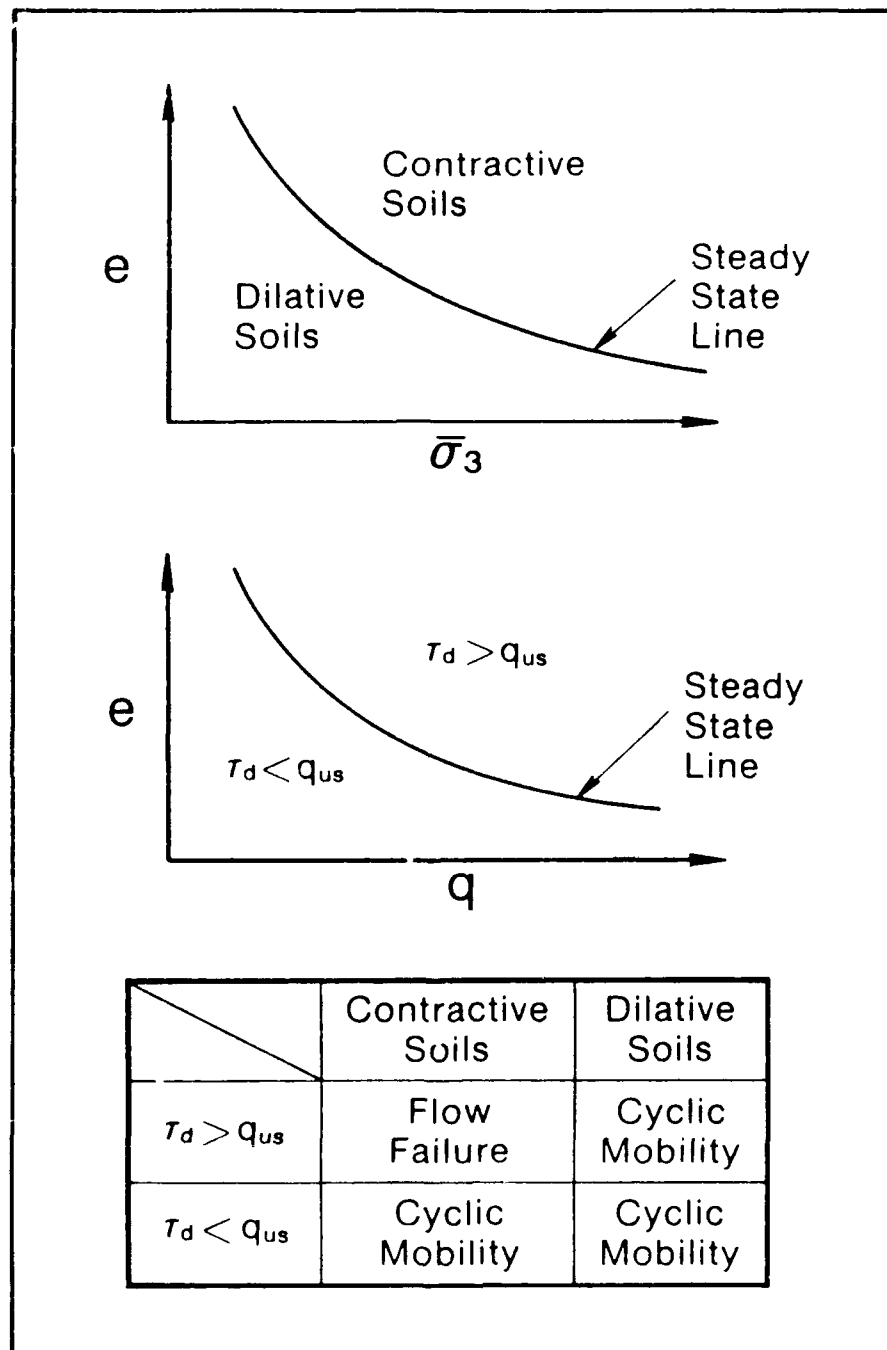


Fig. 2.4. Density and Stress Conditions for Liquefaction Flow Failure and Liquefaction Cyclic Mobility

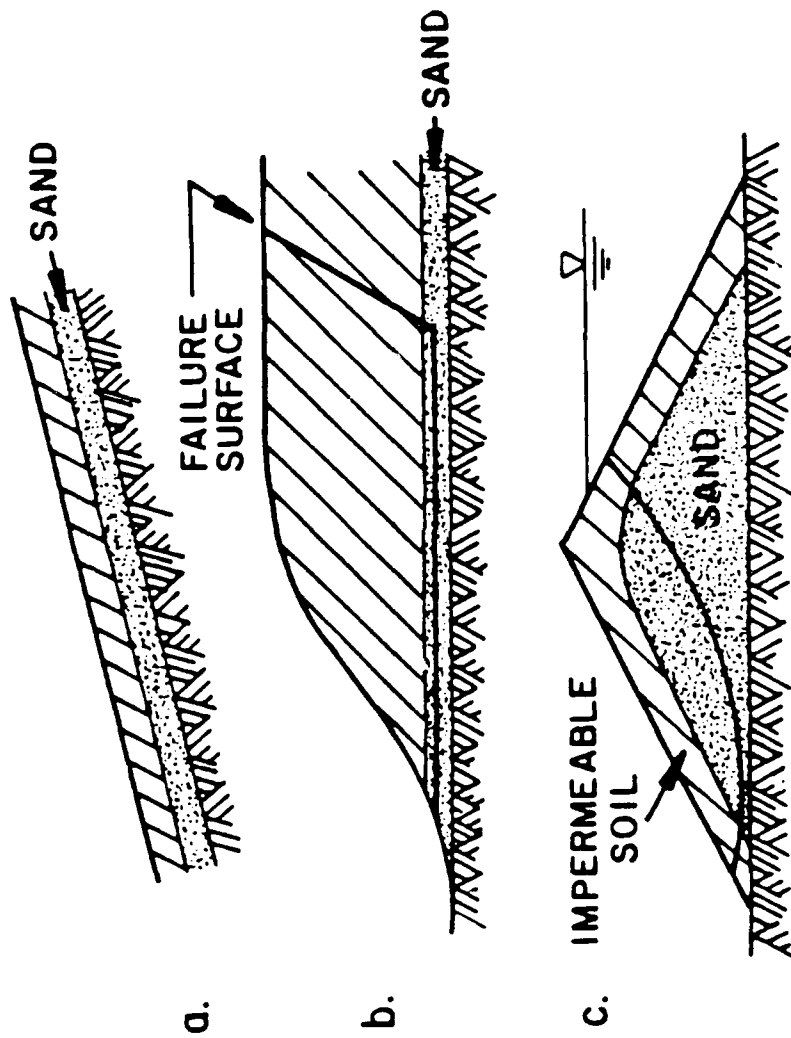


Fig. 2.5. Examples of Flow Failure Mechanism A (NRC, 1985)



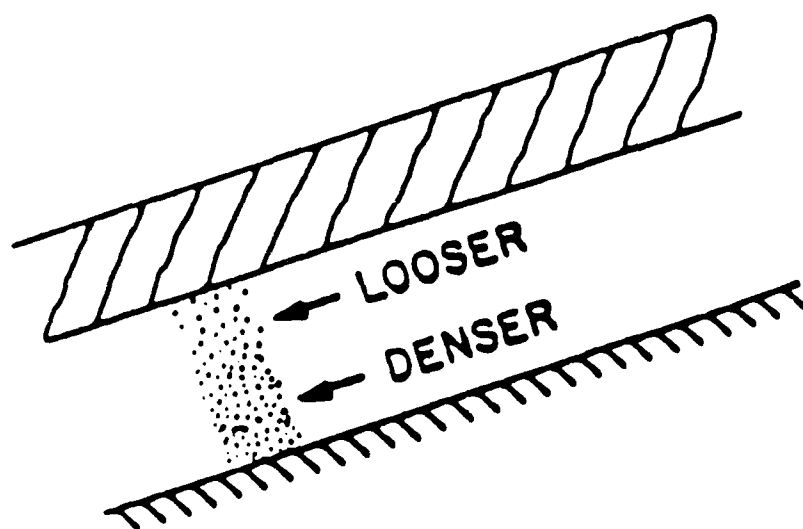


Fig. 2.6. Example of a Potential Situation for Mechanism B Failure. Local Drainage Occurs But It Is Globally Undrained (NRC, 1985)

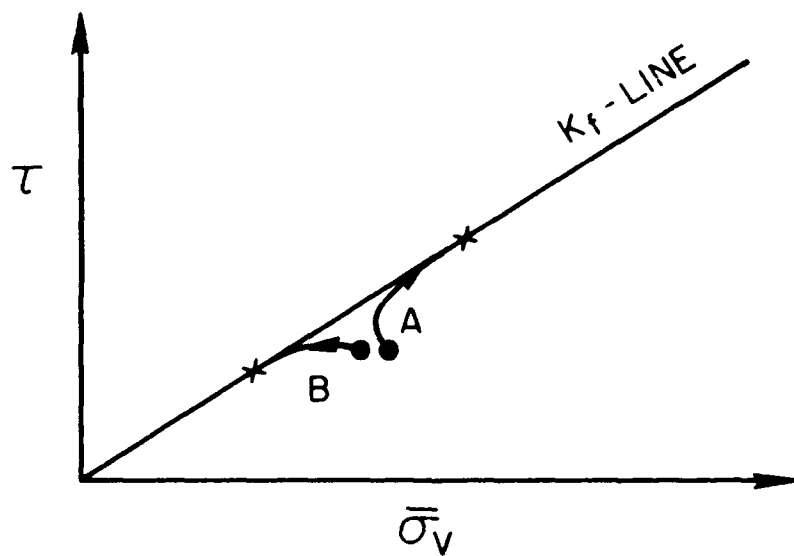


Fig. 2.7. Change in the Undrained Stress Path that a Soil Follows as a Result of Becoming Loosened Because of Local Volume Change. Path A Depicts Stress Path Without Loosening. Path B Depicts Stress Path After Loosening (NRC, 1985)

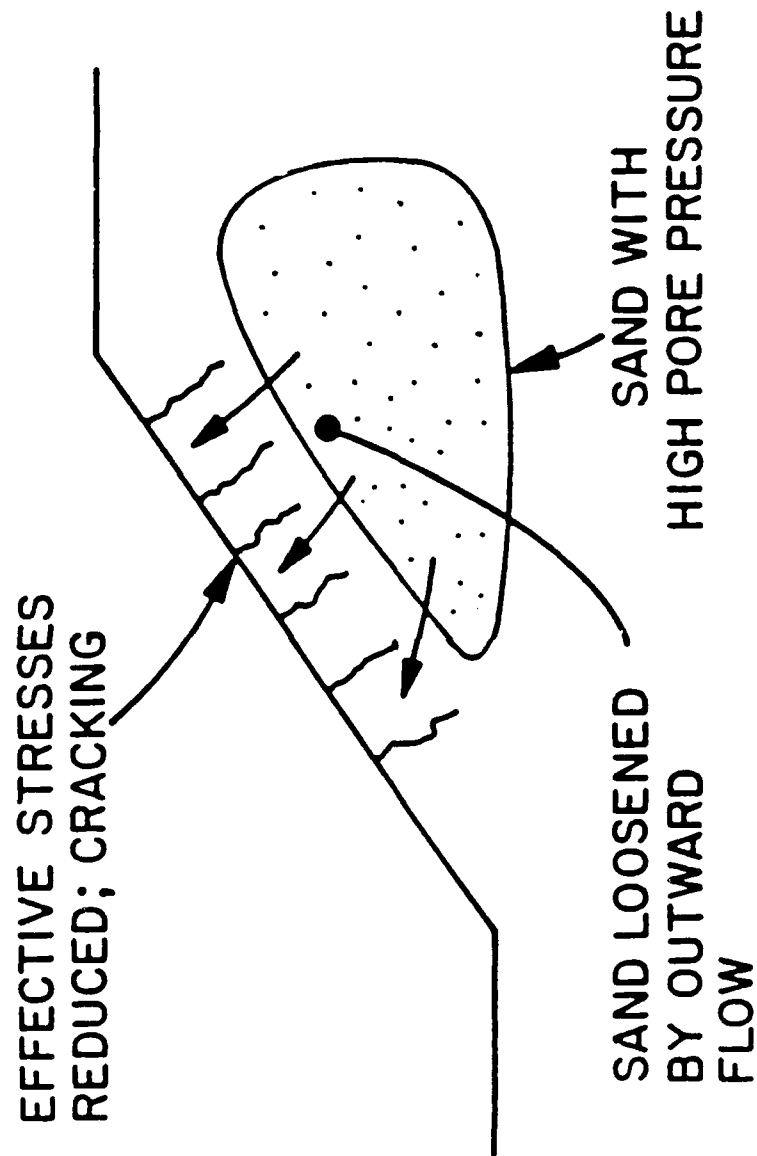


Fig. 2.8. Examples of a Potential Situation for Mechanism C Failure Resulting from Spreading of Pore Pressures and Global Volume Changes (NRC, 1985)

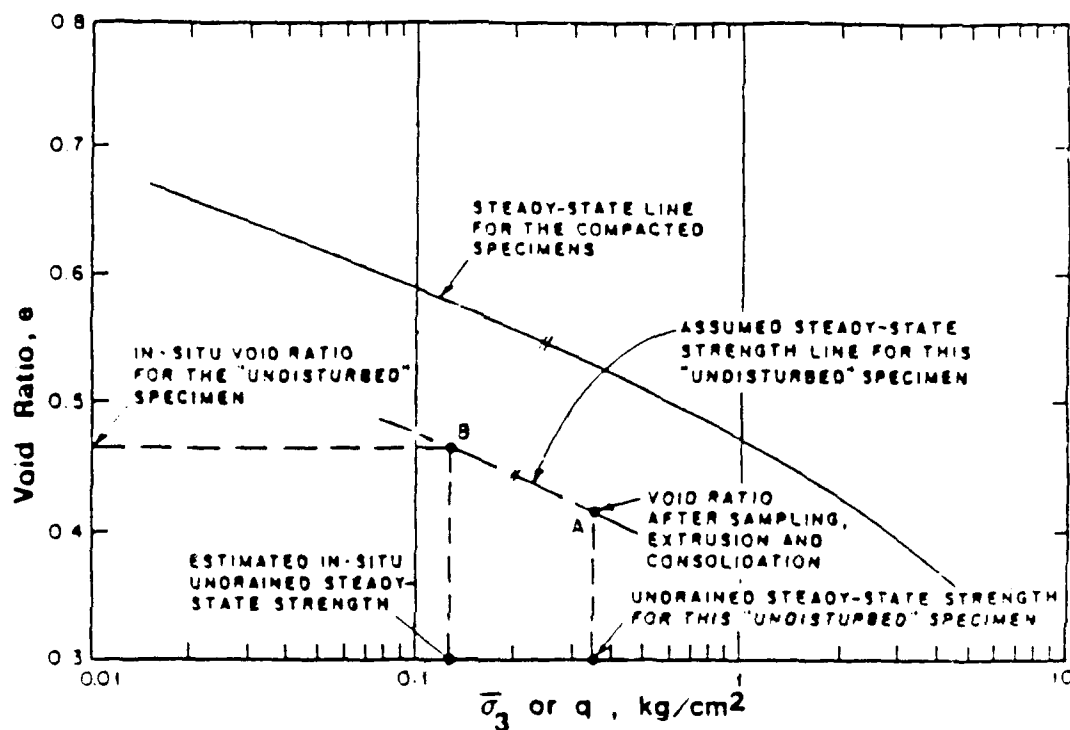


Fig. 2.9. Illustration of Procedure for Obtaining Field SSL from Tests on "Undisturbed" and Reconstituted Specimen (after Poulos et al., 1985)

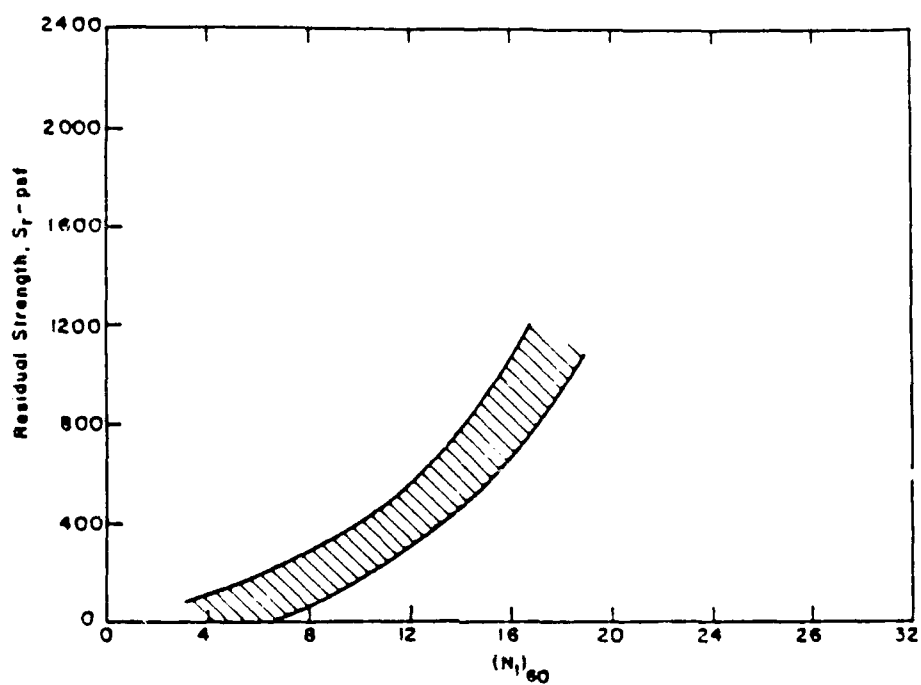


Fig. 2.10. Tentative Relationship Between Residual Strength and SPT N-Values for Sands (after Seed, 1987)

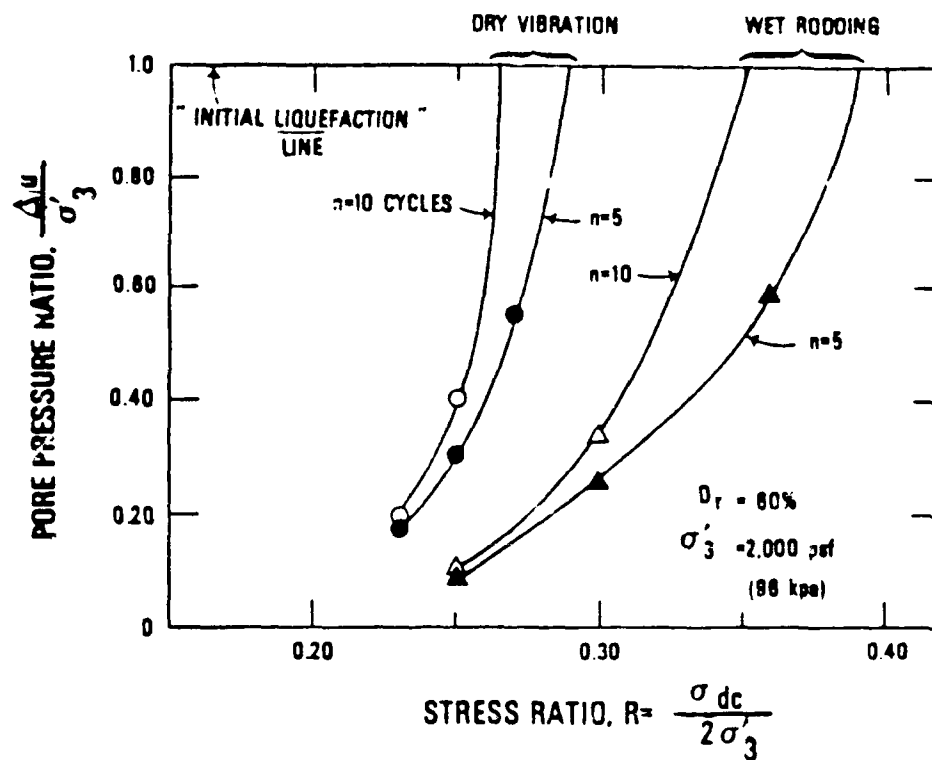
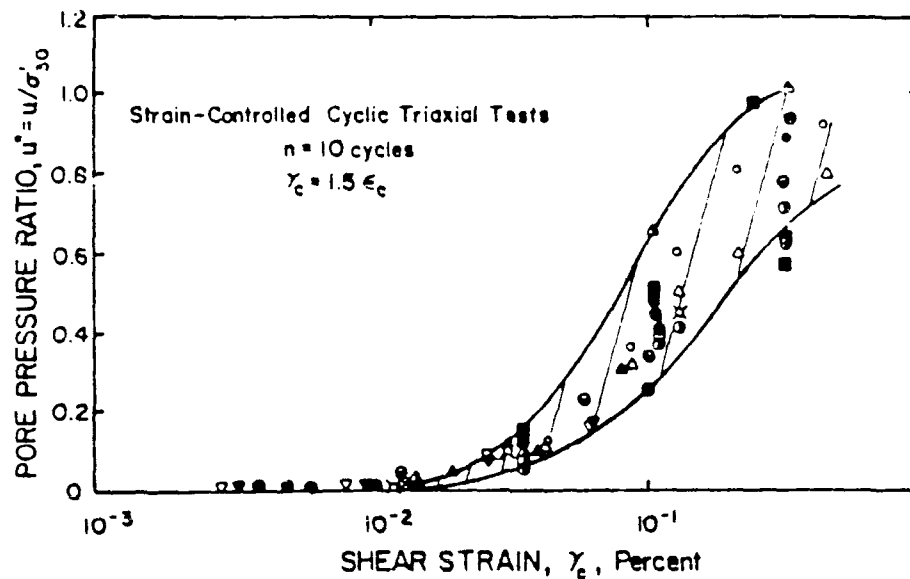


Fig. 2.11. Stress-Controlled Cyclic Triaxial Tests of Saturated Crystal Silica Sand (after Dobry et al., 1982)



Symbol	Sand	$\sigma'_{30}$ (psf)	$D_r$ (%)	Samples/ Fabric	Measured $u$ Peak (P) or Residual (R)
○	Crystal Silica	2,000	60	Dry Vibration	P
△	" "	2,000	60	Wet Rodding	P
▲	" "	2,000	60	Dry Vibration	P
▽	Sand No. 1	2,800	60	Moist Tamping	P
▼	" "	1,400	60	" "	P
○	Monterey No. 0	2,000	60	" "	P
●	" "	2,000	80	" "	P
□	" "	2,000	45	" "	P
■	" "	2,000	45	" "	R
⊕	" "	333	60	" "	P
⊗	" "	4,000	60	" "	P
●	" "	2,000	20	" "	R
●	Banding	2,000	60	" "	R
●	" "	2,000	40	" "	R
●	" "	2,000	20	" "	R
●	Heber Road Point Bar	2,000	Dense	Tube Sample	R
●	Heber Road Channel Fill	2,000	Loose	" "	R
⊗	Owi Island	2,000	40	Moist Tamping	R
○	" "	1,300	40	" "	R
⊕	" "	2,000	Medium Dense	Tube Sample	R
●	Mt. St. Helier Debris	2,000-4,000	50	Moist Tamping	R

Fig. 2.12. Summary of Results from Strain-Controlled Triaxial Tests on Seven Different Sands with Different Specimen Preparation Techniques

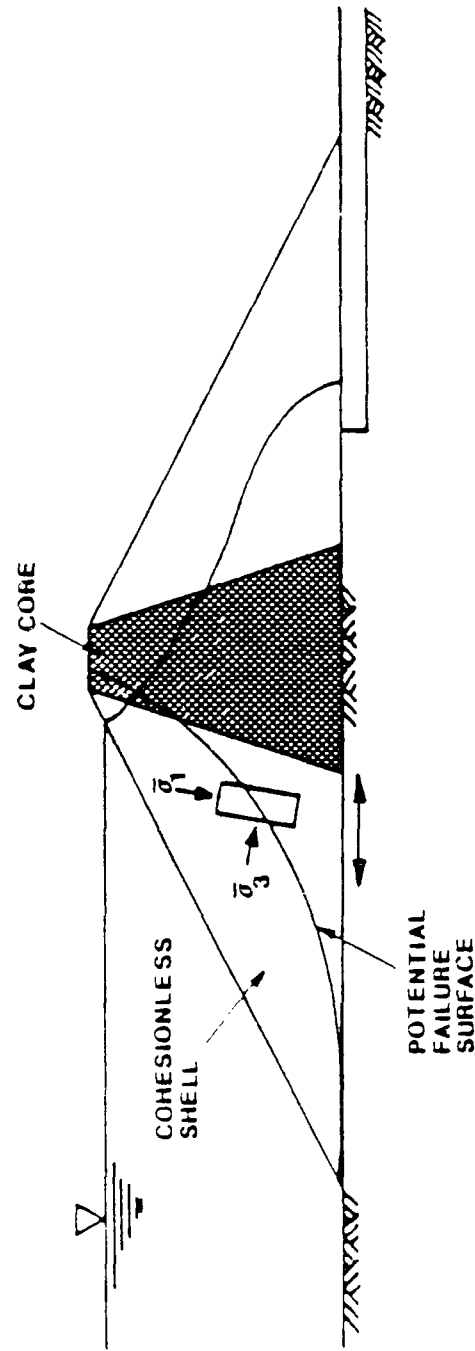


Fig. 2.13. Illustration of Problem of Seismically Induced Liquefaction Flow Failure of an Earth Dam (after Mohamad, 1985)



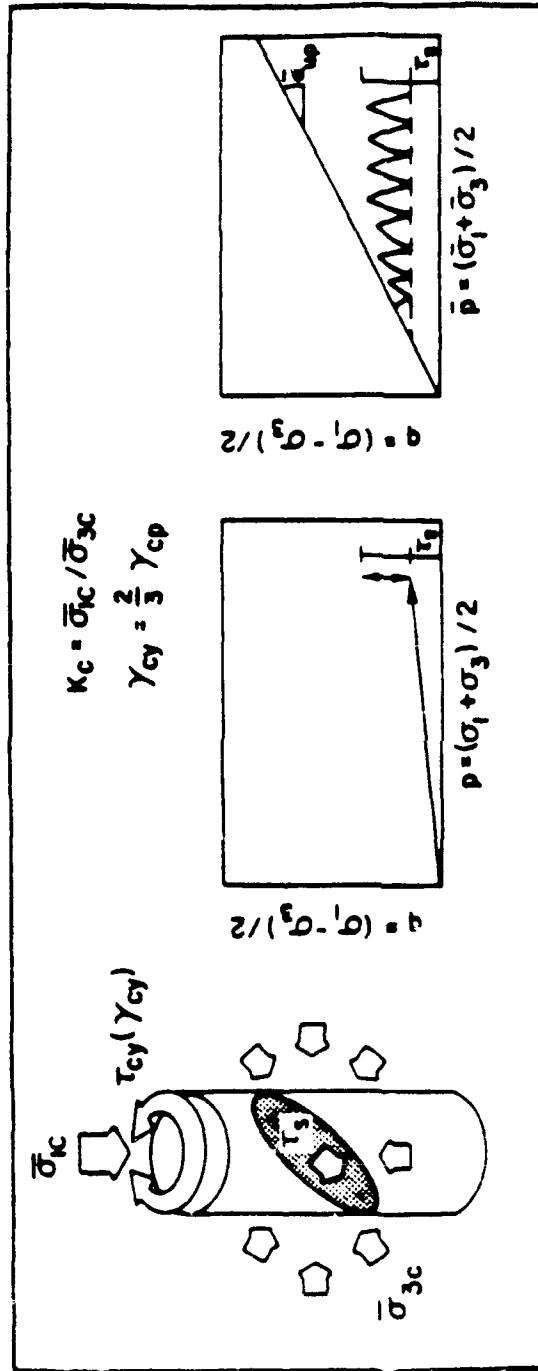


Fig. 2.14. Stress Conditions in Strain-Controlled CyT-CAU Test

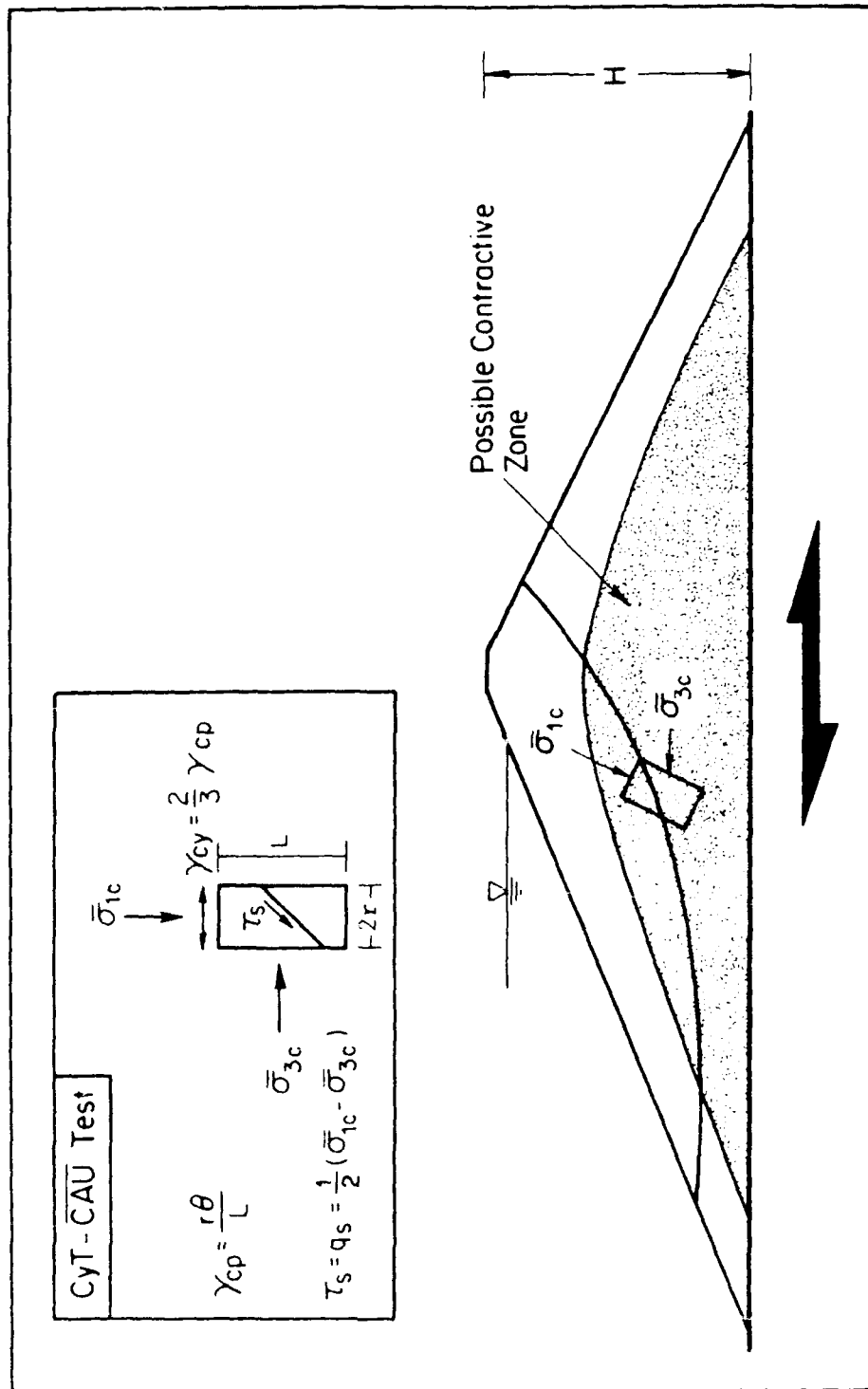


Fig. 2.15. Possible Contractive Zone in a Hydraulic-Fill Dam and the Simulation of Conditions by the CyT-CAU Test

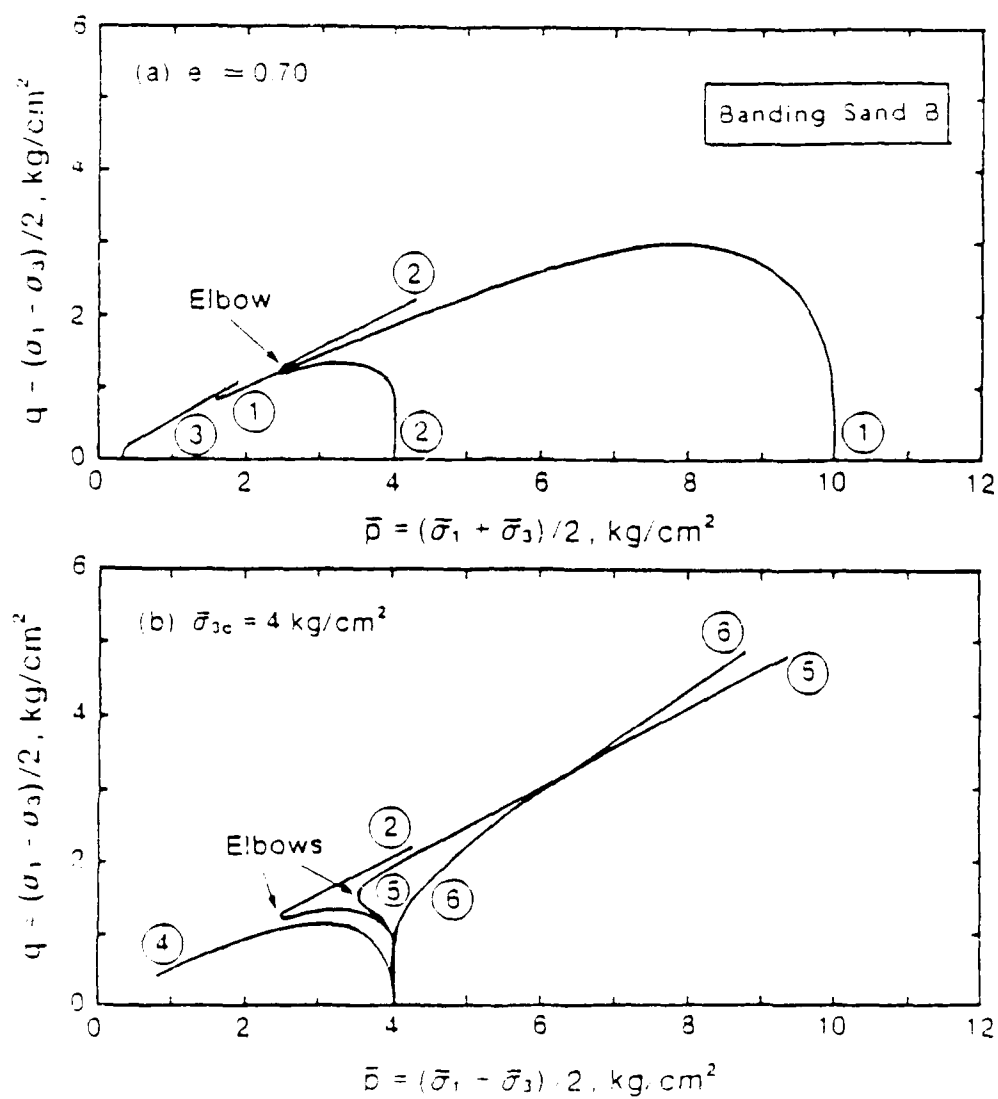


Fig. 2.16. Effective Stress Paths Showing "Elbows" (from Mohamad, 1985)

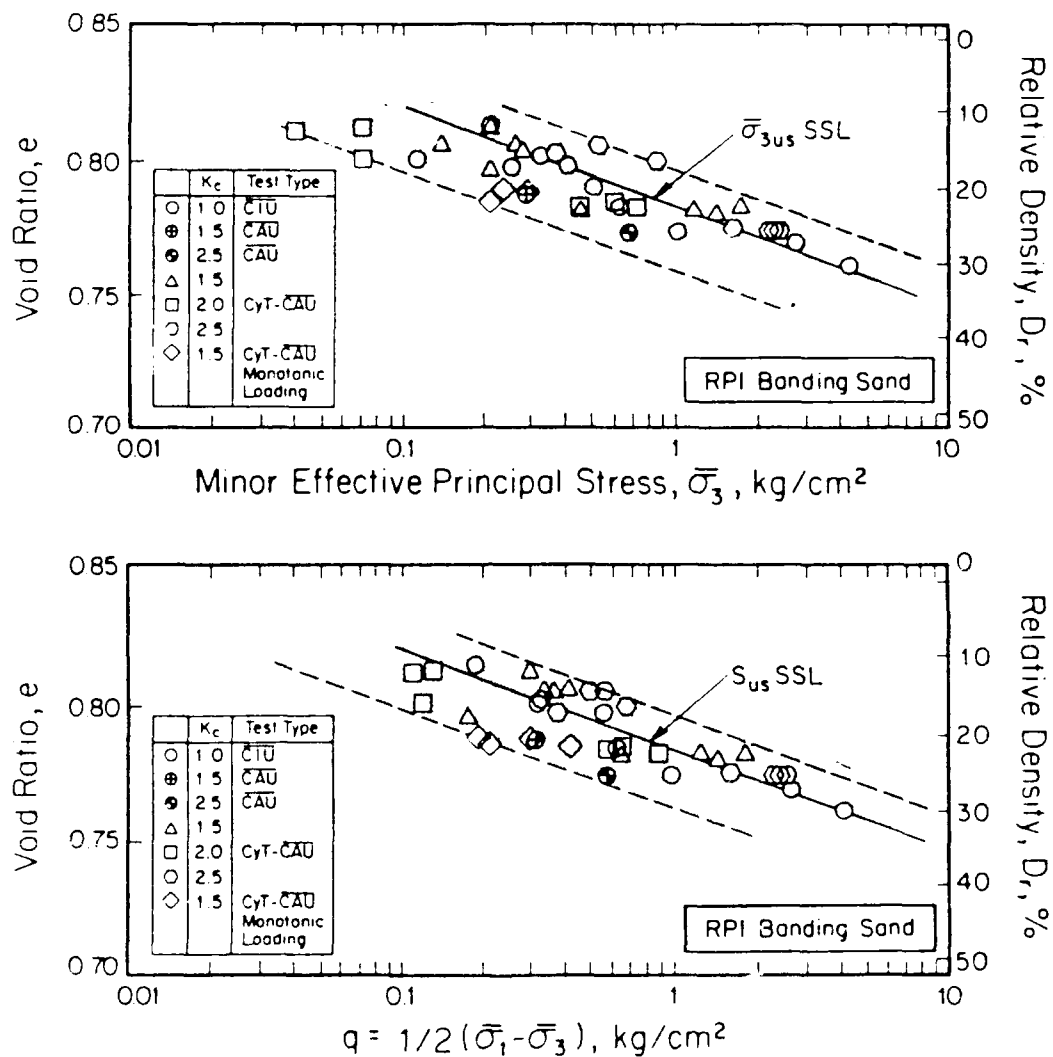


Fig. 2.17. SSL for Banding Sand Determined by Mohamad (1985)

### CHAPTER 3

#### SCOPE AND OBJECTIVES OF THE EXPERIMENTAL STUDY

The main goal of this work is to understand the factors that affect the behavior of contractive sands under static and cyclic undrained loading, and how they influence seismic liquefaction flow failures. Since only contractive sands can develop flow failure in the undrained condition, and the pwp buildup and triggering characteristics of these sands are not well understood, it is extremely important to carry out extensive experimental work to clarify the fundamental behavior of these soils.

Previous work on contractive sands concentrated on steady-state or residual strength considerations, with less attention given to the conditions necessary to trigger flow failure. The experimental work in this thesis, based mainly on cyclic CyT-CAU tests, will give information on both steady-state conditions and triggering conditions; however, the emphasis will be on triggering. This should be emphasized again: each CyT-CAU test used herein reproduces the whole phenomenon of seismically induced flow failure from beginning to end, and thus gives information on both steady-state and triggering characteristics for the specimen tested. This should be contrasted with available state-of-the-art methods, which typically use one kind of

test for predicting triggering and another for evaluating steady-state characteristics.

After the fundamental relevant behavior of contractive soils is understood, improved conceptual frameworks and analytical soil models can be developed. Therefore, one of the objectives of the experimental program herein is to provide the basis for such models and conceptual framework.

The monotonic laboratory tests used herein have been previously used by other researchers (Castro, 1969; Castro et al. 1982), with the emphasis of those investigations being on overall stability and steady-state conditions. Previous work by Mohamad (1985) showed the feasibility of the CyT-CAU test as a tool that could measure both steady-state values after triggering and pwp buildup versus number of cycles before triggering; however, the factors affecting pwp buildup were not systematically studied. The main goal of the experimental program herein is to understand and quantify the factors governing the triggering of liquefaction flow failure; in addition, the issue of steady-state conditions will also be addressed. The parameters affecting liquefaction flow failure triggering that were systematically studied in this work include the minor consolidation effective pressure  $\bar{\sigma}_{3c}$ ,  $K_c = \bar{\sigma}_{1c}/\bar{\sigma}_{3c}$ ,

the cyclic torsional shear strain,  $\gamma_{cy}$ , the number of cycles of  $\gamma_{cy}$  needed to trigger flow failure,  $n_t$ , and soil fabric. The laboratory tests concentrated on three different silty sands to verify that the results and trends were not restricted to one soil, and to find common behavioral characteristics among the three sands. This will enable us to generalize these results to other contractive silty sands and to develop a pore pressure buildup and triggering model (Chapter 7) capable of simulating their behavior.

The experimental work presented herein is directly applicable to Mechanism A type of flow failure which assumes both locally and globally undrained conditions. This is true for both the triggering and stability conclusions to be derived from the laboratory tests.

CHAPTER 4  
FLOW FAILURE LABORATORY TESTING EQUIPMENT  
AND PROCEDURES

4.1 General

Static and cyclic laboratory tests were performed as part of this work on several sands in order to study the cyclic undrained behavior of anisotropically consolidated contractive cohesionless soils.

All tests were conducted in the Class of 1933 Earthquake Engineering and Cyclic Loading Soils Laboratory at Rensselaer Polytechnic Institute (RPI).

The testing techniques and procedures described herein were originally developed by Mohamad (1985); however, in order to decrease the scatter of the experimental data, some new methods were devised and existing ones modified. Results and degree of scatter obtained with the improved procedures were then compared with those reported by other leading soil mechanic laboratories, with excellent agreement.

The focus of this experimental work is to understand the conditions necessary to trigger flow failure and reach steady-state. However, as will be shown later herein, the triggering and steady-state aspects are closely related and cannot be separated; therefore, both are discussed in this



and subsequent chapters.

Although several types of laboratory tests were conducted, all made use of solid triaxial specimens, and therefore the same sample preparation techniques were used in all cases.

#### 4.2 Sands Tested

Five soils were tested for their triggering and flow failure characteristics; however, three sands were more systematically studied. These are Ottawa F125 Sand (called here F125 sand), Lagunillas sand A (called sand A) and Lower San Fernando Dam Sand Batch Mix No. 7 (called SF7 sand). The first of these three soils is an industrially produced and commercially available, slightly silty sand with non-plastic silt, which was used for extensive parametric studies; whereas the latter two are real silty sands obtained from specific engineering projects. Table 4.1 presents some important properties of all sands tested.

The F125 sand is sold by Ottawa Industrial Sand Co. (Ottawa, Illinois) under the trade name F-125. It is a commercially produced sand made of ground crystalline silica (quartz). As shown in Fig. 4.1, it is very fine and uniform. This sand was chosen due to its fineness in order to reduce membrane penetration effects (Lade and Hernandez,

1977; Baldi and Nova, 1984). Membrane penetration has been quantified by the parameter  $S$ , called the normalized membrane penetration. The parameter  $S$  is defined as (Baldi and Nova, 1984):

$$S = \frac{\Delta v_m}{\Delta \log \bar{\sigma}_3}$$

where  $v_m$  is the unit membrane penetration, defined as the volume change due to membrane penetration divided by the membrane area. Therefore, both  $S$  and  $v_m$  have units of length. Figure 4.2 shows the effect of sand mean grain size on the value of  $S$ . It can be seen that for the F125 Sand, with a  $d_{50} \approx 0.1$  mm, the normalized membrane penetration  $S$  is almost zero.

The membrane penetration effect is present in all undrained tests in granular soils where the specimen is surrounded by a rubber membrane, such as an undrained triaxial test. This phenomenon occurs because during consolidation the membrane penetrates the peripheral intergranular voids of the specimen. During undrained shear, the pore pressure pushes out this penetrated membrane and creates partial drainage of the sample towards the periphery. Therefore, as the test is not completely undrained, the values of pore pressure are not correct and

can be much smaller than they should if the test had no membrane penetration. A number of researchers have suggested experimental and analytical methods to account for this phenomenon ( Frydman et al, 1973; Raju and Sadasivan, 1974; Kiekbusch and Schuppener, 1977; Lade and Hernandez, 1977; Martin et al., 1978; Ramana and Raju, 1982; Vaid and Negussey, 1984; Baldi and Nova, 1984; Raines et al., 1987), none of which is simple or can solve the problem completely. By choosing a very fine sand the problem is circumvented. The other soils in this work were either finer than the F125 sand or had enough fines filling the voids so that the membrane penetration effect is practically not present. Therefore, membrane penetration effects did not have to be considered for any of the tests presented in this work, which could then be considered to be essentially undrained.

Lagunillas sands A, B and C are silty sands sampled from a lacustrine, swampy deposit that has experienced liquefaction induced by vibrating machinery in the past. The grain size distributions for these three sands are shown in Figs. 4.3 through 4.5. It can be seen that the three curves are very similar except for their fines content, and would in fact plot very close to each other if the fines under sieve No. 200 ( $< 0.074$  mm) were eliminated

The SF7 Sand was obtained from the Lower San Fernando Dam that liquefied in the 1971 San Fernando earthquake (Seed et al., 1975). In a cooperative effort among various researchers, the US Army Corps of Engineers Waterways Experiment Station (WES) sampled material from the undamaged part of the dam in 1985. Undisturbed as well as disturbed samples were retrieved. The batch tested in this work corresponds to disturbed Batch Mix No. 7, which is in the zone containing most of the material present in the failure. The grain size distribution curve for the SF7 sand is shown in Fig. 4.6.

#### 4.3 The Axial/Torsional Triaxial System

In order to understand the phenomenon of liquefaction flow failure in the field, the stress-strain-pore pressure characteristics of the material has to be investigated. For this work, both static and cyclic tests were conducted using a custom built servo-hydraulic closed-loop testing system built by MTS System Corp. for RPI. All tests made use of some sort of triaxial test equipment and procedure.

The MTS system is logically made up of one large electronic control system that govern two mechanical components. These mechanical components are a Norwegian Geotechnical Institute Direct Simple Shear Device (NGI DSS)

and an Axial/Torsional Cyclic Triaxial frame custom built by MTS. Since only the latter was used in this work we shall explain it in more detail.

The MTS electronic and control components are comprised of a function generator, phase shifter, counter, and signal displays. Two model 442 controller panels control the axial mode and the torsional mode. Each of these control panels in turn includes servo controllers, valve drivers, transducer conditioners, feedback selector modules, limit detector modules and loop stabilization modules. Each panel controls the operation for three channels: force, stroke and strain, and permits any of the three channels to be the controlling parameter. Each mode coupled with their three channels enables the user to control any of the following parameters: axial load, axial strain (small strains), axial stroke (large strains), rotation, torque, and small rotations. At present the small rotation option is disabled and instead pore pressure is used on this channel. Each of the channels has 4 operating ranges (1, 2, 3, and 4) with full scale outputs of 100%, 50%, 20%, and 10%, respectively, of the full range capabilities of the measuring system.

Although the frequency capabilities are a function of system gain and actuator displacement amplitude, the range of most interest in geotechnical studies is easily covered

by the equipment used (from 1 Hz to 0.01 Hz).

The mechanical components are comprised of a 22,000 lb load frame, a 3 gallon per minute hydraulic power supply, a 7.5 gallon hydraulic accumulator system, a 5,500 lb axial actuator (model 204.52) and a 1000 in-lb torsional actuator (model 215.52). The axial/torsional system consists of the axial and torsional actuators located at the top of the frame, whereas the triaxial cell with the specimen is at the bottom of the frame. The two actuators are connected in series by a yoke system but are independently operated by the separate controllers. This provides the capability of performing either cyclic axial triaxial (called cyclic triaxial in the geotechnical literature), cyclic torsional triaxial, or combined cyclic axial-torsional triaxial tests on soil specimens. Either axial and torsional mode can be operated monotonically or cyclically in either load or strain-controlled conditions. Additionally, if a combined cyclic axial-torsional triaxial test is run, an arbitrary phase angle between 0 to 360 degrees may be specified between the two modes. Very large accumulators are incorporated into the system (5 gallons feed, 2.5 gallons return oil), to provide good control and performance at large strains and large frequencies.

The measurement components consist of a thrust/torque load cell, a stroke transducer, a rotational transducer, a small strain transducer, an accelerometer, cell and pore water pressure transducers, digital indicators, XYY recorders and a strip recorder. The MTS thrust/torque load cell is capable of sensing simultaneously both axial load and torque, without the value of one mode influencing the other. The operating ranges are 1000 lb axial force and 500 in-lb torque, respectively, with a linearity of 0.15% full range output (FRO). The MTS stroke transducer is a LVDT (Linear Variable Differential Transformer) with a range of  $\pm 5$  inches and a linearity of 0.5% FRO. The small strain transducer is an LVDT manufactured by Trans-Tek Inc. Model 350-010 with an operating range of  $\pm 0.1$  inches and a linearity of 0.5% FRO. The pore pressure transducers were model 710 by Schaevitz with a linearity of 0.5% and operating ranges varying depending on the pressures used; however, the highest range used was 250 psi. The accelerometer was model LSBC-2 by Schaevitz with a range of 2 g and a linearity of 0.05% FRO. Table 4.2 lists the capabilities of range 1 (the biggest), range 4 (the smallest) and the resolution of range 4 for the measurement components in this study. The axial and torsional displacement transducers are those that come with the

actuator. Due to the small values of rotation angles used and the fact that the rotation transducer is located far from the samples, corrections to obtain the true rotation had to be made by measuring the compliance of the system. Corrections for axial compliance were not necessary because they were very small. The small strain displacement transducer necessary for very small amounts of deformations was externally mounted as close to the specimen as possible.

Problems can occur when trying to run strain-controlled CyT-CAU on samples in which the torque varies during the test due to the sample softening as the pwp increases. If the decrease of the torque is substantial, then the torsional compliance correction factor is not constant and the test is not strain-controlled anymore. This problem is particularly important when large values of torque are present (about 15 in-lb or more), together with large pwp ratios. This occurs mainly in tests on dilative samples. When such conditions exist, the strain-controlled CyT-CAU cannot be used to acquire quantitative information on pwp buildup versus number of cycles. The effect of this problem on the tests reported herein was negligible because no significant degradation of the torque occurred before triggering, and also because the torque values involved were very small (less than 5 in-lb).



Excess pwp within the specimens was measured by means of the very stiff pressure transducer already mentioned. It was attached to a custom-built small stainless-steel solid block with 1/16 inch holes, directly connected to the triaxial cell and located very close to the specimen. This block enabled simultaneous measurements at both specimen top and bottom for fast pwp equalization throughout the soil. Also, flushing of this block was very easy, thereby aiding the de-airing and saturation process.

The accelerometer was used for tests involving very fast flow failures. In computing axial stress during liquefaction failure, the axial force due to the inertia of everything below the load measuring membrane of the load transducer is subtracted from the measured axial load. This inertial force is obtained as  $(m \times a)$ , where  $m$  = mass of all parts (including loading piston and top cap) located between load sensor of transducer and specimen, and  $a$  = measured acceleration of the piston. This mass is obtained in a separate measurement without soil, by applying varying accelerations to a free load cell and plotting measured force versus measured acceleration. The output of this accelerometer was recorded directly and did not go through any of the MTS controlling channels.

The triaxial cell pressure was monitored by means of two instruments: a high accuracy pressure gauge (Heise model CMM), and a pressure transducer of the same type as described as above for the pwp. Having continuous cell pressure readings using the transducer enabled determination of the true cell pressure during the test. This becomes very important at low pressures, because small pressure fluctuations were noted, and also because the cell pressure sometimes changes during fast flow failure, as the piston rod suddenly plunges into the cell and the pressure regulators are not fast enough to discharge the induced excess cell pressure.

The axial load, torque, axial and angular displacement transducers were calibrated by MTS using their calibration standards. The pressure transducers were calibrated using a 36 inch mercury well type manometer accurate to  $\pm 0.2$  psi, and a 400 psi pressure gauge (Heise model CMM) with a maximum nonlinearity and hysteresis of 0.1%. The accelerometer was calibrated simply by noting output values when placing it vertically in both directions.

In order to perform combined axial-torsional tests on the MTS load frame, triaxial cells specially designed and manufactured by Geotechnical Equipment Corporation were used for all tests (Fig. 4.7). These cells have special features

for cyclic axial/torsional tests, such as precise axial alignment of the plattens, the mounting of sintered bronze porous stones directly to the plattens, precision axial-torsional bearings and air bushings, and stiff stainless steel construction. The flexible tubing used was manufactured by Nylo-Seal and it does not expand much under pressure; it also has a burst pressure of 750 psi. The piston entering the triaxial cell rides on an air bearing that is opened just before testing in order to reduce errors in load readings due to friction. The piston rod is screwed directly to the top cap, thereby ensuring good contact. The brass porous stones have different coarseness depending on the type of sand tested; they are screwed into the triaxial cell end plattens to avoid any slippage of the porous stones during torsional loading. In order to consolidate isotropically a soil specimen within this cell, it is necessary to compensate with weights for the cell pressure not acting on the piston rod as this is screwed directly to the top cap.

During cyclic shearing, all parameters were recorded automatically on an 18 channel light pen oscillographic FO-CRT (Fiber Optic Cathode Ray Tube) stripchart recorder (Honeywell Model 1858 Visicorder), and on two XYY recorders (Hewlett Packard Model 7046A). These were digitized

manually and input into a computer program to obtain the necessary information and plots.

#### 4.4 Descriptions of Tests

Six types of undrained cyclic and monotonic tests were used in this research. The monotonic tests applied compression loading to (i) isotropically consolidated samples ( $\overline{CIU}$ ), and (ii) anisotropically consolidated samples ( $\overline{CAU}$ ). Some of these monotonic tests were run strain-controlled while others were load-controlled. The cyclic tests included (iii) threshold strain ( $\overline{TS}$ ), (iv) load-controlled cyclic triaxial on anisotropically consolidated samples ( $\overline{CCAU}$ ), (v) strain-controlled cyclic torsional tests on isotropically consolidated samples ( $\text{CyT-}\overline{CIU}$ ), and vi) strain-controlled cyclic torsional tests on anisotropically consolidated samples ( $\text{CyT-}\overline{CAU}$ ). Most of the experiments were of the  $\text{CyT-}\overline{CAU}$  type, which gives information on pwp buildup before triggering, conditions at triggering, and steady-state conditions after triggering.

Some problems were found when running the strain-controlled  $\overline{CIU}$  and  $\overline{CAU}$  monotonic tests, which did not exist in the corresponding load-controlled tests. Due to the fact that a small weight needs to be added to the piston rod to ensure isotropic conditions, and also considering

that the piston rod is directly screwed to the cap, all the tests were started in the load-controlled mode of the MTS. When switching later to strain-controlled mode, sometimes a minute amount of permanent vertical deformation is applied by the equipment, causing the vertical load, first to increase and then to decrease below its original value as the sample tends to consolidate further. For this reason, performing good monotonic strain-controlled tests in which the axial load did not decrease or decreased very little when switching mode required much care, which would not have been necessary if a traditional triaxial compression frame had been used.

The CTU test is the traditional undrained triaxial compression test of the geotechnical literature. It was performed on the MTS system using either load or strain-controlled mode. In load-controlled tests, the loading rate was usually between 8 lb/min and 1 lb/min depending on the magnitude of the axial force. In strain-controlled tests the strain rate was usually around 0.025 in/min in order to get shearing of the sample to steady-state conditions in roughly 45 minutes. Both rates were considered to be sufficiently slow to guarantee pwp equalization throughout the sample for the types of sands tested. Loading was carried on until failure had been

reached and large strains has occurred. The CAU test was performed in the same way as the CU, except that the sample was consolidated anisotropically to the desired value of  $K_c = \bar{\sigma}_{1c}/\bar{\sigma}_{3c}$  before undrained shearing.

The threshold strain test (TS) methodology is based on previous work done at RPI (Dobry et al. 1981a, 1982; Dyvik et al., 1984; Thomas et al., 1985). It consists of running a succession of short undrained cyclic sequences of 5 sinusoidal axial strain cycles at a frequency dependent on the material (usually between 0.25 and 0.01 Hz); followed by opening the drains and allowing for reconsolidation between sequences. Each sequence was run at a higher cyclic axial strain, until a residual pwp greater than zero was measured. The cyclic axial strain needed to induce this small residual pwp is the axial threshold strain  $\epsilon_{ct}$ . The threshold cyclic shear strain was calculated from  $\gamma_t = 1.5 \epsilon_{ct}$ , which assumes constant volume testing for isotropic or cross-anisotropic soil. This is not a destructive test and therefore the sample can be used again for flow failure.

The cyclic triaxial tests on anisotropically consolidated specimens (CCAU) followed the same general procedure as originally developed by Lee and Seed (1967), and consisted of consolidating the sample to a desired value

of  $K_c$  and then applying a constant axial cyclic shear stress in undrained conditions until failure occurred.

The CyT-CTU and CyT-CAU tests are really two versions of the same type of experiment, conducted on isotropically and anisotropically consolidated samples, respectively. They were carried out by consolidating the soil in load control to the desired value of  $K_c$  ( $K_c=1$  for CyT-CTU or  $K_c > 1$  for CyT-CAU), followed by undrained cyclic loading. This undrained cyclic torsional loading was done in the strain-controlled mode (constant cyclic angle of torque), while the actuator was operated simultaneously in the load-controlled mode to keep the axial stress  $\bar{\sigma}_1$  approximately a constant and equal to  $\bar{\sigma}_{1c}$ . The CyT-CAU experiments were carried on until failure had been triggered and steady state conditions reached. The CyT-CTU experiments were carried on until  $r_u=1.00$  was reached. The frequency used for all these tests was again dependent on the permeability of the material; it was 0.25 Hz for Lagunillas sands A, B, C; 0.1 Hz for Ottawa F125 sand, and 0.01 Hz for San Fernando Dam sand SF7. The appropriate testing frequency was selected for each sand after measuring the time needed for primary consolidation during the isotropic consolidation phase.

specimen.

#### 4.5 Guidelines for Flow Failure Laboratory Testing

Previous results on dilative, isotropically consolidated sands indicate that the relation between pwp and cyclic strain in cyclic strain-controlled tests on these soils is not significantly affected by the specimen preparation technique (Section 2.5). The validity of a similar conclusion for anisotropically consolidated contractive sands was verified in this work by using two different specimen preparation techniques. In this way, the influence of preparation technique on the locations of the SSL lines could also be studied. Some researchers have found different SSL for different specimen preparation methods (Donnely, 1980; Di Gregorio, 1981; Dennis, 1988), while Castro et al. (1982), GEI (1988) and Poulos et al. (1985, 1988) have reported results which were unaffected by the sample preparation technique.

The main method used to prepare specimens in this work was moist tamping using the undercompaction procedure as developed by Ladd (1978). The second method used was wet pluviation, which will be called here sedimentation. However, the sedimentation procedure was only used in four tests conducted on the SF7 sand.



All CyT-CAU and CyT-CTU tests reported herein were on solid cylindrical specimens. Thus the distribution of torsionally-induced cyclic shear stresses  $\tau_{cy}$  on the horizontal plane are not known. The cyclic shear strain  $\gamma_{cy}$  also varies with radius; however, work by Pierce (1985) indicates that a consistent representative cyclic shear strain is  $\gamma_{cy} = (2/3) \gamma_{cp}$ . Here  $\gamma_{cp}$  is the peripheral shear strain in torsional cyclic tests on solid cylindrical specimens, calculated from the cyclic angle of torque with the equation

$$\gamma_{cp} = \frac{\theta_c r}{L}$$

where  $\theta_c$  is the cyclic angle of torque,  $r$  the specimen radius and  $L$  its length. Pierce (1985) showed that  $\gamma_{cy} = (2/3) \gamma_{cp}$  is the uniform cyclic shear strain that would produce the same pwp in an identical specimen. It must be emphasized that the steady-state parameters obtained from the flow failure stage are not affected by the non-uniformity of the cyclic stresses and strains on the horizontal plane, as the flow is driven by the monotonic axial loads. Also, the digitized data points for cyclic tests are taken during zero torque crossings, for which the true stress conditions can be assumed uniform within the

The undercompaction moist tamping method is preferred because it produces a roughly uniform specimen and it is easy to prepare a sample to a target void ratio. Even though the undercompaction procedure was originally developed for stress-controlled cyclic triaxial tests, it was subsequently used for other types of tests in dilative sands (Dobry et al., 1982; Dyvik et al., 1984; Thomas et al., 1985). For cyclic torsional tests on contractive sands some modifications are needed to use this procedure, as described in the following paragraphs.

The undercompaction method is based on the fact that when a sample is compacted in layers, the bottom layers get more compactive energy than the top ones. Therefore, in order to achieve uniform density the bottom layers should be undercompacted with respect to the top layers.

This undercompaction can be done in different ways. For example, layers of equal height can be specified, with each layer having different weights in order to achieve final uniform density. Another procedure could be to have layers of equal weight but to use different compaction energy (combination of weight of tamper and number of tamps) for each layer in order to assure uniformity. The method used in this work was suggested by Ladd (1982), and it utilizes layers of equal weight and different height. The

height of each layer is monitored by using a tamper that can be precisely set to a specified tamping height with a dial gauge accurate to 0.001 inch (Fig. 4.8). In order to use this procedure successfully for liquefaction flow failure testing, three factors must be considered: compaction water content, undercompaction of first layer, and dry unit density.

Since the samples are prepared to be very loose and contractive, they are very sensitive to densification by vibrations during specimen preparation. To avoid densification, a certain amount of water has to be added to give the sample strength through capillary stresses. The method used to find the value of this compaction water content consists of using a small compaction mold of known volume. Different soil mixtures with varying water content are then poured in layers and tamped using specified weights (around 1500 grams tamped 25 times). After repeating the compaction process for different water contents, a curve similar to that shown in Fig. 4.9 is obtained. The compaction water content is selected from the flat part of the curve (Fig. 4.9), so that if the sample dries up due to evaporation, the layer will still have the same dry unit weight. Special considerations are necessary if the soil is silty because then the optimum water content is close to

100% saturation. The compaction water content value finally chosen for the F125 sand was 8% (Baziar, 1987); for sands A, B, and C it was 6% (Vasquez-Herrera et al., 1985); and for the SF7 sand it was 3% (GEI, 1988).

A method to compute the undercompaction value for the first layer ( $U_1$ ) was given by Ladd (1980), making use of stress-controlled cyclic triaxial tests on isotropically consolidated dilative sands.  $U_1$  is the amount by which the first layer is undercompacted so that when the last layer is placed, the sample will have about uniform density.

In this work  $U_1$  was selected using a method based on measuring the uniformity of the sample density with height with a gelatin technique. Emery et al. (1973) used gelatin to measure uniformity of density in sand specimens for cyclic triaxial, simple shear, and shaking table tests. The method used herein follows a suggestion by Woyzichowsky (1986). In this procedure, different sand specimens are prepared using different undercompaction values (for contractive loose sands, between  $U_1 = 0$  and 6%) and saturated with gelatin (concentration = 0.02 grams of gelatin per lcc of water). The triaxial cell, with the sample in it, is then placed in a cold room (10° C) for about 12 hours, to allow the gelatin to solidify. The sample is later cut in horizontal slices which more or less

correspond to the layers used when compacting the sample. Each layer is then trimmed to a specified radial dimensions by using a precisely machined cutting shoe of known area, so that the volume of each individual slice can be obtained by measuring the height of the slice. The individual sliced cylinders are then dried in the oven overnight and later weighed to determine their densities. The weight of the gelatin powder is accounted for in these calculations of the sample density. The densities of the layers were compared and the value of undercompaction selected was that producing the most uniform sample. Figure 4.10 shows the uniformity of three samples with different  $U_1$ . It can be seen that the void ratio distribution is more uniform when  $U_1 = 3\%$ . More details of this technique can be found in Baziar (1987). This selected undercompaction value is dependent on the target initial dry density, and if a different dry density is desired a new  $U_1$  should be determined using the procedure described above.

Since the samples are compacted moist and very loose, the subsequent saturation of the specimen under cell pressure breaks the capillary stresses and tends to collapse a small amount of sand in the radial direction; this radius reduction is not observable by the naked eye. The measured void ratio is very sensitive to small variations of the

measured radius of the soil specimen, and this in turn is crucial for the determination of the SSL of that soil. The magnitude of this collapse depends on the initial dry density and the compaction water content, and it varies from test to test. Therefore, the void ratio of the sample must be determined after the sample has been saturated. This is not the case for dense samples, since at these higher densities collapse does not occur when the specimen is saturated.

The correct evaluation of the void ratio of the specimen can be accomplished using either of two procedures. Procedure 1 involves measuring the height and diameter of the soil specimen after saturation, while Procedure 2 accomplishes this by measuring the water content of the specimen after the end of the test, and obtaining the sample diameter indirectly from this water content. Both methods give reasonable results, and either can be selected depending on the type of soil and the equipment involved. Procedure 1 involves considerable more time and work because the cell water has to be emptied, the sample measured, and the cell water filled again. It also involves having very accurate vacuum regulators in order to maintain the effective stress on the sample during the highest measurement and diameter. Procedure 2 is faster but

involves some careful steps that, if not properly done, can make the whole test useless. In the second method, after the sample has failed, the burette is opened and reconsolidation is allowed. Then specimen drainage values are closed and the specimen is quickly and carefully taken apart in order to obtain a water content using the whole sample. The void ratio before undrained cyclic loading is calculated from the amount of water expelled during reconsolidation, and the water content and dry weight of the specimen after the test. The measured height of the specimen before the test is used to determine the initial radius and area in order to determine the axial stresses and perimeter strains.

The F125 sand samples had their void ratio obtained in both ways, while for the SF7 sand the determinations were conducted using only Procedure 2. Unfortunately, sands A, B, and C, tested at the beginning of this research, used a method that measured diameters before saturation, and therefore the void ratios are not very accurate for these sands, with errors in the void ratio as high as 0.1. Procedure 1 is best suited for sands that have nonplastic silt or are narrowly graded (such as F125 Sand); whereas Procedure 2 is best for samples with plastic silts or better graded materials (such as SF7 sand).

Since a great number of tests involved torsional loading, the specimens needed rough ends to transmit torque. These end restraint effects are known to cause problems such as stress and strain nonuniformities (Shockley and Alvin, 1960; Taylor, 1941; Rowe and Barden, 1964; Bishop and Henkel, 1962; Kirkpatrick and Belshaw, 1968). If the height-to-diameter ratio is such that  $2.0 < L/d < 3.0$  then the average stresses and strains can be assumed to be more uniform (Bishop and Green, 1965).

Another problem that may arise is that if coarse porous stones are used, an extra amount of soil must be added to compensate for the grains that get caught in the voids of these stones. These corrections will result in the top and bottom layers having different amount of soil than the other layers. Unfortunately, the amounts of soil that penetrate both porous stones varies from test to test, and thus the void ratio measurements are affected in a random manner. This correction can be minimized by using a finer grained porous stone. Different grades of sintered bronze porous materials are available, and the proper one to be used is that with sintered grains slightly larger than the tested sand grain size. If this is done, it is possible to eliminate the stone correction completely, and the calculated void ratio will be closer to the true void ratio



of the sample. This method was used to select appropriate porous stones for the F125 and SF7 sands, which could then be tested without the need for stone correction; unfortunately, this was not the case for sands A, B, and C, which were tested at the beginning of the research.

#### 4.6 Moist Tamping and Sedimentation Sample Preparation Procedures

The specimens produced by the moist tamping undercompaction method and used in this work were about 4 inches in height and 2 inches in diameter. The triaxial piston and top cap assembly was installed on the triaxial cell at the outset of the process of assembling the soil specimen, and a carefully machined steel dummy was placed between the top caps. A dial gauge was then locked into position on the piston rod; in this manner the correct specimen height was known at all times. Following this, a membrane was stretched over a carefully machined brass mold in which the sample was to be placed in layers.

A sufficient amount of sand was first dried as much as possible in room temperature and then its lumps were broken down by sieving. The weight of water previously calculated from the selected compaction water content was added to the sand and thoroughly homogenized and mixed inside an airtight

plastic bag. The amount of soil corresponding to each of the six layers of the specimens were then placed in six small airtight plastic bags.

Each layer was added in two steps, each one requiring mixing and spreading in order to eliminate any voids. After all the soil for the layer had been placed, the layer was tamped by using a prescribed lift. Since the top surface of each layer was left smooth after tamping, the soil was scarified before adding the next layer, so as to roughen the contact between layers and to avoid slippage when the axial and torsional loads are applied to the specimen during the test. Good contact between the top cap and the top layer was insured by lowering the piston rod to a predefined position where the sample was to have a height of 4 inches; this lowering was done by careful tamping of the piston rod.

After the specimen was completely formed, vacuum was applied to the soil to a value equal to the effective stress during backpressuring to give it additional strength; and the cell was filled with deaired water. A cell pressure of 3 psi was then applied to the soil while the vacuum was released. The specimen was saturated next. In order to insure good saturation, carbon dioxide ( $\text{CO}_2$ ) was flushed through the sample for one hour; the  $\text{CO}_2$  displaces the air and is substantially more soluble in water than air.

Deaired and dionized water was then percolated slowly from the bottom up until it displaced the  $\text{CO}_2$  (this process also took about an hour). The specimen was then backpressured overnight to a value that varied between 27 psi and 47 psi; however, the effective cell pressure was always kept constant and equal to 3 psi.

Next day the saturation of the soil was verified by Skempton's B parameter, which was checked prior to consolidation. If  $B < 0.95$ , the specimen was left longer under backpressure until  $B > 0.95$  was achieved. After saturation, the specimen was isotropically consolidated to the required pressure  $\bar{\sigma}_{3c}$  before hooking the triaxial cell to the MTS loading machine. If the test was  $\overline{\text{CIU}}$  or  $\text{CyT-}\overline{\text{CIU}}$ , the specimen was then ready for undrained loading. If the test was  $\overline{\text{CAU}}$  or  $\text{CyT-}\overline{\text{CAU}}$ , additional consolidation was performed on the MTS machine under the deviator stress  $\bar{\sigma}_{1c} - \bar{\sigma}_{3c}$ . Finally, the drainage valves were closed and the specimen failed by application of undrained static or cyclic loading.

A few samples of SF7 sand were prepared using a sedimentation method, in order to create a soil fabric similar to the one found in situ where soil has been deposited through water by nature (alluvial, lacustrine and marine deposits) and by man (hydraulic fills) This

preparation procedure has some points in common with that of the undercompaction method already described, but the specimen is formed in a different manner. In this method the mold with the stretched membrane was filled up with boiled deaired water. Sand layers were then formed by dumping equal weights of soil and waiting some time for sedimentation; this time interval was always greater than 30 minutes. When enough soil was added to reach the top of the mold, the placement of soil stopped and the surface was leveled with a fine sharp blade. The triaxial top cap and assembly was then locked and the piston lowered enough to insure good contact between the soil and the top cap. Then the effective cell pressure (3 psi) was applied by vacuum to the sample which was allowed to consolidate. Specimens with very high average void ratios could be prepared by this method, but a specific void ratio could not be targeted. After this fast consolidation period the dimensions of the sample were measured and the cell filled with water. The following steps were the same as in the previous method.

Table 4.1. Properties of Soils Tested

Soil Type	Fine Content (%)	$G_s$	$C_u$	$D_{10}$ (mm)	$D_{50}$ (mm)	Particle Shape
Sand A	13	2.64	2.80	0.07	0.150	Subangular to Angular
Sand B	32	2.64	2.50	0.04	0.090	Subangular to Angular
Sand C	63	2.64	—	$< 0.075$	$< 0.090$	Subangular to Angular
F125	12	2.65	1.80	0.065	0.100	Subangular to Angular
SF7	50.5	2.69	17.0	0.005	0.075	Subangular to Angular

$$C_u = D_{60}/D_{10}$$

**Table 4.2. MTS Measurement Capabilities**

Parameter	Maximum Capability (Range 1)	Minimum Capability (Range 4)	Maximum Resolution (Range 4)
Axial Load	± 1000 lbs.	± 100 lbs.	± 0.1 lbs.
Axial Stroke	± 5.0 inch.	± 0.5 inch.	± $5 \times 10^{-4}$ inch.
Axial Strain	± 0.1 inch.	± 0.01 inch.	± $1 \times 10^{-5}$ inch.
Torque	± 500 inch.-lbs.	± 50 inch.-lbs.	± 0.05 inch.-lbs.
Rotation	± 50 degrees	± 5 degrees	± 0.005 degrees
Pore Pressure	250 psi.	25 psi	0.025 psi

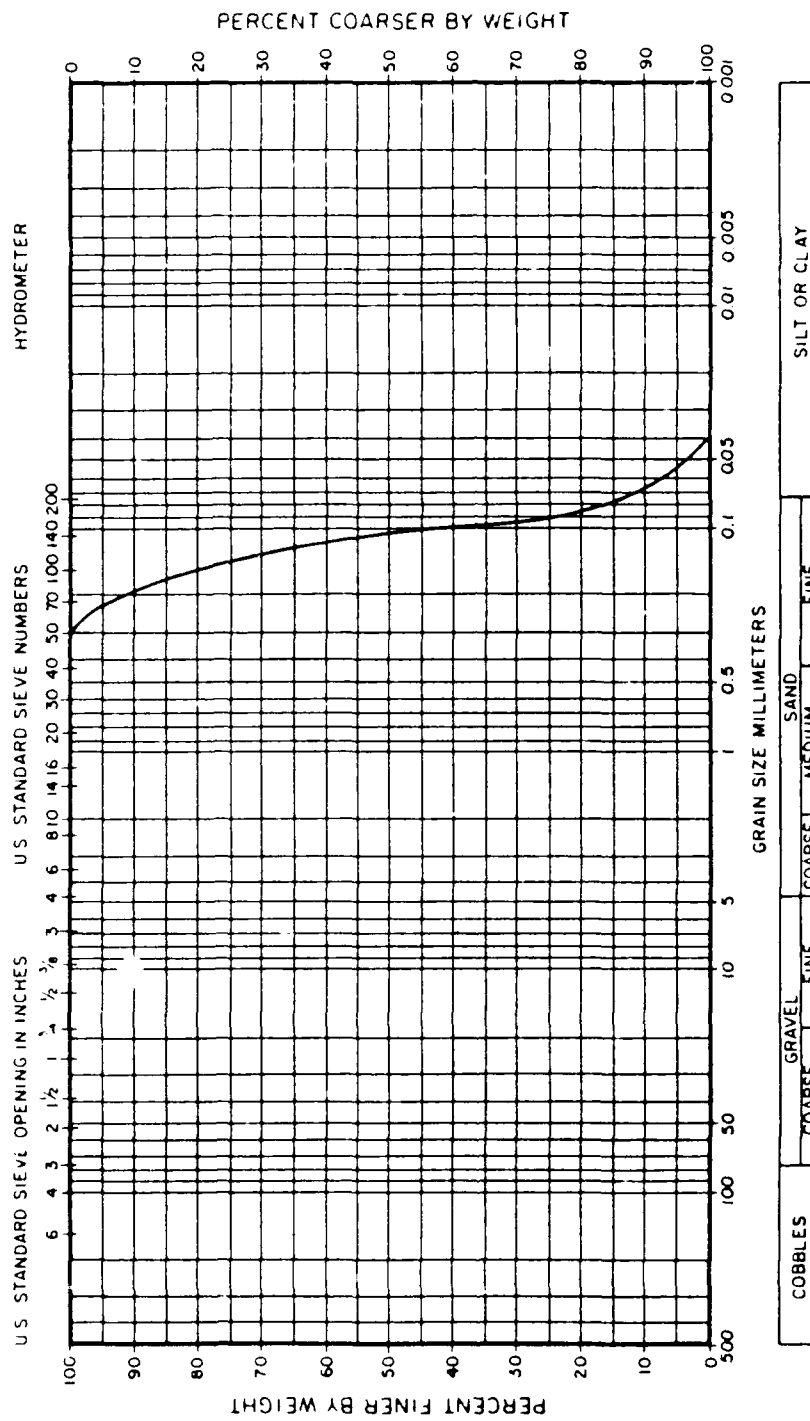


Fig. 4.1. Grain Size Distribution Curves for Ottawa Sand F125

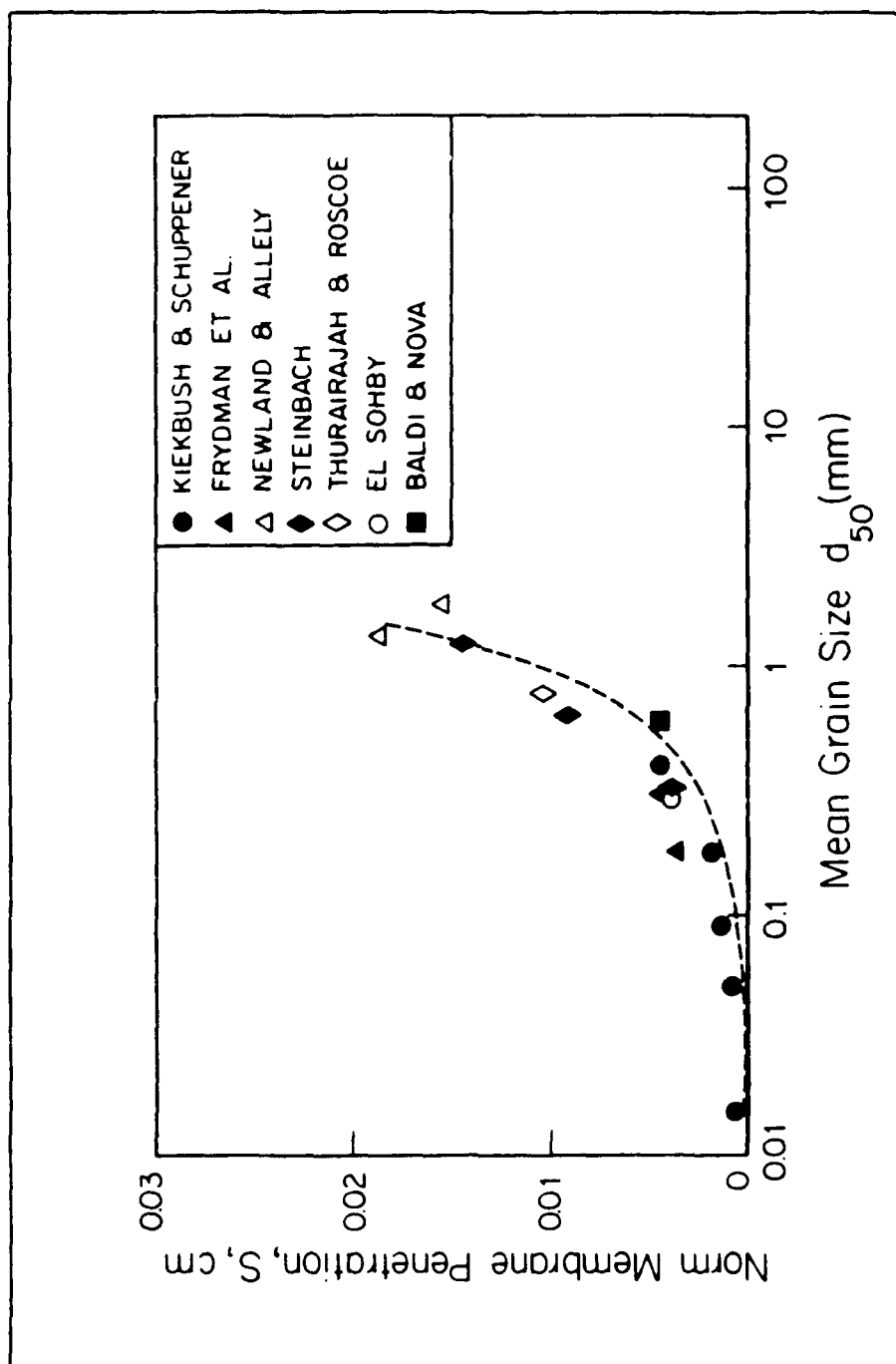


Fig. 4.2. Normalized Membrane Penetration for Various Sands (after Baldi and Nova, 1984)



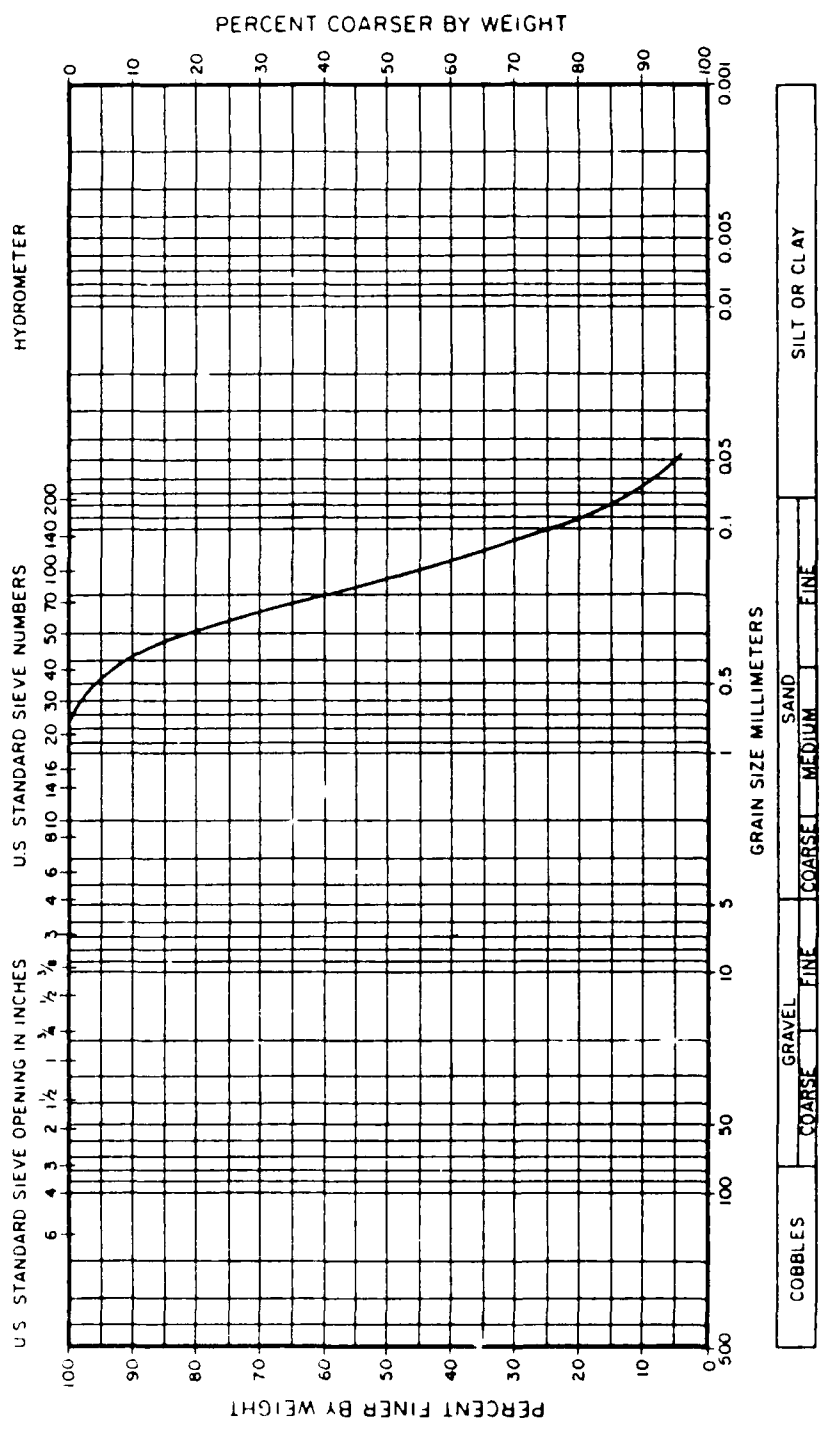


Fig. 4.3. Grain Size Distribution Curve for Sand A

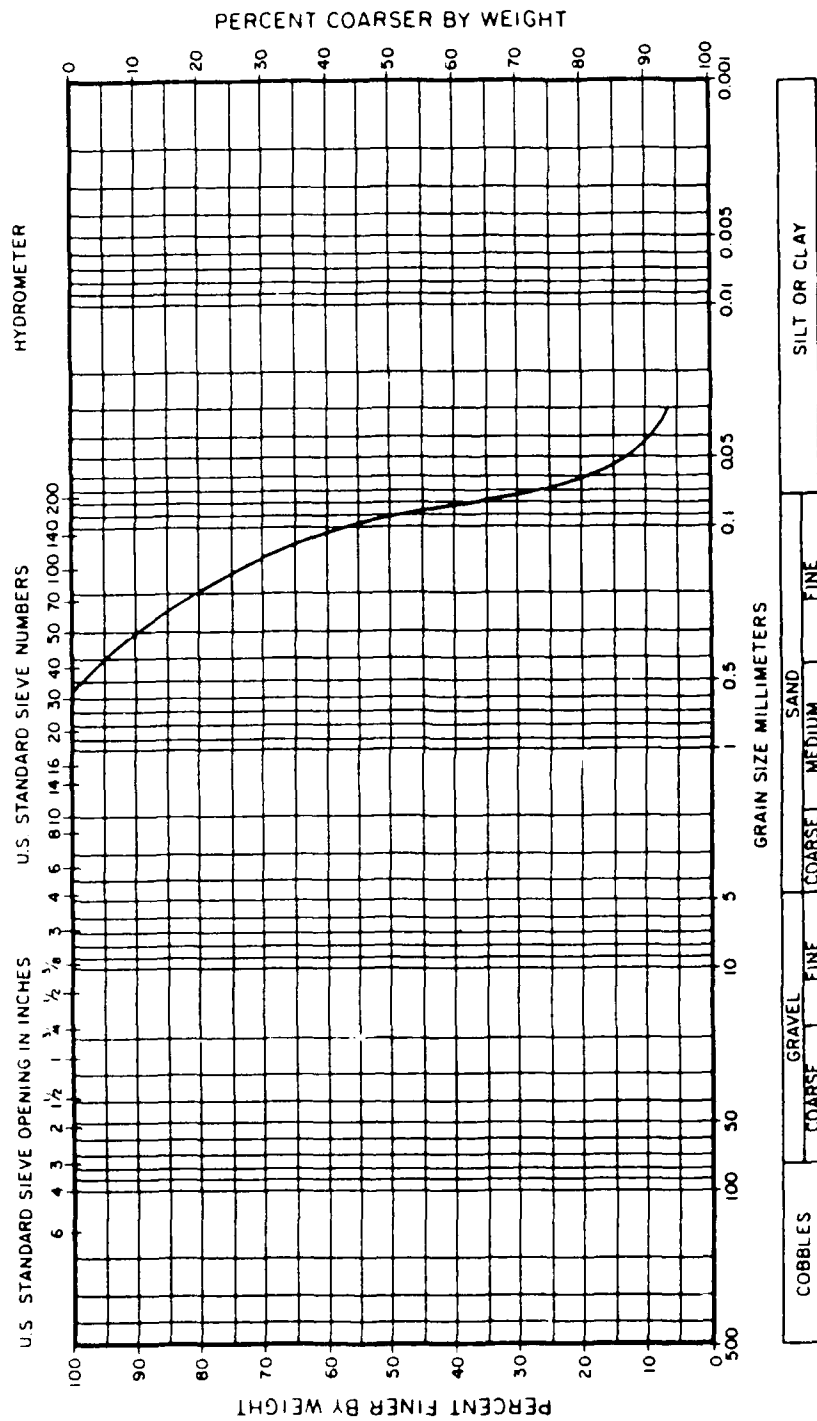


Fig. 4.4. Grain Size Distribution Curve for Sand B

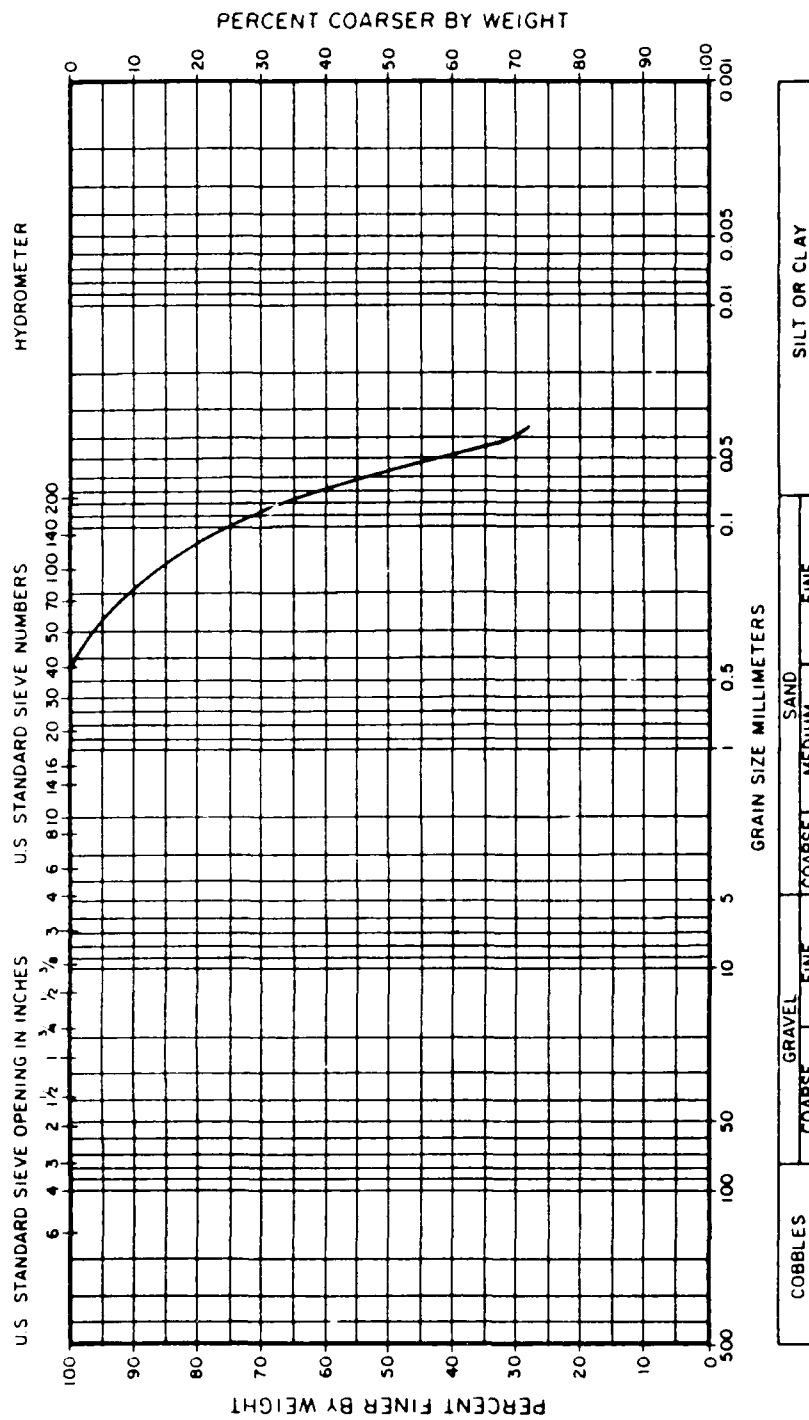


Fig. 4.5. Grain Size Distribution Curve for Sand C

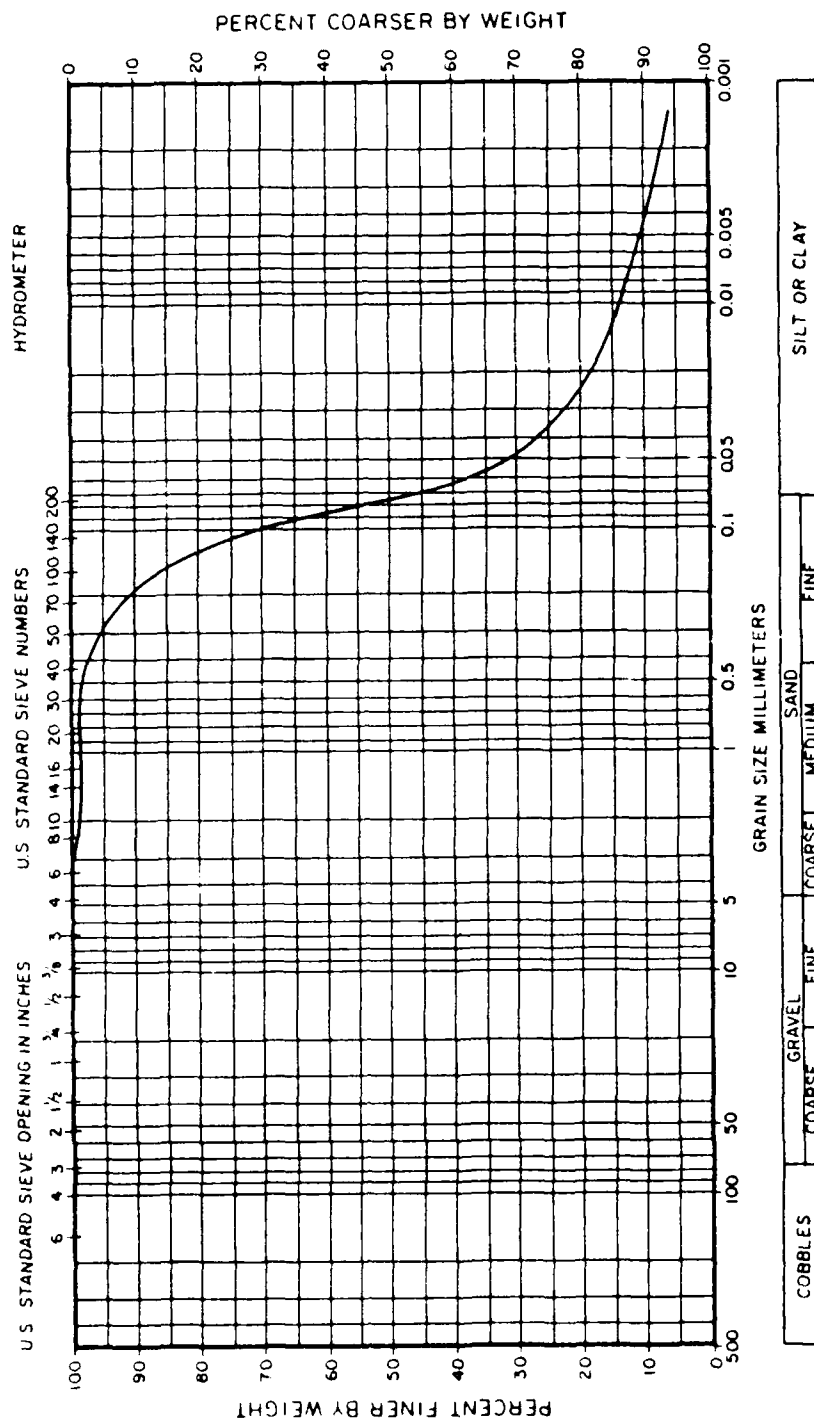


Fig. 4.6. Grain Size Distribution Curve for Sand SF7

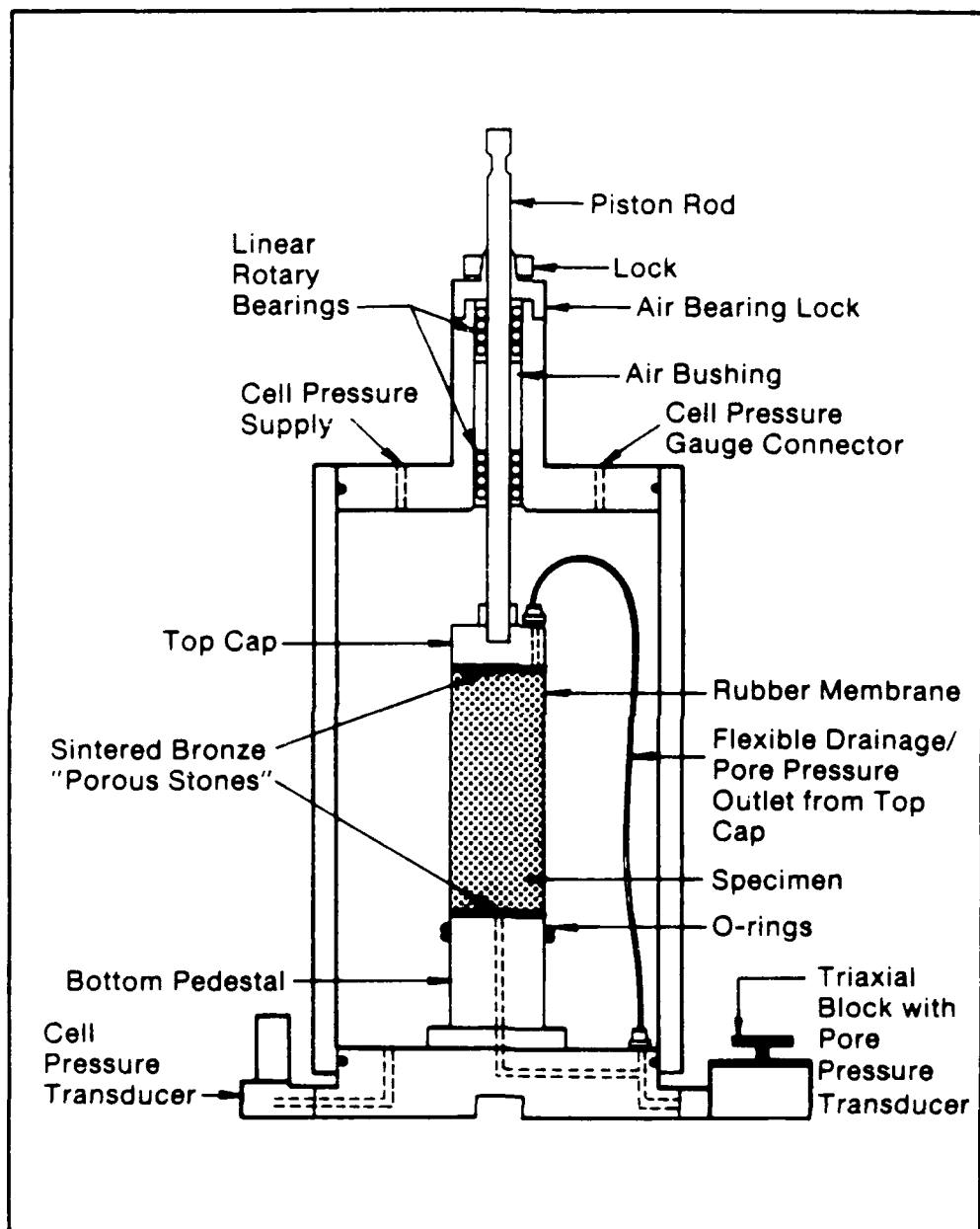


Fig. 4.7. Schematic Diagram of Cyclic Axial/Torsional Triaxial Cell

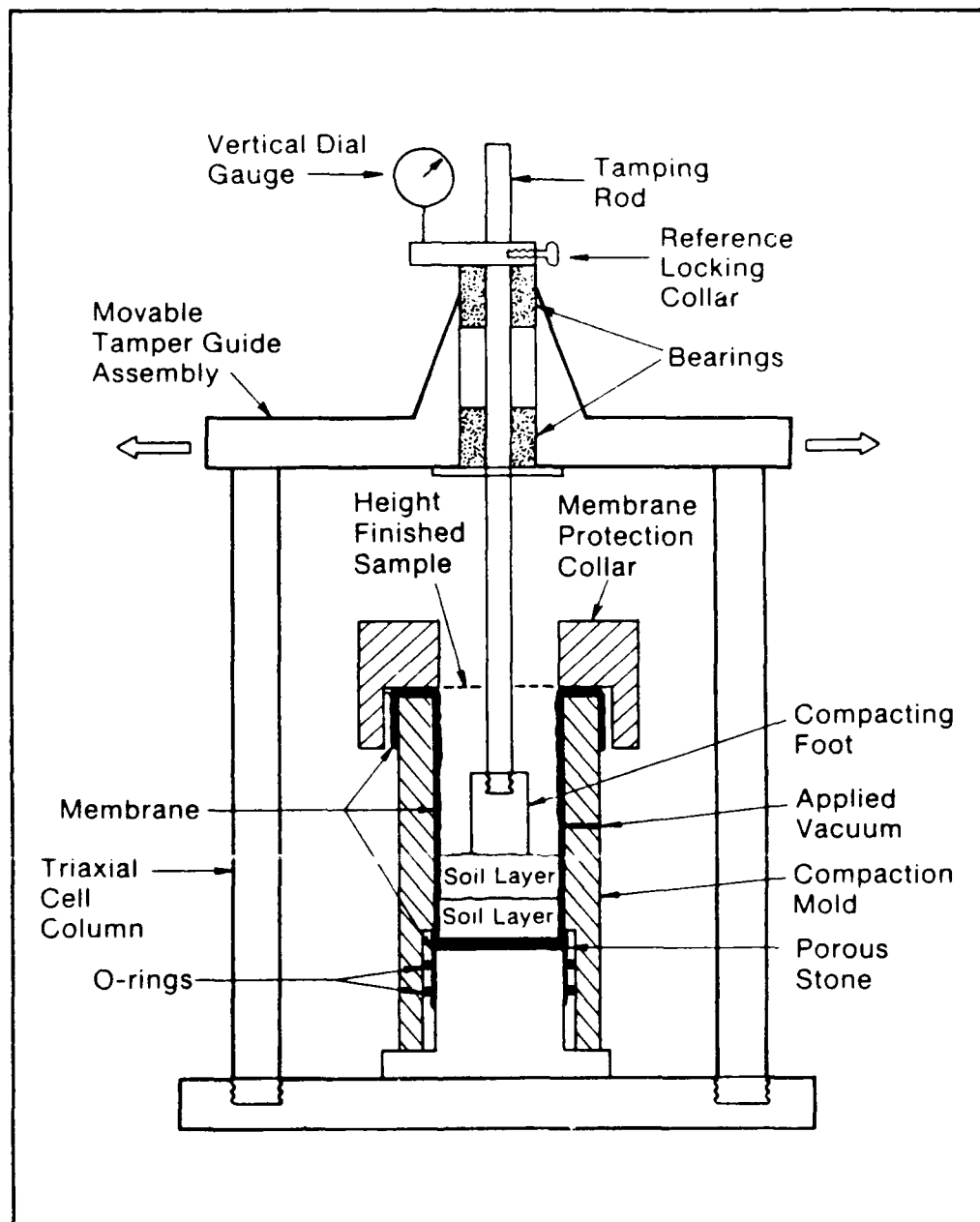
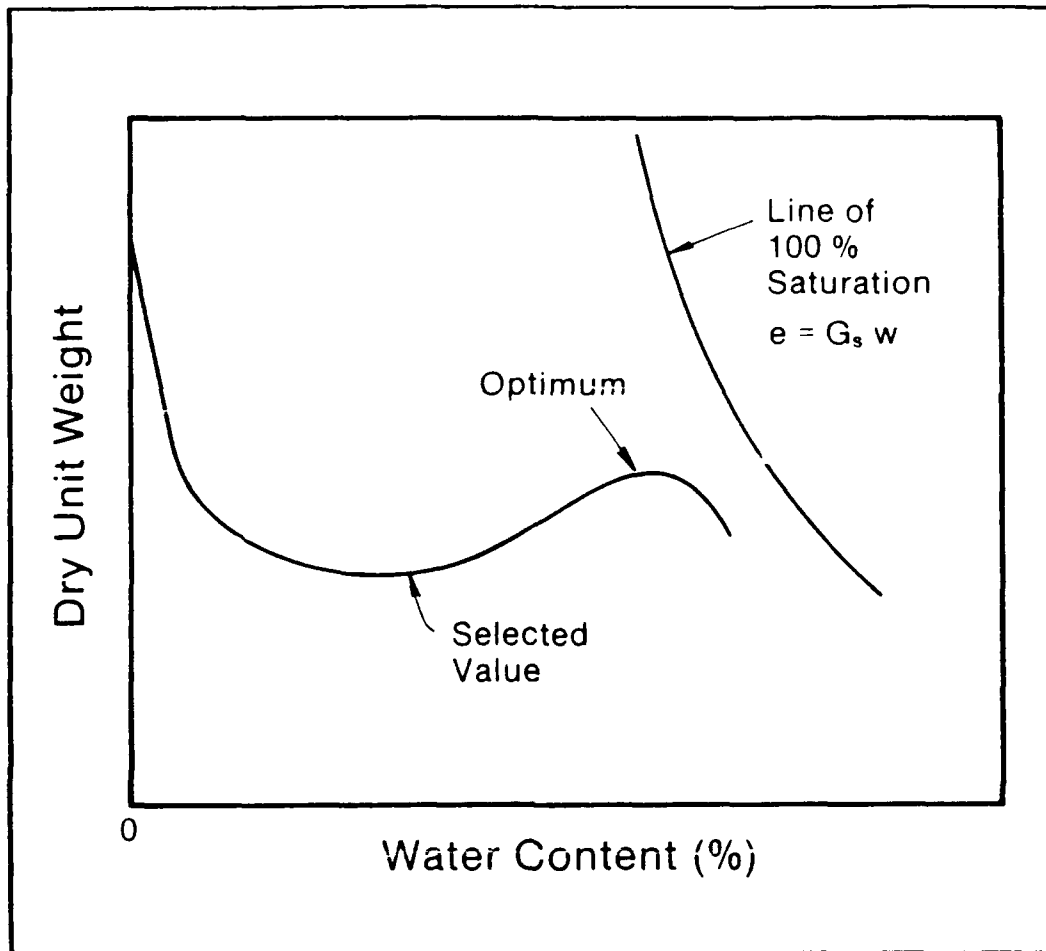
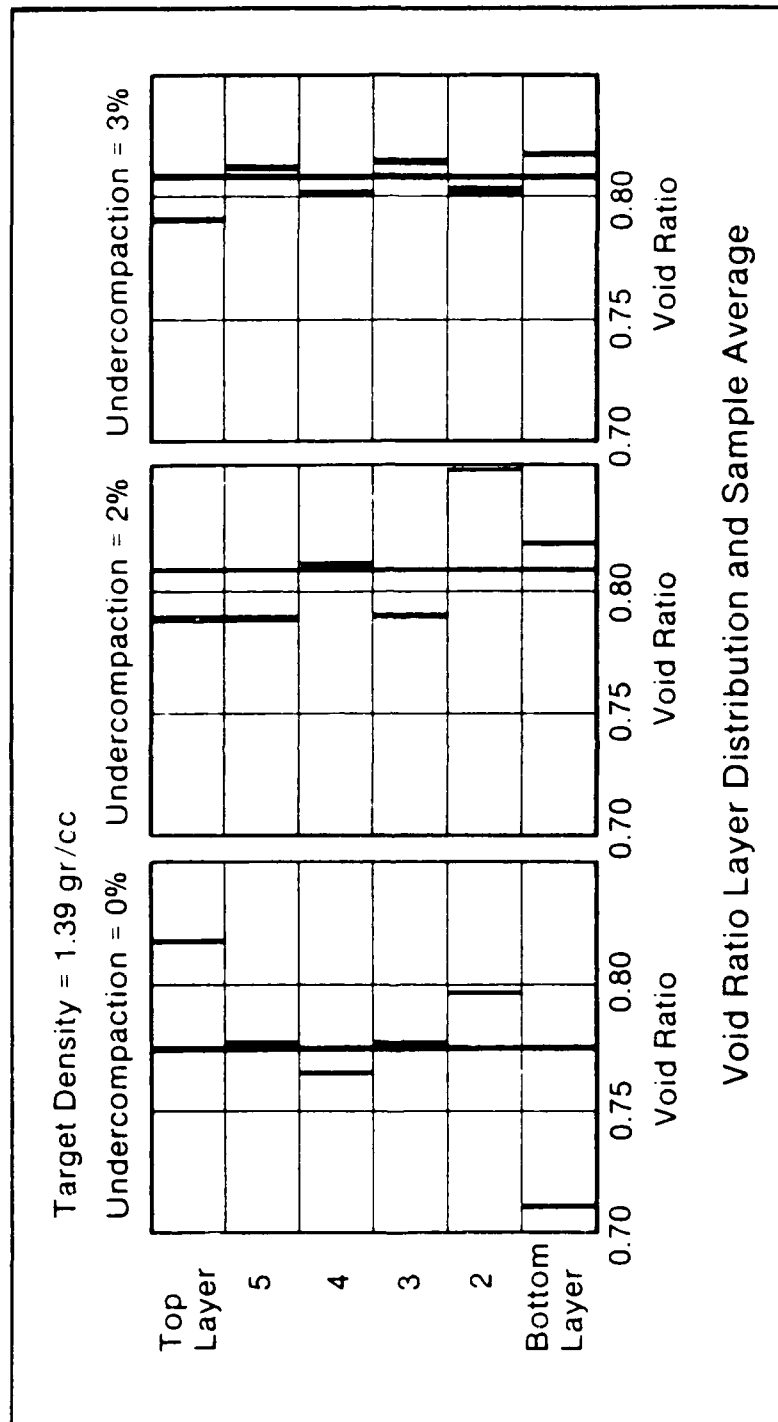


Fig. 4.8. Schematic Diagram of a Specimen Being Prepared in Compaction Mold Attached to the Triaxial Cell



**Fig. 4.9. Schematic of the Process for Selecting the Undercompaction Water Content**



**Fig. 4.10.** Determination of the Undercompaction of the First Layer for a Sample of Sand F125 (data from Baziar, 1987)



## CHAPTER 5

### TESTING PROGRAM

A total of 129 tests were conducted on various sands. Nine of these experiments were done on undisturbed samples while the remaining 120 tests were on remolded specimens. Both cyclic and monotonic tests were performed. Table 5.1 summarizes all types of tests on remolded specimens conducted for each sand. The overwhelming majority of these tests were done on contractive specimens, but some correspond to dilative ones. It can be observed that a large number of tests were done on the industrially produced F125 sand, followed by the 'real world' sands SF7, A, B, and C.

Since the emphasis of this research is to understand the mechanics involved in the liquefaction flow failure triggering of contractive sands due to seismic loading; the majority of the tests were cyclic CyT-~~CAU~~. With this test, information on both the steady-state shear strength characteristics of the sands and the increase of pwp and triggering due to cyclic loading, will be obtained successively in the same experiment. This permits an analysis of the two main issues of liquefaction flow failure evaluation: that of stability and that of triggering.

As indicated by Table 5.1, most of the tests were undrained cyclic torsional tests on anisotropically

consolidated specimens, CyT-CAU, with a smaller number of monotonic CIU and CAU tests also being performed. Four CyT-CIU experiments were also conducted to clarify the behavior of CyT-CAU tests at the limiting case of  $K_c = 1$ . Without exception, all these CyT-CAU and CyT-CIU tests were strain-controlled, with a constant amplitude of cyclic torsional shear strain  $\gamma_{cy}$  used in any given test. Seven cyclic axial triaxial tests (called "cyclic triaxial" in the literature) were also conducted at small values of cyclic strains to obtain a threshold strain of the soil,  $\gamma_t$ . In addition, selected CCAU (cyclic axial triaxial undrained loading on anisotropically consolidated specimen), CAD (drained triaxial compression on anisotropically consolidated specimen), CyT-CAU plus CAU (CyT-CAU test followed by monotonic triaxial test to failure without reconsolidation) tests, as well as CyT-CAU plus CAU tests with variable  $\gamma_{cy}$ , were performed.

The parameters studied that might affect the steady-state shear strength characteristics of the sands tested are shown in Table 5.2. As previously mentioned, tests were done on both contractive and dilative sands in order to see the differences among them and to complete the picture on the general behavior of sands. Both static and cyclic tests were done to see how they relate to each other.

The static monotonic tests were run both load-controlled and strain-controlled to study the effect of strain rate. A couple of drained monotonic tests were done to see if they defined the same SSL as the undrained experiments for sand F125. Some triaxial end restraint (smooth versus rough end caps) effects were also studied with sand F125 in order to see their influence on the testing procedures. The effect of sample fabric was studied on sand SF7 by comparing laboratory test results produced with samples prepared by two different methods, moist tamping using undercompaction and a wet raining technique that produced strongly layered specimens. Finally, the effects of void ratio  $e$ , consolidation stress  $\bar{\sigma}_{3c}$  and  $K_c$  were studied in depth for all three sands.

It must be added that, for sand SF7, steady-state shear strength results were also obtained independently by two other laboratories; GEI and Stanford University. Therefore, the influence of testing at different laboratories could also be evaluated for this sand.

The parameters used to study the pwp buildup and triggering of flow failure are shown in Table 5.3. Some of these parameters were already discussed in the previous paragraphs but in addition, the effect of void ratio,

confining pressure,  $K_c$  and cyclic shear strain on the pwp buildup and on  $n_t$ , were studied.

Table 5.4 shows the ranges of values for the parameters that were investigated using the cyclic CyT-CAU tests on contractive sands. The tables found in Appendix A detail the test parameters and results for each of the tests performed. Due to the differences in testing techniques, to problems with the equipment and the inherent problems present in any laboratory research effort, not all the parameters presented could be directly compared against each other. Therefore, in any of the plots to be presented in Chapters 6 and 7 the total number of tests of a specific type displayed may not match the total number of tests of that type performed.

Some particular experimental problems encountered were the following. The failure of some tests on the Fl25 sand were so fast that the recorder measuring pore pressure could not be read and therefore the value of  $\bar{p}$  at steady-state ( $\bar{p}_{us}$ ) could not be obtained, even though the steady-state shear strength was measured. Another typical problem was that concerning the method of void ratio determination, since in some of the initial tests of this research wrong void ratio measurements were conducted, and the correct void ratios could not be retrieved later. However, in these

tests useful parameters which are not sensitive to accurate void ratio measurements could still be determined and were used for the research, such as pwp, effective stress conditions at triggering,  $n_t$ , and  $u_t$ .

In order for a laboratory test to be a useful engineering tool, it must be performed in a correct manner. Flow failure testing is more complicated than most routine soil mechanics experiments, and thus the equipment used and the procedures followed to achieve these tests were already described in some detail in Chapter 4.

The laboratory shear strength results are discussed in Chapter 6, and they include information on the effective stress conditions at steady-state, effective stress conditions at triggering, and the effect of improper testing techniques on these results. The laboratory pwp buildup and triggering characteristics are presented in Chapter 7. This separation of laboratory test results into two chapters is due to the fact that Chapter 6 can be used to understand monotonic flow failures as well as cyclic flow failures, whereas the results of Chapter 7 are exclusively for flow failures caused by cyclic loading. This is not an arbitrary division, because flow failures are driven by the static shear stresses, whether caused by a seismic event or not. On the other hand, seismically induced flow failures are

triggered due to the pwp induced by the dynamic (cyclic) stresses and strains.

Table 5.1. Numbers and Types of Tests Performed on Remolded Samples

Sand Type	$\overline{CIU}$	$\overline{CAU}$	$\overline{Cyt-CIU}$	$\overline{Cyt-CAU}$	$\overline{CCAU}$	Threshold Strain	CAD	$\frac{\overline{Cyt-CAU}}{\text{plus } \overline{CAU}}$	Variable $\gamma_{cy}$ $\overline{Cyt-CAU}$	Total
Sand A	3	1	0	21	0	1	0	0	0	26
Sand B	1	0	0	3	0	1	0	0	0	5
Sand C	2	0	0	3	0	1	0	0	0	6
Sand F125	8	1	4	36	1	2	2	1	1	56
Sand SF7	2	1	0	22	0	2	0	0	0	27
Total	16	3	4	85	1	7	2	1	1	120

**Table 5.2. Parameters Studied for Laboratory Tests Shear Strength Results**

Sand Type	Dilative vs. Contractive	Static vs. Cyclic	Load vs. Strain Controlled	Drained vs. Undrained	End Restraint Effects	Sample Fabric	e	$\bar{\sigma}_{3c}$	K <sub>c</sub>
Sand F125	✓	✓	✓	✓	✓		✓	✓	✓
Sand A	✓	✓					✓	✓	✓
Sand SF7	✓	✓	✓			✓	✓		✓



**Table 5.3. Parameters Studied for Cyclic Laboratory Test Results for Pore Water Pressure Buildup and Triggering**

Sand Type	Dilative vs. Contractive	Sample Fabric	e	$\bar{\sigma}_{3c}$	$K_c$	$\gamma_{cy}$	$n_t$
Sand F125	✓		✓	✓	✓	✓	✓
Sand A	✓		✓	✓	✓	✓	✓
Sand SF7	✓	✓	✓		✓	✓	✓

**Table 5.4. Ranges of Values for Parameters Studied with Cyclic CYT-CAU Tests on Contractive Sands**

Sand Type	e	$\bar{\sigma}_{3c}$ (Kg/cm <sup>2</sup> )	K <sub>c</sub>	$\gamma_{cy}$ (%)	n <sub>i</sub> (cycles)
Sand F125	0.75 - 0.83	0.5 - 5.5	1.0 - 2.9	0.007 - 0.4	1 - 2160
Sand A	0.71 - 0.84*	2.7 - 4.8	1.22 - 2.25	0.023 - 0.22	1 - 1223
Sand SF7	0.62 - 0.73	1	1.4 - 2.2	0.005 - 0.1	2 - 41

\* Not Accurate

CHAPTER 6  
SHEAR STRENGTH BEHAVIOR: RESULTS OF  
EXPERIMENTAL PROGRAM

6.1 General

This chapter presents the shear strength test results obtained on the several sands tested, in order to understand the behavior of anisotropically consolidated saturated contractive sands subjected to cyclic undrained loading. All experiments involved triggering of flow failure and subsequent large deformations in steady-state condition.

The majority of these flow failure tests performed were monotonic CIU and CAU and cyclic CyT-CAU tests. Therefore, it is useful to present first an example of results for each test type and for the three main sands used in this investigation. Typical experiments on sands A, Fl25 and SF7 are used for this purpose as described in the following paragraphs.

Figure 6.1 shows results of a monotonic triaxial compression test on an isotropically consolidated specimen of loose, contractive sand A (CIU test), consolidated under an all-around pressure  $\bar{\sigma}_{1c} = \bar{\sigma}_{3c} = 6.5 \text{ Kg/cm}^2$  to a void ratio  $e=0.76$ . That is, in this test,  $K_c = \bar{\sigma}_{1c}/\bar{\sigma}_{3c} = 1.0$ . The shear stress,  $q = 1/2 (\bar{\sigma}_1 - \bar{\sigma}_3)$ , which was initially zero after consolidation, was then increased in undrained

condition until a peak (triggering) point T was reached. After point T,  $q$  decreased very rapidly to the constant, steady-state or residual strength value,  $q = q_{us} = 0.52 \text{ Kg/cm}^2$ . The excess pore pressure ratio,  $r_u = u/\bar{\sigma}_{3c}$  in Fig. 6.1(b) increased all the time, even beyond point T, until it stabilized and remained constant at steady-state with a value of  $r_u = 0.935$ . Thus, during steady-state failure, identified in the figure by the letter S, unlimited strains developed under constant normal and shear stresses,  $\bar{\sigma}_{3us} = 0.42 \text{ Kg/cm}^2$  and  $q_{us} = 0.52 \text{ Kg/cm}^2$ . Figure 6.1(c) shows the effective stress path in  $\bar{p}$ - $q$  space; the stress path always curves to the left,  $q$  reaches a maximum at point T, and then decreases until the stress path arrives to point S, where it stays deforming in steady-state condition.

Figure 6.2 presents results of a monotonic triaxial compression loading test on an anisotropic sample of loose silty sand A (CAU test). It was anisotropically consolidated under principal stresses  $\bar{\sigma}_{1c} = 10.2 \text{ Kg/cm}^2$  and  $\bar{\sigma}_{3c} = 5.1 \text{ Kg/cm}^2$ ,  $K_c = 2.0$ . In this test, there is an applied static shear stress  $\tau_s = q_s = 1/2 (\bar{\sigma}_{1c} - \bar{\sigma}_{3c}) = 2.55 \text{ Kg/cm}^2$  before undrained loading starts. During undrained shearing,  $q$  increased slightly in Fig. 6.2(a) until a peak was reached at point T (triggering) with a value of  $q = 2.9 \text{ Kg/cm}^2$ ; then the strength decreased to the constant

steady-state value  $q = q_{us} = 1.30 \text{ Kg/cm}^2$ . This steady-state failure stage is entirely similar to that already described for the CTU test in Fig. 6.1; flow failure with unlimited strains at constant stresses  $\bar{\sigma}_{3us}$  and  $q_{us}$ .

It must be noted that in load-controlled monotonic tests such as those presented in Figs. 6.1 and 6.2, the sand goes from the triggering point T to large strains in a very short time, of the order of 1/3 to 1/2 seconds. Therefore, precise and quick response transducers and recording equipment are needed to perform the test. This presents a problem for data collection, whether done by a recorder or a computer. Since the pre-triggering part of the test is done very slowly, and the unannounced triggering occurs suddenly with everything changing rapidly afterwards, the data scanning has to be done using two vastly different rates. If only the slow rate is used, many readings occurring during failure will be missed. On the other hand, if the recording rate is too fast, the computer can run out of memory or the recorder out of paper before the test is over.

Figures 6.3 and 6.4 show results of a typical cyclic strain-controlled torsional triaxial test on an anisotropically consolidated specimen of loose silty sand A (CyT-CAU test). In this test,  $\bar{\sigma}_{1c} = 8.34 \text{ Kg/cm}^2$ ,  $\bar{\sigma}_{3c} = 4.07$

$\text{Kg/cm}^2$  ( $K_c = 2.05$ ) and the void ratio after consolidation is  $e = 0.75$ . The sample was cyclically sheared undrained in the torsional mode using a constant angle of rotation which created a representative torsional cyclic shear strain,  $\gamma_{cy} = 0.05\%$ . In this test, the pore pressure increased during cyclic straining while the locked in static stress remained constant,  $r_s = 0.5(\bar{\sigma}_c - \bar{\sigma}_{3c} = 2.13 \text{ Kg/cm}^2$ . At point T, after  $n = n_t = 11$  cycles, flow failure was triggered, the axial strain increased more than 20% in about 0.5 seconds,  $q$  decreased from its static value to its steady state shear strength,  $q = q_{us} = 0.99 \text{ Kg/cm}^2$ ; and the pore pressure ratio rose to its steady-state value  $r_u = 0.77$ . Point S in Figs. 6.3 and 6.4 correspond to the steady-state conditions, similar to the monotonic tests in Figs. 6.1 and 6.2. The same as those monotonic tests, during the steady-state flow triggered by cyclic loading in Fig. 6.3 the stresses also remained constant:  $\bar{\sigma} = \bar{\sigma}_{3us} = 0.93 \text{ Kg/cm}^2$  and  $q = q_{us} = 0.99 \text{ Kg/cm}^2$ .

Figures 6.5 through 6.8 include similar CIU, CAU, and CyT-CAU test results on sand Fl25. Figure 6.5 presents a CIU test on an isotropically consolidated contractive sand sample. The behavior is similar to that on sand A. After some loading, the sample exhibited a peak in the stress-strain curve when flow failure was triggered, after

which the sample developed very large strains in steady state condition. Triggering and steady-state flow were also observed in the CAU test on the same sand shown in Fig. 6.6. The cyclic CyT-CAU test on sand F125 shown in Figs. 6.7 and 6.8 were similar to those for sand A in Figs. 6.3 and 6.4.

CIU, CAU and CyT-CAU test results corresponding to sand SF7 are shown in Figs. 6.9 through 6.12.

Figure 6.9 shows a typical CIU experiment on this soil. The results are not as dramatic as those shown previously on sands A and F125, because now there is only a very small decrease in shear strength after triggering. The steady-state condition is not so clearly defined, because the stress-strain curve in Fig. 6.9(a) appears to continue decreasing without reaching a constant value even after an accumulated axial strain of 28%. The reason for this is the fact that the permeability of the sand was low enough to inhibit instantaneous pwp readings and pwp equalization throughout the sample right after flow failure was triggered. However, after some time during steady-state deformation a constant value of pwp was reached. The decreasing straight line of the stress-strain curve is a combination of two factors related to the speed of failure: the axial load staying nearly constant while the area of the specimen was changing with strain and the low permeability,

of the sand sample. This effect was not noticed in sands A, B or C because even though they had large amounts of fines, these fines were less plastic than those on sand SF7.

The values defining the steady-state condition in Figs. 6.9 to 6.11 were chosen by looking at the deformation velocity of the sample (not shown in the figures but read from the stripcharts) as it was noted that after a while it remained constant; after this point of constant velocity, the chosen point for steady-state conditions was when the pwp value became constant. The incorporation of the constant velocity criterion was explicitly taken into account for sands A and F125 because, when the stress-strain curve becomes flat, the velocity is constant and the pwp is also constant. It is important to note that Castro et al. (1982) include a constant velocity criterion in the definition of steady-state of deformation. This procedure insured consistent readings of load, stroke and pore pressure at steady-state and produced very reliable results when compared to those produced by other laboratories.

In order to prove that the fast straining rate involved in load controlled tests was the reason for the stress-strain curve being a decreasing straight line, a monotonic strain-rate controlled CAU test was also performed on sand SF7 and is shown in Fig. 6.10. The strain rate



during undrained loading was 0.5% axial strain per minute. The stress-strain curve now looks more familiar, with an almost constant plateau reached by both the stress-strain and the pore pressure curves at steady state.

A CyT-~~CAU~~ test on silty sand SF7 is shown in Figs. 6.11 and 6.12. Flow failure triggered in this anisotropically consolidated sample after a certain number of strain cycles, in a manner similar to those previously presented for sands A and F125. After triggering, the steady-state conditions were determined in the same manner as that for the ~~CTU~~ test.

## 6.2 The Steady State Lines

This section presents the steady-state lines (SSL) and steady-state strength envelopes for sands F125, A, B, C, and SF7. The results on the effective steady-state strength envelope will be shown first, followed by the SSL results.

The SSL is usually plotted either in semi-log plots of  $e - \bar{\sigma}_3$  and  $e - q$  spaces or, alternatively, in  $e - \bar{p}$  and  $e - q$  spaces. In these plots the SSL's can often be approximated by straight lines. The steady-state strength envelope is plotted in  $\bar{p}$ - $q$  space.

### 6.2.1 Results on Ottawa Sand F125

The steady-state strength envelope is plotted in Fig. 6.13 for all tests with sand F125. A unique steady-state failure envelope of angle  $\bar{\alpha}_{us} = 29^\circ$ , corresponding to a friction angle,  $\bar{\phi}_{us} = 33.6$ , is defined by the data points. Of particular importance is the fact that a unique steady-state strength envelope is obtained, unaffected by consolidation conditions (isotropic or anisotropic), type of test or stress path (monotonic or cyclic), with the envelope being independent of the value of  $K_c$ .

Figure 6.13 does not include all tests performed on sand F125. The reason has to do with the very fast speed of failure, where sometimes the strip chart recorder measuring the pwp was not running at a fast enough speed to catch the failure, and the value of  $u_{us}$  was not obtained; therefore,  $\bar{p}_{us}$  needed for Fig. 6.13 could not be computed. This problem did not occur with the triggering conditions because up to that point rate of the straining was very slow.

The SSL for sand F125 is plotted in Figs. 6.14 and 6.15 using the two different types of plots as graphs of  $\bar{p}$  vs  $e$ ,  $\bar{\sigma}_3$  vs  $e$  and  $q$  vs  $e$  at steady-state. Here again it can be observed that the steady state of deformation can be achieved from totally different types of tests, whether

cyclic or monotonic, and is unaffected by  $K_c$ . The steady-state shear strength is only dependent on the void ratio of the sand. The figures also show that due to the flatness of the SSL lines, and to the fact that strength is in logarithmic scale, small changes in void ratio produce large variations in shear strength. Therefore, if accurate values of  $\bar{p}_{us}$  or  $q_{us}$  are required, extremely accurate determinations of the void ratio are necessary.

Two drained laboratory tests were also performed on anisotropically consolidated samples (CAD tests). to see if the steady-state line is the same for drained and undrained testing. Both tests presented problems in measuring some parameters because the recorders were not turned on; however, a final value of void ratio and shear stress were made manually during the steady-state of deformation. The results are shown in Fig. 6.16, where it is apparent that the same line can be defined using drained as well as undrained laboratory tests. This confirms the results on other sands (Seed and Lee, 1967; Castro et al., 1988) that the SSL can be determined by using either drained or undrained tests if proper testing techniques are used.

### 6.2.2 Results on Sand A

The SSL for these three sands will not be presented in this section because the measured void ratio values are not correct; this effect will be discussed in more detail in the last section of this chapter. Since these wrong measurements of void ratios do not affect the steady-state strength envelope, these results for the three sands will be shown.

The steady-state strength envelope for sands A, B, and C are presented in Figure 6.17 where it can be seen that a constant value of  $\bar{\alpha}_{us} = 29^\circ$  is defined. The fact that these three sands have the same steady state strength envelope is probably due to the fact that these sands come from the same geologic condition and have similar grain size distribution curves but with varying silt content.

Since more extensive testing was carried out on sand A, these results are shown separately in Figure 6.18 where a more detailed description of the types of tests are given. It can clearly be seen that the unique steady-state strength envelope is not affected by the fact that the tests are monotonic or cyclic; and is also unaffected by the value of  $K_c$ .

### 6.2.3 Results on San Fernando Sand SF7

The steady-state strength envelope for sand SF7 is shown in Fig. 6.19. Again, a unique steady-state strength envelope  $\bar{\alpha}_{us} = 29^\circ$  is defined regardless of test type, of soil fabric (moist tamping versus sedimentation) or  $K_c$ . Even though the tests on sedimented samples plot somewhat lower than those tests using moist tamping samples, they are all very close among themselves and to the  $\bar{\alpha}_{us} = 29^\circ$  line. An identical value of  $\bar{\alpha}_{us} = 29^\circ$  was also obtained in this sand using many monotonic strain rate controlled tests by another laboratory (Castro et al., 1988). The accuracy of the results shown in Fig. 6.19 is exceptionally good considering that the values of  $\bar{p}_{us}$  range between 0.2 and 1.0  $\text{Kg/cm}^2$ .

The steady-state lines for sand SF7 are shown in Figs. 6.20 and 6.21. The sand specimens used were prepared by two different methods (moist tamping and sedimentation; see Section 4.6) and yielded two different but seemingly parallel SSL. The curve for moist tamping specimens in Fig. 6.21 includes results by two other laboratories (GEI, 1988; Seed et al., 1987). The laboratory results presented in these reports (GEI, 1988; Stanford University, presented by Seed et al., 1987) were done on samples prepared by moist tamping techniques similar, but not identical to those used

herein. This good agreement between the three laboratories gives added confidence to the validity of the results presented herein. The four samples prepared by the sedimentation procedure and included in Figs. 6.20 and 6.21 produced specimens that were substantially looser than those prepared by the moist tamping methods used at RPI, GEI and Stanford University. This difference is due to the internal structure of the specimens. The sedimented samples have an internal layering caused by the different sand size particles being deposited through water and settling at different times (the coarser particles first and the finer ones later). This sedimentation produces an internal stratigraphy, where the different layers have different void ratios within the sample, and with the overall average void ratio being larger than that of a homogenous moist tamped specimen, as illustrated in the figures. This is not contradictory with the basic assumption, validated by Figs. 6.20 - 6.21, that the SSL is unaffected by fabric and specimen preparation details, provided that this fabric is roughly homogeneous throughout the specimen. Additional evidence supporting this hypothesis is the fact that Castro et al. (1988) found a unique SSL for sand SF7 by using specimens in the lab prepared by two different methods that create a roughly similar homogenous fabric. On the other

hand, the sedimentation method, and presumably also the hydraulic fill method in the field, creates a layered heterogenous fabric. In some liquefaction evaluation procedures such as Poulos et al. (1985), the value of  $e$  needs to be determined in order to calculate  $S_{us}$ . Since fabric affects this value of  $e$ , then it will also affect  $S_{us}$ , and the effect of fabric needs to be accounted for. More discussion on this subject will be given in the following section and in Chapters 8 and 9.

#### 6.2.4 Discussion

The angle of the steady-state strength envelope  $\bar{\alpha}_{us}$  depends only on the frictional characteristics of the soil and does not change because of isotropic versus anisotropic consolidation, monotonic versus cyclic loading, variations in the value of  $K_c$  or differences in soil fabric due to the placement method. This implies that probably the most important factor in defining this angle is the sand particle shape. Strong evidence for this is the unique strength envelopes shown in Fig. 6.17 for sands A, B, and C, which are sands coming from the same lacustrine deposit and thus have the same grain characteristics but varying silt content. It can be seen that a unique steady-state strength envelope is defined for the three sands.

As already discussed in Section 2.7, Mohamad (1985) attempted to extract from the available literature results of strength envelope angles at steady-state. However, some of these results were obtained by him using the line of phase transformation or characteristic line (Ishihara et al., 1975; Luong and Sidaner, 1981), which occurs in dilative sands not susceptible to flow failure. The line of phase transformation is close but still different from the flow failure envelope, which in contractive sands is the steady-state strength envelope. The effective stress path curves sharply to the right in monotonic tests crossing the line of phase transformation. In a previous publication, this behavior was called an elbow (Mohamad and Dobry, 1986), and was hypothesized to correspond to the steady-state line. In this respect, two types of elbows should be distinguished. In one type, corresponding to partially contractive specimens where there is a shear stress drop, and flow occurs for a limited strain range, the elbow is always at steady-state, as illustrated by monotonic results on Banding sand (Castro, 1969, Mohammad and Dobry, 1986). In the other type, corresponding to dilative specimens where there is no shear stress drop nor flow, the elbow is by definition on the line of phase transformation, but it may or may not coincide with the steady-state envelope.



Although in the same Banding results just discussed the lines of phase transformation and steady-state were the same (Mohamad and Dobry, 1988), in general this is not the case, and the elbow occurs at a higher shear stress  $q$  and lower obliquity  $q/\bar{p}$  than the values  $q_s$  and  $q_s/\bar{p}_s = \tan \bar{\alpha}_{us}$  corresponding to steady-state. This is illustrated by Fig. 6.22, which shows laboratory tests results on undisturbed, very dense, dilative sand specimens of sands A, B and C. The implicit assumption in Fig. 6.22 is that  $\bar{\alpha}_{us}$  is the same for remolded and undisturbed specimens having different fabric; this assumption is supported by Fig. 6.19. All the samples except one developed elbows, and when compared against the steady-state strength envelope of true flow failures, it is clear that the elbows are below the steady-state strength envelope. Table 6.1 contains the strength envelopes of the line of phase transformation for a number of sands; as already observed by Mohamad (1985), when the particles become more angular, the angle tends to be larger. This is intuitively appealing since as a frictional material those sands having more angular particles should have a higher friction angle. Table 6.2 shows the steady-state strength envelope angles  $\bar{\alpha}_{us}$  for a variety of sands. Even though a relationship exists between an

increasing particle angularity and a larger  $\bar{\alpha}_{us}$  steady-state angles  $\bar{\alpha}_{us}$ , the differences is not very large, and  $\bar{\alpha}_{us}$  is close to  $29^\circ$  in most cases.

Since a contractive sand sample cannot exist beyond the steady state strength envelope, this envelope then becomes the ultimate failure surface or state boundary. A concept analogous to this exists in the critical state theory (Schoefield and Wroth, 1968). Problems have arisen with this latter theory when applied to sands, mainly because it is very difficult to reach the critical state using dilative sands (see Section 2.2), and also because sands can be placed at different initial densities, and thus a normalization procedure used for clays cannot be extended for sands (Atkinson and Bransby, 1978). At this moment, the steady-state in sands is not considered by many researchers to be equal to the critical state. Critical state and steady or residual state are different in clays because there is reorientation and realignment of clay particles at large strains (residual strength) in laboratory tests, as a specific failure surface develops instead of there being a homogenous strain field (Lupini et al., 1981). Therefore, in clays, the residual or steady-state strength is a combination of particle reorientation and dilation. On the other hand, in granular soils dilation is the dominant

effect, and this has led some reseachers to state that for sands critical state and steady-state are from a practical viewpoint one and the same (Castro et al., 1982; Sladen et al., 1985).

The tests on San Fernando SF7 sand in three different laboratories and using different moist tamping compaction techniques, confirmed that SSL lines are insensitive to fabric, provided that the resulting specimen is roughly homogeneous. On the other hand, tests on the same sand prepared by sedimentation, and thus having a nonhomogeneous layered fabric gave a different SSL location. The SSL's obtained for these sedimented specimens are above the corresponding SSL's for moist tamping specimens, and they are in general in good agreement with the steady-state values obtained by GEI (1988) on undisturbed specimens of the same San Fernando sand (see Chapter 9). This difference in SSL between moist tamping and sedimented remolded specimens is consistent with Poulos et al. (1985) recommendation of using the in-situ, layered fabric to determine the in-situ SSL. In the case of a hydraulic fill dam, this in-situ fabric can be simulated in first approximation by the sedimented method used herein, as the dam is built by dumping soil through water over long periods of time. Visual descriptions of this layering have been

provided for hydraulic fills and tailings dams by a number of authors (e.g., Dobry and Alvarez, 1966; Seed et al., 1973). Similar layering is often found in alluvial, lacustrine and marine deposits (Vasquez-Herrera et al., 1985).

Of course, there is no guarantee that the specific wet raining technique used herein for the sedimented specimens gives an identical layering to that in the field, and it may well be that different layerings may produce different and parallel SSL's (GEI, 1988). This requires further research, for example studying the effect of different amounts of soil placed in the water at a given time when preparing the sedimented samples. However, it is expected that the method used herein is a reasonable representation of typical in-situ layering and SSL. This assumption will be verified in Chapter 9 and Fig. 9.13 by a comparison with in-situ SSL's obtained by GEI (1988) using a different method. If, as assumed, the wet raining technique with its resulting segregation and layering, followed by the consolidation of the silty sand under  $\bar{\sigma}_{3c}$  and  $\bar{\sigma}_{1c} = K_c \bar{\sigma}_{3c}$ , produces naturally a soil fabric similar to that of an hydraulic fill in situ, then the fact that the resulting soil is contractive in the laboratory has important practical implications. That is, it suggests that hydraulic fill

deposits of silty sand in the field can be contractive and can experience flow failure in undrained condition. This will be further discussed in Chapter 9 in connection with the 1971 flow slide in the Lower San Fernando Dam.

In the GEI method, suggested by Castro and Poulos (Poulos et al., 1985; GEI, 1988) for liquefaction flow failure evaluation, the fabric is taken into account by testing undisturbed (inhomogeneous) specimens and correcting to the in-situ void ratio along a line parallel to the SSL generated using remolded homogeneous specimens. In that method, the usage of undisturbed specimens takes care of the fabric issue by keeping the in-situ fabric; however, these samples are very dense, and achieving flow failure in anisotropically consolidated undisturbed samples is often difficult or impossible. The method used herein of preparing inhomogeneous layered specimens by sedimentation is attractive in that they are very loose and contractive, they flow at realistic void ratios, and no correction for void ratio is necessary.

A fundamental assumption in the liquefaction evaluation procedure suggested by Castro and Poulos (Poulos et al., 1985) is that the in-situ and the remolded SSL are parallel. In their publication, they give some evidence as to why the in situ SSL and the remolded SSL must be parallel. The work

presented herein tends to support this assumption as the moist tamping and sedimentation SSL's seem indeed to be parallel (Figs. 6.20 and 6.21). Some additional support for the sedimented SSL in Fig. 6.20 is provided by test SF7-24 (see Appendix III), on a dilative specimen that did not flow. This test, not included in the figure, with  $\bar{\sigma}_{3c} = 1$  kg/m and  $e = 0.657$ , would plot slightly below the dashed portion of the sedimented SSL in Fig. 6.20.

### 6.3 Effective Stress Conditions at Triggering of Flow

The  $\bar{p} - q$  points at which flow failure is triggered (point T in Figs. 6.1 - 6.3) in the tests of sand F125, A and SF7, are shown in in this section.

#### 6.3.1 Results on Ottawa Sand F125

The number of tests and test conditions performed on sand F125 allowed conducting a complete study on the triggering behavior for both monotonic and cyclic loading. In what follows, the locations of the triggering points, called T in Figs. 6.1 to 6.3, are plotted and discussed.

Figure 6.23 shows the triggering (peak) points for all monotonic CTU tests conducted on this sand, such as point T in Fig. 6.1, including those experiments done in this work and others presented elsewhere (Baziar, 1987).

The figure includes load-controlled and strain-controlled CIU tests performed with rough and smooth end conditions. It can be seen that the load-controlled tests define an envelope of angle  $\bar{\alpha}_{up} = 17^\circ$ , while the strain-controlled tests define a lower envelope  $\bar{\alpha}_{up} = 14^\circ$ , with these envelopes being valid for both rough and smooth ends. The two triggering envelopes in Figs. 6.23 are unaffected by the value of confining pressure, which varied between 1.0 and 6.5 Kg/cm<sup>2</sup>, or by the value of the void ratio of the contractive specimens. In what follows, only load-controlled tests will be used to compare with the cyclic CyT-CAU tests, since the cyclic tests are always load-controlled in the axial direction.

Of course, at the end of consolidation, the stress point for a CIU test is always below the triggering envelope such as defined by  $\bar{\alpha}_{up} = 17^\circ$  in Fig. 6.23. However, this is not necessarily the case for CAU or CyT-CAU tests, where the effective stress point after consolidation may be below or above, which in the latter case would mean between the  $\bar{\alpha}_{up} = 17^\circ$  line and the steady-state  $\bar{\alpha}_{us} = 29^\circ$  line. In this case, the boundary between specimens consolidated above and below the  $\bar{\alpha}_{up}$  line corresponds to  $K_c = (1 + \tan \bar{\alpha}_{up}) / (1 - \tan \bar{\alpha}_{up}) = 1.88$ .

The triggering points for all monotonic and cyclic tests consolidated with  $1 \leq K_c \leq 1.5 < 1.88$  for sand F125, that is below the  $\bar{a}_{up} = 17^\circ$  line, are shown in Fig. 6.24. It can be seen that the triggering points defined by the monotonic and cyclic tests are very similar, regardless of the value of  $K_c$ , even for a combination test of CyT-CAU followed by CAU loading to failure. That is, the "triggering" envelope  $\bar{a}_{ut}$  previously defined by CyT-CAU tests seems to be the same as the "peak" envelope  $\bar{a}_{up}$  for the CIU tests, with  $\bar{a}_{ut} \approx \bar{a}_{up} = 17^\circ$ . In reality, more refined calculations reveal that the average value of  $\bar{a}_{ut}$  for the tests with  $K_c = 1.5$  is  $\bar{a}_{ut} \approx 17.5^\circ$ , slightly larger than  $\bar{a}_{up} = 17^\circ$  obtained for the CIU tests. Those values of  $\bar{a}_{ut} = 17^\circ$  to  $17.5^\circ$ , in addition of being almost independent of  $K_c$  for the range of  $K_c$  between 1 and 1.5, are also unaffected by the value of the confining pressure, which was between 1.0 and 6.5 Kg/cm<sup>2</sup>. The value of the void ratio did not seem to matter either as long as the samples were clearly contractive.

For those monotonic and cyclic tests consolidated above  $K_c = 1.2$  or 1.5, the triggering envelope becomes a rapidly increasing function of  $K_c$ . This is illustrated by Figs. 6.25, 6.26 and 6.27, which present the triggering points for



tests with  $K_c$  values of 2.0, 2.5 and 2.9, respectively. It is clear that as  $K_c$  increases, the slope of the triggering envelope,  $\bar{\alpha}_{ut}$ , also increases.

Figure 6.26 shows test results done with  $K_c = 2.0$  which define a triggering envelope  $\bar{\alpha}_{ut} = 21^\circ$ . It can be seen that this envelope is unaffected by confining pressure or type of test (cyclic or monotonic). The cyclic triaxial (CAU) test, which has been used widely in the geotechnical literature also triggered at the same envelope. Similar results can be seen for the other two values of  $K_c$  in Figs. 6.26 and 6.27, where tests with different confining pressures also triggered on the same envelope.

The triggering envelopes thus obtained for all the tests on sand F125 are summarized without data points on Fig. 6.28. The corresponding  $\bar{\alpha}_{ut}$  angles are shown in Fig. 6.29 as a function of  $K_c$ , including  $\bar{\alpha}_{ut} = \bar{\alpha}_{us} = 29^\circ$  for  $K_c = 3.48$ . It can be seen that  $\bar{\alpha}_{ut} = \bar{\alpha}_{up} = 17^\circ$  for  $K_c = 1.0$  and 1.2; and then  $\bar{\alpha}_{ut}$  increases for  $K_c = 1.5, 2.0, 2.5$  and 2.9.

The triggering points are also plotted in  $e - q$  and  $e - \bar{p}$  spaces in Fig. 6.30. All points plot to the right of the corresponding steady-state line, thereby showing that the triggering stresses are larger than the steady-state stresses. It can be observed that even though there is a trend for the triggering stresses to increase as the void

ratio decreases, the points define a band rather than a line. It has been suggested that triggering of monotonic samples occurs at a collapse surface (Sladen et al., 1985) in  $e - \bar{p} - q$  space; This does not occur here and a collapse surface is not defined, due to the fact that the confining pressure and void ratio have no effect on the triggering strength envelopes as long as the sample is contractive.

There is a possibility that this triggering band in  $e - \bar{\sigma}_3$  space such as in Fig. 6.30 could be a boundary, where tests consolidated to the right of it are completely contractive, whereas samples consolidated between it and the SSL would produce partially contractive specimens. This hypothesis deserves further research.

### 6.3.2 Results on Sand A

The triggering (peak) points for the monotonic  $\overline{\text{CU}}$  tests on sand A are shown in Fig. 6.31, and they define an envelope  $\bar{\alpha}_{\text{up}} = 23^\circ$  corresponding to  $K_c = 2.475$ . All anisotropically consolidated  $\overline{\text{CAU}}$  and  $\text{CyT-}\overline{\text{CAU}}$  tests on this sand were conducted with  $K_c < 2.475$ . Therefore, after the previous discussion in Section 6.3.1, it should be expected that all should trigger on or close to the same envelope,  $\bar{\alpha}_{\text{ut}} = \bar{\alpha}_{\text{up}} = 23^\circ$ . This is verified by Fig. 6.31, which includes all triggering points for sand A. Although the

plot has more experimental scatter than Fig. 6.24, it does define a unique line, independent of test type and value of  $K_c$ . Triggering in monotonic and cyclic tests on more silty sand B and C and  $K_c < 2.475$ , not included in Fig. 6.31, also exhibited the same  $\bar{\alpha}_{ut} = 23^\circ$  (Vasquez-Herrera et al., 1988).

### 6.3.3 Results on San Fernando Sand SF7

Figs. 6.32 through 6.36 presents the triggering envelopes for tests done on sand SF7. They include monotonic and cyclic tests done with five different values of  $K_c$ : 1.4, 1.7, 1.87, 2.0 and 2.2. Figure 6.32 shows the triggering points of load-controlled CIU and cyclic CyT-CAU tests with  $K_c$  values up to 1.87 for both moist tamped and sedimented specimens. It can be seen that the triggering envelope defined by the CIU tests is roughly the same than that for cyclic tests with  $K_c$  less than 1.87, even though the scatter is larger than that for sand F125. The triggering envelope defined has an inclination  $\bar{\alpha}_{up} = \bar{\alpha}_{ut} = 22^\circ$ , which corresponds to a  $K_c$  of about 2.4. However, the results on  $K_c = 2.0$  and 2.2 shown in Figs. 6.35 and 6.36, respectively, are substantially higher, with  $\bar{\alpha}_{ut} = 24^\circ$  and  $25.5^\circ$  respectively. There is no doubt that the triggering envelope tends to increase as the value of  $K_c$  increases in all cases (see Figure 6.37). In Fig. 6.37, the

extrapolation of the band at high value of  $K_c$  was guided by the fact that, for  $K_c = 3.48$ ,  $\bar{a}_{ut} \approx \bar{a}_{us} = 29^\circ$ .

Four tests were done on samples prepared by the sedimentation method described in Chapter 4. These samples were failed in cyclic tests with  $K_c = 1.7, 1.87$  and  $2.0$ , and are included in Figs. 6.33, 6.34 and 6.35. It can be seen that the triggering envelope was not affected by the method of sample preparation.

#### 6.3.4 Discussion

The monotonic and cyclic triggering results presented here show a very clear and consistent picture, based mainly on the tests on sand F125 but also confirmed by those on sands A and SF7. As summarized by Figs. 6.24 and 6.29 for sand F125, and by Fig. 6.31 for sand SF7, triggering in monotonically load-controlled triaxial compression of isotropically consolidated contractive samples always occurs on a constant strength envelope of angle  $\bar{a}_{up}$ . Any sample consolidated anisotropically sufficiently below the  $\bar{a}_{up}$  line triggers at that envelope or slightly above it, whether the test is monotonic, cyclic or a combination of cyclic and monotonic. In general, the triggering envelope  $\bar{a}_{ut}$  is a function of  $K_c$  alone; in the limit, when the effective stress state at consolidation is on the steady-state

strength envelope, this and the triggering envelope become identical.

The exact determination of the locus of triggering for CyT-CAU tests is extremely important for practical applications, as this determines how much pwp buildup can occur in a given soil element before triggering of liquefaction flow failure occurs. Once the triggering envelope  $\bar{\sigma}_{ut}$  is known, and using the fact that the effective stress path of a CyT-CAU test is a horizontal line moving to the left, we can then find what is the maximum allowable residual pwp increase which can be caused by an earthquake before triggering (Mohamad and Dobry, 1986).

The framework just discussed also helps explain the results obtained by Mohamad (1985) on Banding sand, already discussed in Section 2.7, and throws light on the reasons for the scatter and differences found by Mohamad between his monotonic and cyclic tests. As presented in more detail in Section 2.7, he found that triggering in the anisotropically consolidated cyclic tests occurred when the effective stress path reached the steady-state envelope for that sand. On the other hand, for the monotonic tests on the same sand triggering occurred along a lower, peak undrained strength envelope. He then ran a CAU test by anisotropically consolidating the sample above the monotonic triggering

envelope; and this sample also failed in what he called the steady-state strength envelope. The behavior of this was not well understood at the time but the results presented herein (e.g., Fig. 6.28) would predict this kind of behavior for the testing conditions used by Mohamad.

The effective stress conditions at triggering are related to those at steady-state, and to describe this some parameters need to be defined. Casagrande (1976) suggested the term liquefaction potential ( $L_p$ ) to quantify how far to the right a sample is consolidated from the steady-state line  $L_p$  is defined as follows:

$$L_p = \frac{\bar{\sigma}_{3c} - \sigma_{3us}}{\bar{\sigma}_{3us}} \quad (6.1)$$

where  $\bar{\sigma}_{3c}$  and  $\bar{\sigma}_{3us}$  are the minor effective principal stresses at end of consolidation and steady-state, respectively. Increasing positive values of  $L_p$  imply increasing contractiveness of a soil sample. Alternatively, Bishop (1967), defined the term brittleness index ( $I_b$ ) to denote the strength loss of a clay sample when strained monotonically by using the peak strength and residual strength. In order to apply it to contractive sands we use instead the triggering and steady-state shear stresses. In this fashion,  $I_b$  is defined by:

$$I_b = \frac{q_{ut} - q_{us}}{q_{ut}} \quad (6.2)$$

where  $q_{ut}$  and  $q_{us}$  are the triggering shear stress and steady-state shear stress, respectively. An increasing  $I_b$  implies greater strength reduction.

The implication of Eq. 6.2 is that, if  $I_b$  can be predicted for a given soil, the steady-state strength becomes a fraction of the triggering shear stress:

$$q_{us} = (1 - I_b) q_{ut} \quad (6.3)$$

Equation 6.3 is extremely significant for anisotropically consolidated specimens subjected to a driving static shear stress  $q_d$ . In CyT-CAU tests, essentially  $q_{ut} = q_d$ . That is, it is always  $q_{ut} \geq q_d$ , and Eq. 6.3 can be rewritten:

$$q_{us} \geq (1 - I_b) q_d \quad (6.4)$$

Therefore, if  $I_b$  can be predicted, Eq. 6.4 provides a lower bound for the steady-state shear strength,  $q_{us}$ .

Figure 6.38 plots  $I_b$  versus  $L_p$  for all CTU, CAU and CyT-CAU tests performed herein on sand Fl25. Of particular importance is the fact that there is a upper limit of  $I_b = 0.85$ , regardless of how high  $L_p$  goes. In practical terms this means that after a certain point it doesn't matter how

contractive a soil sample is (as measured by  $L_p$ ); the strength drop after liquefaction has triggered (measured by  $I_b$ ) has an upper bound irregardless of how far to the right of the SSL a sample is consolidated. After Eq. 6.4, this translates into a lower bound for  $q_{us}$ , that is  $q_{us} \geq 0.15 q_d$ . Therefore, Fig. 6.38 also suggests that  $I_b$  is a better parameter to quantify the behavior of sands susceptible to flow failure because it takes into account the shear strength drop, of primary importance in stability calculations.

It is hypothesized that the triggering of flow is also related to  $I_b$  in addition to the influence of  $K_c$  already discussed. The brittleness index takes into account the fact that, as a sample is being consolidated anisotropically, not only its driving shear stresses increase but also at the same time the steady-state shear strength increases due to consolidation. As soon as the degree of anisotropic consolidation, as measured by  $K_c$ , becomes so large that the sample starts increasing the value of  $q_{us}$  faster than the sample gains driving shear stress  $q_d$ ; then Eq. 6.3 suggests  $I_b$  should decrease. This is shown in Fig. 6.39 for all  $\overline{CTU}$ ,  $\overline{CAU}$  and  $CyT-\overline{CAU}$  tests done on sand Fl25, that is, for the same tests plotted in Fig. 6.38. It



can be seen in Fig. 6.39 that the value of  $I_b$  remains constant up to about  $K_c = 2.0$ ; and after that it decreases. The importance of this finding will become more apparent in the next chapter when discussing other aspects of flow failure triggering.

#### 6.4 Pore Water Pressure Needed for Triggering

It was shown in the previous section that the strength envelope of a specific sand at which flow failure is triggered was constant for a given value of  $K_c$ . Since the stress path of the CyT - CAU is a horizontal line travelling from the point of consolidation (on a  $K_c$  line) to the triggering envelope, the amount of pwp ( $u_t$ ) generated when reaching the triggering envelope is given by (Mohamad, 1985).

$$r_{ut} = \frac{u_t}{\bar{\sigma}_{3c}} = 0.5 \left[ K_c + 1 - \frac{(K_c - 1)}{\tan \bar{\alpha}_{ut}} \right]$$

If the value of  $\bar{\alpha}_{ut}$  of the triggering envelope were constant, this expression would represent a linear relationship between  $r_{ut}$  and  $K_c$  for a given material; however, since  $\bar{\alpha}_{ut}$  can change as a function of  $K_c$ , the relationship becomes a curve. Figures 6.40 and 6.41 present the experimental relationships between  $r_{ut}$  and  $K_c$  for sands

F125 and SF7, respectively. They clearly demonstrate that as the value of  $K_c$  increases, the pwp necessary to trigger flow failure decreases.

It is very important to point out that the values of  $r_{ut}$  in cyclic tests are never one unless  $K_c = 1.0$ , and that generally the higher the value of  $K_c$ , the smaller is  $r_{ut}$ . This demonstrates that the concept of initial liquefaction usually obtained from cyclic undrained loading of isotropically consolidated sands (contractive or dilative) can be unconservative if used to predict undrained liquefaction flow failure in contractive sands.

The role of  $r_{ut}$  will be shown to be of fundamental importance in the next chapter where the behavior of contractive sands during cyclic loading are studied. As a matter of fact, it will become the link between the parameters controlling pwp buildup and those determining the effective stress conditions at triggering.

### 6.5 Tests on Dilative Samples

Since not all soil elements within an earth structure will be contractive, it is important that the stress-strain behavior of sands not susceptible to flow failure be studied. For this purpose, undrained monotonic and cyclic laboratory tests were also carried out on dilative soil

specimens. These soil tests represent different levels of dilatancy, depending on how far they are consolidated to the left of the steady-state line. The results of monotonic tests will be presented first, followed by the cyclic tests.

Figure 6.42 shows a monotonic triaxial compression CTU test on sand A. As the sample is loaded axially, positive values of pwp cause the effective stress path to curve towards the failure envelope, which in this case is also  $29^\circ$ , the same as the steady-state strength envelope. Upon further loading and after an elbow, the effective stress path reaches the strength envelope and runs up along this failure envelope. This change of direction is brought about by a change in the rate of pore pressure buildup, that ceases to increase and start decreasing while the imposed shear stresses are still going up. Of special interest is the fact that the stress-strain behavior of this sample is totally different from that of contractive sands. No decrease in shear strength occurs, and the large strains associated with flow failure are not present.

As discussed before, the change in direction of the effective stress path before it reaches the ultimate strength envelope is called an elbow (Mohamad, 1985), and these elbows occur along a strength envelope that has been called the line of phase transformation or characteristic

line.

The aforementioned elbow can occur in a more pronounced manner, as shown in Figure 6.43. Here the elbow marks the end of pwp buildup with increasing stress and a leveling of the stress-strain curve. After this elbow, the effective stress path again runs along the failure envelope. In Figs. 6.42 - 6.43, elbows have not involved a decrease in shear strength; however, this can also occur in what has been called limited liquefaction flow failure. When a sample exhibits this behavior, it is said to be partially contractive. In these tests, flow failure occurs for a limited range of strain, before the sample regains its strength (Castro, 1969, Mohamad and Dobry, 1986).

A somewhat similar result occurs in cyclic CyT-CAU tests. Figs. 6.44 and 6.45 show results for a dilative sample of sand SF7. It can be seen that as the number of cycles of uniform shear strain increases, the pwp increases to a constant value. This increase in pore pressure causes the effective stress path to stop on the failure envelope, and stay there oscillating with constant pwp under any further cyclic straining. After the effective stress path reaches this envelope during cyclic loading, further increases of pwp are inhibited; however, the sample continues to experience an increase in permanent axial

deformations. Again, it is important to note that the decrease in shear strength and large strains associated with liquefaction flow failure does not occur, even if relatively high pwp are generated. Any increase in shear stress due to monotonic load will cause the effective stress path to curve sharply upwards as it moves along the failure envelope; this is shown using another test on sand SF7 in Figs. 6.46 and 6.47. The sudden change in direction of the effective stress path is brought about due to the sudden decrease in pwp when monotonic loading starts; further loading causes the pwp to continue decreasing. Even though the cyclic loading caused the pwp to build up to significant values, the soil did not lose its strength when further sheared monotonically. Therefore, large values of pwp alone are not necessarily indicative of flow failure; as a matter of fact, cyclic tests with  $K_c = 1.00$  will buildup a pore pressure ratio  $r_u = 1.00$ , and these tests cannot produce flow failure.

Another very interesting condition can occur with tests on dilative samples. Figs. 6.48 and 6.49 show a cyclic CyT-CAU test followed by monotonic loading similar to that of a CAU test; this is known as a CyT-CAU+CAU test. Due to the cyclic straining, the pwp buildup causes the effective stress path to reach the failure envelope and remain there

even while cyclic loading continues. When cyclic loading is stopped and the sample is loaded monotonically without allowing for reconsolidation, there is an immediate drop in the pwp that causes the effective stress path to curve upwards and progress along the failure envelope. If the  $q_{us}$  is close to the consolidation stress, very large monotonic stresses are not necessary to cause the sample to reach its steady-state. At this point, the stress-strain curve reaches a plateau of constant shear strength and the value of pwp is also constant for increasing strain as the sample reaches its steady-state.

The above point is very important when analyzing flow failures of an earth structure, because during cyclic loading, as contractive elements along the failure surface reach failure, there is a redistribution of shear stresses among all the elements in the failure surface. This redistribution of stresses creates an increase in monotonic stresses over those already existing on the elements that have not triggered. If the sample is dilative, this can cause additional elements to fail with the increasing monotonic load; however, the shear strength retained by the sample can be very large, as shown in Figure 6.48. On the other hand, if the sample is contractive and the cyclic loading stops short of the triggering envelope, it will not

only the value of void ratio. Effective stress conditions at steady-state and triggering are not affected by these factors. The results of pwp buildup were also not affected by the specimen nonuniformities; this is probably due to the robustness of the cyclic strain method. Cyclic strain-controlled test results on isotropically consolidated dilative samples (Dobry, 1982) have showed that different testing preparation techniques do not affect much the pwp buildup; this conclusion from dilative samples can also be extended to contractive samples.

When incorrect procedures are used to measure void ratio, the experimental scatter can be quite large. This is mainly due to the collapse of some sand grains during saturation of the specimen; therefore, the specimen diameter should be measured after the sample is saturated (see Chapter 4). The potential error preventing an accurate measurement of void ratio due to collapse upon saturation was also noted by Sladen and Hanford (1987).

Since this collapse is not uniform, even the slope of the SSL is not correct. The slope of the remolded SSL is important when applying the liquefaction evaluation procedure developed by Castro and his coworkers (Poulos et al., 1985).

fail; but additional monotonic loading can cause it to reach the triggering envelope. This is clearly shown in Figs. 6.50 and 6.51, using a CyT-CAU+CAU test done on a contractive sample of sand F125, where the cyclic loading was stopped before it reached the triggering envelope and later, without allowing for reconsolidation, the sand was axially loaded undrained until liquefaction flow failure was triggered.

Therefore, flow failure by monotonic loading of a soil element can also occur due to redistribution of stresses due to cyclic triggering in other contractive elements. In dilative soil elements, the steady-state shear strength can also be reached due to additional monotonic loading following the cyclic loading.

## 6.6 Influence of Testing Procedures

As mentioned in Chapter 4, incorrect testing procedures can lead to erroneous results. This section will compare test results using correct testing procedures with those using incorrect testing procedures.

The testing techniques to be discussed are the following: measurement of void ratio after saturation, the use of correct end plattens, and reuse of the tested sand. The influence of the above factors were found to influence



Figure 6.52 shows comparisons of test results on sand F125 using the two different methods of void ratio measurements. The correct procedure is the one that measures the void ratio after saturation. It can be seen that the method that measures void ratios after saturation produces results with large scatter, while at the same time the cluster of points are above the correct SSL. It also shows that if the correct position of the SSL is not known, a line with a different slope could be drawn to best fit these data points. Figure 6.52 also shows that the collapse upon saturation causes sufficient rearrangement of some particles in the sand grains skeleton to influence the position of the SSL; it also indicates that this collapse is more or less random, and that a constant factor cannot be used to correct the results.

The other parameter that can influence the determination of the void ratio is that involving the triaxial end plattens. The problem arises because rough ends have to be used in torsional tests, and these rough porous stones cause the sand grains to penetrate into the porous stone. In order to make the first and last soil layers uniform with the rest of the sample, a stone correction factor in the form of additional soil is added to keep the uniformity constant. This correction factor is

later subtracted from the total soil weight when computing the void ratio. Figure 6.53 illustrates the use of this correction factor with sand F125 results. It can be seen that the tests with smooth ends, and those with rough ends done in this work which did not need a correction factor, plot on the same line. This is also true for those tests using significantly rougher ends performed by Baziar (1987) on this sand. Despite this good agreement, the use of a stone correction factor is not recommended. One reason is that the factor is probably not constant from specimen to specimen. The conditions that are ideal involve no correction factor and smooth end plattens; however, this limits the tests to only monotonic compression. For tests involving torsional loading, the next best thing is to use porous stones that are rough enough to transmit torque but smooth enough to avoid using a stone correction factor. This would mean that the grain of the porous stone should match as closely as possible the sand grains; therefore, finer sands will require finer porous stones. For this reason, it is suggested that no correction factor be used, and that the porous stone grain match the sand grain size as much as possible.

The last concern test procedures involves reuse of . . . If the grain size distribution before and

after the test are compared, it is very clear that a substantial amount of sand grain crushing occurs. This is illustrated by Figure 6.54, where the crushing before and after the test is apparent. Since small variations in grain size are known to influence the position of the SSL for a particular sand, this implies that the crushed sand will have a different SSL than the original uncrushed sand. Therefore, sand should not be reused in flow failure tests if crushing of particles is present. Although the mechanism of sand crushing during flow failure tests is not well understood, it appears to be related to the sudden drop in shear stress from peak to steady-state and not to the amount of isotropic effective normal stresses involved, which were in all cases quite small.

The original tests on sands A, B, and C were done using these incorrect procedure; their SSL can be seen in Figs. 6.55, 6.56, and 6.57, respectively (Vasquez-Herrera et al., 1985). By looking at the results on sand A in Figure 6.55 it can be clearly observed that the scatter of these tests is large; even worse, the absolute position of the SSL is a priori known to be wrong because the collapse due to saturation makes the sample denser. The results on sands B and C would appear to be better if it were not known that the testing procedures are wrong; therefore, the fact that

they are a straight line is a product of chance and the slopes and positions of these SSL are also incorrect.

The SSL's for sands A, B, and C were determined using some of the incorrect procedures mentioned before, because cronologically they were the first sands tested, and because at the time it was not known that these factors affected the measurement of void ratio. The amount of scatter in Fig. 6.55 is quite large when compared to the SSL found for sands F125 and SF7 (e.g., see Figs. 6.14 and 6.21). Also, the correct position of the SSL is not known, but it must certainly be lower than that shown. This figure shows the cummulative effects of the following incorrect testing procedures: incorrect undercompaction value, incorrect tamping water content, incorrect measurement of  $e$ , use of incorrect stone correction factor, and reusing of the sand.

The effect of these factors is probably what caused the large scatter in the results presented by Mohamad (1985) on Banding Sand. His testing results were already discussed in Section 2.7, where it can be seen that the scatter is similar to that found here for sand A. It is believed that much better results would have been found if the following procedures had been followed: the sand was not reused, void ratios were determined after saturation, use of the correct undercompaction value, and elimination of the stone

correction factor.

Table 6.1. Strength Envelopes of Lines of Phase Transformation for Various Sands

Sand	$\bar{\alpha}_{pt}$	$\bar{\phi}_{pt}$	Particle Shape	Reference
Fountainebleau Sand	26.1°	29.3°	Unknown	Luong (1980) Luong (1981) and Sidaner
Ottawa Sand	26.5°	29.9°	Rounded	Vaid and Chern (1983)
Reid-Bedford Sand	27.7°	31.6°	Subrounded with Rounded and Angular	Durham and Townsend (1972)
Fuji Sand	28.1°	32.4°	Subangular	Ishihara et. al (1975)
Antelope Valley Sand	30.1°	35.4°	Subangular to Angular	Lade and Hernandez (1977)

Table 6.2. Steady-State Strength Envelopes for Various Sands

Sand	$\bar{\alpha}_{us}$	$\bar{\phi}_{us}$	Particle Shape	Reference
Sacramento River Sand	30.5°	36.1°	Subangular to Subrounded	Seed and Lee (1967)
RPI Banding Sand	28.5°	32.9°	Subrounded	Mohamad (1985)
Ottawa C109 Sand	29.0°	33.7°	Rounded	Vaid and Chern(1982)
Lornex Mine Tailing	29.7°	34.8°	Angular	GEI (1982)
Alcan Mine Tailing	32.9°	40.3°	Angular	Poulos et. al (1985)
Sand SF7	29.0°	33.7°	Angular	This Study
Sand A,B,C	29.0°	33.7°	Subangular to Angular	This Study
Sand F125	29.0°	33.7°	Subangular	This Study
Leighton Buzzard Sand	28.0°	32.1°	Rounded	Succarieh et. al (1987)

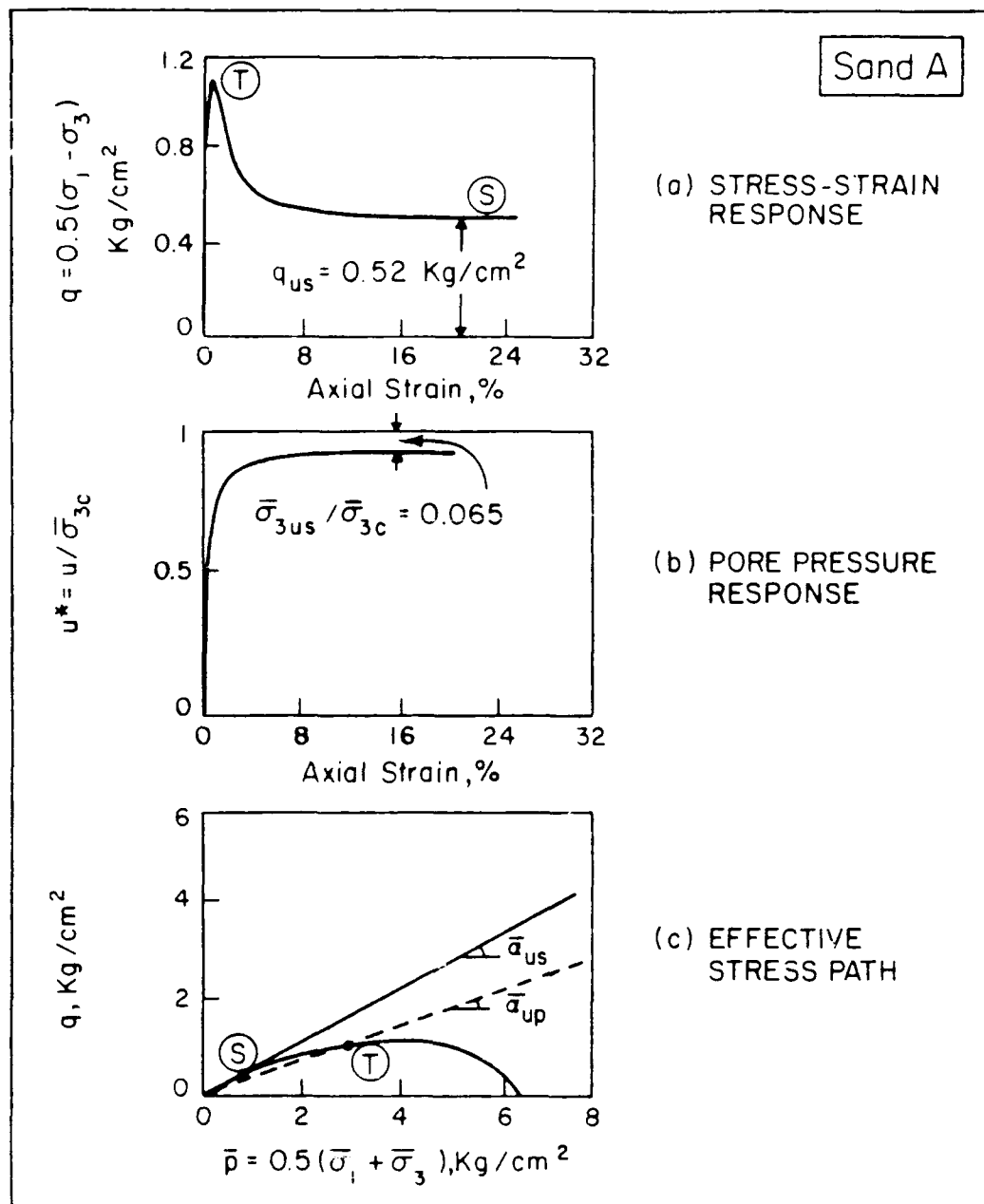


Fig. 6.1. Monotonic Triaxial CTU Test on Silty Sand A  
 $(\bar{\sigma}_{1c} = \bar{\sigma}_{3c} = 6.5 \text{ kg/cm}^2)$



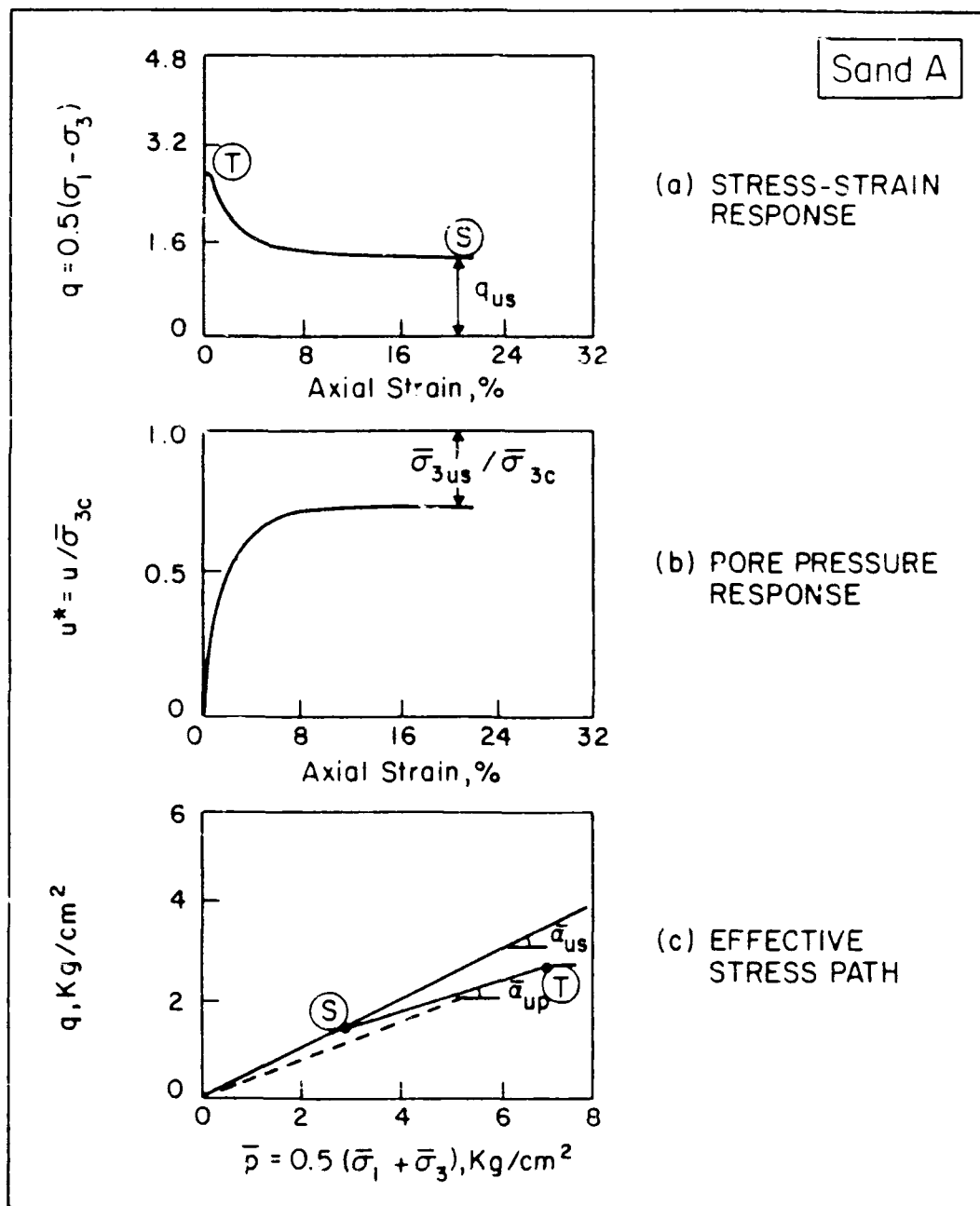


Fig. 6.2. Monotonic Triaxial CAU Test on Silty Sand A  
 $(\bar{\sigma}_{3c} = 5.1 \text{ kg/cm}^2, \bar{\sigma}_{1c} = 10.2 \text{ kg/cm}^2)$

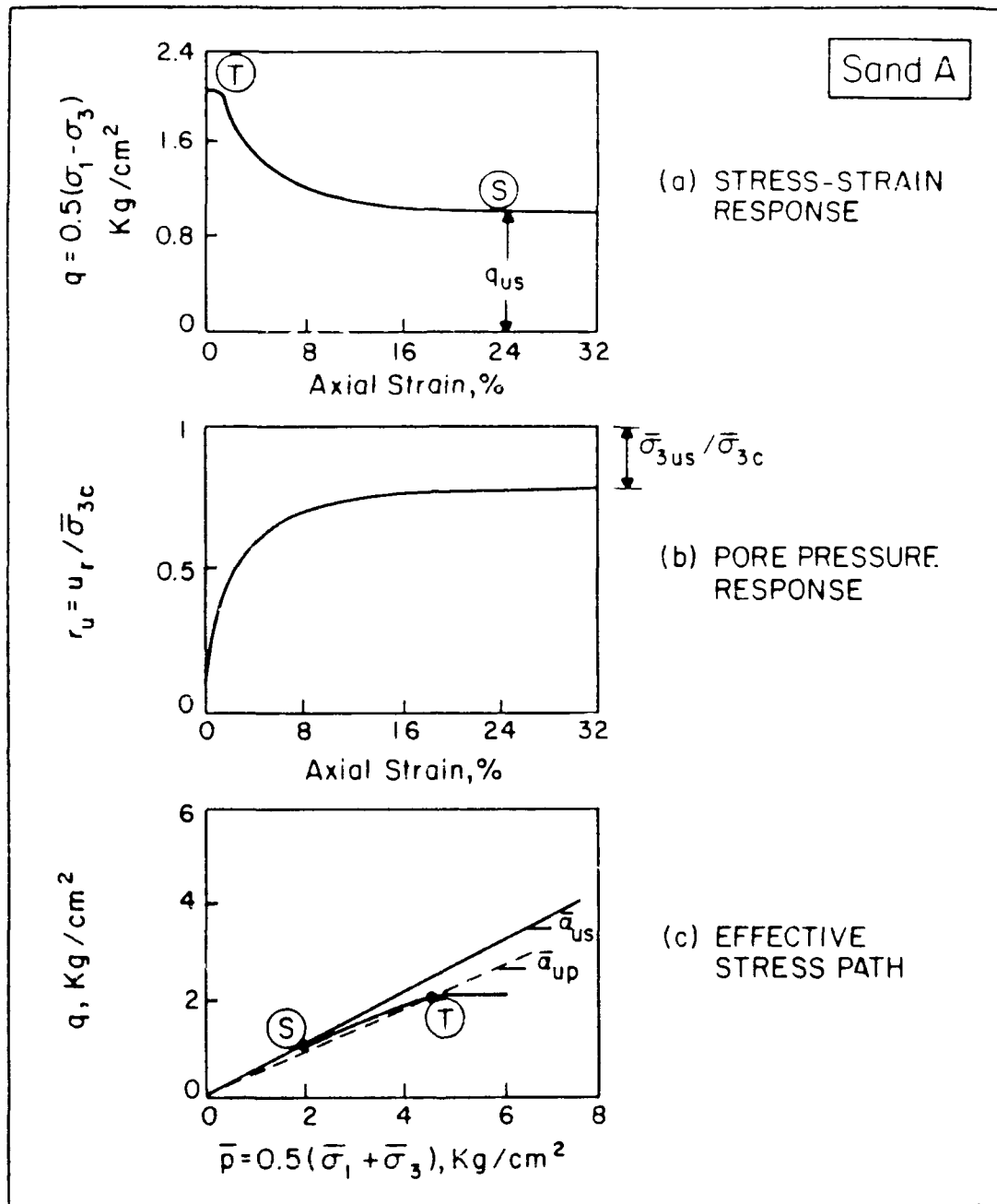


Fig. 6.3. Cyclic Torsional Triaxial CyT-CAU Test on Silty Sand A ( $\bar{\sigma}_{3c} = 4.07 \text{ kg/cm}^2$ ,  $\bar{\sigma}_{1c} = 8.34 \text{ kg/cm}^2$ ,  $\gamma_{cy} = 0.05\%$ )

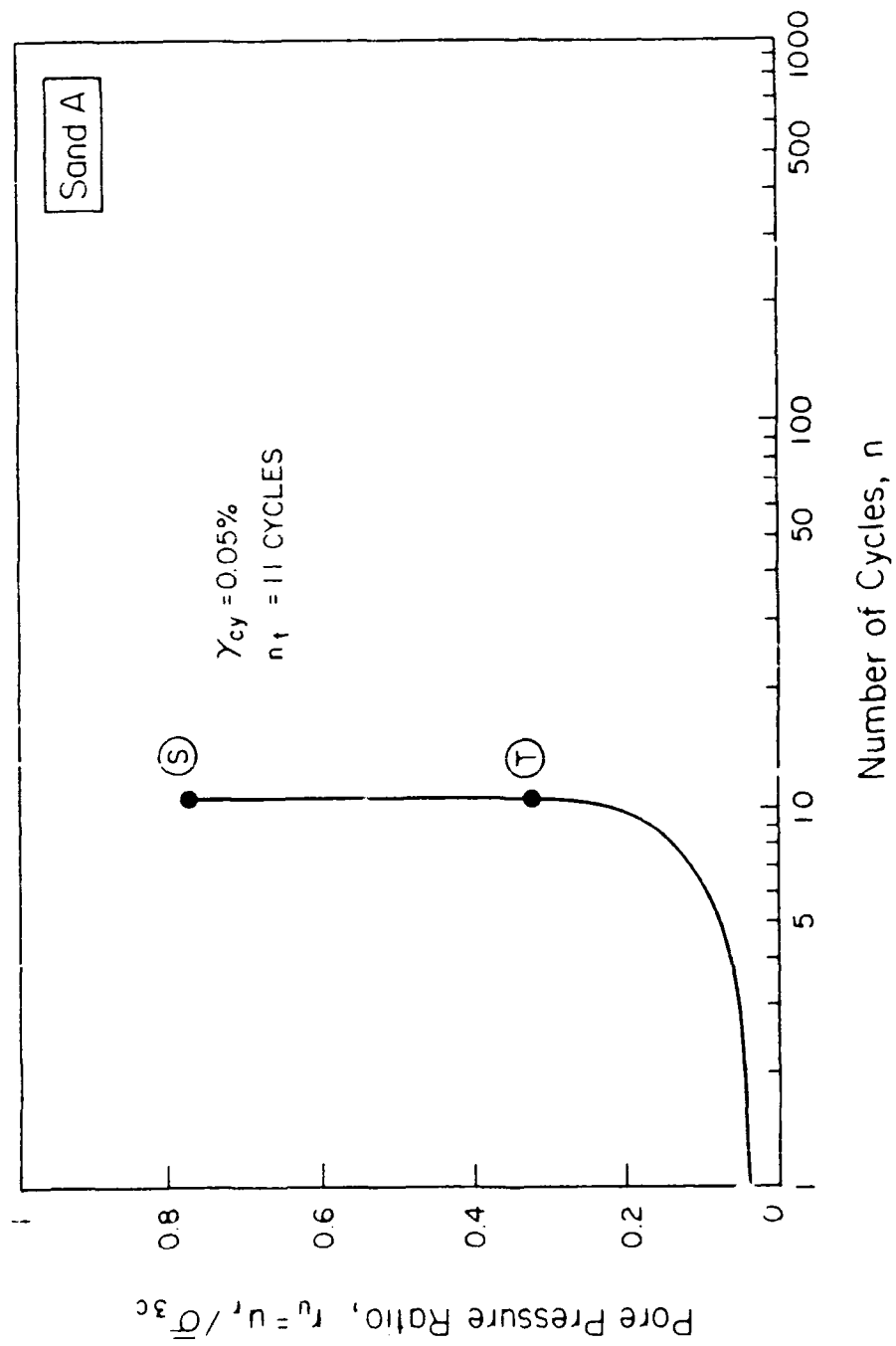


Fig. 6.4. Pore Water Pressure Buildup During CyT-CAU Test on Silty Sand A shown in Fig. 6.3

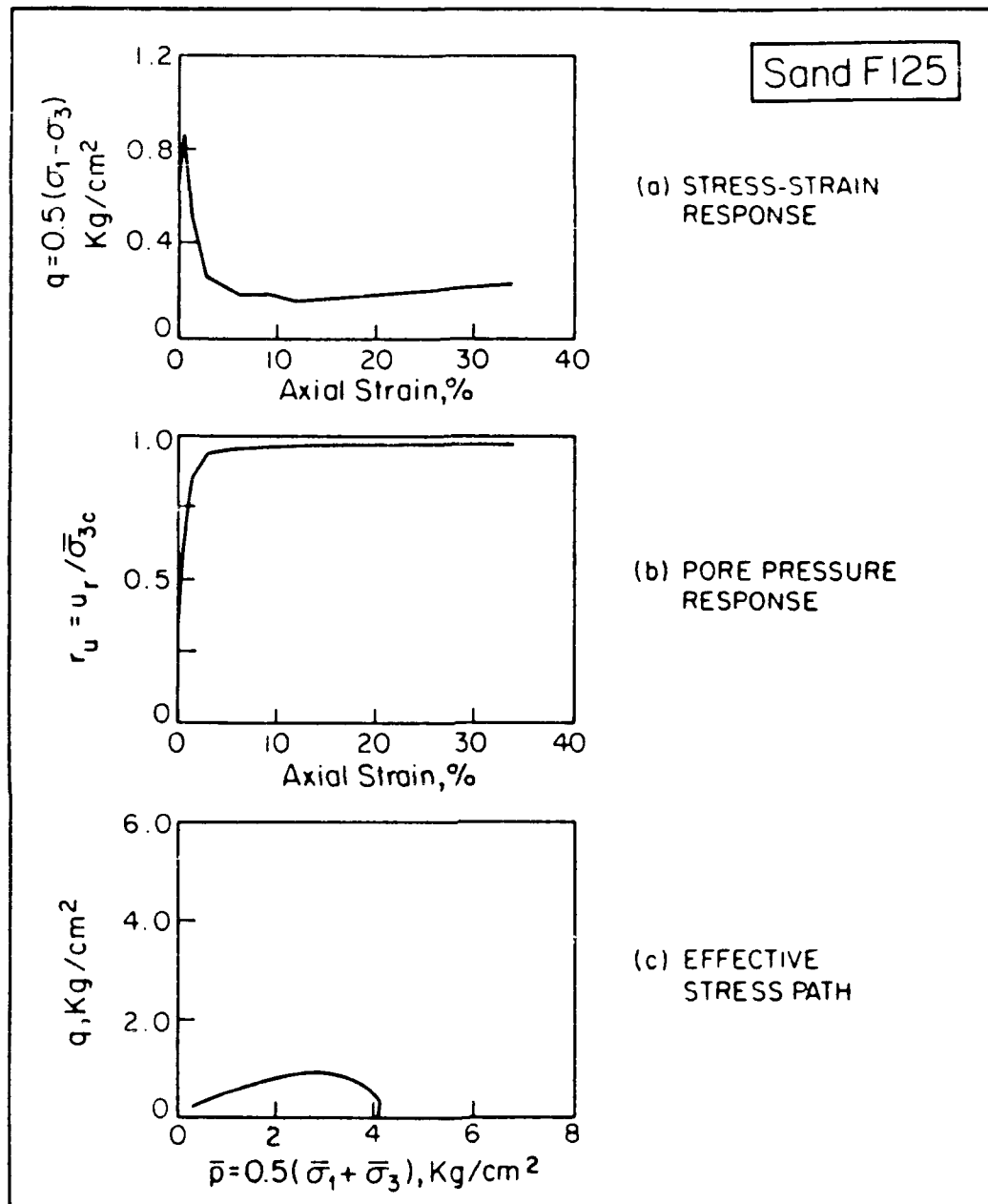


Fig. 6.5. Monotonic Triaxial CIU Test on Ottawa Sand F125  
 $(\bar{\sigma}_{3c} = \bar{\sigma}_{1c} = 4.08 \text{ kg/cm}^2)$

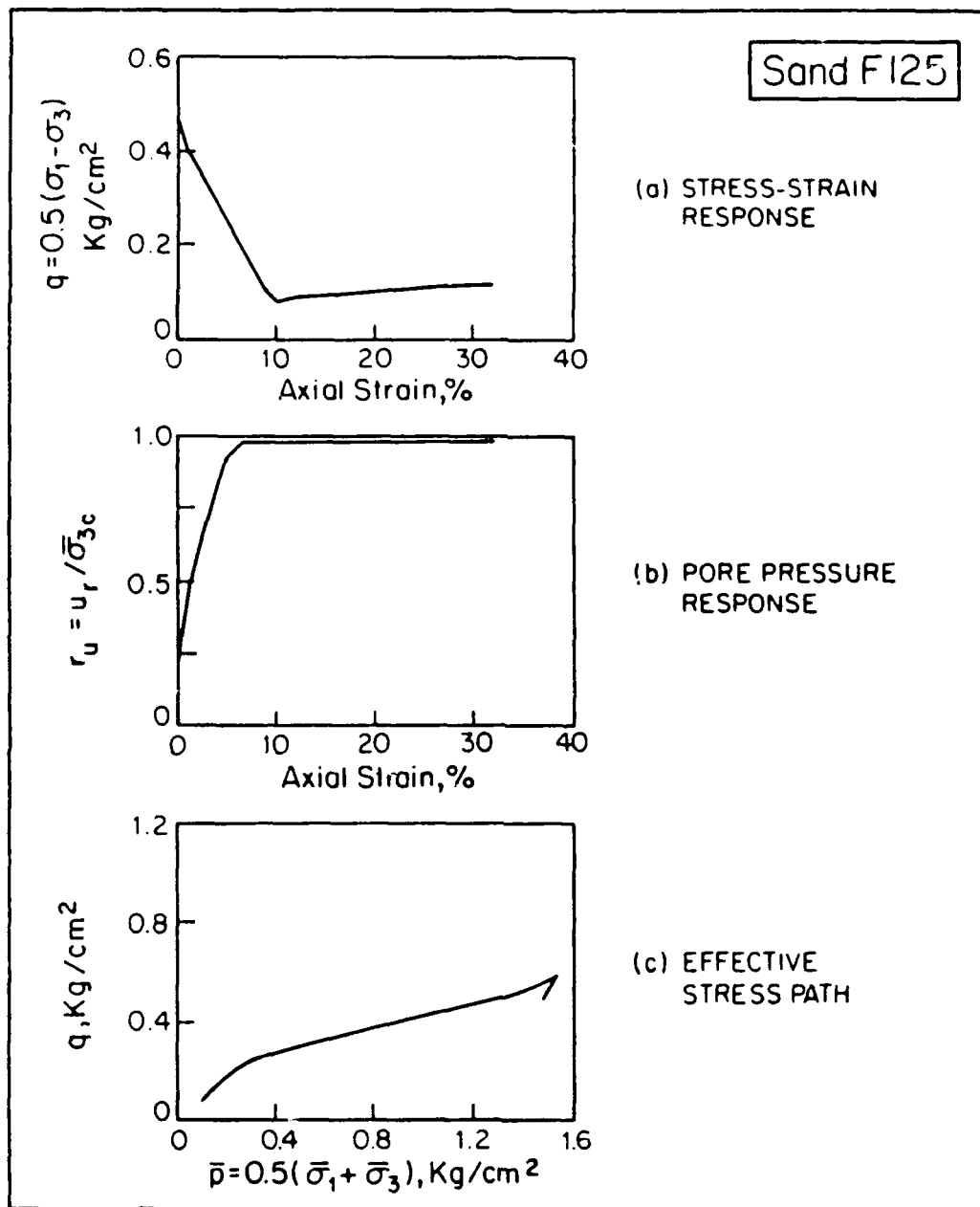


Fig. 6.6. Monotonic Triaxial CAU Test on Ottawa Sand F125  
 $(\bar{\sigma}_{3c} = 0.98 \text{ kg/cm}^2, \bar{\sigma}_{1c} = 1.97 \text{ kg/cm}^2)$

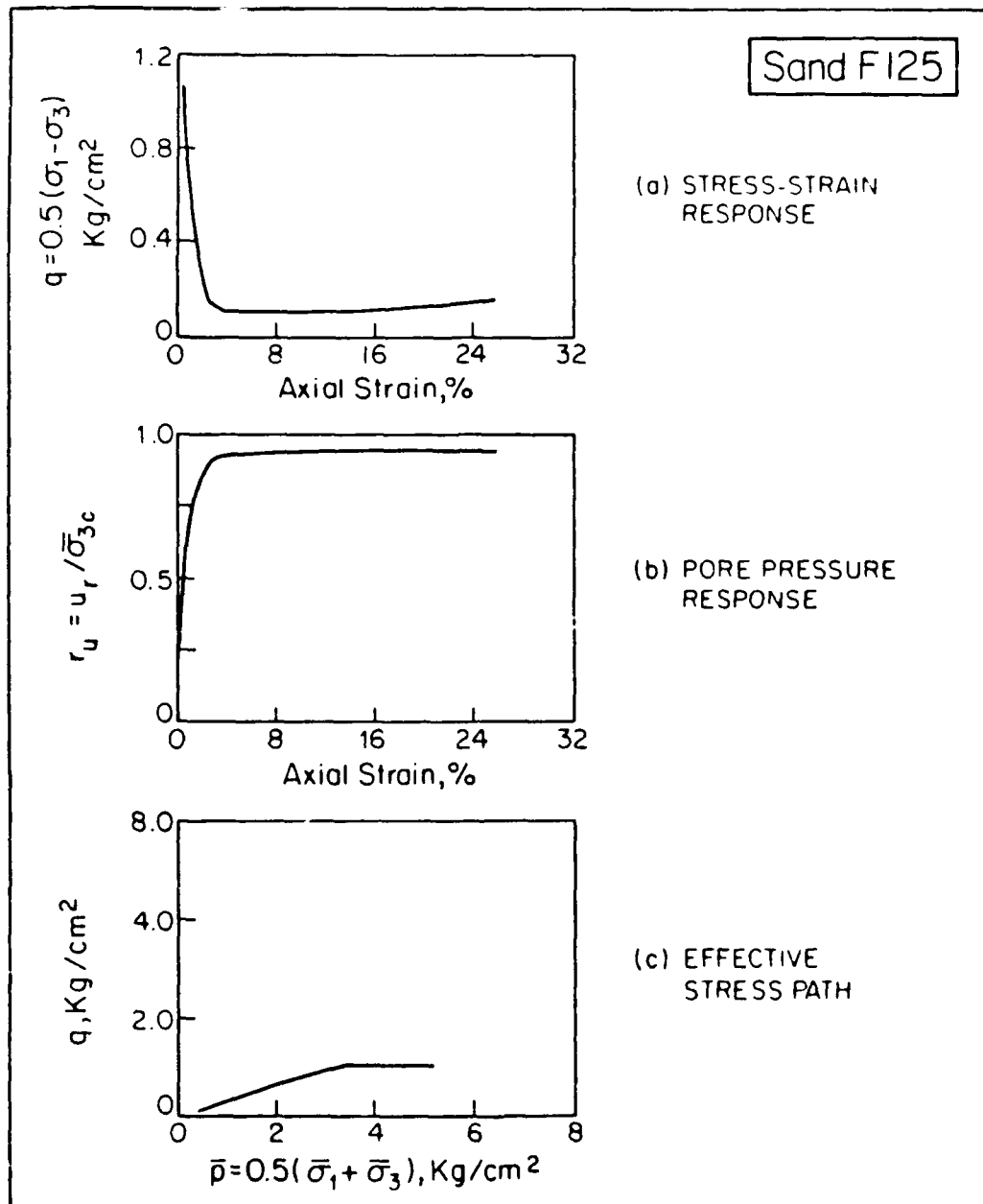


Fig. 6.7. Cyclic Torsional Triaxial CyT-CXU Test on Ottawa Sand F125 ( $\bar{\sigma}_{3c} = 4.07 \text{ kg/cm}^2$ ,  $\bar{\sigma}_{1c} = 6.20 \text{ kg/cm}^2$ ,  $\gamma_{cy} = 0.116\%$ )

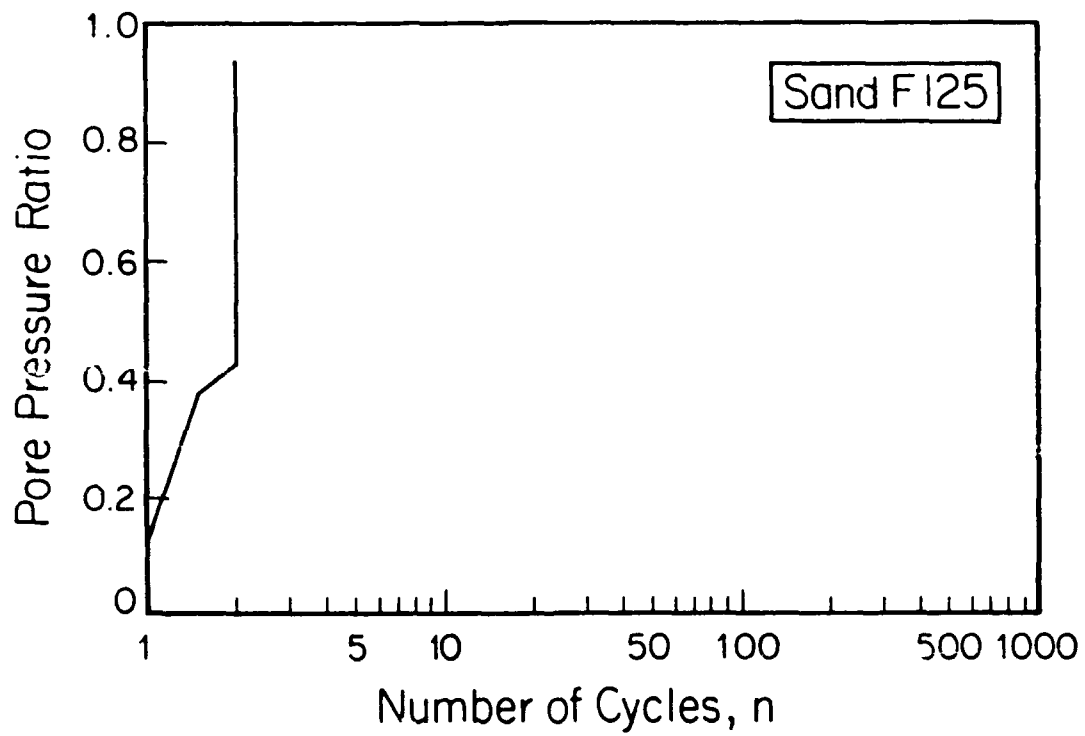


Fig. 6.8. Pore Water Pressure Buildup for the CyT-CAU Test in Figure 6.7

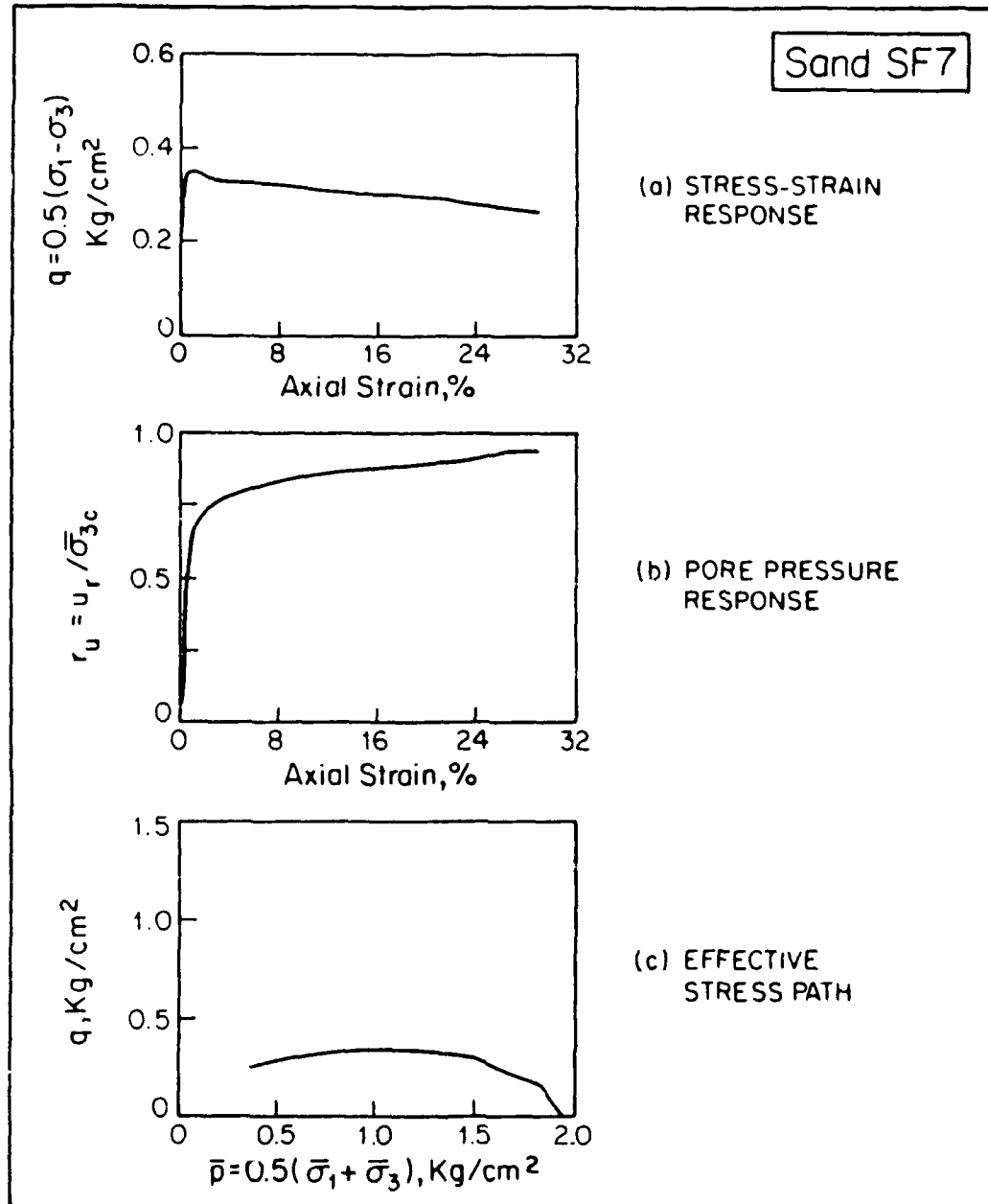


Fig. 6.9. Monotonic Triaxial CTU Test on Sand SF7  
 $(\bar{\sigma}_{3c} = \bar{\sigma}_{1c} = 1.98 \text{ kg/cm}^2)$



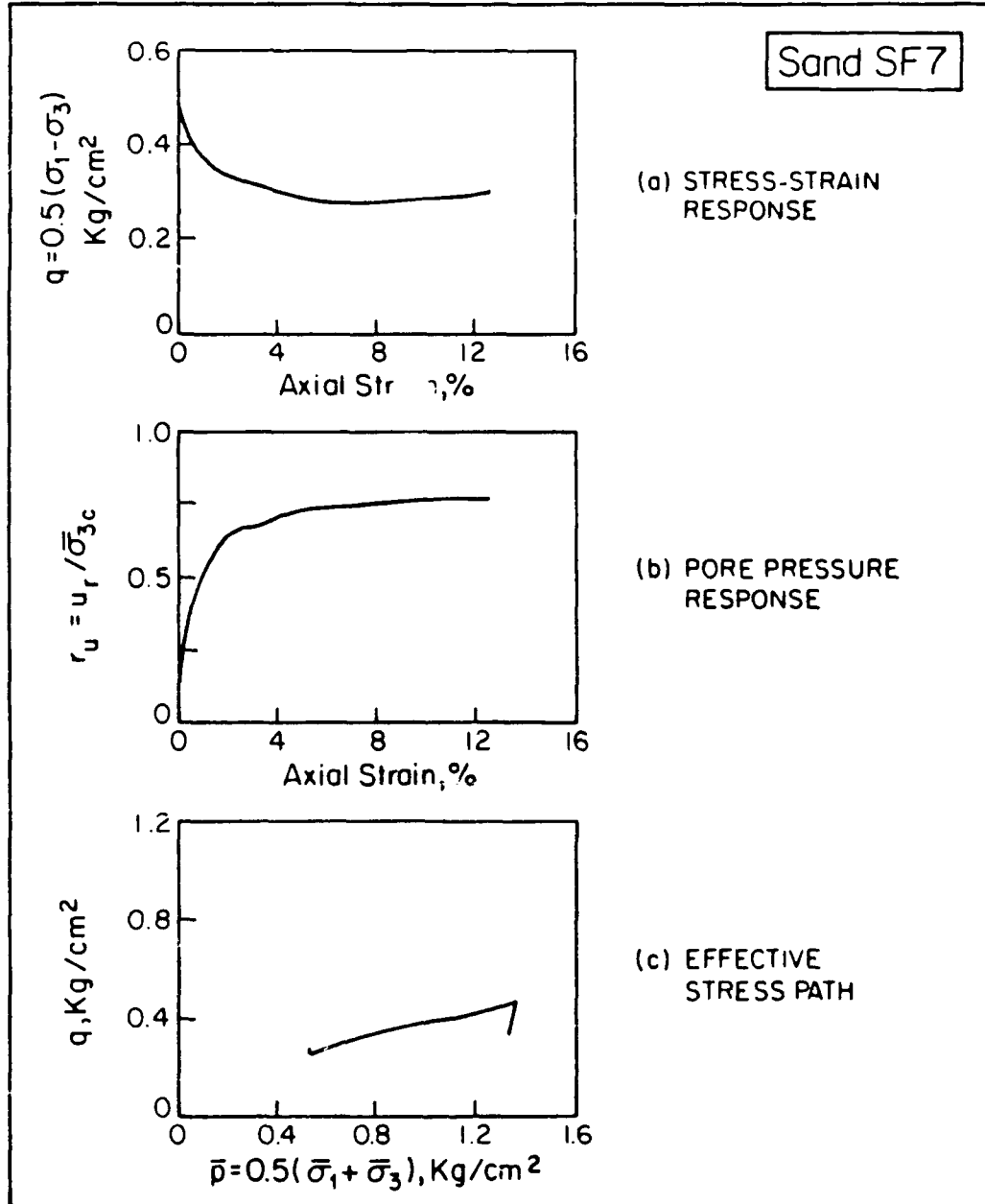


Fig. 6.10. Monotonic Triaxial Strain-Controlled CAU Test on Sand SF7 ( $\bar{\sigma}_{3c} = 0.98 \text{ kg/cm}^2$ ,  $\bar{\sigma}_{1c} = 1.67 \text{ kg/cm}^2$ )

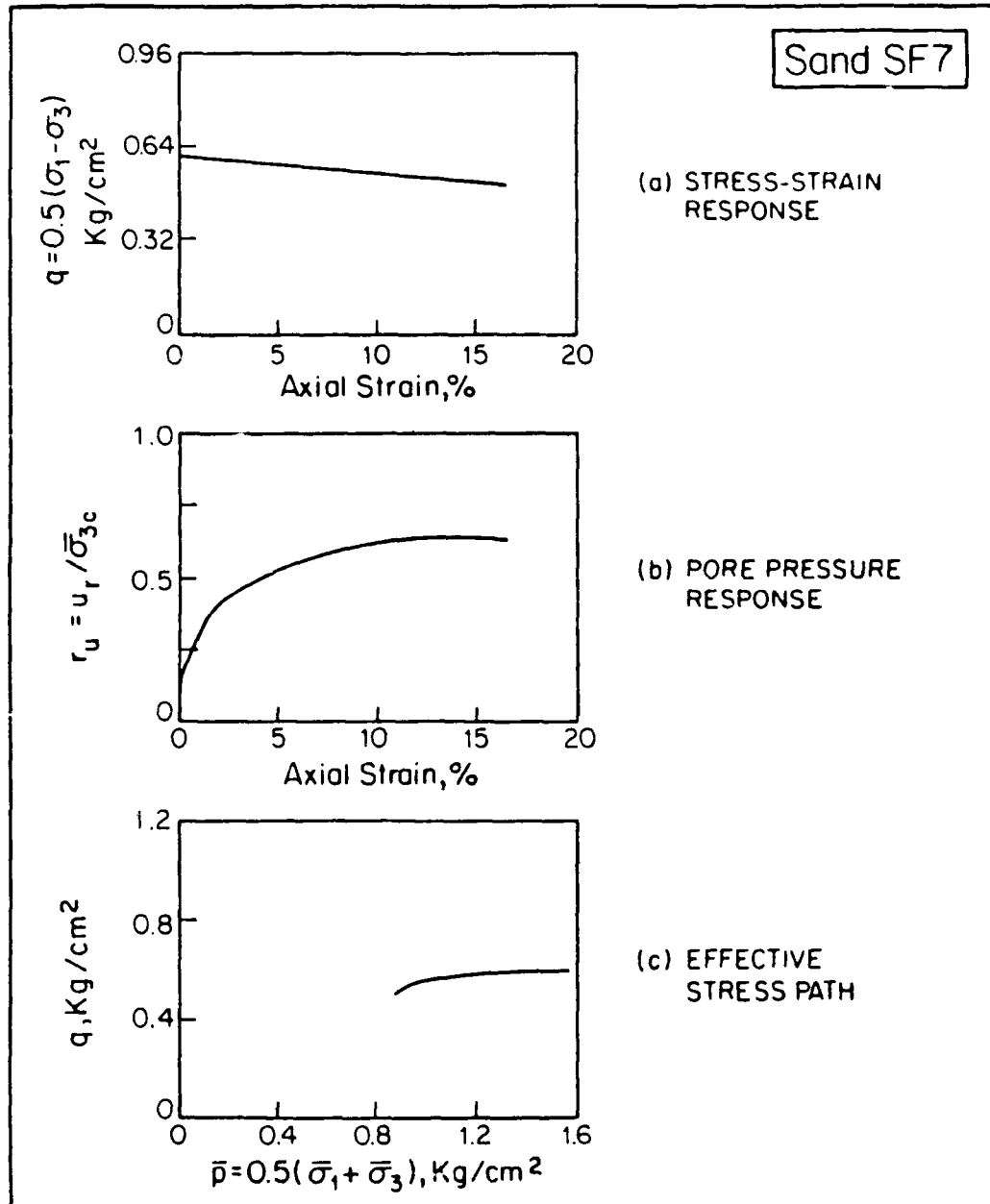


Fig. 6.11. Cyclic Torsional Triaxial CyT-CAU Test on Sand SF7 ( $\bar{\sigma}_{3c} = 0.98$  kg/cm<sup>2</sup>,  $\bar{\sigma}_{1c} = 2.17$  kg/cm<sup>2</sup>,  $\gamma_{cy} = 0.0107\%$ )

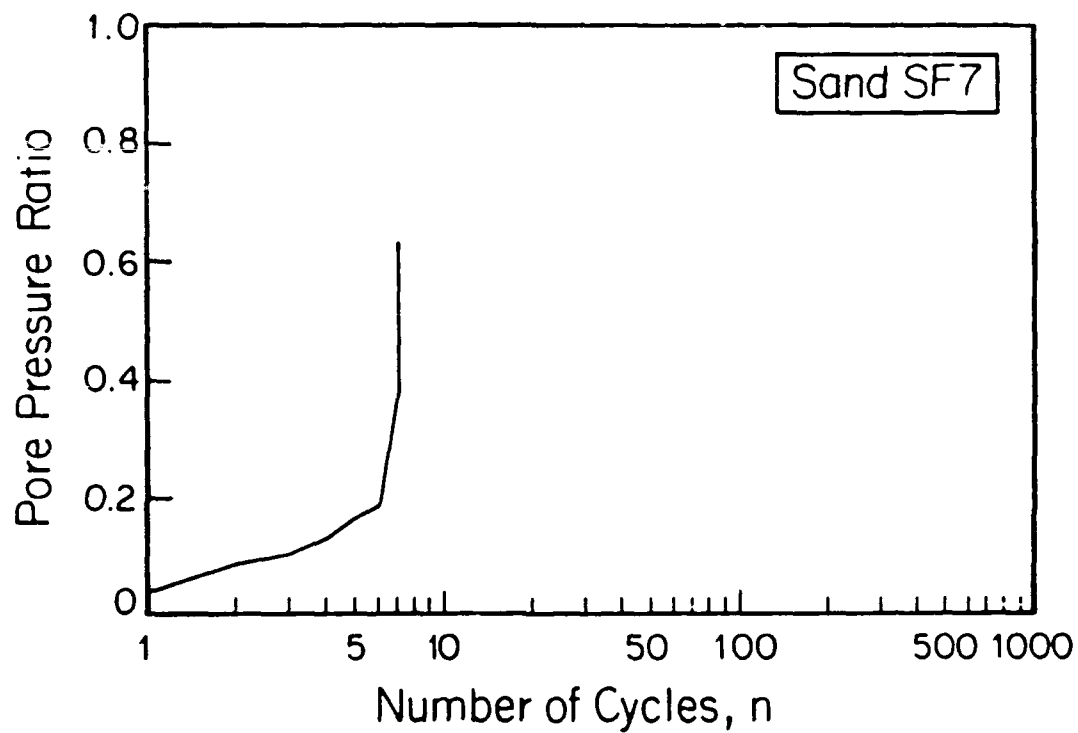


Fig. 6.12. Pore Water Pressure Buildup Versus Number of Cycles for the CyT-CAU Test in Figure 6.11

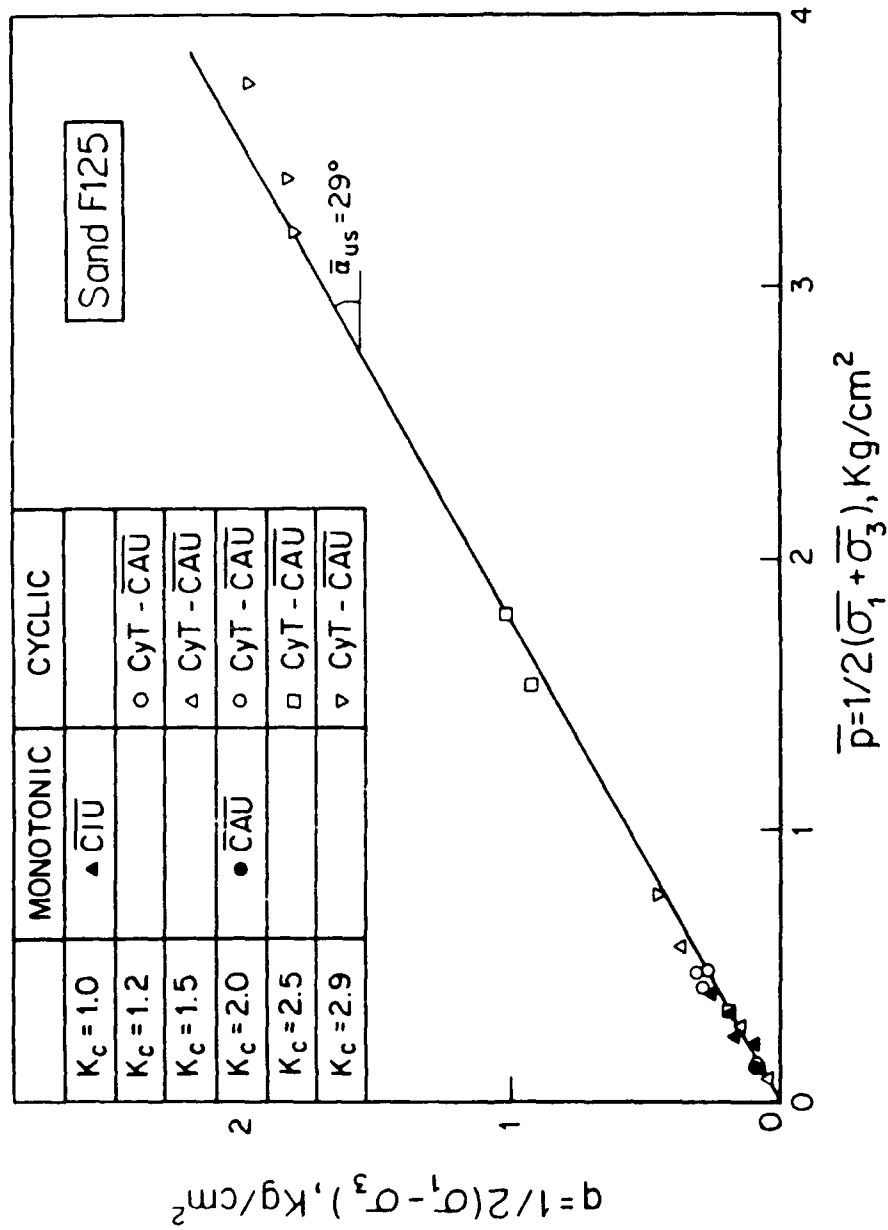


Fig. 6.13. Steady-State Strength Envelope for Ottawa Sand F125

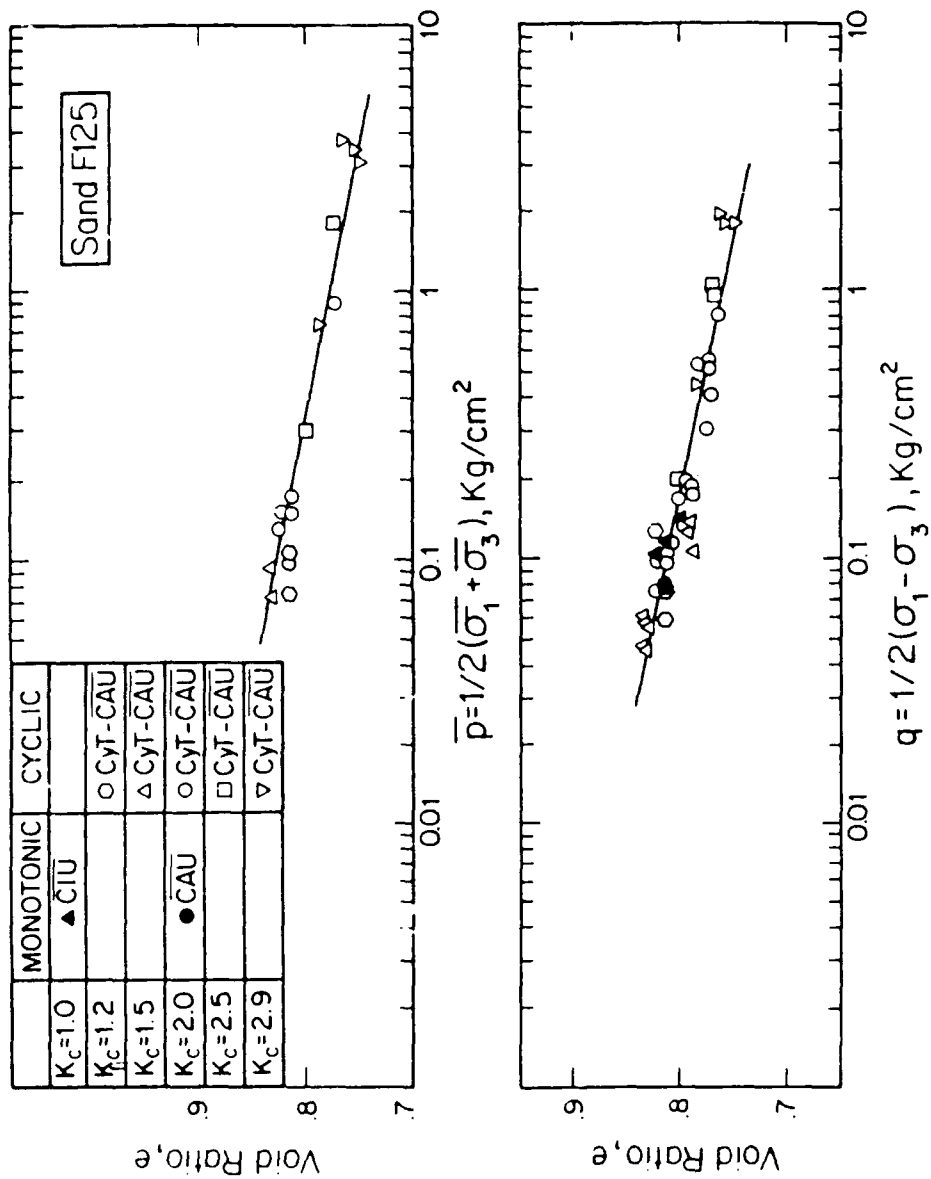


Fig. 6.14. Steady-State Lines of Ottawa Sand F125 in  $e-\bar{p}$  and  $e-q$  space

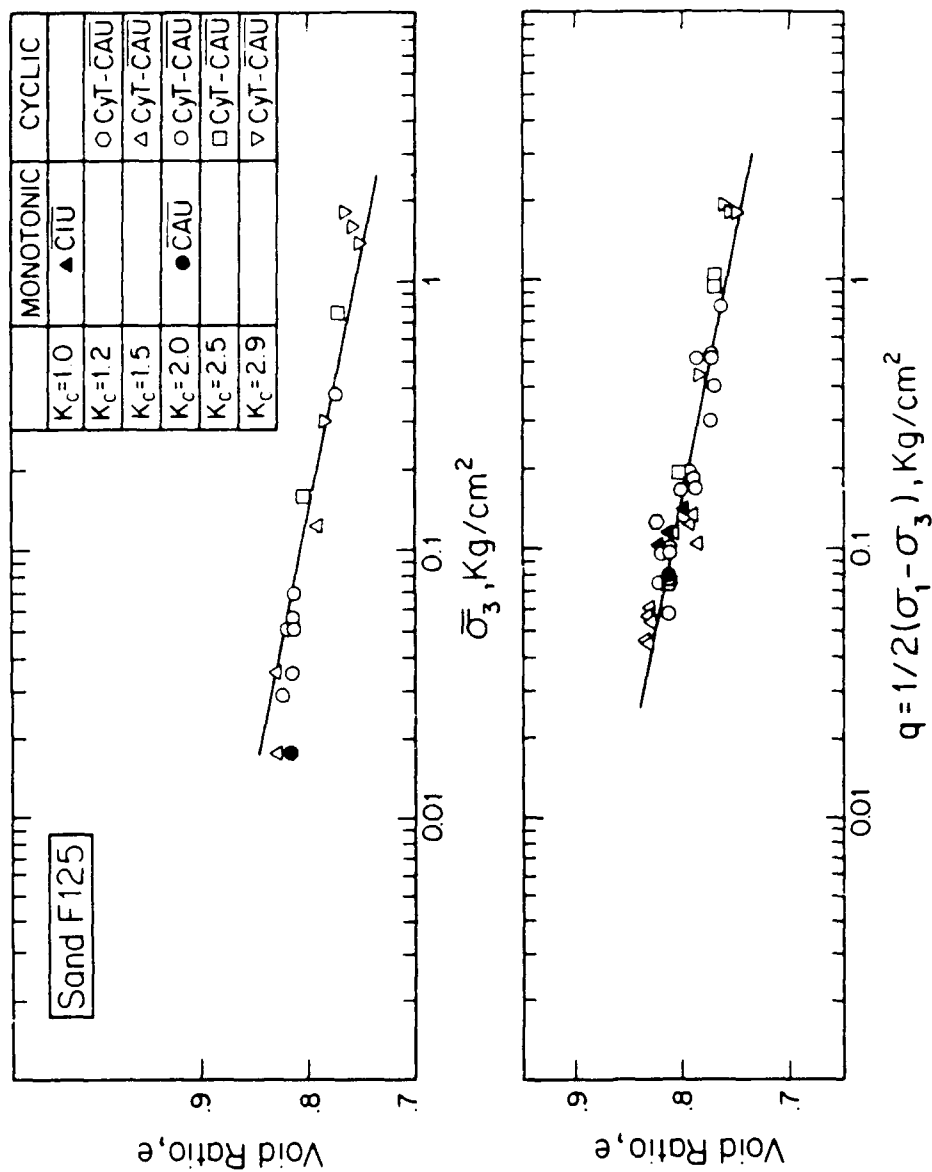


Fig. 6.15. Steady-State Lines for Ottawa Sand F125 in  $e-\bar{\sigma}_3$  and  $e-q$  space

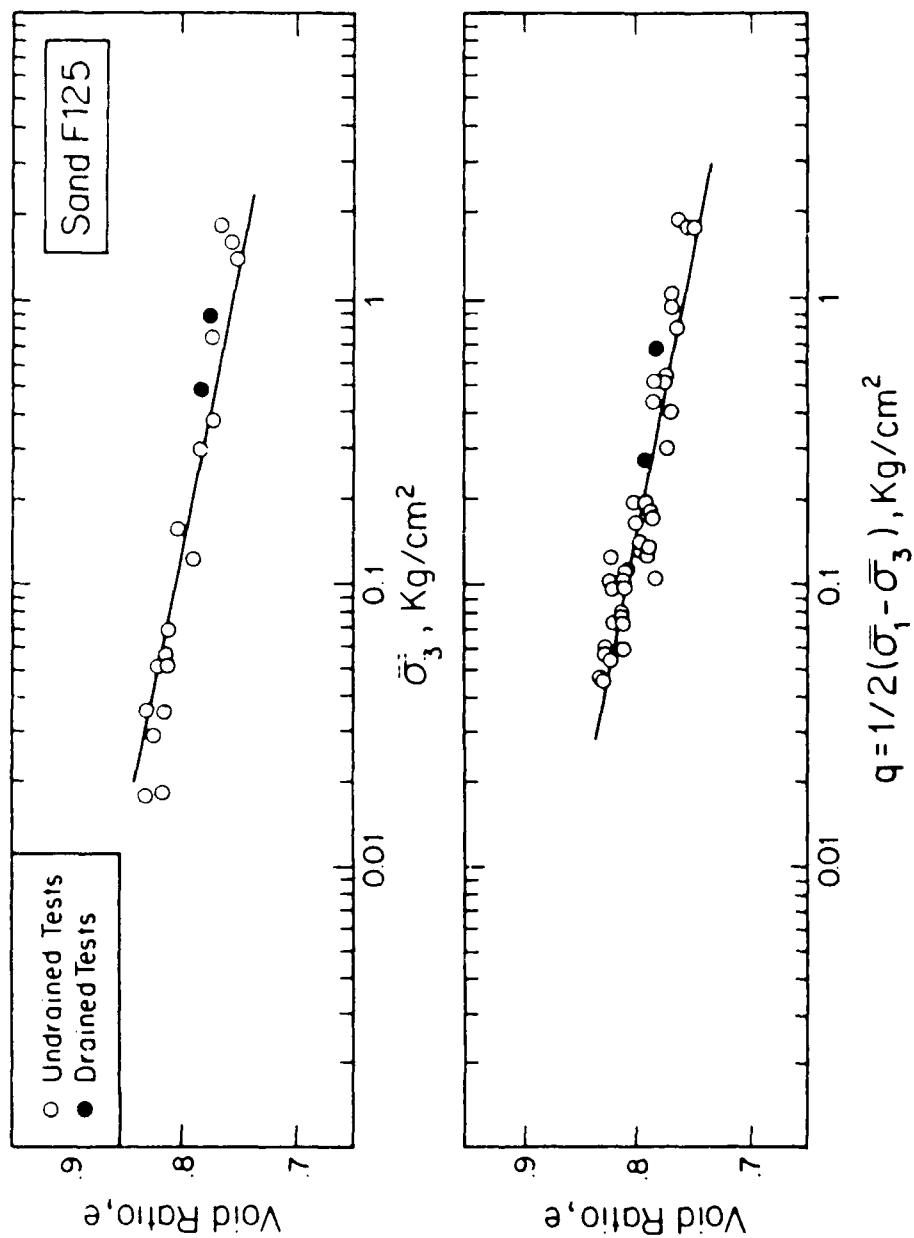


Fig. 6.16. Comparison Between Drained and Undrained Tests Defining the SSL of Ottawa Sand F125

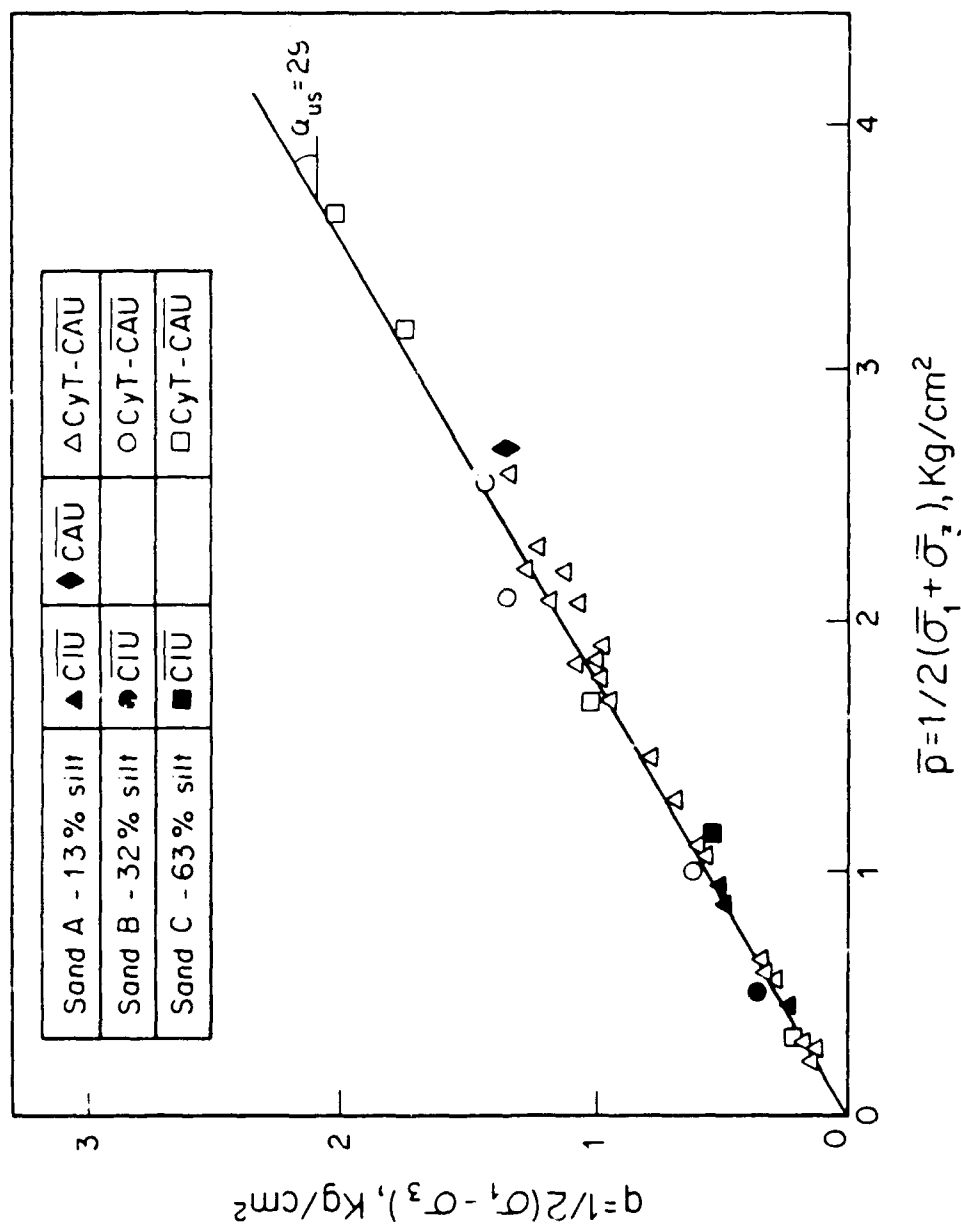


Fig. 6.17. Steady-State Strength Envelope on Silty Sands A, B and C



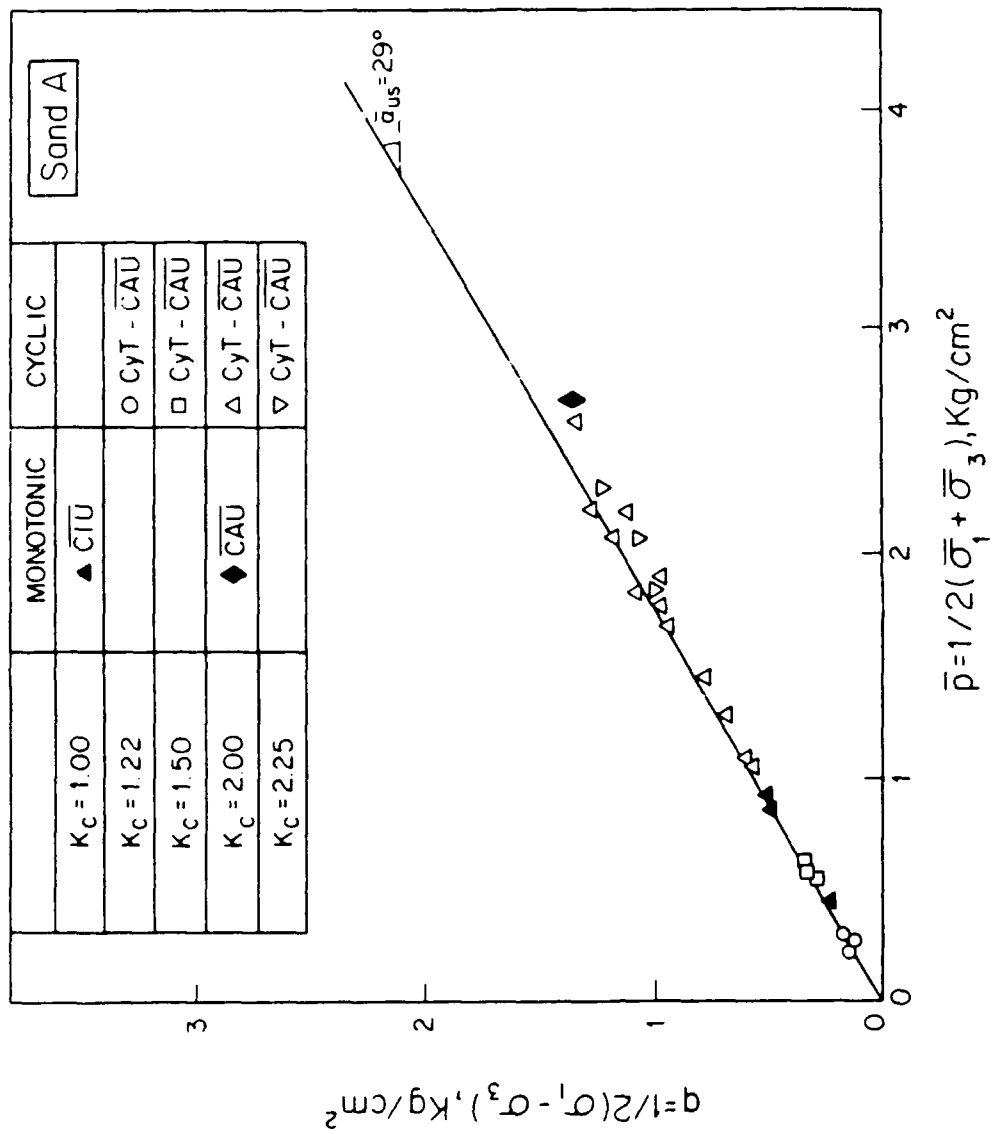


Fig. 6.18. Steady-State Strength Envelope on Silty Sand A

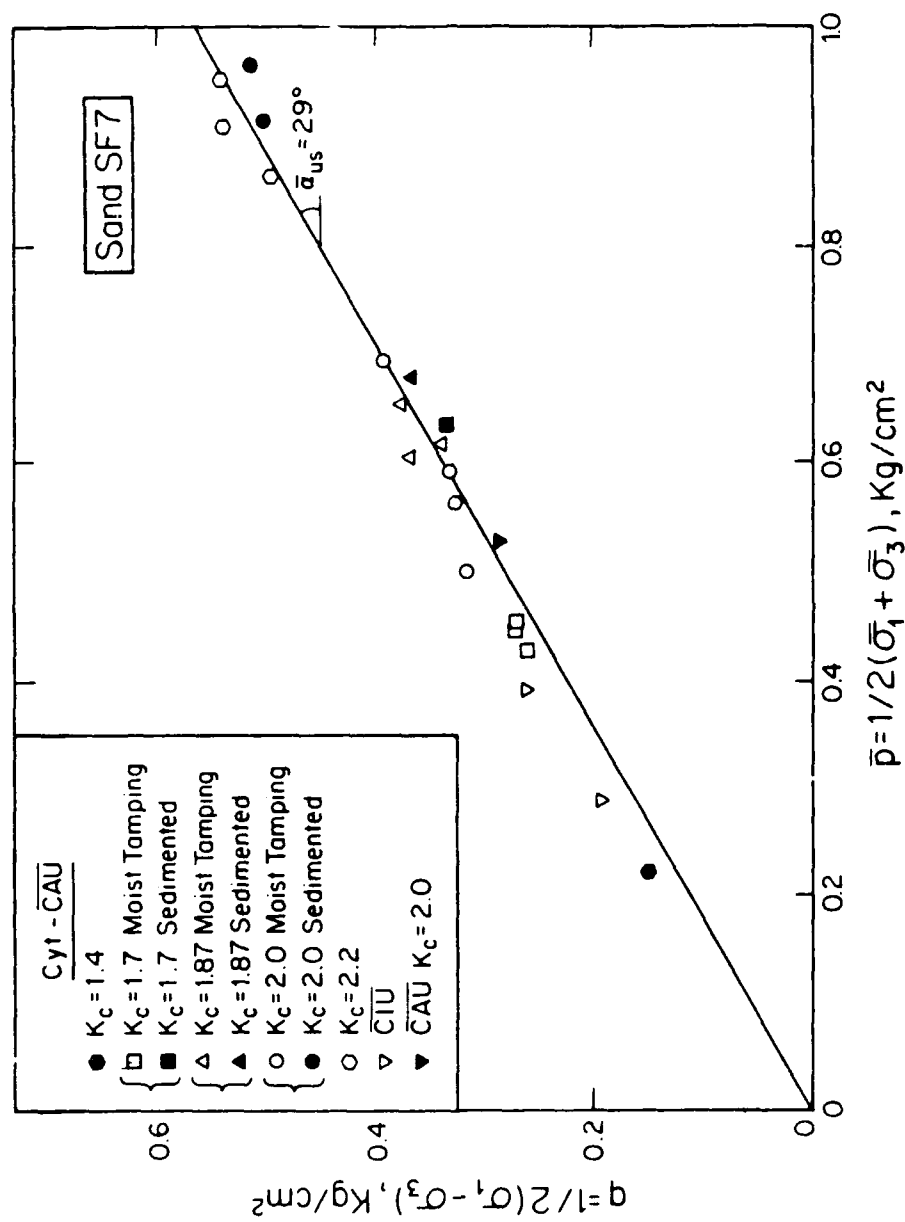


Fig. 6.19. Steady-State Strength Envelope on Silty Sand SF7

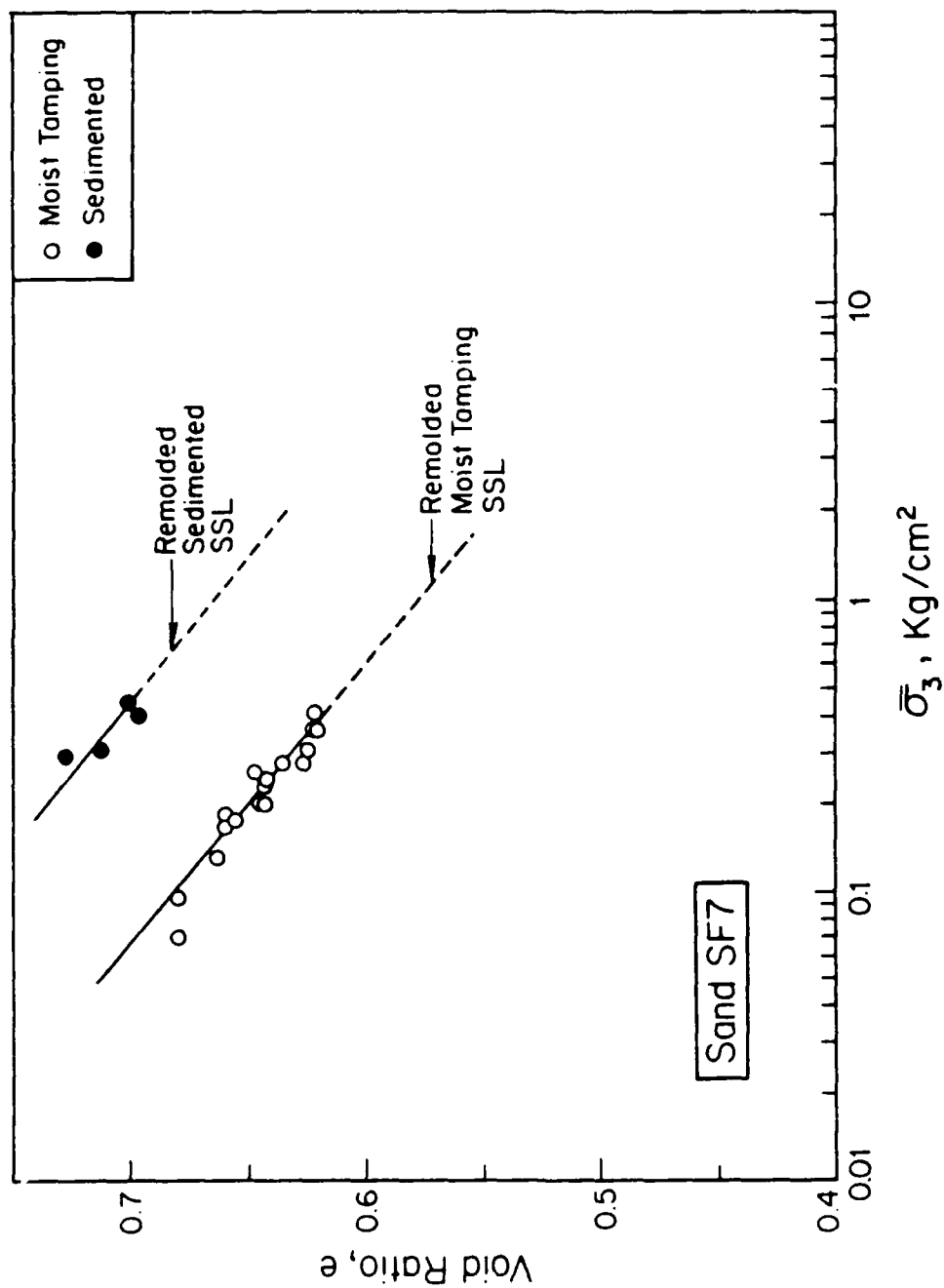


Fig. 6.20. Steady-State Strength Envelope on Silty Sand SF7 in  $e-\bar{\sigma}_3$  Space for Sedimented and Moist Tamped Specimens

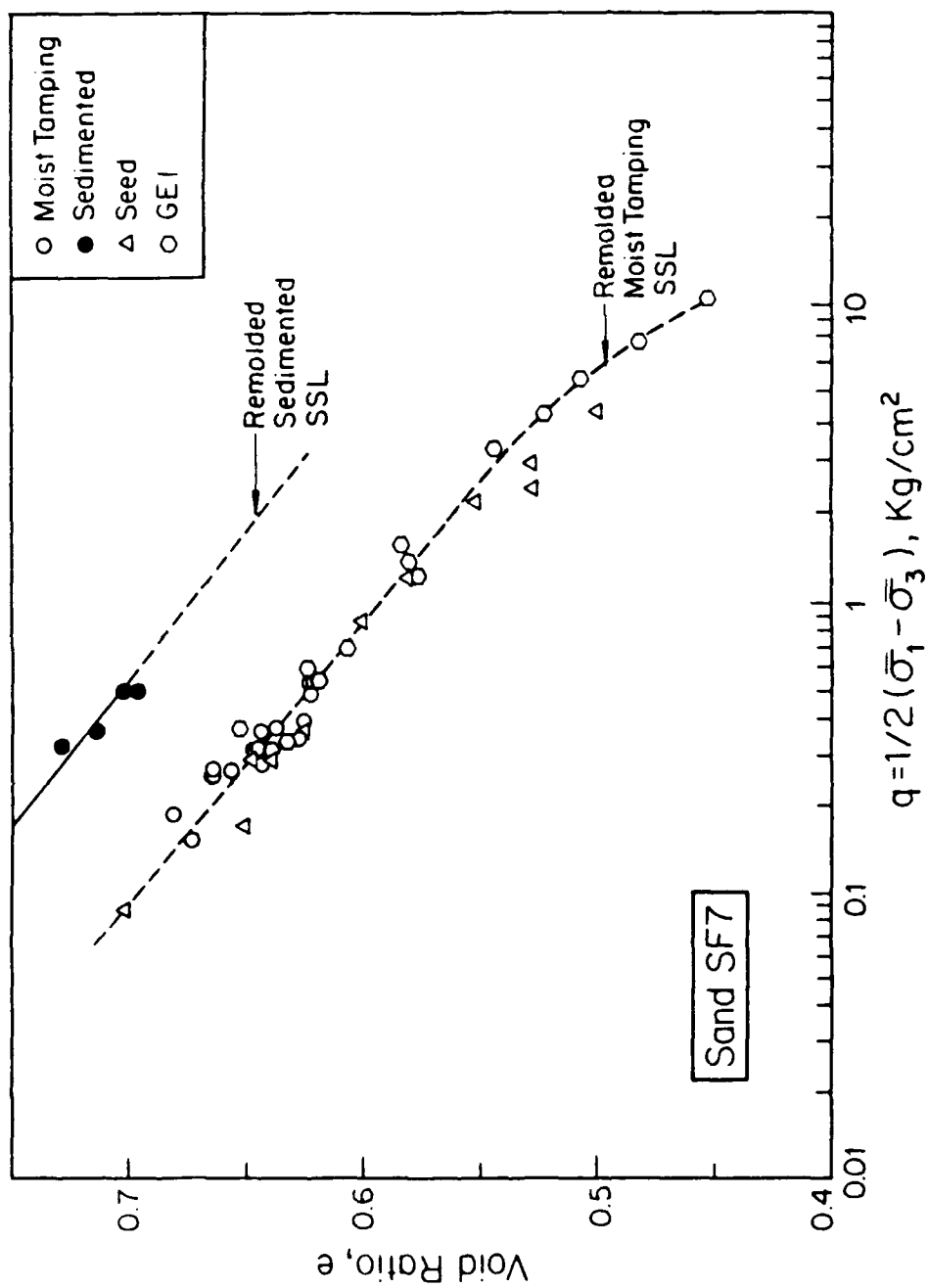


Fig. 6.21. Steady-State Strength Envelope on Silty Sand SF7 in  $e$ - $q$  Space for Sedimented and Moist Tamped Specimens

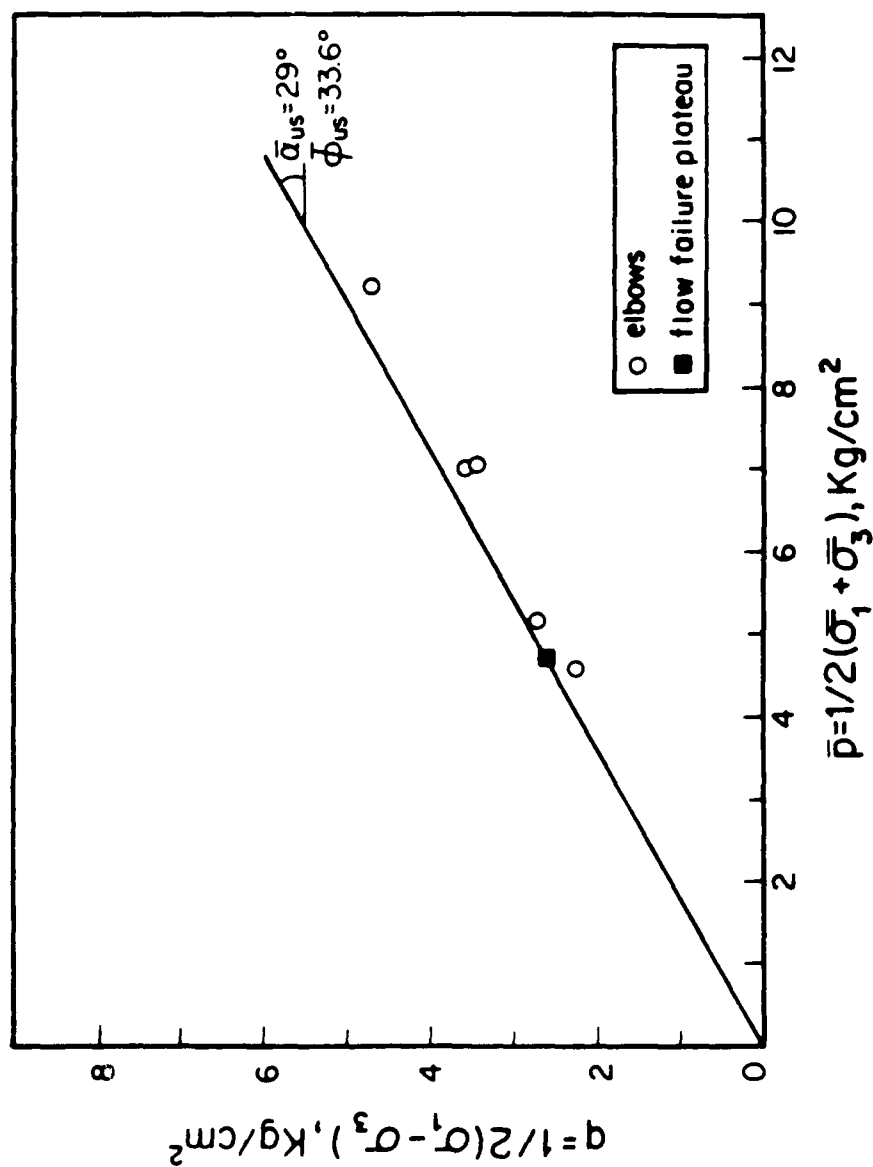


Fig. 6.22. Steady-State Strength Envelope Points for the Intact Specimens and Comparison with  $\bar{q}_{us}$  Obtained from Remolded Specimens

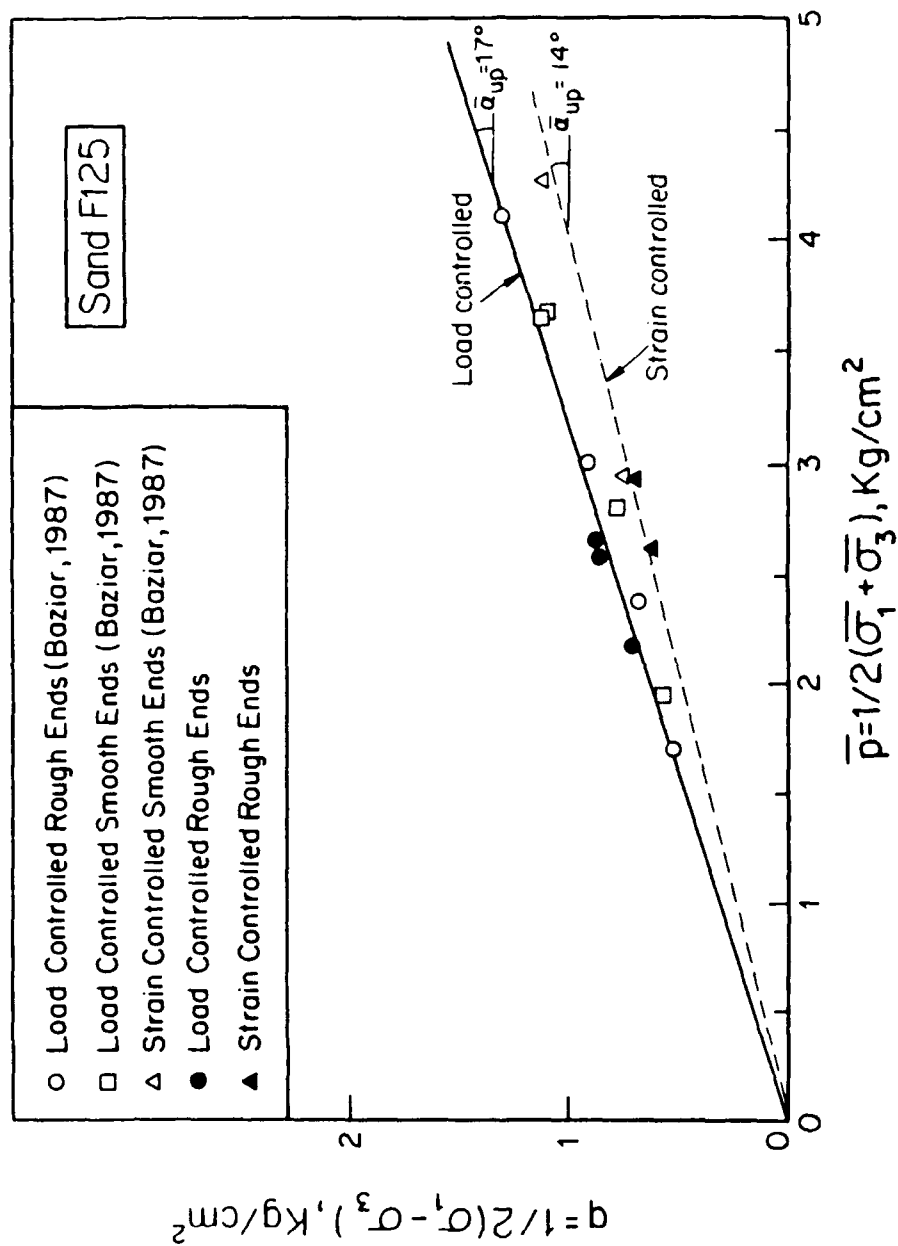


Fig. 6.23. Comparison of Peak Strength Envelopes Between Load and Strain-Controlled Monotonic CU Tests on Ottawa Sand F125

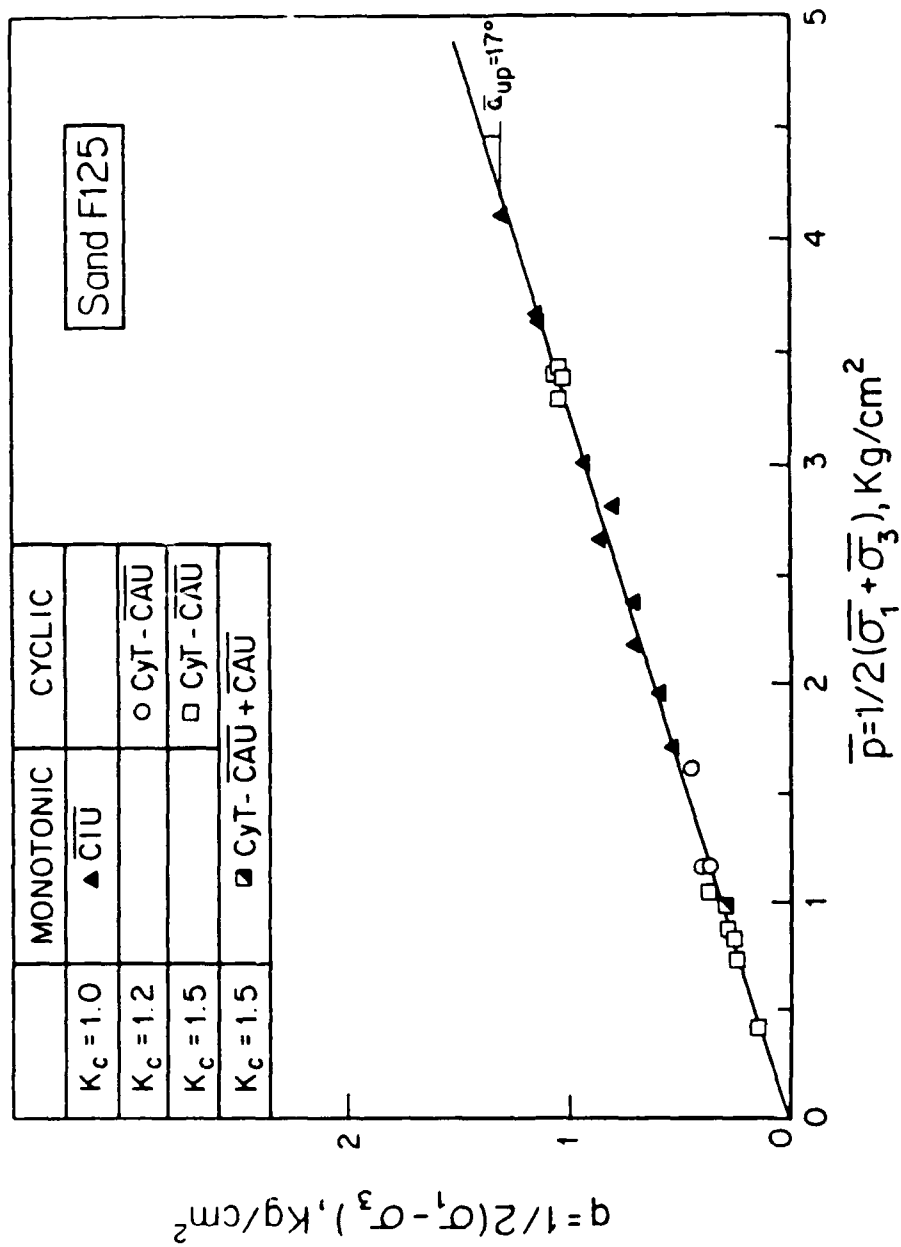


Fig. 6.24. Triggering Envelope for Ottawa Sand F125 with Specimens Consolidated Below  $\bar{\sigma}_{up} = 17^\circ$

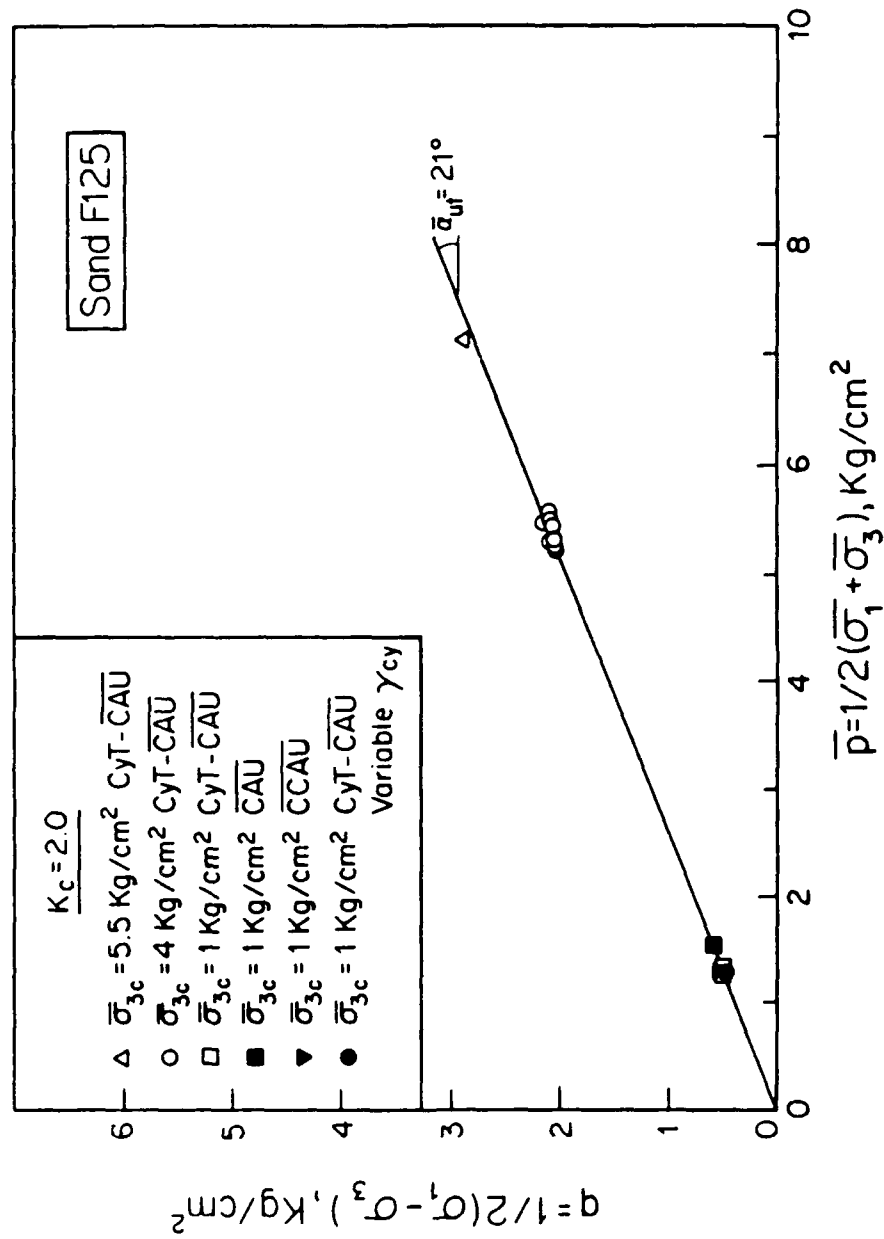


Fig. 6.25. Triggering Envelope for Ottawa Sand F125 Specimens Consolidated with  $K_c = 2.0$



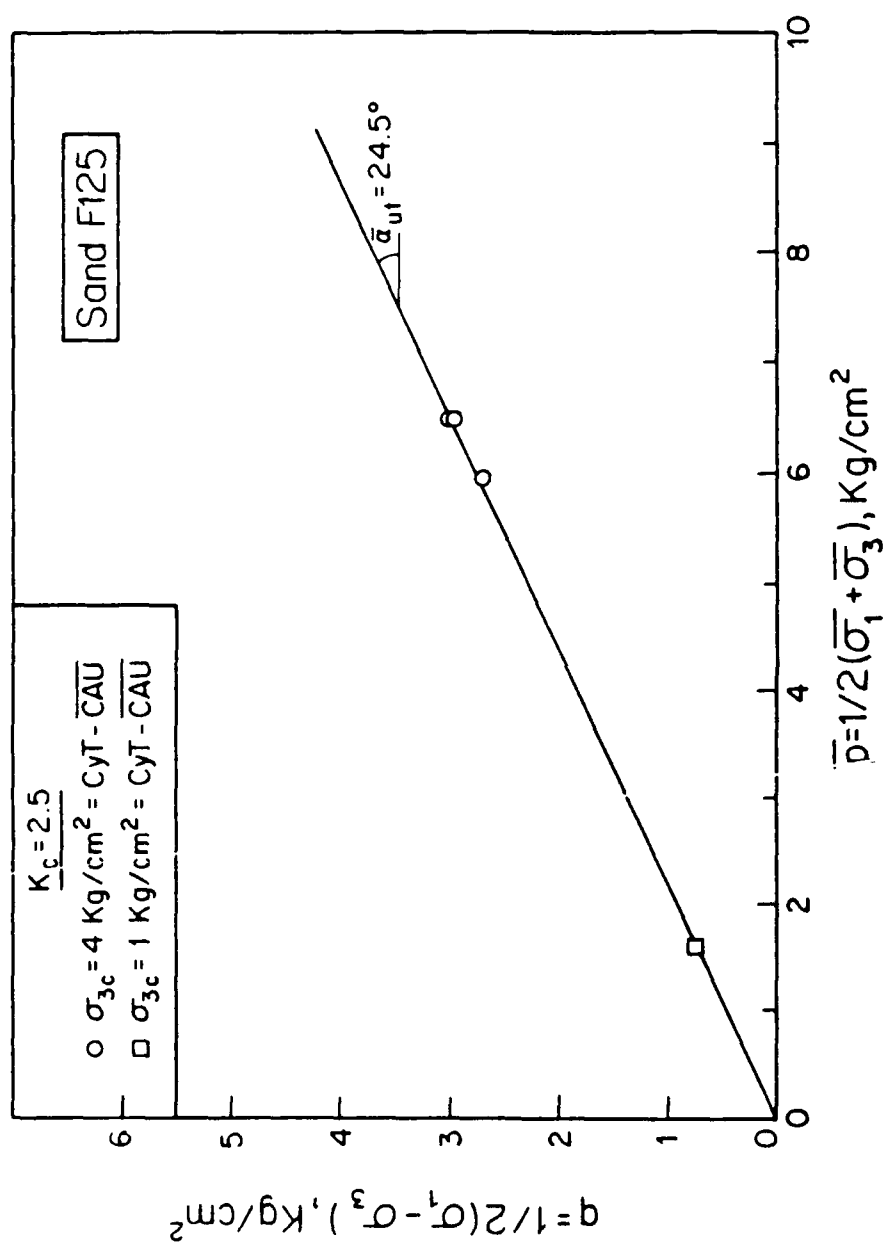


Fig. 6.26. Triggering Envelope for Ottawa Sand F125  
Specimens Consolidated with  $K_c = 2.5$

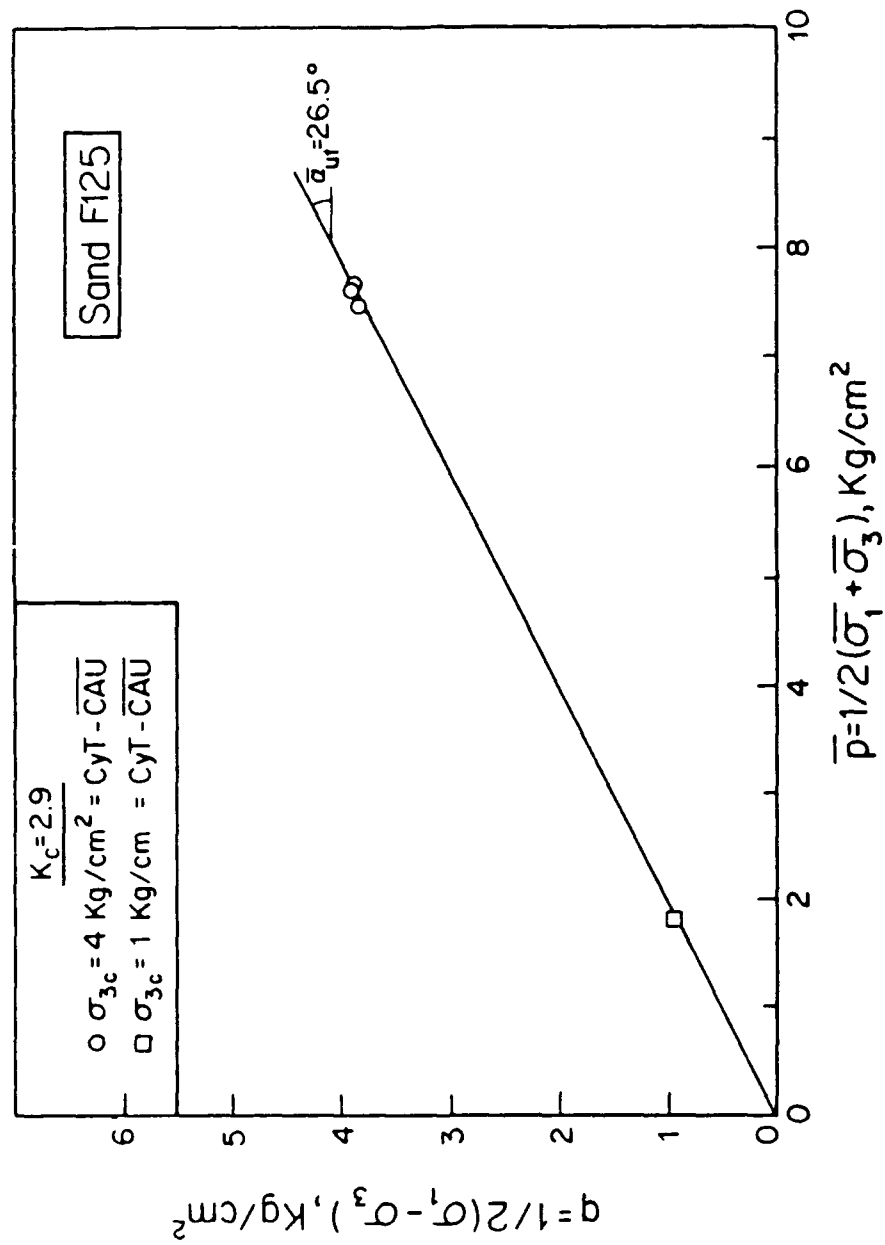


Fig. 6.27. Triggering Envelope for Ottawa Sand F125 Specimens Consolidated with  $K_c = 2.9$

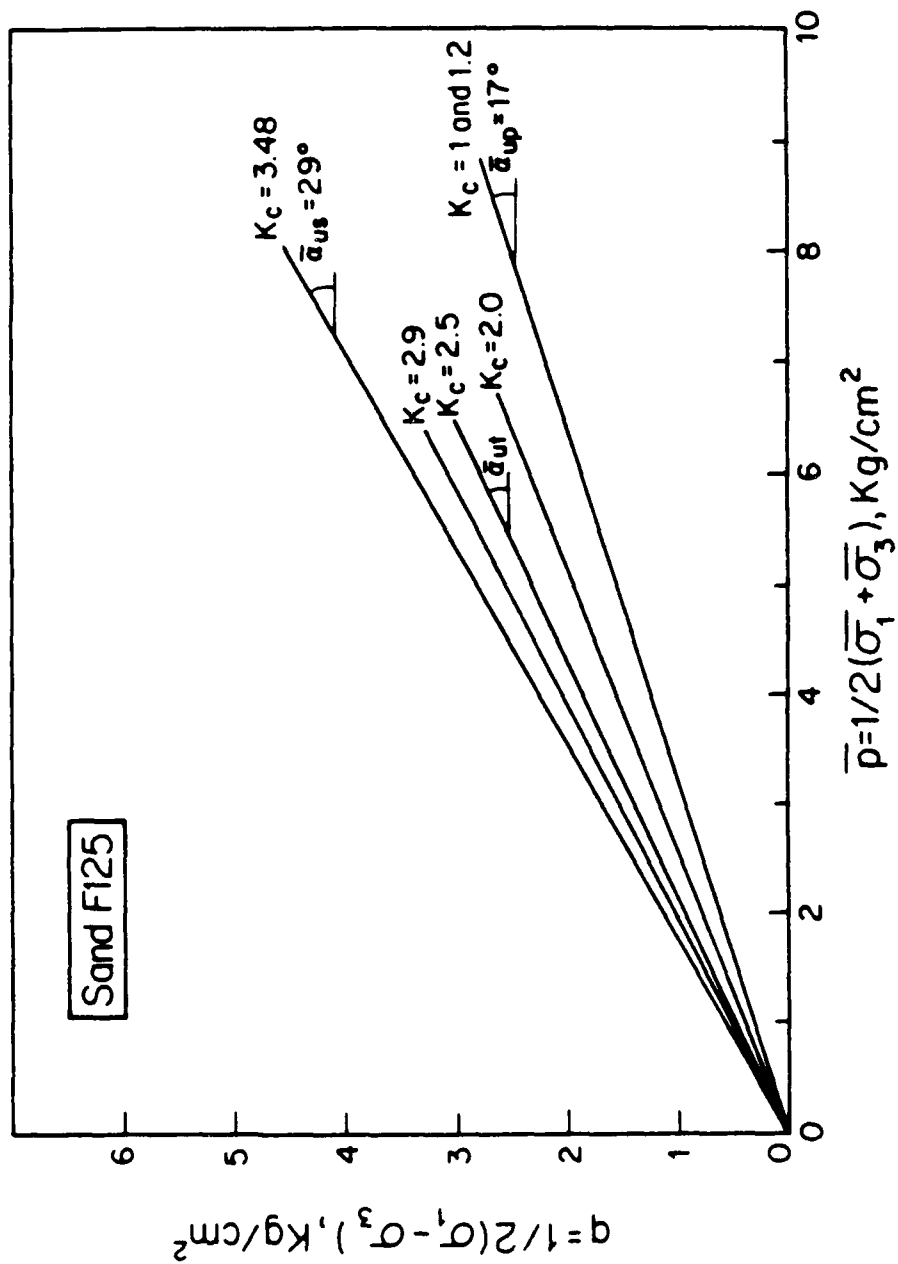


Fig. 6.28. Comparison Between Triggering Envelopes of Ottawa Sand F125 Showing the Influence of  $K_c$

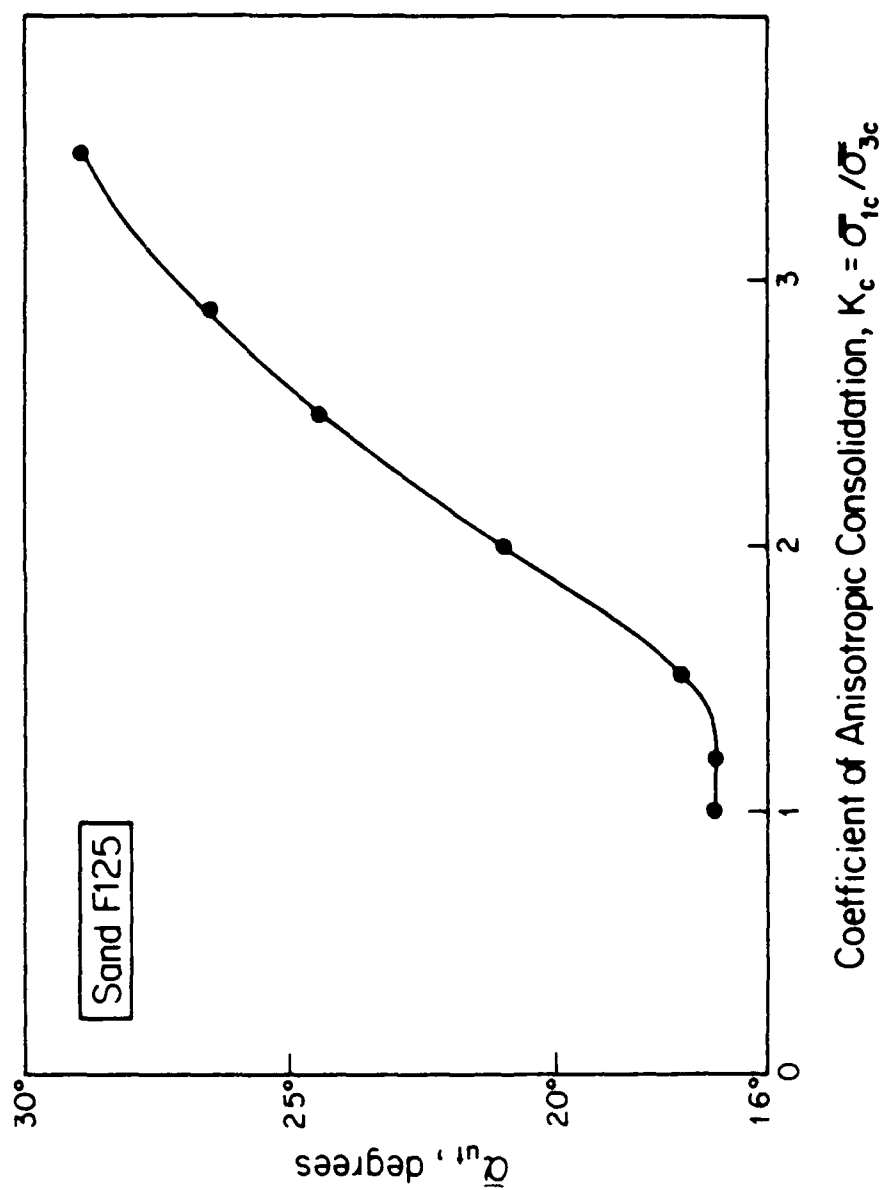


Fig. 6.29. Influence of  $K_c$  on  $\alpha_{ut}$  for Ottawa Sand F125

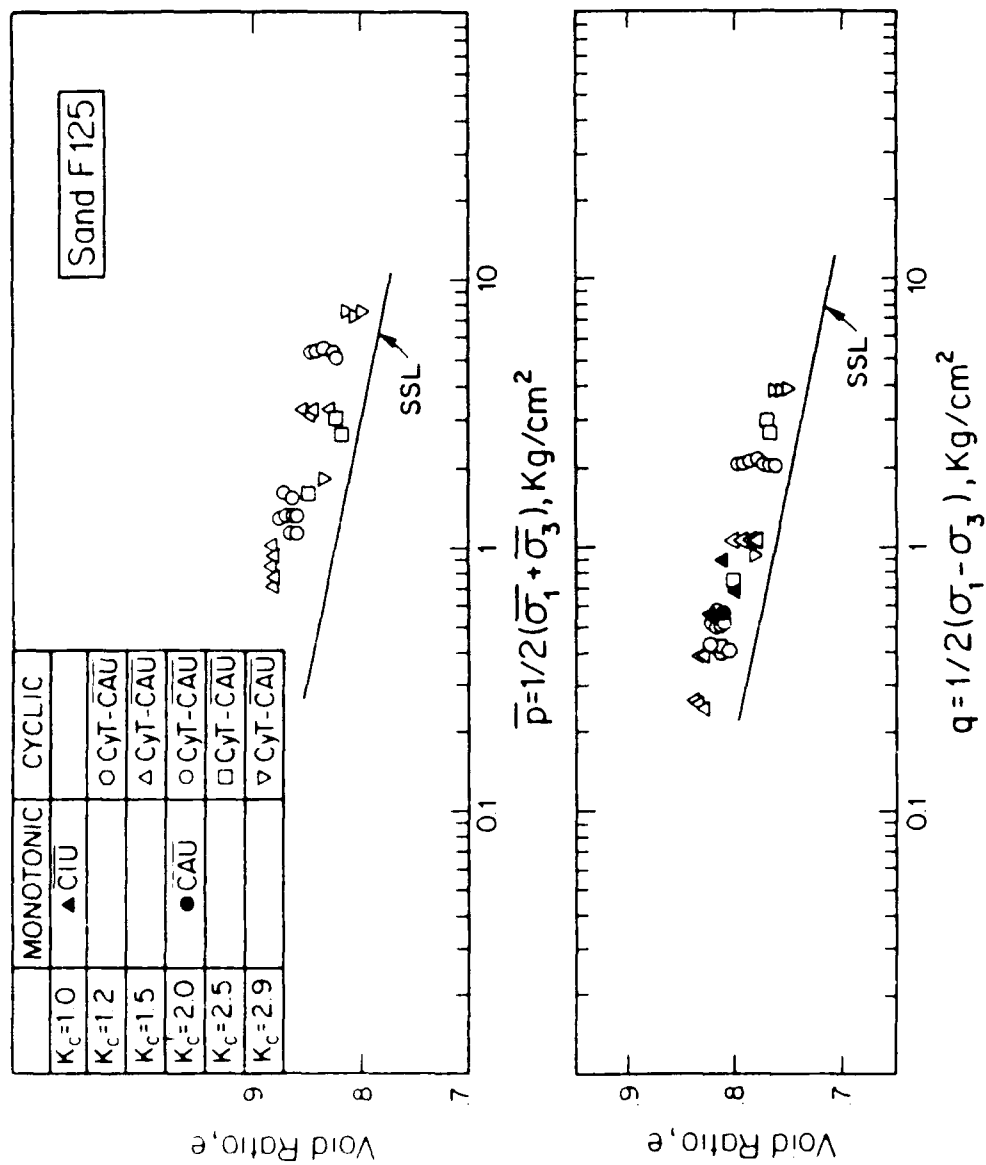


Fig. 6.30. Comparison Between SSL and Triggering Conditions in Ottawa F125 Sand

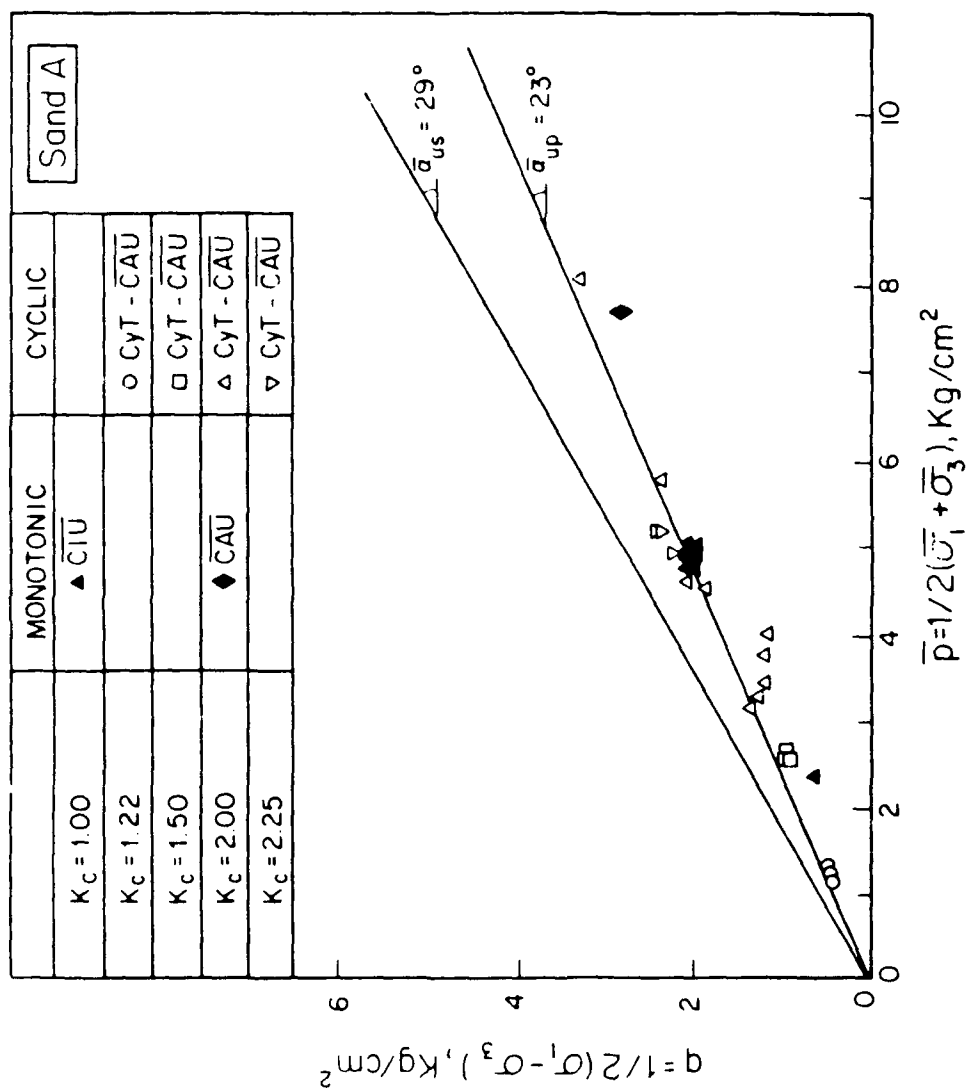


Fig. 6.31. Triggering of Flow Failure Strength Envelope for Sand A

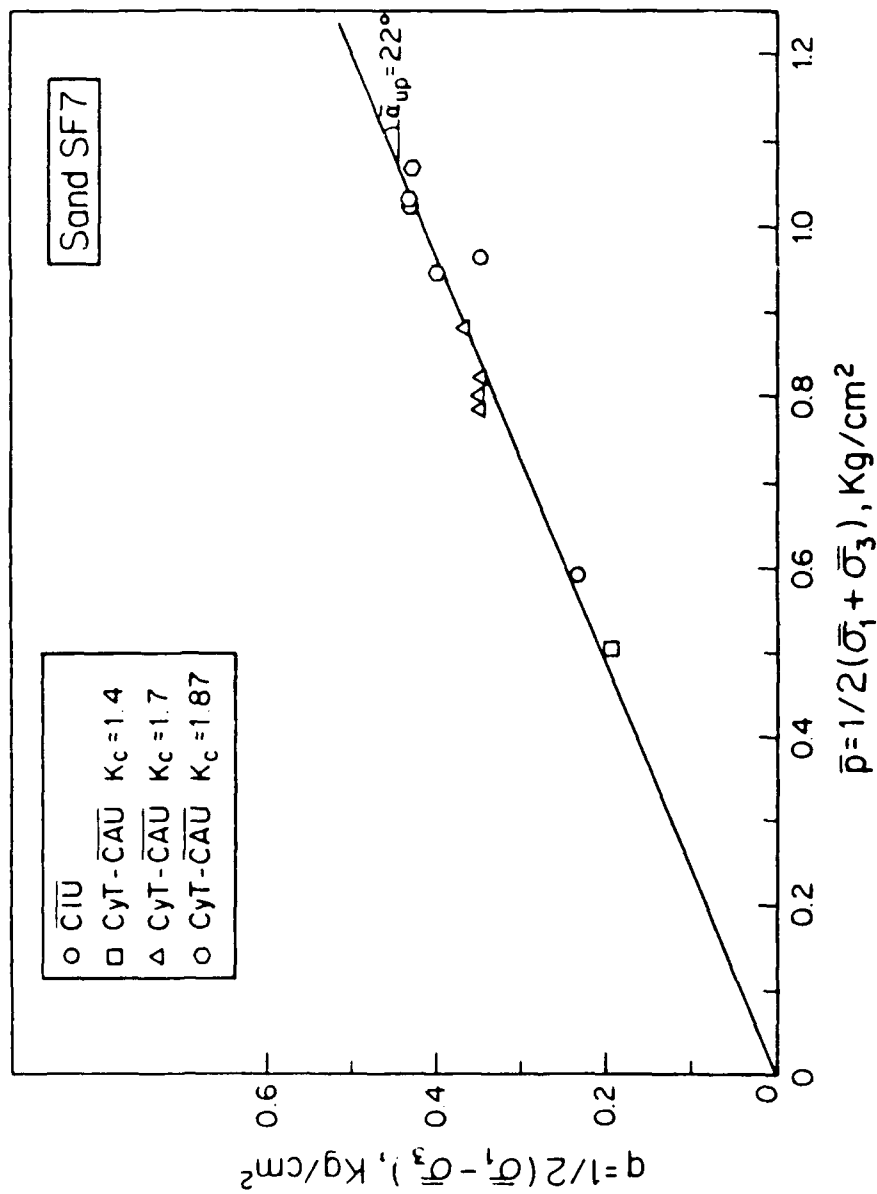


Fig. 6.32. Triggering Envelope of Sedimented and Moist Tamped Specimens of Sand SF7 Consolidated with  $K_c \leq 1.87$  Using Sedimented Specimens

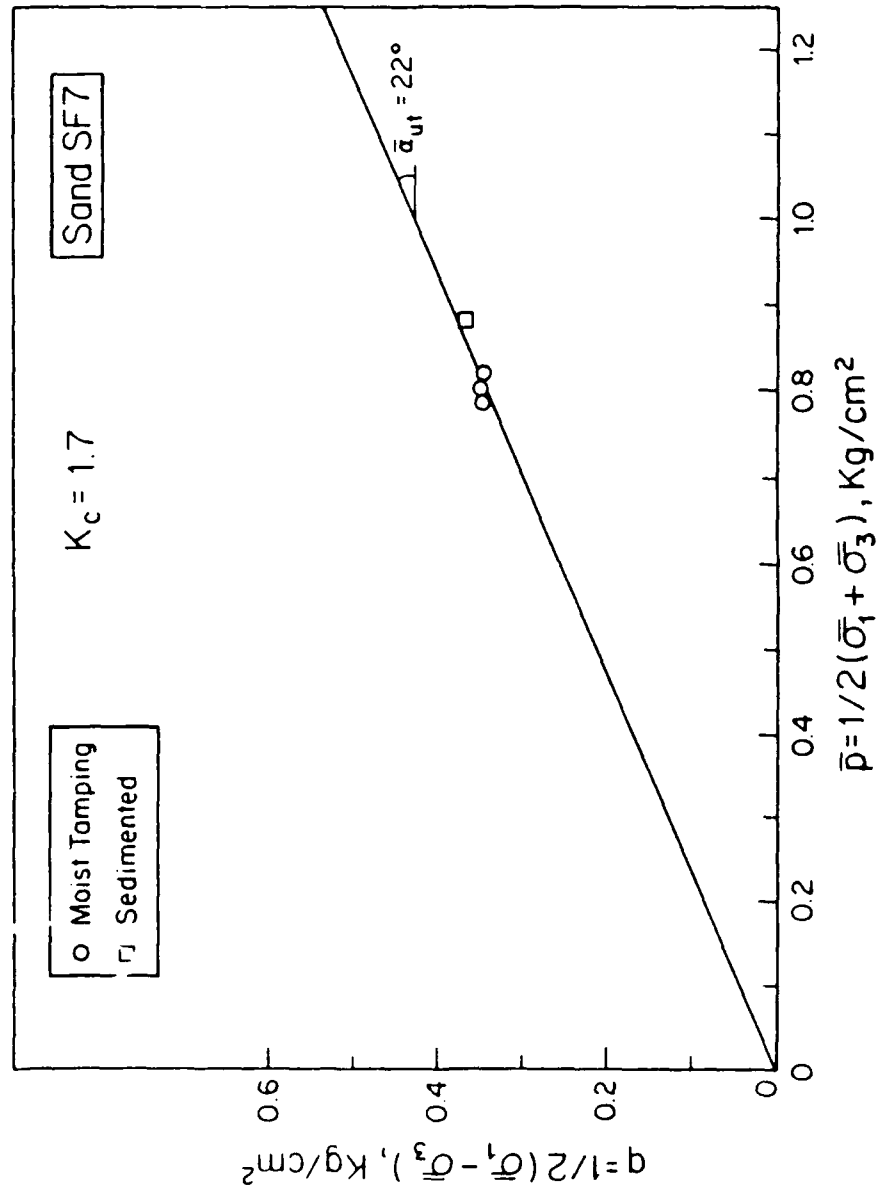


Fig. 6.33. Triggering Envelope of Sedimented and Moist Tamped Specimens of Sand SF7 with  $K_c = 1.7$



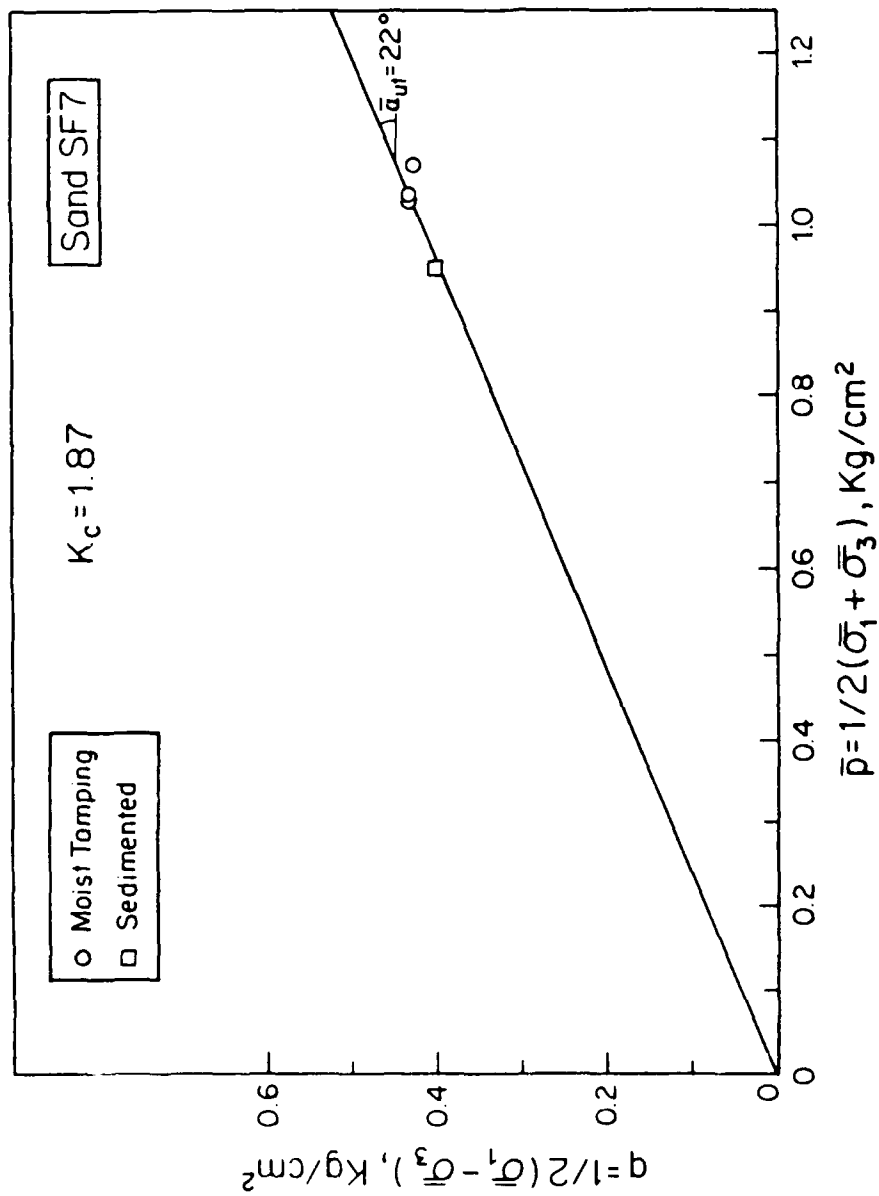


Fig. 6.34. Triggering Envelope of Sedimented and Moist Tamped Specimens of Sand SF7 with  $K_c = 1.87$

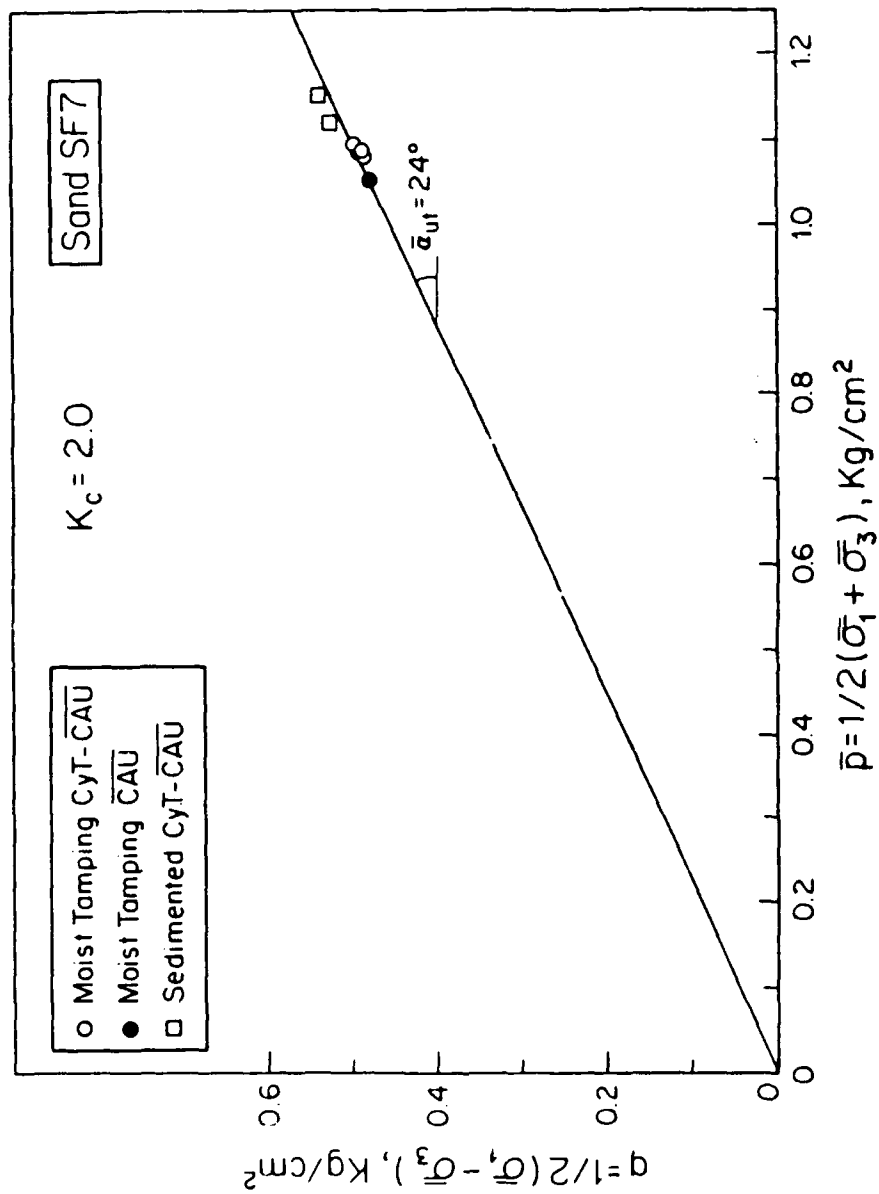


Fig. 6.35. Triggering Envelope of Sedimented and Moist Tamped Specimens of Sand SF7 with  $K_c = 2.0$

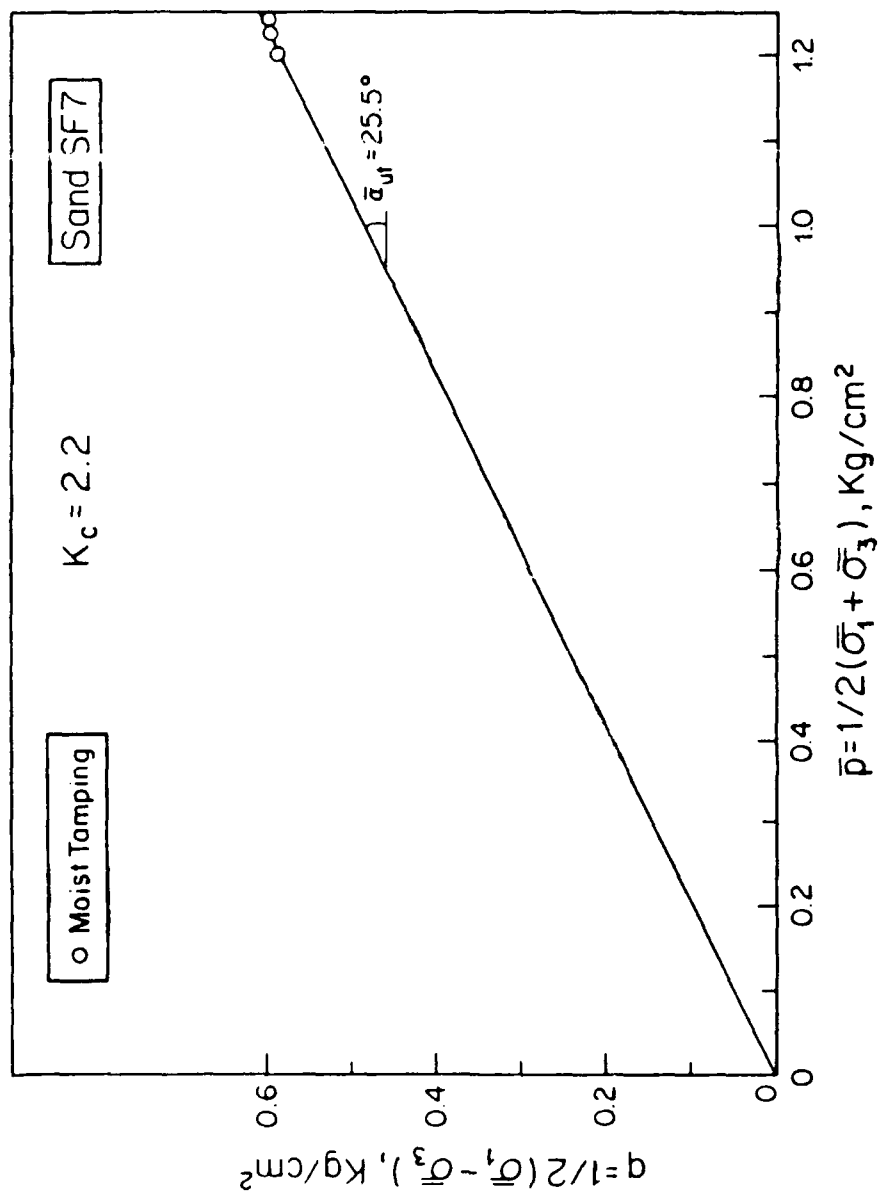


Fig. 6.36. Triggering Envelope of Sedimented and Moist Tamped Specimens of Sand SF7 with  $K_c = 2.2$

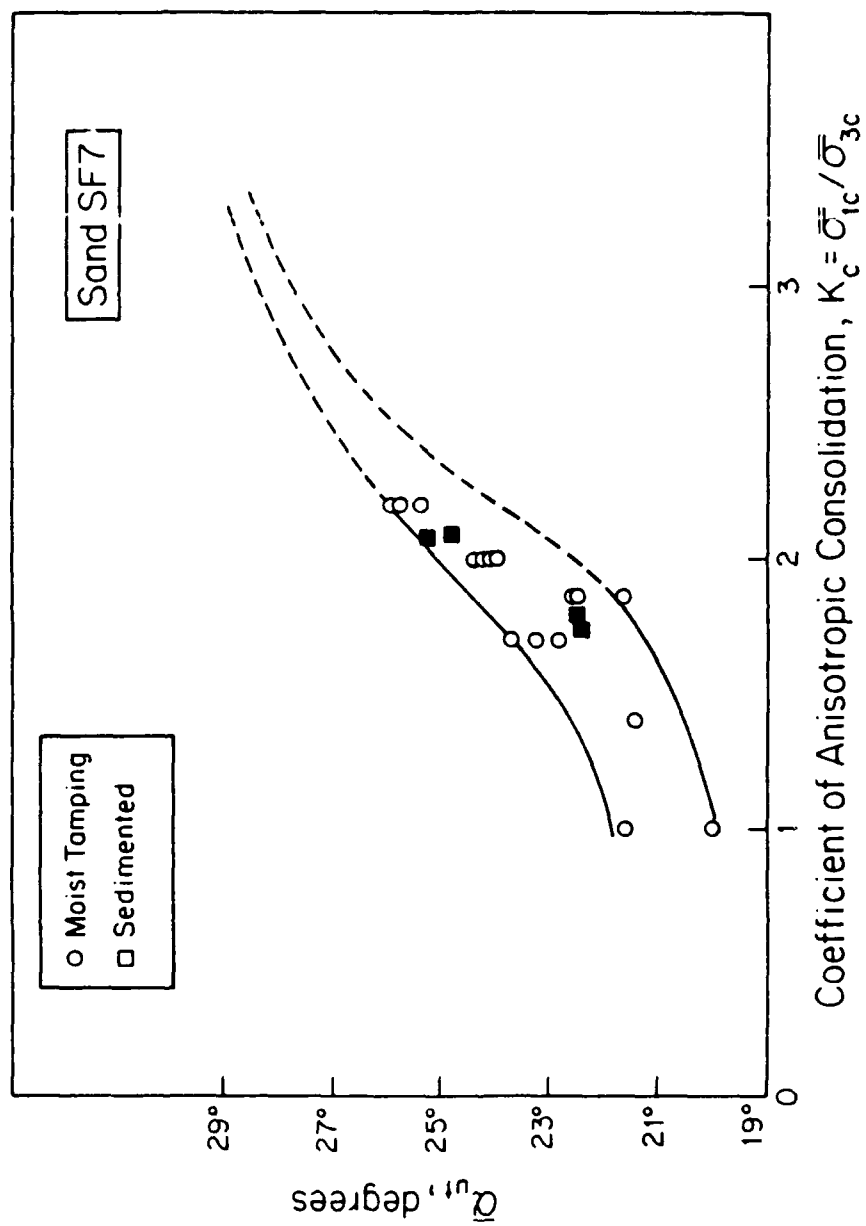


Fig. 6.37. Variation of  $\alpha_{ut}$  as a Function of  $K_c$  for Sand SF7

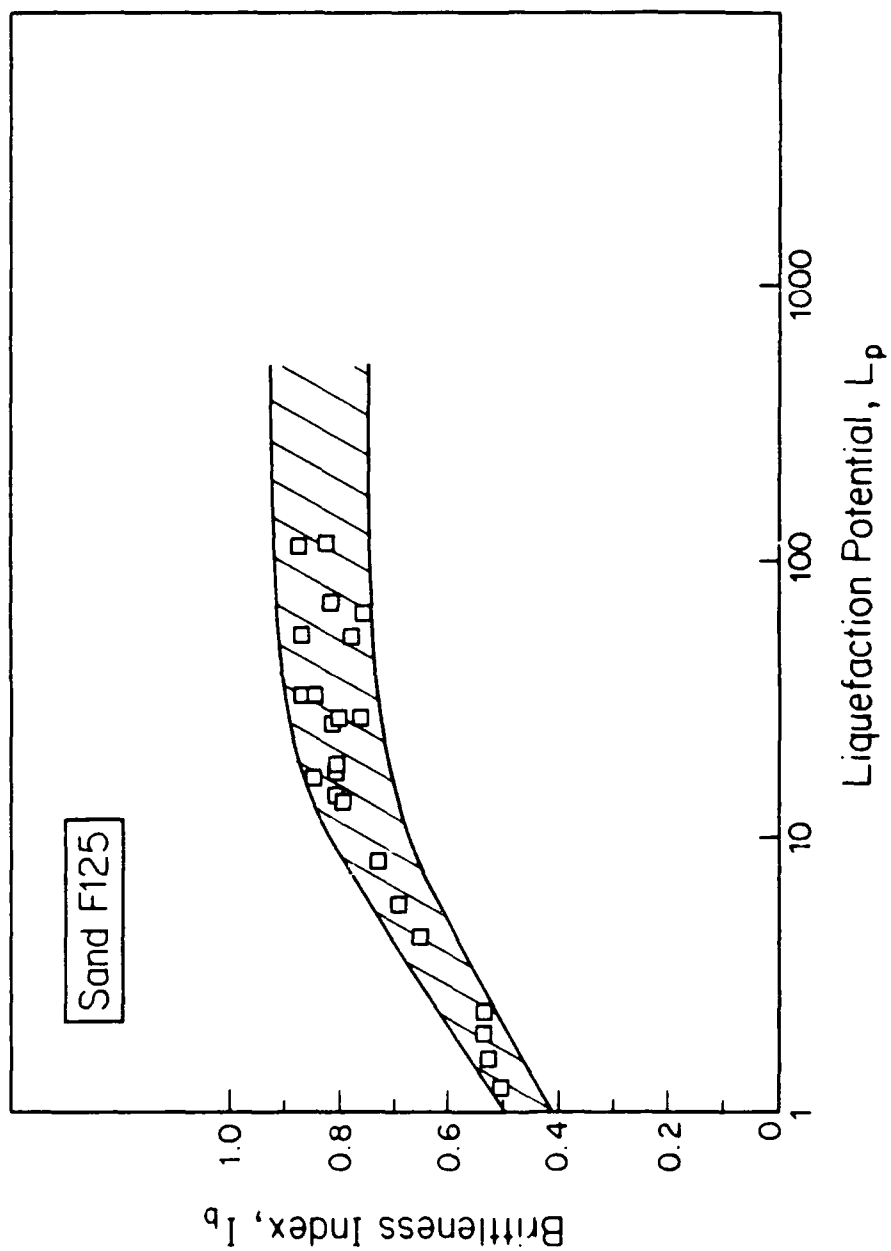


Fig. 6.38. Comparison Between Brittleness Index and Liquefaction Potential in Ottawa Sand F125

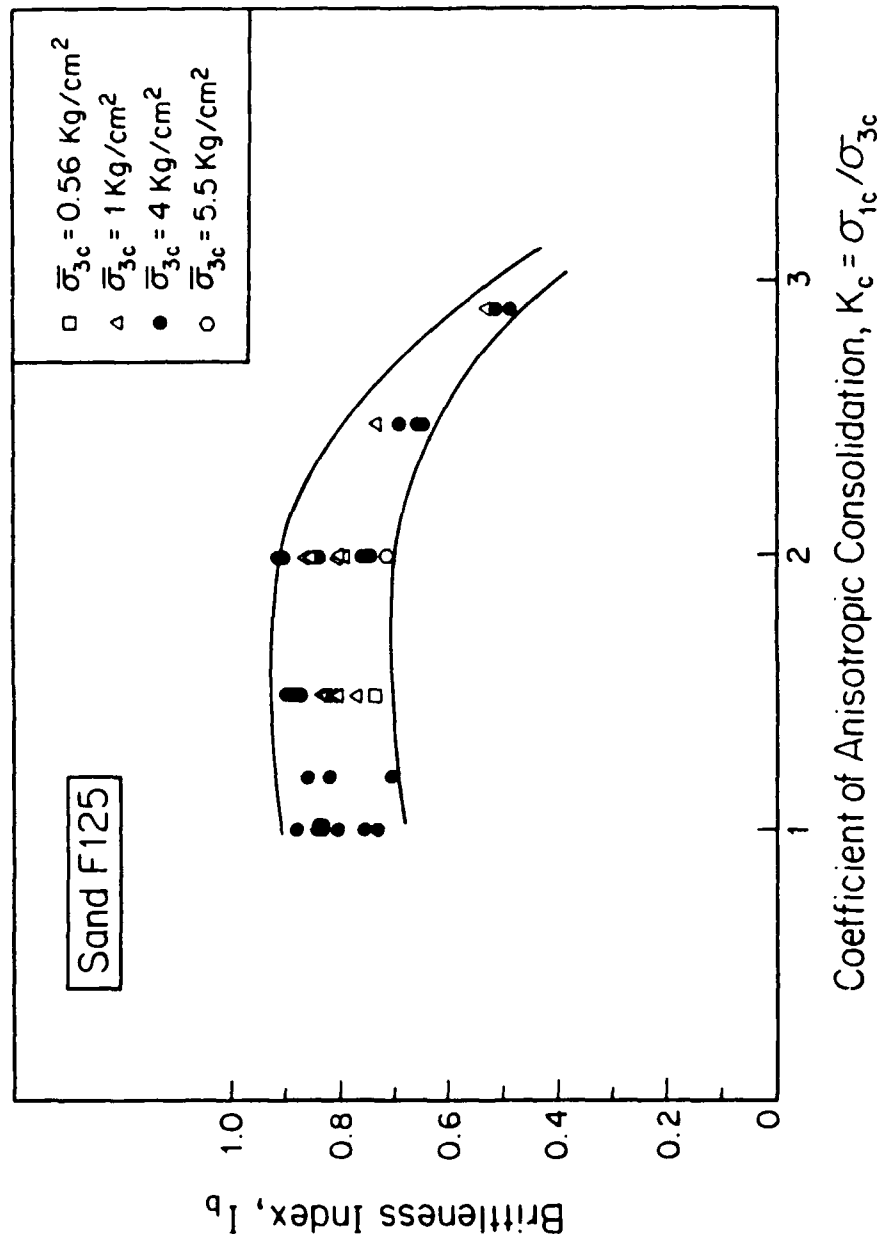


Fig. 6.39. Variation of Brittleness Index as a Function of  $K_c$  for Ottawa Sand F125

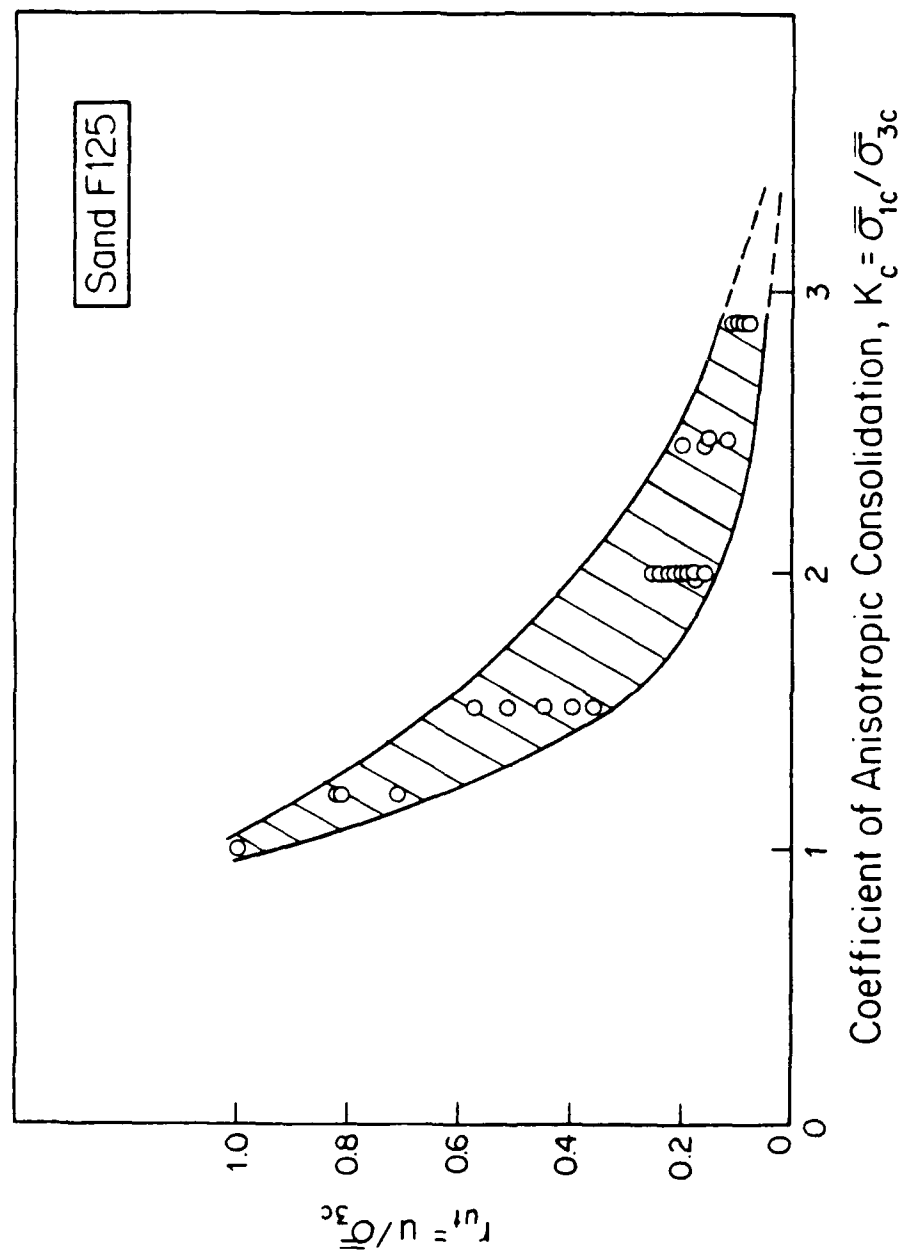


Fig. 6.40. Variation of  $r_{ut}$  with  $K_c$  for Ottawa Sand F125

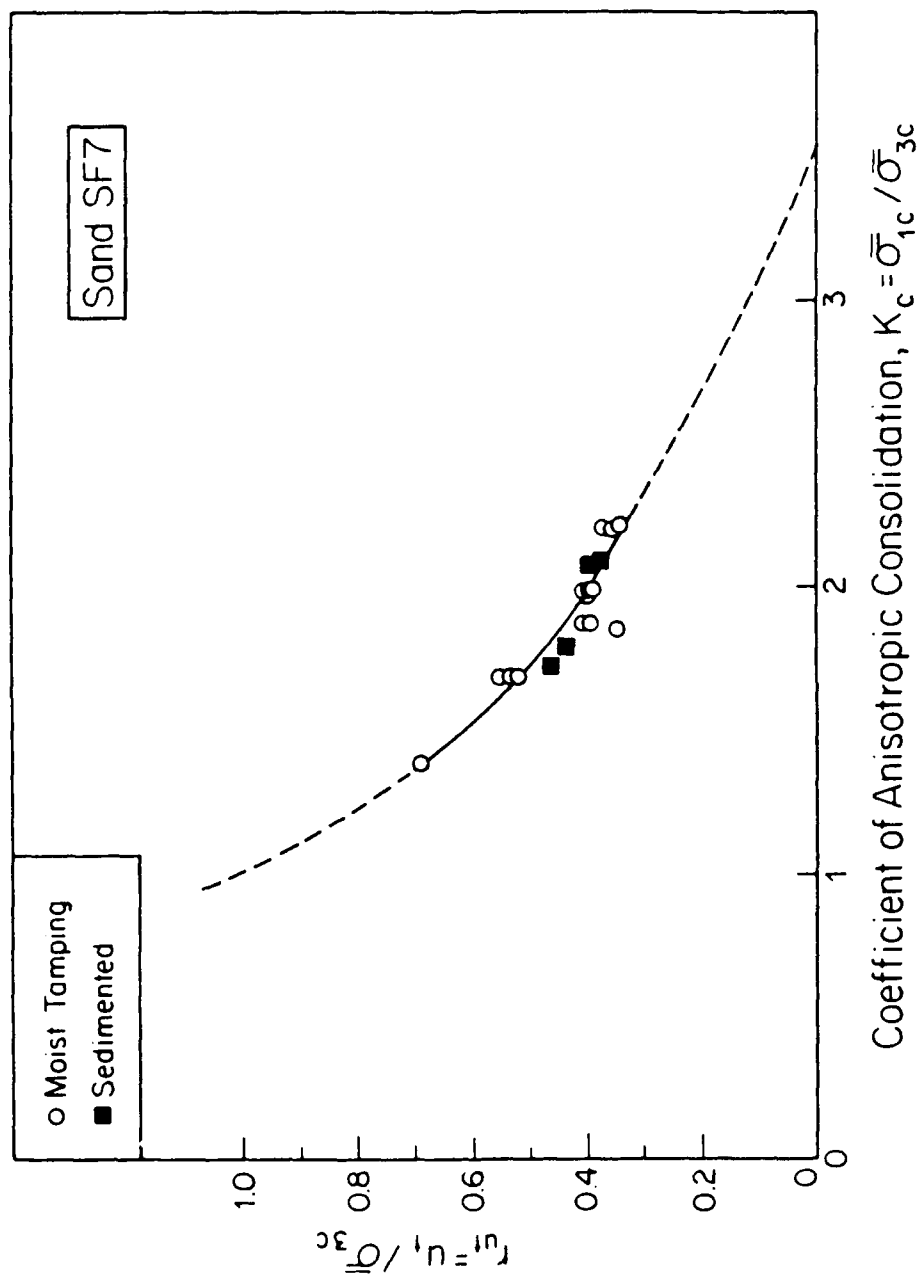


Fig. 6.41. Variation of  $r_{ut}$  as a Function of  $K_c$  for Sand SF7



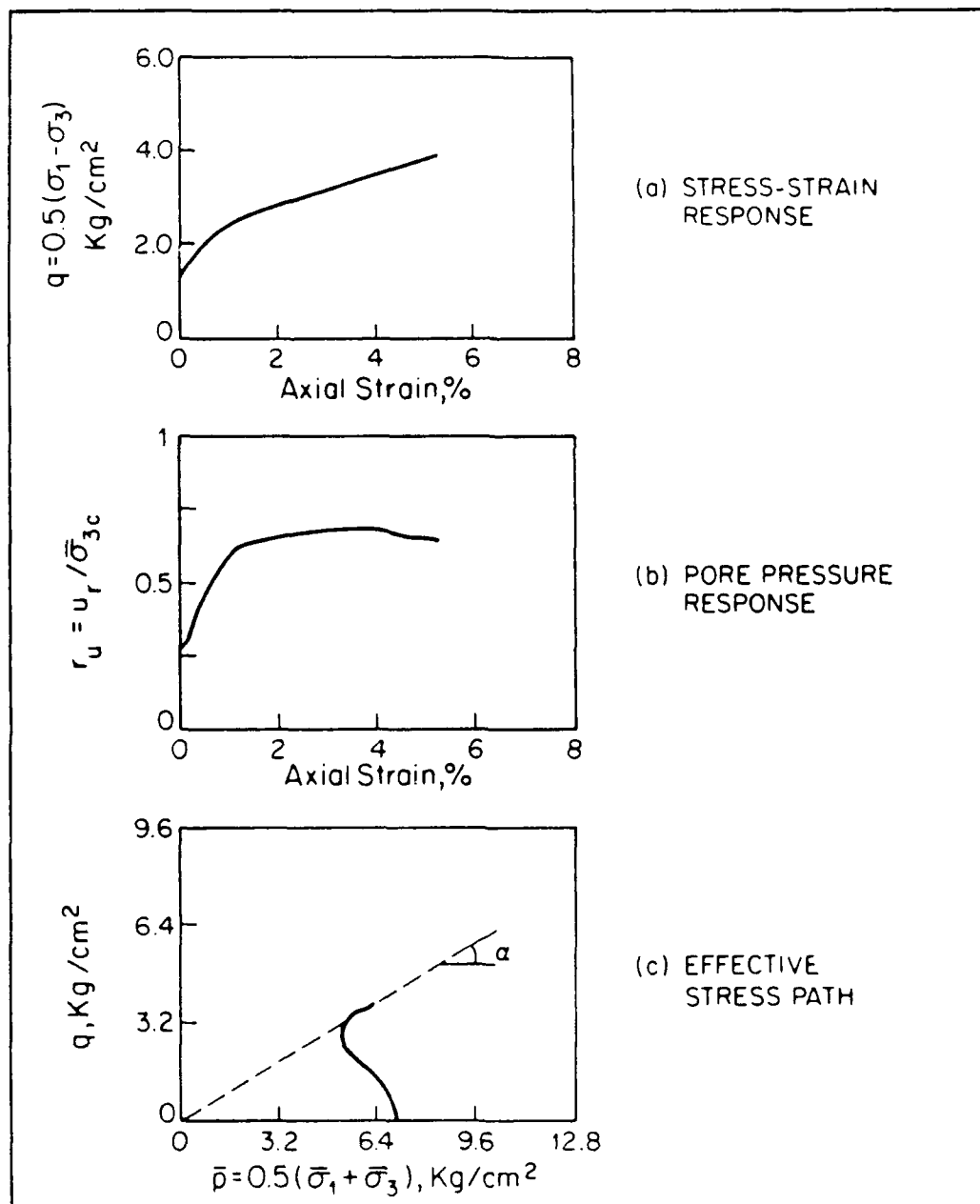


Fig. 6.42. Monotonic Triaxial CIU Test on Dilative Specimen of Sand A ( $\bar{\sigma}_{1c} = \bar{\sigma}_{3c} = 6.98 \text{ kg/cm}^2$ )

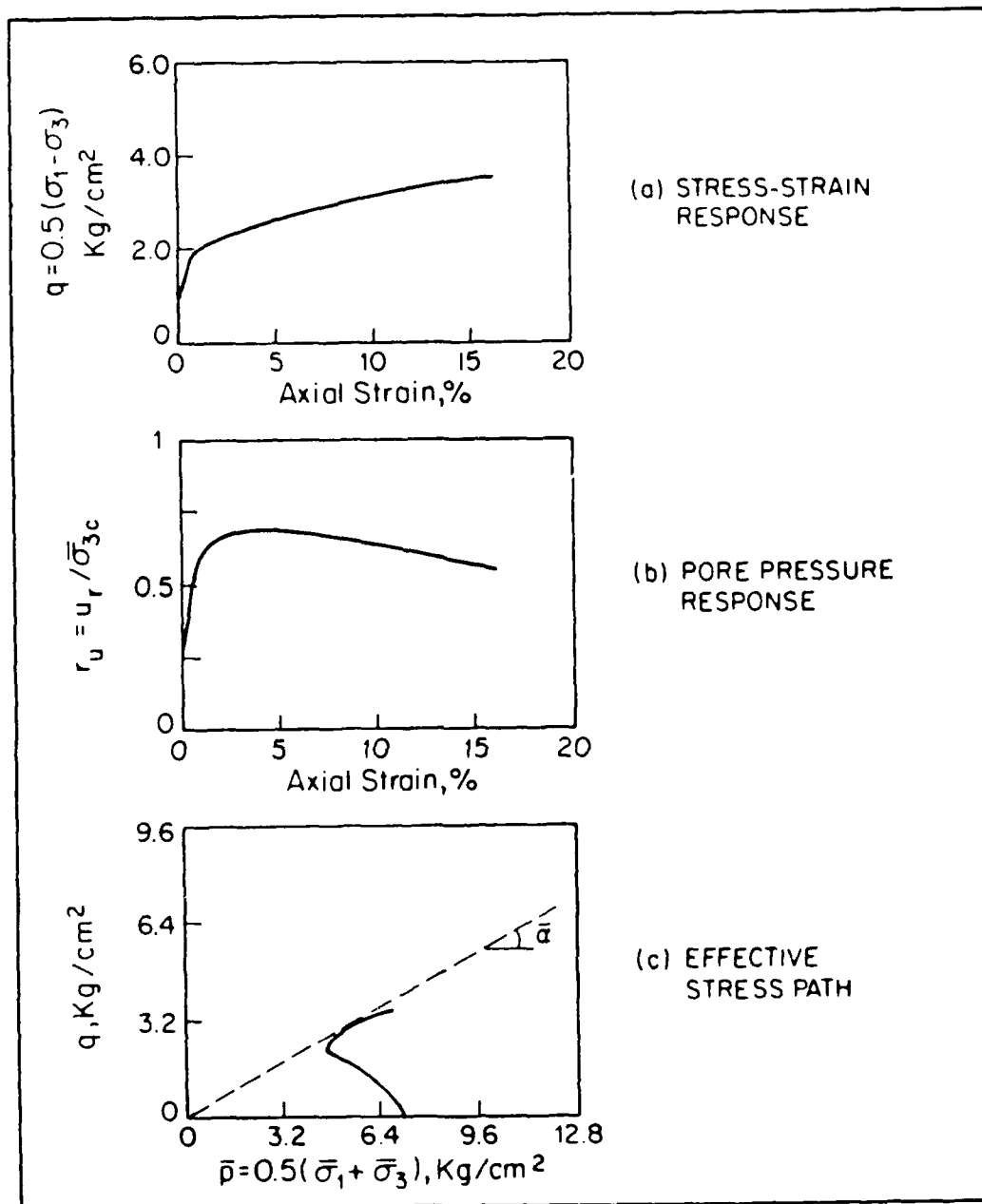


Fig. 6.43. Monotonic Triaxial CTU Test on Dilative Specimen of Sand A Showing a More Pronounced Elbow ( $\bar{\sigma}_{1c} = \bar{\sigma}_{3c} = 7.1 \text{ kg/cm}^2$ )

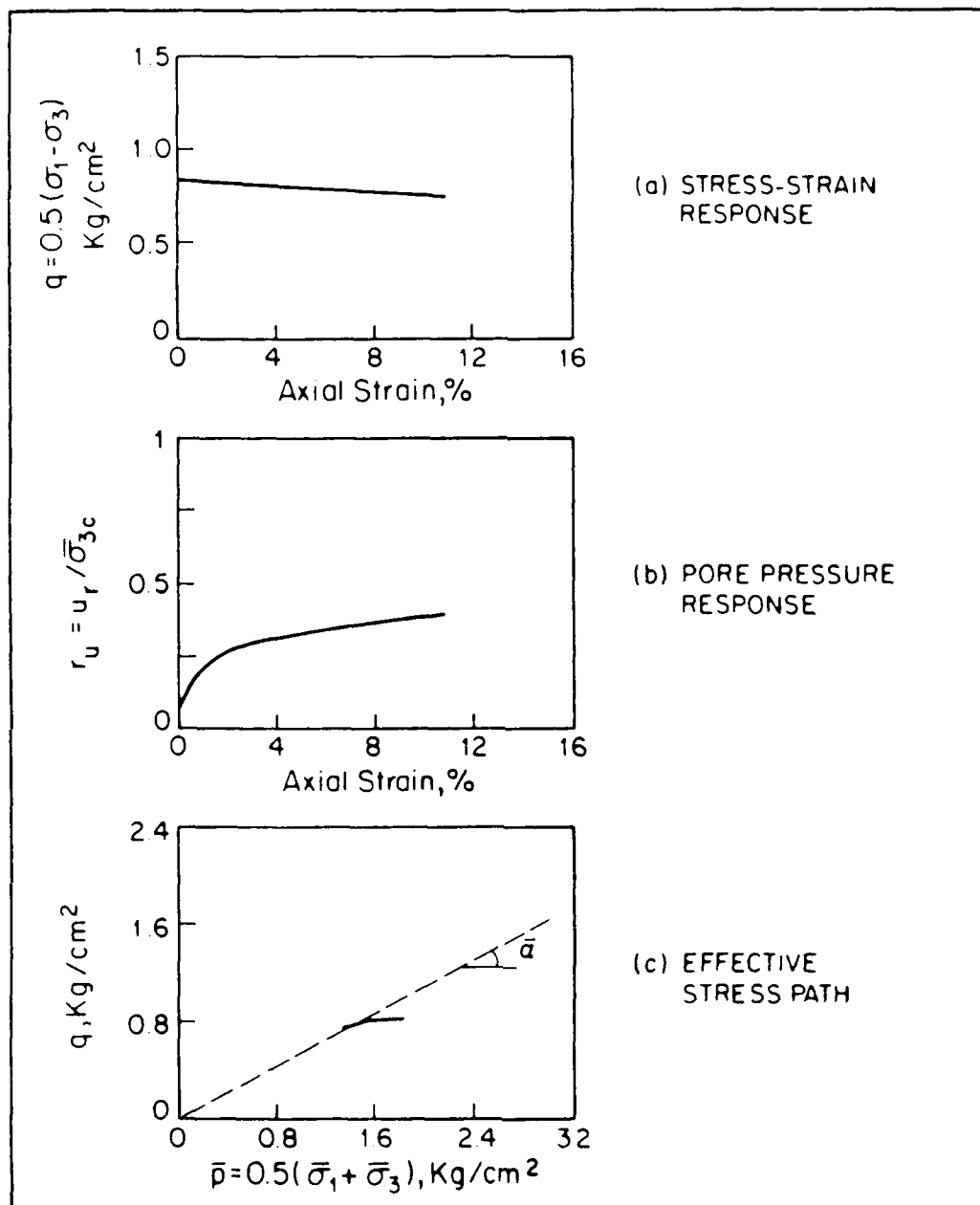


Fig. 6.44. Cyclic Torsional Triaxial CyT-CAU Test on Dilative Sample of Sand SF7 ( $\bar{\sigma}_{3c} = 0.98 \text{ kg/cm}^2$ ,  $(\bar{\sigma}_{1c} = 2.63 \text{ kg/cm}^2, \gamma_{cy} = 0.053\%)$ )

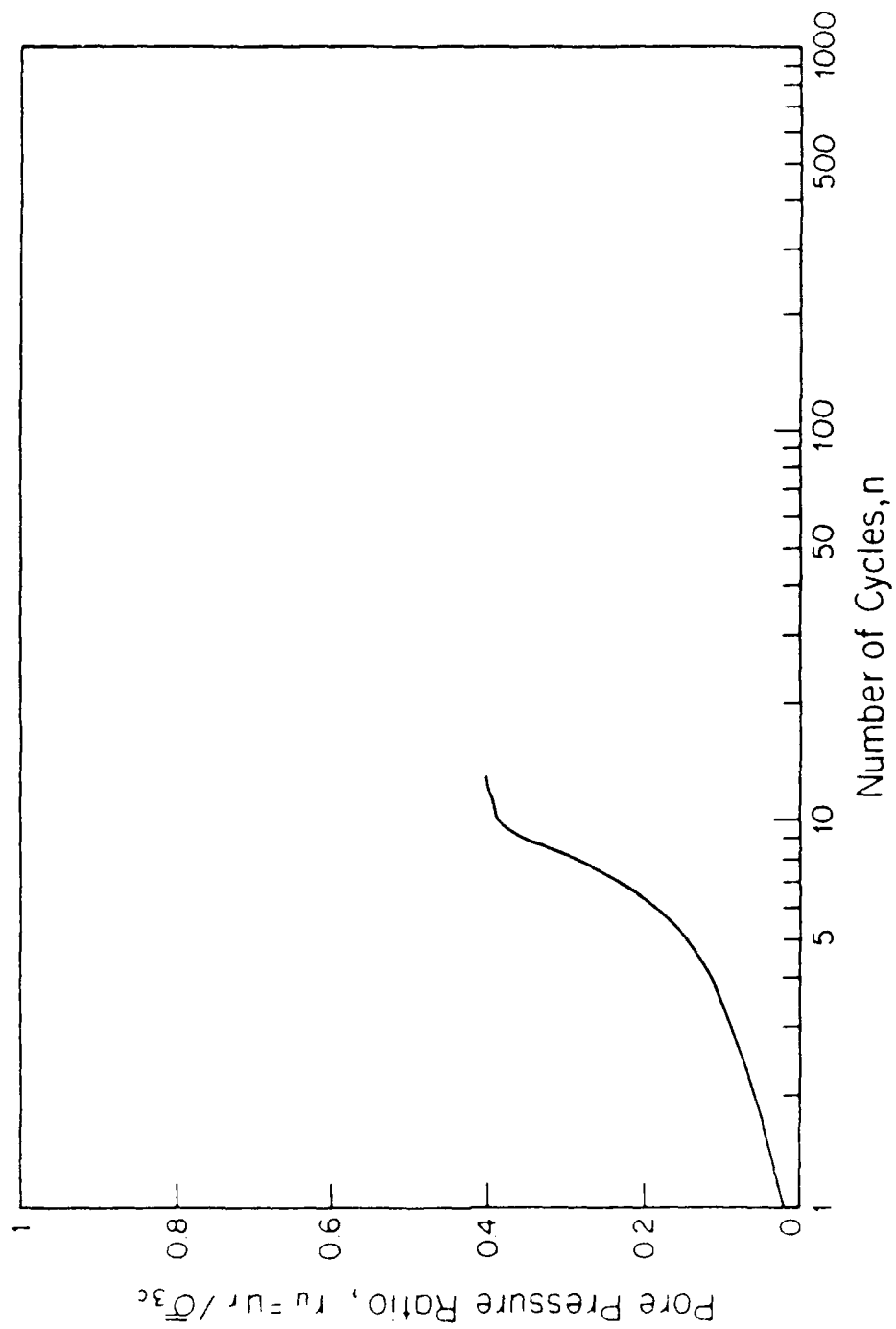


Fig. 6.45. Pore Water Pressure Buildup for the Cyt-CXU Test in Fig. 6.44

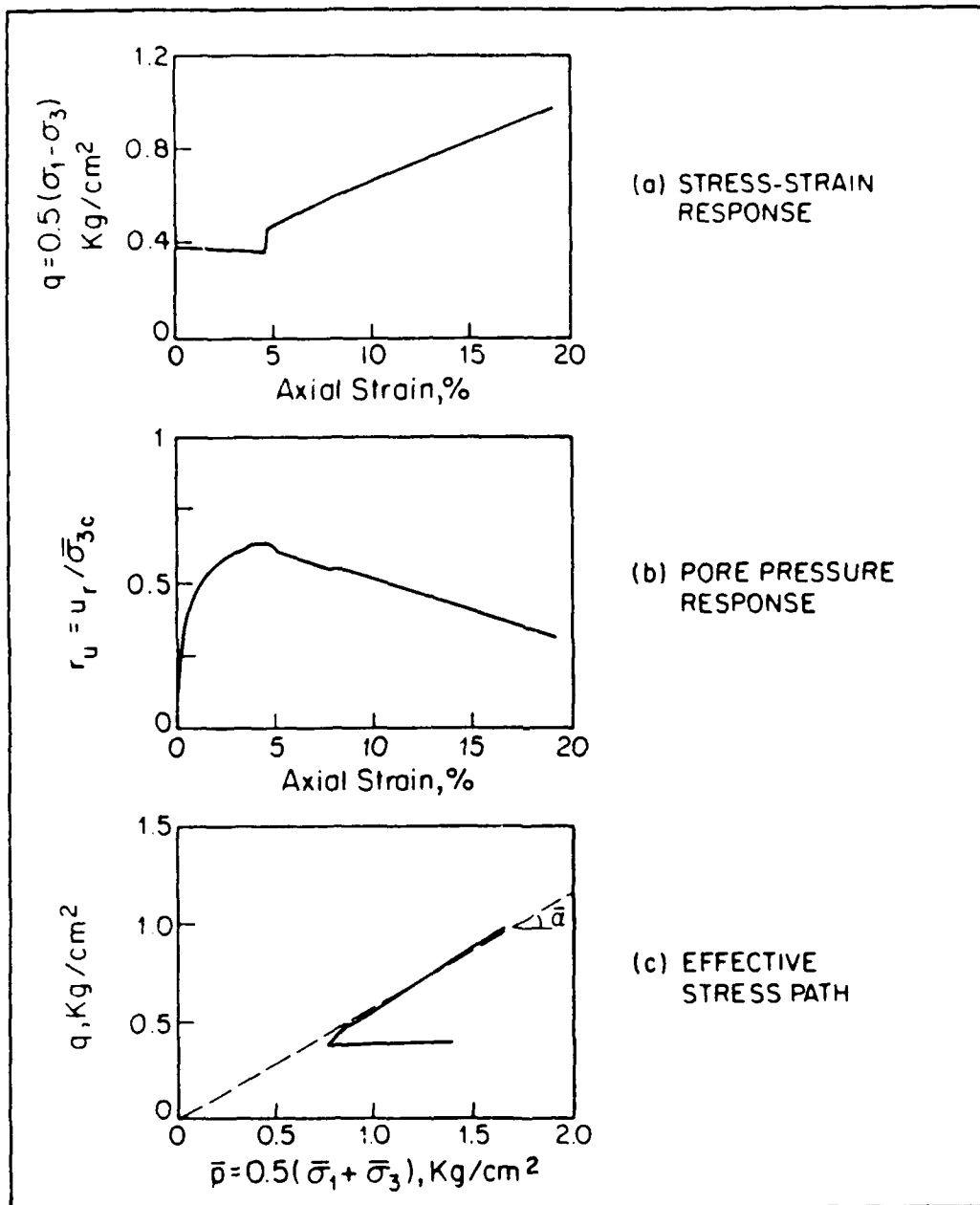


Fig. 6.46. Results of a CyT- $\overline{\text{CAU}}$  Test on a Dilative Sample of Sand SF7 Carried Out Until It Reached the Strength Envelope  $\bar{\alpha} = \bar{\alpha}_{\text{US}} = 29^\circ$  followed by Monotonic Loading (CyT- $\overline{\text{CAU}}$ + $\overline{\text{CAU}}$  Test)

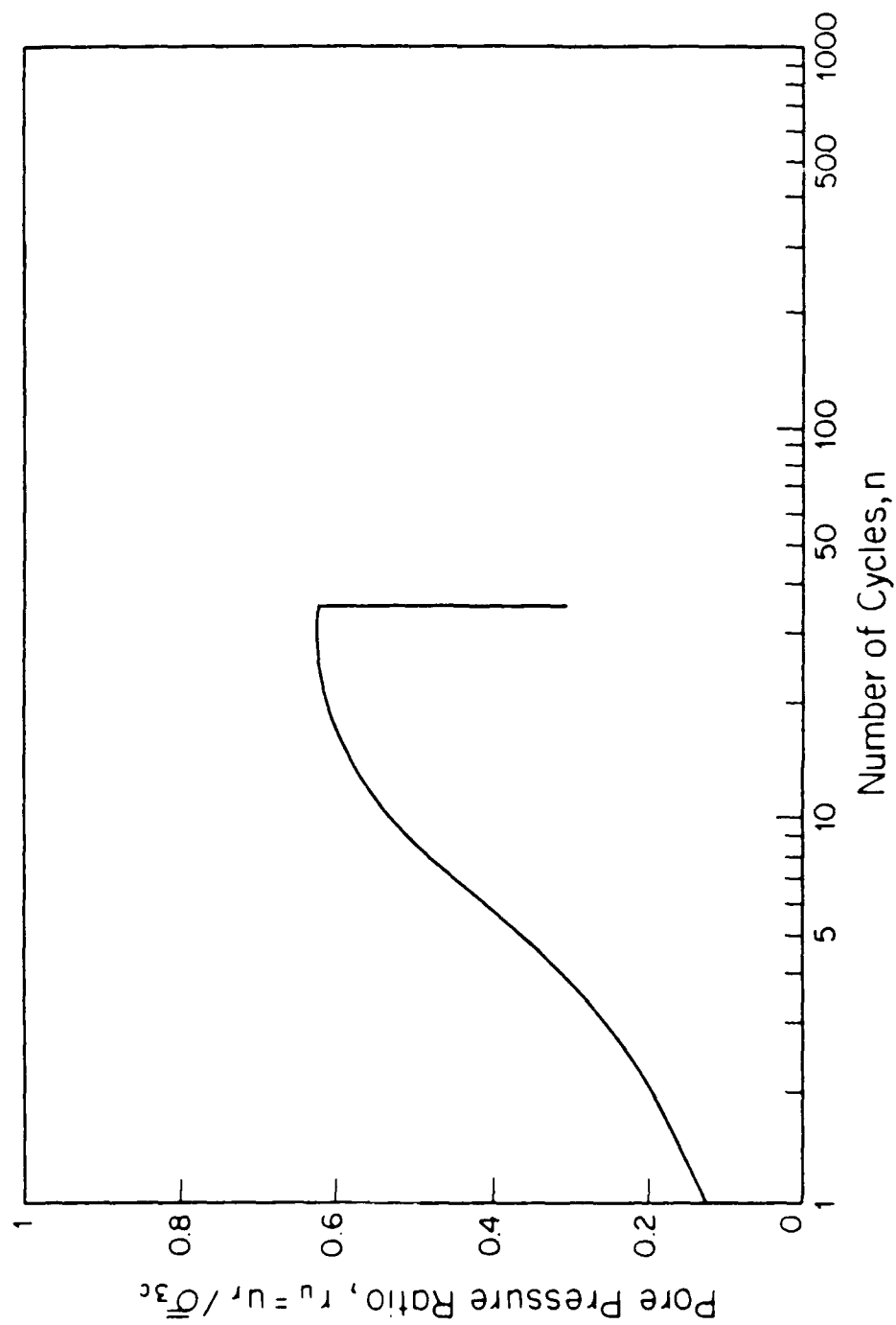


Fig. 6.47. Pore Water Pressure Buildup of the Cyt-Cau-Cau Test Shown in Fig. 6.44

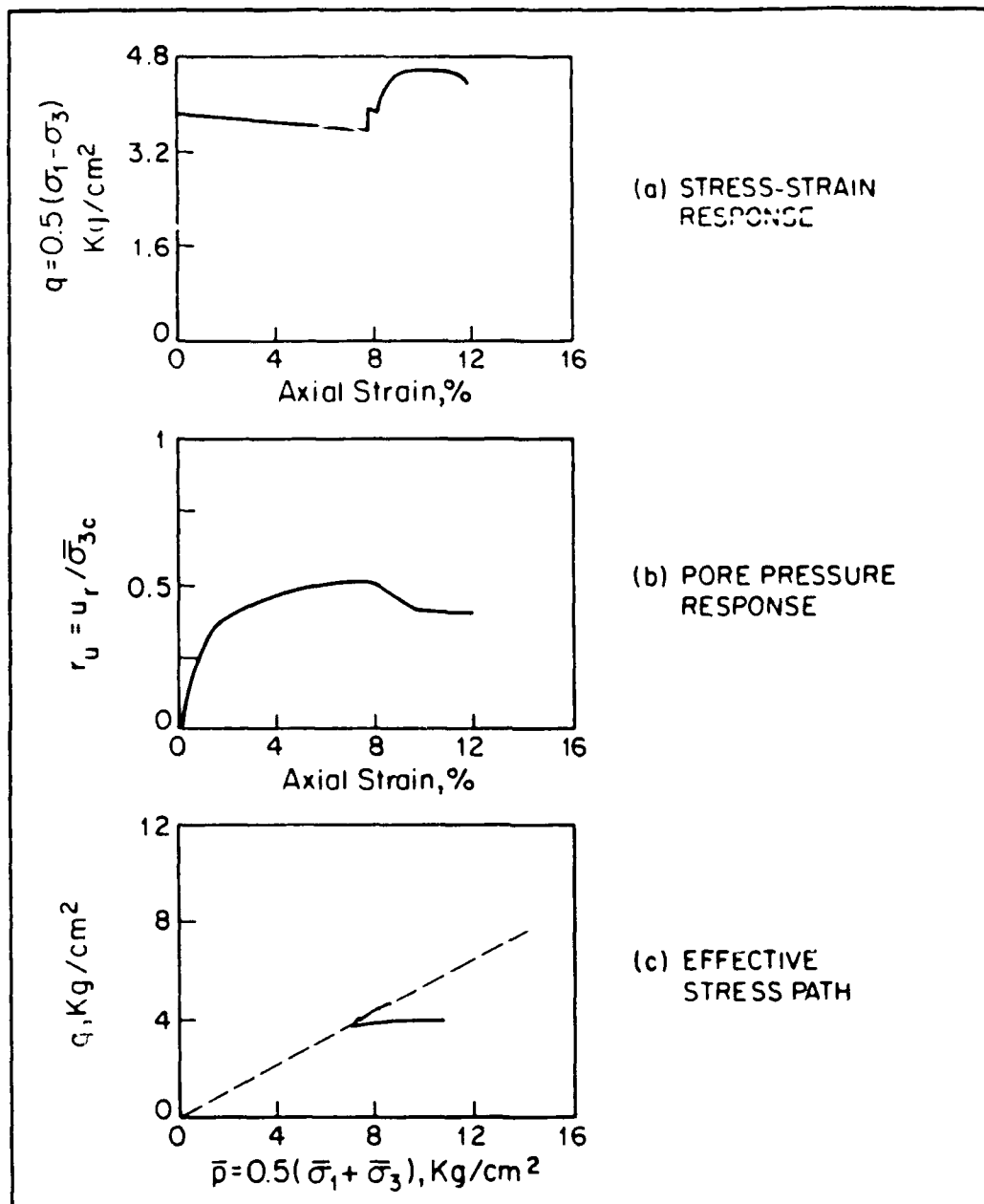


Fig. 6.48. CyT-CAU+CAU Test On An Initially Dilative Sample of Sand A Showing Steady-State Conditions at Higher Stresses

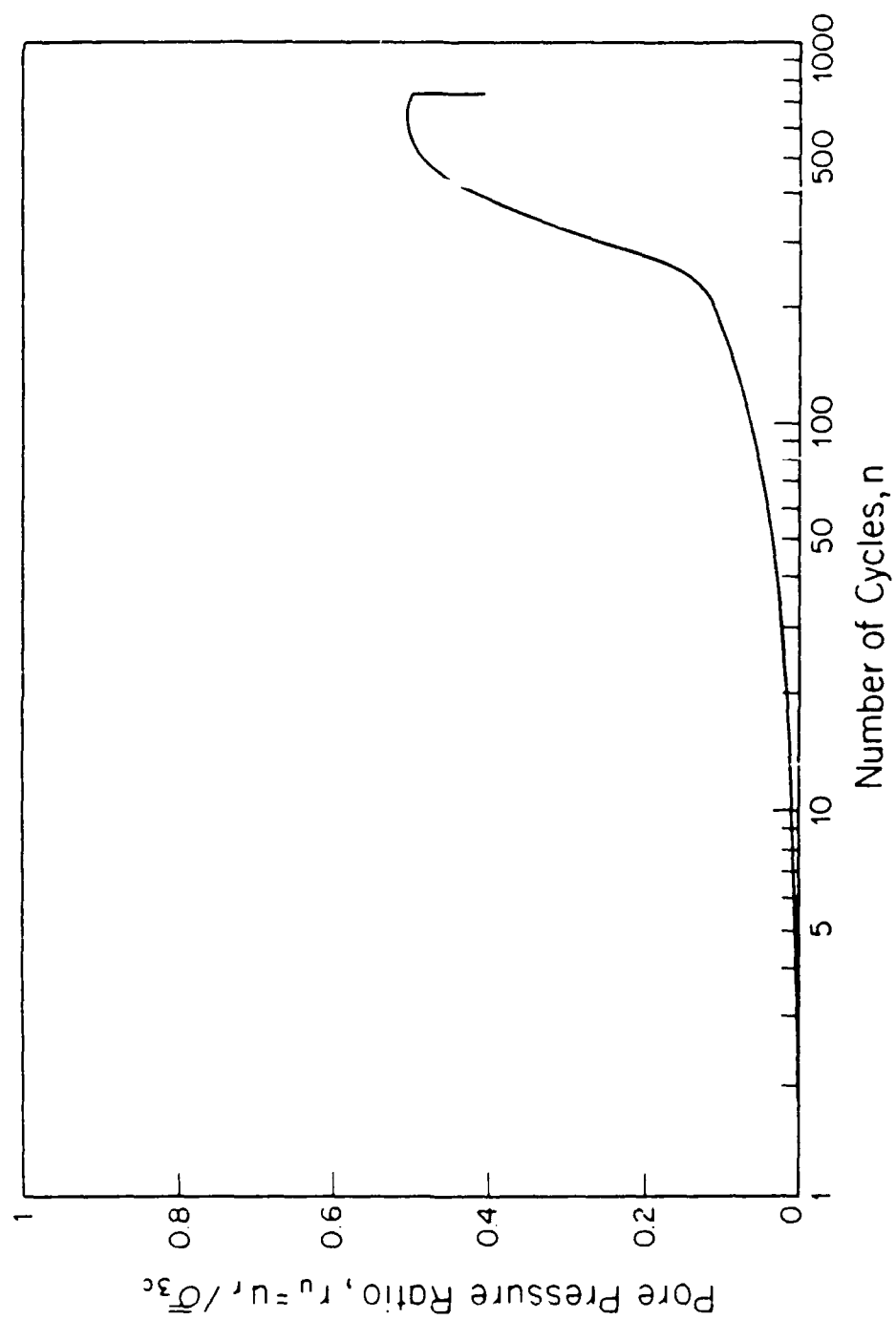


Fig. 6.49. Pore Water Pressure Buildup of the CyT-CAU+CAU Test Shown in Fig. 6.48



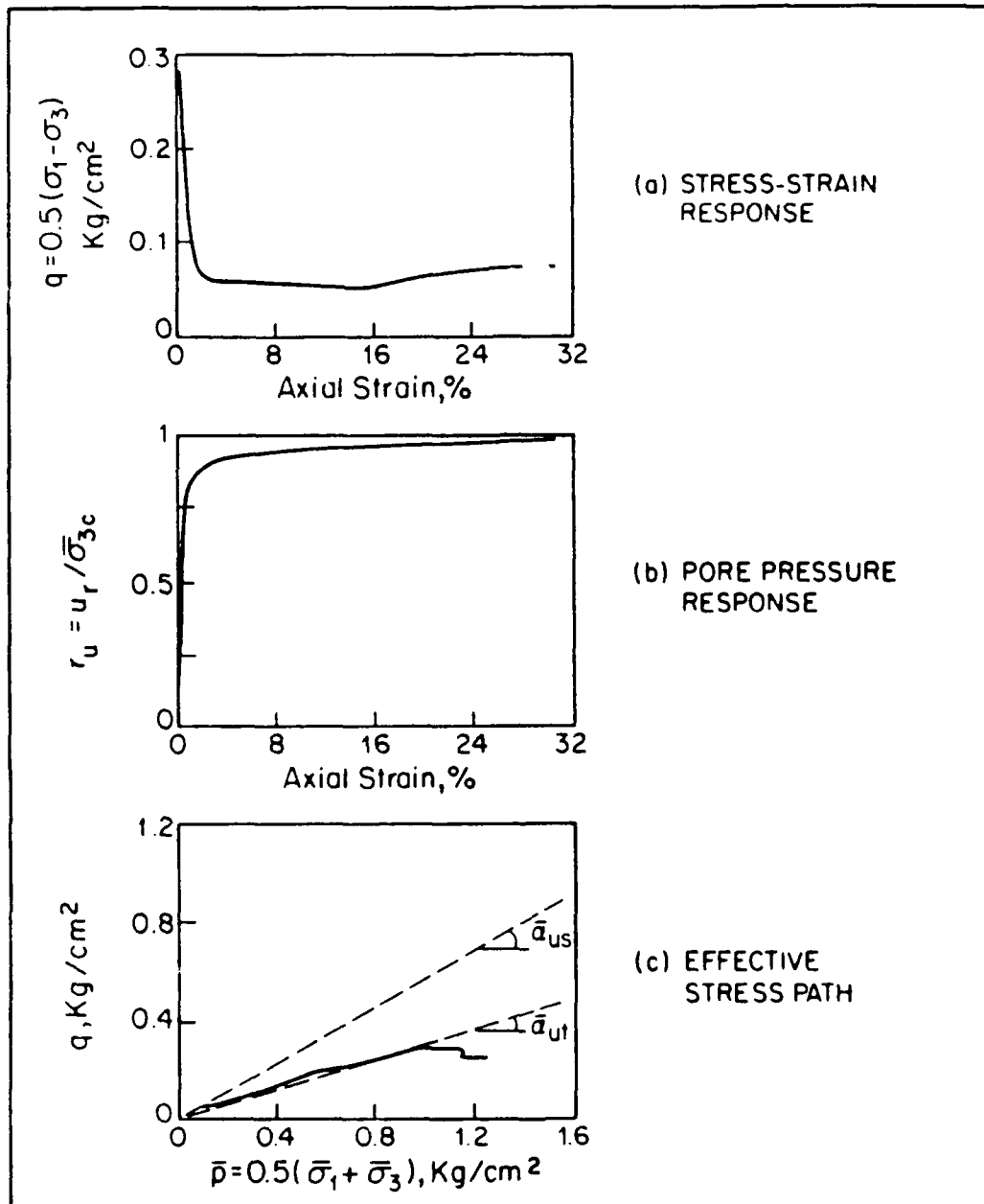


Fig. 6.50. Cyt-~~CAU~~+CAU Test on a Contractive Specimen of Sand F125 Showing Triggering and Steady-State Conditions

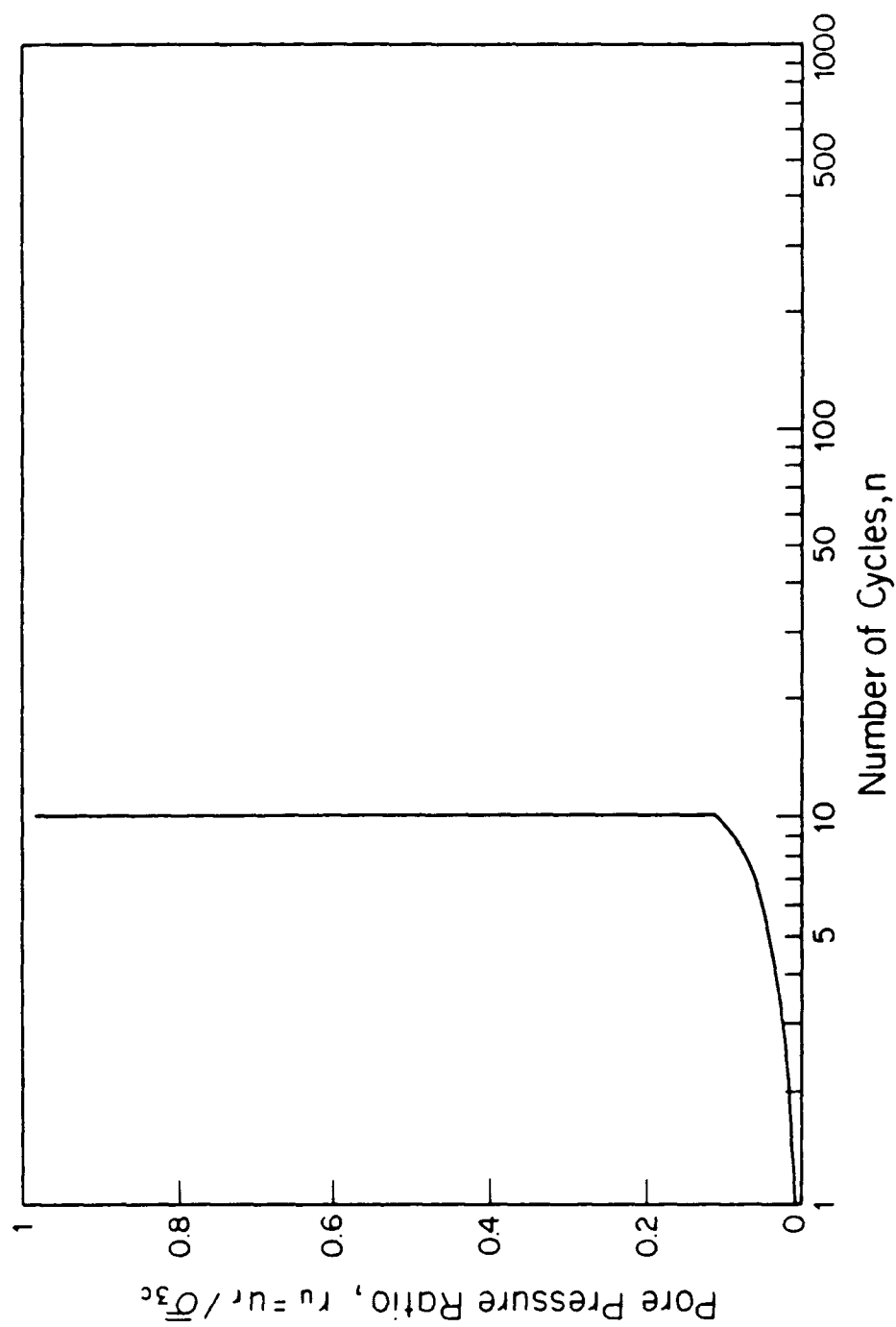


Fig. 6.51. Pore Water Pressure Buildup of CyT-CAU+CAU Test Shown in Fig. 6.50

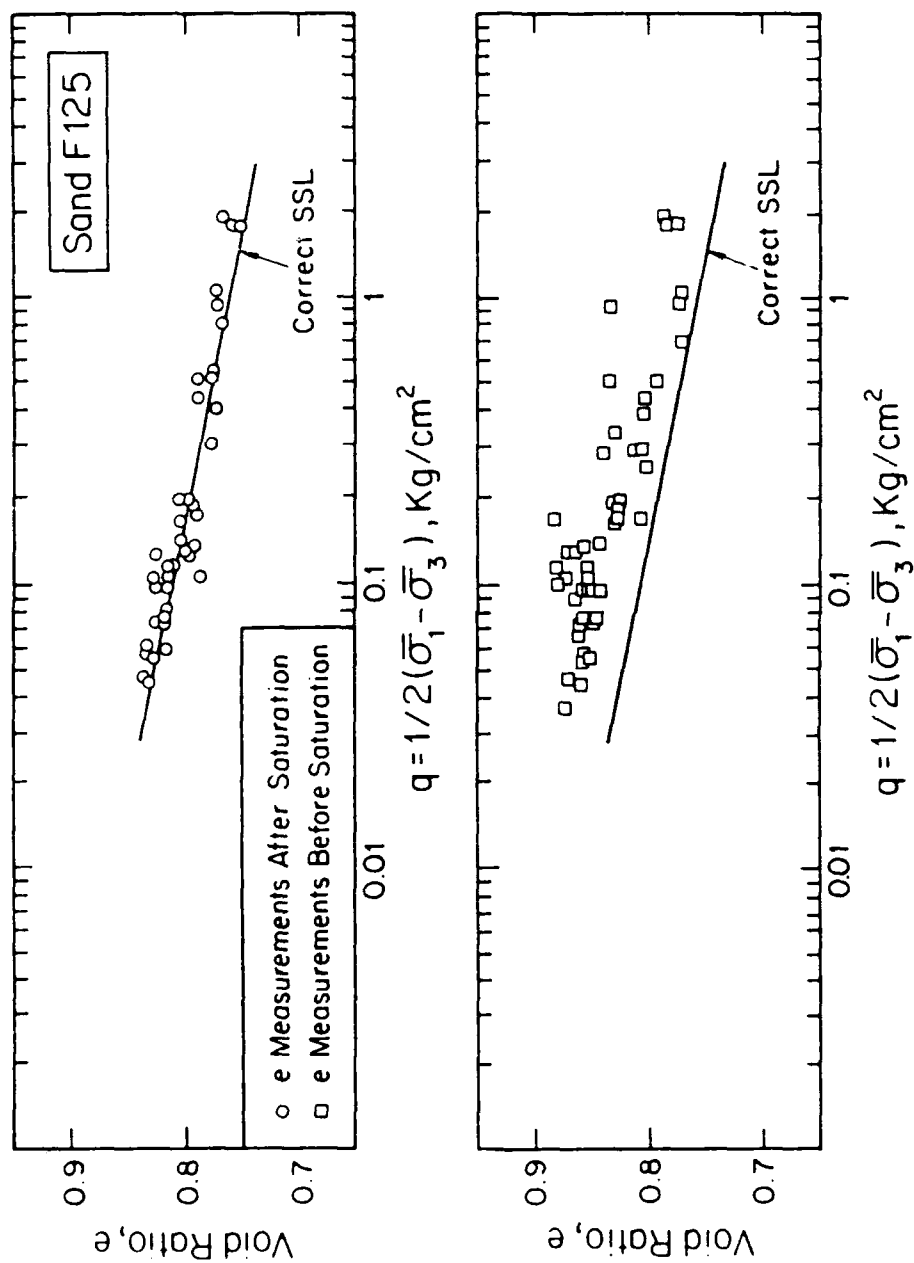


Fig. 6.52. Effect of Void Ratio Measurements Before Saturation on the SSL of Ottawa Sand F125

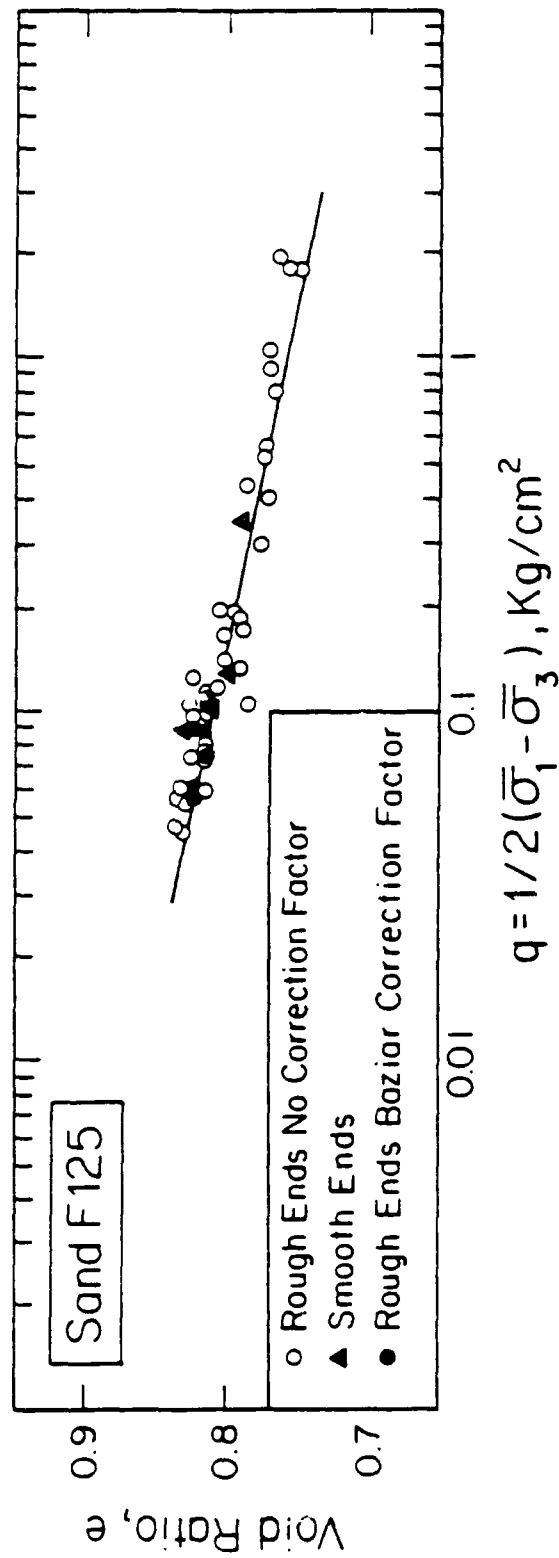
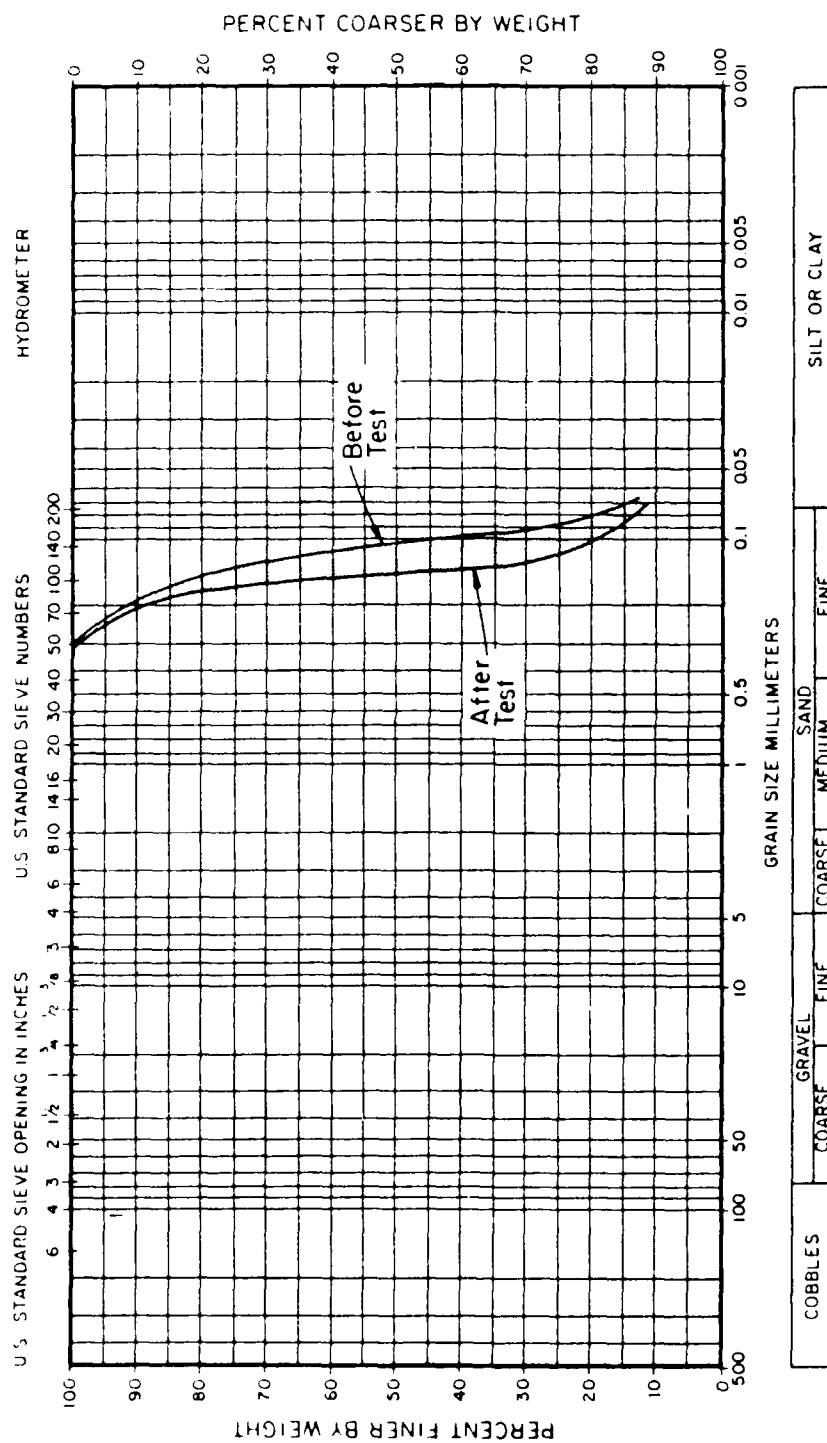


Fig. 6.53. Effect of Stone Correction Factor for the Triaxial Ends on the SSL of Ottawa Sand F125



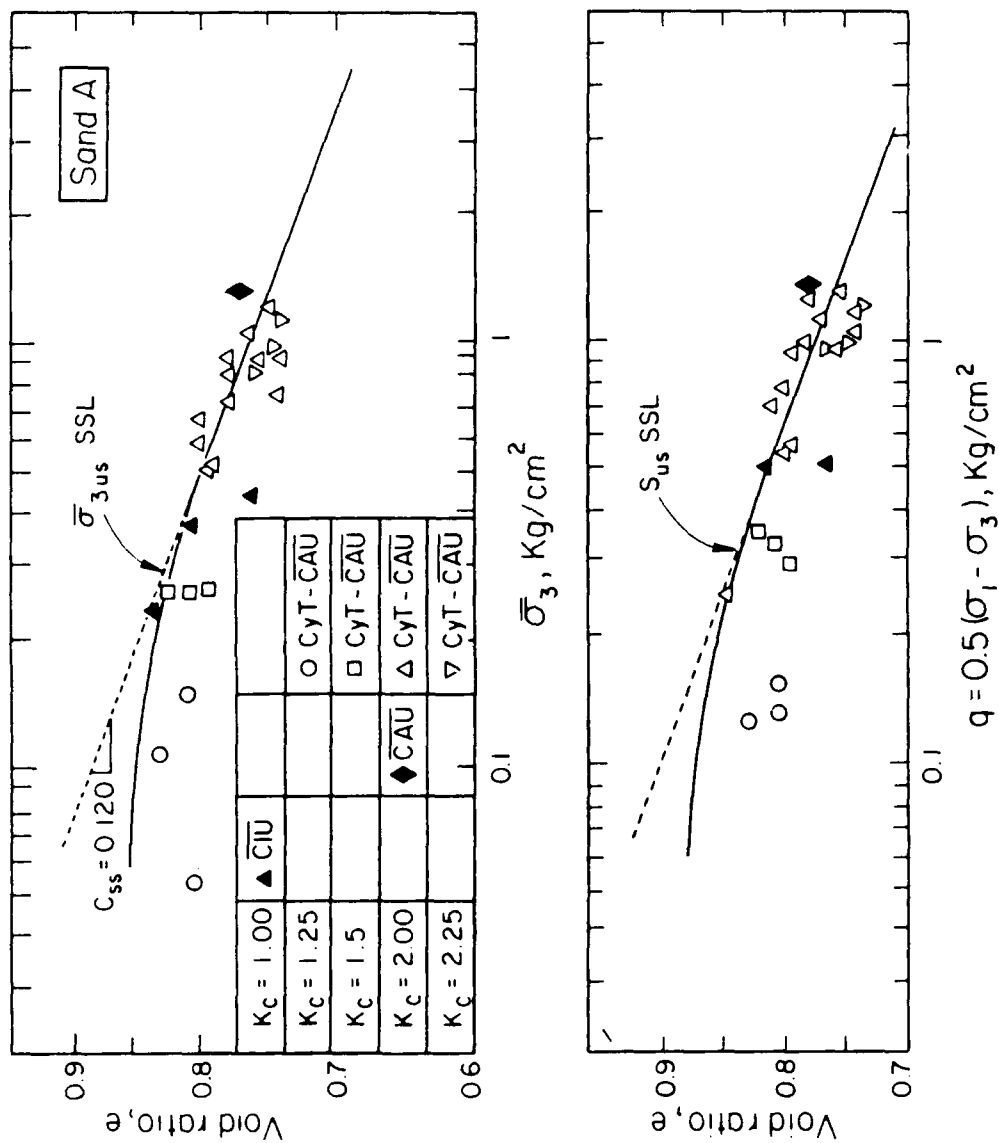


Fig. 6.55. SSL for Sand A Showing Cumulative Effects of Incorrect Testing Procedures

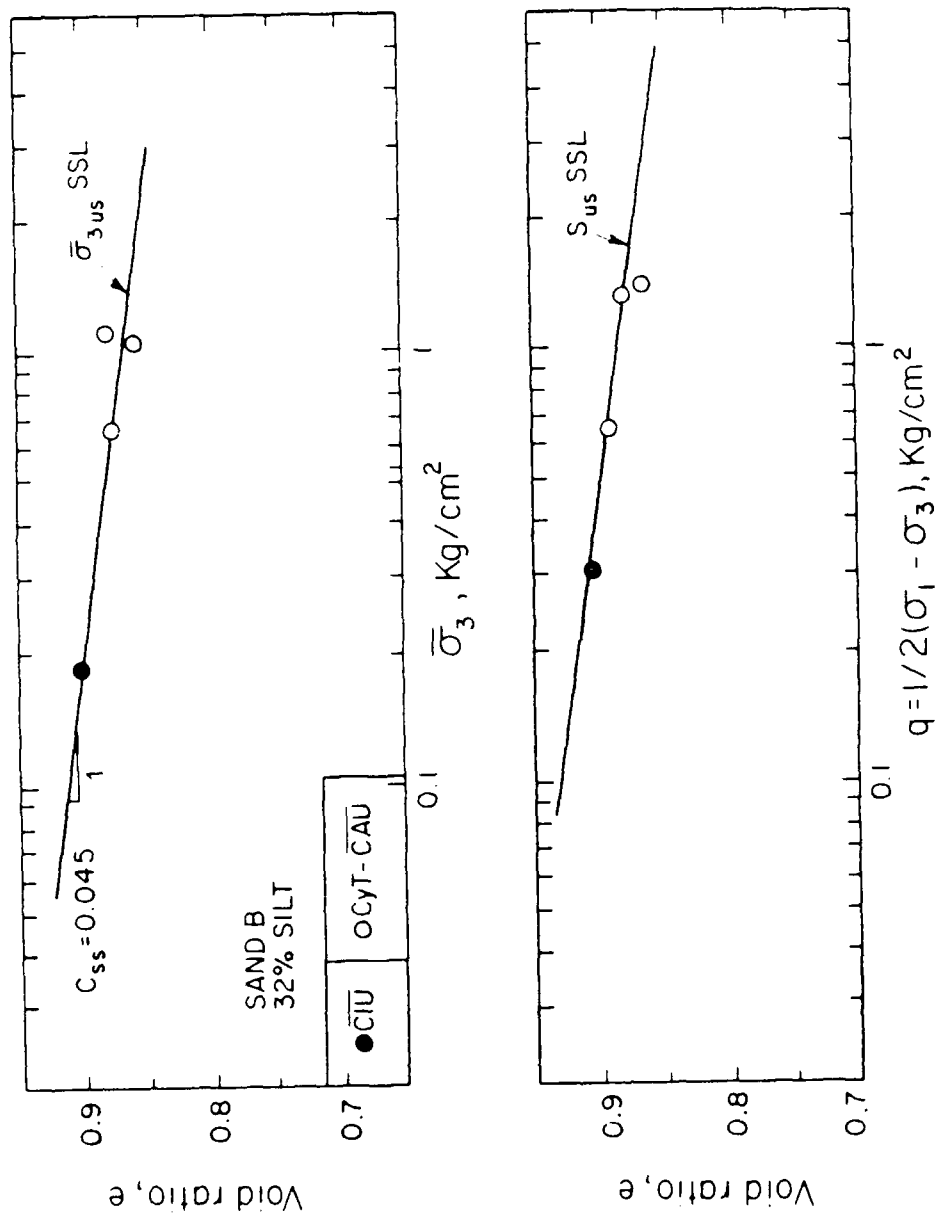


Fig. 6.56. SSL for Sand B Obtained Using Incorrect Testing Procedures

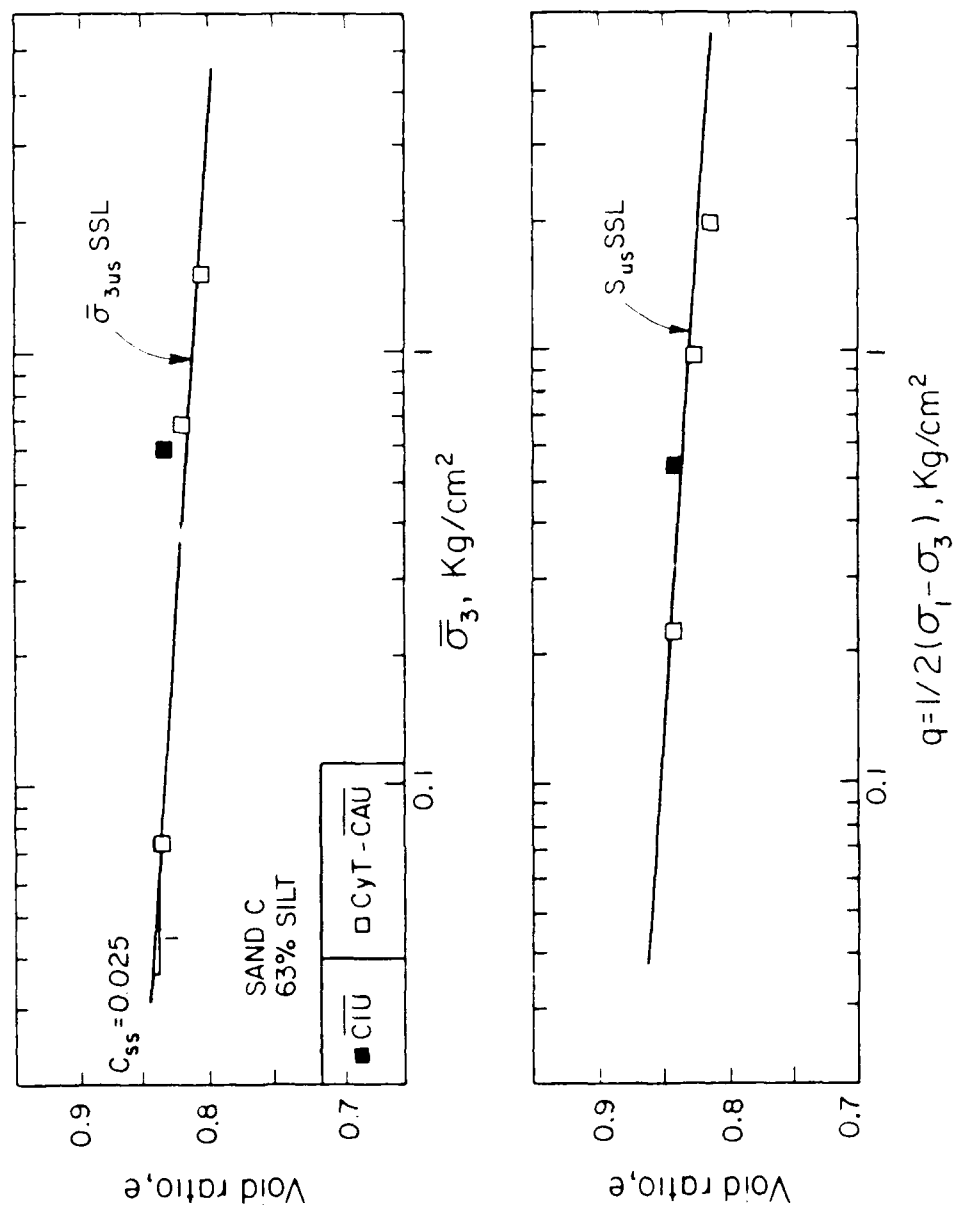


Fig. 6.57. SSL for Sand C Obtained Using Incorrect Testing Procedures



CHAPTER 7  
PORE PRESSURE BUILDUP AND TRIGGERING DUE  
TO CYCLIC STRAINING: RESULTS OF  
EXPERIMENTAL PROGRAM

7.1 General

Although the stress conditions needed to trigger liquefaction flow failure, already discussed in Chapter 6, constitute a useful concept in earthquake engineering, it does not take into account the magnitude and number of cyclic stresses and strains induced by an earthquake. From the viewpoint of evaluating triggering for a given seismic shaking, the most important data obtained in the experimental study reported here relate to the pwp buildup and number of cycles needed to trigger flow failure during the first stage of the CyT-CAU tests. Unlike the  $q_{us}$  values and other characteristics of steady-state failure, which can be determined from either cyclic or monotonic tests, pwp buildup and number of cycles to failure can be obtained only from cyclic tests such as the CyT-CAU.

The pore pressure and pore pressure ratio at triggering were defined in Section 6.4 as  $u_t$  and  $r_{ut} = u_t/\bar{\sigma}_{3c}$ , respectively. As discussed there and illustrated by Figs. 6.40 and 6.41, for a given sand the value of  $r_{ut}$  is determined mainly by  $K_c = \bar{\sigma}_{1c}/\bar{\sigma}_{3c}$ , and is relatively

independent of  $\bar{\sigma}_{3c}$ , cyclic strain  $\gamma_{cy}$ , and sand fabric. On the other hand, the number of cycles of cyclic strain needed for triggering,  $n_t$ , is very much a function of  $\gamma_{cy}$ .

Section 7.2 discusses the issue of the number of cycles to trigger flow failure, while the pwp buildup results are displayed in Section 7.3. Other sections at the end of this chapter present, respectively, a comparison of triggering and pwp buildup among the sands tested, the development of a pwp model for earthquake engineering applications, and a discussion of the cumulative axial strains at triggering.

The pwp buildup, that is the increase in pore pressure  $u$  and pore pressure ratio  $r_u = u/\bar{\sigma}_{3c}$ , versus number of cycles  $n$ , will be discussed in Section 7.3 and modeled in Section 7.4 up to the value,  $r_{ut}$ , where the sample fails by liquefaction flow failure triggering. After triggering, the pwp increases to its steady-state value as the sample strains. However, if the sample is constrained, it will not achieve its steady-state values of  $r_{us}$  or  $q_{us}$ .

Although flow failure does not exist in isotropically consolidated samples subjected to cyclic loading because  $r_d = 0$ , it is interesting to compare this different physical phenomenon with the pwp buildup and flow failure triggering.

For isotropically consolidated samples ( $K_c = 1$ ) such as those in CyT-CTU tests, triggering is defined when the

sample reaches a pwp ratio  $r_{ut} = 1.00$ . This may appear to be arbitrary at first sight, as in these tests flow failure does not happen at all. However, as previously shown in Section 6.3, in the CyT-CAU tests in which flow failure does occur, failure starts when a specific triggering envelope is reached. Therefore, we can consider the origin of the effective,  $\bar{p}$ - $q$  stress space as part of all the triggering envelopes; for isotropically consolidated samples, this corresponds to  $r_{ut} = 1.0$ . This will enable direct comparisons between CyT-CIU and CyT-CAU tests.

Figure 7.1 shows results of two strain-controlled torsional triaxial CyT-CIU tests on sand F125. Strain controlled tests on isotropically consolidated samples always produce pwp buildup curves that are concave downwards in arithmetic plots, with triggering ( $u = \bar{\sigma}_{3c}$  or  $r_u = r_{ut} = 1$ ) occurring in less cycles when  $\gamma_{cy}$  is larger. Concave downward curves in dilative specimens were also found by Pierce (1985), who used strain-controlled cyclic axial triaxial tests on isotropically consolidated samples.

A different picture occurs when the value of  $K_c$  is higher than 1.00. Fig. 7.2 shows results of four strain-controlled CyT-CAU tests on sand F125 with different values of  $\bar{\sigma}_{3c}$  and  $\gamma_{cy}$ . The pwp buildup curves are no longer concave downwards; on the contrary, they are concave upwards

with the concavity increasing as the sample approaches triggering. Therefore, for cyclic strain-controlled tests, pwp buildup data from isotropically consolidated specimens cannot be used to predict results on anisotropically consolidated specimens. The curves in Figs. 7.1 and 7.2 show fundamental differences between the pwp buildup of isotropically and anisotropically consolidated contractive sands. Isotropically consolidated specimens (Fig. 7.1) will experience faster rates of pwp buildup at the beginning of cyclic loading, whereas anisotropically consolidated specimens (Fig. 7.2) will have a faster rate of pwp buildup at the end, closer to triggering. Figure 7.2 also illustrates the fundamental fact, previously discussed in Section 6.4, that the value of  $r_u$  at triggering,  $r_u = r_{ut}$ , decreases as  $K_c$  increases. For example, in Fig. 7.1,  $r_{ut} = 1$  for  $K_c = 1.0$ , while in Fig. 7.2  $r_{ut} = u/\bar{\sigma}_{3c} \approx 0.2$  for  $u_c = 2.0$ .

As will be discussed later in this chapter in Section 7.2, if an anisotropically consolidated contractive sand specimen is subjected to cyclic shear strains above the threshold strain, it will fail after a number of cycles,  $n_t$ , when its pwp ratio reaches  $r_{ut}$ . If a series of tests at the same values of  $K_c$  and  $\bar{\sigma}_{3c}$  are carried out with different

levels of cyclic shear strain,  $\gamma_{cy}$ , then we can construct what we will call here a triggering relationship. A triggering relationship is defined as a log-log plot of  $n_t$  versus  $\gamma_{cy}$ , as shown schematically in Fig. 7.3. This will become a main vehicle to portray the results concerning the number of cycles to failure.

In order to compare tests with different confining pressures, traditionally the value of pwp is normalized by using  $r_u = u/\bar{\sigma}_{3c}$ . However, since the value of  $r_{ut}$  is affected by  $K_c$ , it is convenient to normalize again the pwp by using the value of pwp at triggering. This leads us to use the ratio  $u/u_t = r_u/r_{ut}$ , as a convenient way to allow direct comparisons of pwp buildup between different tests, regardless of the values of  $\bar{\sigma}_{3c}$  and  $K_c$ .

Also, in order to be able to compare tests with different number of cycles to failure, and thus with different  $\gamma_{cy}$  we normalize the number of cycles,  $n$ , with the number of cycles at failure,  $n_t$ .

In this way, the curves of  $u$  versus  $n$  such as in Figs. 7.1 and 7.2 are transformed into normalized dimensionless curves of  $r_u/r_{ut}$  versus  $n/n_t$ . It will be shown throughout this chapter that the use of this normalization procedure allows a direct comparison of all test results on a particular sand in a single plot, regardless of the values

of  $\gamma_{cy}$ ,  $\bar{\sigma}_{3c}$  and  $K_c$ . A schematic drawing showing this normalization procedure for pwp buildup is shown in Fig. 7.4. The generated curves of  $r_u/r_{ut}$  versus  $n/n_t$  will be called the pwp buildup curves.

## 7.2 Number of Straining Cycles to Trigger Flow Failure

The triggering relationships will be presented for each of the tested sands. Test results on sand F125 will be shown first followed by those on sands A, B and C, and finally those for sand SF7. A brief discussion of all these results will also be presented at the end of the section.

### 7.2.1 Results on Ottawa Sand F125

The triggering relationships for cyclic CyT- $\overline{CU}$  and CyT- $\overline{CAU}$  tests on sand F125 are shown in Figs. 7.5 through 7.10 for soil samples tested with  $K_c = 1.0, 1.2, 1.5, 2.0, 2.5$  and  $2.9$ , respectively, and using a range of consolidation pressures  $\bar{\sigma}_{3c}$ .

By looking at the test results on isotropically consolidated contractive sands with a constant value of  $\bar{\sigma}_{3c}$ , shown in Fig. 7.5, it is clear that there is a trend for  $n_t$  to decrease as  $\gamma_{cy}$  increases. This is intuitively appealing because since pwp buildup is mainly controlled by  $\gamma_{cy}$ , then larger values of cyclic shear strain should build up pwp

faster and therefore also reach failure faster. Similar results have been found by Park and Silver (1975) and Pierce (1985) using strain-controlled tests. In stress-controlled tests it has also been shown that pwp increases with number of cycles (Seed and Lee, 1966; Lee and Seed, 1967) and that larger values of cyclic stress produce a faster pwp buildup.

The triggering relationships tend to show that as  $\gamma_{cy}$  become smaller the number of cycles to cause triggering  $n_t$  becomes very large, and close to the value of the threshold strain for this sand,  $n_t$  tends asymptotically to infinity. This is physically correct because the threshold strain is the minimum value of  $\gamma_{cy}$  that causes any pwp buildup.

Figure 7.11 shows the determination of the threshold strain for contractive sand F125 consolidated to  $\bar{\sigma}_{3c} = \bar{\sigma}_{1c} = 4 \text{ Kg/cm}^2$ , and determined in a cyclic triaxial test. The threshold strain is shown to be  $\gamma_t = \gamma_{cy} = 0.006\%$ . This is the asymptotic value shown in the triggering relationships where the number of cycles to failure become very large.

For each of the triggering curves of constant  $K_c$  in Figs. 7.5 - 7.10, there is a strong influence of the confining pressure, causing  $n_t$  to increase as  $\bar{\sigma}_{3c}$  increases. For example, in Fig. 7.7, for  $K_c = 1.5$  and  $\gamma_{cy} = 0.2\%$ , a sample consolidated to  $\bar{\sigma}_{3c} = 0.562 \text{ Kg/cm}^2$  will trigger after 3 cycles, whereas that consolidated to  $4 \text{ Kg/cm}^2$  will trigger

after 50 cycles.

This means that the magnitude of confining pressure has a very strong influence on the rate of pwp buildup of contractive sands. The effect was observed in all tests where different values of confining pressure were used. This trend may also be present to a smaller degree in strain-controlled tests of dilative sands, but few experimental results covering a large range of  $\bar{\sigma}_{3c}$  are available.

The effect of confining pressure on number of cycles to triggering can be better visualized by arithmetic plots such as those shown in Figs. 7.12 through 7.17. These are the same results already shown in Figs. 7.5 to 7.10, but now plotting  $n_t$  versus  $\bar{\sigma}_{3c}$  for a given  $\gamma_{cy}$ . This type of plot will be referred to as a modified triggering relationship. For example, the triggering relationship in Fig. 7.7 for  $K_c = 1.5$  has been transformed into the modified triggering relationship of Fig. 7.14. Since sometimes in Figs. 7.5 to 7.10 there are no tests at the same cyclic strain with different confining pressures, in some cases the values were chosen by interpolation among the existing laboratory tests using the curves of the triggering relationships.

The modified triggering relationships in Figs. 7.12 to 7.17 clearly show the dramatic effect of confining pressure



on the triggering of flow failure for sand F125. Very significantly, a linear relationship was found between  $n_t$  and  $\bar{\sigma}_{3c}$  for a given  $\gamma_{cy}$  in all cases for which enough data was available. The wealth of data in Fig. 7.14 is especially convincing on the existence of this linear relation, with all straight lines passing by the origin, that is, suggesting a tendency for triggering to occur in contractive specimens at  $n_t = 0$  cycles when  $\bar{\sigma}_{3c} = 0$ , independently of  $K_c$  and  $\gamma_{cy}$ .

The fact that the lines of constant  $\gamma_{cy}$  in the plot of modified triggering relations pass by the origin with  $n_t = 0$  for  $\bar{\sigma}_{3c} = 0$  is intuitively appealing. This is probably due to the fact that at  $\bar{\sigma}_{3c} = 0$  (no gravity), the sand grains are close to being in suspension floating in water, thus offering minimal or no resistance to any disturbance. The effect of confining pressure is very important when analyzing the liquefaction flow failure of earth structures where a large range of  $\bar{\sigma}_{3c}$  is usually present.

Results such as in Fig. 7.14 can be expressed analytically as:

$$u_t = T(K_c, \gamma_{cy}) \cdot \bar{\sigma}_{3c}$$

Figs. 7.18 and 7.19 are log-log plots showing the values of  $T$  as a function of  $\gamma_{cy}$  for all  $K_c$  used in the tests on sand Fl25. Although in all cases these  $T$ - $\gamma_{cy}$  plots are parallel straight lines in these log-log graphs, it is understood that as the cyclic shear strains approach the threshold strain, they must curve upwards to very large values of  $T$ . However, for earthquake engineering studies, where the main concern is for a short number of cycles at relatively large strains, the linear approximation between  $T$  and  $\gamma_{cy}$  is perfectly suitable.

Figs. 7.18 and 7.19 clearly show the value of  $T$  decreasing with increasing  $\gamma_{cy}$  for a given  $K_c$ . The figures also show that, for a given  $\gamma_{cy}$  and increasing  $K_c$ ,  $T$  decreases between  $K_c = 1.0$  and  $2.0$  but increases between  $K_c = 2.0$  and  $2.9$ . This behavior is not well understood, but it could be related to the sudden change in  $\bar{a}_{ut}$  when  $K_c$  approaches  $1.88$  (Fig. 6.29); and also to the lower brittleness index of those tests with  $K_c = 2.5$  and  $2.9$ , compared to those with  $K_c \leq 2.0$  (Fig. 6.39).

The data just presented for sand Fl25 also allow comparing  $n_t$  with  $\gamma_{cy}$  at a given  $\bar{\sigma}_{3c}$  but for all possible values of  $K_c$ . This is done in Fig. 7.20, which shows the range of triggering relationships for all tests with  $\bar{\sigma}_{3c} = 1$

$\text{Kg/cm}^2$  and  $K_c$  between 1.5 and 2.9. As can be seen, the value of  $K_c$  does not seem to affect the relation between  $\gamma_{cy}$  and  $n_t$  as much for a low value of  $\bar{\sigma}_{3c}$  as much as it did for higher values (compare Fig. 7.20 with the curves in Figs. 7.6 - 7.10 corresponding to  $\bar{\sigma}_{3c} = 4 \text{ Kg/cm}^2$ ).

### 7.2.2 Results on Sands A, B and C

The triggering relationships for sand A are shown in Figs. 7.21 through 7.24 for  $K_c = 1.22, 1.5, 2.0$ , and  $2.25$ . In these figures the trend for the number of cycles to trigger flow failure,  $n_t$ , to increase as the magnitude of the cyclic shear strain decreases is very clear. Again  $n_t$  tends to very large values as  $\gamma_{cy}$  gets closer to the threshold strain. All the tests were run at  $\bar{\sigma}_{3c} = 3.72 \text{ Kg/cm}^2$ , except for some tests with  $K_c = 2.0$  for which  $\bar{\sigma}_{3c}$  was between  $2.67$  and  $4.78 \text{ Kg/cm}^2$ .

The threshold strain for sands A, B, and C was determined by using the laboratory test results shown in Fig. 7.25. It is clear that for 5 cycles of strains with  $\gamma_c$  less than  $0.01\%$ , no pwp buildup was experienced. This threshold strain corresponds to the asymptotic values the triggering curves approach as the number of cycles becomes very large.

Figure 7.26 shows  $n_t$  for tests cycled at  $\gamma_{cy} = 0.05\%$  with  $K_c = 2.0$ , and for different values of confining pressure. Again a linear relationship such as given for sand F125 also holds true for this data set. This effect of  $\bar{\sigma}_{3c}$  has important practical consequences. For example, a sample consolidated to  $\bar{\sigma}_{3c} = 2.67 \text{ Kg/cm}^2$  will trigger after 4 to 5 cycles, whereas a sample consolidated to  $\bar{\sigma}_{3c} = 4.78 \text{ Kg/cm}^2$  will need 14 cycles to trigger.

Since Fig. 7.26 is the modified triggering relationship for  $K_c = 2.0$  and  $\gamma_{cy} = 0.05\%$ , it is of interest to see if the results shown for sand F125 are also applicable to the results on sand A. The linear relationship for  $\gamma_{cy} = 0.05\%$  in Fig. 7.26 for sand A has somewhat more scatter than that found for sand F125. This scatter is believed to be a direct consequence of the fact that the true sample diameter is not very accurate due to the unrecorded collapse of the specimen during saturation (see discussion in Chapter 4). Since the radius of the sample is not known and changes from test to test; therefore the exact values of cyclic shear strain are not completely reliable.

For sand A the magnitude of  $K_c$  also plays an important role in the triggering relationships; for a given cyclic shear strain  $\gamma_{cy}$ , the test with a higher value of  $K_c$  fails

with less number of cycles (smaller  $n_t$ ). The lines used to fit the data points for each value of  $K_c$  and  $\bar{\sigma}_{3c} = 3.72$  kg/cm<sup>2</sup>, and already included in Figs. 7.21 - 7.24, are plotted together in Fig. 7.27. By looking at this figure we can see that, for example, a soil element with  $\bar{\sigma}_{3c} = 3.72$  Kg/cm<sup>2</sup> and  $\gamma_{cy} = 0.2\%$  needs about 8 cycles to reach failure if  $K_c = 1.22$ , whereas it will take only 2 cycles if  $K_c = 2.0$ .

### 7.2.3 Results on San Fernando Sand SF7

The triggering relationships for sand SF7 and  $K_c$  between 1.4 and 2.0 are shown in Fig. 7.28; these were generated using tests with confining pressures  $\bar{\sigma}_{3c} = 1.00$  Kg/cm<sup>2</sup> and samples prepared using the moist tamping undercompaction method. It can be seen that the graph also follows the general behavior pattern found previously for the other two sands. For a given  $K_c$ , as the magnitude of  $\gamma_{cy}$  increases,  $n_t$  decreases. Also, for a given value of  $\gamma_{cy}$ , the sample with a higher value of  $K_c$  triggers before that with a lower value of  $K_c$ .

Figures 7.29 through 7.31 repeat the same triggering relationships of sand SF7 for  $K_c = 1.7$ , 1.87, and 2.0, respectively. What is of particular interest in these plots is that they present results on samples prepared by two

different methods: moist tamping and sedimentation. It can be seen in these figures that the method of sample preparation does not have a significant influence on the triggering relationships, despite the fact that the sand fabric produced by these two methods is totally different. The fabric produced by the sedimentation process mimics the in-situ structure of hydraulically produced sand deposits and creates an internal layering within the sand specimen. The consequences of this finding illustrated in Figs. 7.29 - 7.31 are extremely important, because it justifies applying directly the laboratory test results presented herein to the field conditions. This confirms again the validity of doing cyclic shear strain-controlled tests; and it clearly shows that cyclic shear strain is a very robust parameter not only for pwp buildup in isotropically consolidated dilative sands (Dobry, 1982), but also for triggering relationships in contractive sands.

Figure 7.32 shows that for sand SF7, the triggering relationship at a high  $K_c = 2.21$  is not consistent with those at low  $K_c$  in Figs. 7.29 - 7.31; because the effect of  $n_t$  to decrease as  $K_c$  decreases suddenly is reversed. This was also observed for  $K_c = 2.5$  and  $2.9$  in sand F125 (see Figs. 7.18 and 7.19), and the discussion on this behavior in Section 7.2.1 is also applicable to sand SF7.

The threshold strain was also determined for sand SF7 using isotropically and anisotropically consolidated specimens. The results are shown in Fig. 7.33, where it can be observed that in both cases,  $\gamma_t \approx 0.005\%$ . The data for this sand have some more scatter than those of the other contractive sands previously shown, but they do show that the value of  $K_c$  does not affect the threshold strain. This result on contractive sands completes the picture of the influence of  $K_c$  on  $\gamma_t$  for all sands, contractive or dilative; because it has also been shown that  $K_c$  does not affect  $\gamma_t$  in dilative sands (Dyvik et al., 1984). The value of  $\gamma_t$  is again shown to be the asymptotic value of cyclic shear strain where the triggering relationships give very large values.

Finally, the modified triggering relationships for sand SF7 and  $K_c = 1.7, 1.87$  and  $2.0$  are shown in Figs. 7.34 through 7.36. Although all tests were run at one confining pressure, the figures assume that the linear relationships between  $\bar{\sigma}_{3c}$  and  $n_t$  found for sands F125 and SF7 are still true.

Figure 7.37 shows a similar trend of variation of the parameter  $T = n_t / \bar{\sigma}_{3c}$  as  $\gamma_{cy}$  and  $K_c$  change, already found for the other sands. That is,  $\log T$  versus  $\log \gamma_{cy}$  plots as a

straight line for constant  $K_c$ , and the location of the line is lower as  $K_c$  increases from 1.4 to 2.0.

#### 7.2.1 Discussion

The effect of various parameters on the number of cycles to trigger flow failure,  $n_t$ , was investigated using cyclic torsional tests on triaxial samples. The parameters studied were  $\gamma_{cy}$ ,  $\bar{\sigma}_{3c}$ , and  $K_c$ .

The parametric study showed that for constant values of  $\bar{\sigma}_{3c}$  and  $K_c$ ,  $n_t$  decreases as  $\gamma_{cy}$  increases. It also revealed that for constant values of  $K_c$  and  $\gamma_{cy}$ ,  $n_t$  increases linearly as  $\bar{\sigma}_{3c}$  increases. Another conclusion reached in sand F125 for the range between  $K_c = 1.0$  and 2.0, was that  $n_t$  decreases as  $K_c$  increases; however, the opposite trend was found when  $K_c > 2.0$ . At values of  $\bar{\sigma}_{3c} = 1$  the triggering relationships with  $K_c = 1.5, 2.0, 2.5$  and 2.9 were quite close; showing that at low values of  $\bar{\sigma}_{3c}$ , the effect of  $K_c$  on  $n_t$  is not very significant. The change of behavior at  $K_c = 2.0$ , especially illustrated by the data on sand F125, may be related to the decrease in  $I_b$  and increase in  $\bar{a}_{ut}$  observed as  $K_c$  increases above 2.0.

Using sand SF7, the effect of specimen fabric (sedimentation versus moist tamping) was evaluated in terms



of its effect on  $n_t$ . No significant influence was found on the triggering relationships for the two types of samples, having, respectively, homogenous and layered fabrics. Therefore, it can be assumed that the triggering relationships developed in the laboratory can be directly applicable to the field without any correction. This is another confirmation of the robustness of the cyclic strain approach.

The triggering relationships take into account the effect of cyclic shear strain on the necessary number of cycles a particular soil element will need to trigger liquefaction flow failure. However, it should not be forgotten that these triggering relationships are related to the triggering strength envelope in  $\bar{p}$ - $q$  space, since the effective stress path of the CyT-CAU test is a horizontal line travelling towards the triggering envelope, with the horizontal distance measuring the pwp generated at triggering,  $r_{ut}$  (see Section 6.4).

The role of  $r_{ut}$  is of fundamental importance in understanding the behavior of contractive sands during cyclic loading. As a matter of fact, it becomes the link between the parameters controlling triggering and the parameters controlling pwp buildup.

### 7.3 Pore Water Pressure Buildup During Cyclic Straining

This section will discuss the build up of pore water pressure (pwp) in strain-controlled CyT-CTU and CyT-CAU tests on contractive samples of sands Fl25, A and SF7. The material to be presented in this section is very much related to number of cycles to trigger failure  $n_t$  previously discussed in Section 7.2 and to the value of pwp at triggering  $r_{ut}$  discussed in Section 6.4.

#### 7.3.1 Results on Ottawa Sand Fl25

The pwp buildup curves are presented as plots of  $r/r_{ut}$  versus  $n/n_t$  in Figs. 7.38 through 7.44 for  $K_c = 1.0, 1.2, 1.5, 2.0, 2.5$  and  $2.9$ .

Figure 7.41 is especially interesting, as it includes 13 tests having a wide variation of testing parameters. Fig. 7.41(a) shows the pwp buildup curves for all tests with  $K_c = 2.0$  on sand Fl25, and Fig. 7.41(b) includes the corresponding testing parameters, with  $\bar{\sigma}_{3c}$  between  $1.0 \text{ Kg/cm}^2$  and  $5.5 \text{ Kg/cm}^2$ ,  $\gamma_{cy}$  between  $0.0065\%$  and  $0.05\%$ , and  $n_t$  varying between 3 and 139 cycles. It can be observed that this normalization procedure produces very consistent results despite these large variations in  $\bar{\sigma}_{3c}$ ,  $\gamma_{cy}$  and  $n_t$ .

The same normalization procedure was also employed to reduce the other tests on sand F125 with other  $K_c$ . The figures show that this results in very consistent plots, despite the differences in  $\bar{\sigma}_{3c}$ ,  $\gamma_{cy}$  and  $n_t$ . The biggest scatter occurs in the tests with  $K_c = 1.0$ . It is believed that this may be caused by the fact that in this case the test is no longer strictly strain-controlled, since the pwp causes the torque to drop and therefore the compliance corrections, though not large (as explained in Chapter 4) are not constant during the test.

Careful examination among the figures shows that these normalized pwp build up curves are essentially a function of  $K_c$ . This is more clearly demonstrated by comparing the best fit curves for each set of tests with constant  $K_c$ , as done in Fig. 7.44. It can be seen that a family of curves is generated, each corresponding to a different  $K_c$ . However, for the values of  $K_c = 2.5$  and  $2.9$  the curves are essentially the same as that for  $K_c = 2.0$ . As a matter of fact, the pwp buildup curves for  $K_c = 1.0$  on one side, and that for  $K_c = 2.0, 2.5$  and  $2.9$  on the other, constitute the boundaries of this family of curves. The fact that these normalized curves for  $K_c = 2.0, 2.5$  and  $2.9$  are identical is probably related to the change in behavior at  $K_c \approx 2.0$ .

already noted before, and affecting  $\bar{a}_{ut}$  and  $I_b$  (Chapter 6), and  $n_t$  (Section 7.2).

Therefore,  $K_c$  has a significant influence on the rate of pwp buildup in contractive sands. Sands with lower values of  $K_c$  build up most of their pwp at the beginning of cyclic loading; whereas sands with higher values of  $K_c$  build up their pwp faster towards the end of the cyclic loading, right before triggering.

### 7.3.2 Results on Sands A, B and C

The same type of pwp generation behavior was found in sand A. Figs. 7.45 through 7.48 show the normalized pwp buildup curves for tests with  $K_c = 1.22, 1.5, 2.0, 2.25$ . These figures demonstrate a similar behavior to that found previously for sand Fl25. Figure 7.47 shows the pwp buildup curves for tests on sand A with  $K_c = 2.0$ . The uniqueness of the curve is again witness to the power of the normalization procedure in cyclic strain-controlled tests; since we again have a wide range of confining pressure, cyclic shear strain and number of cycles to failure. The best fit curves for different values of  $K_c$  are compared in Fig. 7.49. The curves follow again the same trend seen in sand Fl25.

### 7.3.3 Results on San Fernando Sand SF7

The same pwp generation behavior was observed for tests on sand SF7, as shown in Figs. 7.50 through 7.54 for  $K_c = 1.4, 1.7, 1.87, 2.0$  and  $2.2$ . In these figures, the open data points are tests in which the specimen was formed using the moist tamping undercompaction procedure, whereas the solid data points represent specimens prepared by the sedimentation method. It can be seen that the normalization procedure also works well for all tests on sand SF7, regardless of the specimen preparation procedure. For the tests on sedimented samples with  $K_c = 1.7$  and  $1.87$  the points are somewhat higher than the data points for the moist tamped samples. The maximum discrepancy occurs in Fig. 7.52, and there part of the explanation is that  $K_c = 1.8$  for the sedimented sample but  $K_c = 1.87$  for the two moist tamped specimens, and thus the sedimented data should be bigger (compare curves in Figs. 7.51 and 7.52). Therefore, the results on sand SF7 are also consistent with the rest of the results on other sands; and they also show that rate of pwp buildup is controlled mainly by the magnitude of the cyclic shear strain and value of  $K_c$ , and is not significantly affected by the fabric of the sand specimen.

Finally, Fig. 7.55 shows the effect of  $K_c$  on the pwp build up curves of sand SF7; the trend is again similar to that previously presented in the other two sands.

#### 7.3.4 Discussion

Results were presented regarding the rate of pwp buildup in contractive sands. It was found that the normalized plot of  $r_u/r_{ut}$  versus  $n/n_t$  is a very useful tool to understand pwp buildup. A totally different behavior was found between isotropically and anisotropically consolidated samples, with the value of  $K_c$  playing a fundamental role. For small  $K_c$ , the rate of pwp buildup is faster at the beginning of cyclic loading, whereas for large values of  $K_c$  the rate of pwp buildup is very small at the beginning and increases as the sample is close to triggering.

The triggering relationships for  $r_{ut}$  and  $n_t$  presented in Sections 6.7 and 7.2 are very much related to these results on pwp buildup, as reflected in the use of  $r_{ut}$  and  $n_t$  for the normalized pwp buildup curves.

Using the normalization procedure presented herein, it is shown that essentially only  $K_c$  affects the pwp buildup curves for a given sand. The confining pressure does not have a significant effect on the normalized rate of pwp

buildup, even though a sample with a smaller value of  $\bar{\sigma}_{3c}$  will trigger in less cycles. The reason for this is that the value of  $r_{ut}$  depends on  $K_c$  and the soil characteristics and not on  $\bar{\sigma}_{3c}$ .

The results on the San Fernando Sand showed that fabric does not have a significant influence on the pwp buildup curves. Therefore, the pwp buildup curves generated in the laboratory and presented herein, can be directly applied to predict the pwp generation in the field for that particular sand.

Three facts concerning pwp buildup and triggering of flow failure are apparent. First of all, small values of  $r_{ut}$  are needed to trigger flow failure if  $K_c$  is high. Second, at those high values of  $K_c$ , pwp does not build up much until close to triggering. Finally, triggering occurs at very small values of accumulated axial strains, as illustrated by Fig. 6.3 and discussed later in more detail in Section 7.6. These three facts point out that for situations in the field fitting the above conditions, seismic liquefaction flow failure could occur without much of an external manifestation; and by the time an earth structure can be seen to deform excessively, triggering has long time occurred.

#### 7.4 Pore Pressure Buildup and Triggering for Different Sands

This section will compare the triggering relationships and the pwp buildup curves for the three sands tested (sands Fl25, A, and SF7).

Figure 7.56 shows a band enclosing all data from the triggering relationships for the three sands, for  $\bar{\sigma}_{3c} = 1$  Kg/cm<sup>2</sup> and  $K_c = 2.0$ . These values of  $\bar{\sigma}_{3c}$  and  $K_c = 2.0$  are typical of many earth structures. Even though the range of  $n_t$  for a given  $\gamma_{cy}$  is large, it still gives a useful indication of general behavior. The values of  $\gamma_{cy}$  producing triggering in contractive samples with this  $K_c > 1$  are much smaller than for strain-controlled tests on isotropic consolidated samples. It was already shown in Fig. 2.12 that for  $K_c = 1$  and a range of  $\bar{\sigma}_{3c} = 0.25$  to 2 Kg/cm<sup>2</sup>, the  $r_{ut} = 1.0$  condition occurs in 10 cycles when  $\gamma_{cy} = 0.3\%$  to 0.5% in most dilative sands (NRC, 1985). Also the extrapolation to  $\bar{\sigma}_{3c} = 1$  Kg/cm<sup>2</sup> in Fig. 7.12 suggests that, for contractive sand Fl25 and  $K_c = 1$ ,  $\gamma_{cy} \approx 0.1\%$  for  $u_t = 10$  cycles. As shown in Fig. 7.56, this range of strains 0.1% to 0.5% is substantially to the right of the curve presented in Fig. 7.56, with this showing very clearly the detrimental effect of  $K_c$  on  $n_t$ .



Figure 7.57 shows the limiting ranges of the normalized pwp buildup curves for the three sands tested. All test data fall within the shaded region regardless of the values of  $K_c$ ,  $\bar{\sigma}_{3c}$ ,  $\gamma_{cy}$  and  $n_t$ . This shaded region is bounded on the left hand side by the pwp buildup curves for tests with  $K_c = 1.0$  and, on the right hand side by the highest values of  $K_c$  used ( $K_c = 2.9$  in sand F125, 2.25 in sand A and 2.2 in sand SF7).

### 7.5 A Pore Pressure and Triggering Model for Cyclic Straining of Contractive Sands

On the basis of the consistent results obtained with totally different types of sand; it is believed that most or all contractive sands behave in a similar fashion. In order to fit the behavior of any arbitrary contractive sand to the experimental evidence presented herein, a simple pwp model is presented in this section, along with the necessary procedures to calibrate the model parameters for that particular sand. This model is an effective stress path based pwp buildup and triggering of flow failure model, as it attempts to model the effective stress path of a CyT-CAU test from its point of consolidation to the triggering of liquefaction flow failure, by modelling the effect of various factors on the pwp buildup that will eventually lead

it to failure.

Experimental evidence was already shown indicating that pwp build up in contractive sands is related to the following four main factors:

- 1) Consolidation Stress,  $\bar{\sigma}_{3c}$
- 2) Coefficient of Anisotropic Consolidation,  $K_c$
- 3) Magnitude of Cyclic Shear Strain,  $\gamma_{cy}$
- 4) Number of Cycles of Strain,  $n$

The proposed model will take into account the above factors, and when incorporated into a dynamic response analysis package, it should be able to perform a dynamic effective stress analysis of an earth structure susceptible to liquefaction flow failure.

The proposed pwp model is based on several experimentally observed results on contractive sands as presented in this work. These results are:

- 1) Only contractive soils with driving shear stresses greater than  $S_{us}$  are susceptible to flow failure in an undrained, Mechanism A situation.

- 2) Triggering of liquefaction flow failure occurs when certain effective stress conditions are met which are dependent on the sand properties (friction angle) and on  $K_c$ .

- 3) After triggering, the sample loses its shear strength while straining until the steady-state shear

strength is reached.

4) A sufficient amount of pwp must be generated to trigger flow failure. This pwp can be generated by either monotonic or cyclic loading. Any perturbation that induces pwp buildup in contractive sands will be detrimental to the stability of the soil element.

5) There is a threshold cyclic strain below which no permanent sand rearrangement occurs; therefore, below this threshold strain no pwp will be generated.

6) For given values of  $\bar{\sigma}_{3c}$  and  $K_c$ ; as the magnitude of  $\gamma_{cy}$  increases, the number of cycles to trigger flow failure decreases

7) For given values of  $\gamma_{cy}$  and  $K_c$ ; as the magnitude of  $\bar{\sigma}_{3c}$  increases, the number of cycles to trigger flow failure also increases in a linear manner.

8) If  $\bar{\sigma}_{3c}$  and  $\gamma_{cy}$  are given and  $K_c \leq 2$ , as the magnitude of  $K_c$  increases the number of cycles to trigger liquefaction flow failure,  $n_t$  decreases. For values of  $K_c > 2$ , the trend may reverse itself, with  $n_t$  now increasing.

9) The normalized pwp buildup curves presented in this work,  $r_u/r_{ut}$  versus  $u/u_t$ , are mainly affected by the magnitude of  $K_c$ .

Of the above nine experimental facts, the first one can be easily described by the SSL for a particular soil. The

remaining eight facts can be visualized by three types of graphs shown schematically in Fig. 7.58. The three figures are: (a) the location of the triggering ( $\bar{\alpha}_{ut}$ ) and steady-state strength ( $\bar{\alpha}_{us}$ ) envelopes for a particular sand; (b) the triggering relationships that quantify the effects of  $\bar{\sigma}_{3c}$ ,  $K_c$  and  $\gamma_{cy}$  on the number of cycles  $n_t$  to trigger liquefaction flow failure; and (c) the pwp buildup curves which portray the effect of  $K_c$  on the rate of normalized pwp buildup.

By modelling each of the above three figures separately, it will be possible to construct the desired pwp model.

The triggering strength envelope of angle  $\bar{\alpha}_{ut}$  and the magnitude of  $K_c$  define the necessary amount of pwp necessary to trigger flow failure, as given by:

$$r_{ut} = 0.5 \left[ K_c + 1 - \frac{K_c - 1}{\tan \bar{\alpha}_{ut}} \right] \quad (7.1)$$

where now  $\bar{\alpha}_{ut}$  might not be a constant as it may vary with  $K_c$ . The pwp ratio at triggering  $r_{ut}$  is a fundamental variable in the model, and it will be seen later that  $r_{ut}$  is the parameter linking the triggering relationships, the pwp buildup curves and the effective stress conditions at triggering.

The pwp buildup curves are a family of curves whose shape changes as a function of  $K_c$  (Fig. 7.58c). For  $K_c = 1.0$  the curve is always concave downwards for all  $(n/n_t)$ . As  $K_c$  increases, the curves start becoming concave upwards at earlier values of  $(n/n_t)$ . The family of curves can be represented by the following equation:

$$\frac{r_u}{r_{ut}} = \frac{P \left( \frac{n}{n_t} \right)}{1 + Q \left( \frac{n}{n_t} \right)} + R \left( \frac{n}{n_t} \right)^S \quad (7.2)$$

where the parameters  $P$ ,  $Q$ ,  $R$ , and  $S$  are determined by fitting the experimental results. These parameters are chosen so that the first term becomes the dominant one for low values of  $K_c$ , while the second term controls for high values of  $K_c$ . Therefore, at  $K_c = 1.0$ ,  $R = 0.0$ ; and at large  $K_c$ ,  $P$  will be close to zero. The parameters  $Q$  and  $S$  are constants chosen to better fit the results. The factors  $P$  and  $R$  are calculated using the general expressions:

$$P = j - f K_c \quad (7.3)$$

$$R = g K_c - k \quad (7.4)$$

where  $j$ ,  $f$ ,  $g$  and  $k$  are constants fitted to the data.

Applying this scheme to the results of sand A we obtain that parameters P and R are given by the following expressions as functions of  $K_C$ :

$$P = 5.279 - 2.133 K_C$$

$$R = 0.677 K_C - 0.677$$

and the constants Q and S are  $Q = 2.182$  and  $S = 8$ . The resulting model curves for sand A are shown in Fig. 7.59 for  $K_C = 2.0$  and in Fig. 7.60 for all values of  $K_C$  used in the tests. Notice that the normalized pwp buildup curves in Fig. 7.60 are identical to those previously included in Figs. 7.45 to 7.49.

The final, and probably most important part of the model relates to the triggering relationships. Two methods were developed that determine  $n_t$  and they are presented here: one of them takes into account  $\bar{\sigma}_{3C}$  whereas the other does not. The method that does not take into account the confining pressure was developed earlier and applied to sand A. The more realistic model incorporates the value of  $\bar{\sigma}_{3C}$  and will be shown later.

The triggering relationship not incorporating  $\bar{\sigma}_{3C}$  is given by the following equation:

$$n_t = \frac{r_{ut}}{h(2-r_{ut})} \quad (7.5)$$

where  $h$  is a function of both  $K_c$  and  $\gamma_{cy}$ . The function  $h(\gamma_{cy}, K_c)$  must also take into account the fact that there exists a threshold strain  $\gamma_t$  below which no pwp are generated. The function  $h$  is given by the following equation:

$$h = a (\gamma_{cy} - \gamma_t)^\beta \quad (7.6)$$

where  $a$  and  $\beta$  are linear functions of  $K_c$ :

$$a = a - b K_c \quad (7.7)$$

$$\beta = c - d K_c \quad (7.8)$$

The function  $h$  can be graphically obtained if we solve Eq. 7.5 for  $h$  giving the following expression:

$$h = \frac{r_{ut}}{n_t(2-r_{ut})} \quad (7.9)$$

and we plot  $h$  as a function of  $\gamma_{cy}$  from the experimental data. This should create unique curves for tests with constant  $K_c$  and different  $\gamma_{cy}$ . This is shown in Fig. 7.61 for tests on sand A with  $K_c = 1.5$ . Using the above mentioned procedure with the test results for sand A yields

$a = 4.78$ ,  $b = 1.91$ ,  $c = 2.96$  and  $d = 0.78$ , and Eq. 7.6 becomes:

$$h = (4.78 - 1.91 K_c) (\gamma_{cy} - 0.01) (2.96 - 0.78 K_c)$$

$$r_{ut} = 0.5 \left[ K_c + 1 - \frac{(K_c - 1)}{\tan 23^\circ} \right] \quad (7.11)$$

These expressions for  $h$  and  $r_{ut}$  when combined with Eq. 7.5 allow predicting number of cycles to triggering any  $n_t$ . The corresponding predicted triggering relationships for all values of  $K_c$  used in the tests are shown in Fig. 7.62. Notice that these are the same curves of  $n_t$  versus  $\gamma_{cy}$  plotted before in Figs. 7.21 to 7.24, and that Fig. 7.62 is identical to Fig. 7.24. Using the triggering relationships in Fig. 7.62,  $r_{ut}$  given by Eq. (7.11), and the expression in Fig. 7.60 for the normalized pwp buildup, a CyT-CAU test was modelled and compared against the actual measurements in Fig. 7.63, with very good agreement.

The second method to derive the triggering relationships is more powerful as it incorporates the value of  $\bar{\sigma}_{3c}$ , and it is also easier to use than the first method just discussed.

Recalling the results of Section 7.2, we found that the triggering relationships can also be displayed in the



arithmetic plots of  $n_t$  vs  $\bar{\sigma}_{3c}$ , which we called modified triggering relationships. In this type of representation,  $n_t$  is related to  $\bar{\sigma}_{3c}$  by the following linear relation:

$$n_t = T \bar{\sigma}_{3c} \quad (7.10)$$

where  $T$  is the slope of the radial lines of equal  $\gamma_{cy}$ , and is a function of  $K_c$

It was also shown in Section 7.2 that if  $T$  is plotted versus  $\gamma_{cy}$  in a logarithmic plot, a straight line appears which is dependent on  $K_c$  only. For different values of  $K_c$  the lines appeared to be parallel, and  $T$  could therefore be expressed as:

$$\log T = \log I - F \log \gamma_{cy} \quad (7.13)$$

where  $F$  is the constant slope of all lines and  $I$  their intercepts. This can be rewritten as:

$$T = I \gamma_{cy}^{-F} \quad (7.14)$$

where  $F$  is a constant and  $I$  is a function of  $K_c$  only.

Using the modified triggering relationships for moist tamped sand SF7 with  $K_c = 1.4, 1.7, 1.87$  and  $2.0$ , the curves for  $T$  could be determined for this sand, and were shown

previously in Fig. 7.37. In that plot,  $I$  is a function of  $K_c$  given by:

$$I = \kappa + \ell K_c \quad (7.15)$$

where  $\kappa$  and  $\ell$  are constants.

This relationship for  $I$  can be found in a plot of  $\log I$  versus  $K_c$ , and is shown as an example for sand SF7 in Figure 7.64, which provides  $\kappa = 1.230$  and  $\ell = 1.114$ . Also, for Eq. 7.13,  $F = 1.2374$  was found.

Summarizing the results on sand SF7, the pwp triggering equations to determine  $n_t$  are the following:

$$I = 1.230 - 1.114K_c$$

$$T = I \gamma_{cy}^{-1.2374}$$

$$n_t = T \bar{\sigma}_{3c}.$$

and they are calculated in that specific order when used to predict  $n_t$ . The rest of this pwp buildup model including  $\bar{\sigma}_{3c}$  is identical to that before without  $\bar{\sigma}_{3c}$ . That is,  $n_t$  is combined with  $r_{ut}$  and with the curves of  $r_u/r_{ut}$  versus  $u/u_t$  to predict  $r_u$  versus  $n$ .

Either of the two pwp models just described can be easily applied to variable cyclic shear stress time

histories such as occurring during seismic loading. The only input that is needed is the shear strain time history, as well as the value of the consolidation pressure  $\bar{\sigma}_{3c}$  and  $K_c = \bar{\sigma}_{1c}/\bar{\sigma}_{3c}$  for the soil element in question.

The algorithm to account for a variable shear strain time history using either pwp model would be the following. From  $K_c$  and  $\bar{\sigma}_{3c}$ ,  $r_{ut}$  and the shape of the curve of  $r_u/r_{ut}$  versus  $n/n_t$  can be determined for the whole strain history. However, as  $n_t$  depends on the cyclic strain  $\gamma_{cy}$ , which is changing,  $n_t$  has to be updated in every cycle (or half-cycle). Figure 7.65 sketches the calculation along the corresponding line of  $r_u/r_{ut}$  versus  $n/n_t$ . The procedure is as follows:

- at the end of cycle  $i$  of cyclic strain  $\gamma_i$  a pore pressure  $u_i$  has been calculated. To this cyclic strain corresponds a value of  $n_{ti} = n_t(\gamma_i)$ . Therefore, at this point in time the element is at point A in Fig. 7.65, of coordinates  $r_{ui}/r_{ut} = u_i/(\bar{\sigma}_{3c} r_{ut})$  and  $n_t/n_{ti}$
- to calculate the pore pressure  $u_{i+1} \geq u_i$  at the end of cycle  $i+1$  of strain  $\gamma_{i+1}$ , first the "equivalent number of cycles" of  $\gamma_{i+1}$  needed to cause  $u_i$ ,  $n_{i+1}$ , and the "equivalent number of cycles to triggering"

of  $\gamma_{i+1}$ ,  $n_{ti+1}$ , must be calculated. The ratio  $n_{i+1}/n_{ti+1} = n_i/n_{ti}$ , as we are still at point A in Fig. 7.64. The value  $n_{ti+1}$  is obtained from  $\gamma_{i+1}$ , and  $n_{i+1} = n_{ti+1} (n_i/n_{ti})$ .

- finally, point B is located, corresponding to the end of cycle  $i+1$ . This point has an abscissa  $(n_{i+1}+1)/n_{ti+1}$ , and the corresponding coordinate  $r_{ui+1}/r_{ut} = u_{i+1}/(\bar{\sigma}_{3c} r_{ut})$  is read from the curve.

This algorithm was incorporated into a dynamic analysis using the test results on sand A, and was used to analyze the possibility of liquefaction flow failure of an earth structure (Dakoulas et al., 1988).

#### 7.6 Accumulated Axial Strain at Triggering

Castro et al. (1988) have proposed to analyze the problem of flow failure triggering using an accumulated axial strain criteria. Therefore, it is of interest to see how this method relates to the one previously shown herein. Figs. 7.66 through 7.68 show the relationship between the pwp value at triggering,  $r_{ut}$ , and the accumulated axial strain,  $\epsilon_t$  obtained experimentally for sands A, SF7 and Fl25, respectively. In general, a very small value of cumulative axial strain is needed to achieve liquefaction

flow failure; in these silty sands the triggering axial strains were on the order of 1% or less. This is in contrast with cyclic triaxial test results on anisotropically consolidated dilative sands (Seed, 1973), in which the failure criteria was arbitrarily set as 5% accumulated axial strain. Here again we see that it can be very unconservative to use laboratory test results on dilative sands to model a situation in the field involving contractive sands. Figures 7.66 through 7.68 also appear to show that as the value of  $r_{ut}$  increases, the accumulated axial strain,  $\epsilon_t$ , also increases; however, there is significant scatter. Figure 7.68 suggests that the relation between  $r_t$  and  $\epsilon_t$  is not greatly affected by the fabric of the soil specimen. Figure 7.66 indicates that samples involving large values of  $K_c = 2.5$  and  $2.9$  tend to fail at larger  $\epsilon_t$ , even though the corresponding magnitudes of  $r_{ut}$  are very small ( $r_{ut} < 0.2$ ). The reason for this is not well understood but could be related to the differences in  $I_b$  (see Fig. 6.39). Figure 7.66 suggests that predicting triggering based on number of cyclic strain cycles and pwp buildup, gives more consistent and uniform results than relying on an accumulated strain criteria assumed valid for different loading conditions,  $K_c$  and  $r_{ut}$ .

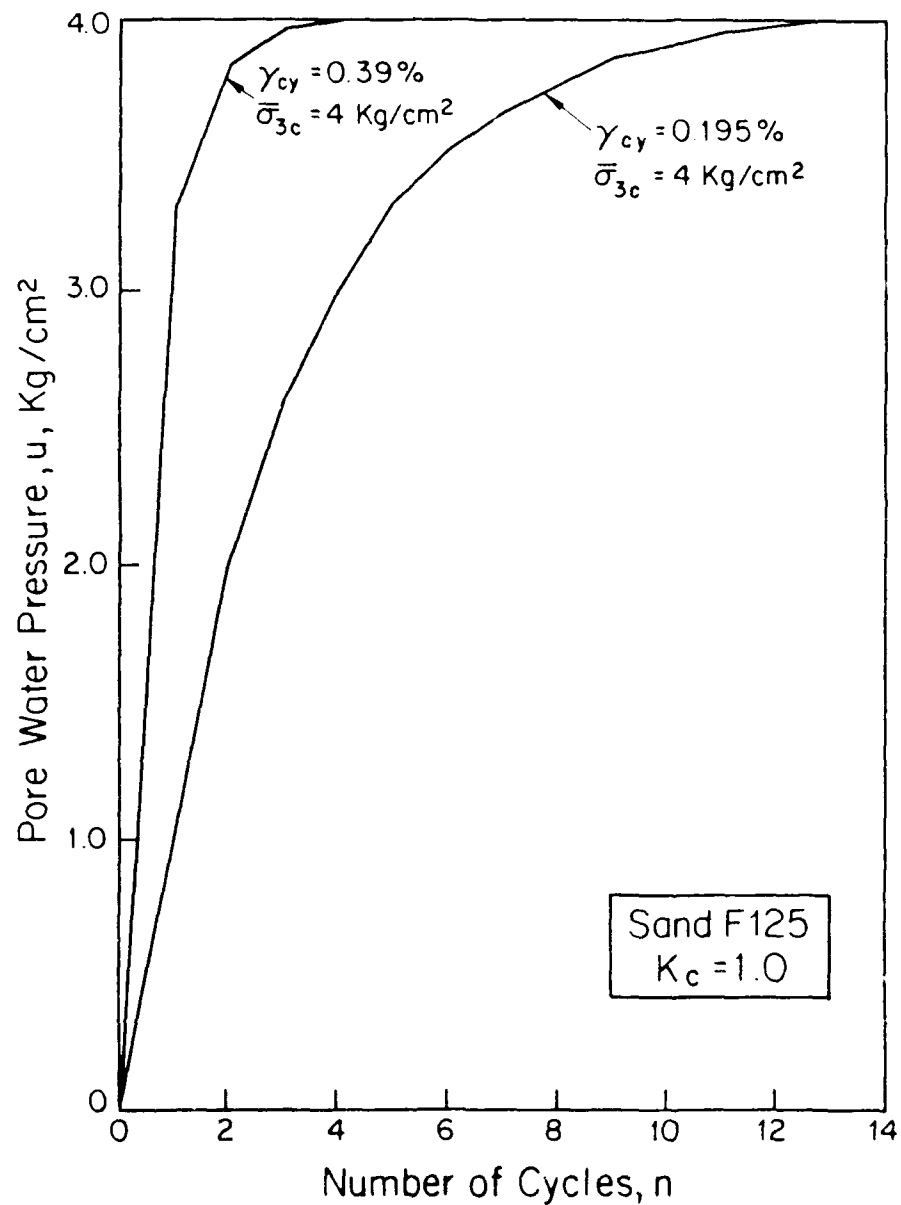


Fig. 7.1. Pore Water Pressure Buildup in Strain-Controlled CyT-CIU Tests on Isotropically Consolidated Samples of Ottawa Sand F125

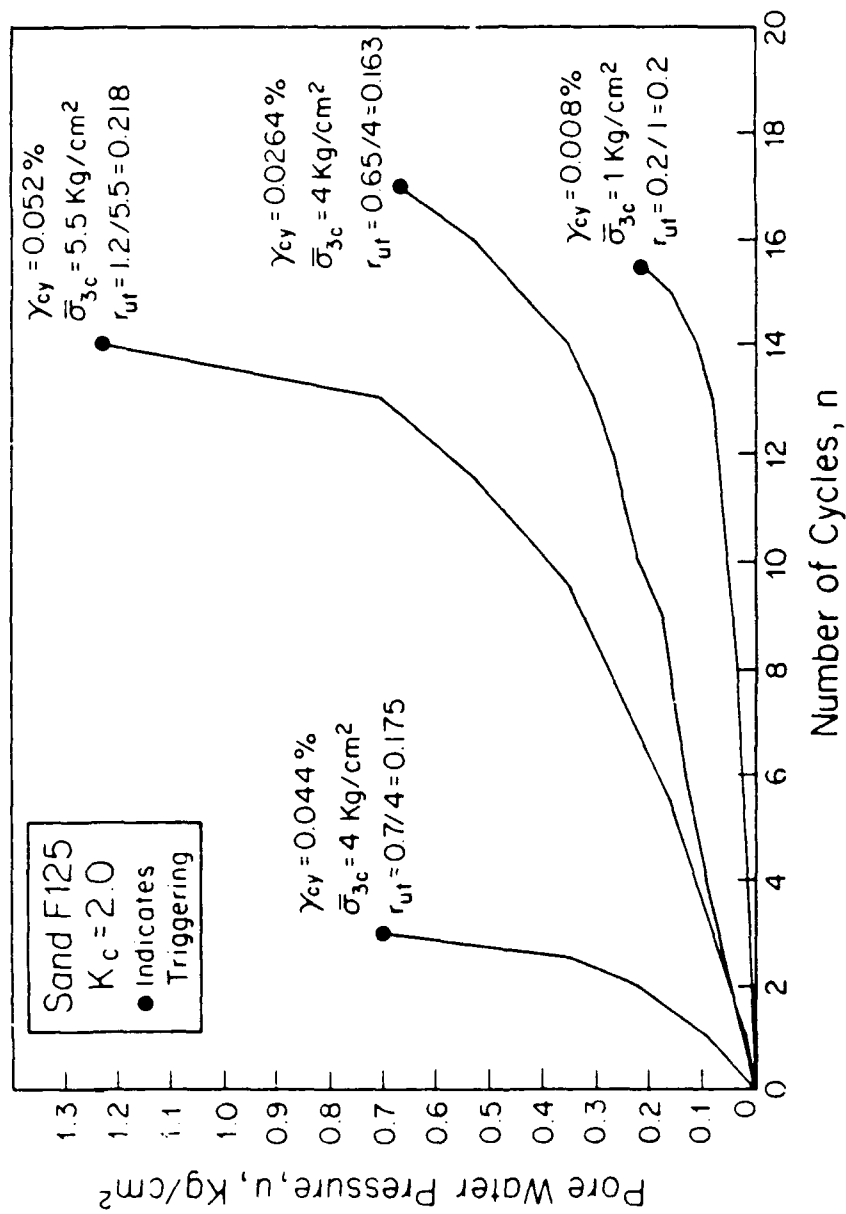


Fig. 7.2. Pore Water Pressure Buildup in Strain-Controlled Cyt-CTU Tests on Anisotropically Consolidated ( $K_c = 2.0$ ) Samples of Ottawa Sand F125)

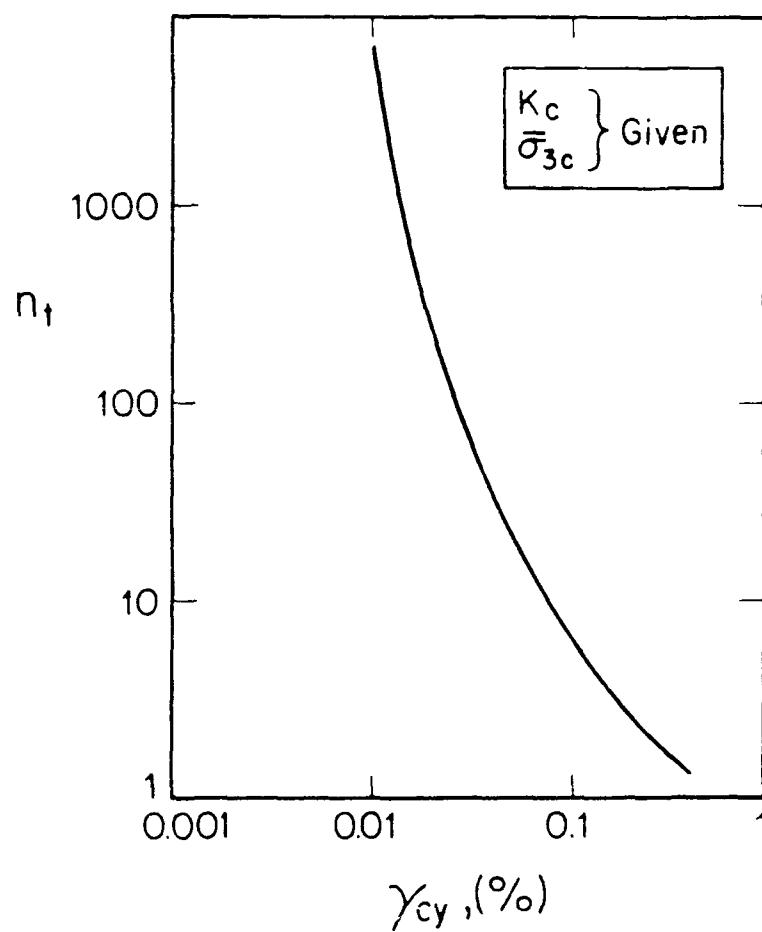


Fig. 7.3. Schematic Diagram of the Triggering Relationship



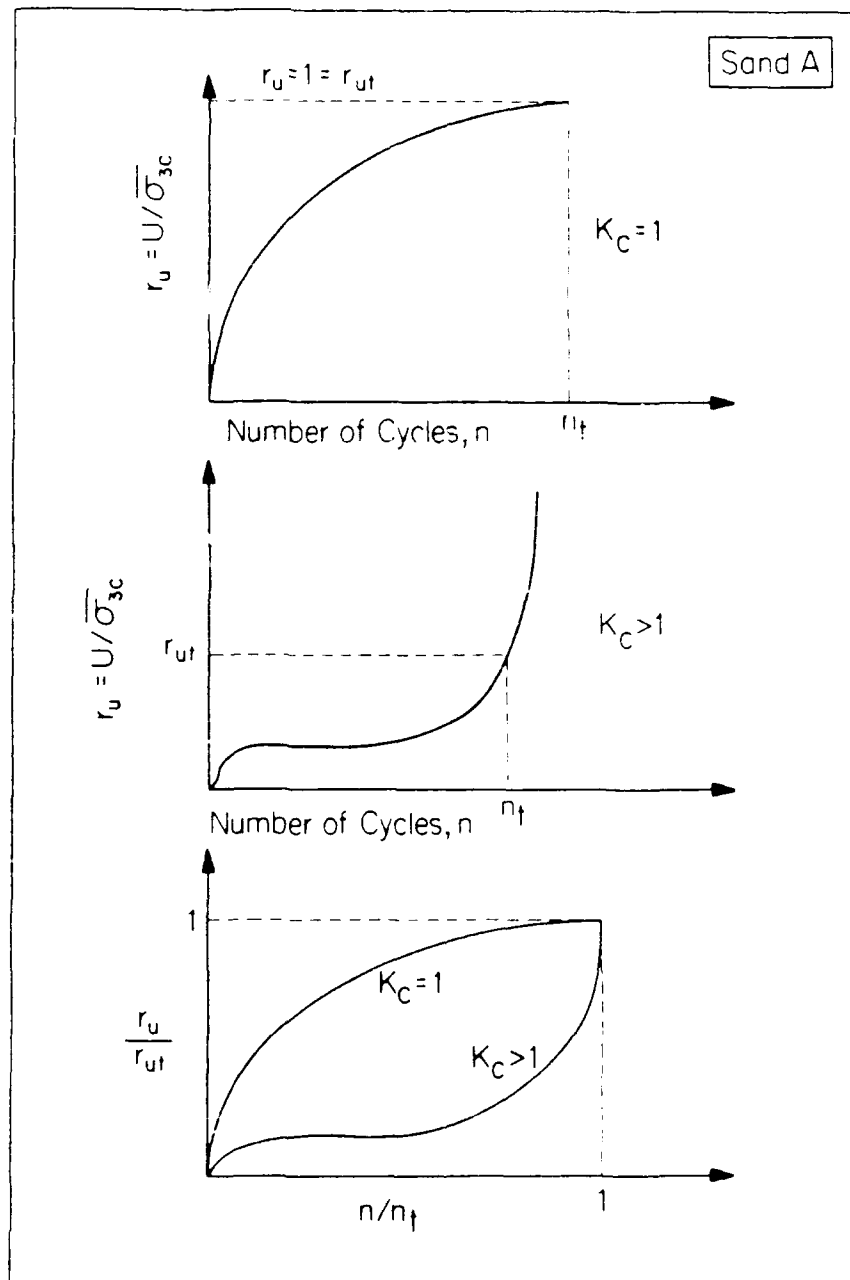


Fig. 7.4. Schematic Diagram for the Normalization Procedure to Generate the PWP Buildup Curves

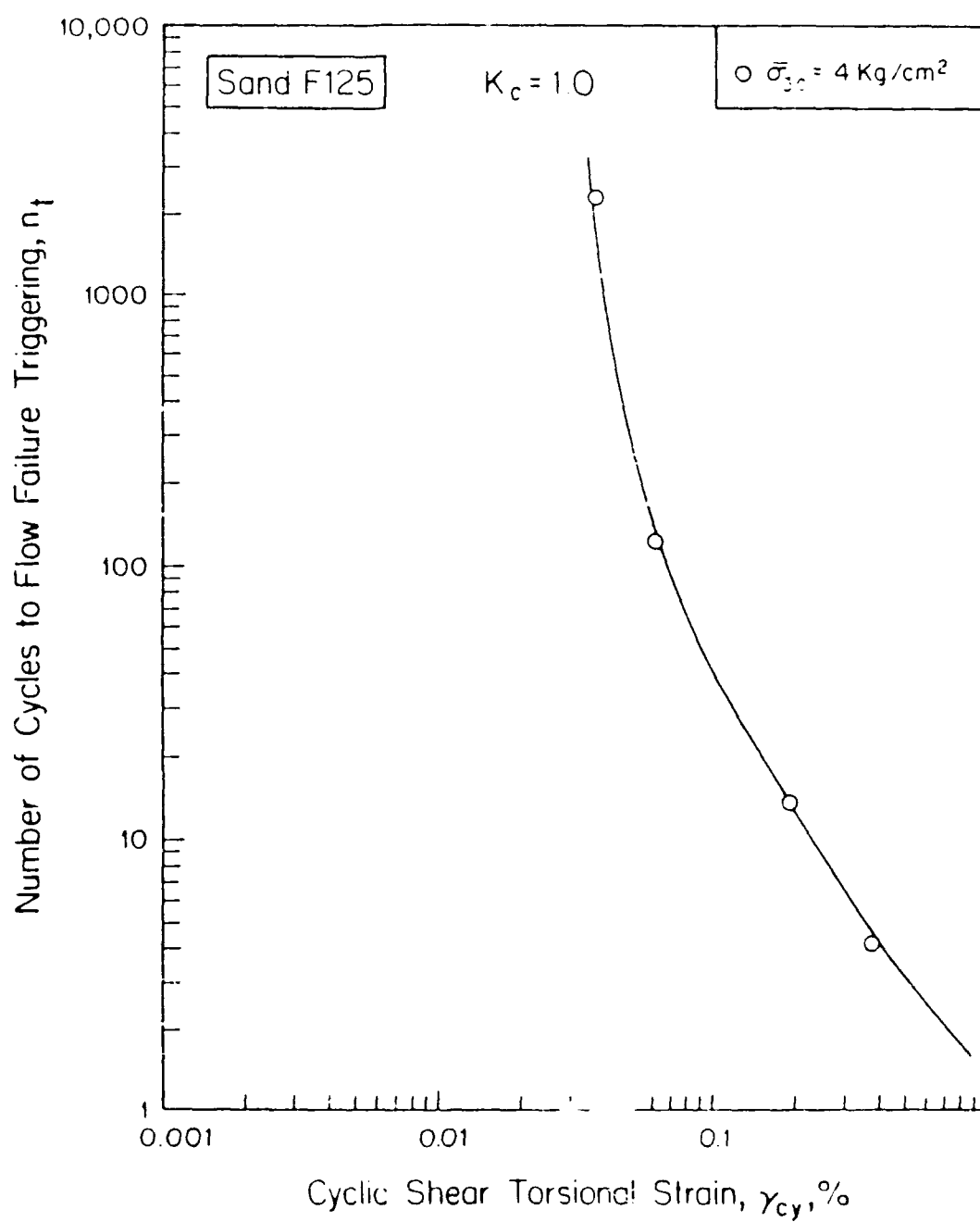


Fig. 7.5. Triggering Relationship for CyT-CIU Tests on Sand F125,  $K_c = 1.00$

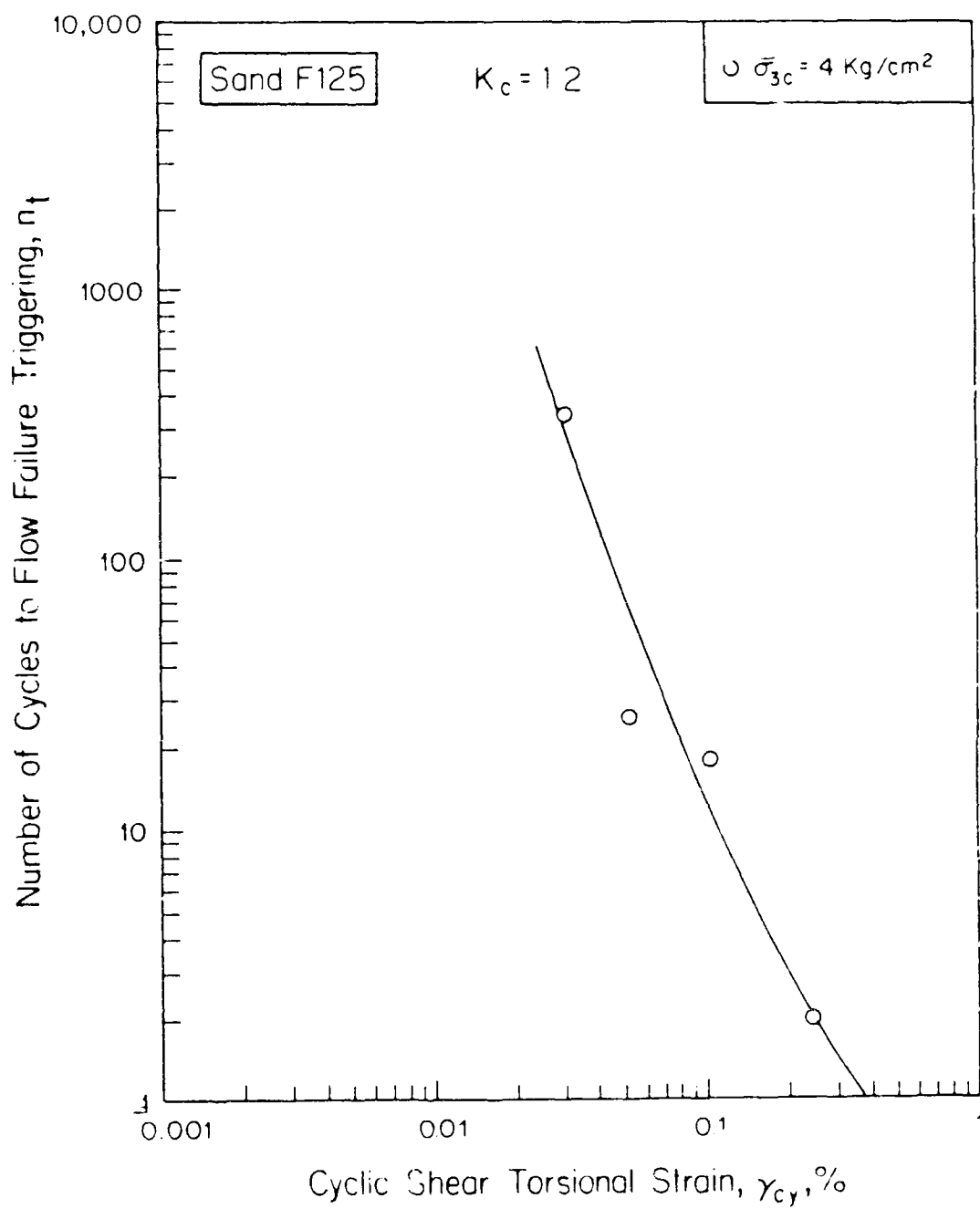


Fig. 7.6. Triggering Relationship for CyT-CAU Tests on Sand F125,  $K_c = 1.2$

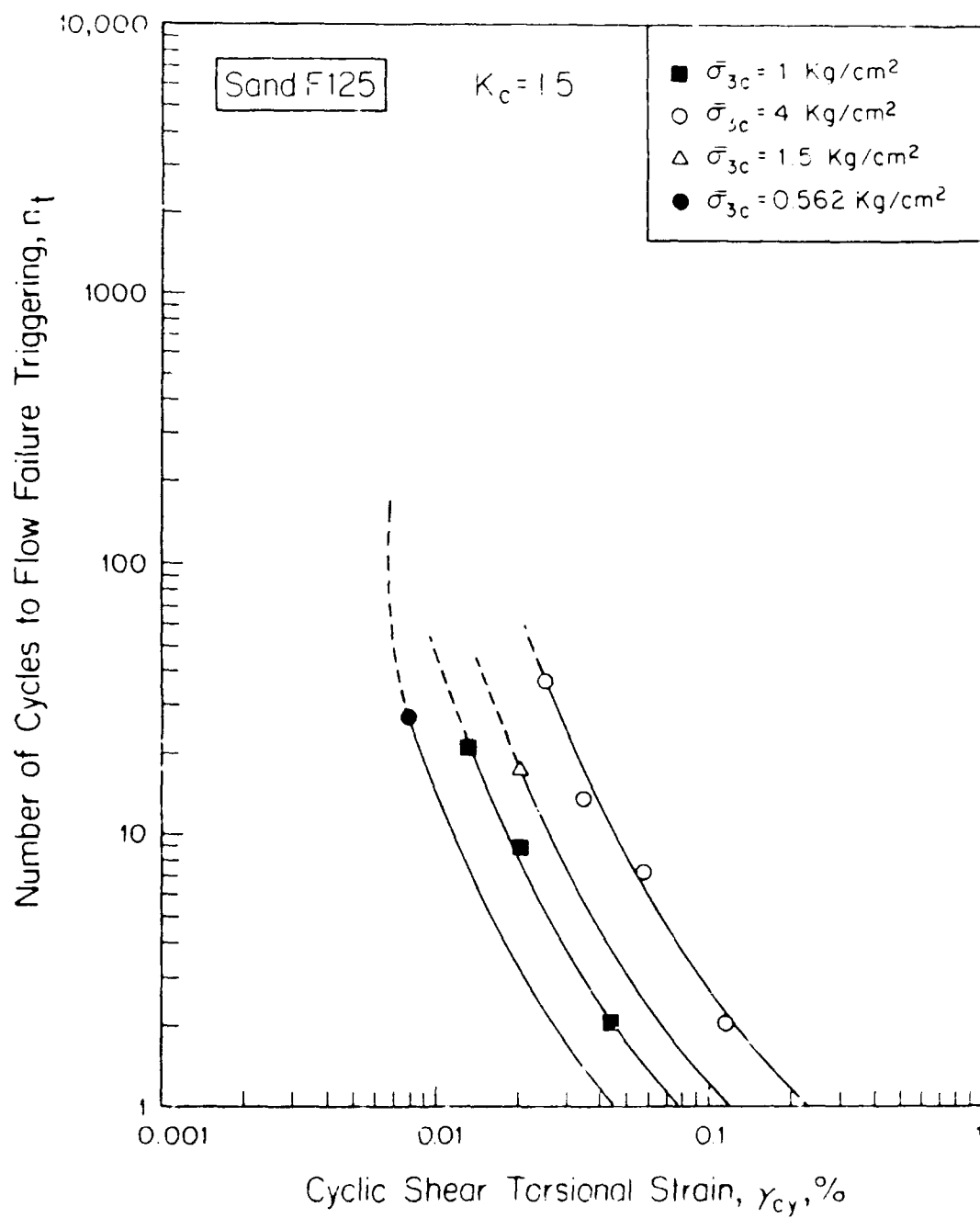


Fig. 7.7. Triggering Relationship for CyT-CAU Tests on Ottawa Sand F125,  $K_c = 15$

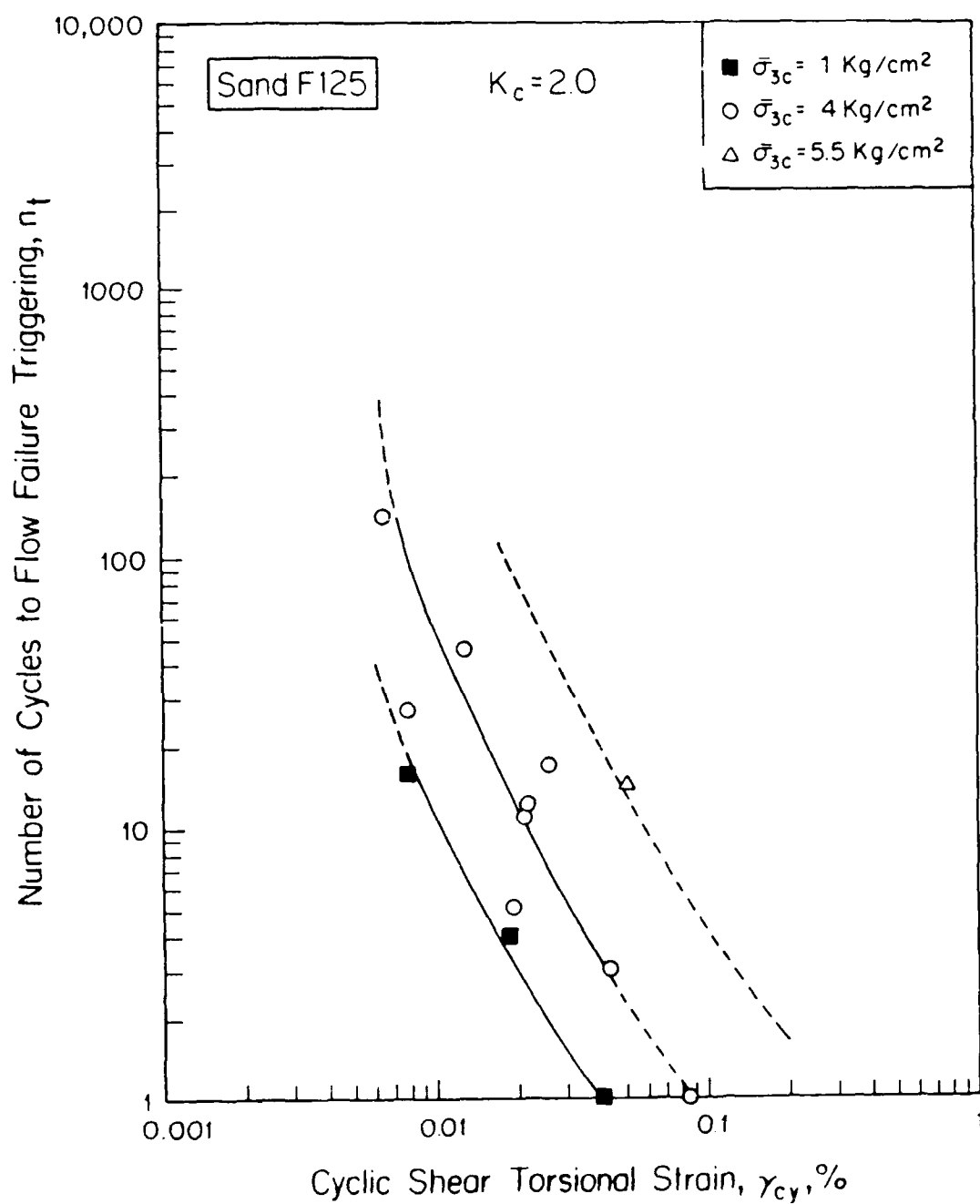


Fig. 7.8. Triggering Relationship for CyT-CAU Tests on Ottawa Sand F125,  $K_c = 2.0$

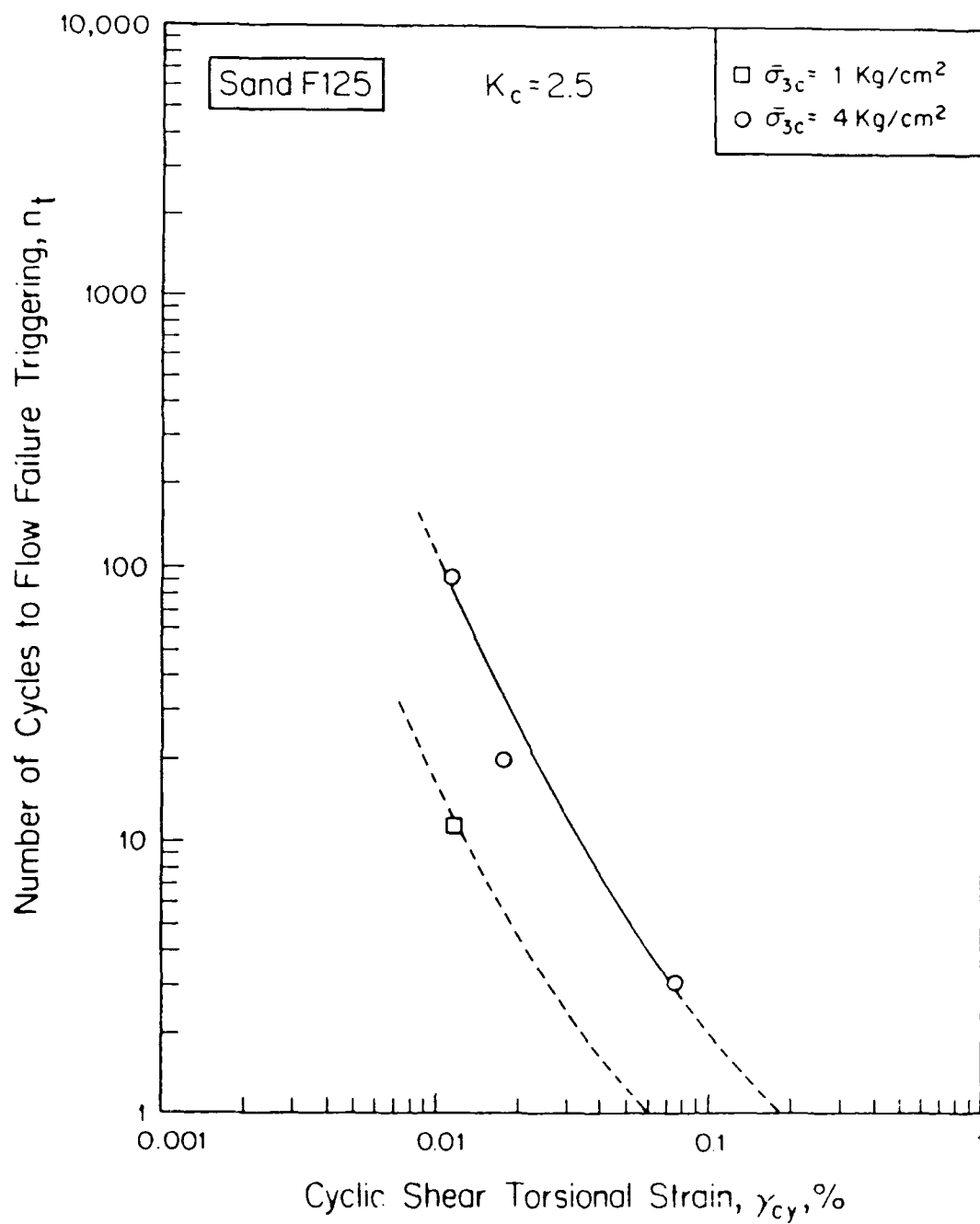


Fig. 7.9. Triggering Relationship for CyT-CAU Tests on Ottawa Sand F125,  $K_c = 2.5$

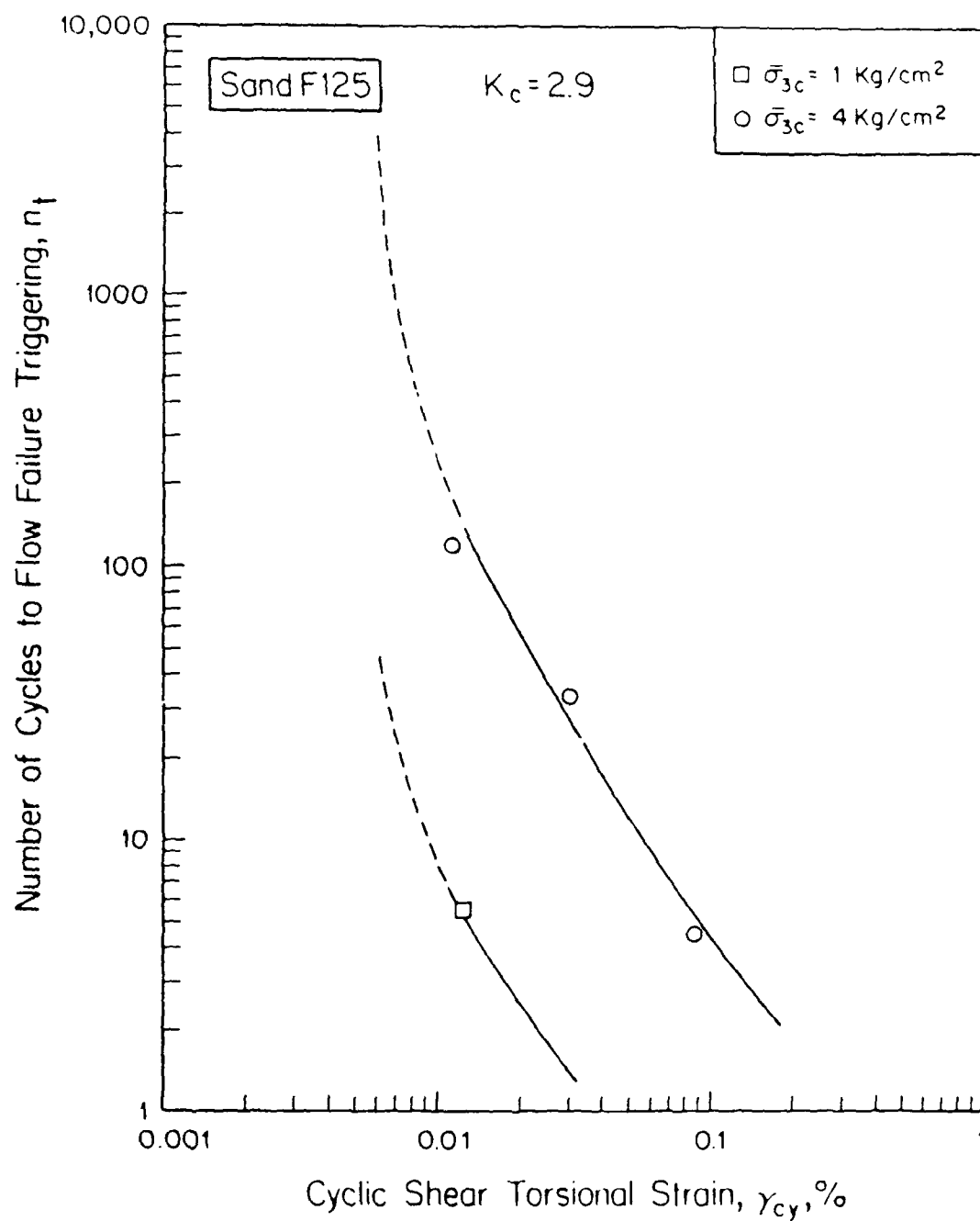


Fig. 7.10. Triggering Relationships for CyT-CAU Tests on Ottawa Sand F125,  $K_c = 2.9$

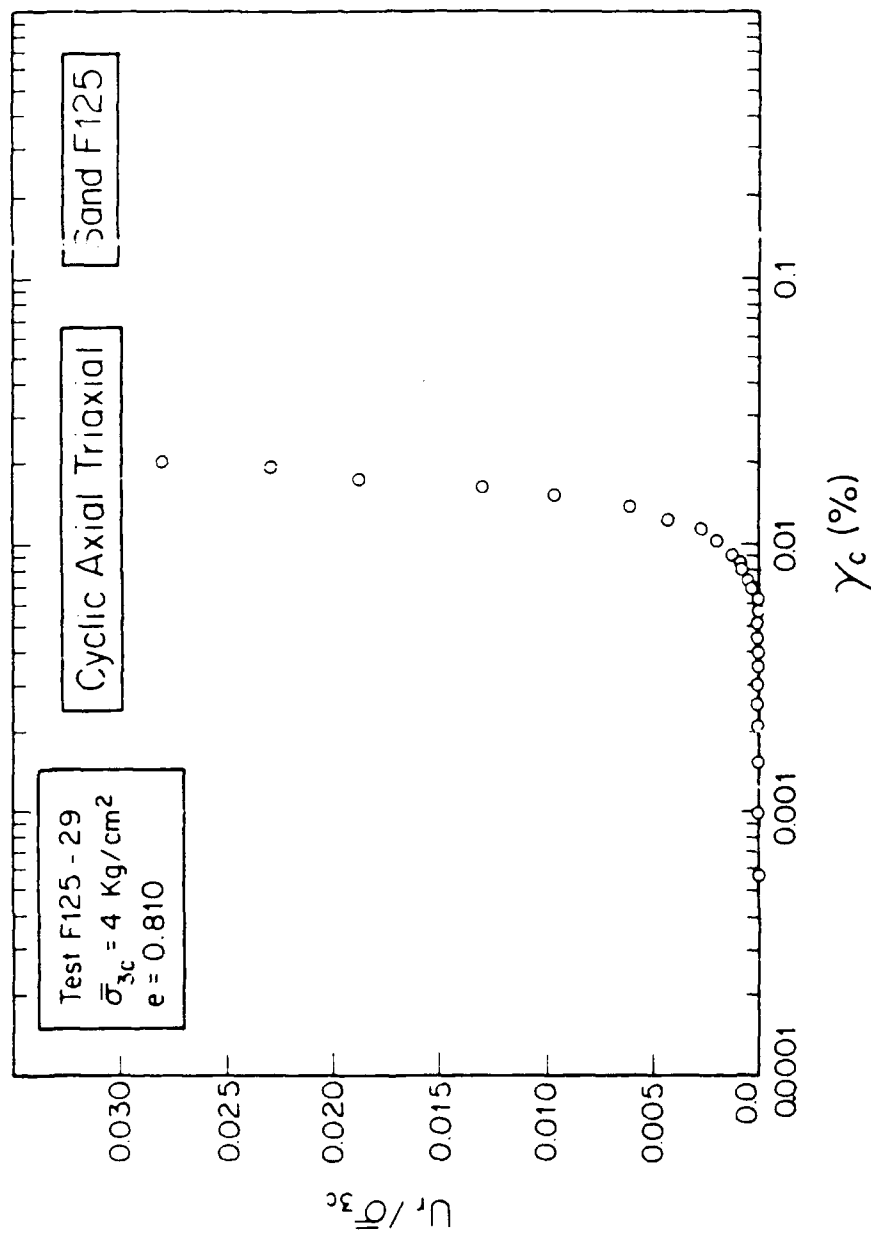


Fig. 7.11. PWP Buildup After 5 Cycles of Constant Shear Strain in Ottawa Sand F125



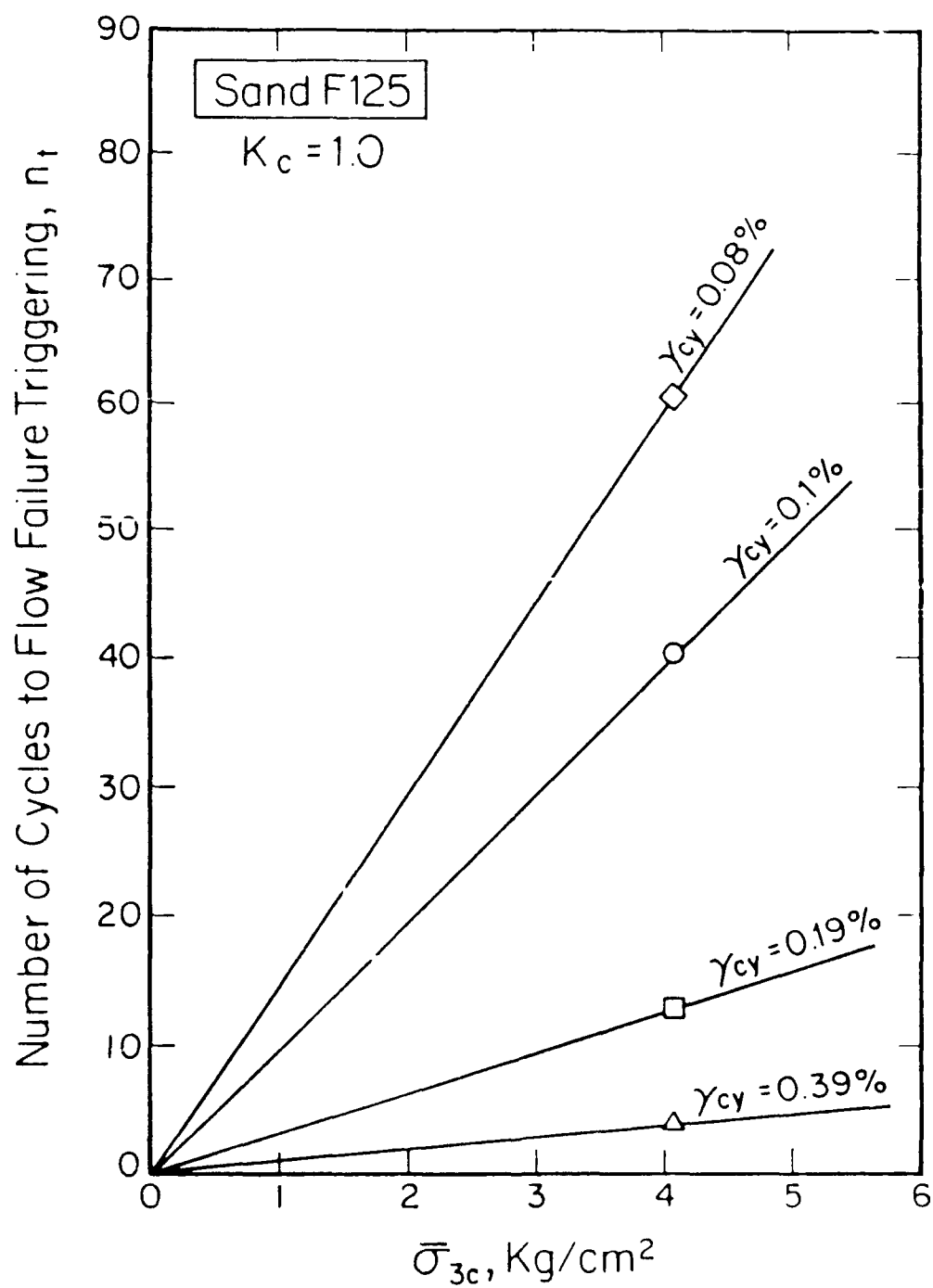


Fig. 7.12. Modified Triggering Relationships of Ottawa Sand F125, K<sub>c</sub> = 1.0

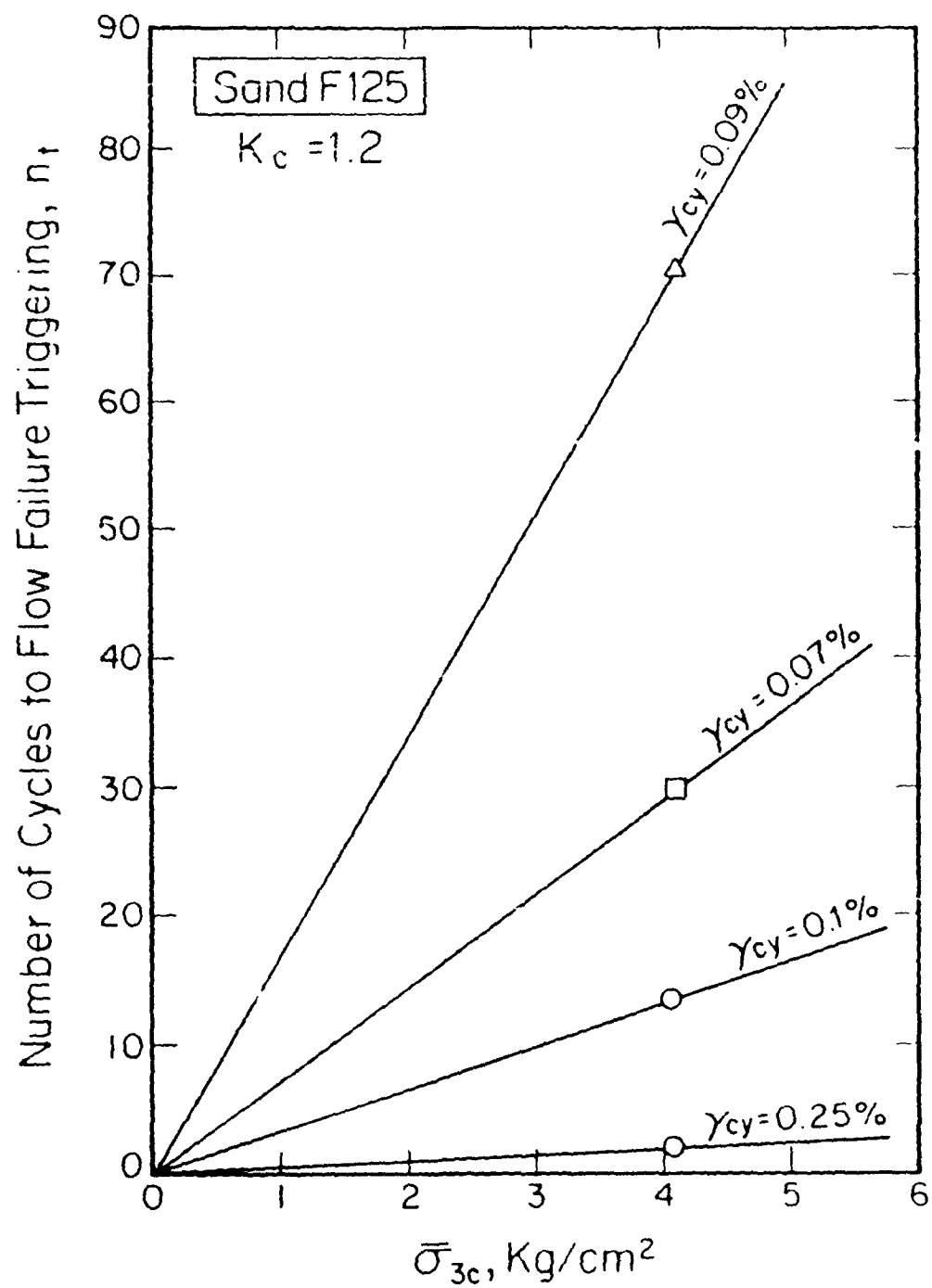


Fig. 7.13. Modified Triggering Relationships of Ottawa Sand F125,  $K_c = 1.2$

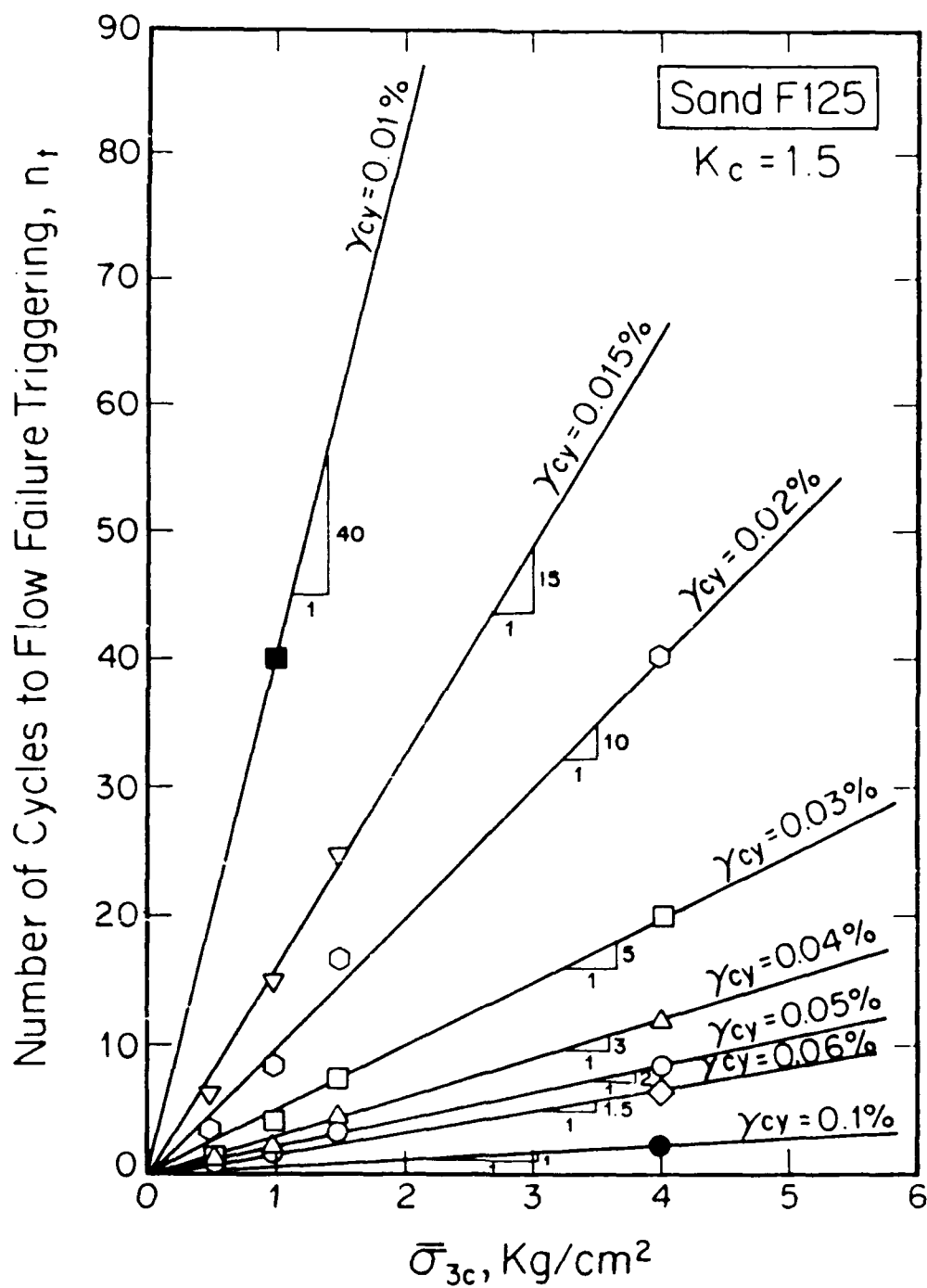


Fig. 7.14. Modified Triggering Relationships of Ottawa Sand F125,  $K_c = 1.5$

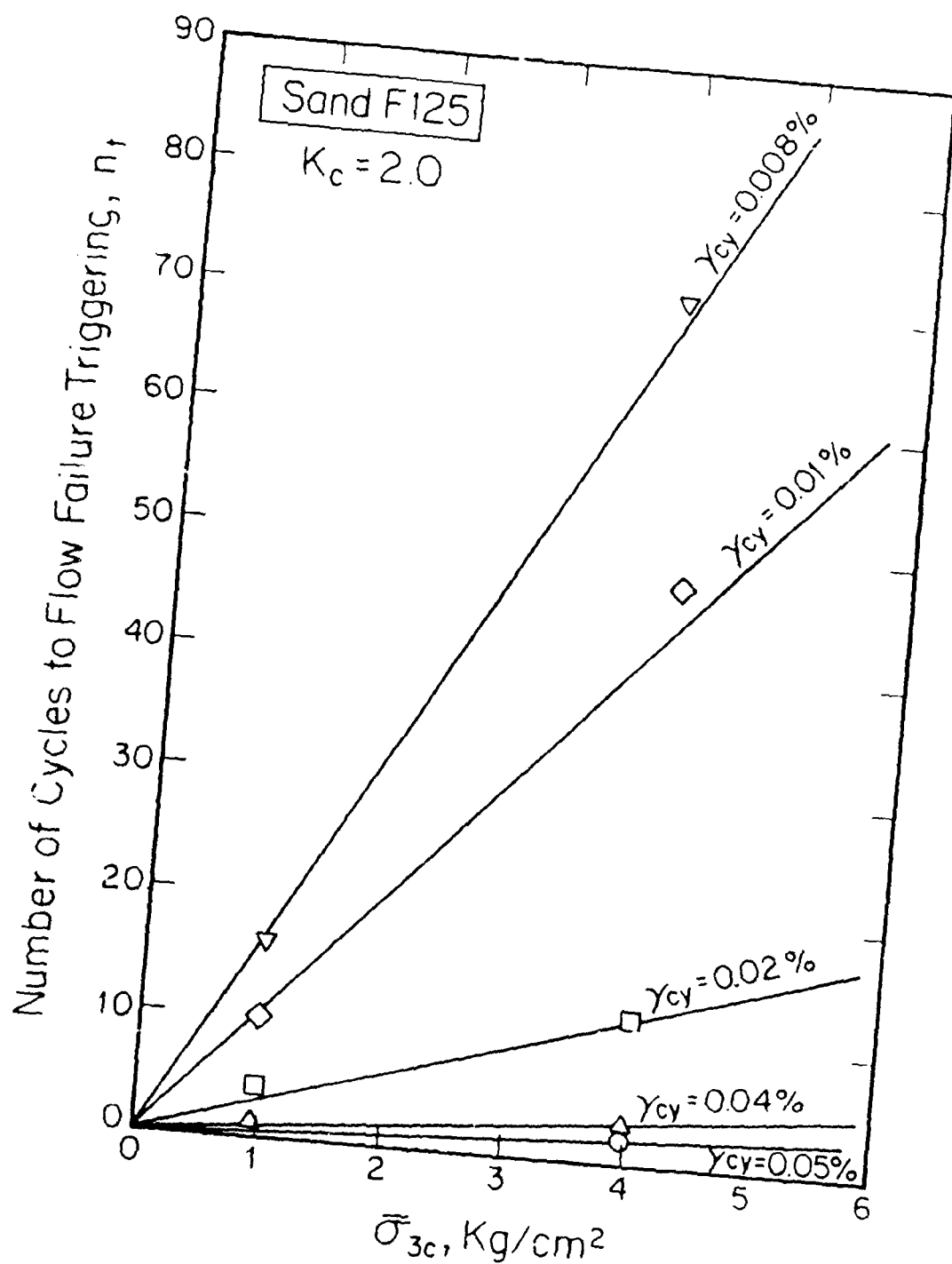


Fig. 7.15. Modified Triggering Relationships of Ottawa Sand F125,  $K_c = 2.0$

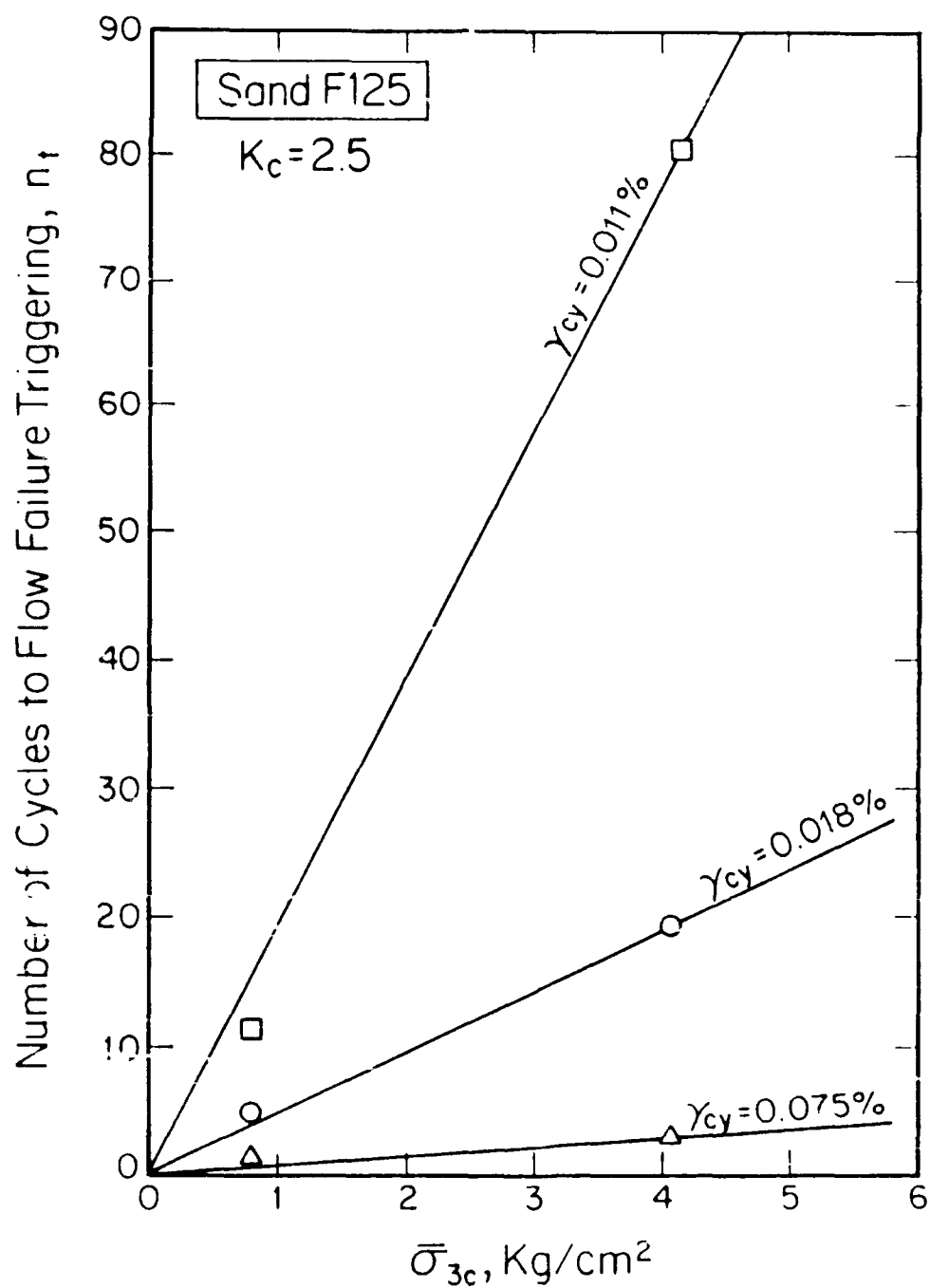


Fig. 7.16. Modified Triggering Relationships of Ottawa Sand F125,  $K_c = 2.5$

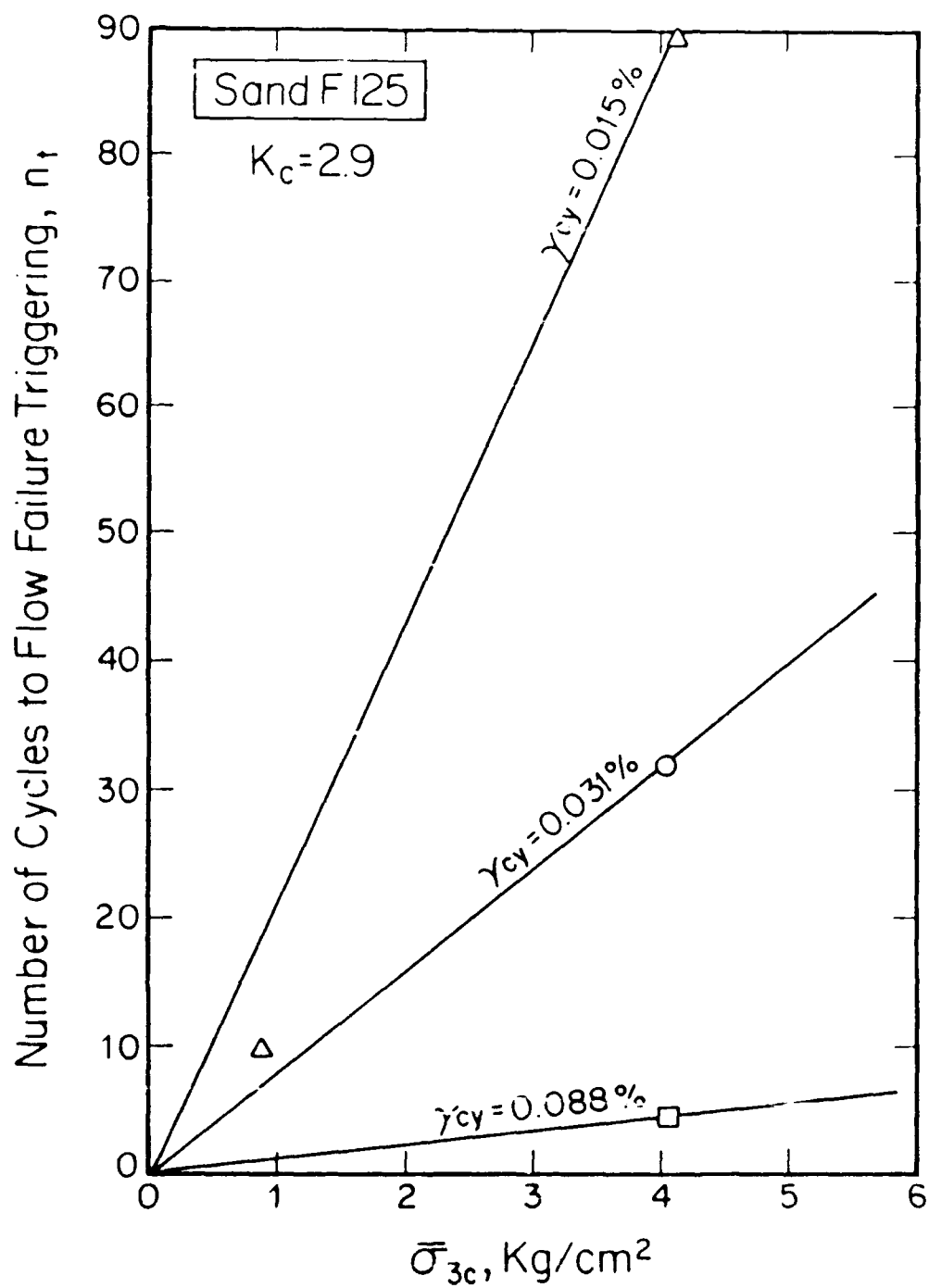


Fig. 7.17. Modified Triggering Relationships of Ottawa Sand F125,  $K_c = 2.9$

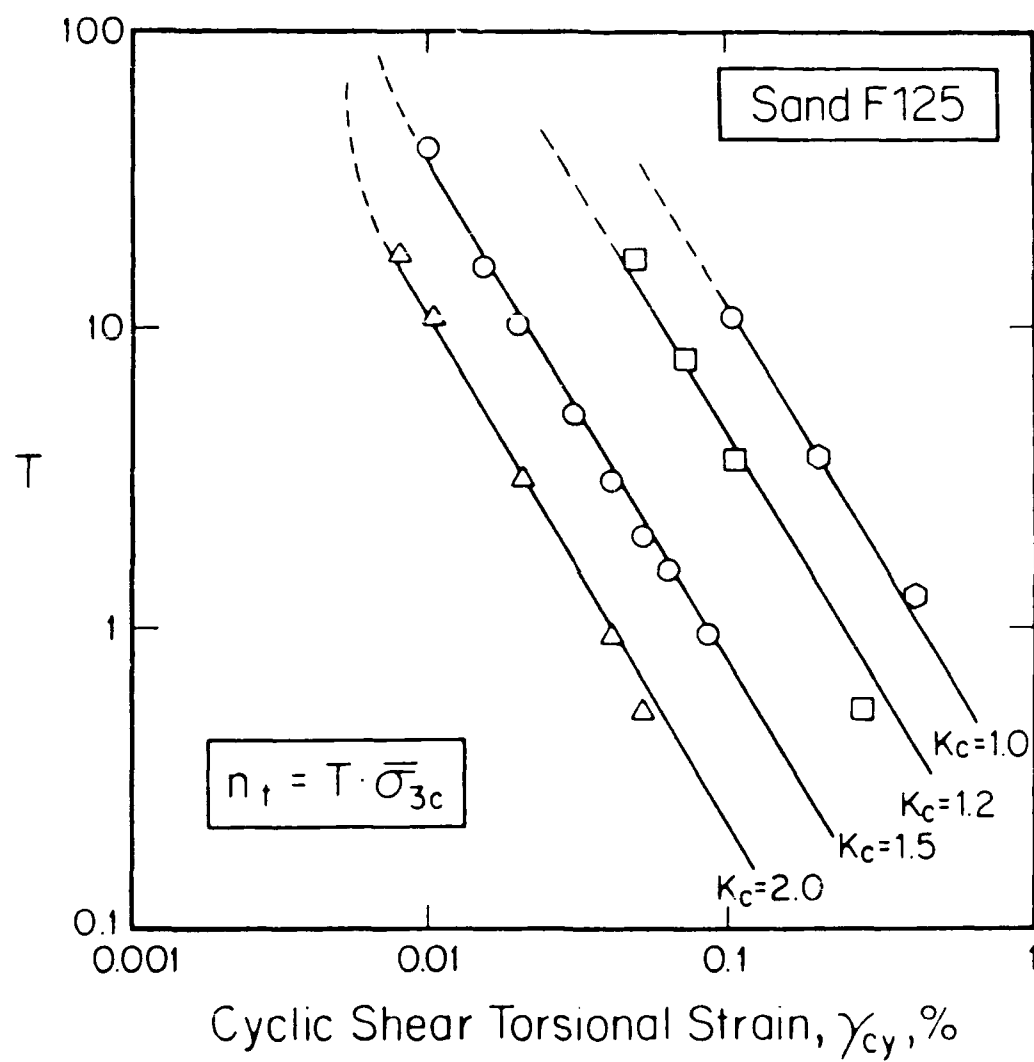


Fig. 7.18. Curves of the Function  $T$  in Ottawa Sand F125 for  $K_c=1.0-2.0$  ( $n_t$  in cycles,  $\bar{\sigma}_{3c}$  in  $\text{kg}/\text{cm}^2$ )

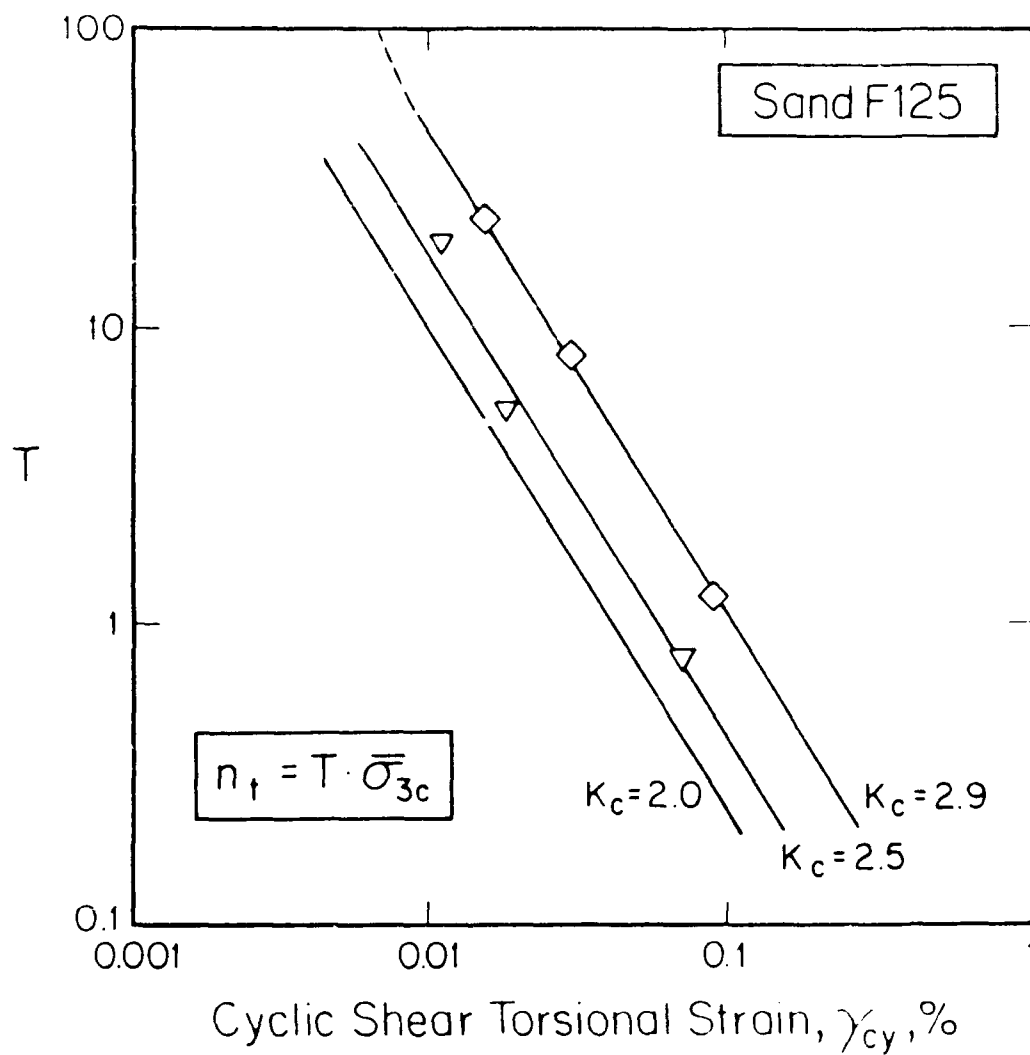


Fig. 7.19. Curves of the Function  $T$  in Ottawa Sand F125 for  $K_c = 2.5-2.9$  ( $n_t$  in cycles,  $\bar{\sigma}_{3c}$  in  $\text{kg/cm}^2$ )



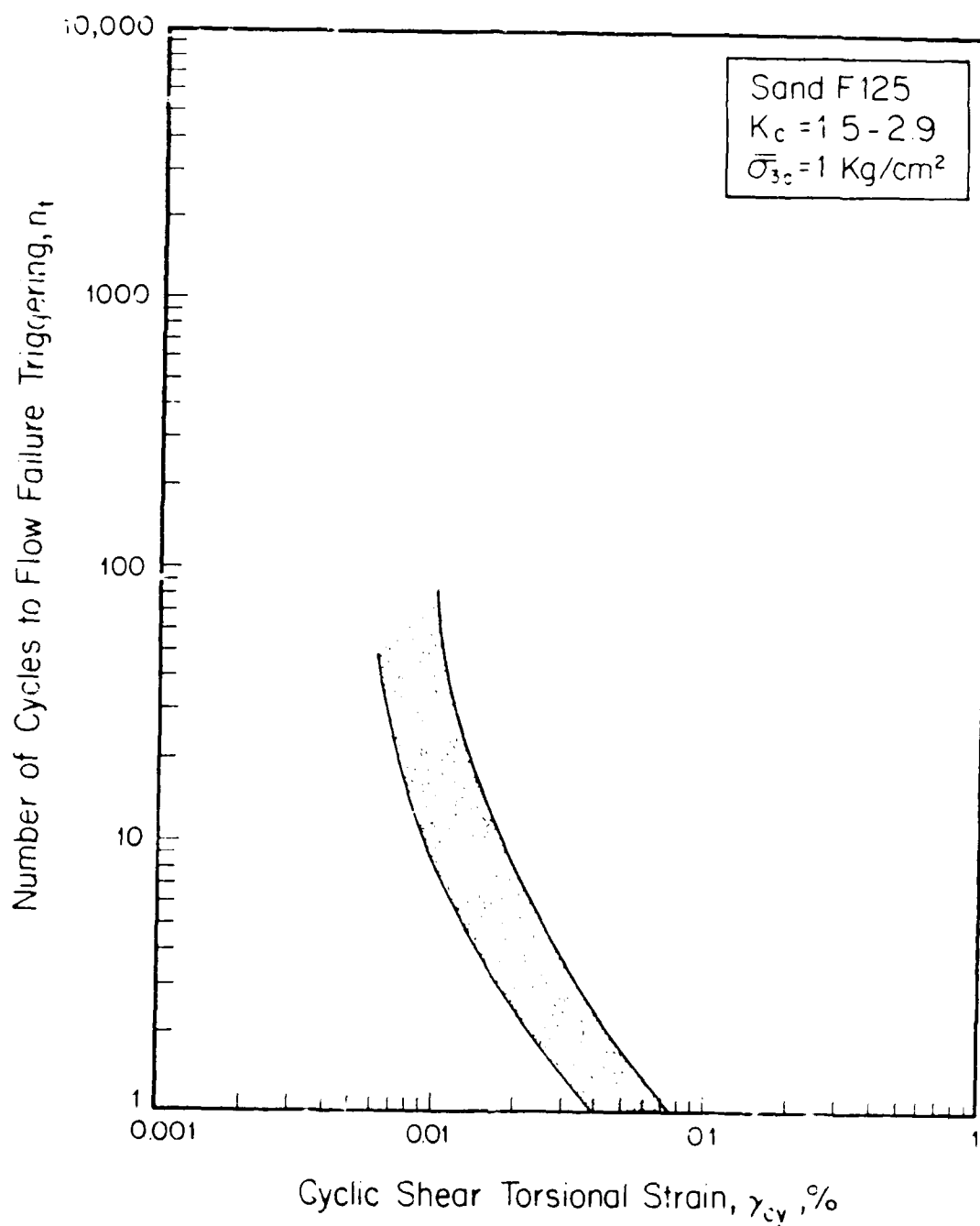


Fig. 7.20. Triggering Relationship Range of Ottawa Sand F125 for all Tests with  $K_c = 1.5-2.9$ ,  $\bar{\sigma}_{3c} = 1 \text{ kg/cm}^2$

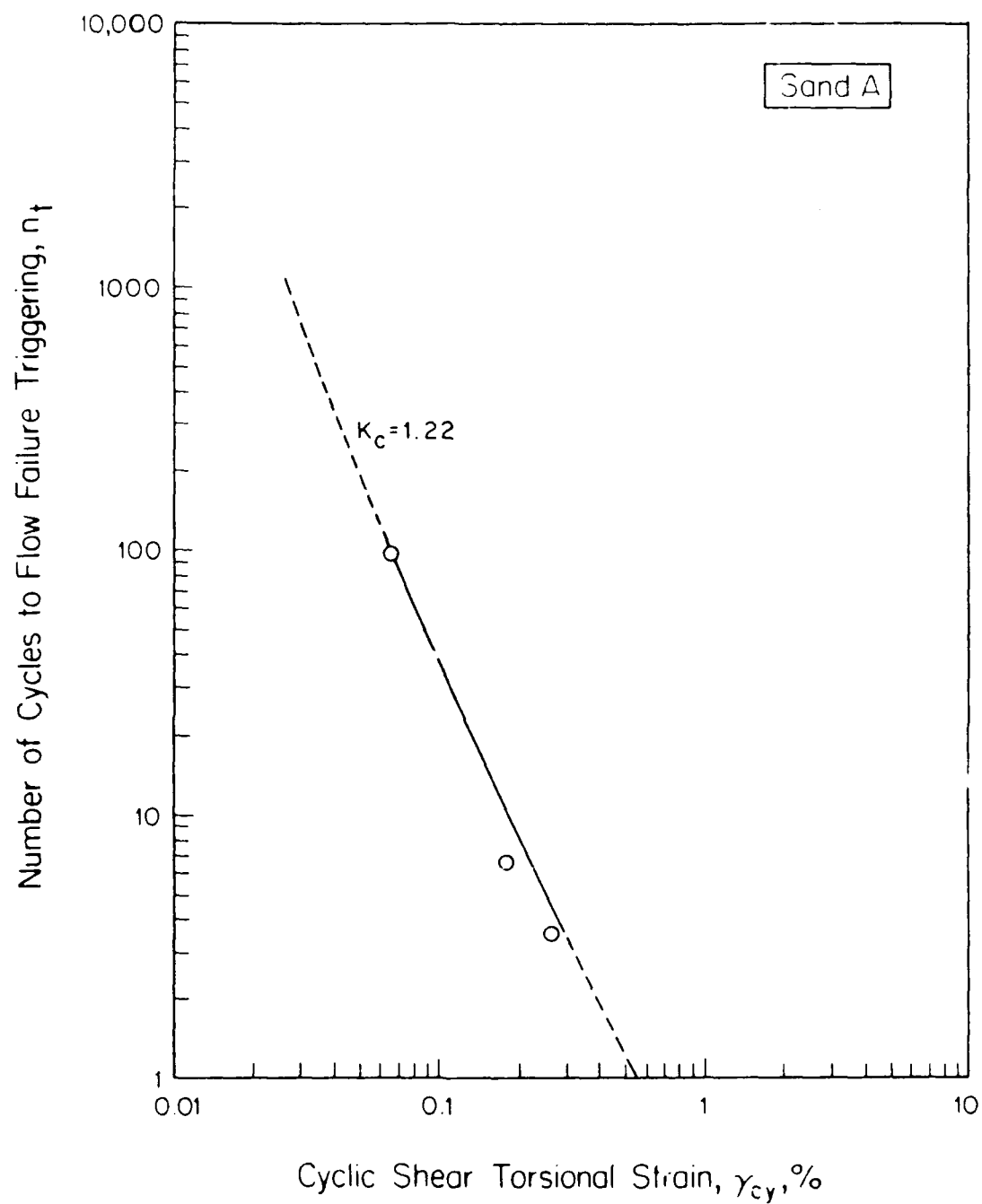


Fig. 7.21. Triggering Relationship for CyT-CAU Tests on Sand A,  $K_c = 1.22$ ,  $\bar{\sigma}_{3c} = 3.72 \text{ kg/cm}^2$

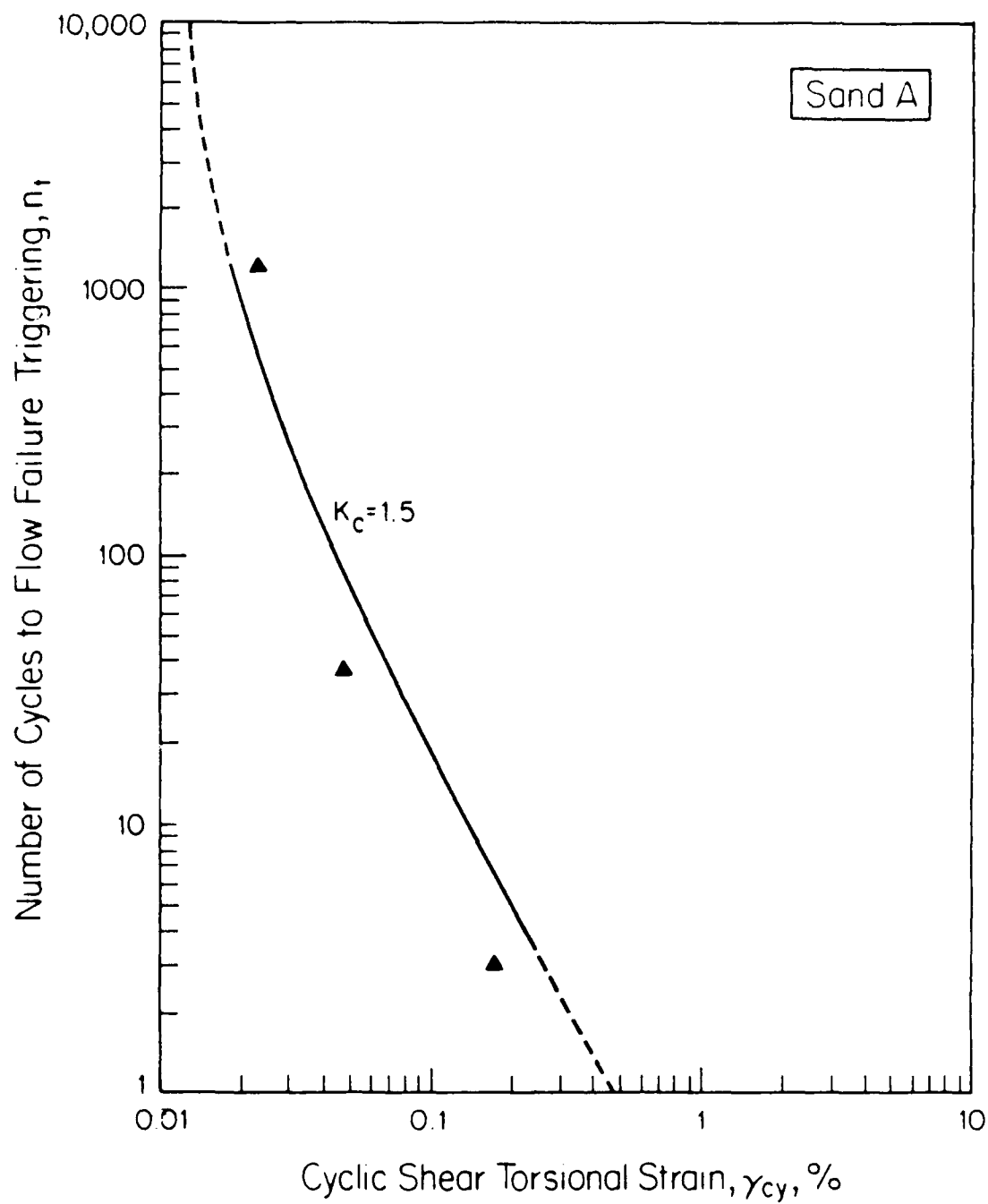


Fig. 7.22. Triggering Relationship for CyT-CAU Tests on Sand A,  $K_c = 1.5$ ,  $\bar{\sigma}_{3c} = 3.72 \text{ kg/cm}^2$

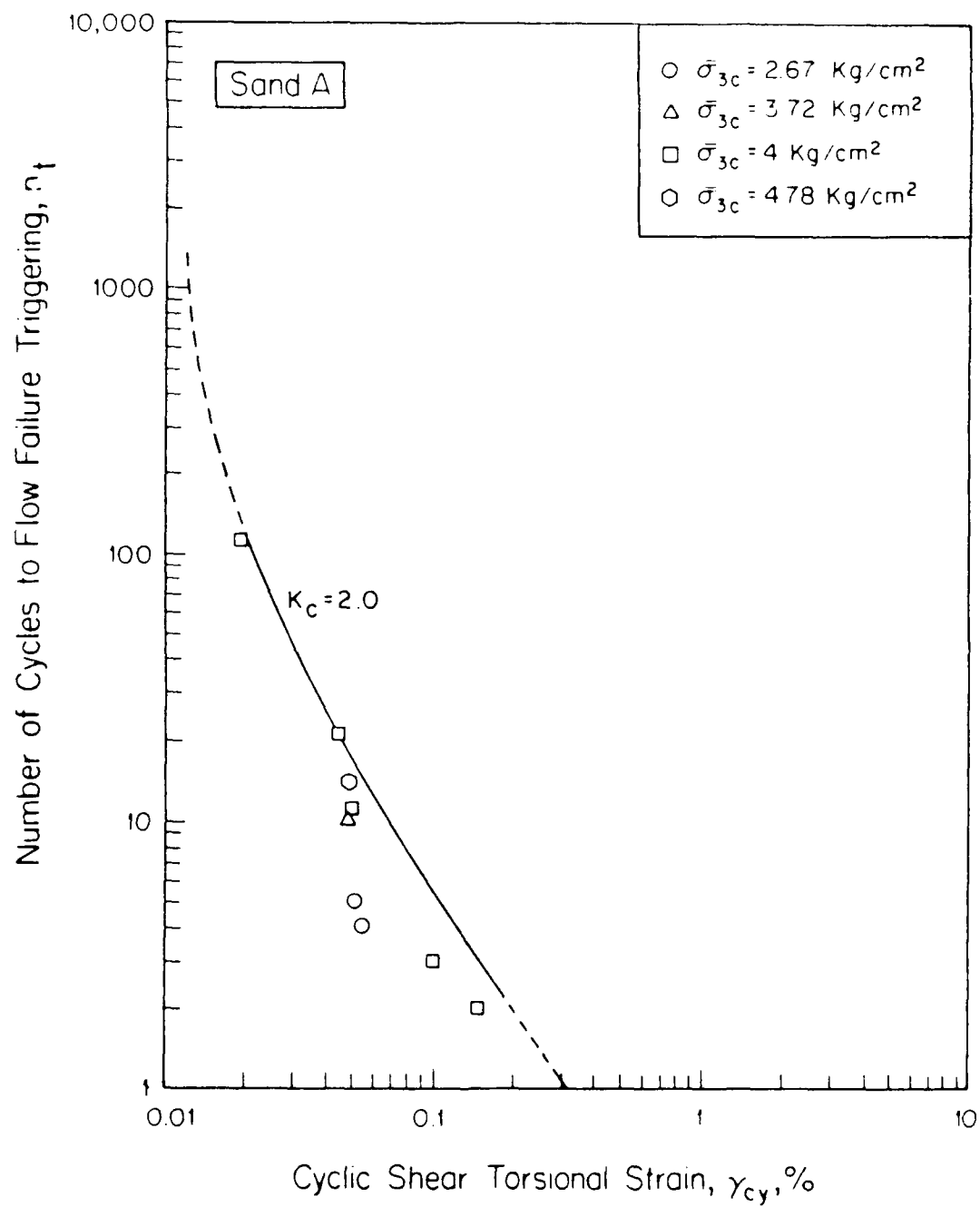


Fig. 7.23. Triggering Relationship for CyT-CAU Tests on Sand A,  $K_c = 2.0$

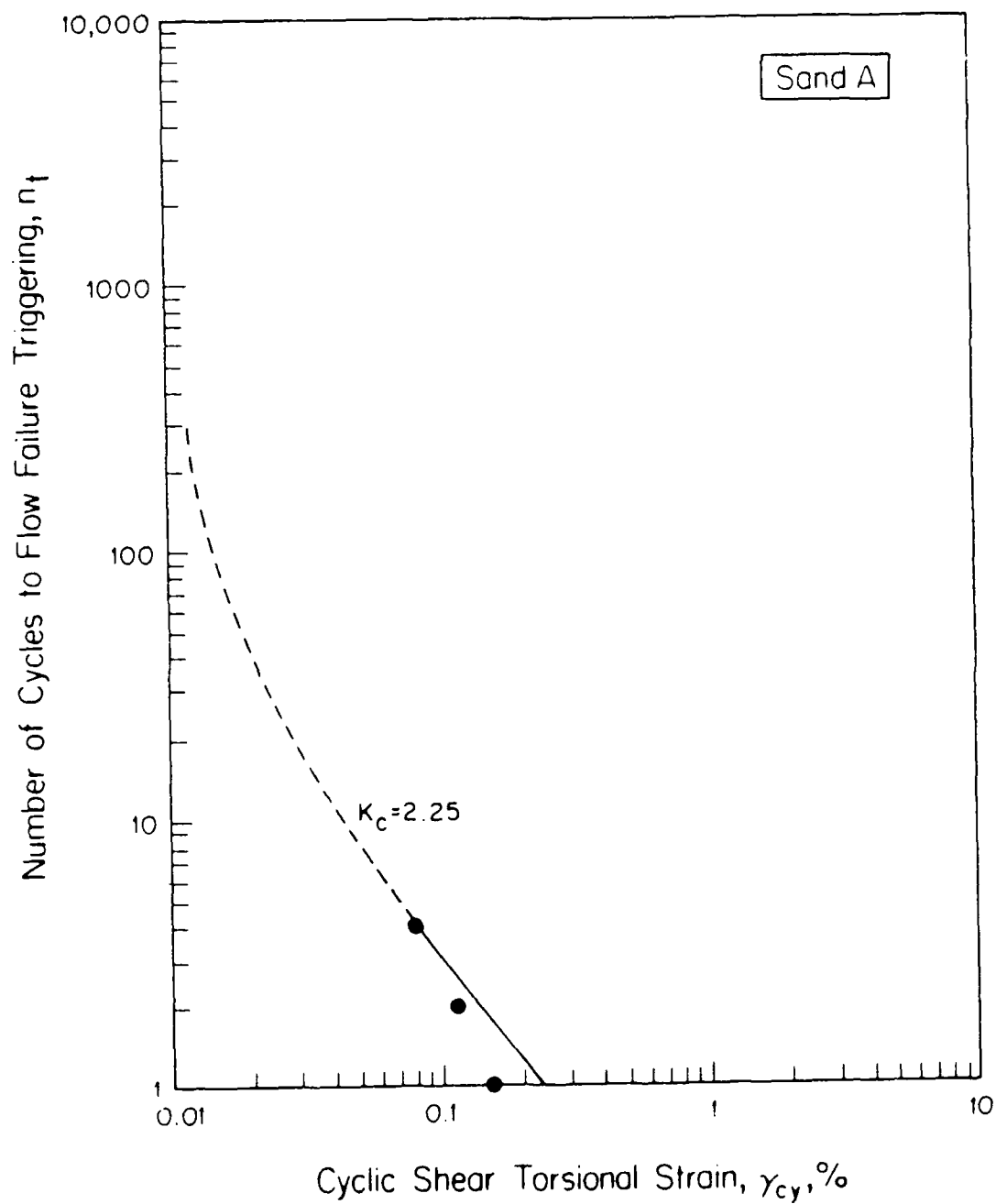


Fig. 7.24. Triggering Relationship for CyT-CAU Tests on Sand A,  $K_c = 2.25$ ,  $\bar{\sigma}_{3c} = 3.72 \text{ kg/cm}^2$

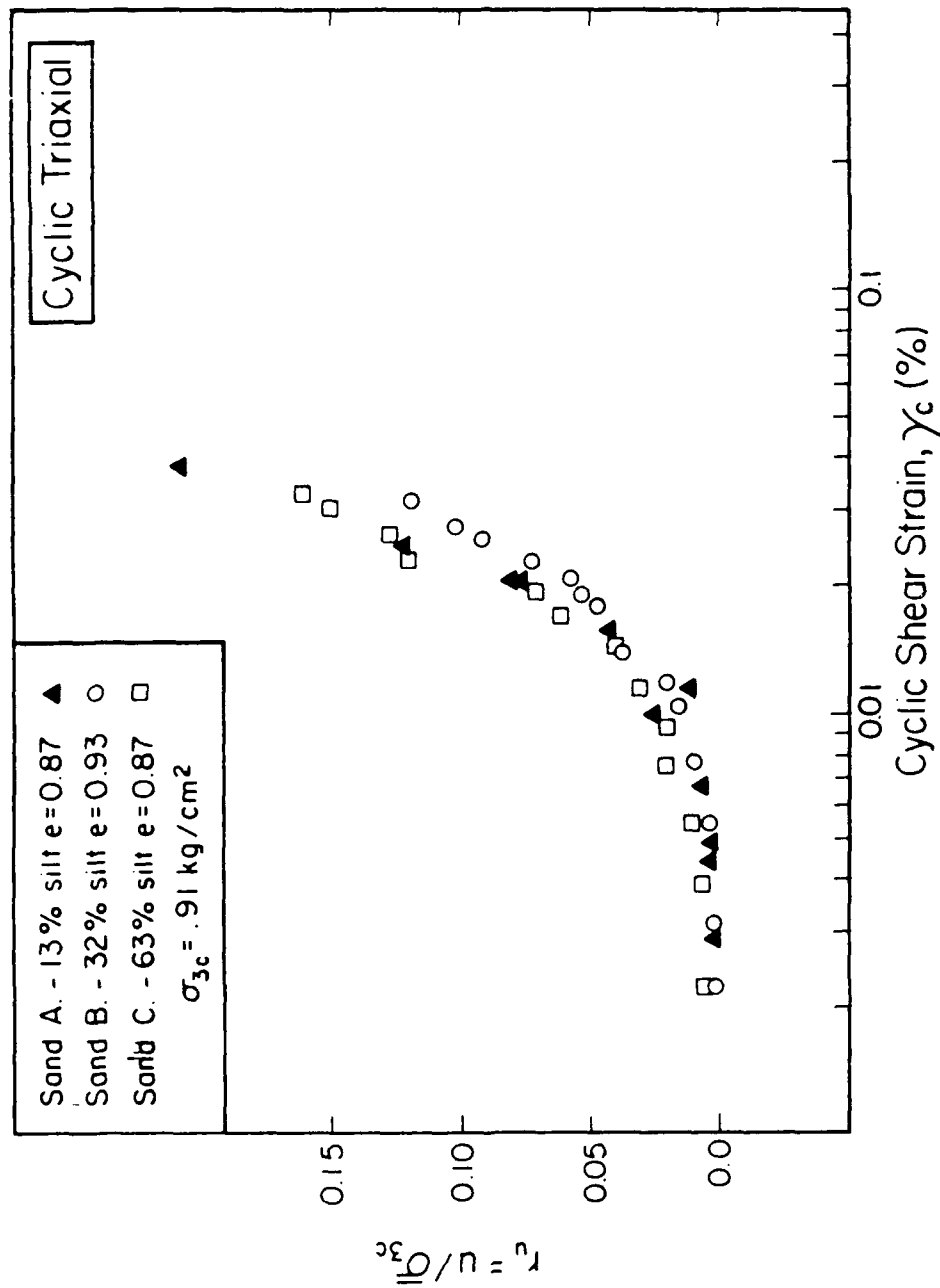


Fig. 7.25. PWP Buildup After 5 Cycles of Constant Shear Strain in Sands A, B, and C

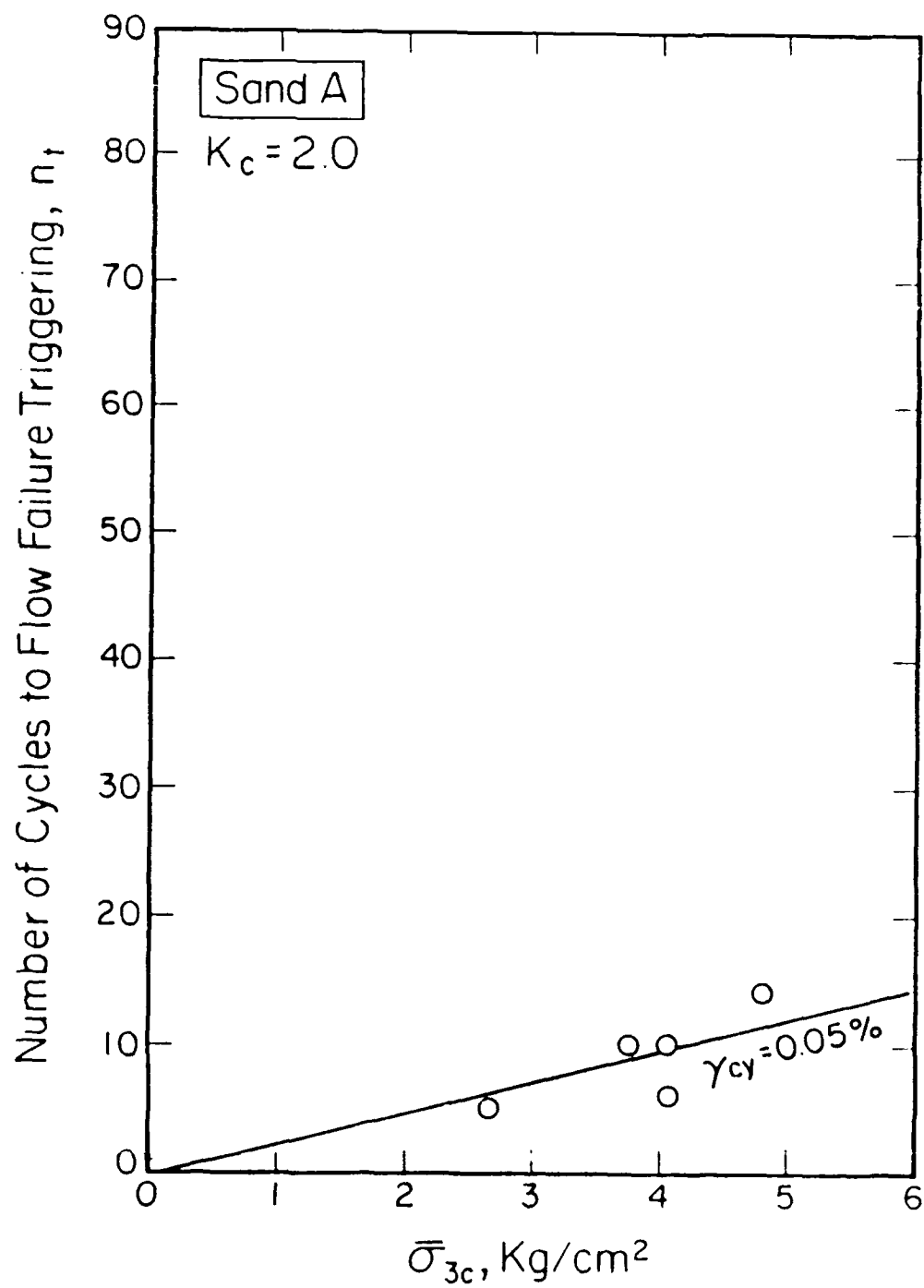


Fig. 7.26. Modified Triggering Relationship for Sand A,  $K_c = 2.0$

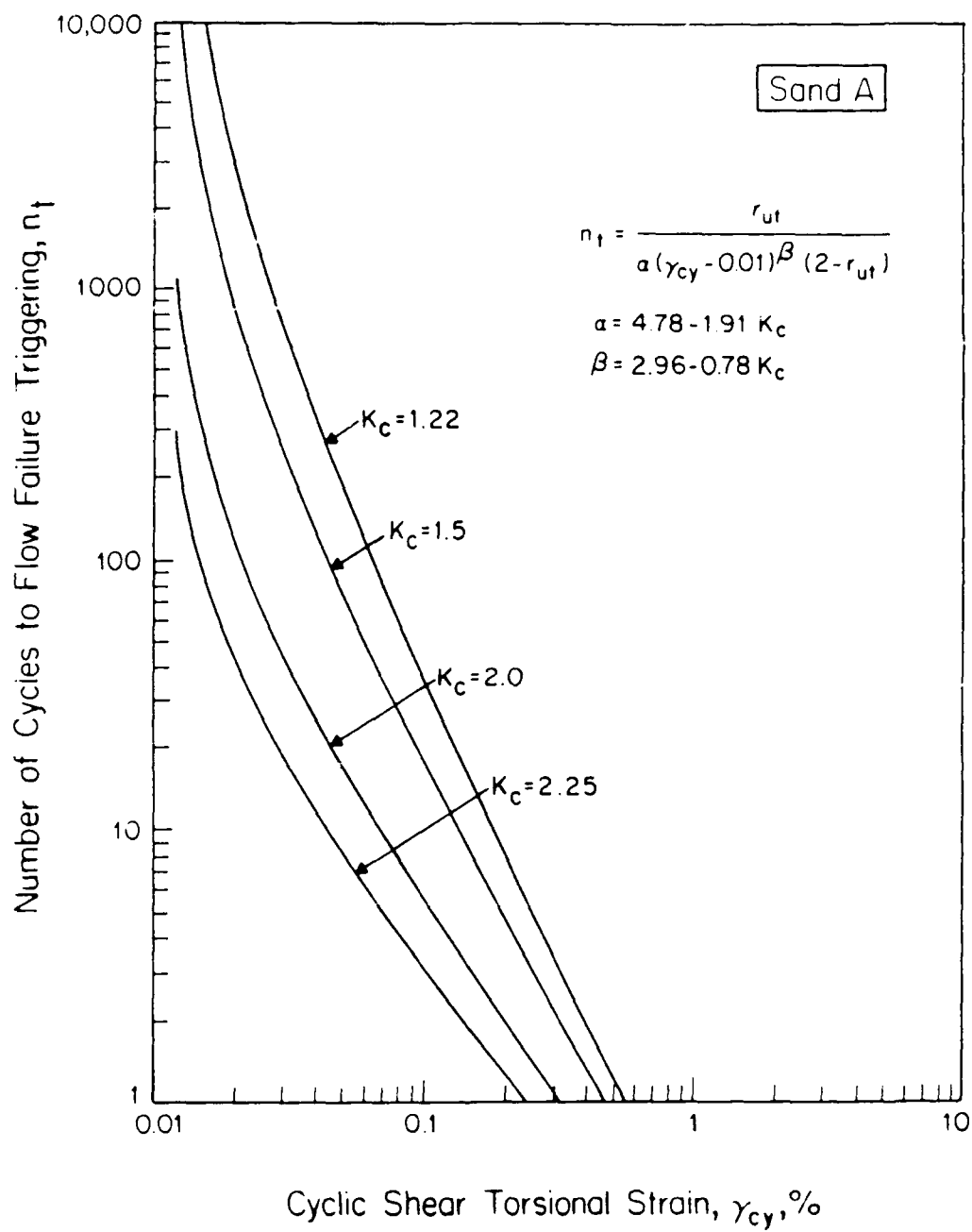
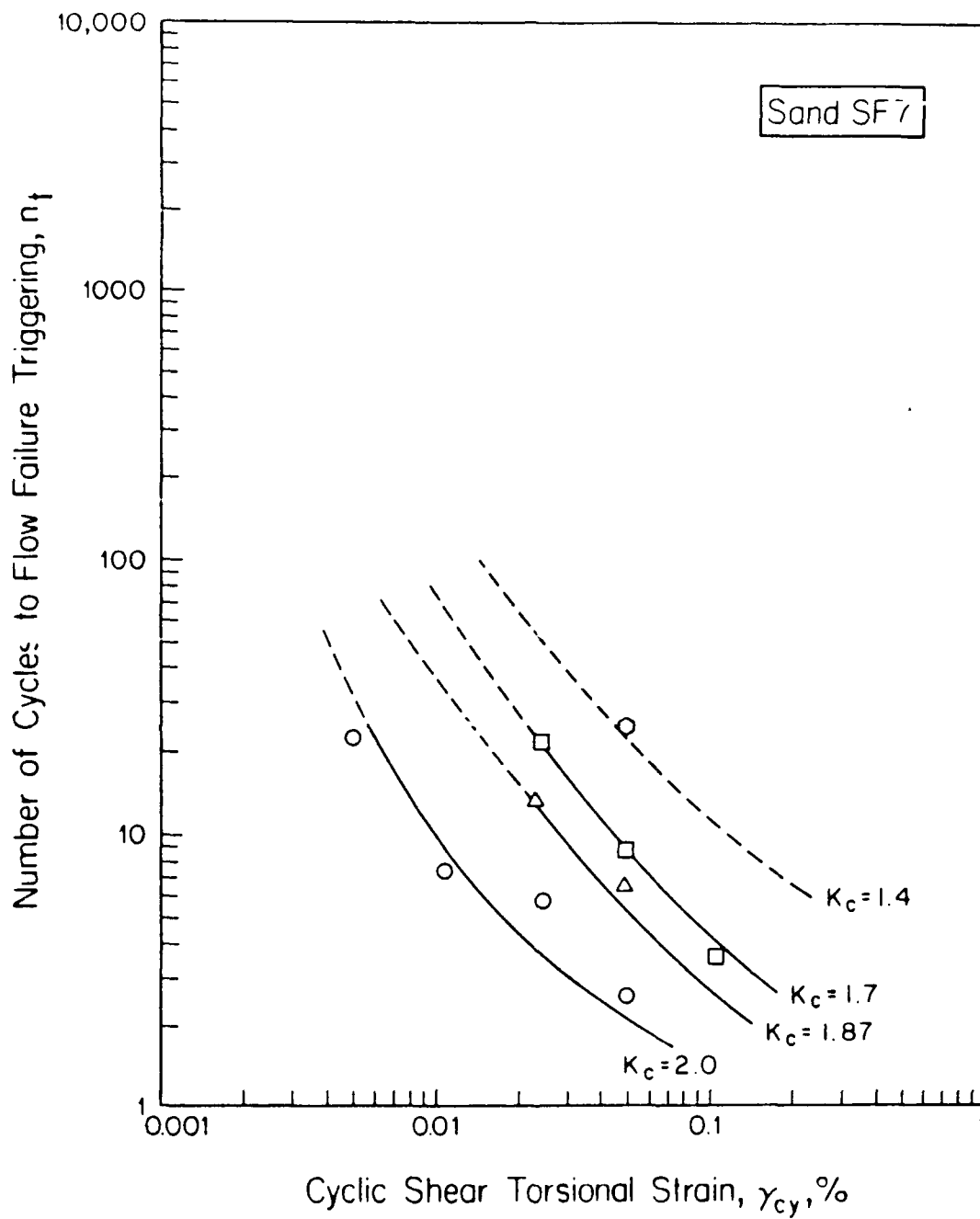


Fig. 7.27. Triggering Relationships for Sand A,  $\bar{\sigma}_{3c} = 3.72$  kg/cm<sup>2</sup>





**Fig. 7.28. Triggering Relationships for Moist Tamped Specimens of Sand SF7,  $\bar{\sigma}_{3c} = 1 \text{ kg/cm}^2$**

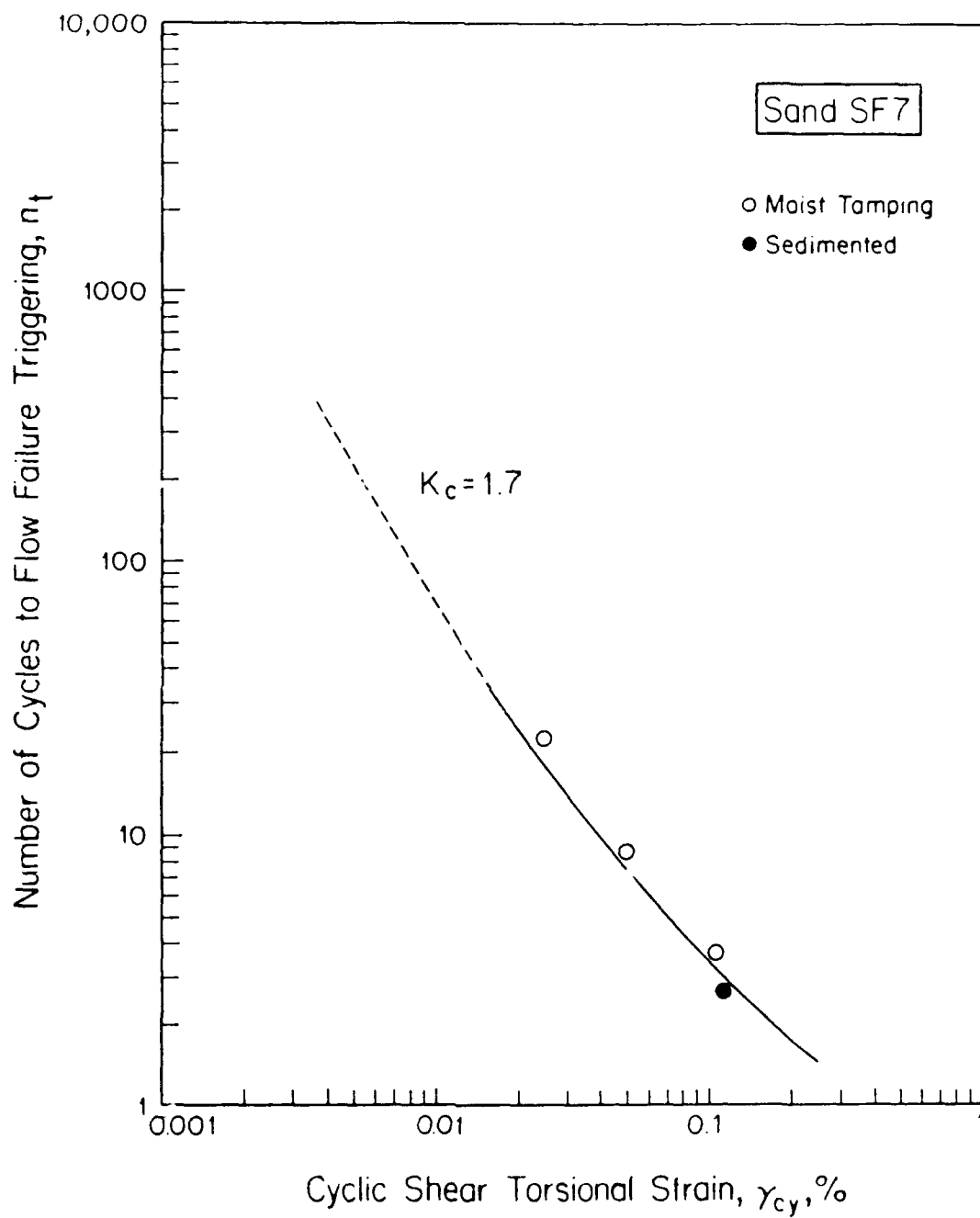


Fig. 7.29. Comparison of Triggering Relationships Between Moist Tamped Specimens and Sedimented Samples of Sand SF7,  $K_c = 1.7$ ,  $\bar{\sigma}_{3c} = 1 \text{ kg/cm}^2$

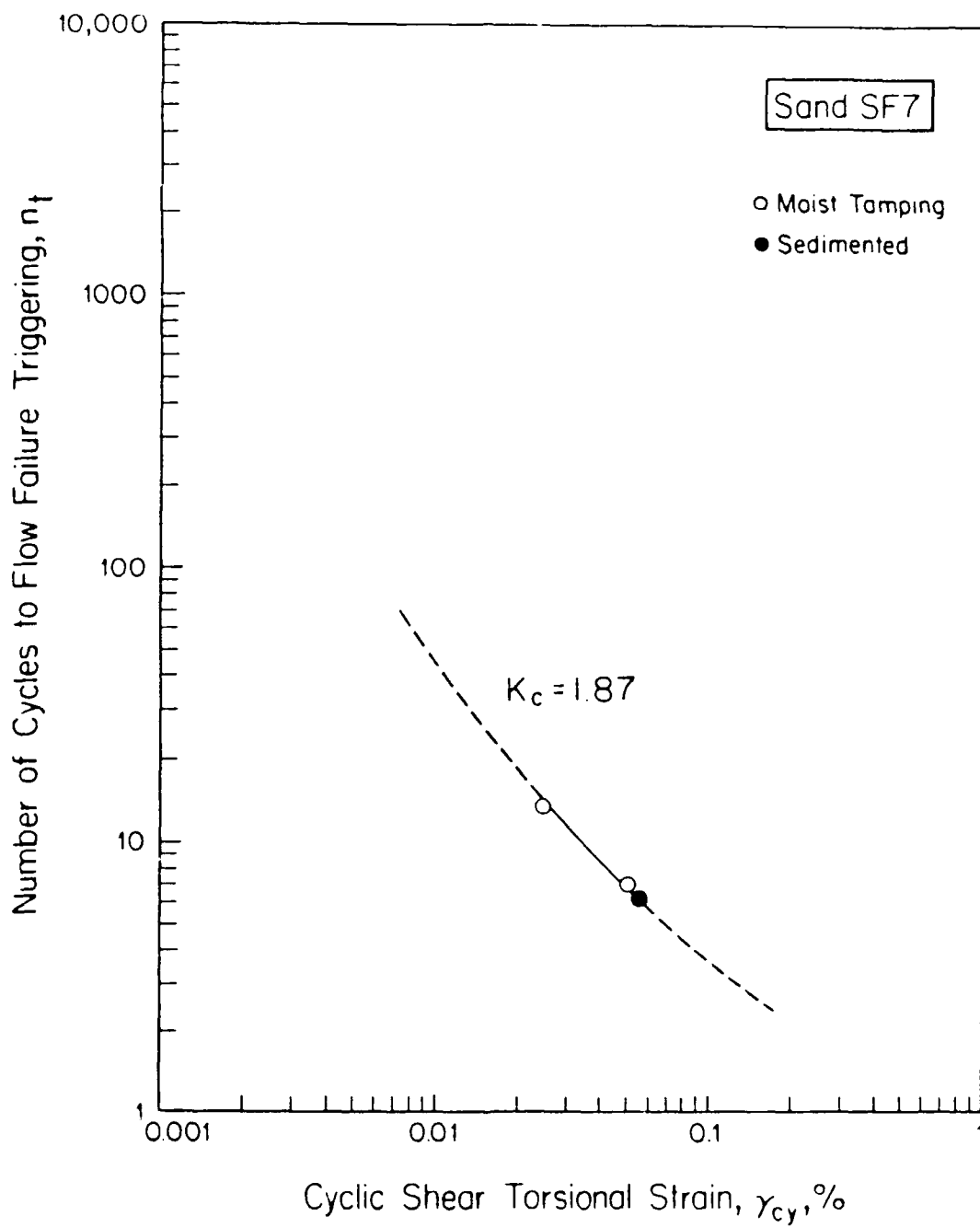


Fig. 7.30. Comparison of Triggering Relationships Between Moist Tamped Specimens and Sedimented Samples of Sand SF7,  $K_c = 1.87$ ,  $\bar{\sigma}_{3c} = 1 \text{ kg/cm}^2$

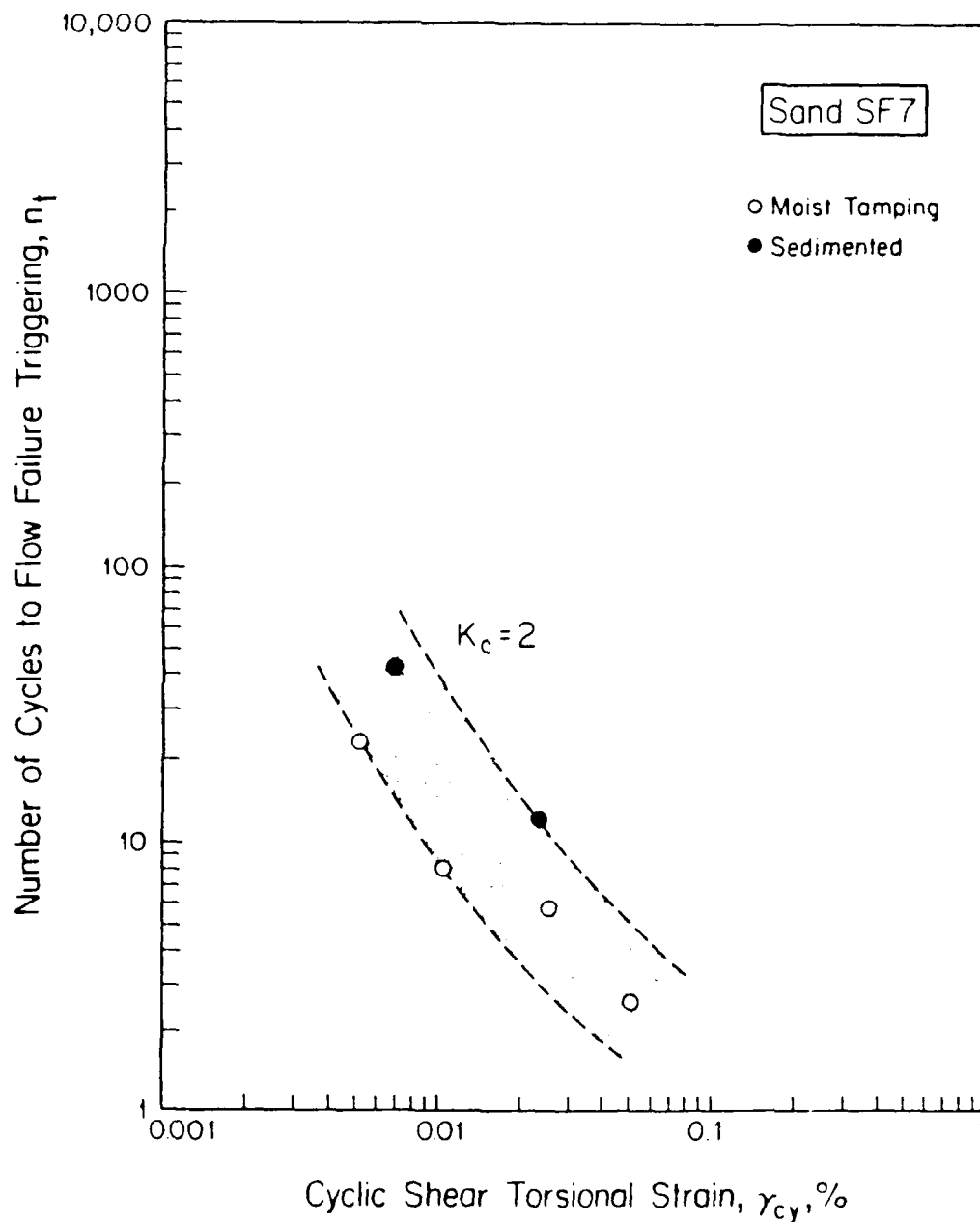


Fig. 7.31. Comparison of Triggering Relationships Between Moist Tamped Specimens and Sedimented Samples of Sand SF7,  $K_c = 2.0$ ,  $\bar{\sigma}_{3c} = 1 \text{ kg/cm}^2$

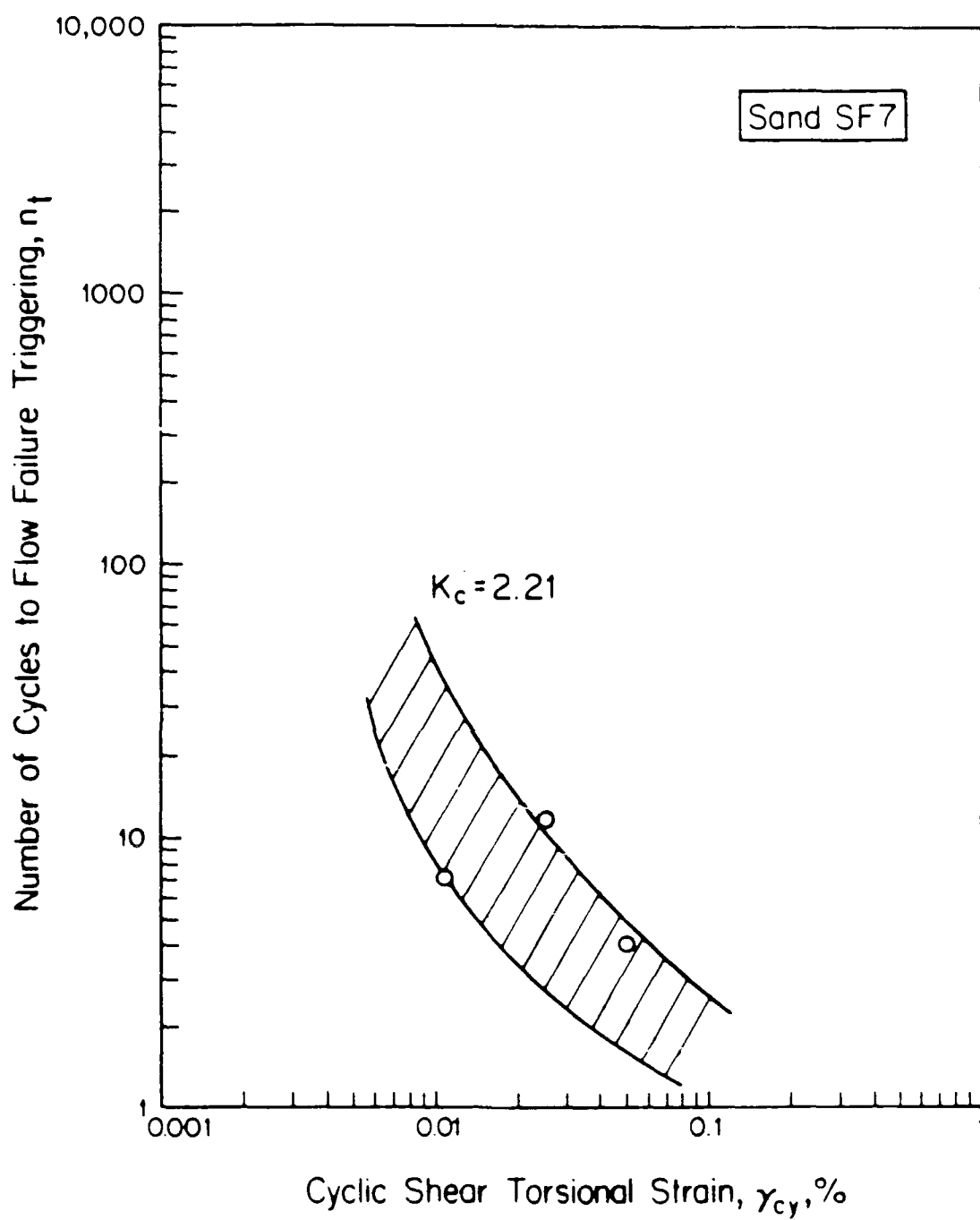


Fig. 7.32. Triggering Relationships for Moist Tamped Specimens of Sand SF7,  $K_c = 2.2$ ,  $\bar{\sigma}_{3c} = 1 \text{ kg/cm}^2$

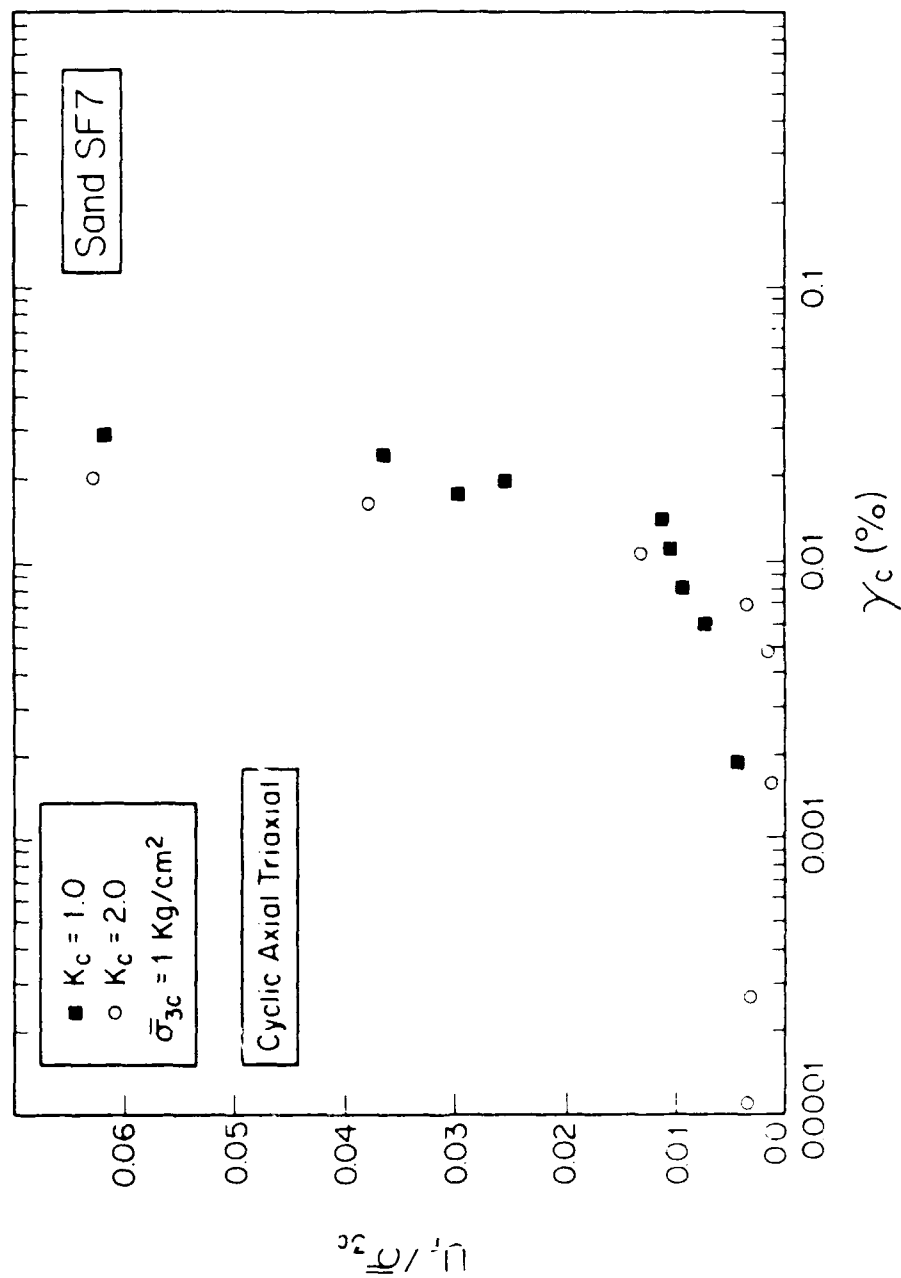


Fig. 7.33. PWP Buildup after 5 Cycles of Constant Shear Strain with Different  $K_c$  in Sand SF7

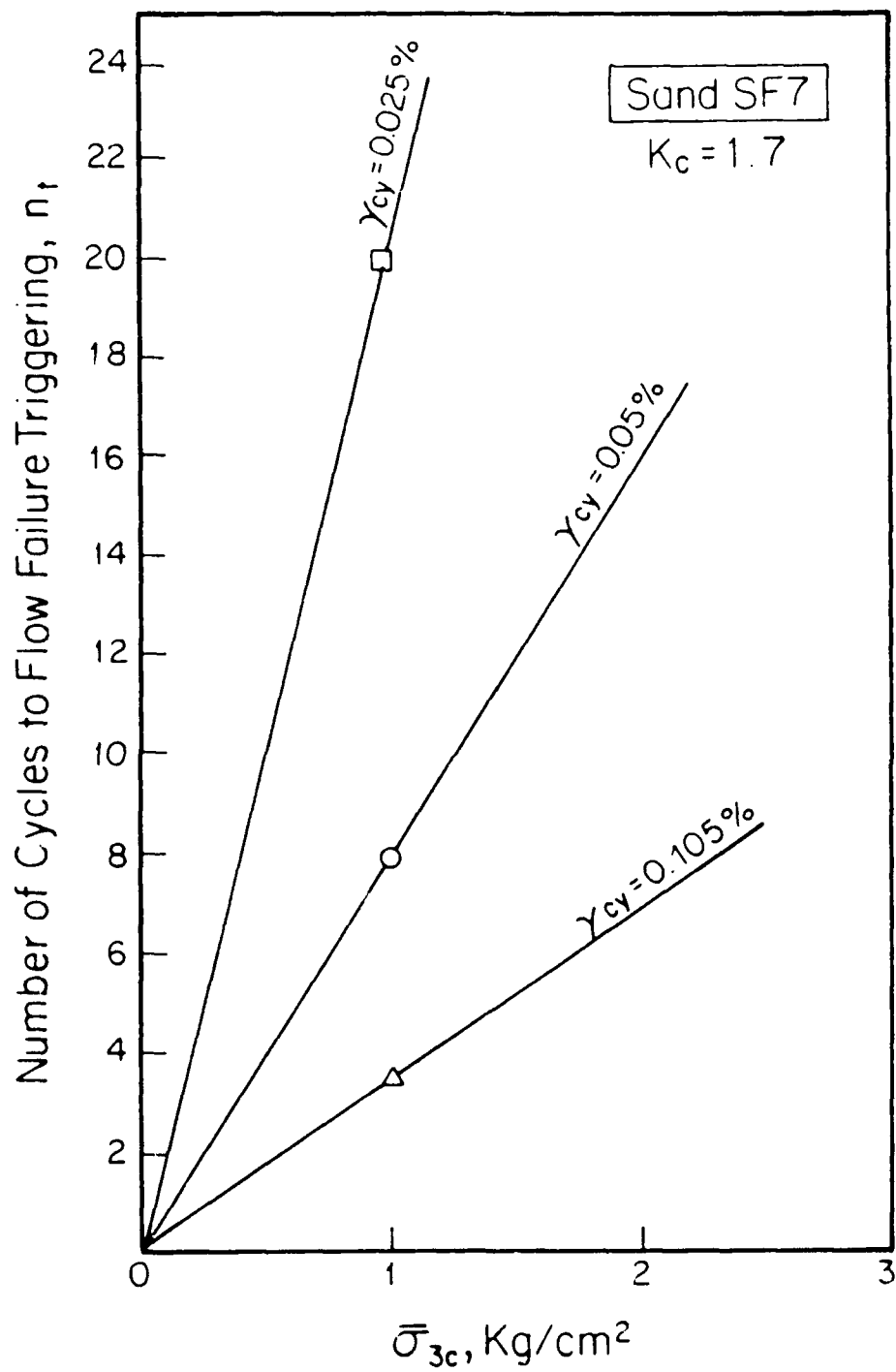


Fig. 7.34. Modified Triggering Relationships for Sand SF7,  $K_c = 1.7$

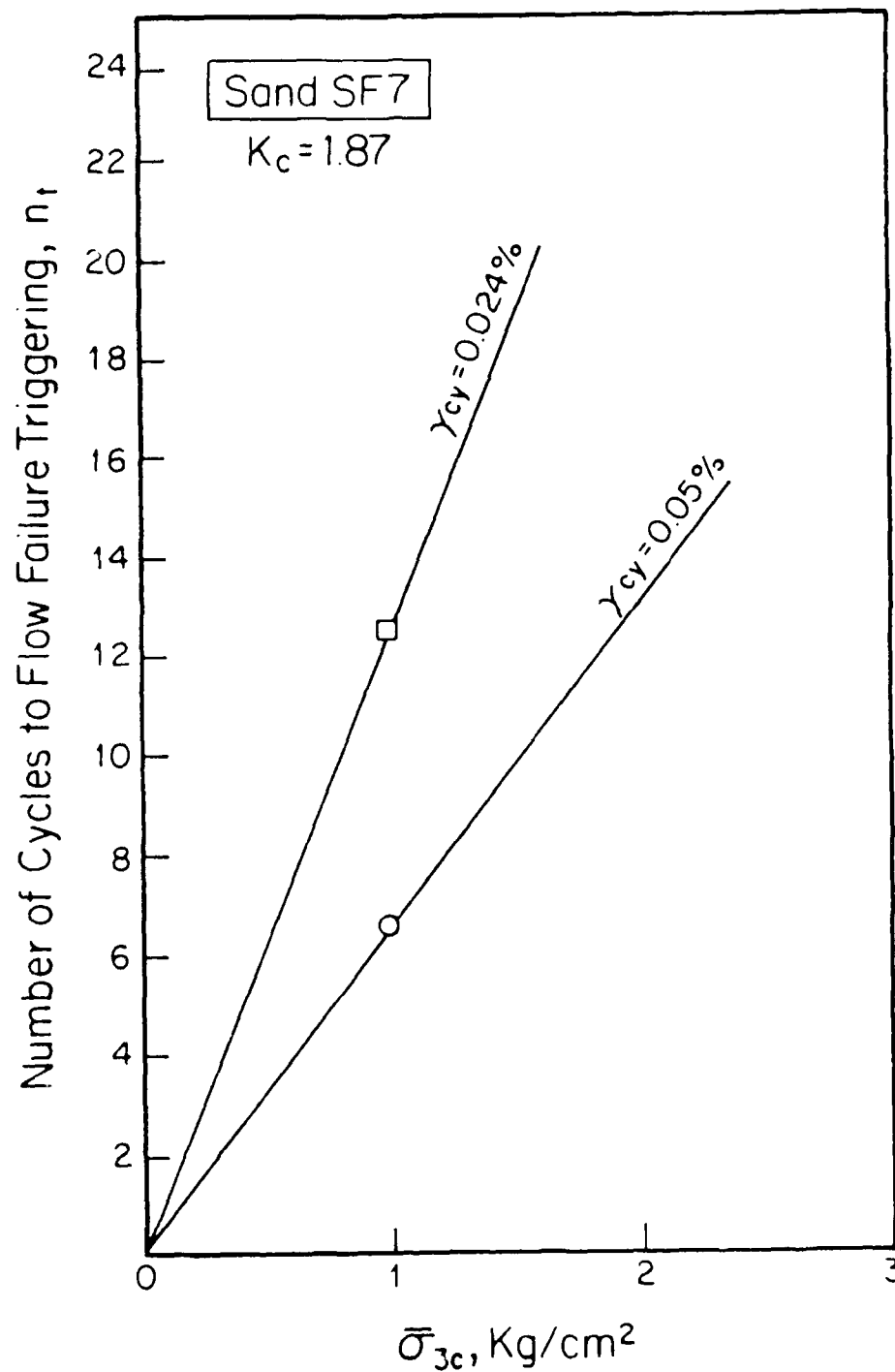


Fig. 7.35. Modified Triggering Relationships for Sand SF7,  $K_c = 1.87$



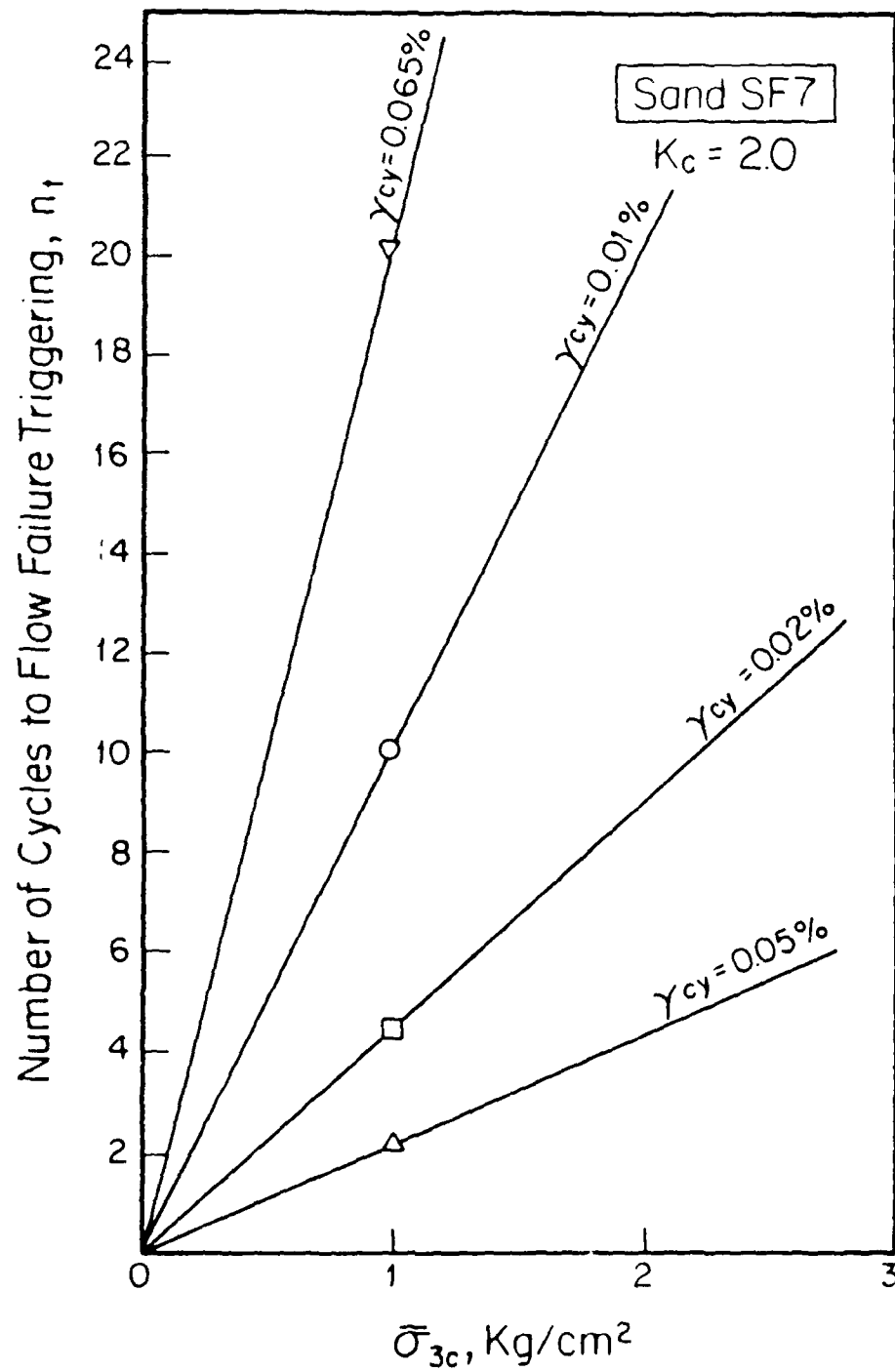


Fig. 7.36. Modified Triggering Relationships for Sand SF7, K<sub>c</sub> = 2.0

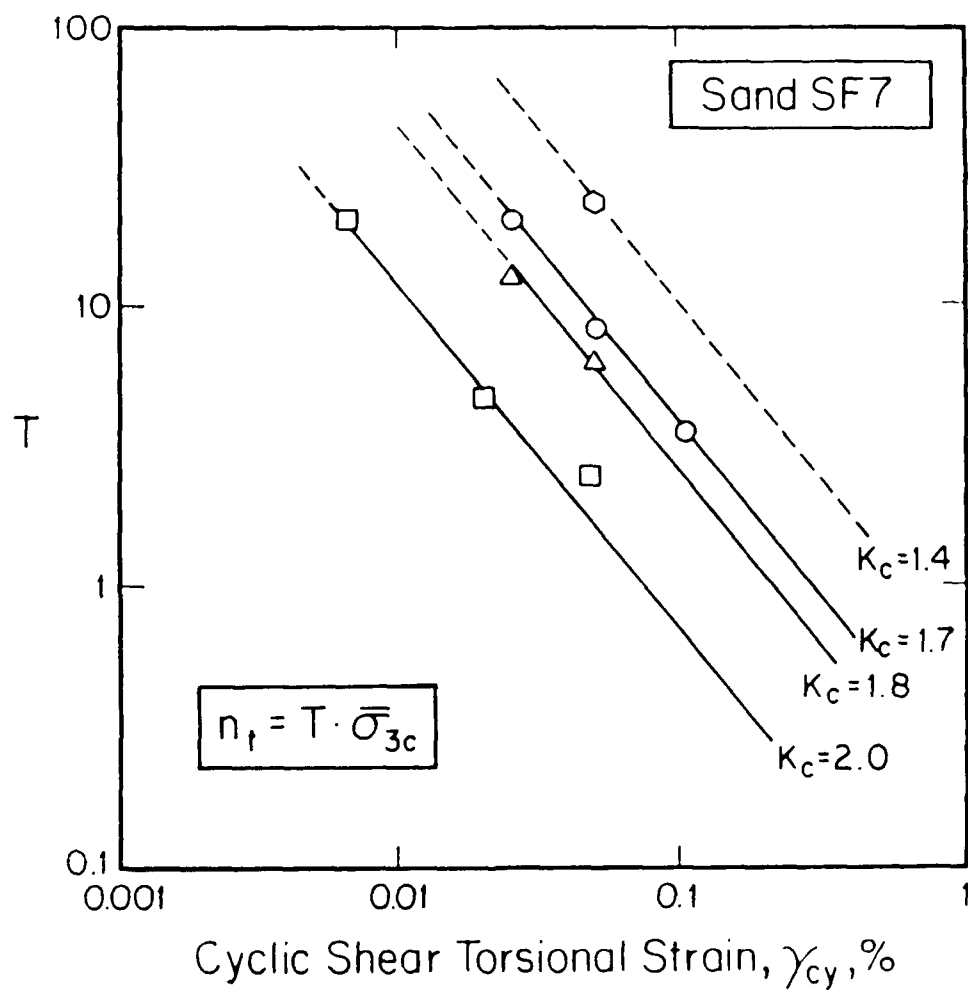
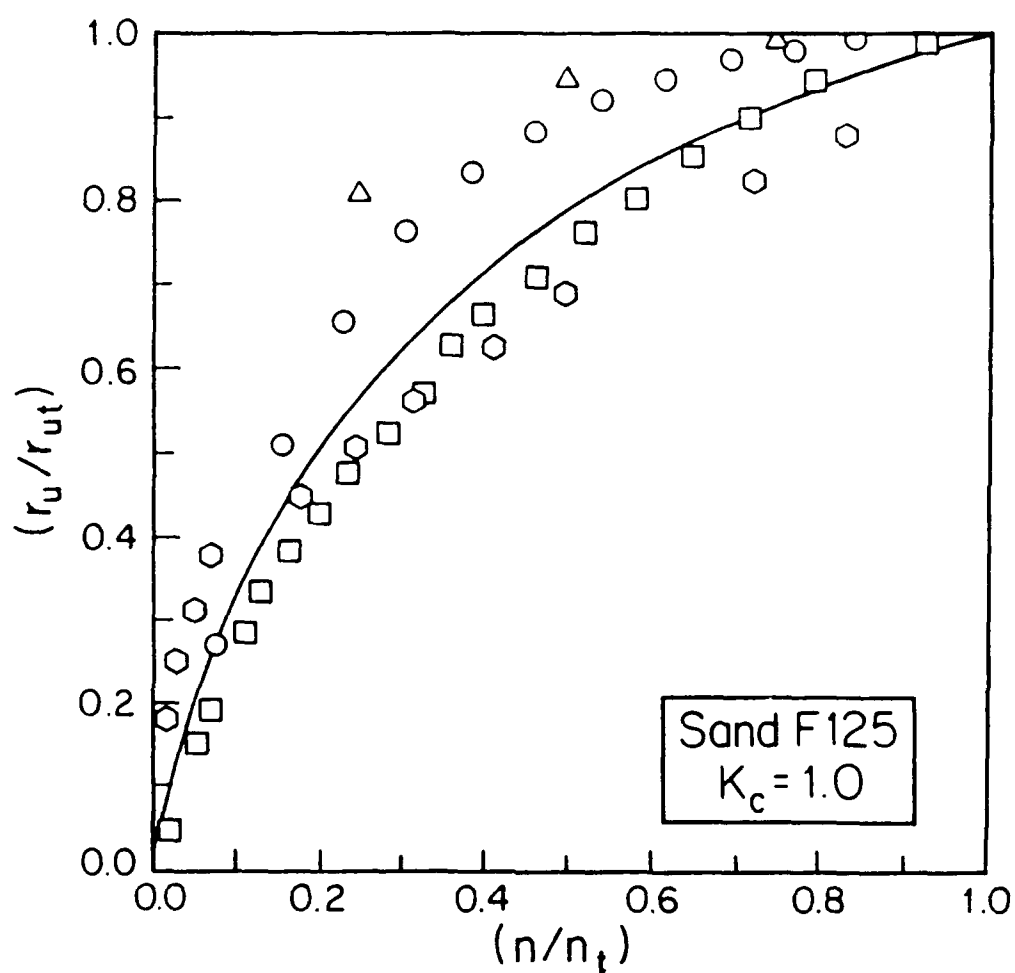
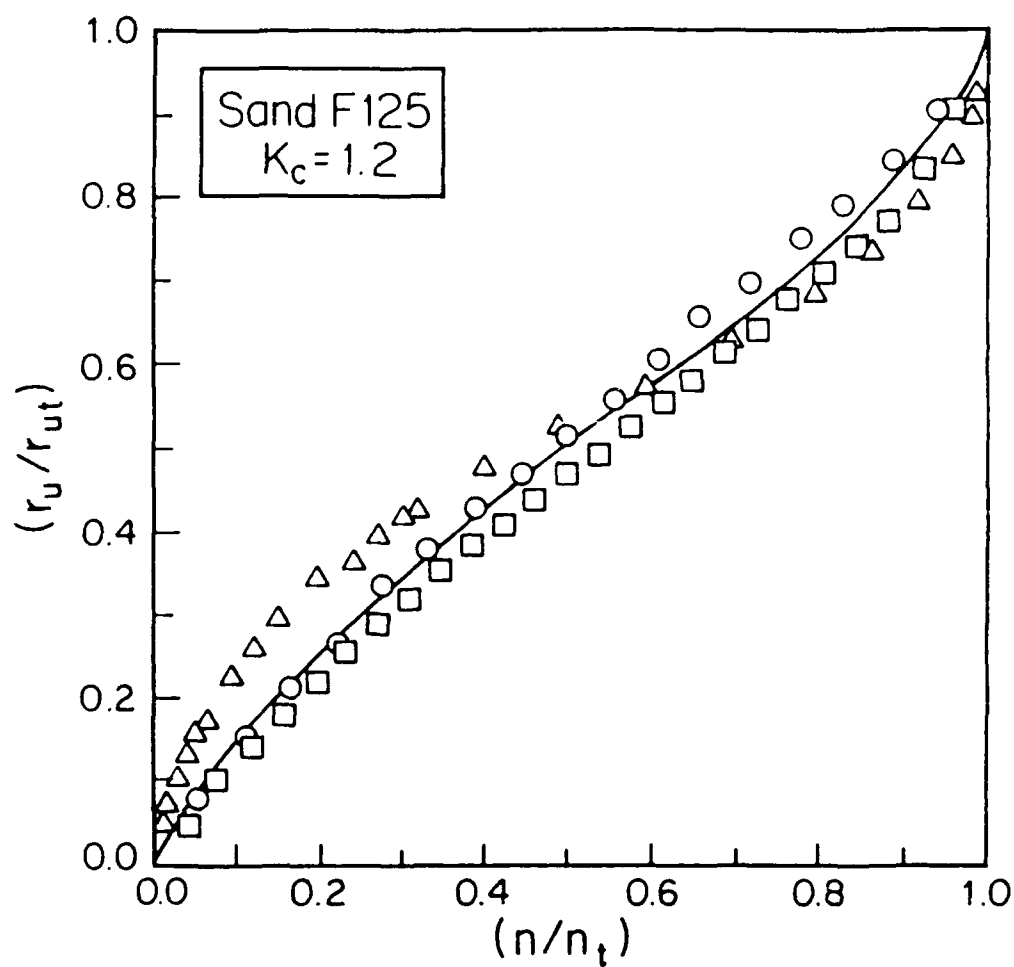


Fig. 7.37. Curves of the Function  $T$  in Sand SF7 ( $n_t$  in cycles,  $\bar{\sigma}_{3c}$  in  $\text{kg/cm}^2$ )



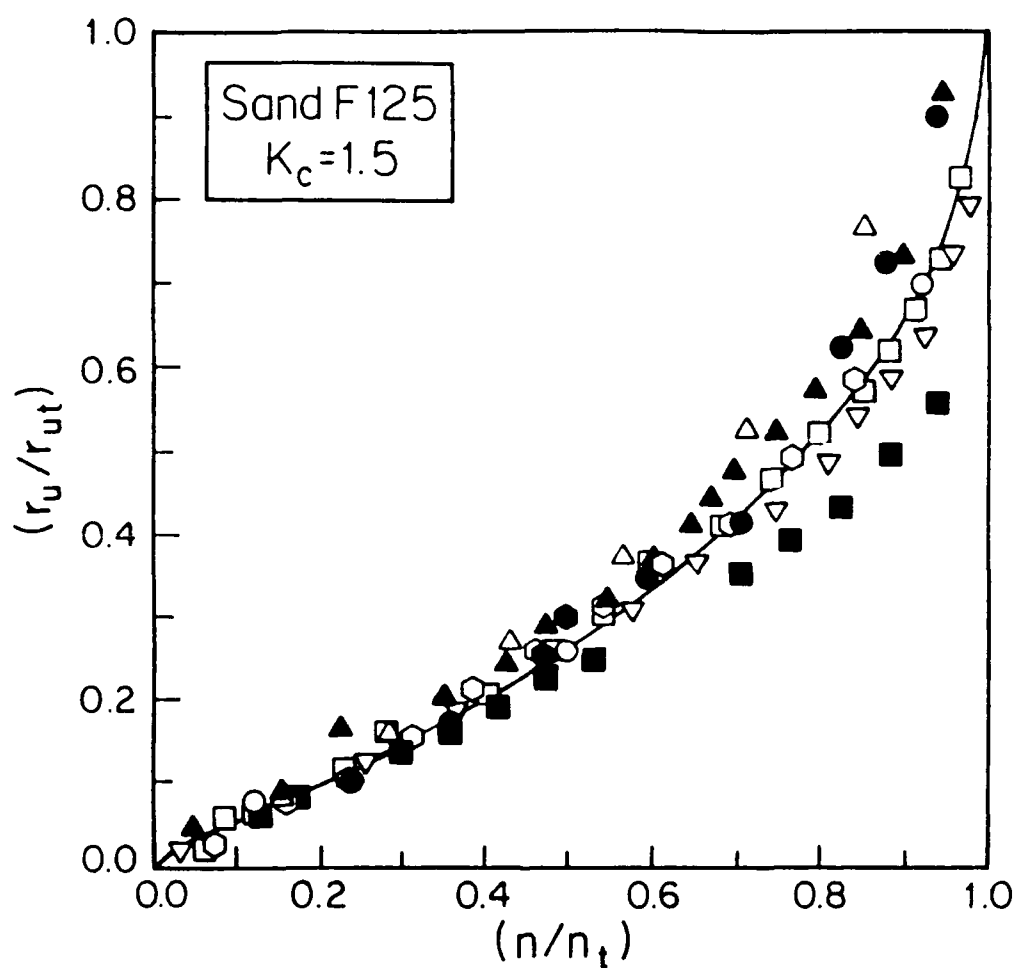
Test		$\bar{\sigma}_{3c}$ (Kg/cm <sup>2</sup> )	$\gamma_{cy}$ (%)	$n_t$ (cycles)	$r_{ut}$
△	F125-2	4.00	0.3873	4	1.00
○	F125-6	4.00	0.1956	13	1.00
□	F125-7	4.00	0.0620	115	1.00
◇	F125-8	4.00	0.0377	2160	1.00

Fig. 7.38. PWP Buildup Curves of Ottawa Sand F125, for  $K_c = 1.0$



Test		$\sigma_{3c}$ (Kg/cm <sup>2</sup> )	$\gamma_{cy}$ (%)	$n_t$ (cycles)	$r_{ut}$
○	F125-24	4.00	0.1087	18	0.819
□	F125-25	4.00	0.0540	26	0.711
△	F125-26	4.00	0.0321	332	0.819

Fig. 7.39. PWP Buildup Curves of Ottawa Sand F125, for  $K_c = 1.2$



Test	$\bar{\sigma}_{3c}$ (Kg/cm <sup>2</sup> )	$\gamma_{cy}$ (%)	$n_t$ (cycles)	$r_{ut}$
○ F125-17	4.00	0.0356	13	0.381
○ F125-18	4.00	0.1161	2	0.357
□ F125-19	4.00	0.0253	35	0.515
△ F125-20	4.00	0.0586	7	0.453
● F125-31	1.00	0.0440	2	0.393
● F125-32	1.00	0.0210	8.5	0.518
▽ F125-33	0.56	0.0082	26	0.516
▲ F125-34	1.00	0.0130	20	0.446
■ F125-35	1.50	0.0200	17	0.570

Fig. 7.40. PWP Buildup Curves of Ottawa Sand F125, for  $K_c = 1.5$

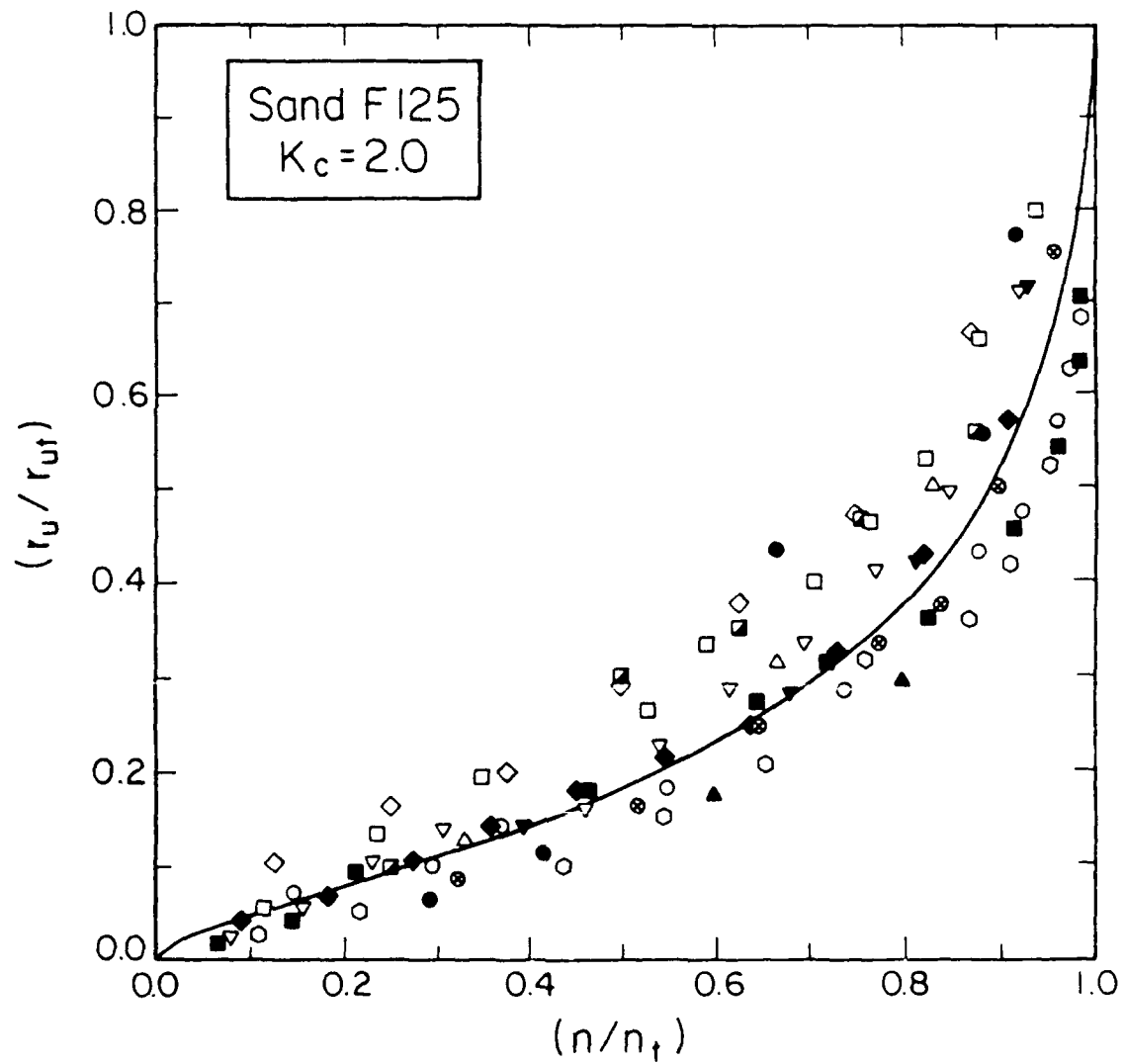
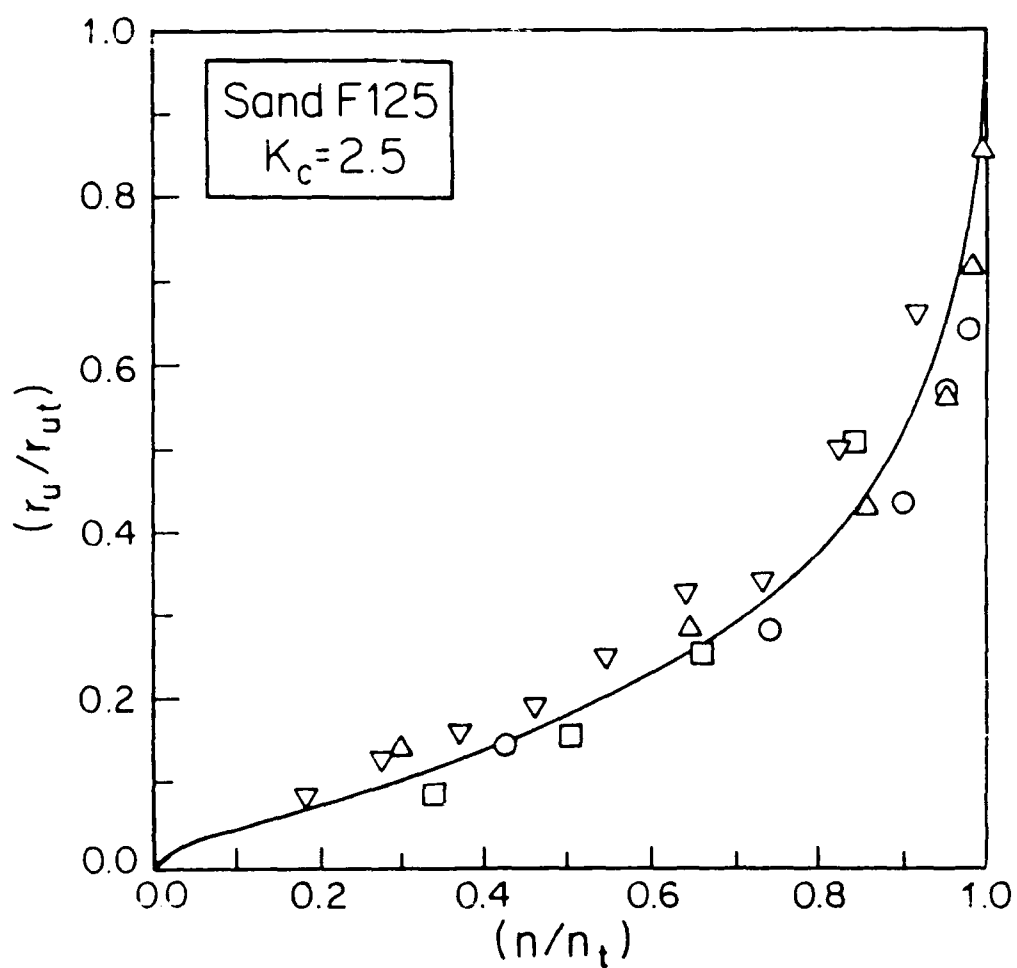


Fig. 7.41(a). PWP Buildup Curves of Ottawa Sand F125, for  $K_c = 2.0$  (Legend of Points in Fig. 7.41(b))

Test		$\bar{\sigma}_{3c}$ (Kg/cm <sup>2</sup> )	$\gamma_{cy}$ (%)	$n_f$ (cycles)	$r_{ut}$
◇	F125-1	4.00	0.0383	8	0.207
◆	F125-3	4.00	0.0374	11	0.241
▽	F125-4	4.00	0.0338	13	0.207
▼	F125-5	5.50	0.0520	14	0.224
●	F125-10	4.00	0.0220	12	0.194
△	F125-11	4.00	0.0440	3	0.172
▲	F125-12	4.00	0.0196	5	0.172
○	F125-13	4.00	0.0129	46	0.205
□	F125-14	4.00	0.0264	17	0.162
○	F125-15	4.00	0.0080	27	0.151
■	F125-16	4.00	0.0065	139	0.237
▣	F125-48	1.00	0.0190	4	0.179
⊗	F125-49	1.00	0.0080	15.5	0.214

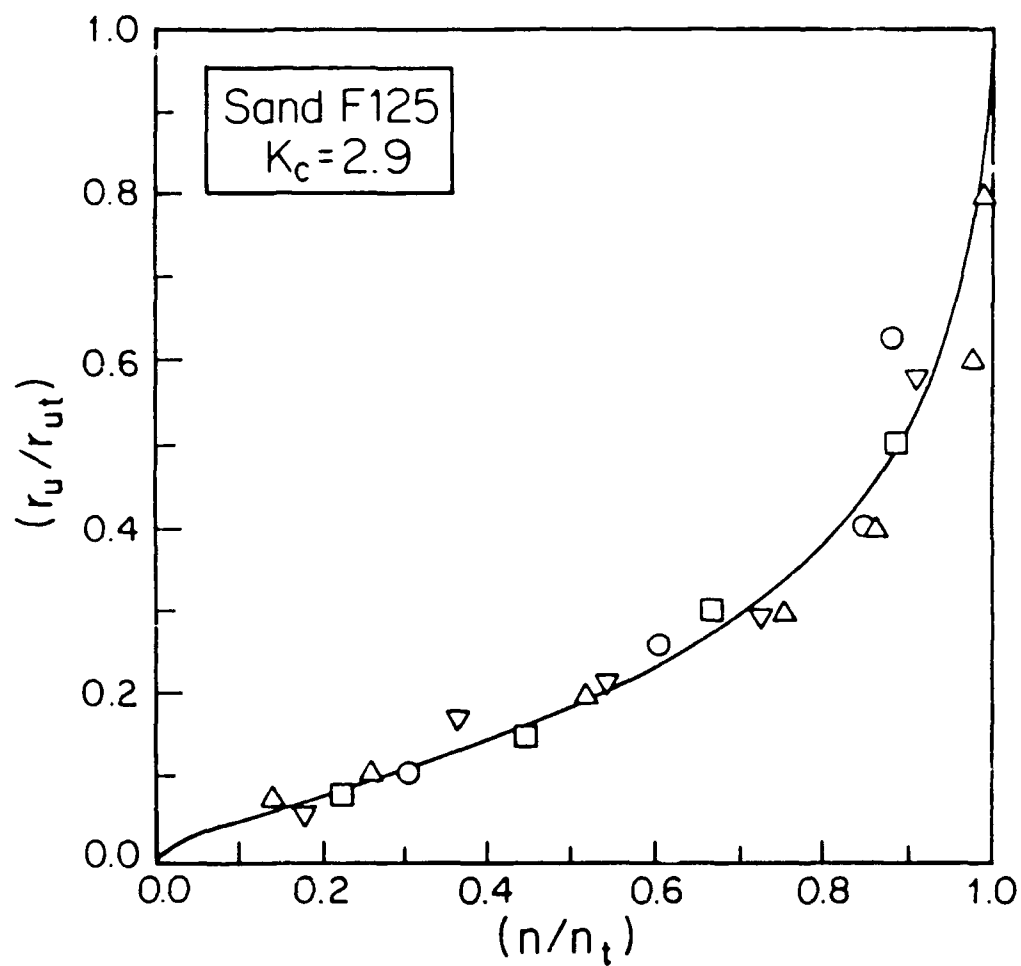
Fig. 7.41(b). Legend of Data Points Presented in Fig. 7.41(a)



Test	$\bar{\sigma}_{3c}$ (Kg/cm <sup>2</sup> )	$\gamma_{cy}$ (%)	$n_t$ (cycles)	$r_{ut}$
○ F125-36	4.00	0.0180	19	0.151
□ F125-37	4.00	0.0760	3	0.194
△ F125-38	4.00	0.0100	89	0.151
▽ F125-46	1.00	0.0116	11	0.107

Fig. 7.42. PWP Buildup Curves of Ottawa Sand F125, for  $K_c = 2.5$





Test		$\bar{\sigma}_{3c}$ (Kg/cm <sup>2</sup> )	$\gamma_{cy}$ (%)	$n_t$ (cycles)	$r_{ut}$
△	F125-39	4.00	0.0150	115.5	0.108
○	F125-40	4.00	0.0330	33	0.086
□	F125-41	4.00	0.0870	4.5	0.073
▽	F125-45	1.00	0.0123	5.5	0.093

Fig. 7.43. PWP Buildup Curves of Ottawa Sand F125, for  $K_c = 2.9$

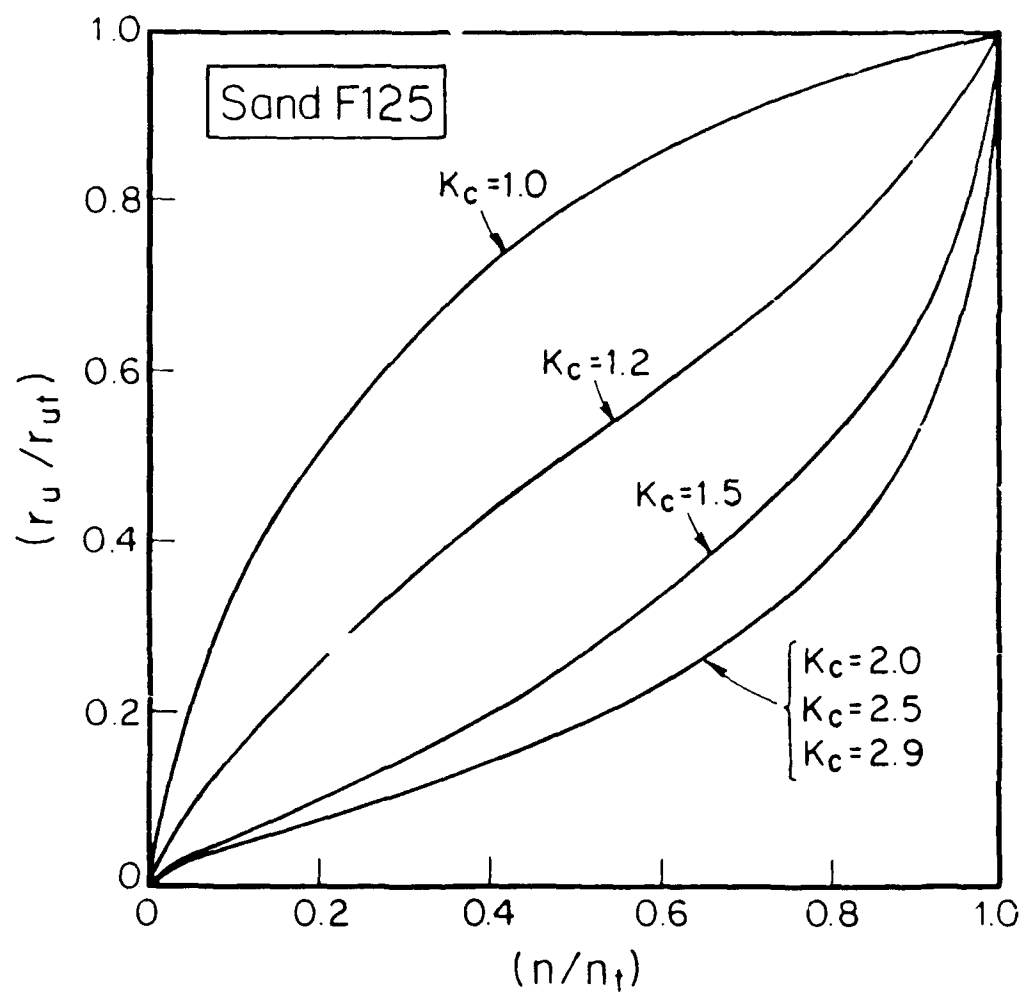
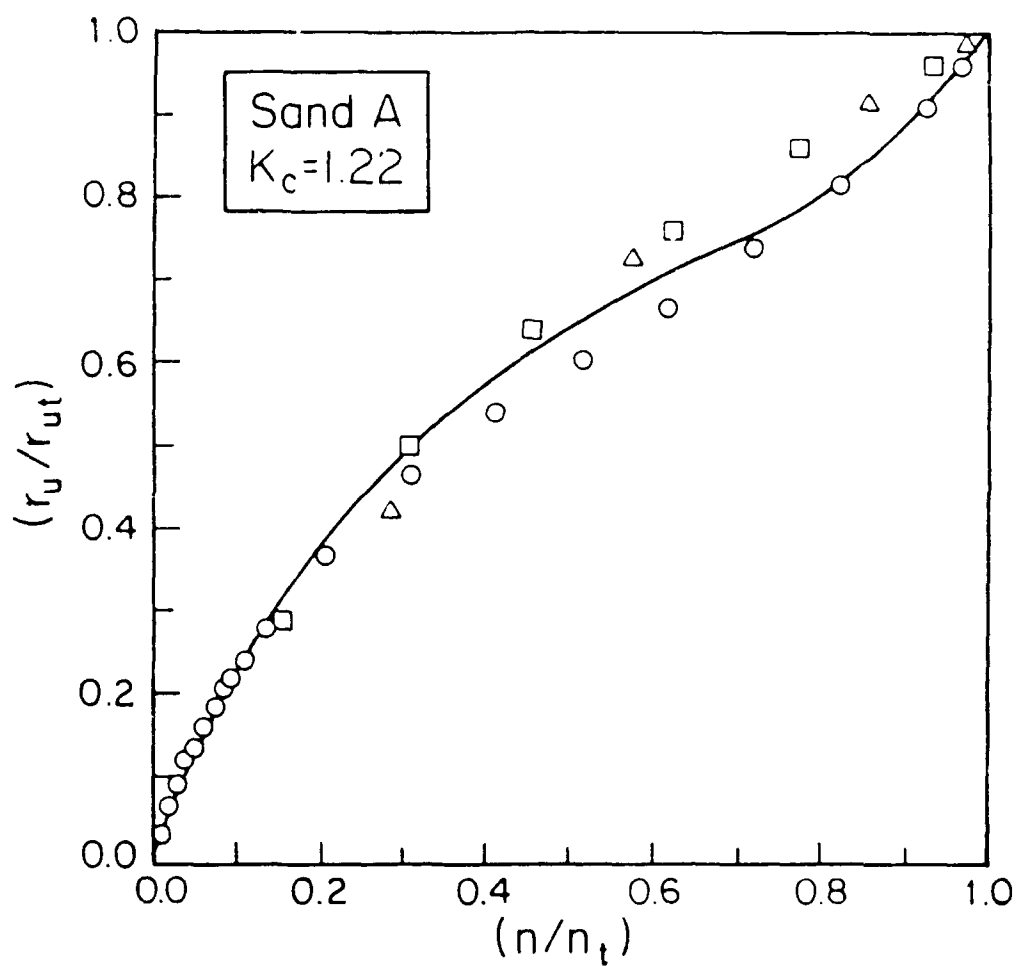
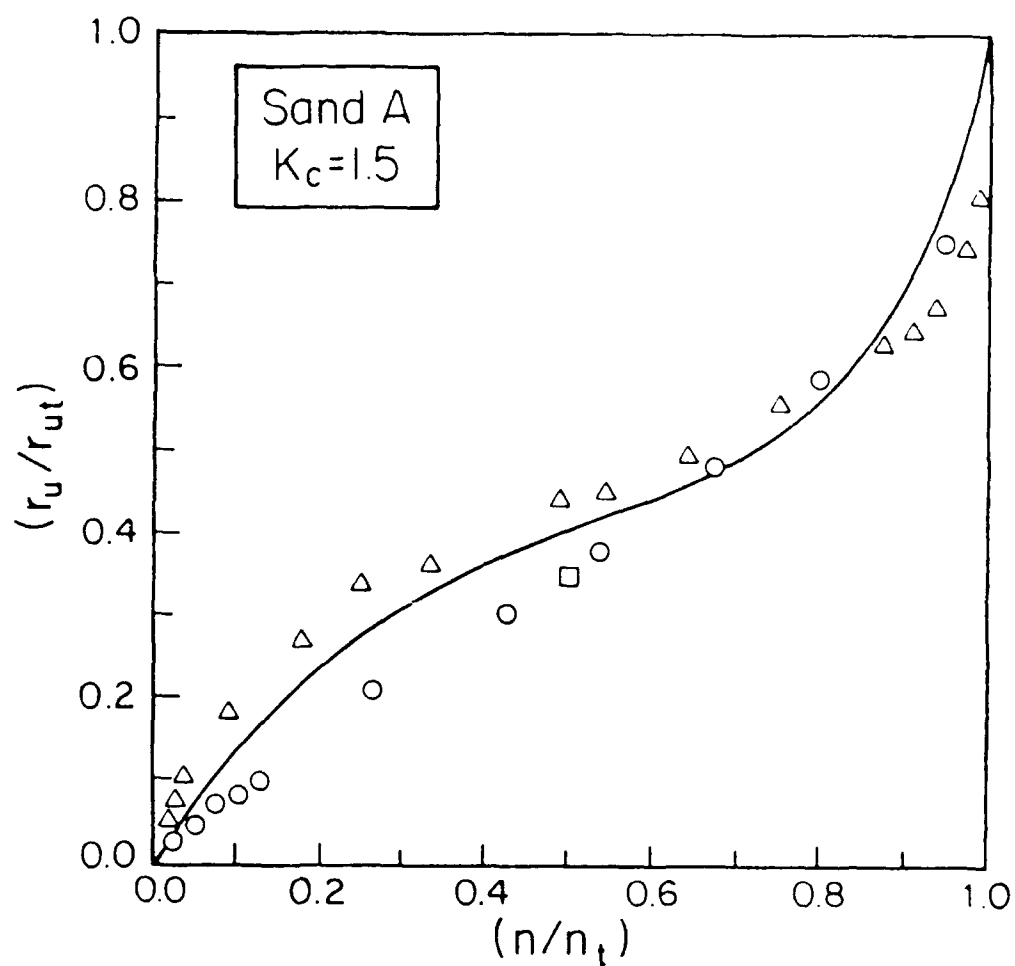


Fig. 7.44. PWP Buildup Curves of Ottawa Sand F125, for  $K_c=1.0-2.9$



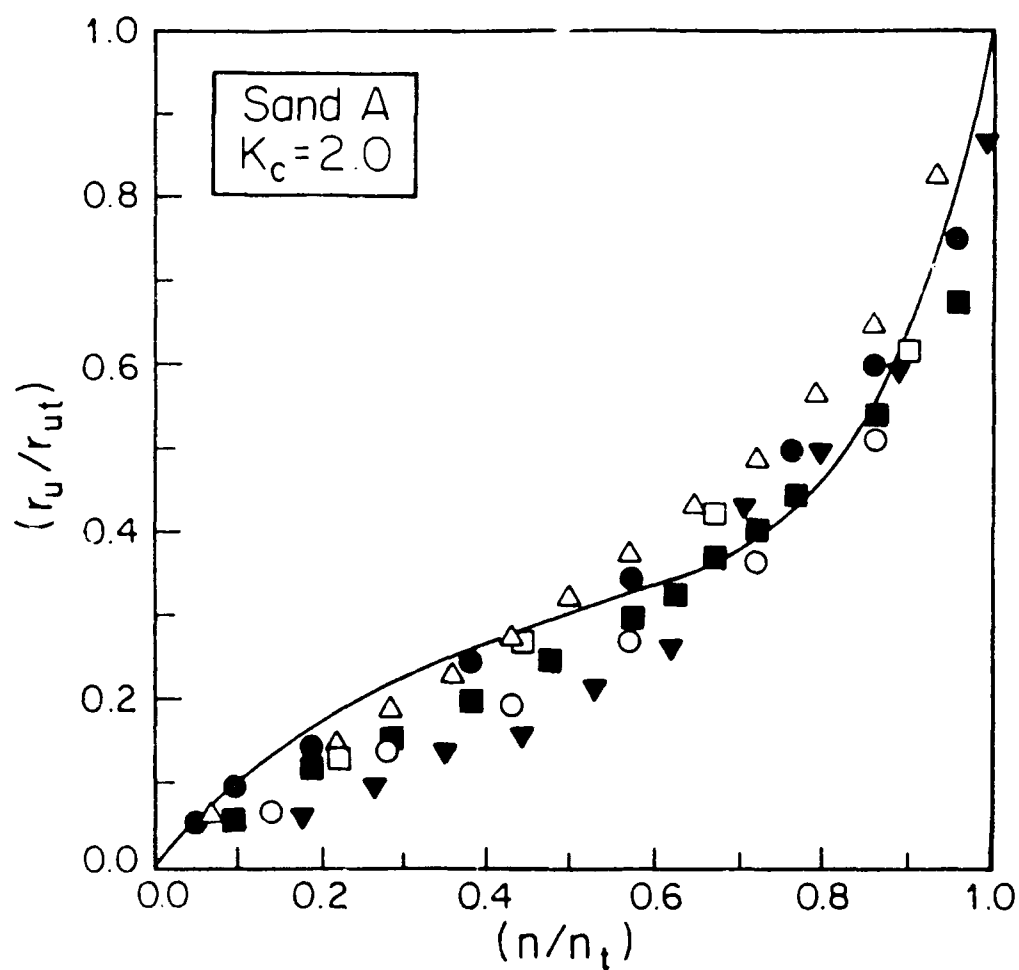
Test		$\bar{\sigma}_{3c}$ (Kg/cm <sup>2</sup> )	$\gamma_{cy}$ (%)	$n_t$ (cycles)	$r_{ut}$
○	LAGA-47	3.73	0.066	9.6	0.849
□	LAGA-48	3.73	0.18	6.5	0.816
△	LAGA-49	3.73	0.266	3.5	0.830

Fig. 7.45. PWP Buildup Curves of Sand A, for  $K_c = 1.22$



Test	$\bar{\sigma}_{3c}$ (Kg/cm <sup>2</sup> )	$\gamma_{cy}$ (%)	$n_t$ (cycles)	$r_{ut}$
○ LAGA-44	3.73	0.047	37	0.599
□ LAGA-45	3.73	0.171	3	0.604
△ LAGA-46	3.73	0.023	1223	0.612

Fig. 7.46. PWP Buildup Curves of Sand A, for  $K_c=1.5$



Test	$\bar{\sigma}_{3c}$ (Kg/cm <sup>2</sup> )	$\gamma_{cy}$ (%)	$n_t$ (cycles)	$r_{ut}$
○ LAGA-6	4.00	0.0462	7	0.283
□ LAGA-10	2.67	0.0545	4	0.251
■ LAGA-11	4.07	0.0494	11	0.316
△ LAGA-13	4.78	0.0490	14	0.292
● LAGA-22	4.00	0.0447	21	0.345
▼ LAGA-25	4.00	0.0193	113	0.270

Fig. 7.47. PWP Buildup Curves of Sand A, for  $K_c = 2.0$

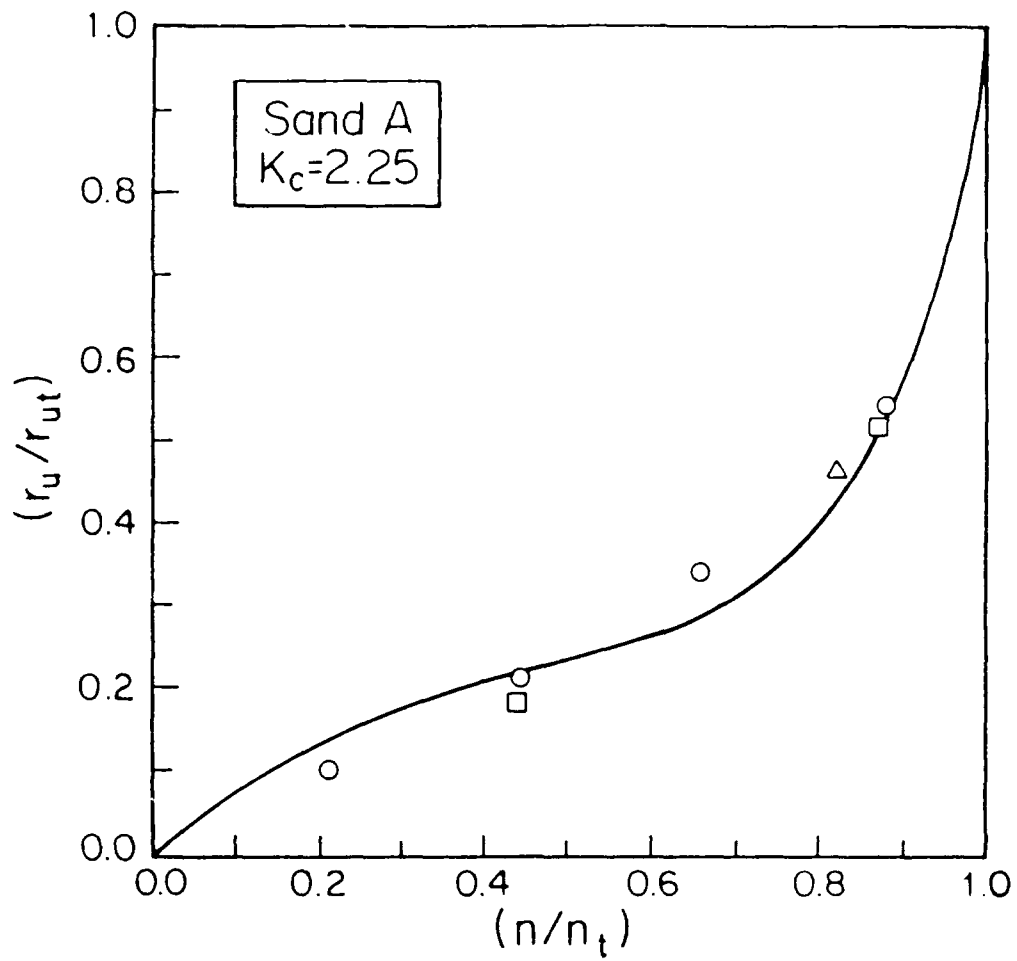


Fig. 7.48. PWP Buildup Curves of Sand A, for  $K_c=2.25$

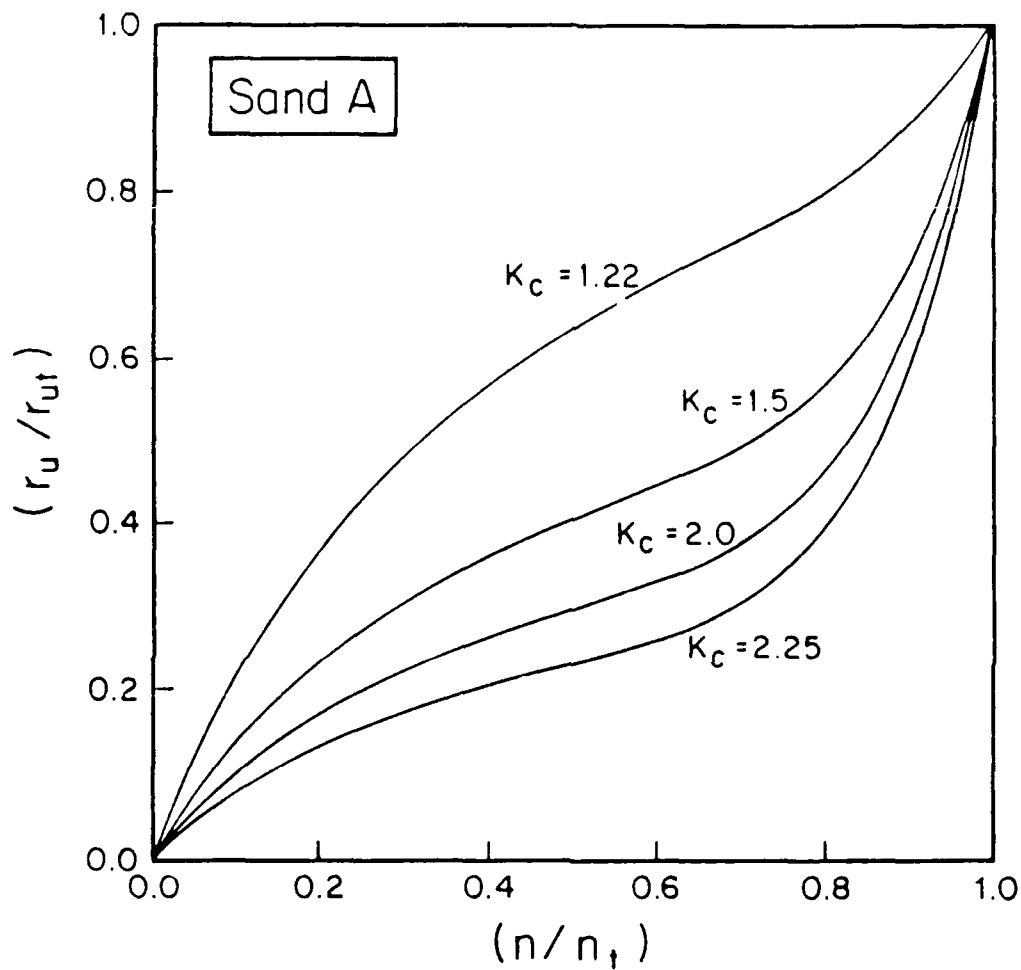
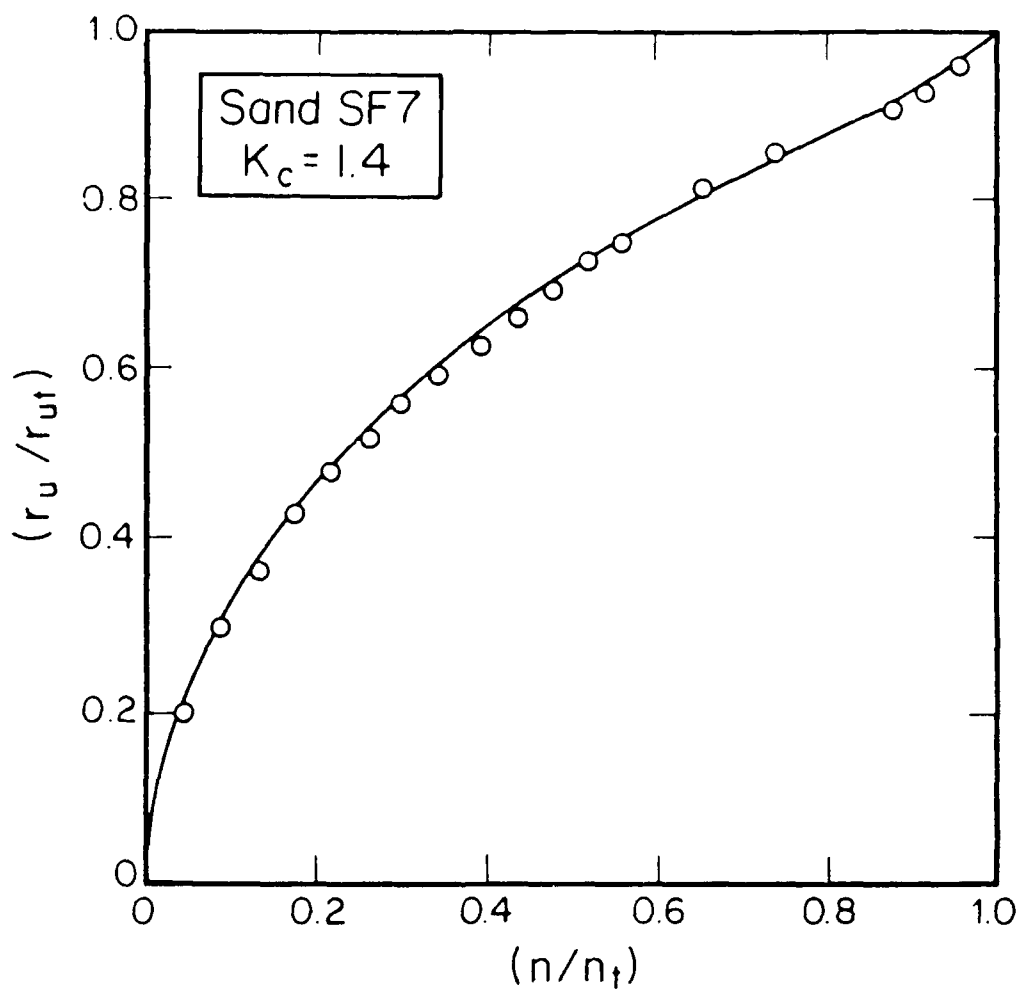


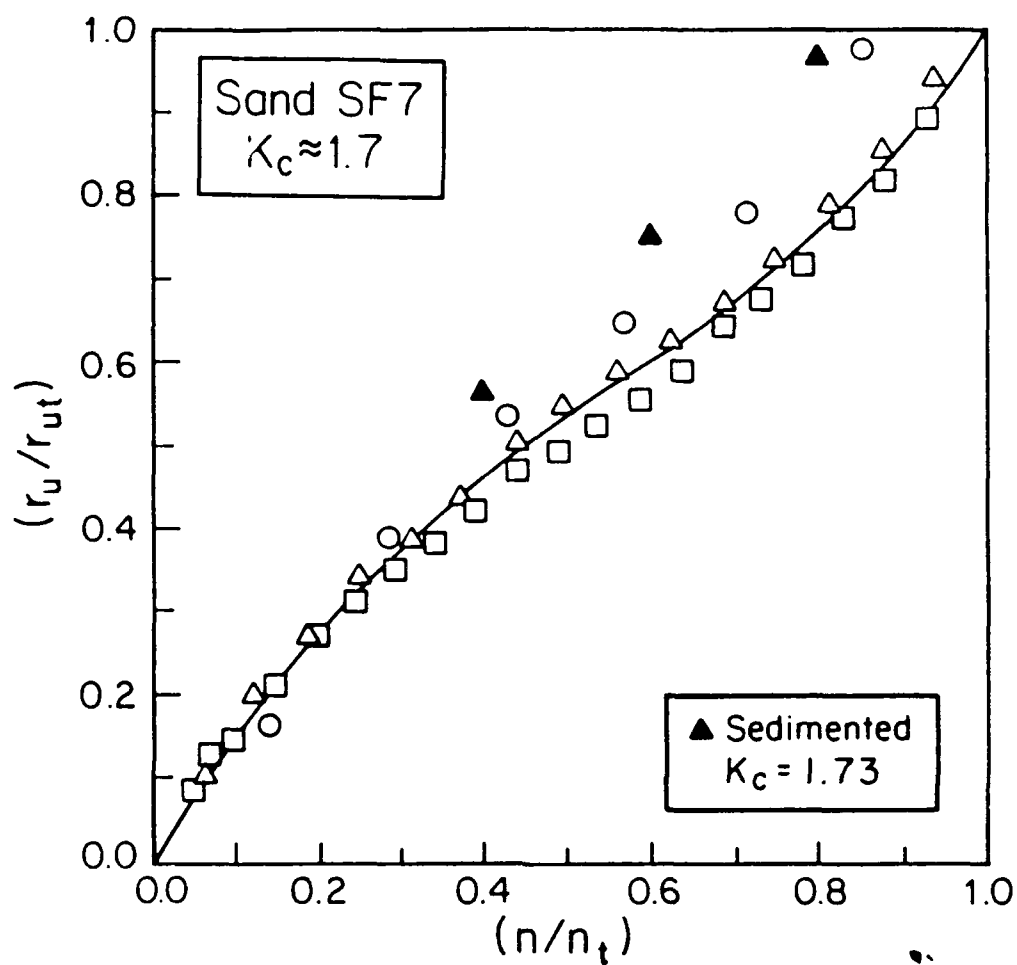
Fig. 7.49. PWP Buildup Curves of Sand A, for  $K_c = 1.22-2.25$



Test		$\bar{\sigma}_{3c}$ (Kg/cm <sup>2</sup> )	$\gamma_{cy}$ (%)	$n_t$ (cycles)	$r_{ut}$
o	SF7-1	1 Kg/cm <sup>2</sup>	0.05	23	0.688

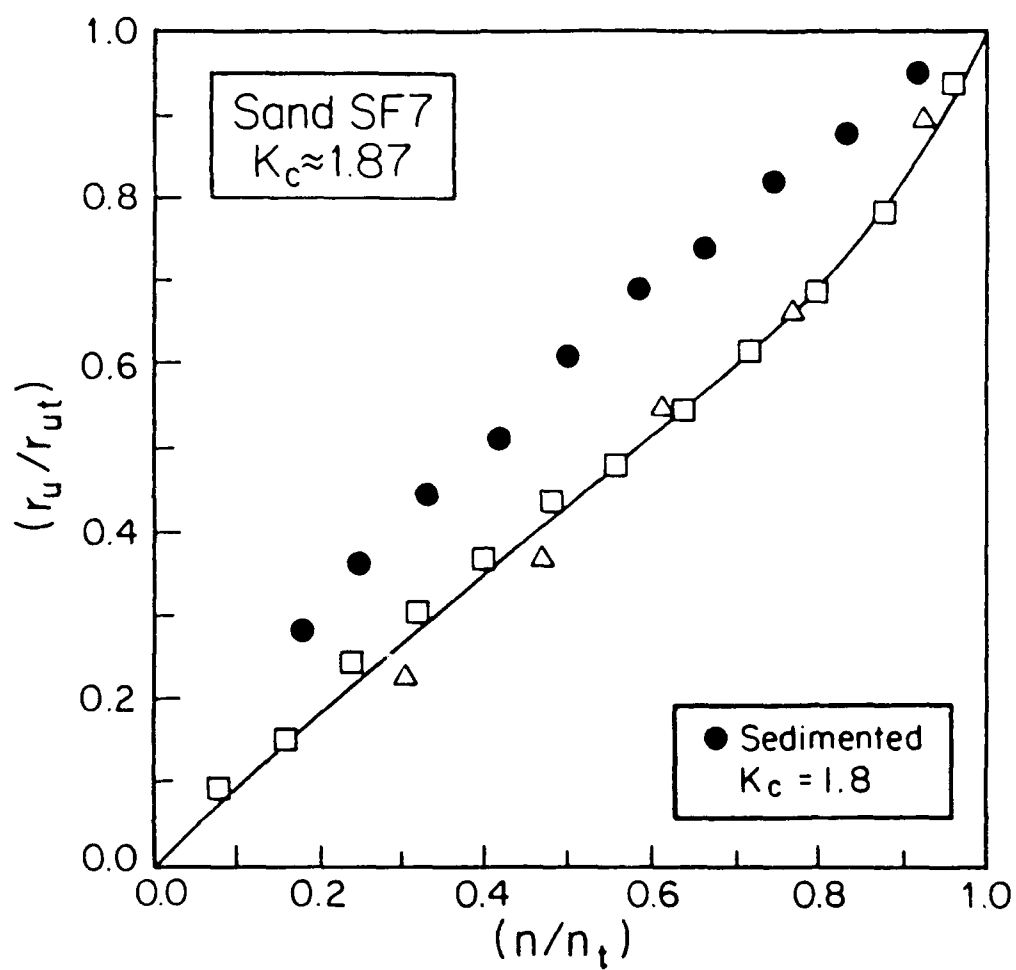
Fig. 7.50. PWP Buildup Curves of Sand SF7, for K<sub>c</sub>=1.4





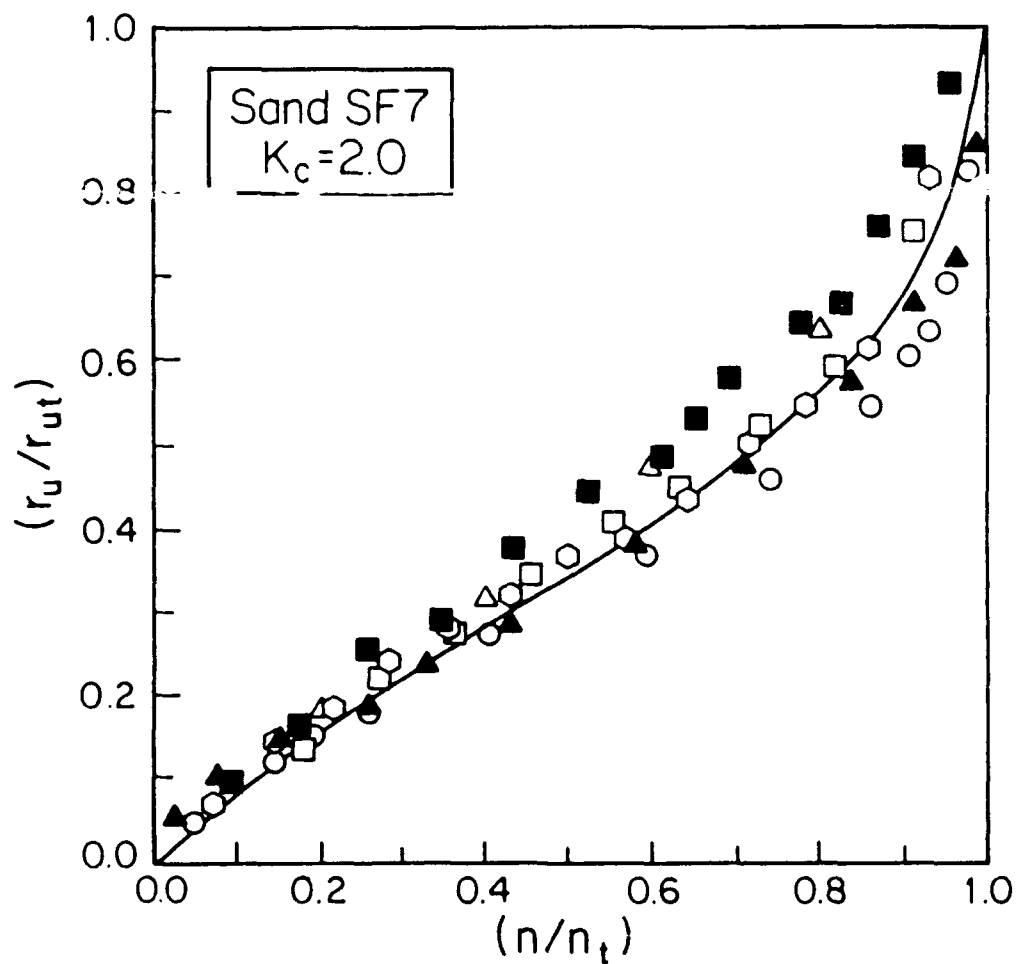
Test		$\bar{\sigma}_{3c}$ (Kg/cm <sup>2</sup> )	$\gamma_{cy}$ (%)	$n_t$ (cycles)	$r_{ut}$
△	SF7-1	1.00	0.0493	8	0.536
□	SF7-8	1.00	0.0245	20.5	0.518
○	SF7-9	1.00	0.1027	3.5	0.554
▲	SF7-23	1.00	0.1100	2.5	0.464

Fig. 7.51. PWP Buildup Curves of Sand SF7, for  $K_c \approx 1.7$   
(Solid Points Represent Sedimented Sample)



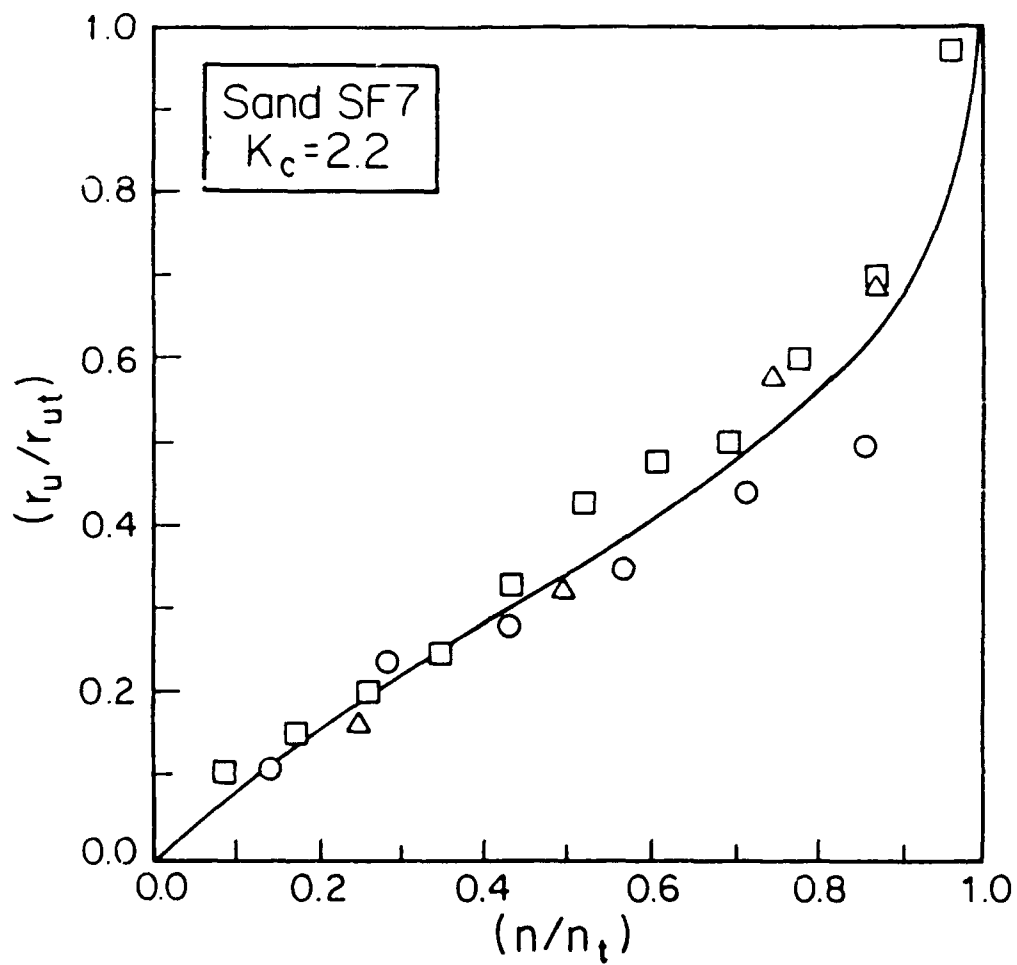
Test	$\bar{\sigma}_{3c}$ (Kg/cm <sup>2</sup> )	$\gamma_{cy}$ (%)	$n_t$ (cycles)	$r_{ut}$
△ SF7-15	1.00	0.0500	6.5	0.393
□ SF7-16	1.00	0.0245	12.5	0.393
● SF7-22	1.00	0.0568	8.5	0.437

Fig. 7.52. PWP Buildup Curves of Sand SF7, for  $K_c \approx 1.87$   
(Solid Points Represent Sedimented Sample)



Test		$\bar{\sigma}_{3c}$ (Kg/cm <sup>2</sup> )	$\gamma_{cy}$ (%)	$n_t$ (cycles)	$r_{ut}$
△	SF7-2	1.00	0.0518	2.5	0.393
□	SF7-4	1.00	0.0257	5.5	0.393
○	SF7-5	1.00	0.0050	21	0.393
⊙	SF7-6	1.00	0.0107	7	0.393
▲	SF7-25	1.00	0.0072	39.5	0.375
■	SF7-26	1.00	0.0240	11.5	0.402

Fig. 7.53. PWP Buildup Curves of Sand SF7, for  $K_c=2.0$   
(Solid Points Represent Sedimented Sample)<sup>c</sup>



	Test	$\bar{\sigma}_{3c}$ (Kg/cm <sup>2</sup> )	$\gamma_{cy}$ (%)	$n_t$ (cycles)	$r_{ut}$
○	SF7-11	1.00	0.010	7	0.375
□	SF7-17	1.00	0.026	11.5	0.357
△	SF7-18	1.00	0.051	4.0	0.339

Fig. 7.54. PWP Buildup Curves of Ottawa Sand SF7, for  $K_c = 2.2$

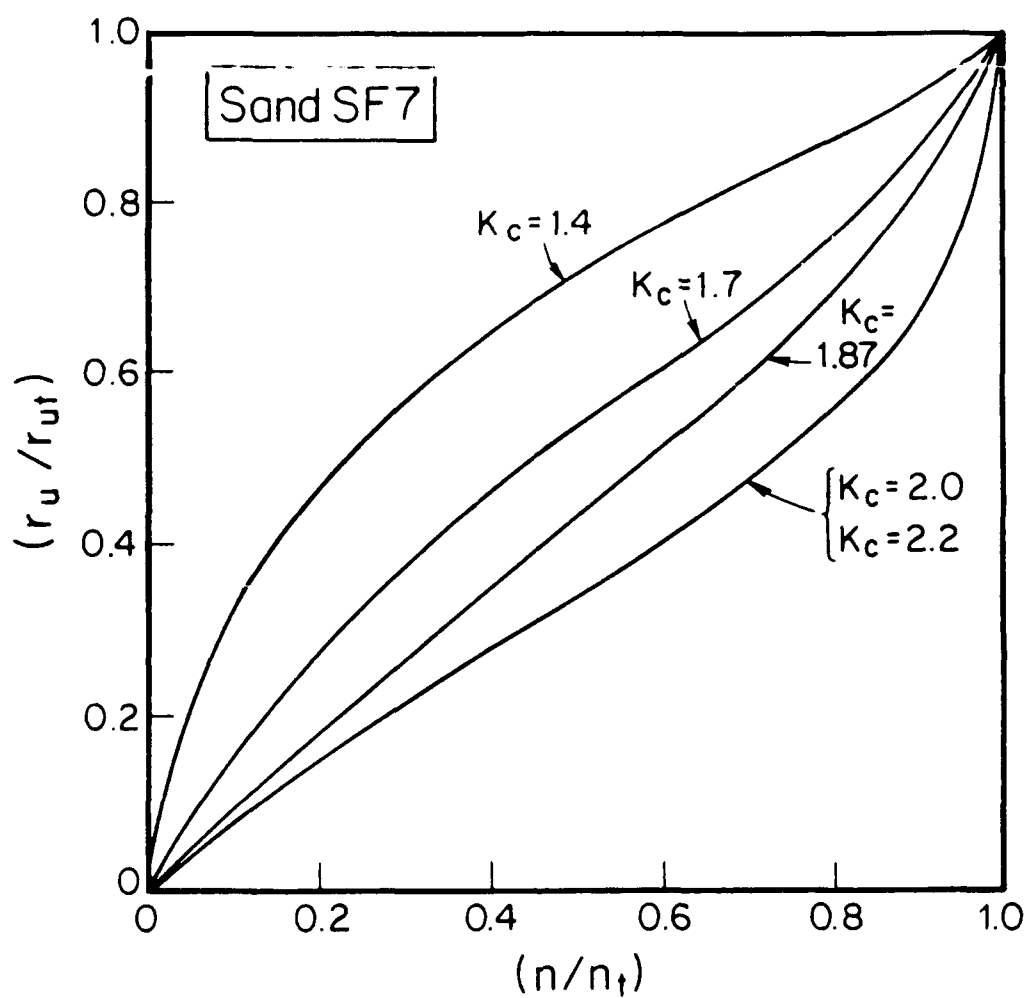


Fig. 7.55. PWP Buildup Curves of Ottawa Sand SF7, for  $K_c = 1.4-2.2$

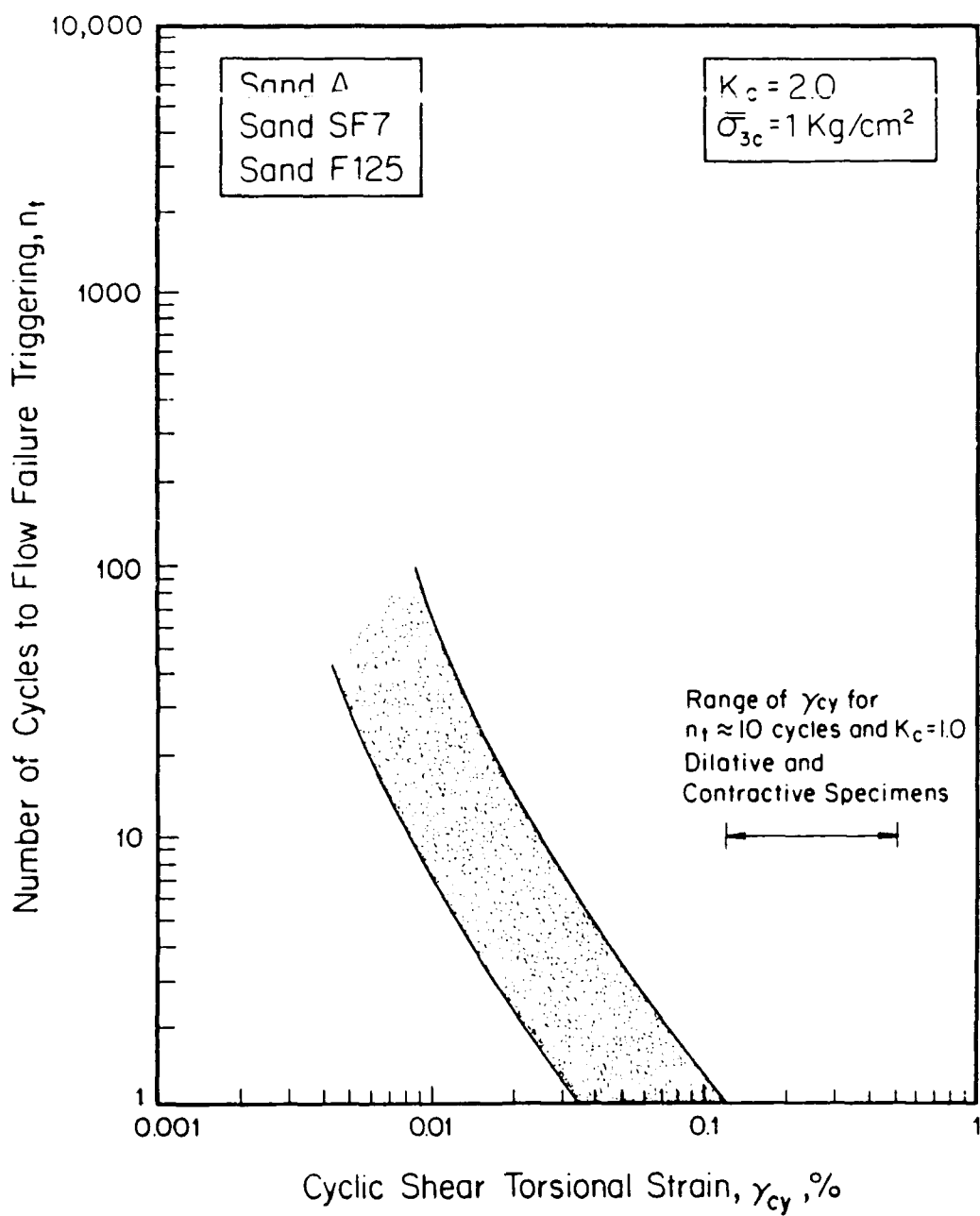


Fig. 7.56. Band of Triggering Relationships for all Tests with  $K_c = 2.0$ ,  $\bar{\sigma}_{3c} = 1 \text{ kg/cm}^2$  in Three Sands

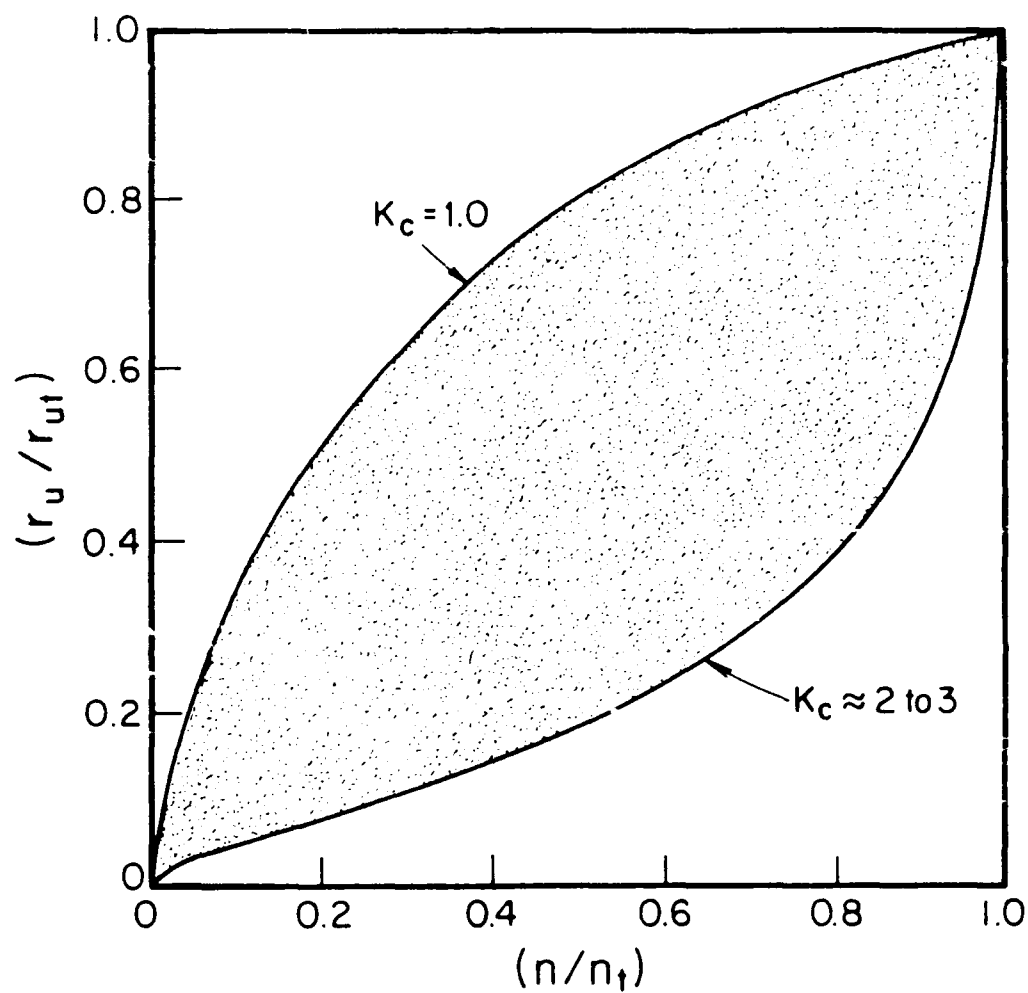


Fig. 7.57. PWP Buildup Bands for All Tested Sands, for  $K_c = 1.0-3.0$

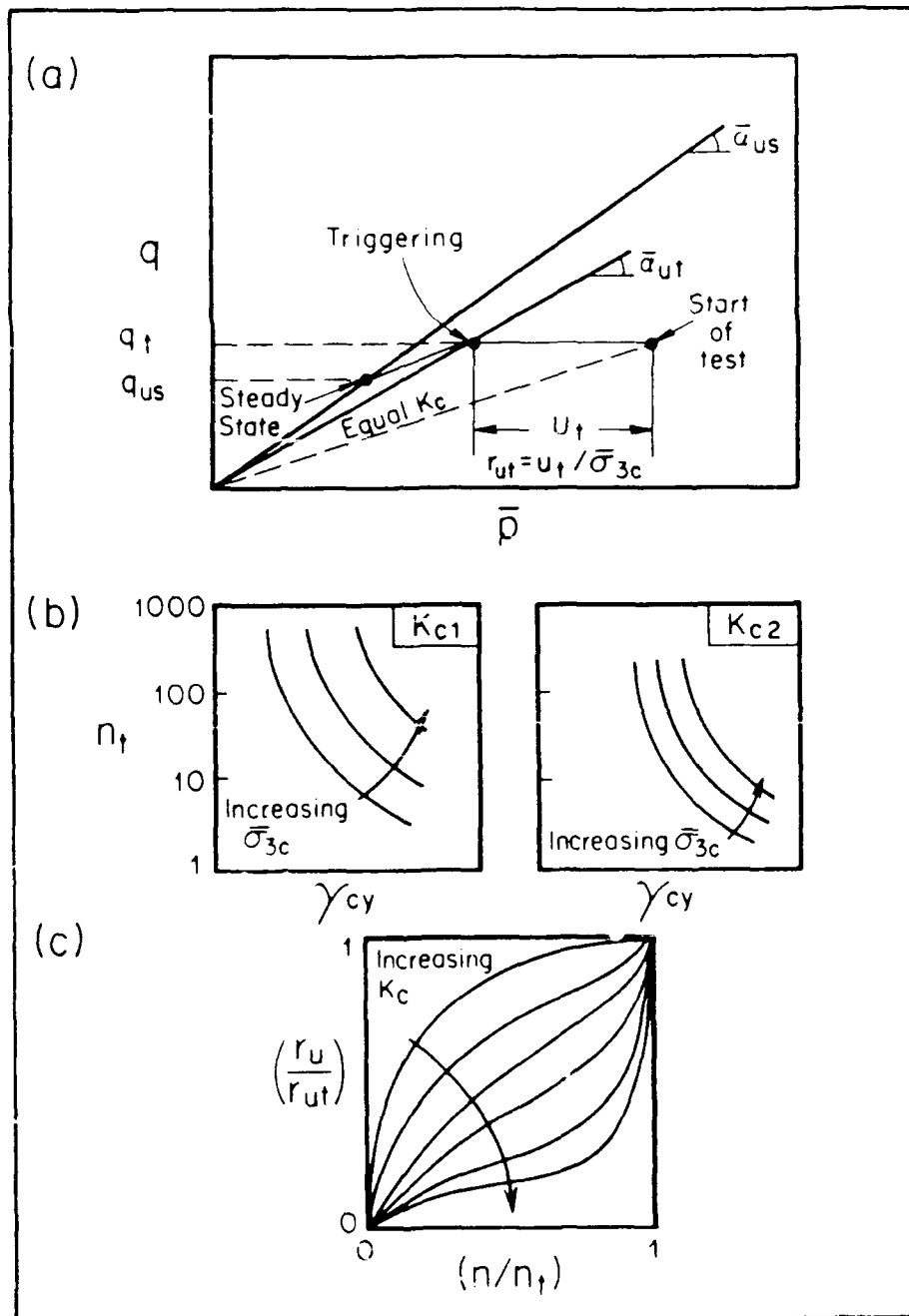


Fig. 7.58. Schematic Diagram of the 3 Criteria Comprising the PWP Triggering Model



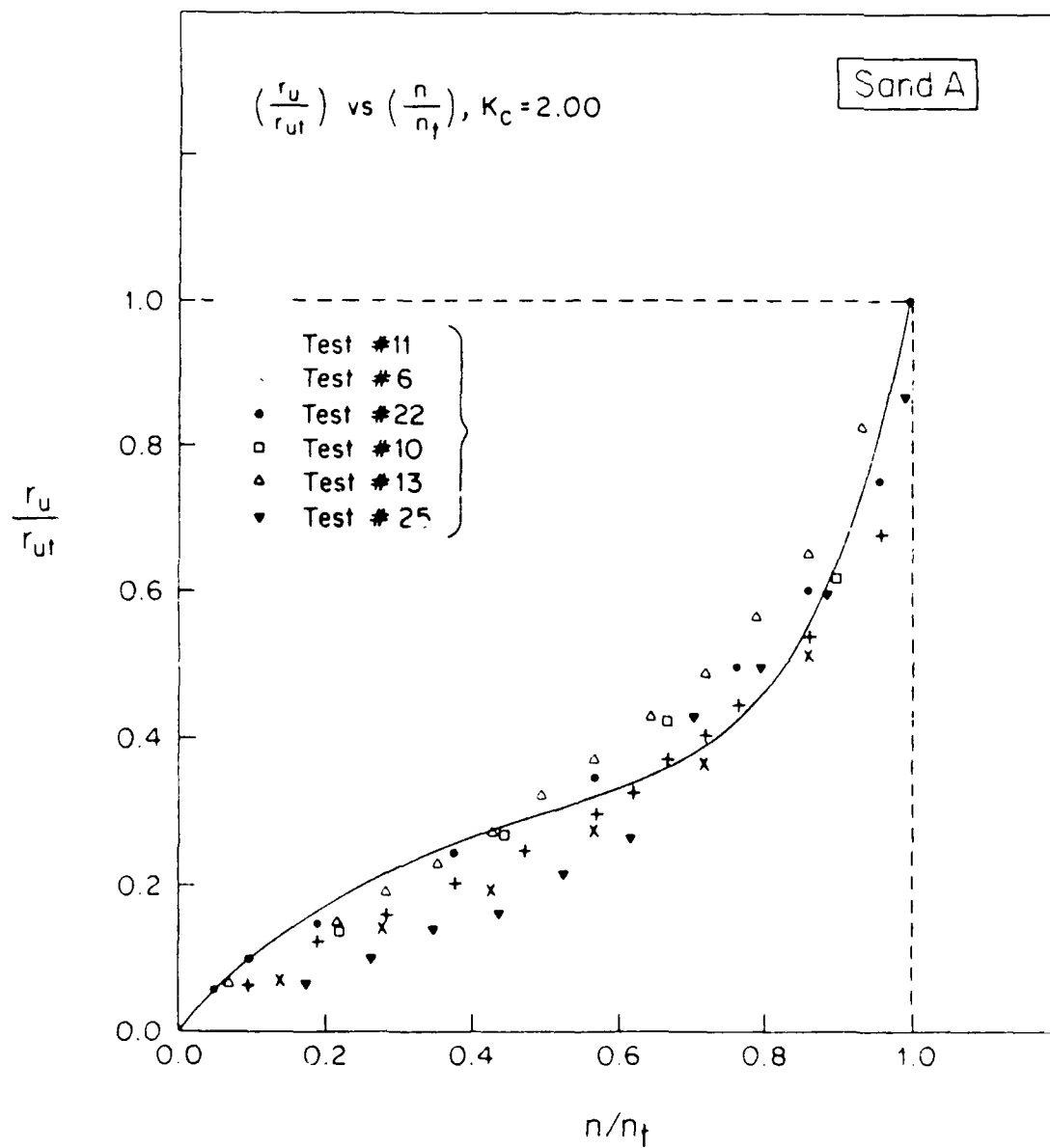


Fig. 7.59. PWP Buildup Curve Approximation for Sand A, for  $K_c = 2.0$

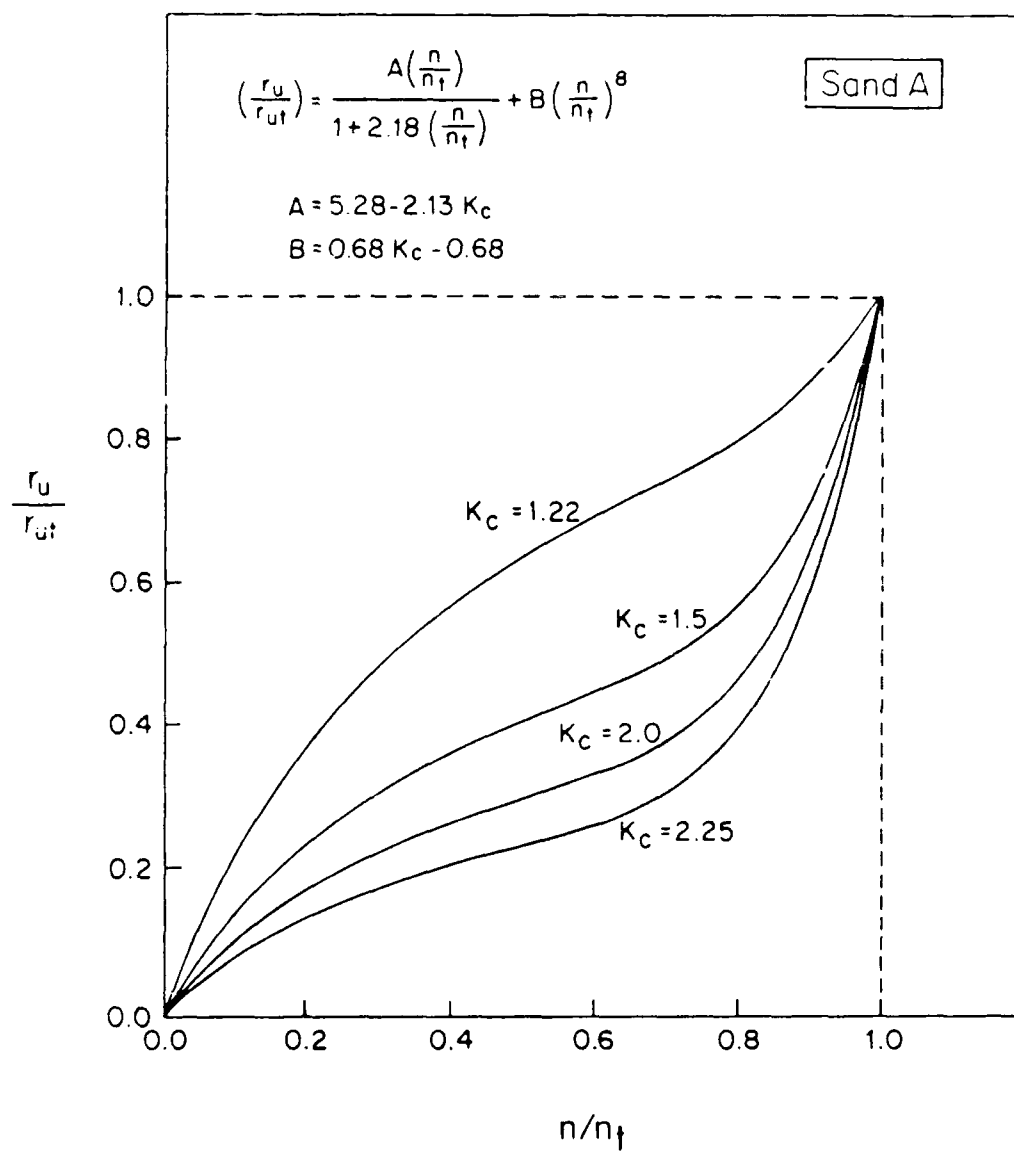


Fig. 7.60. PWP Buildup Curve Approximation for Sand A, (all  $K_c$ )

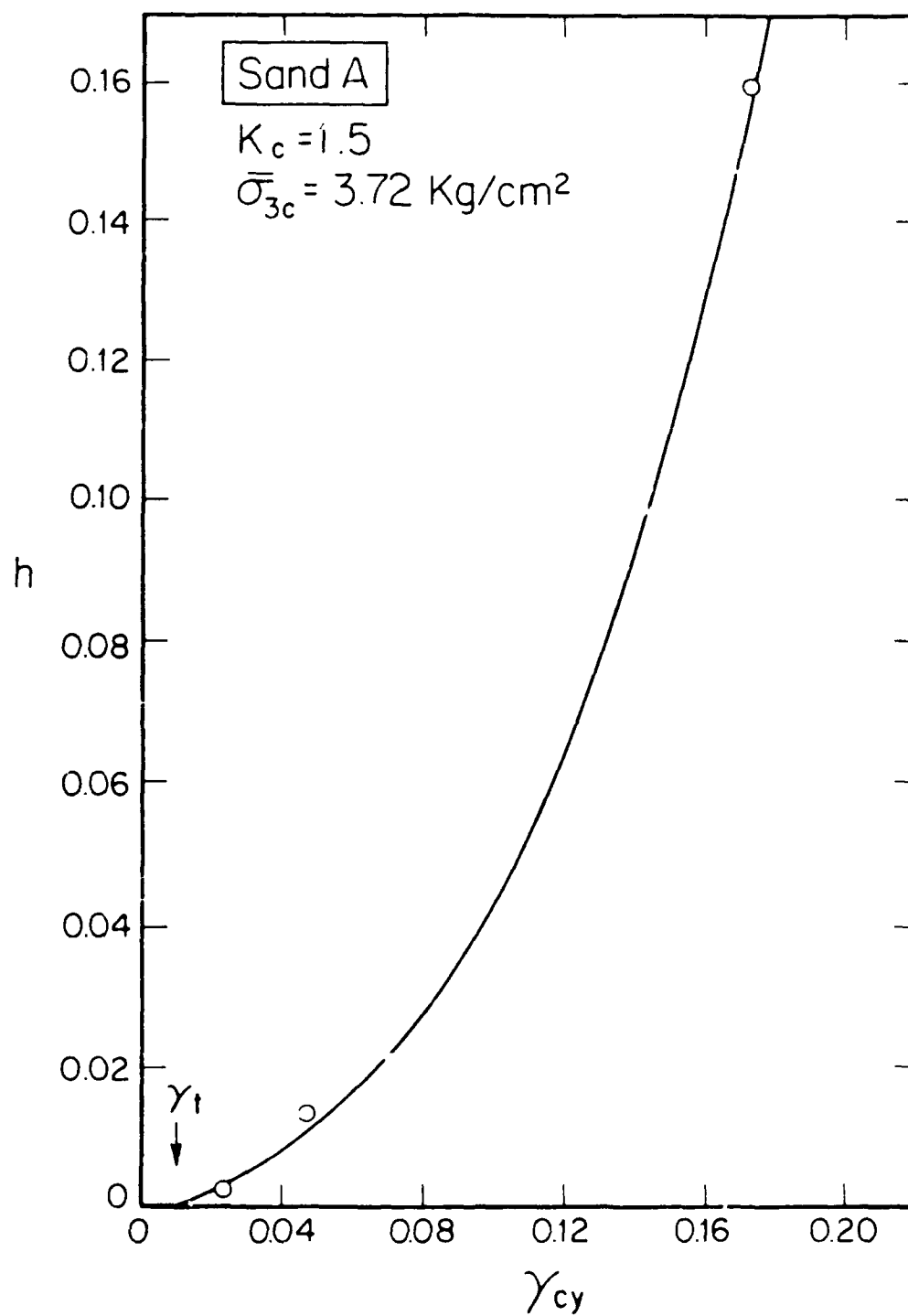


Fig. 7.61. Evaluation of Function  $h$  for the Modelling of the Triggering Relationships

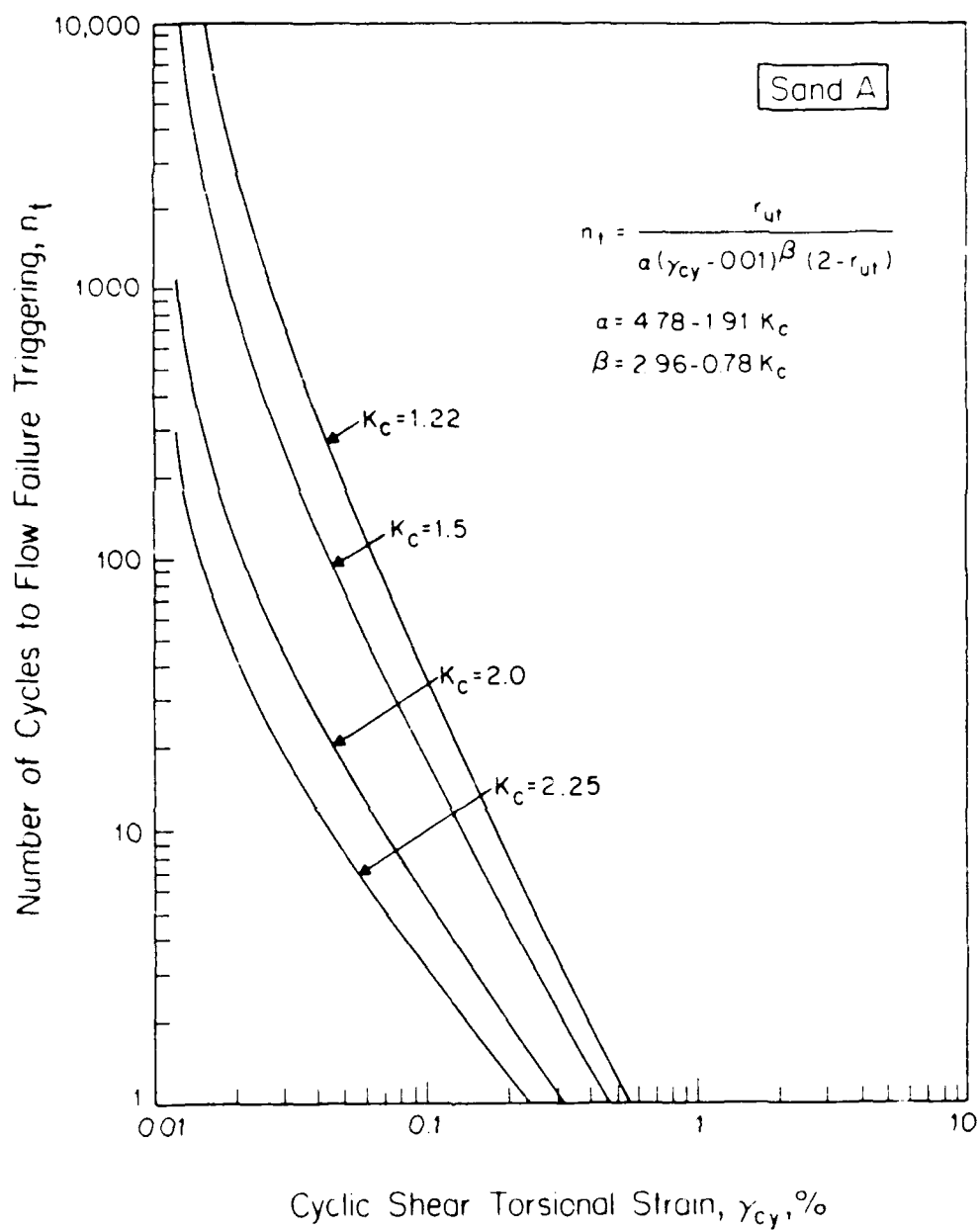


Fig. 7.62. Approximation of Triggering Relationships for Sand A ( $\bar{\sigma}_{3c} = 3.72 \text{ kg/cm}^2$ )

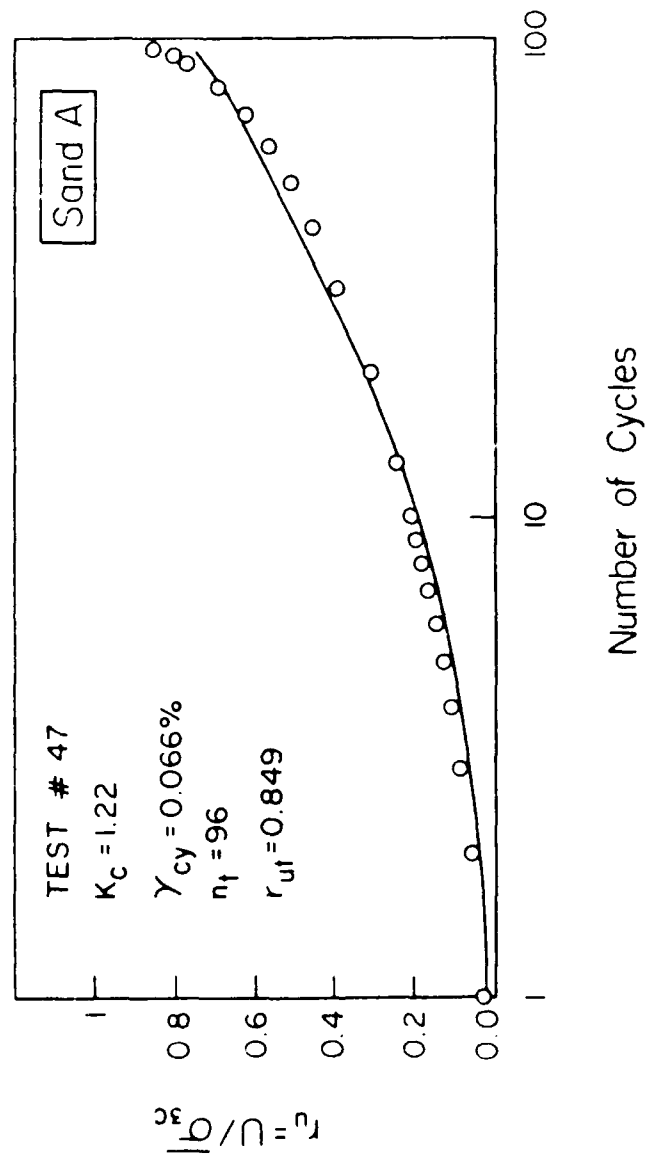


Fig. 7.63. Comparison Between Predicted and Actual Results of a Cyt-CAU Test on Sand A Using the PWP Triggering Model

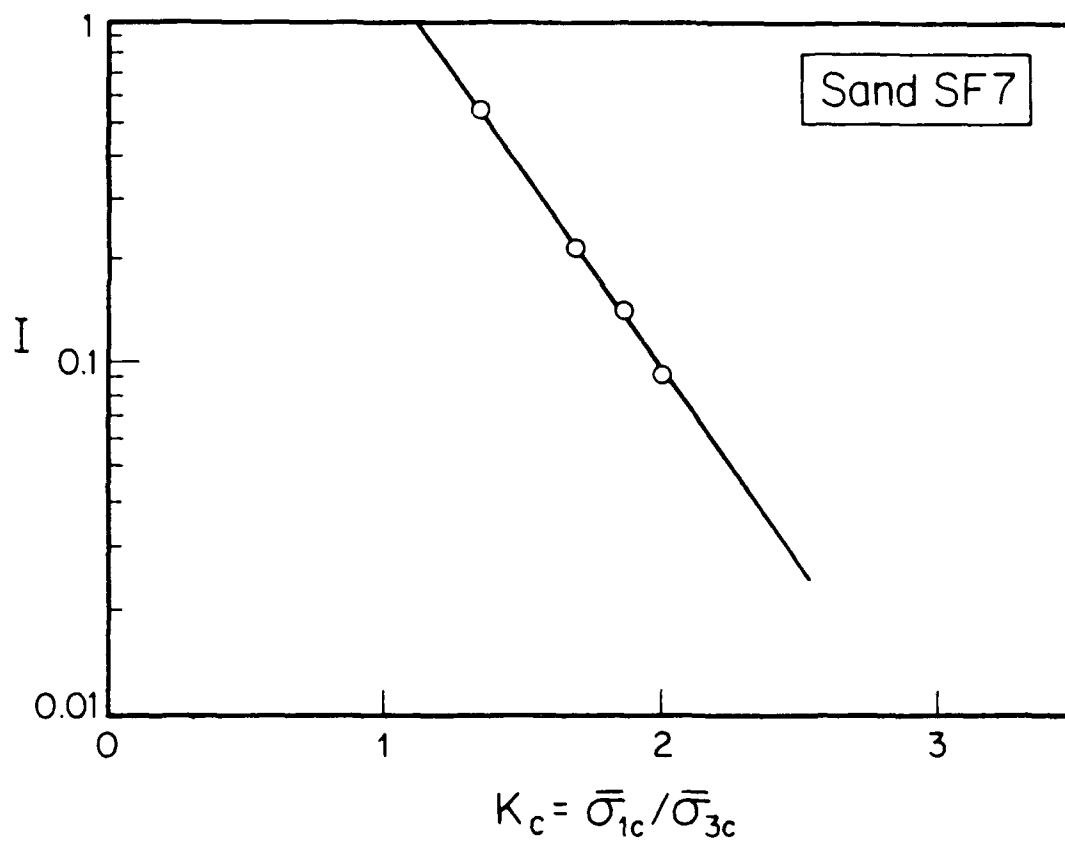


Fig. 7.64. Evaluation of the Function  $I$  for the Triggering Relationship of Sand SF7

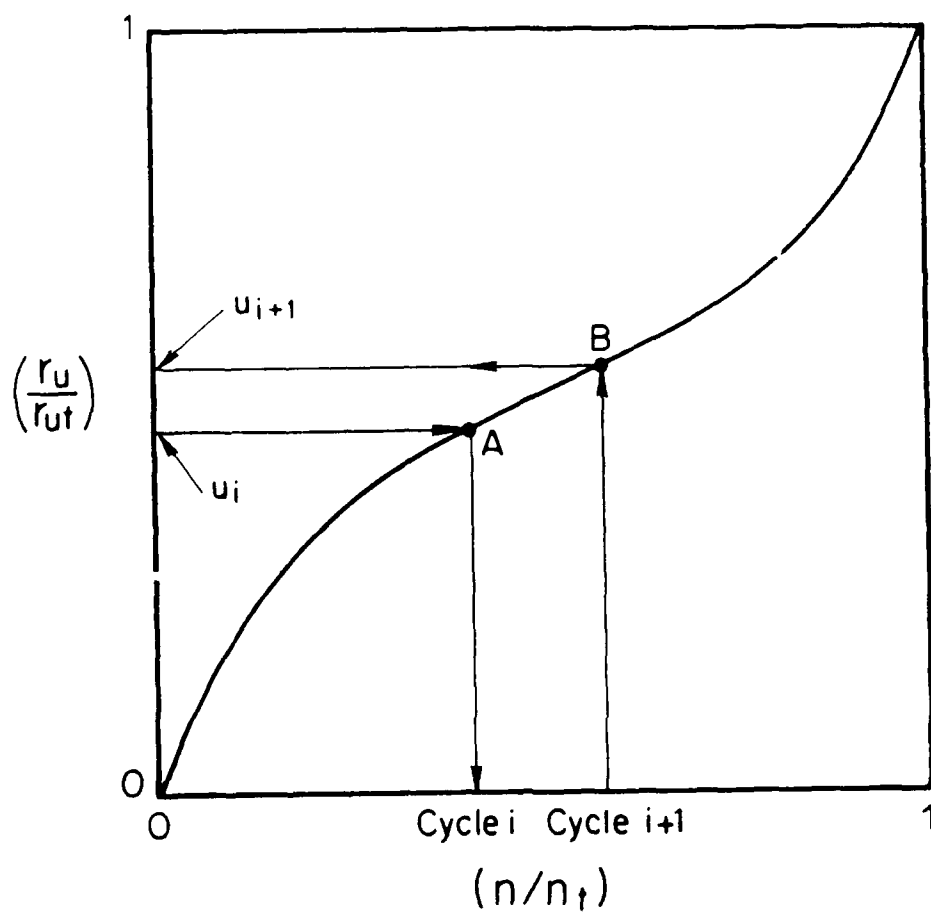


Fig. 7.65. Use of the PWP Buildup Curves to Account for the Incorporation of Variable Shear Strains into the PWP Triggering Model

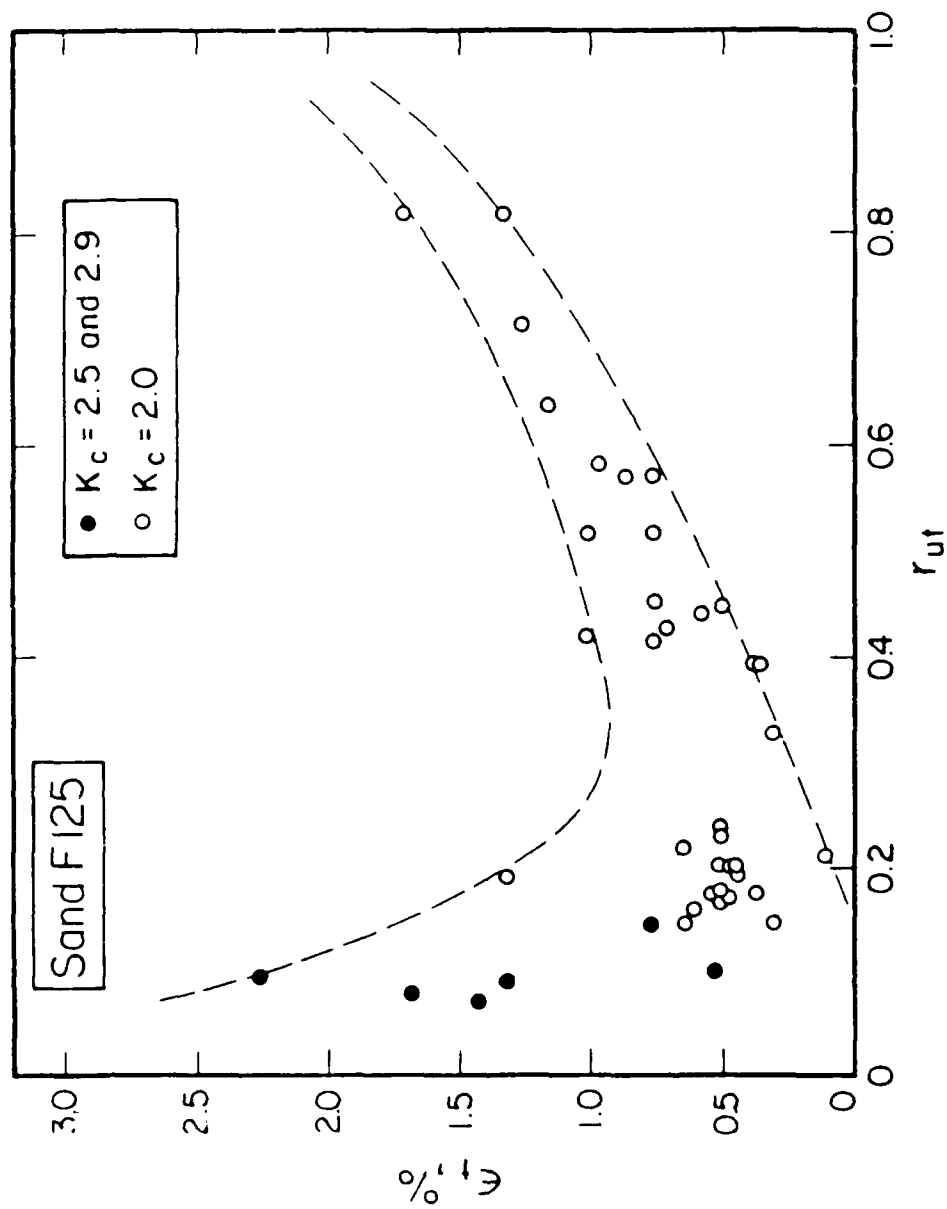


Fig. 7.66. Cumulative Axial Strain at Failure Compared to PWP at Failure for Ottawa Sand F125



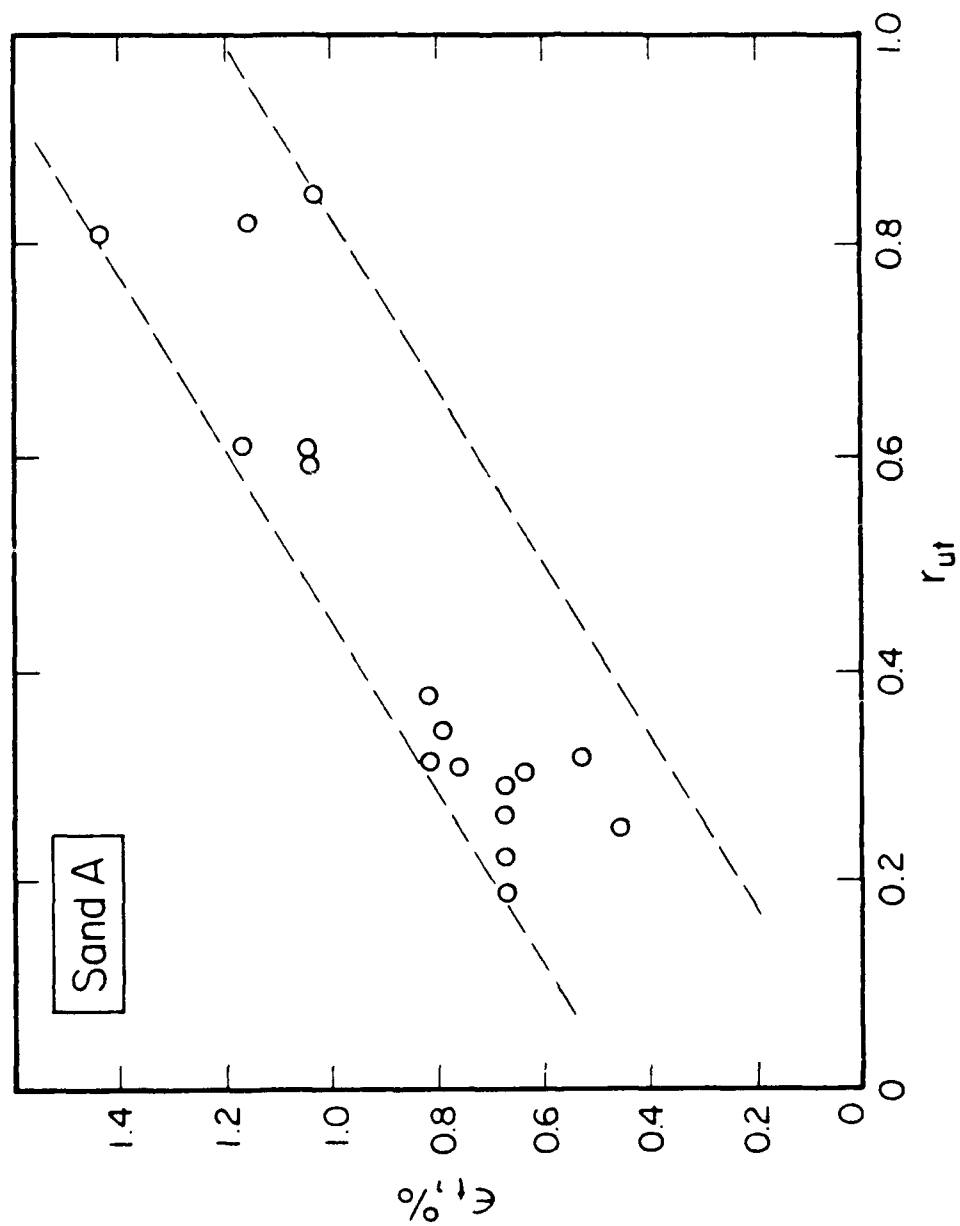
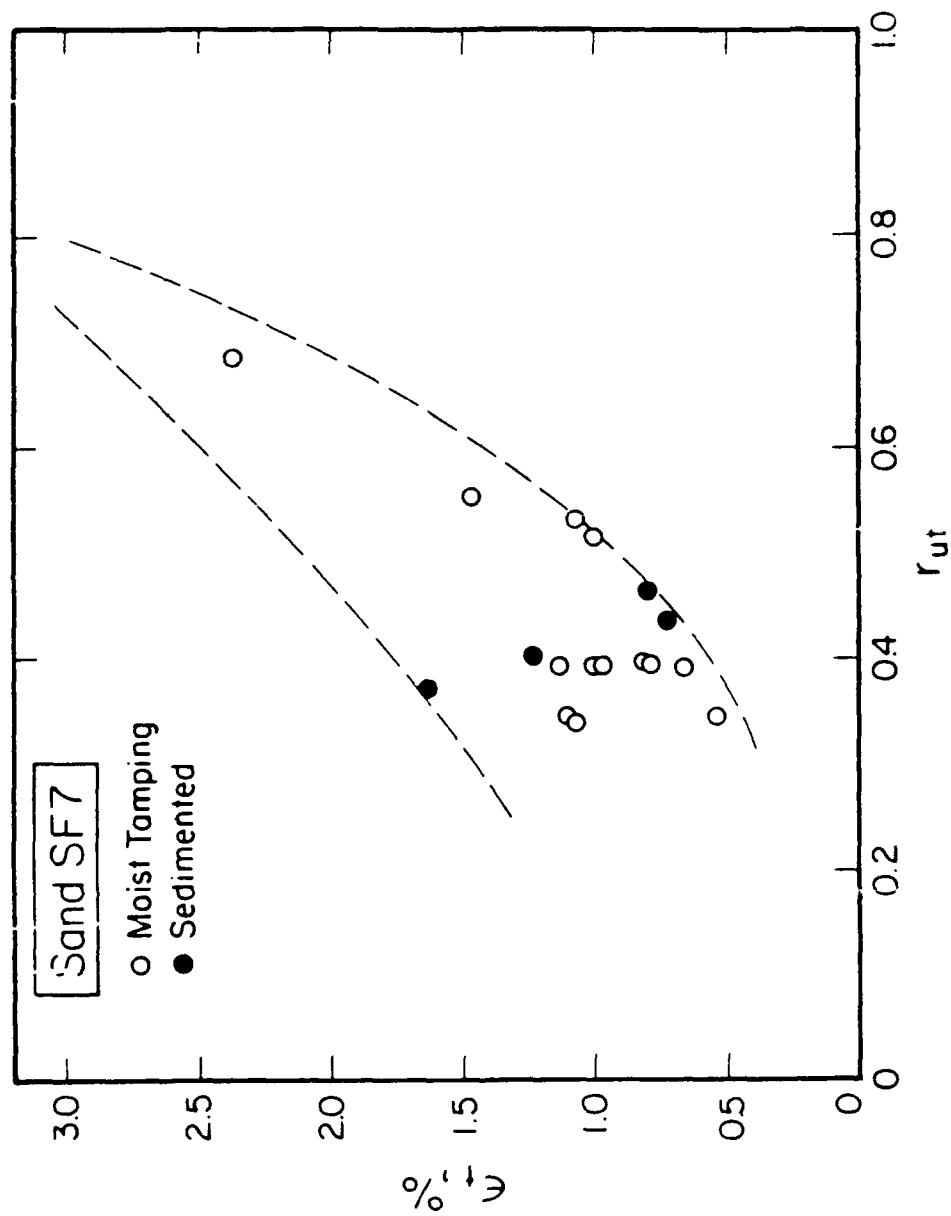


Fig. 7.67. Cumulative Axial Strain at Failure Compared to PWP at Failure for Sand A



**Fig. 7.68.** Cumulative Axial Strain at Failure Compared to PWP at Failure for Sand SF7

CHAPTER 8  
CONSIDERATIONS ON LIQUEFACTION  
FLOW FAILURE EVALUATION

8.1 General

Chapters 6 and 7 presented a number of experimental results pertaining to the pore pressure buildup and flow failure triggering of a very loose contractive sand subjected to undrained cyclic straining. A consistent picture was obtained from tests on several sands, as summarized in Section 7.4 and quantified by the model of Section 7.5. Therefore, it is reasonable to assume that this behavior is common to other contractive sands similarly loaded.

In this chapter, a number of liquefaction flow failure case histories are examined and contrasted with the experimental results already discussed. These case histories focus on situations involving slopes and embankments, and they include both seismically induced failures and static failures, for which more information is available in the literature. Static situations are relevant to seismic failure as in both cases, after triggering, the flow failure is driven by the monotonic driving shear stresses regardless of the causes triggering the failure. As a matter of fact, the Lower San Fernando Dam failed after

the earthquake had ended (Seed, 1979).

As essentially no measurements taken during a flow failure or just prior to it are available, only a qualitative examination and discussion is possible on the characteristics of the case histories. This case history evaluation has two main purposes in the context of this work: a) to examine aspects common to the failures which may throw light on the failure mechanism(s), including the basic question of how undrained the failures were; and b) to contrast the available observations with the predictions from the laboratory tests summarized in Section 7.4.

The evidence from field case histories is presented in Sections 8.2, 8.3 and 8.4, for both seismic and monotonic flow failures. Relevant shaking table and centrifuge model test data are discussed in Section 8.5.

It is possible to use the model of Section 7.4, in conjunction with shear strain time histories computed using a dynamic response analysis program, to evaluate the pwp buildup and triggering of an earth structure or foundation soil subjected to a specific seismic ground shaking. This is done in Chapter 9 for the Lower San Fernando Dam in the 1971 earthquake, and has also been applied by the authors to another project in a previous report (Dakoulas et al., 1988).

Ideally, these same computer programs and model could be compared and validated against the actual seismic case histories discussed in Section 8.4. Unfortunately, not enough information exists in most cases, with San Fernando being by far the best documented. This is a consequence of the unpredictable and uncommon nature of earthquakes, and of the large destruction caused when they happen and a failure occurs. The problem then becomes almost like a black box, in which the assumptions and developed models are used to compare their output against what happened in the field. If the agreement is good then the model gains a certain level of confidence which increases as more and more case histories are successfully predicted with it. The obvious problem is that by changing assumptions and conditions, an extremely broad range of possible answers can be achieved and sometimes opposite conclusions can be justified. The problem can be decreased to a certain extent by looking at as many different cases as possible, even if this has to be done qualitatively rather than quantitatively.

Section 8.6 summarizes important factors for seismic liquefaction flow failure evaluation obtained from the previous discussions on case histories and experimental results. Section 8.7 proposes a possible conceptual framework for the analysis and quantitative evaluation of

flow failure of a slope, earth embankment or foundation subjected to seismic shaking.

## 8.2 Evidence of Liquefaction Flow Failure

The first problem encountered in any compilation of case histories has to do with identifying the particular problem or phenomenon. In this case, it translates into being able to distinguish a liquefaction flow failure from other liquefaction phenomena.

The word liquefaction appears to have been first used by Hazen in 1920 to describe a slide that happened at Calaveras Dam (Hazen, 1920).

A number of different but related phenomena have also been called liquefaction. One of them relates to upward flow of water occurring through a soil deposit at the critical hydraulic gradient, also called a quick sand condition. Lateral spread failures in the field, involving large pwp and deformations but not flow as they involve relatively small driving shear stresses, are called liquefaction. Still another is associated to large values of excess pwp and strains created by undrained cyclic laboratory tests on medium-dense and dense dilative sands; however, in these tests the strains are limited and no flow failure occurs.

Several characteristics are typical of flow failures, and are clues to be looked for when searching for case histories. Based on the case histories presented herein, these characteristics are as follows:

1) In earth structures and slopes, the material typically travels a long distance because of a decrease in its shear strength, which makes it unable to sustain the load applied to it. It will continue flowing until the driving shear stresses are reduced. In liquefaction flow failures of foundations, the material does not travel such long distance but does suffer very large shear strains such as those present in total bearing capacity failures. This bearing capacity failure is due to the fact that the strength of the soil supporting the foundation suffers a decrease in its shear strength.

2) The path left by the liquefied material of an earth structure or slope leaves marks typical of a fluid of high specific gravity flowing down a surface. It flows around objects in its path leaving a sort of channel when it has ended.

3) From the time of initiation until its end, the failure usually occurs very fast, with durations ranging from seconds to a couple of minutes as a maximum, depending on the volume of material flowing and the soils present.

4) When the flow failure of an earth structure or slope has stopped, the flow surface slope is usually very flat. Typical values of this slope are as low as a few degrees, thereby indicating that the soils present suffered a decrease of shear strength.

5) During and after the failure, there is evidence of high values of pwp and large volumes of water present in the soils through which the failure is taking place. The presence of sand boils is typical of these failures.

Even though these characteristics exist, it is by no means an easy task to identify flow failures, because the evidence is often not clear. This evidence may be disguised and affected by the other conditions particular to a site. Therefore, each case history needs to be carefully studied by itself on an individual basis. Another problem that may arise is that the person originally describing the case history sometimes leaves facts out and emphasizes others depending on the perceived reasons for the failure.

### 8.3 Cases Involving Monotonic Flow Failures

There have been many more cases of liquefaction flow failures of large earth structures and slopes reported in the absence of seismic events than those involving earthquake shaking. These monotonic flow failures can be



subdivided into two categories:

- 1) Flow Slides in Coastal Deposits
- 2) Flow Slides in Hydraulic Fill Earth Structures

#### 8.3.1 Monotonic Flow Slides in Coastal Deposits

Loose silty fine sand deposits are easily created by nature and some spectacular flow slides have involved these deposits. A brief description of some of these cases are given in the following paragraphs.

##### Coastal Slides in Holland

In the Dutch province of Zeeland there is a group of islands separated by wide estuaries. The inhabitants of these islands have built dykes to guard themselves against high water tides. Many of these dykes have failed due to flow slides that occurred frequently between years 1881 and 1946 (Koppejan et al., 1948).

The soils involved in these failures were very fine and uniform silty sands, some of them with some small amounts of clay. In plan, the flow slides left a typical fan shape with the width increasing towards the coast. The slides develop through a gradual process, with intervals of few minutes between one shallow slide and the next, with the

silty sand mass sliding downward and flowing out. Since these disturbances occur almost completely underwater, their progress has been observed only when the disturbance progresses above the water line. When this happens, a crack appears a few meters inland followed by the slide of the mass behind the crack. This retrogressive sliding goes on for a period ranging from a few hours to a day, propagating at a speed of about 50 meters/hr. A profile through a typical flow slide is shown in Fig. 8.1.

The explanation which has been given for the initiation of these flow slides is that since they occur in periods of low tide, scouring at the base of the slope creates a very steep slope that stands for a short time until it fails. After failure, the remaining portion of the slope tends to expand slightly due to the decrease of lateral support, thereby causing a replenishment of pore water which takes some time. This water flow, in turn, induces in the soil seepage forces directed inwards, thereby creating temporary support of the sand skeleton. While this process is occurring and water is flowing in, the shear strength of the sand is decreasing due to swelling. Eventually the sand elements fail due to the fact that their density is below the critical density and the factor of safety of the slide drops below unity. The slides are then progressive in

nature and repeat itself as more and more slices flow out. After the slide has ended, no more slides are ever noted again through the sediments that flowed once (Koppejan et al., 1948). The surface of the flow slides after failure are characterized by slopes of 3 to 4 degrees.

Summarizing, this case history reveals the possible importance of dilation and void ratio increase in making a slope more contractive, or switching it from mildly dilative to contractive. It also shows that slides occur very easily at extremely low confining pressures since the failures are shallow. It also points out that the failure is progressive in nature. The flow slide involved silty sands and sandy silts deposited through water. The slope of the surface left after failure was extremely flat thereby indicating small values of shear resistance.

#### Flow Slides of the Mississippi River Banks

The Reid-Bedford Bend in the Louisiana side of the Mississippi river has been subjected to numerous flow slides of its banks (Senour and Turnbull, 1948). The soils present consist of clays as well as sandy and clayey silts. These flow slides resemble a cup or pocket shape near the shore with their maximum width adjacent to the bank. An example of a failure that occurred in June of 1947 is shown in Fig.

8.2. Since many of the failures happened when no one was present, a description of the progression of the failure does not exist.

Field investigation and laboratory test results showed that failure could not have occurred due to a soil slide through a failure plane, or due to scouring alone, and could only be explained by a flow failure. The first liquefaction flow failure tests ever run on the triaxial machine were done in connection with this problem, and they revealed that the shear strength of the sand could be greatly reduced; this strength reduction could explain the flow slides that had occurred. The flow failure explanation was further strengthened by the gentle slope at the end of the slide, the pocket shape plan of the failure scar and the lack of a shear slide mud wave at the toe of the slide. Centrifuge work modelling these flow slides of levees on the Mississippi River has been reported by Padfield (1978) and Schoefield (1980). These references, as well as Torrey and Weaver (1984) and Hadala and Torrey (1987) suggest that these failures occur in originally dense, dilatant sand slopes by a continuous "cascading" process of the sand grains close to the face of the slope.

### Flow Slides in Scandinavian Countries

Numerous cases of subaqueous slope failures have occurred in the Scandinavian countries, especially in the Norwegian Fjords. The "above water" appearance of the scars left by the flow slide is very small when compared to the volumes of soils involved below water (Terzaghi, 1956; Andresen and Bjerrum, 1968; Bjerrum, 1971). The soils involved in the slides were loose fine sands, silty sands and silty clays that had been deposited in post glacial deltas and estuaries.

Some of the flow slides that have been recorded occurred at Trondheim Harbor in 1888 and 1950, Helsinki Harbor in 1936, Orkdalsfjord in 1930, Hømmelvika in 1942, Follafjorden in 1952 and Finnvika in 1940 (Andresen and Bjerrum, 1968; Bjerrum, 1971).

An example is the slide in Helsinki Harbor shown in Fig. 8.3. An extension of the Helsinki Harbor was being built by placing sand underwater behind a small rockfill embankment that created a basin. Even though the rockfill was not completed and a 25 meter gap remained, the pumping of sand to fill the basin began. During the process of filling, a small slide occurred at the gap but work still continued. Shortly thereafter, a large flow slide of the hydraulically placed sand released about  $6000 \text{ m}^3$  through the

small gap in the bank. The displaced sand flowed out for 100 meters and deposited itself in a horizontal layer above the sea bed, leaving a failure surface after the slide of about 3 to 4 degrees in the basin.

The scenario for these flow slides proposed by Bjerrum (1971) is as follows. It starts as an initial slide, caused usually by the low tide or by accumulation of sediments that loads the banks of the fjord. After this initial slide, more slides occur as the flowing mass leaves the faces of the scarps unsupported. These faces will later fail and flow away as the shallow slide develops retrogressively when the different slices of sand fail. This retrogressive flow slide continues until the slope of the material left standing is very low.

Summarizing, it can be seen that this scenario is very similar to the mechanism proposed by Koppejan et al. (1948) for the Zeeland flow slides. Undrained triaxial tests on a fine sand from Norway showed that very small shear resistances could be generated if the samples were very loose, and thus the reason for the flow slide was tied to the loss of strength of these sands at small strains (Andresen and Bjerrum, 1968; Bjerrum et al., 1961).

### 8.3.2 Monotonic Flow Slides in Hydraulic Fill Earth Structures

Flow slides have occurred in a number of embankment dams constructed by the hydraulic fill method. Five static dam failures will be presented in this section in which major or total failures happened due to liquefaction flow failure. The dam failures are Necaxa Dam in 1909, Calaveras Dam in 1918, Alexander Dam and Saluda Dam in 1930, and Fort Peck Dam in 1938.

#### Necaxa Dam Failure

Construction of the Necaxa Dam by the hydraulic fill method started in 1907. On May 20, 1909, about 550,000 cubic meters of the upstream portion of this hydraulic fill dam slid into the reservoir (Schuyler, 1906, 1909). A sketch of the dam with its failure surface is shown in Fig. 8.4. It was to be the tallest dam in the world when completed, with a final height around 60 meters and upstream and downstream slopes of 3 on 1 and 2 on 1, respectively.

Prior to the accident, the reservoir had been emptied due to draught, whereas the central pool on top of the dam was raised very fast in order to speed construction. The gap left by the slide in the upstream slope was about 120 meters long, roughly equivalent to about one-third of the

length of the dam. The above two facts, together with the type of volcanic material used for the upstream section, led to the hypothesis that the failure had occurred due to the pressure exerted by the unconsolidated central core which would have exceeded the strength of the soil in the upstream slope. The failure occurred at 6.05 a and the time needed for the development of the slide was said to have been about one minute. A detailed description of the slide initiation does not exist, but there is evidence of prior dam movement because "bulging or mammaling of the upstream slope" was observed before failure (Hazen and Metcalf, 1918). Unfortunately, four workers caught in the flow slide were drowned (Schuyler, 1909).

Summarizing, the failure of this tall dam shows that large values of driving shear stress can cause liquefaction flow failure by monotonic loading. It also shows that some straining occurred prior to the failure. The materials involved were cohesionless silty sands and sandy silts deposited through water by the hydraulic fill process.

#### Calaveras Dam Failure

Calaveras Dam in California was to be the tallest dam of its time with a final height of 73 meters. Construction of this hydraulic fill structure started in 1914, but on



March 24, 1918, the central section of the upper part of the upstream side and core of the dam slid into the reservoir (Cleary, 1914; Hazen and Metcalf, 1918; Hazen, 1918).

A sketch of the dam and its failure surface is shown in Fig. 8.5. The slide happened in the morning, probably close to the east side of the dam; the dam started to move towards the reservoir and part of it rotated horizontally like a door hinged vertically at the abutment. The dam revolved about  $30^{\circ}$  from its original direction, leaving an opening. Before the movement had gone very far, the material in the core and central pool began to come through this opening as the central part of the dam was released and flowed through the gap. As the central pool level fell, the material from the core appeared to flow towards the center and out into the reservoir through the opening (Hazen and Metcalf, 1918). Witnesses said the following (Hazen, 1918):

"...the material was carried forward on a good lubricant, and that the lubricant first became used up or expelled near the center of the dam and left the higher parts of the dam on solid bottom while there was still lubricant to carry forward the lower and more advanced portions."

This observation was in disagreement with the inspection of the dam after the failure where it was noted that the material that moved was "hard and solid and apparently entirely outside the range of materials that

would flow" (Hazen, 1918).

Many movements occurred in the dam during construction and most of them took place in the downstream embankment, as far back as a year before the failure. On June 18, 1917 the deformations of the upstream part of the dam were estimated to be 18 inches horizontally and in the following 12 hours an additional 6 inch movement was observed. With these movements, cracks were observed for a distance of 700 ft across the dam on the upstream concrete facing. Cracks were also observed at an angle of  $45^{\circ}$  with the crest line, converging towards the reservoir. Because of these movements, sluicing was stopped and almost instantly the rate of movement decreased until they practically ceased. The sluicing would be resumed again until the movements were considered to be excessive and then it was stopped; this cycle was repeated twice during construction of the dam. On the day before the failure of the dam, the horizontal movement totalled about 4 feet (Hazen and Metcalf, 1918).

The failure of the dam was observed by people on the dam and represent a very interesting description of a flow failure (Hazen and Metcalf, 1918):

"The final movement at the time of failure on Mar. 24, 1918 was very rapid. The greater part of it probably took place within a space of not more than five minutes. The reinforced-concrete outlet tower was thrown forward

into the reservoir. The noise and splash and waves of this drew attention of those who were nearby to what was going on. Alice Epsy, the nine-year old daughter of the construction engineer, saw the tower fall. Her attention was drawn to it by noise, which some of the men also noticed. Looking toward the dam she saw the tower swaying back and forth for a moment, after which it fell in a direction straight away from the dam. It has not been seen since.

It seems likely that the first considerable movement was a drop in the level of the central pool on the top of the dam, accompanied by a slow lifting, or moving forward, of the surface of the upstream toe above the water line. The lower part of the toe had been paved with concrete, and this extended about 13 ft. above the water level. Above that point the face was covered with heavy stone riprap. The top of the concrete formed a conspicuous line, and observers say this seemed to rise several feet. This may have represented an actual rise, or it may simply have been a lifting at the edge by the forward movement of the mass. There was then a foreward movement of the whole central section. The section that moved was about 700 ft. long."

"... when the material was released it started to flow almost like water. At first it came through the narrow breach as a turbid cataract with a steep slope, but the opening rapidly widened and the slope flattened until the center was drained down to within a few feet of the water level in the reservoir. Probably within five minutes the rapid movement was over, although the clay continued to flow at a reducing rate for some time. The more solid material of the upstream part of the dam, consisting largely of heavy rock fill, had then moved foreward and downward and had filled a space for several hundred feet beyond where the toe had been. This material must be piled up to a height in places of 70 ft., and it stands high above the water and far into the reservoir."

Later, this failure was reanalyzed (Hazen, 1920), and it was found that failure must have occurred due to a condition where the shear strength dropped significantly because of trapped water pressures in the voids of the sand,

turning the soil mass into something like water. This represents the first explanation of liquefaction flow failure ever given.

Summarizing, this case history shows that volume changes took place prior to failure accompanied by movement of the dam. The volume changes were swelling somewhere in the dam probably in the upstream part. The soils that failed were silty sands deposited through water. The failure occurred due to a decrease in the shear strength of the soils in the upstream portion of the dam until they could no longer support the static shear stress due to the weight of the dam. The driving shear stresses caused the large unidirectional deformations.

#### Saluda Dam Failure

Saluda Dam was a 200 ft. high dam built using semi-hydraulic fill methods on the Saluda River in South Carolina. At 6.05 a.m. on Feb. 19, 1930, a section of the downstream portion of the dam slumped and broke out releasing the water in the segregation pool. A sketch of the dam is shown in Fig. 8.6. The water took a total of 20 minutes to flow out and left a 300 ft. wide washed out area where 125,000 cu. yds of the downstream embankment rushed out.

Summarizing, a great deal of information was not available concerning the propagation of the flow failure, except for the fact that some small movement of the slope occurred in a narrow area right before the failure (Engineering-News Record, 1930a).

#### Alexander Dam Failure

On March 26, 1930 the hydraulic fill Alexander Dam in Hawaii failed due to flow failure of the downstream slope. The dam was nearly 80% completed and was to be a trapezoidal embankment 125 ft. high and 620 ft. long. A sketch of the dam is shown in Fig. 8.7. About 257,000 cu. yd. of soil flowed out with the slide causing the loss of 6 lives. The failure occurred suddenly without warning, although in the previous 2.5 months, a total of 0.23 ft of horizontal movement had been noted in the downstream side; and ten days before the break drainage through the area that failed came to a halt for no apparent reason (Engineering-News Record, 1930b).

The best description of the failure was given by the engineer in charge of the work at the dam at the time (Engineering-News Record, 1930b):

"At 3.45 p.m., March 26, 1930, just after the men had finished building the downstream dyke and had left the

dam, a major slide occurred. I had just completed a trip across the downstream beach where sluicing was going 80 ft. from the south abutment. Going to the top of the bank I saw Natao talking with his son in the center of the dam on the upstream beach, and as I wished to give him some instructions regarding the night's work, I met him at the junction of the embankment and the top of the dam. While indicating some detail by tracing a design of it in the ground, I saw him give a violent start. I was facing northeast (slightly upstream), and upon turning my head saw a section of the downstream flume, probably that beginning about 150 ft. from the north abutment, sink slowly down out of sight. There appeared to be a pause, after which the core pool went down and out."

"The overhanging upstream beach with its flume also went down, the upper portion going down the gulch, while that underlying remained in the dam."

"I estimate the time of the entire occurrence from the time the downstream flume was first noticed by me as sinking, to the large slough of the overhanging upstream beach, at less than 30 seconds."

Some witnesses said that the downstream bank bulged out immediately over the rockfill at the toe and moved outward with a gush of liquid mud. They also say that this gush occurred much before any movement was observed in the core pool, which remained intact until it was released due to the portion of the dam sliding out.

Another interesting observation was the fact that the gush of fluid mud that smashed against the valley wall was not core material, and could have only come from the downstream portion of the embankment that was hydraulically placed. Therefore large values of pwp must have been present there.

Summarizing, this case history clearly shows that large pore pressures are present in a flow failure. This is represented by the gush of liquid mud which originated in the downstream portion of the embankment and not in the core. The failure of the core of the dam came later as the downstream portion of the dam slid out and therefore is a consequence of the sliding and not a cause of it. The failure occurred due to a decrease in the shear strength of the silty sands which at the time of failure could not support the static shear stresses imposed by the dam. These driving shear stresses caused the large deformations in one direction.

#### Fort Peck Dam Failure

Fort Peck dam was being constructed, in Montana, using hydraulic fill methods when, on September 22, 1938 a major flow slide in the upstream portion of the dam killed 8 men and released 8,000,000 cu. yd. of fill. The dam was planned to be about 200 ft. high, 3000 ft. wide and 9000 ft long along the crest and would have been at completion one of the largest dams in the world containing approximately 100,000,000 cu. yd. of hydraulic earth fill. A sketch of the dam is shown in Fig. 8.8 (Engineering News Record, 1938; Middlebrooks, 1942).

The failure occurred before the dam was finally completed and with reservoir partially filled. The part of the dam involved in the failure was a 1700 ft. long section of the upstream shell, near the east abutment, which slid into the reservoir. The progress of the failure (Casagrande, 1965) tells us that the movement started by a bulging of the upstream slope near the location of the slide with a simultaneous lowering of the core pool. Then transverse cracks appeared, and these later widened forming a gap as a portion of the slope started to move and rotate in a manner similar to a door hinged at the abutment. Through this gap the core pool rapidly drained. Some material was found to have travelled as much as 1500 ft. from their original position as the material flowed and came to rest with slopes of 1:20. Intact blocks of soils were carried by the flowing sand as if they had been floated. The flowing sand was found to be still in a very quick condition even after 10 days following the failure, and the surface was dotted with sand boils, some of which were still discharging sand and water.

Historically, this dam is very important for liquefaction flow failure studies because it marks the beginning of the use of the critical density concept in flow failure evaluation (Engineering News Record, 1938;



Middlebrooks, 1942) Due to its dramatic failure, a nine-man board was appointed to investigate the slide; among them was Casagrande who with few others suspected that the failure was due to liquefaction (Gilboy, 1942; Casagrande, 1965).

The first triaxial tests used for defining the critical void ratio of a sand were performed in this project, and they appeared to show that the silty sands involved were denser in situ than their critical value. These were triaxial compression drained tests. Because of this, liquefaction flow failure was thought not to be the fundamental reason for the flow slide. Instead, the main reason given by the panel for the flow failure was sliding through the bentonite seams of the Bearpaw shale underlying the dam.

Casagrande (1965) later said that it was impossible to determine the critical void ratio using triaxial tests and the prevailing knowledge at the time. Even though the tests then showed that the shell material could not have liquefied, he never abandoned the notion of liquefaction, and always stated that liquefaction was the cause of failure, which had been started by movements of the Bearpaw shale due to filling up of the reservoir. Some of the evidence he gave for this were:

1) Due to the topography of the dam after the slide, it was obvious that the shear strength decreased with increasing strains to very low values.

2) The largest displacements occurred where the thickness of the foundation sand was the greatest.

3) The speed and distance covered by the slide could not have been a product of local shale failure alone; this probably triggered liquefaction flow failure of the loose sands.

4) Movements were noticed for a number of hours before the slide in the surface of the fill; therefore, the sand must have been straining. As discussed in Chapter 7, a certain amount of straining is a necessary condition for liquefaction flow failure to trigger.

5) The sliding mass stretched out longitudinally as well as radially because it was riding on a liquefied layer that was getting thinner.

This case history represents the best documented case of a monotonically induced liquefaction flow failure. The triggering loads were generated by local shear failure of the bentonite seams in the Bearpaw shale underlying the dam.

### Mine Tailing Dam Failures

Mine tailing dams are especially susceptible, and they have experienced liquefaction flow failure because they are very loose and traditionally they have not had a high level of engineering (Brawner and Campbell, 1972; Smith, 1969. 1972; Jeyapalan et al., 1983a, 1983b). Unfortunately, no detailed information of these dams are usually available, although most of them share a number of features in common. These commonalities include great heights, loose and saturated very fine silty sand deposits achieved by water pluviation, and large available quantities of water.

### 8.4 Cases Involving Seismic Flow Failures

There have been fewer cases of liquefaction flow failure of large earth structures occurring due to earthquake shaking. When evaluating case histories involving liquefaction of earth structures, a difference must be made between those involving flow failures and those involving cyclic mobility, even though both can be associated with large deformations and high values of pwp. The deformations in cases of cyclic mobility are a result of both the cyclic and driving shear stresses, and these deformations generally stop after the earthquake has ended. These movements are then an accumulation of the strains

produced by the different elements during cyclic loading. On the other hand, the deformations involved in cases of liquefaction flow failure are due mainly or exclusively to the driving shear stresses. They are dependent on the cyclic stresses to build up the pwp and trigger the failure but only need the driving shear stresses to push the flow failure. The cases shown here will be those considered to have involved liquefaction flow failure rather than cyclicly induced deformations; however, the line differentiating both of these problems is sometimes not so well defined.

The liquefaction flow failure cases to be presented fall in the following categories:

- 1) Flow Slides in Natural Deposits
- 2) Flow Slides in Hydraulic Fill Earth Structures

#### 8.4.1 Flow Slides in Natural Deposits

In the cases to be described in this section a sand layer liquefied and the overlying material flowed on top of it with the soil mass being moved mainly by the driving shear stresses and not by the seismically induced cyclic stresses. In some cases the movements had not even started when the shaking ended and developed completely under the driving static shear stresses alone. A similar but

different problem exists with liquefaction in almost level ground where lateral spreading occurs; however, the deformations there are caused by some combination of cyclic and driving shear stresses, and the movements generally stop after the shaking ends.

Liquefaction flow failure cannot occur in level ground in the free field even if the soil is contractive, because in this particular case the driving shear stresses are zero or very small. However, once a structure is placed on it the conditions change and flow failure becomes possible. This points out that driving shear stresses are a very important factor in a liquefaction flow failure. Sand boils are associated with liquefaction in level ground even when flow failure cannot occur; therefore, the presence of sand boils alone cannot be identified with the flow failure phenomenon. On the other hand, sand boils are representative of loose sand with high pwp and large volumes of water being expelled, and the existence of a structure in such soils (making it non-level ground) can cause large deformations or even flow failure.

The experimental tests results presented in this work showed that if  $K_c$  is large, very small values of the triggering pwp ratio  $r_u$  are needed ( $r_{ut} \approx 0.2$ ) for

liquefaction flow failure, with this value of  $r_{ut}$  increasing as  $K_c$  approaches 1. These low values of  $r_{ut}$  are probably significantly smaller than that needed for sand boils to form. Therefore, in principle liquefaction flow failure in contractive soil could be triggered even if there is no manifestation of sand boils nearby. However, after triggering, a soil element would reach conditions with high values of pwp such as  $r_u = 0.95$  during steady-state. After the flow failure has come to rest these large values of pwp could form sand boils such as in the case of the Fort Peck slide (Casagrande, 1965).

Some of the best known and spectacular flow failures will be summarized in the following paragraphs. They include the slides at Valdez and Seward (Alaska, 1964), Lake Merced (California, 1957) and Lake Rinihue (Chile, 1960).

During the Alaska earthquake of 1964 very large flow slides occurred at different locations. In Valdez, very large masses of soils slid underwater together with the waterfront area, both of which were carried by the slide. An artist's conception of the flow slide is shown in Fig. 8.9. In Seward, the flow slides involved 4000 ft. of coastline where fuel storage tanks, warehouses, boat harbors and docks that were situated on the shoreline completely disappeared under water (Seed, 1967).

Flow slides also occur in smaller proportions where the soil conditions are appropriate for them; such was the case of the flow slides of the highway bordering Lake Merced during the 1957 San Francisco earthquake. The highway was built on fill resting on a deposit of loose saturated sand. The magnitude of the translations were characteristic of flow slides, as the highway disappeared in some places under the lake (Seed, 1967).

Flow slides have also occurred in clay deposits containing many seams of silt and fine sand. This was the case of the slides on the San Pedro River near Lake Rinihue during the Chilean earthquake of 1960. One of these, shown in Fig. 8.10, involved 30,000,000 cu. yd. of soils which moved 1000 ft. horizontally during the failure. Studies performed on this slide revealed that they were produced by liquefaction of the many silt and sand seams in the clay deposit (Seed, 1967).

Summarizing, these cases of liquefaction flow failures in natural deposits show that large amounts of deformation in one direction are caused mainly by the driving shear stresses and a decrease in the soil shear strength. This drop in shear strength is due to the pwp buildup of sand and silty sand deposits as a consequence of the seismic stresses. Therefore, liquefaction flow failure can be

separated into two parts: (i) one of pwp buildup caused by seismic stresses which lead to a reduction in shear strength of the sand mass until it can no longer carry the static shear stresses, and (ii) a second part of unidirectional large displacements as a consequence of the driving shear stresses exceeding the residual strength available in the sand mass.

#### 8.4.2 Flow Slides in Hydraulic Fill Earth Structures

Hydraulic fill dams and mine tailing dams have been particularly susceptible to liquefaction flow failure. Other types of dams have suffered lesser degrees of failure, usually not flow slides but rather permanent deformation problems. Unfortunately, eyewitness detailed account regarding the triggering of flow failure is missing from most of the cases surveyed; in only one case (the Lower San Fernando Dam) is adequate geotechnical field work available for further study.

##### Lower San Fernando Dam (1971)

The flow failure of the upstream slope of this hydraulic fill dam during the 1971 San Fernando Earthquake (Magnitude 6.6) represents the best documented case history



of seismically induced liquefaction flow failure of an earth structure. This dam was built by hydraulic fill methods at the beginning of the century using the best available techniques, and when finished it was a 140 ft. high. In 1966 it was analyzed using pseudo-static methods for earthquake effects and was found to be safe. The 1971 earthquake produced peak ground surface accelerations in the free field of 0.55 - 0.60 g and caused a major flow slide of the upstream side of the dam leaving only 5 ft. of freeboard. Had this dam failed, 80,000 residents downstream from the dam would have been killed or seriously hurt; they were evacuated until the reservoir elevation was dropped to a safe level. The failed area of the dam had large pieces of cohesive materials that broke as the underlying soil liquefied; this liquefied soil flowed between the large chunks of soil and disappeared into the reservoir bottom. No available information concerning the slide mechanism is available, except for the fact that the slide occurred about 26 seconds after the shaking ended and the slide itself took about 50 seconds to occur (Seed, 1979). This implies that the flow failure was driven by the static weight of the dam and was not due to the seismic loads. However, clearly it was the earthquake which caused enough pwp buildup to soften the soil and made the flow failure possible. A sketch of

the dam before and after the slide is shown in Fig. 8.11, and this case history will be studied in detail in the next chapter. It is also interesting to note that less than 2 miles from the Lower San Fernando Dam is the Upper San Fernando Dam, with both of them making the Van Norman Lake complex. This other dam was also built by the hydraulic fill method at about the same time as the Lower Dam and had a final height of 80 ft. when finished. The Upper Dam did not experience flow failure although it did suffer severe longitudinal cracks in the upstream side. These cracks were a product of the dam moving downstream about 5 ft. and settling about 3 ft (Seed et al., 1973, 1975).

Summarizing, this case history clearly shows that the flow failure was driven by the static weight of the dam and was not due to the seismic loads because it failed after the earthquake had ended. The failure occurred because of the softening of the soil as the pwp increased due to the seismic strains. More information on this case history will be given in Chapter 9. The liquefied area was a narrow wedge in the upstream zone of the dam, and when this liquefied material flowed out it carried the overlying cohesive soils broken into more or less intact blocks floating on it.

### Sheffield Dam Failure (1925)

On June 29, 1925 the Santa Barbara Earthquake caused the Sheffield Dam to fail by what is believed to be liquefaction (Fig. 8.12). Estimates of the free field peak ground surface acceleration experienced by the dam was about 0.15 g, and the earthquake must have lasted between 15 and 18 seconds (Seed et al., 1969). Failure occurred due to sliding of the whole dam along a horizontal surface near the base of the embankment. This sliding caused the whole dam to translate downstream and rotate horizontally as if it were hinged on one of the sides. Since a large section of the dam moved as a rigid body, the plant growth of the downstream slope was not disturbed. Unfortunately, there were no witnesses when the failure occurred but a survey a few days later accurately described the failure (Willis, 1925):

"The foundations of the dam had become saturated and the rise of water as the ground was shaken formed a liquid layer of sand under the dam, on which it floated out, swinging about as if on a hinge."

The floating of large pieces of soil masses such as that involving the Calaveras, Fort Peck and San Fernando Dams appears to be characteristic of dams having large liquefied zones underlying stronger more cohesive materials. Fig. 8.12 shows a profile of the dam before and after the

failure where the large section of the dam that moved into the reservoir can be seen.

Summarizing, this case history shows the effect of the decrease in shear strength of a horizontal layer near the base of the embankment. When the driving shear stresses became larger than the shear strength of this critical layer, a flow failure driven by the static stresses, ensued. The decrease in shear strength was probably due to an increase in pwp as a consequence of the cyclic stresses.

#### Mine Tailing Dams in Chile (1965)

On March 28, 1965 a strong earthquake (Magnitude 7 to 7-1/4) shook some mine tailings dams in the central portion of Chile. In one tailings dam, the released material flowed down a valley towards the town of El Cobre where it killed more than 200 people. The failure was identified as being caused by liquefaction of the hydraulically deposited core material which caused breaching of the exterior embankment creating a gap where the material flowed downstream. The materials involved were very fine silty sands and nonplastic silt. A total of 12 tailings dams ranging in height between 5 and 35 meters failed leaving characteristic semicircular failure scarps. In one case, the flowing mud came rushing out and climbed 8 meters on the mountain in front of it, and

later flowed down the valley. In another case, eyewitness reported hearing a sound like an explosion followed by sounds like a waterfall, indicating the violent nature of the flow slide. In many of the cases it was observed that chunks of dry exterior crust floated out on the liquefied mud. The presence of large values of pwp was evident in the numerous silt and fine sand boils present in the material that flowed and on the material that stayed on the dams. Fig. 8.13 shows the profile of one of the failed tailings dams (El Cobre Old Dam), before and after the earthquake. It is believed that all the failures occurred during the shaking (Dobry, 1965; Dobry and Alvarez, 1967).

Summarizing, these case histories point out that mine tailing dams are particularly susceptible to seismically induced liquefaction flow failures. The reason for this is that these earth structures are composed of extremely loose and saturated silty sand deposits created by hydraulic deposition. These silty sands were probably contractive and the seismic stresses caused sufficient pwp buildup to make the driving shear stresses larger than the shear strength of the soil; therefore  $FS < 1$ .

### Mochikoshi Tailings Dams (1978)

The Izu-Ohshima-Kinkai earthquake (Magnitude 7.0) struck the central portion of Japan on January 14, 1978. The main shock was followed by numerous aftershocks, the largest of which happened 18 hours later and had a magnitude of 5.8. During these earthquakes, the Mochikoshi Tailings Dams of a gold and silver mine failed due to liquefaction flow failure of very fine silty sand and non-plastic silt soils (Okusa and Anma, 1980; Okusa et al, 1980; Marcuson et. al, 1979).

The tailings dams were composed of three dykes, with two failing as shown in Fig. 8.14. Dyke No. 3 did not suffer any failure. Dyke No. 1 failed right after the main shock, releasing 80,000 cu. meters of the dike material through a breach that was 73 meters in width and 14 meters in height. The valley along which the tailing material had travelled showed white tailings-water splash marks on the trees and branches that were as high as 30 meters. What was left of the pond showed a gentle slope of about 10°. A worker was swept away by the liquefied tailings and his body was found 300 meters downstream.

Dyke No. 2 slowly broke 5 hours and 20 minutes after the main aftershock and the breach of the dyke had dimensions of 12 meters high and 55 meters wide, through

which 3,000 cu. meters flowed out. Again it is clear here that the flow failure was driven by the static shear stresses. It has been suggested that the failure occurred by propagation of pwp throughout the mass after the earthquake, causing the factor of safety for the failure surface to drop continuously from the end of the earthquake to a value of unity.

Many sandy silt volcanoes were found near the pond of the Dyke No.2 after the flow failure; sand boils were also observed in the nearby Hirayama and Norosawa dams, where flow failure did not occur.

Summarizing, these case histories point out again that liquefaction flow failure is driven by the static shear stresses and not by the seismic loads. This is very clear in the tailings dam that failed more than 5 hours after a strong aftershock. Another tailings dam nearby failed by liquefaction flow failure during the earthquake. The fact that one of the tailings dam suffered the failure so long after the aftershock suggest some level of drainage involved. An explanation based on pwp redistribution causing the FS to decrease appears to be the main reason for this failure.

## 8.5 Cases Involving Physical Model Studies

Liquefaction flow failure by ground shaking has also been attempted on physical model studies using shaking table and centrifuge models; unfortunately, these efforts so far have been unsuccessful. This section will examine why flow failure has not been achieved, and will discuss some relevant results concerning fabric.

### 8.5.1 Shaking Table Tests

Some interesting results of a foundation on a liquefiable sand deposit were presented by Huishan et al. (1984); the observations showed that there is a fundamental difference between sand deposits that are homogenous and those having stratification. The stratification was achieved in these tests by water pluviation, similarly to the sedimentation method used herein to prepare specimens for the CyT-CAU tests (see Chap. 4); therefore, each layer had two sublayers, one of coarser material underlying one of finer material.

The shaking table tests on homogenous, normally consolidated sand deposits produced results that were consistent with others with similar conditions (e.g., Florin



and Ivanov, 1961). That is, liquefaction ( $r_u = 1.00$ ) starts at the upper part and then proceeds downward in what has been called the liquefaction front. The pwp buildup was almost the same for the same elevation, whereas it increased almost linearly from top to bottom and moved up. For the sand deposits that were denser in the top because of compaction of the surface, the opposite occurred, liquefaction started from the bottom. The dissipation of pwp occurred in the same fashion for both types of homogenous deposits; dissipation began from the bottom of the soil as the consolidation front proceeded upwards. This upward migration of pwp caused the pwp of the upper strata to continue increasing (Huishan et al., 1984). This mechanism might explain the tilting of the Kawagishi-cho apartment buildings during the Niigata earthquake of June 16 1964. These buildings took several minutes to overturn and the directions of tilting (some of them as much as 60° from their original position) were not equal (Kawakami and Asado, 1966). The excess water from the deeper sands started to flow upwards thereby causing the pwp of the upper strata to keep increasing. This also probably increased the volume and thus caused a drop in the steady-state shear strength of the sands under the building foundations. When the decreasing shear strength of the sands approached the

driving shear stresses due to the foundation, a bearing capacity failure ensued. This points out the importance of water redistribution, caused in this case by the upward flow of water.

A total different picture occurred in Huishan's shaking table tests when foundations were placed on the surface of the deposits. The pwp distribution was no longer the same at the same elevation and it appears to have been greatly influenced by the consolidation and driving stresses induced by the foundation.

In the model with the foundation resting on the stratified soil, the pwp increased and caused the formation of a water interlayer between the sublayers of coarse and fine materials. These water interlayers grew and caused the soil overlying it to be uplifted. Other water interlayers at the same elevation sometimes joined together to form longer water interlayers. When the thickness of the water interlayer reached a certain value, the water burst out through the overlying stratum and created sand boils. A simplified sketch of the conditions in one of these tests is shown in Fig. 8.15. The same as with the tests on homogeneous deposits: the values of  $r_u$  directly under the foundation were smaller than those in the free field at the same elevation; therefore, both the confining and driving

shear stresses influence the pwp buildup. If the foundation is resting on a homogenous sand deposit, the results are quite similar except that water interlayers do not form and the sand boils are smaller in size. It could be speculated that these larger sand boils in the stratified sedimented sand model carry more water to the surface than that expelled by the homogeneous deposit. This larger amount of water may be perhaps related to the significantly higher void ratios achieved by the sedimentary fabric (see Section 6.2).

This phenomenon of the water interlayers was confirmed in the investigation herein by a simple procedure in the laboratory consisting of pouring silty sand in a graduated glass cylinder full of water. If the amounts of soils added are the same and they are poured at the same time intervals, then a stratified system with layers of equal height is formed. By slight tapping of the cylinder an immediate buildup of pwp is noted, because formation of water interlayers start. Even after shaking has stopped, these water interlayers grow from the flow of water from other soil elements. Other water interlayers at the same elevation might also join to form one very large interlayer. At one point in time, this large water interlayers suddenly break up through the overlying stratum and a connection is

established between two water interlayers at different elevations. After this, the water of the interlayers proceeds at a faster rate upwards until the surface is reached where it suddenly blows through. It continues to do so for long periods of time (3 minutes) until all the water in the interlayer has been expelled.

The above descriptions of shaking table and glass cylinder experiments point out that the water interlayers are formed due to the stratification of the sand deposit, and that this stratification appears to facilitate the formation of sand boils. It also clearly shows that the formation of water interlayers is related to the amount of water being expelled by the surrounding elements into this interlayer. Even though no flow failure was observed in the model foundation cases, the experiments show that consolidation stresses and driving shear stresses do affect the generation and distribution of pwp.

The reason why flow failure was not seen in these tests was because the soils were too dense and/or because there were not enough driving shear stresses to drive the failure. However, it is possible to speculate that if these conditions had been different, the failure surface could have passed through these water interlayers and could have a factor of safety less than one, thus precipitating a flow

failure (Seed, 1987).

Summarizing, the shaking table test results point out the importance of driving shear stresses on pwp distribution in a sand body. The presence of the model foundation altered the generation and distribution of pwp. The model studies also showed that the fabric of the silty sand deposits also affects the distribution of pwp throughout the soil mass. In particular, water interlayers formed between some layers of the stratified deposit. The water interlayers clearly had an effect on the formation of sand boils. No liquefaction flow failure was noticed in these tests. Flow failures due to the formation of loose zones between layers of the same materials or among layers of different materials has been identified as Mechanism B (National Research Council, 1985).

#### 8.5.2 Centrifuge Tests

The centrifuge has been unable to create a seismically induced liquefaction flow failure of an earth structure, even though a number of attempts have been made to achieve it.

The first centrifuge tests that tried to simulate seismically induced flow failures in earth embankments were

done by Schofield at Cambridge University, England (Dean and Schofield, 1983). In this initial work, two centrifuge models of submerged embankments were subjected to cyclic loads using the shaker of the Cambridge Centrifuge (also called the 'bumpy road apparatus'). The two models were homogenous saturated sand embankments with water (silicon oil in the tests) on both sides of the embankment, which rested on an impermeable rigid foundation. Both models were supposed to approximate the 5 meter high prototype structure shown in Fig. 8.16. The piezometric readings did show that the values of pwp rose to their maximum attainable value (on the  $K_f$  line) during the shaking, thereby indicating pwp triggering. However, no flow failure was noted in these tests because the embankments were quite dense, with  $D_r = 50 - 80\%$ . At these values of relative density and for the stress levels involved, almost all sands are dilative. However, the dyke did suffer some slumping due to the cyclic stresses, as shown in Fig. 8.16.

The next series of centrifuge models involved testing homogenous compacted silt embankments resting on a foundation layer of Leighton Buzzard Sand and having steady seepage from upstream towards the downstream side (Schofield, 1984). The model section is shown in Fig. 8.17. Therefore, two very important conditions were brought into

play here: the interaction of the foundation and the embankment, and the effect of steady-state seepage on pwp buildup. The introduction of these factors showed that the dyke experienced rocking, causing the pwp at each end of the embankment to be out of phase  $180^\circ$  during the earthquake; and that the patterns of pwp after the end of the earthquake were very much affected by the steady-state seepage. The dyke model also cracked extremely, as can be seen in Fig. 8.17. The patterns of pwp during and after the earthquake are shown in Fig. 8.18, where it can be seen that large gradients were generated at the downstream toe of the dyke due to the pwp redistribution. That is, the seepage forces generated by the excess pwp were added to those due to the steady state seepage and made the stability conditions worse than before the earthquake. Despite the cracking of the dyke, the large hydraulic gradients, and the large values of pwp generated in these tests, no flow failure developed because the foundation sand had a  $D_r$  larger than 50%.

The reason for liquefaction flow failure not having been observed in these centrifuge tests is that the sands involved have not been contractive in any of the experiments. In order to prove this, a centrifuge model of a dyke made of cohesive material resting on a loose foundation and subjected to shaking (Habibian, et al., 1985)

will be shown. This centrifuge model, also performed at Cambridge University, was made using the best available procedures and technology to make the sand as loose as possible. A bag of the foundation soil provided by the Cambridge University researchers was tested at RPI using monotonic  $\bar{C}IU$  tests to define its steady-state line (Succarieh et al., 1987). It is a mix of Leighton Buzzard Sand 52/100 mixed with 10% by weight of 120/200 fine sand of the same type. This Leighton Buzzard sand is a uniform rounded sand with maximum and minimum void ratios of  $e_{max} = 0.94$  and  $e_{min} = 0.65$  respectively. The steady-state strength envelope for this sand from the  $\bar{C}IU$  tests is shown in Fig. 8.19, where they are compared with results on Leighton Buzzard (all 52/100) using drained direct simple shear (DSS) tests (Atkinson and Bransby, 1978, see also Section 2.2 herein). It must be noted that the sand used in these DSS tests is not identical to that of the  $\bar{C}IU$  tests, as it does not have the 10% fine sand. As expected, it can be seen in Fig. 8.19 that the plane strain simple shear produced a slightly higher friction angle than triaxial compression (Lambe and Whitman, 1969). The undrained triaxial tests gave  $\bar{\alpha}_{us} = 28^\circ$ , which is consistent with results on other rounded sands (see Chapter 6). The SSL for the Leighton Buzzard sand is shown in Fig. 8.20, but since



only four closely spaced points were generated, a slope of the line could not be accurately determined. In order to be able to more accurately determine the slope of the SSL, the results of the drained simple shear tests were used as shown in Fig. 8.20; since the sand is basically the same with only a slight gradation difference, the two lines can be assumed to be parallel (Poulos et al., 1985). The SSL of the Leighton Buzzard Sand is compared against that of the Ottawa F125 sand used herein where they can both be seen in Fig. 8.21. It can be seen that the SSL of the Leighton Buzzard sand is substantially above and to the right of that belonging to the Ottawa F125 sand; therefore it would appear to be more difficult to make a soil deposit that is contractive using this sand than that of sand F125. This is confirmed if we look at Fig. 8.22, where many published SSL for different soils are shown; it is clear that the SSL of the Leighton Buzzard sand is farther to the right than most other sands.

The centrifuge model using the loose Leighton Buzzard Sand tested in the centrifuge is shown in Fig. 8.23 where a loose sand layer was sandwiched between two denser layers. This is the same sand tested by Succarieh et al. (1987). The test again produced the highest possible pwp attainable although the dyke did not crack; therefore the loose sand

layer can be considered to have triggered. The void ratios were estimated for the sand layers and are shown in Table 8.1, where it can be seen that for the loose sand layer under the dyke the value of void ratio is about 0.91. The value of  $\bar{\sigma}_{3c}$  under the dyke in the loose layer is about 0.3 Kg/cm<sup>2</sup>, and using Fig. 8.21 it can be seen that this layer is still dilative despite being very loose. On top of all this, the values of void ratios are not very accurate when measured in the centrifuge; for example, in this sand, an error of 1 mm in measuring the loose layer will translate in an error of 0.1 in the void ratios which would represent more than one order of magnitude in the consolidation stress,  $\bar{\sigma}_{3c}$ .

Since flow failure by Mechanism A has not been achieved due to the problems mentioned before; other researchers have started looking at Mechanism B. Recently, work done at the University of California at Davis on a small centrifuge suggested that liquefaction by flow failure Mechanism B was achieved (Arulanandan et al., 1988). An embankment with water at both sides was built by placing fine sand over water to a height of 7.0 cm., and then placing a layer of soft clay 1.5 cm. thick over the sand. The clay layer was prepared at a water content above the liquid limit. A schematic representation of the model before and after the

shaking is shown in Fig. 8.24. After some shaking, the sand portion of the embankment settled, and the clay layer flowed off the sand and collected in the form of a mudslide at the end of the toe. It was suggested that the densifying sand expelled pore water which could not escape through the clay layer and accumulated at their interface leaving the overlying clay layer in an unstable condition. However, in this centrifuge model the clay was so soft that perhaps it would have flowed anyway regardless of the material underlying it. Clays at their liquid limit are extremely soft since they are almost in a semiliquid state. Therefore, this flow slide of a very soft clay layer is inconclusive, because it is not clear if the failure was due to the clay alone or to the water expelled from the sand embankment.

Summarizing, the centrifuge model tests did not produce flow failures but did point out some important factors involved in the pwp buildup of saturated sands. The reason for the lack of flow failure was that the soil was dilative rather than contractive. In these dilative sands, large deformations can occur but not of the magnitude of a flow failure. These deformations were induced by a combination of the cyclic loads and the driving shear stresses, but basically ceased after cyclic loading was over. The pwp of

these dilative sands increased during cyclic loading and reached a maximum value of  $r_u$  corresponding to an increase in pwp until it reached its particular failure envelope ( $K_f$  line); it then stayed there until dissipation began. The centrifuge tests also pointed out importance of the seepage conditions before the earthquake, as these affect the distribution of pwp during and after shaking.

#### 8.6 Some Important Factors in Liquefaction Flow Failure Evaluation

Even though monotonically induced and seismically induced flow failures were presented separately, they do share a number of features. At the end of each case history, a brief summary of the important factors present in the particular failure was given. In this section, these factors will be compared between case histories and some of them will be related to the laboratory results.

The following characteristics were found to be present in one or more of the case histories studied in the previous three sections:

- Liquefaction flow failure is clearly a complex problem involving the interaction of many factors, many of which are not well understood.

- Some level of drainage clearly occurred before liquefaction flow failure was triggered in several cases. This happened in the monotonically induced flow failures and also in hydraulic fill structures that failed hours after the earthquake.
- Significant values of excess pwp were apparent during or after the flow failures, whether monotonically or seismically induced.
- The actual failure slides occurred very fast.
- Several failures appeared to be progressive.
- The presence of substantial static driving shear stresses in both loose and dense sands affected the pwp buildup in cohesionless soils. These are the same shear stresses which invariably drove the flow failure slides when they occurred.
- In dilative sands, a maximum value of  $r_u$  was reached which corresponds to the value of pwp needed to get to the failure envelope.
- The amounts of deformations involved were very large in liquefaction flow failures of earth structures and slopes.
- Centrifuge shaking model tests confirmed the laboratory prediction that pwp increases with shaking duration.

- The stratification of the sand deposit influences the generation and distribution of pwp, as well as the development and characteristics of sand boils.
- The amount of water expelled by the soils in one part of the system can be detrimental to soils in another part through drainage, because it can lower the undrained strength of dilative soils to the drained strength.
- A stratified sedimented deposit may have a significant higher overall void ratio than a homogeneous one.
- The fact that the FS is greater than but close to 1 after the earthquake does not guarantee the stability of a potentially liquefiable structure, because pwp and volume redistribution in dilative soils could cause a decrease from their undrained strength towards its drained strength thereby causing a further reduction in the factor of safety.

First and foremost, liquefaction flow failure is a boundary value problem where the effect of all soils involved affect the overall stability; that is, the whole system of soils with their multiple interacting factors needs to be considered. When evaluating the susceptibility of an earth structure to liquefaction flow failure,

engineers have often focused on the soils susceptible to flow failure, without consideration of the different effects neighboring soils may have on the liquefiable soil. These effects are mainly stress redistribution and water-solid transfer across soil boundaries.

All liquefaction flow failures discussed in this chapter clearly involved the reaching of some pwp buildup when the failures occurred. This is supported by the laboratory test results presented herein; in fact, triggering is defined in this work by a necessary value of  $r_u$  at which large, uncontrollable deformations start to occur. The laboratory test results presented in this work assume the pwp to be generated in a locally and globally undrained situation, and thus pertain directly to the conditions associated with undrained liquefaction Mechanism A. However, their use is also indirectly related to Mechanisms B and C. This is because, if Mechanism A flow failure does not occur, then the possibility of other mechanisms involving some sort of drainage (mechanisms B or C) will be controlled to a large extent by the amount and location of the pwp generated during the earthquake.

Most failures occur in loose saturated uniform silty sands and sandy silts, and in some cases the silt represents most of the liquefied material. Most of the real world case

histories evaluated herein involved silty sands, and this may suggest that silt content might somehow have a detrimental effect on the development of liquefaction flow failure. This is not to say that pwp buildup and triggering are necessarily worse in silty sands than in clean sands, but that for the whole system, taking into account such things as fabric, void ratio redistribution and pwp migration, a system containing silty sands could perhaps behave worse than that comprised only of clean sands.

Another common characteristic among the case histories is that the majority occur in loose silty sands and sandy silts deposited through water (hydraulic fill methods, alluvial sediments, etc.). It has been known for a long time that granular soils deposited through water can achieve a very loose structure (Kolbuszewski, 1948a, 1948b). It was also shown herein that this deposition or sedimentation process produces a stratification that makes the overall void ratio of these samples much looser than those created using homogenous samples. This stratification was shown to generate concentrations of water at the interlayers, and a failure surface going through these interlayers would produce a low factor of safety (Huishan, 1984). If two different soil deposits liquefy and have the same  $r_u$ , the one which can expel more water is more hazardous to the



whole soil system because it will affect the surrounding soils more. Therefore, additional research is necessary to clarify the amounts of water generated by reconsolidation of clean sands, silty sands, and layered complex sedimented systems of these soils.

The redistribution of pwp and water throughout the system will be strongly influenced by the permeability of the soil. In stratified soils such as the sedimented soils discussed in this research, the horizontal permeability is significantly larger than the vertical permeability. This means that excess pwp will extend faster in the horizontal direction than a vertical direction. If this redistribution of water and pwp causes the strength of these soils to decrease, then horizontal failure planes can be more easily formed.

Some of the monotonic case histories showed that water movement prior to failure was noticed. In those cases, the water transfer invariably consisted of the sands swelling and sucking in water; this dilation was always accompanied by movements of the soil mass as its undrained strength decreased to its drained strength. In some cases, the level of some water deposit connected to the dam soil was found to drop and since it can be considered to be like a piezometer, it shows that negative pwp were present. This can lead to

the conclusion that a sample that is mildly dilative (near and to the right of the SSL) is not necessarily safe to liquefaction flow failure. Obviously, the more dilative a sample is, the safer to liquefaction flow failure it will be, but near the SSL a gray area exists which should be analyzed on a case by case basis using careful engineering judgement.

For earthquakes in level ground, a dense sand can generate  $r_u = 1.0$  conditions, but very little volumetric strain is necessary for reconsolidation to reach again the  $r_u = 0.0$  conditions; the reverse is true in loose sand where the soil needs to expel a lot of water to reconsolidate. This has been shown to be a very important parameter in level ground cases (Dobry, 1988) but the idea can be extended to 2D or 3D cases involving earth structures. For these problems, the redistribution of water is very much affected by the seepage conditions before the earthquake, as pointed out by the results on the centrifuge (Schofield and Venter, 1985).

The above discussion points out that contractive sands are dangerous not only because their shear strength is lower but also due to the amount of water they can expel. This amount of water is probably related to the position of the soil with respect to its SSL, because an increasing

contractiveness of a soil should make it generate more water, and increasing dilativeness should make it generate less water. Therefore, in first approximation, the position of a soil relative to the SSL can be used for two purposes; as a measure of how much water can be expelled by the soil element (even if flow failure does not occur but pwp are generated), as well as for the conventional use in overall stability as described herein.

Another common characteristic among the liquefaction flow failures is the fact that significant driving shear stresses are invariably present, and that by reducing them the susceptibility to liquefaction flow failure can be reduced.

The experimental fact that the value of  $\bar{\sigma}_{3c}$  affects the number of cycles to failure in contractive sands is probably an important part of the explanation of why submarine flow failures occur, such as those in Holland and Scandinavia. These are soils deposited by nature through water, and they fail with very shallow failure surface which obviously have very small values of  $\bar{\sigma}_{3c}$ . The laboratory test results in Chapter 7 show that very small perturbations are necessary in this case to trigger flow failure.

Several of the case histories previously discussed in this chapter involving liquefaction flow failures showed

signs of progressive failure. This occurred due to strength reduction of the elements in the liquefied soil, possible driving shear stress redistribution throughout the soil system, and changes in geometry as liquefied parts of the slope flowed out. The shear stress redistribution arises because as an element liquefies and cannot take the shear stresses imposed on it, the surrounding elements must take additional shear stresses. These additional shear stresses can then cause other elements to fail. The strength drop situation is further complicated because beyond triggering, the shear strength of the soil drops with increasing strain; therefore, if the surrounding elements do not let it strain, the sample may not quite drop to its steady-state shear strength. Here again the system analysis concept appears and shows that interaction between different elements in the system is very important for a whole picture of the process. This becomes especially clear by considering that strength reduction and stress redistribution are dependent on the stress-strain relationships of all soils present.

The case histories involving seismically induced liquefaction and the laboratory test results presented herein point out that the two dimensionality of the problem is of fundamental importance. Therefore, for liquefaction flow failure evaluation, two-dimensional (or 3D) dynamic

finite element analyses need to be performed. The driving shear stresses are of fundamental importance in evaluating pwp buildup and number of cycles to failure; and only 2D (or 3D) analyses such as produced by Finite Elements techniques can handle this problem. One dimensional models, and models where the soil properties of an element cannot be changed during shaking, may not be able to capture some important aspects of the seismic liquefaction flow failure process.

#### 8.7 Proposed Conceptual Framework

This section proposes a logical conceptual framework for the evaluation and analysis of flow failure of a specific slope, earth embankment or foundation subjected to seismic shaking. This framework is based on the previous discussions on case histories and model tests, as well as on the pwp buildup and triggering experimental results on the contrative sands reported herein.

The framework is presented in Fig. 8.25 by using a flowchart of logical steps to be followed in an analysis; this will enable a more clear visualization of the whole problem. The flowchart incorporates the laboratory test results presented herein, together with some of the procedures and techniques used by other researchers in previously developed liquefaction evaluation procedures

(Poulos et al, 1985; Seed, 1987). It also includes the concepts of liquefaction Mechanisms A, B and C (NRC, 1985).

Due to its general and comprehensive nature, the conceptual framework presented in the flowchart incorporates some processes that are not yet completely understood and require more research. These include stress, pore water and solid redistribution, as well as loss of solids to the system. Nonetheless, these processes are believed to be potentially important factors in liquefaction flow failure and thus were included. The fact that the conceptual framework includes these processes currently not well understood should not be a reason for not using them and wait for results of future research; very often these processes can be dealt with by acknowledging their existence and using experience and engineering judgement.

The conceptual framework requires a calculated or estimated shear strain time history or representative cyclic strain and number of cycles caused by the seismic shaking input for all potentially liquefiable soil elements, and therefore can be considered to be an extension of the cyclic strain approach to liquefaction. The reason for using cyclic strain instead of cyclic stress is that cyclic strain is a more robust parameter for modelling pwp buildup, as it is affected less by soil fabric and void ratio than cyclic

stress. In the application of the cyclic strain approach, the fundamental material parameter is  $G_{\max}$ , which can accurately be measured in-situ from shear wave velocity measurements using the cross-hole technique (Stokoe and Hoar, 1978). It should also be pointed out that  $G_{\max}$  is a required parameter for any dynamic response analysis of the earth structure, needed to evaluate either seismic stresses or strains.

The different steps of the conceptual framework shown in Fig. 8.25 are discussed in the following paragraphs.

First, Step 1 verifies if the particular design earthquake will produce shear strains above the threshold strain,  $\gamma_t$ . If they are all below  $\gamma_t$  then no pwp buildup will be experienced and no permanent deformations will occur. This step takes into account that small earthquakes which may be a common occurrence will not cause any damage, regardless of any other consideration.

Step 2 checks if the majority of the cohesionless soils are strongly dilative, as these soils are not expected to experience a decrease in soil strength, and they also exhibit large stiffness during cyclic loading. Even though pwp may be generated in these strongly dilative soils, no large strains will occur; instead, smaller permanent deformations dependent on the level of shaking and looseness

of the material may develop. These deformations will include contributions from both constant-volume distortions and volume changes (settlements). How dilative a soil element is can be evaluated experimentally in the lab by knowing how far the soil state is from the SSL, or alternatively by penetration tests performed in situ. Given the current state-of-the-art, it seems advisable to assume conservatively that all cohesionless soils which are not strongly dilative are contractive and can experience flow failure. This decision may also be influenced by the amounts of water that can be expelled in looser areas in the system during or after the shaking, which may then reach a dilative zone and make it contractive (Step 9).

Step 3 involves checking if there are significant amounts of driving shear stresses  $\tau_d$ . If they are small, flow failure cannot occur and the magnitude of permanent displacement will be associated mainly with the level of shaking and looseness of the material. Lateral spreadings belong in this category. The contribution of permanent volume changes (settlement) is obviously still present in this case as it was in Step 2. Driving shear stresses are analyzed by performing limit equilibrium analyses such as in slope stability on the whole earth structure system. If there are significant driving shear stresses, and



contractive or mildly dilative soils are present, there is a risk that liquefaction flow failure can take place.

Step 4 calculates the amount of pwp generated in the soils present assuming a totally undrained condition. The pwp model presented in this work can be used for this purpose in contractive sands, but other similar models can also be used. The relevancy of evaluating the generation of pwp at all soil elements that can develop them will become more important in the later steps of this methodology, when redistributing water and pwp throughout the system.

Step 5 finds those contractive elements that have triggered because their predicted value of pwp exceeds  $r_{ut}$ . This triggering analysis can be performed by using the results presented in the previous chapter. These triggered elements will be assigned either their steady-state shear strength,  $S_{us}$ , or in a more refined analysis, a decreased stress corresponding to the cumulative strain. (It should be remembered that a contractive soil element that has triggered will not reach its steady-state if it is constrained by the neighboring elements.)

Step 6 checks if the most critical failure surface (that having the lowest factor of safety) is below 1.0. The strength of the contractive sands that triggered can be

conservatively chosen to be  $S_{us}$ , while the dilative soils should be assumed to have their drained strength in order to account for potential flow of water into these soils. If the FS is below 1.0, then liquefaction flow failure by completely undrained mechanism A is predicted. The reason for not introducing drainage at this point is that in most instances involving strong ground shaking both pwp and triggering occur very fast (a few seconds to a few minutes), so that in most silty sands there may not be much possibility for dissipation. Also, the assumption of no drainage is usually conservative at this stage as it increases the magnitude of pwp and number of triggered elements. So, in first instance the process can be considered to be essentially undrained, and if under this assumption the FS is below 1, then a flow failure will occur. This is probably what happened in some flow failures that occurred during strong ground motions, such as the Chilean tailing dams (Dobry and Alvarez, 1965) and the Mochikoshi tailings dams (Okusa and Anma, 1980).

If some elements have failed, they must redistribute the shear stresses they can no longer carry to the surrounding elements. This is taken care by Steps 7 and 8. The loop in the figure redistributes the stress in undrained conditions because this stress redistribution can be assumed

to occur instantaneously. This process continues until there are no more soil elements failing by stress redistribution. This monotonic stress redistribution was illustrated in the laboratory results presented herein by the monotonic CAU test data, where it could be seen that monotonic loads induce additional pwp buildup and triggering.

If after the stress redistribution is completed the FS is still greater than 1, then flow failure by mechanism A cannot occur, but still the possibility of the other, not fully undrained mechanisms must be taken into account. The earth structure cannot be considered safe until the effect of pore water transfer and void ratio redistribution has taken place.

Step 9 starts redistributing pore water and void ratios throughout the whole system, allowing for the fact that the water supplied by any soil in the system will influence the overall stability of the system. Also, the water flow regime before the earthquake must be incorporated, as this has been shown to influence the evolution of pwp distribution with time. Possible ways to handle this problem would be a combination of analytical tools involving theories of consolidation and flow through porous media; however, significant additional research is needed in this

area.

If the pwp of an element rises to its pwp triggering value  $r_{ut}$  due to pwp redistribution, or by an increase in void ratio; there is the possibility that it will trigger and the strength in that element will reach its steady-state. Step 10 finds all these elements that might trigger due to void ratio increase or pwp redistribution. Additional considerations can be made at this point on possible void ratio increases in some elements due to loss of solids to the system (such as caused by sand boiling, Mechanism C). Special care should be taken for cracking induced by the seismic stresses because it might influence the stability analysis (it drops the factor of safety) and because it might accelerate Mechanism C due to the flow of water through the cracks.

Step 11 checks to see if the FS of the most critical failure surface drops below 1.0. If it does, then liquefaction flow failure by Mechanism B or C is predicted due to pwp and/or void ratio redistribution.

Since some additional elements may have triggered and dropped their strength to the steady-state value, these driving shear stresses must be redistributed throughout the system. Steps 12 and 11 perform a loop that takes care of the redistribution of void ratio and pwp until steady-state

seepage conditions are restored or the FS drops below 1, whichever comes first. This process could probably take many hours in the field such, as the case involving the Mochikoshi tailings dam that failed 8 hours after the aftershock.

Only after the steady-state seepage conditions have been reestablished with  $FS > 1$  can a dam be considered safe against liquefaction flow failure by Mechanisms B and C.

**Table 8.1. Estimated Void Ratios for the Centrifuge Test  
Shown in Fig. 8.23 (after Habibian et al.,  
1985)**

	Seaward side		Under the dyke		Landward side	
	Before test	After test	Before test	After test	Before test	After test
Top layer	0.72 (67%)	0.72 (67%)	0.68 (79%)	0.64 (92%)	0.65 (88%)	0.65 (88%)
Middle layer	0.94 (0%)	0.78 (47%)	0.91 (9%)	0.64 (90%)	0.85 (27%)	0.76 (55%)
Bottom layer	0.72 (67%)	0.69 (77%)	0.56 (85%)	0.63 (95%)	0.75 (57%)	0.75 (57%)

Note: The numbers in parentheses are the Relative Densities.

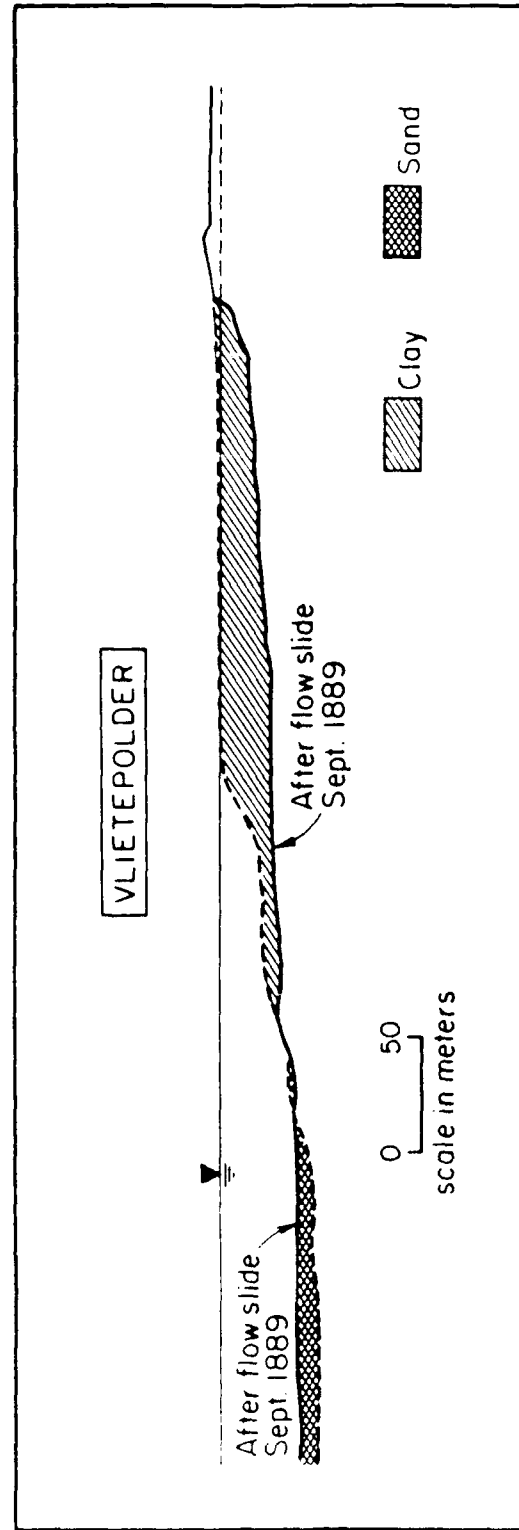


Fig. 8.1. Profile of Flow Slide at Vlietepolder, Holland  
(after Koppejan, et al., 1948)

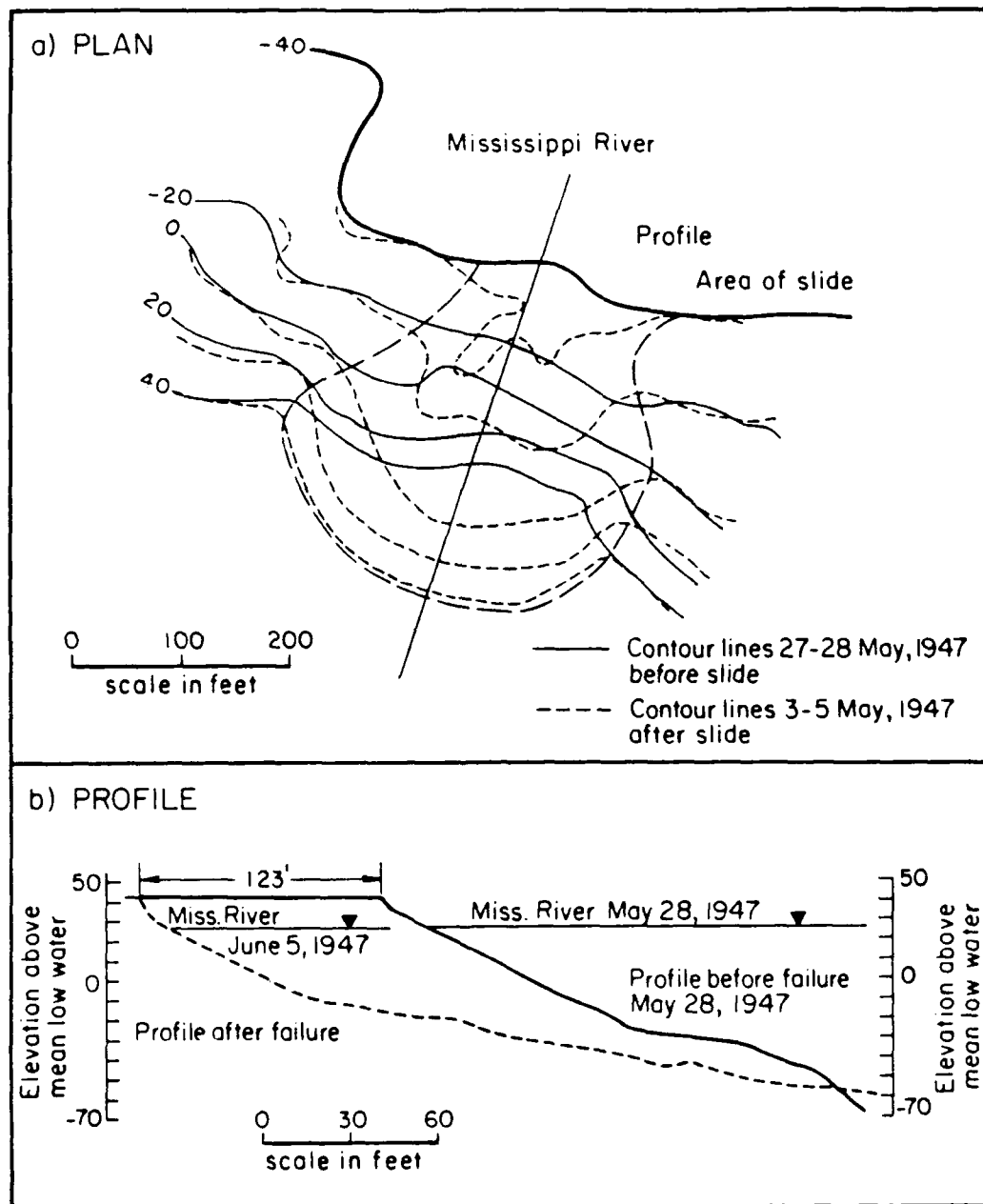


Fig. 8.2. Profile of Flow Slide in Mississippi River Bank  
(after Senour and Turnbull, 1948)



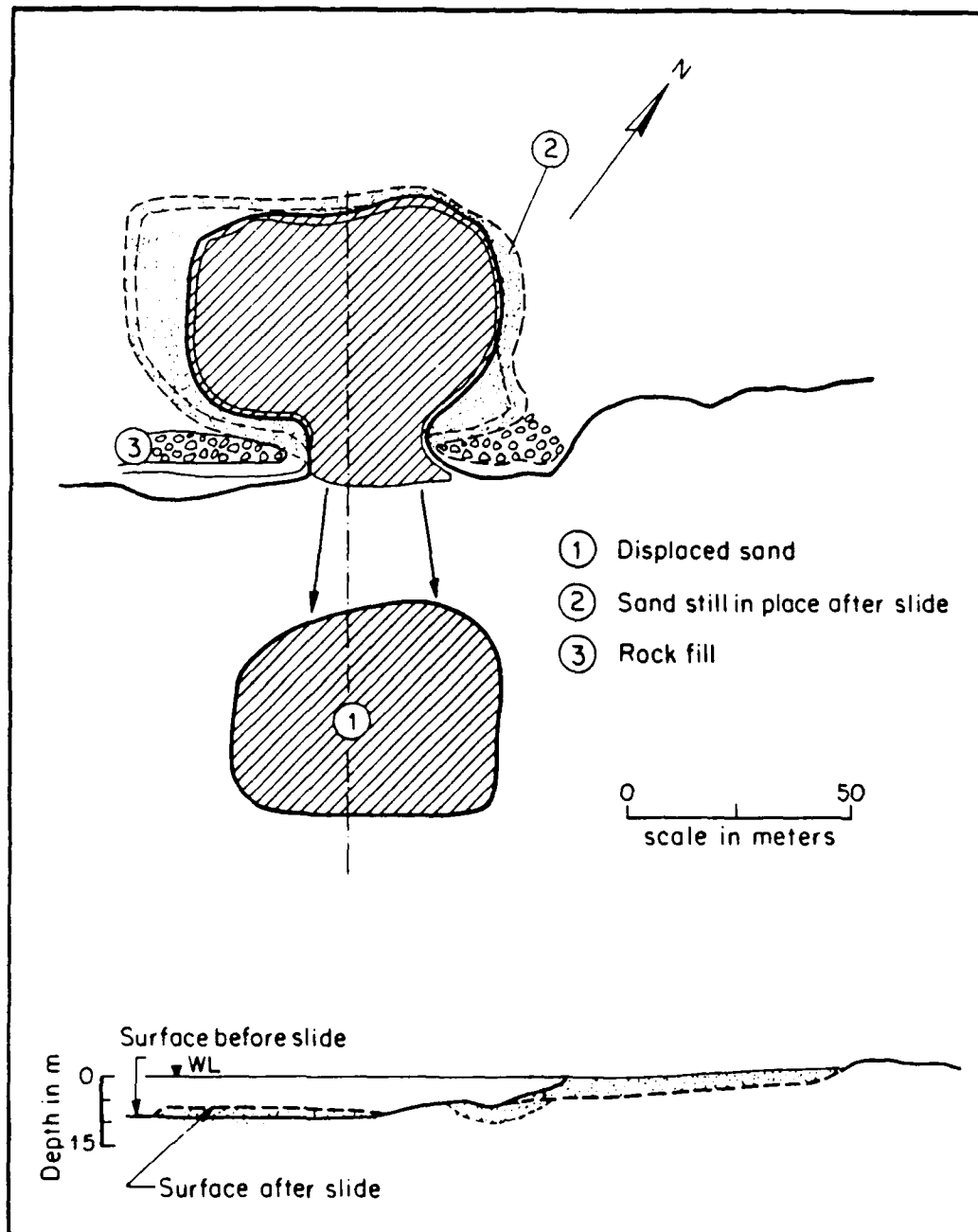


Fig. 8.3. Profile and Plan of Slide in Helsinki Harbor  
(after Andersen and Bjerrum, 1968)

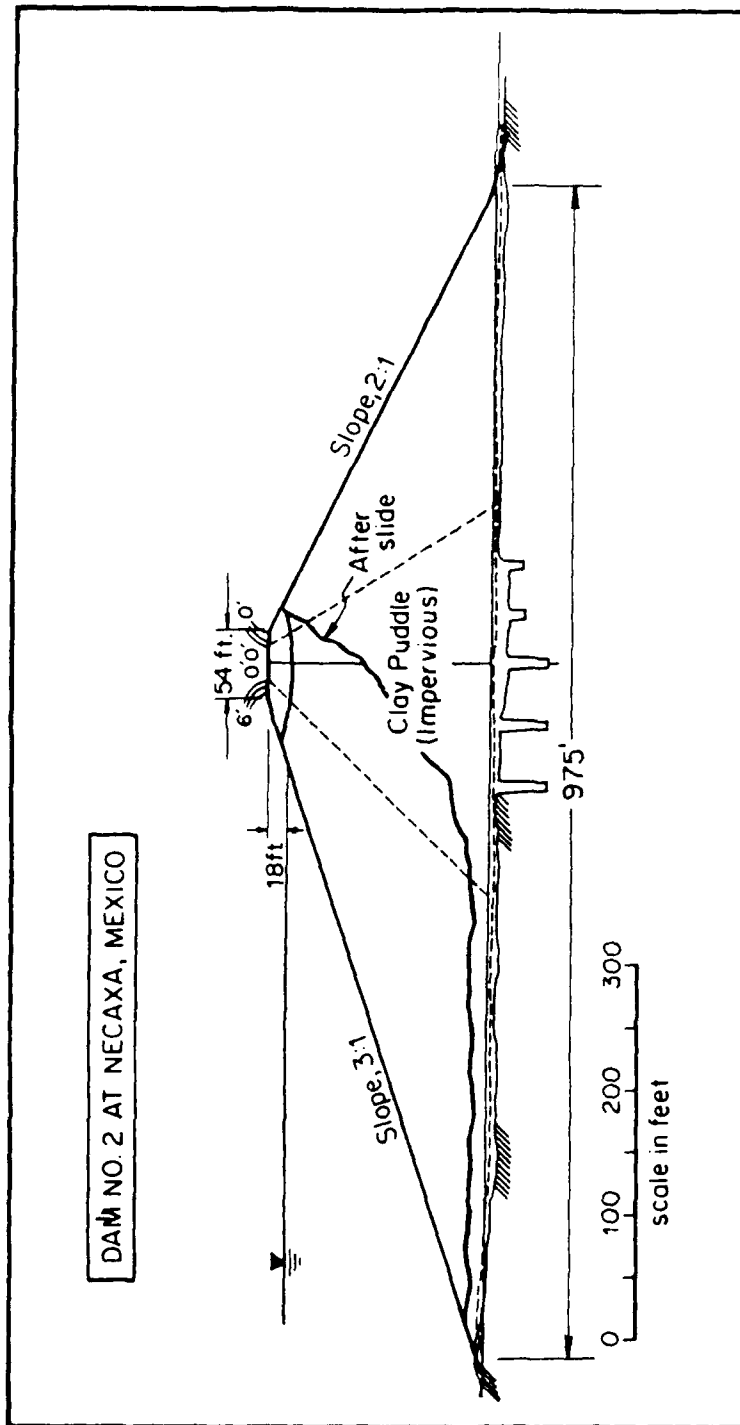


Fig. 8.4. Cross Section of Necaxa Dam No. 2 (after Schuyler, 907; 1909)

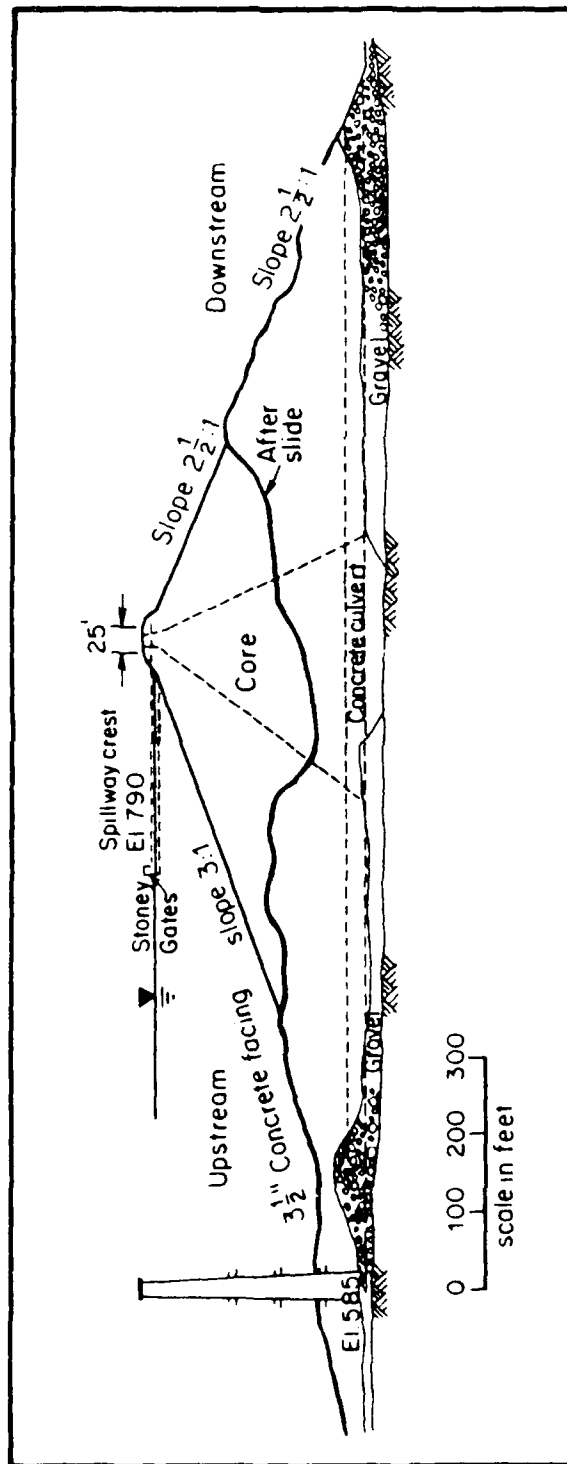


Fig. 8.5. Cross Section of Calaveras Dam (after Hazen, 1918)

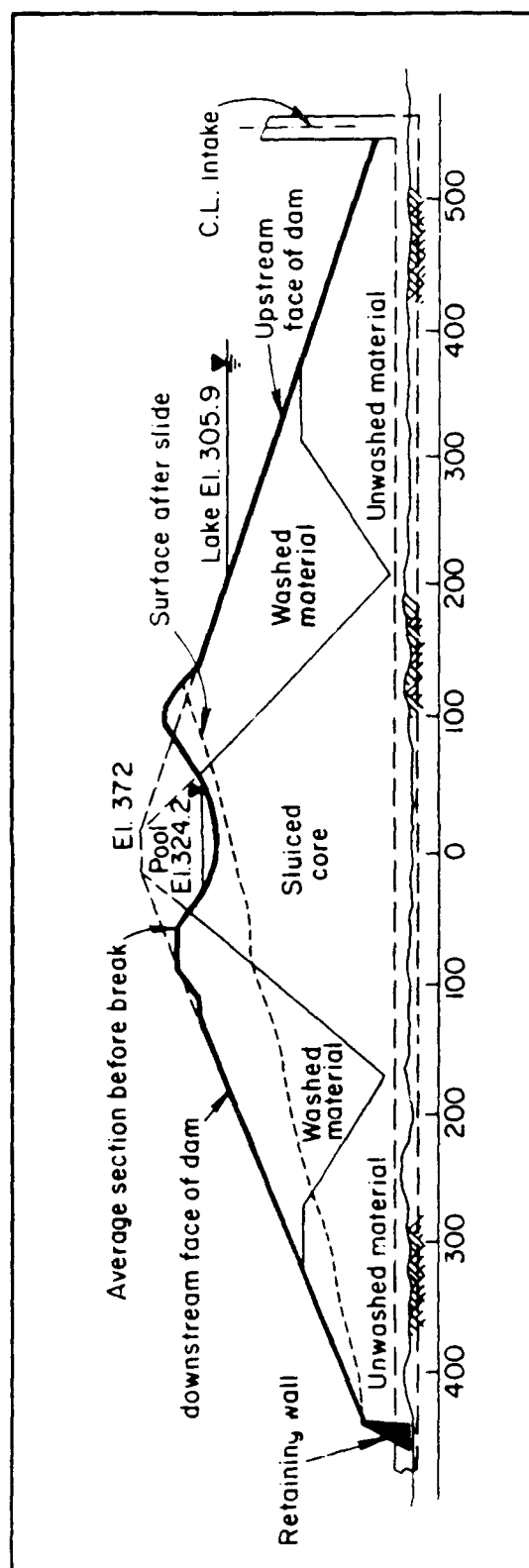


Fig. 8.6. Cross Section of Saluda Dam (after Engineering News Record, 1930a)

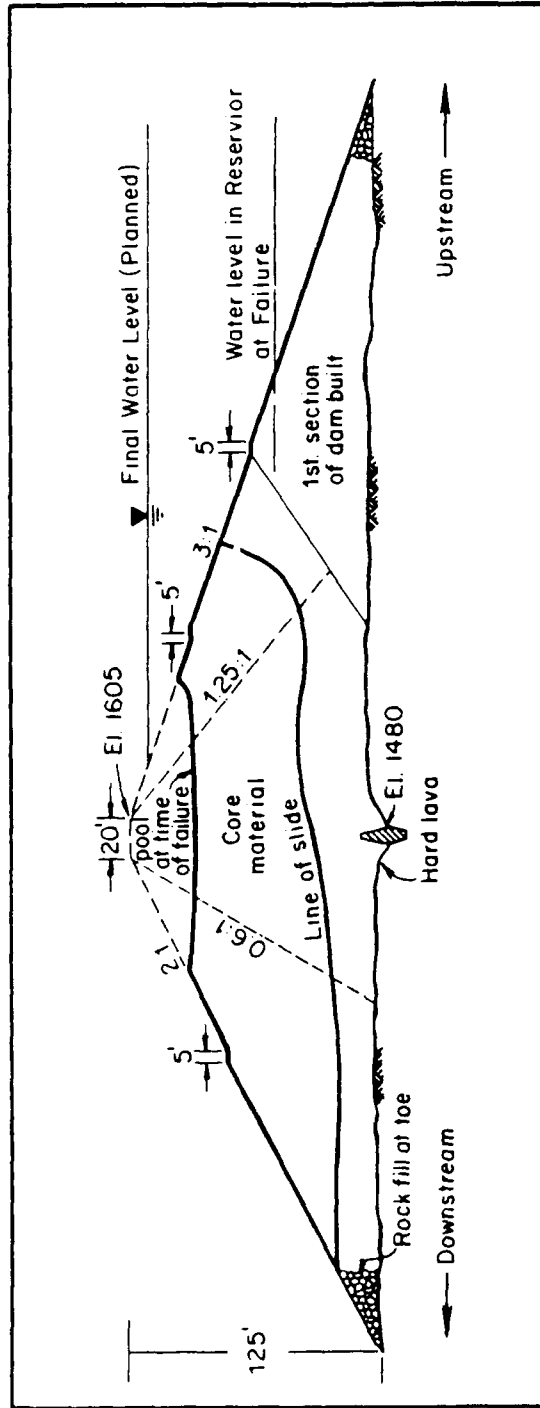


Fig. 8.7. Cross Section of Alexander Dam (after Engineering News Record, 1930b)

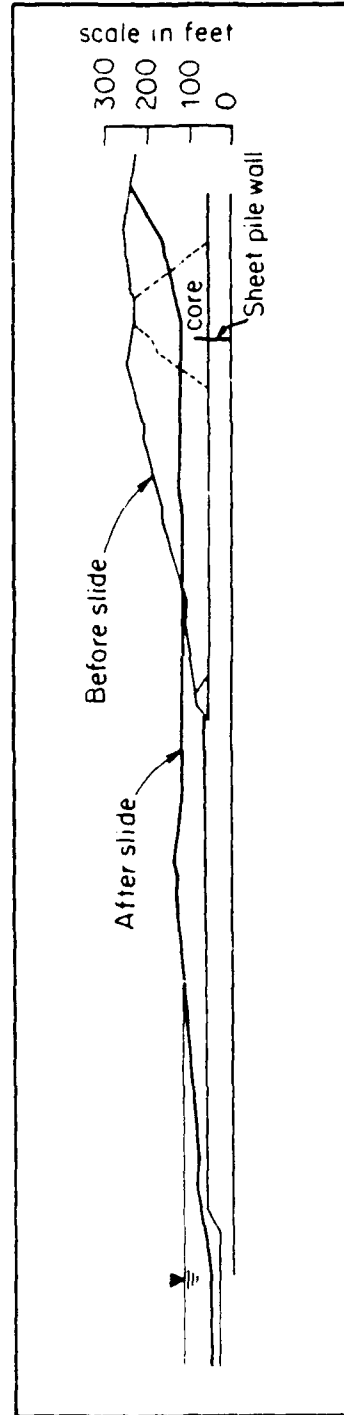


Fig. 8.8. Cross Section of Fort Peck Dam (after Casagrande, 1965)

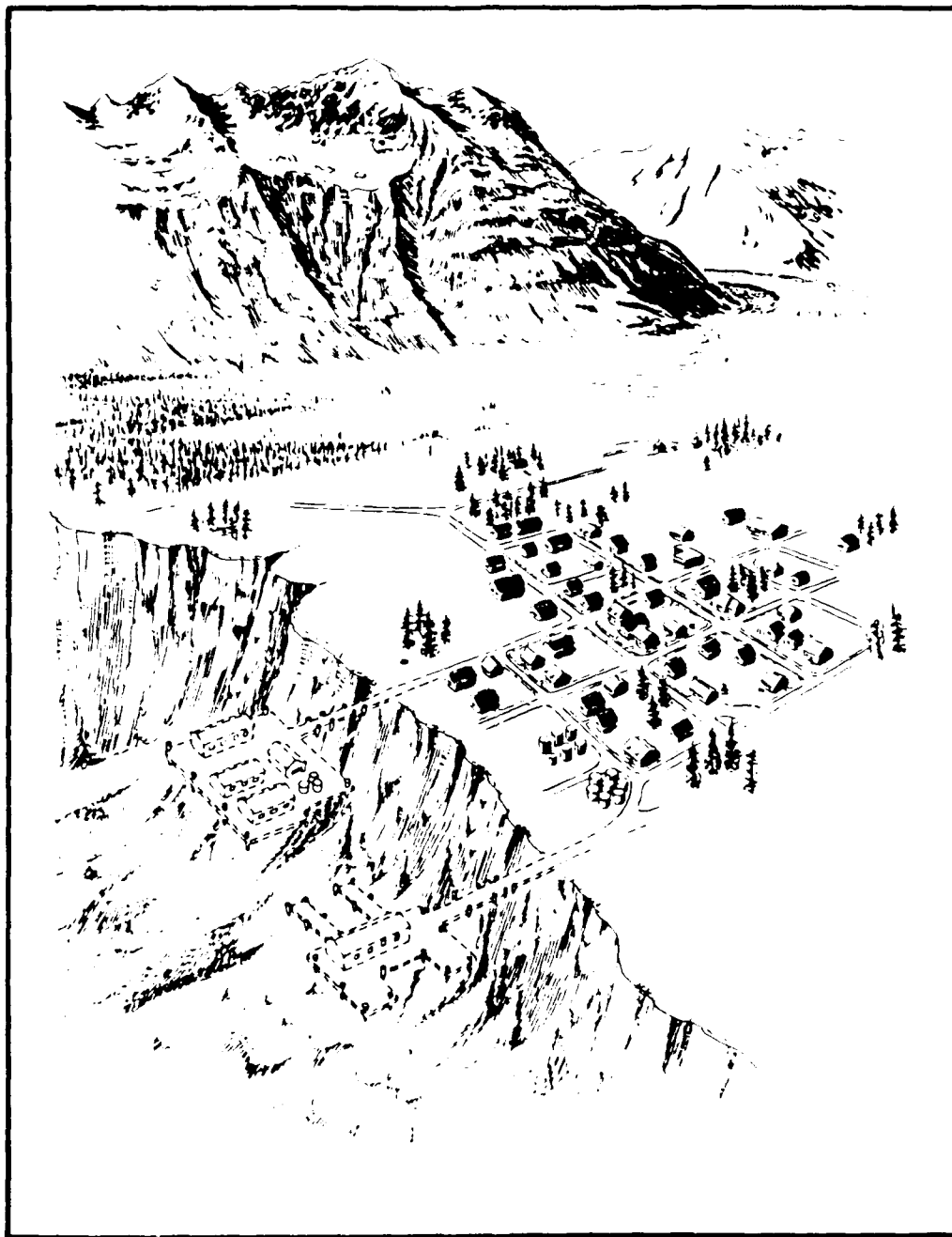


Fig. 8.9. Artist's Concept of Flow Slide at Valdez (after Seed, 1967)

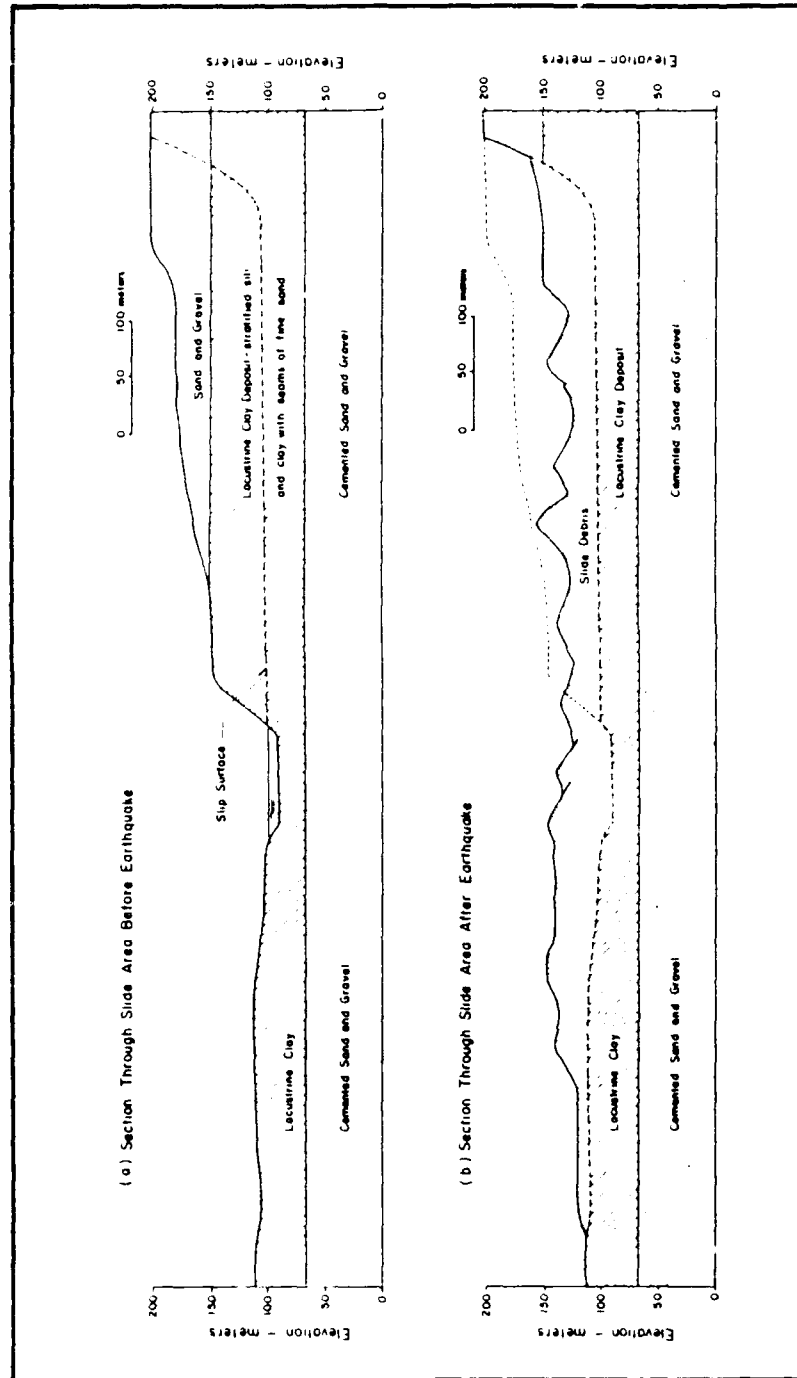


Fig. 8.10. Approximate Sections Through Large Slide Area Near Lake Riñihue, Chile (after Seed, 1967)



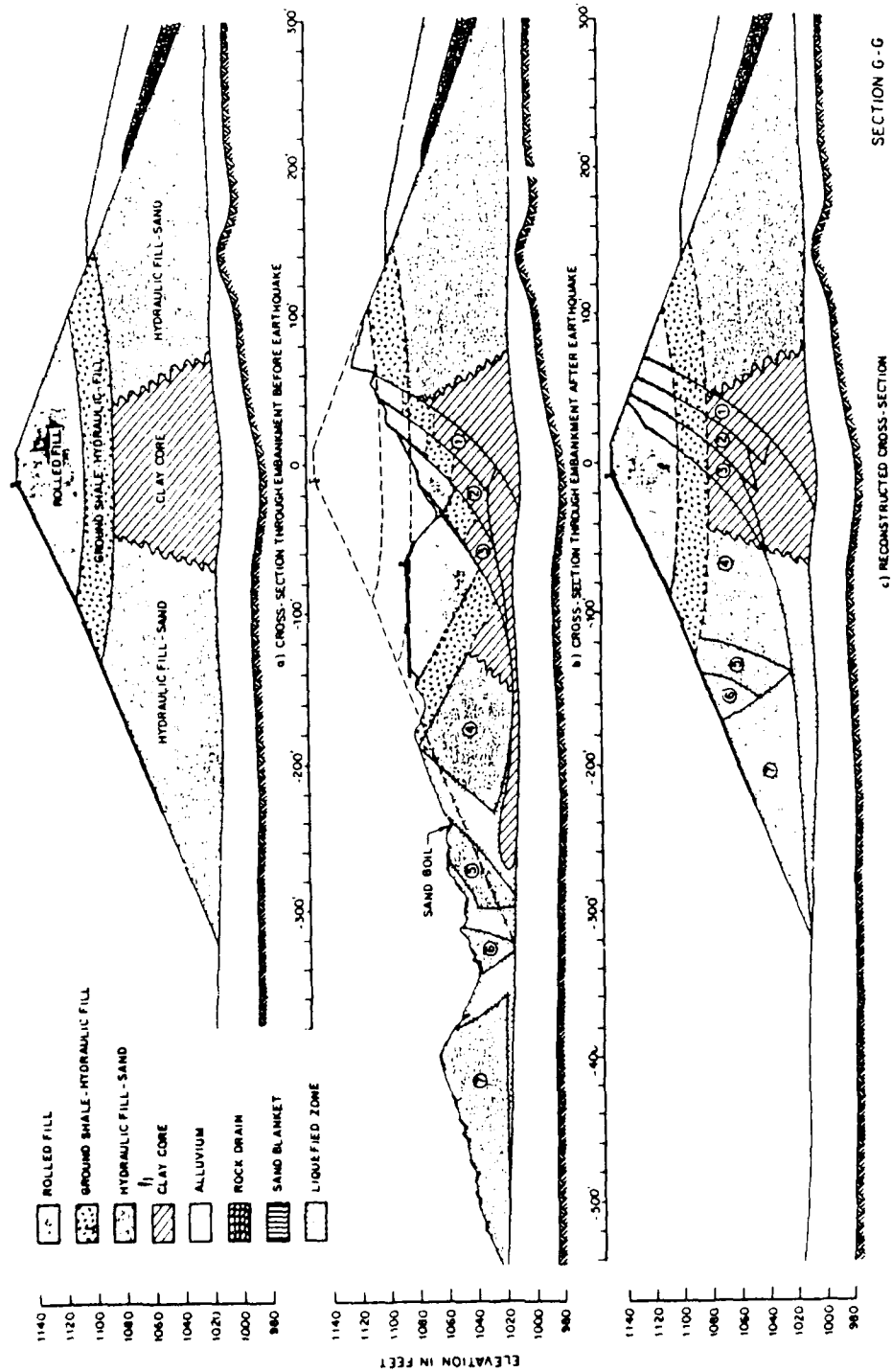


Fig. 8.11. Cross Section of Slide in the Lower San Fernando Dam (after Seed et al., 1973)

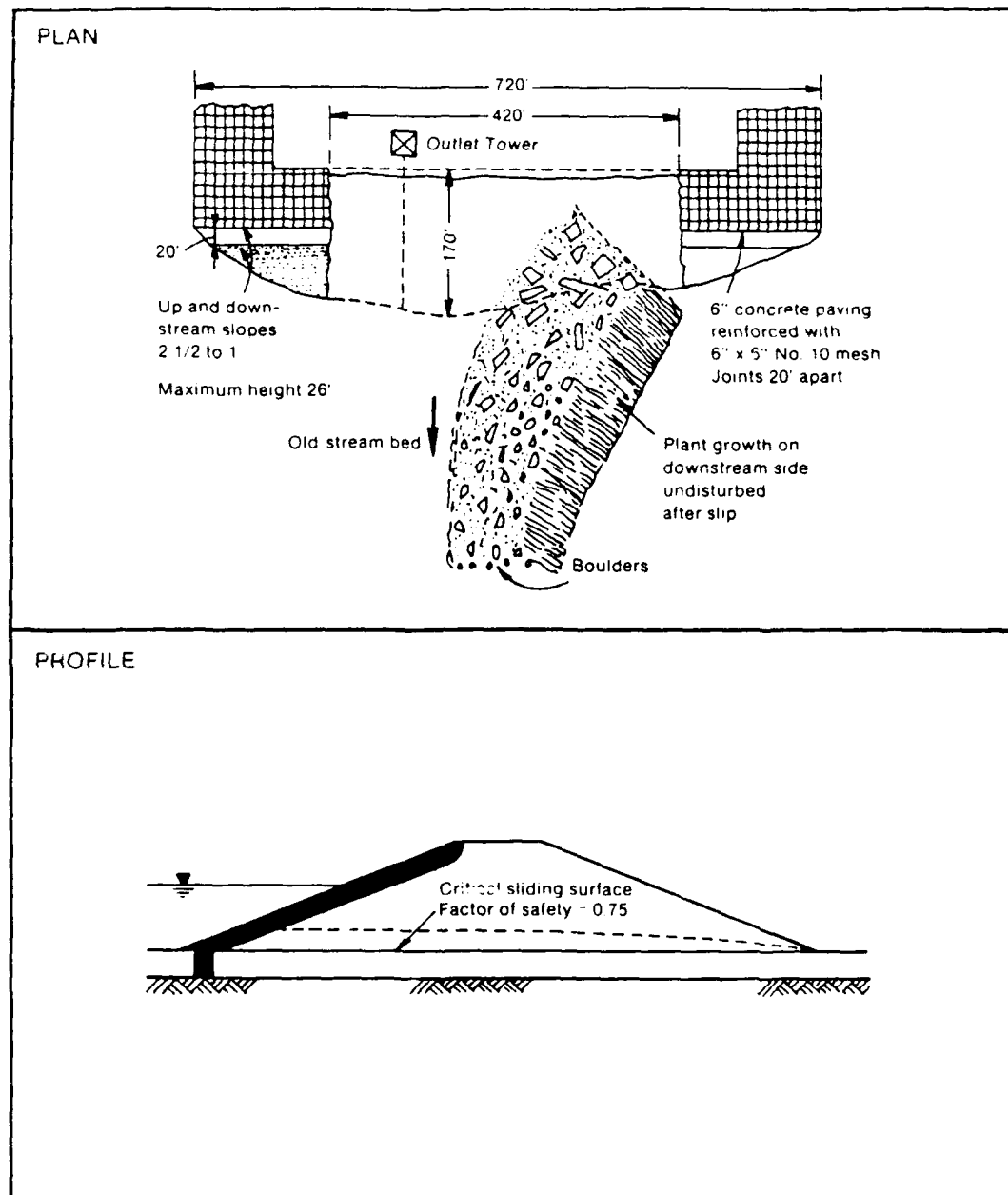


Fig. 8.12. Plan and Profile of the Slide in the Sheffield Dam (after Engineering News Record, 1925; Seed et al., 1969)

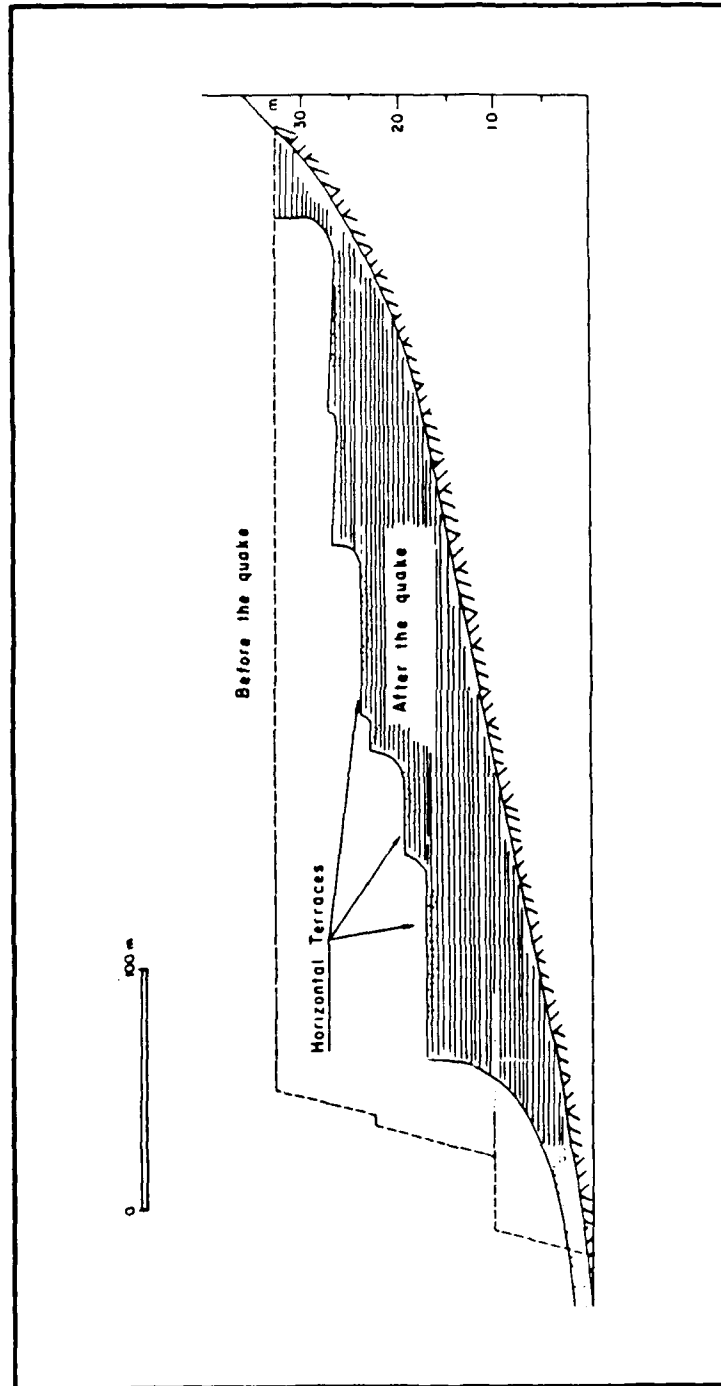


Fig. 8.13. Profile of El Cobre Old Dam (after Dobry and Alvarez, 1967)

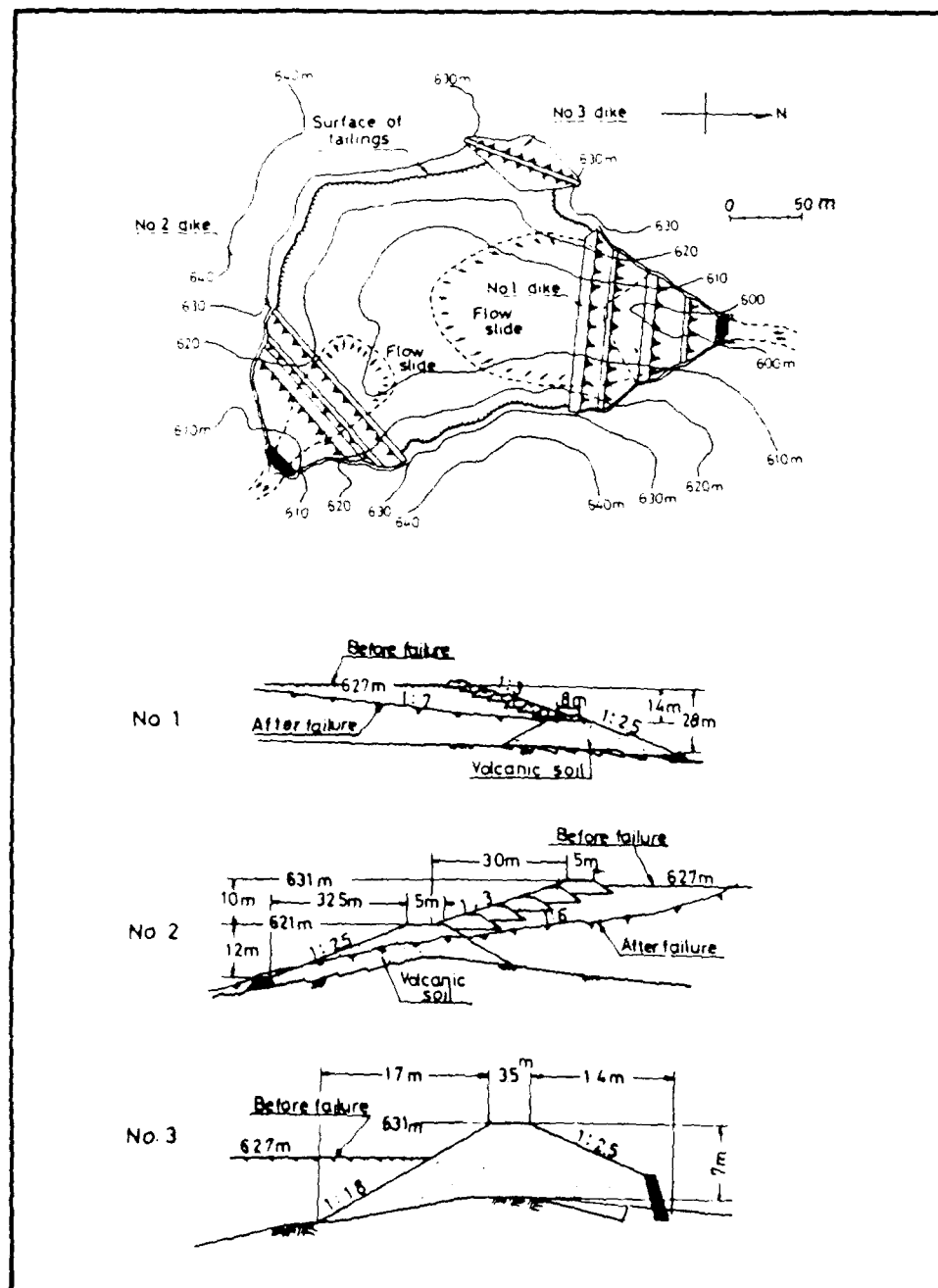


Fig. 8.14. Profile of the No. 1, No. 2 and No. 3 Dykes of Mochikoshi Tailings Dam (after Okusa and Anna, 1980)

# SHAKING TABLE TEST OF STRATIFIED SAND DEPOSIT

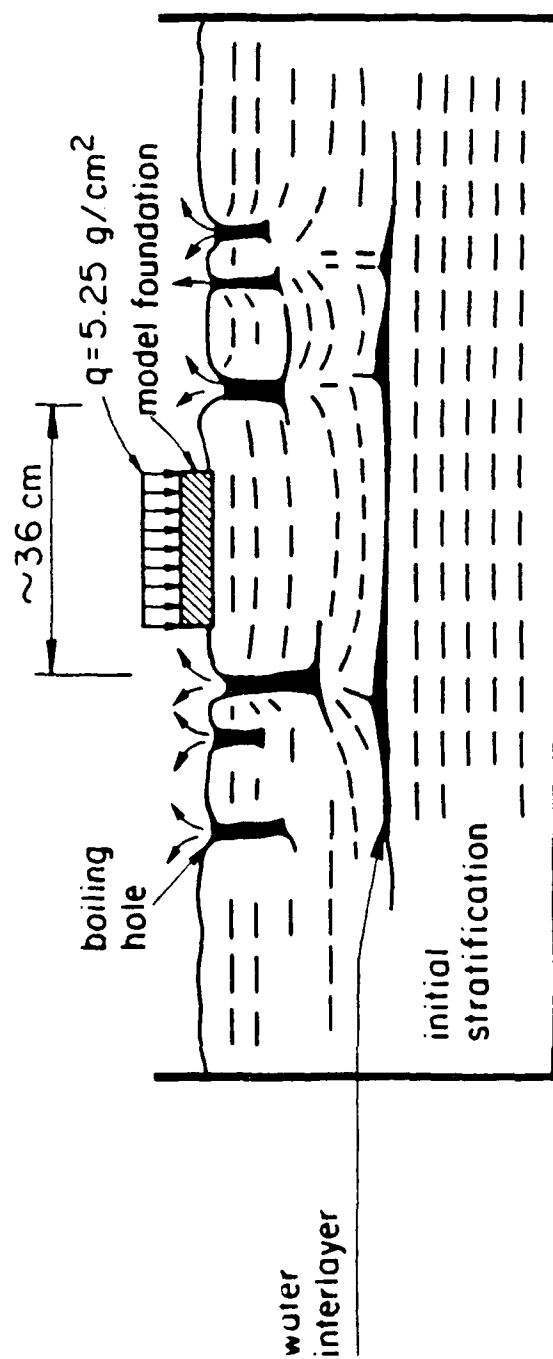


Fig. 8.15. Shaking Table Test of Model Foundation on a Stratified Sand Deposit (after Huishan and Taiping, 1984)

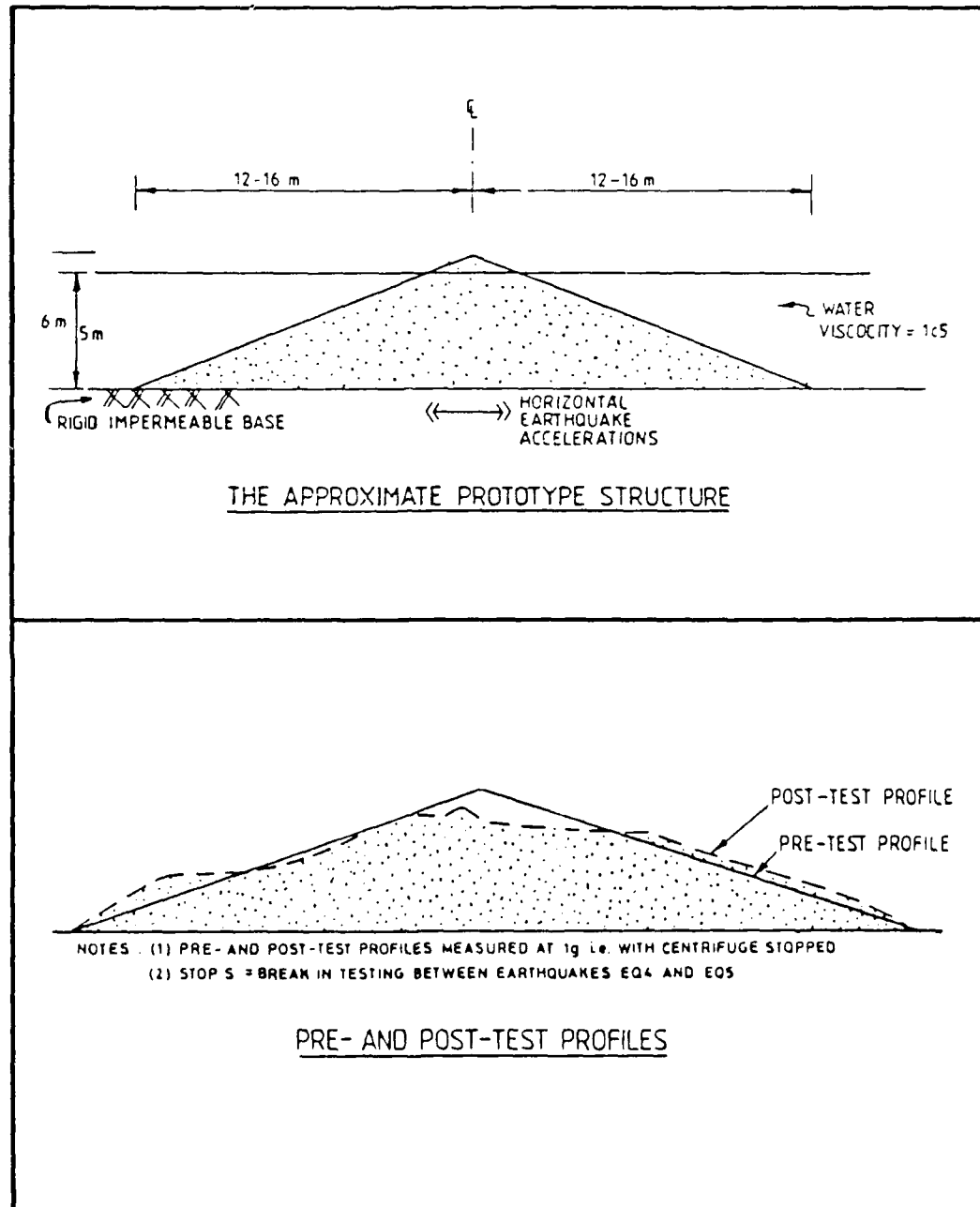


Fig. 8.16. Centrifuge Model of a Submerged Embankment Subjected to Earthquakes (after Dean and Schofield, 1983)

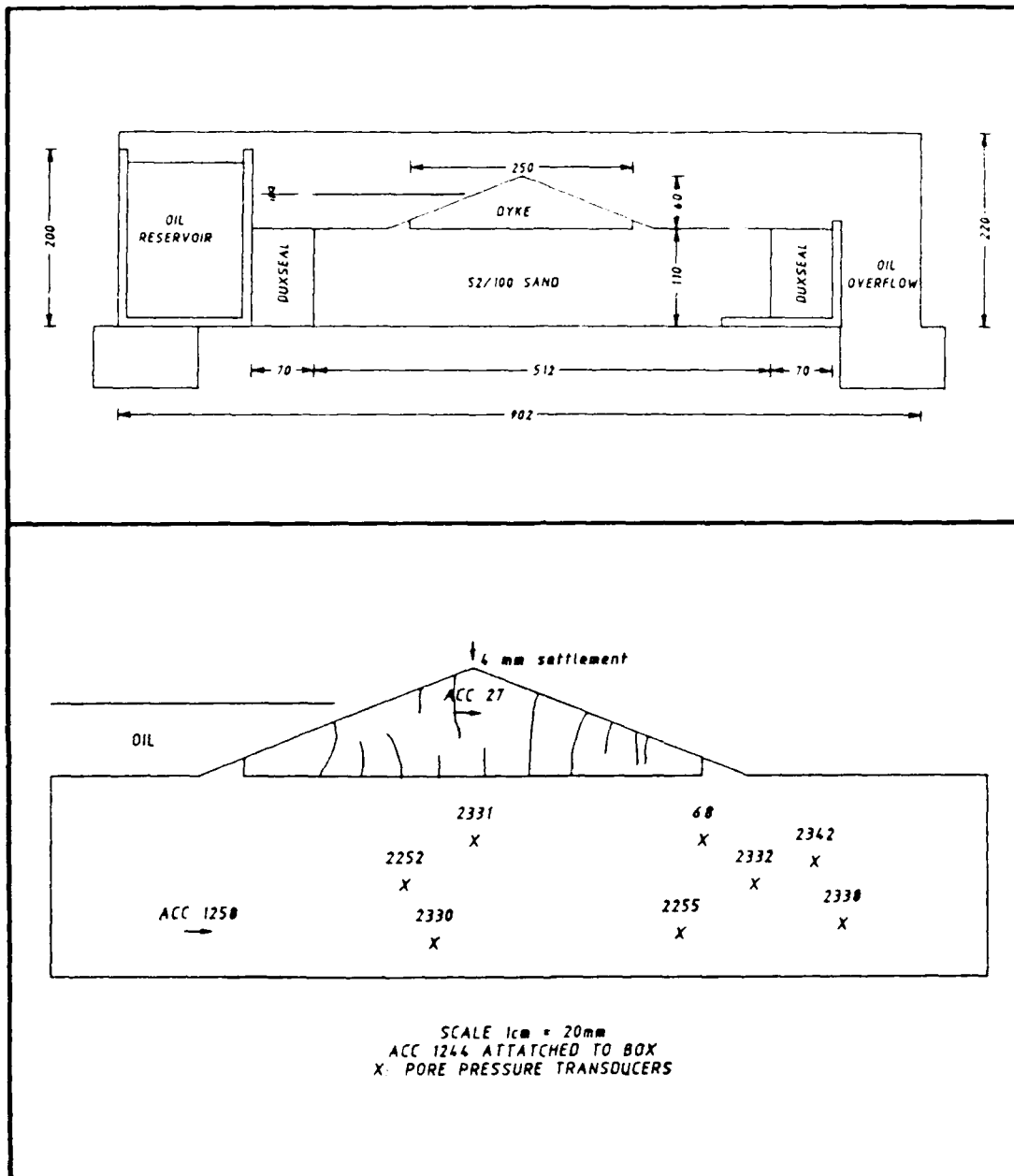


Fig. 8.17. Centrifuge Model of a Compacted Silt Embankment Resting on a Sand Foundation Showing Model Geometry Before Earthquake, and Crack Pattern after Earthquake (after Schofield and Venter, 1984)





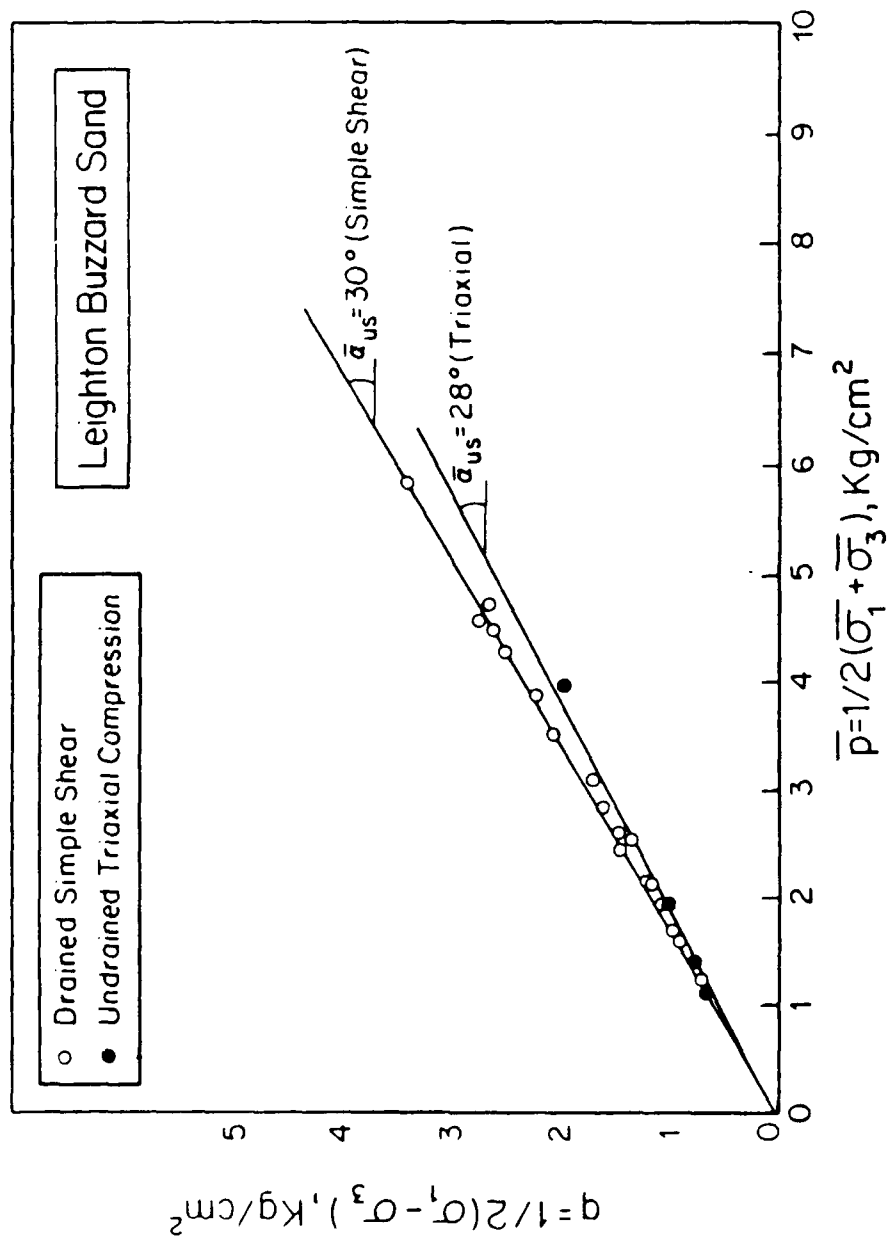


Fig. 8.19. Steady-State Strength Envelopes for Leighton Buzzard Sand Using Drained Simple Shear and Undrained Triaxial Compression

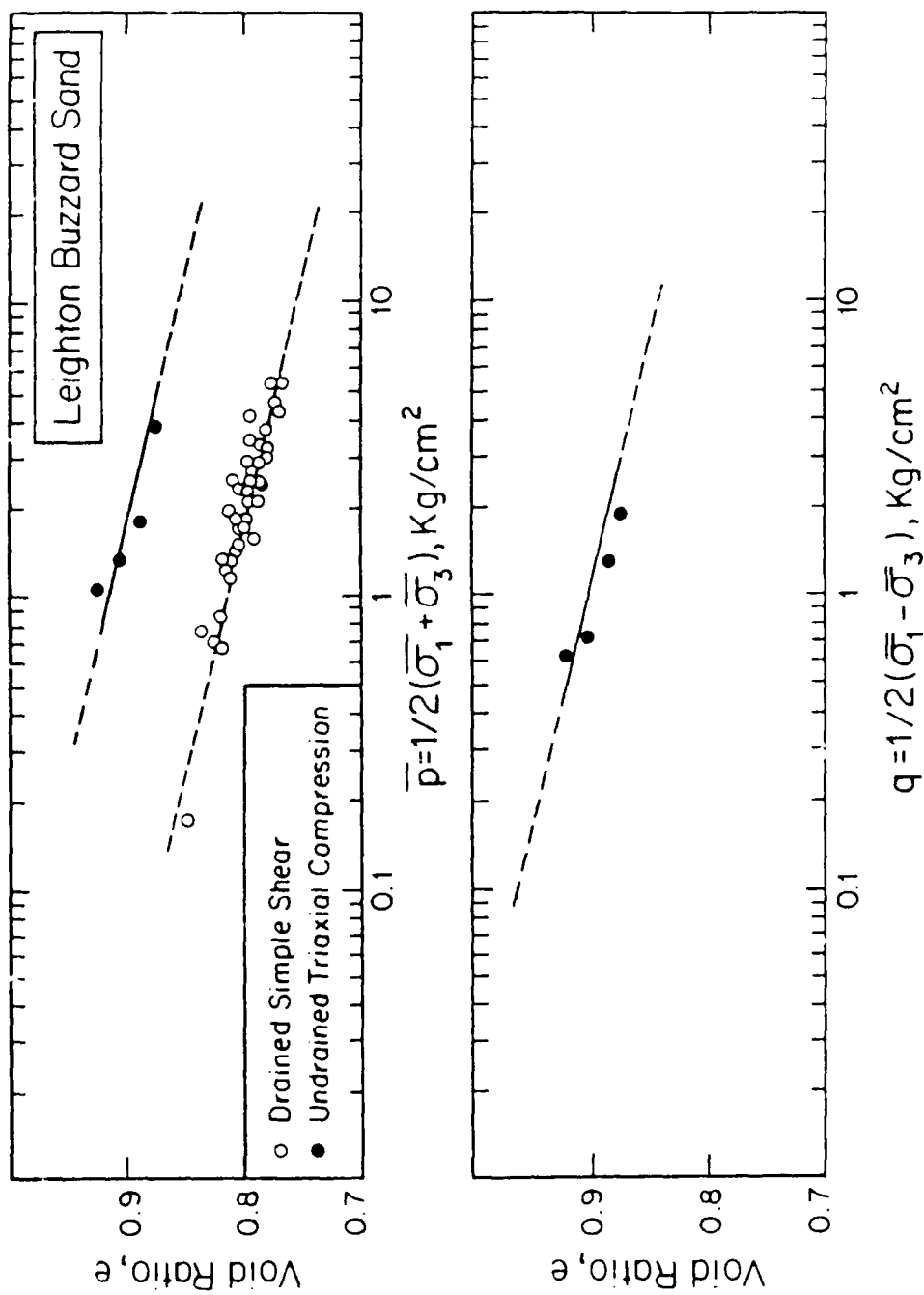


Fig. 8.20. Determination of SSL for Leighton Buzzard Sand Used in the Centrifuge Model Shown in Fig. 8.23 (data from Atkinson and Bransby, 1978; Succarieh et al., 1987)

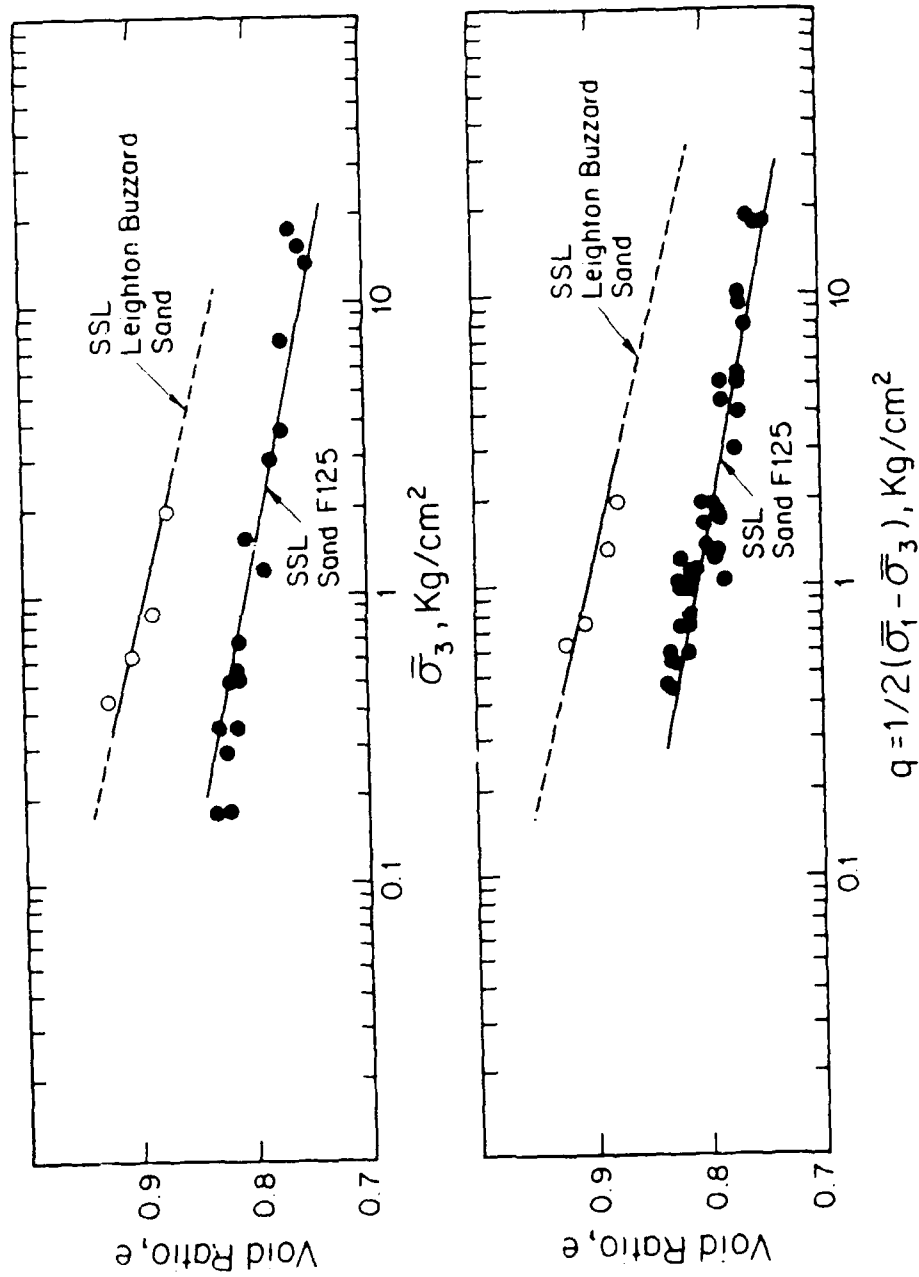


Fig. 8.21. Comparison Between SSL of Leighton Buzzard Sand and Ottawa Sand F125

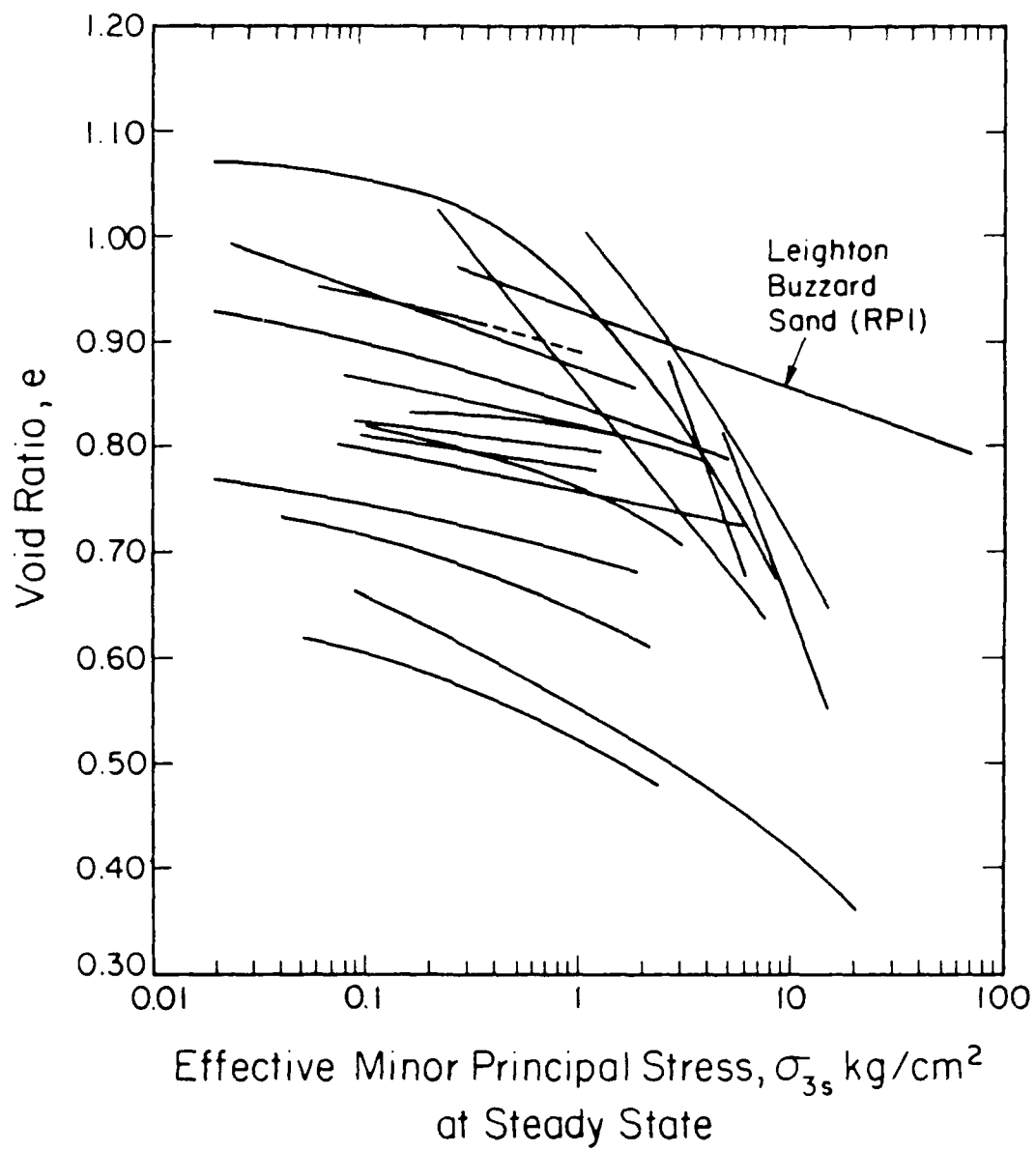


Fig. 8.22. Position of SSL of Leighton Buzzard Sand Compared to Other Sands

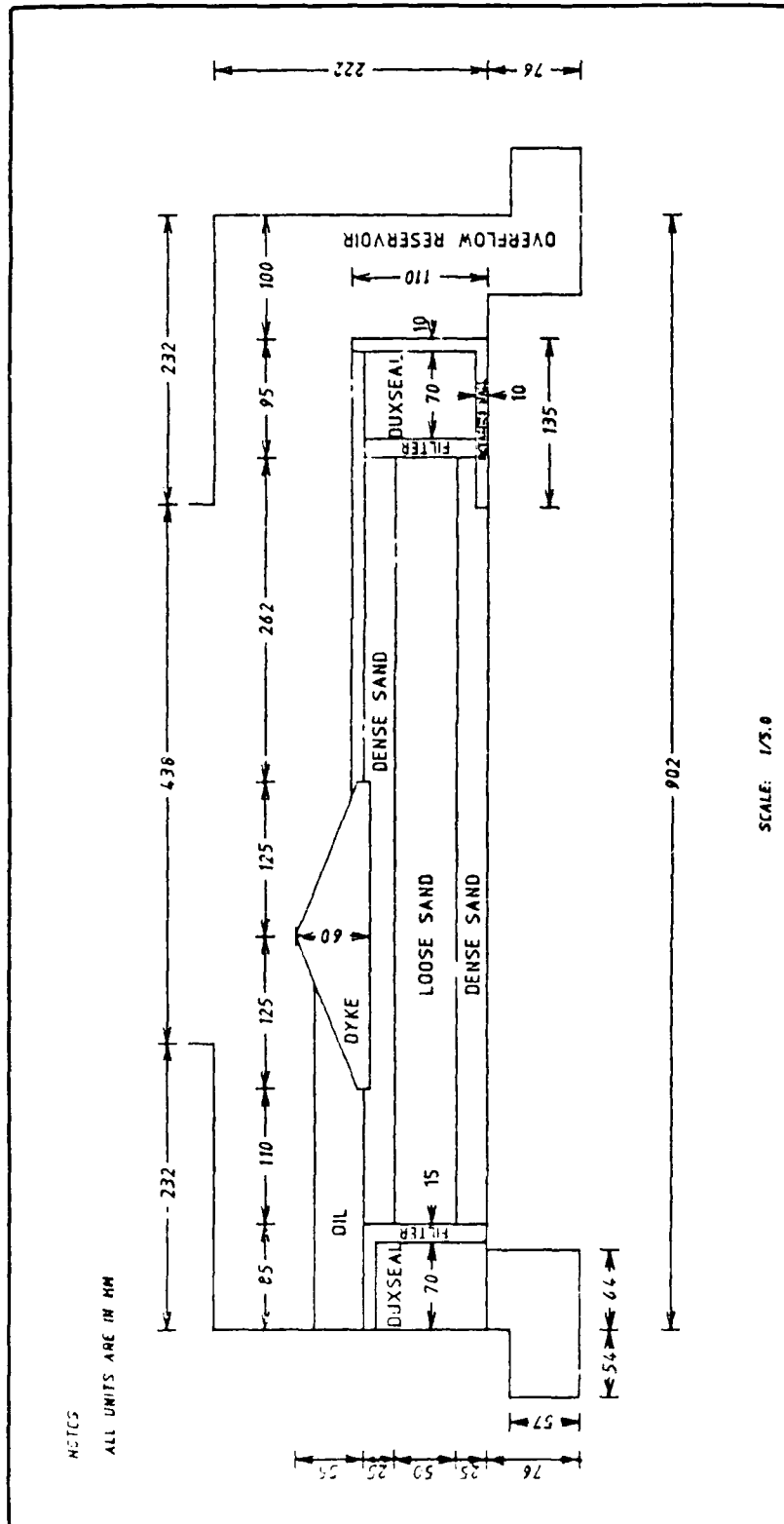


Fig. 8.23. Centrifuge Test of a Well Compacted Dyke Resting on Foundation with Layer of Loose Sand (after Habibian et al., 1985)

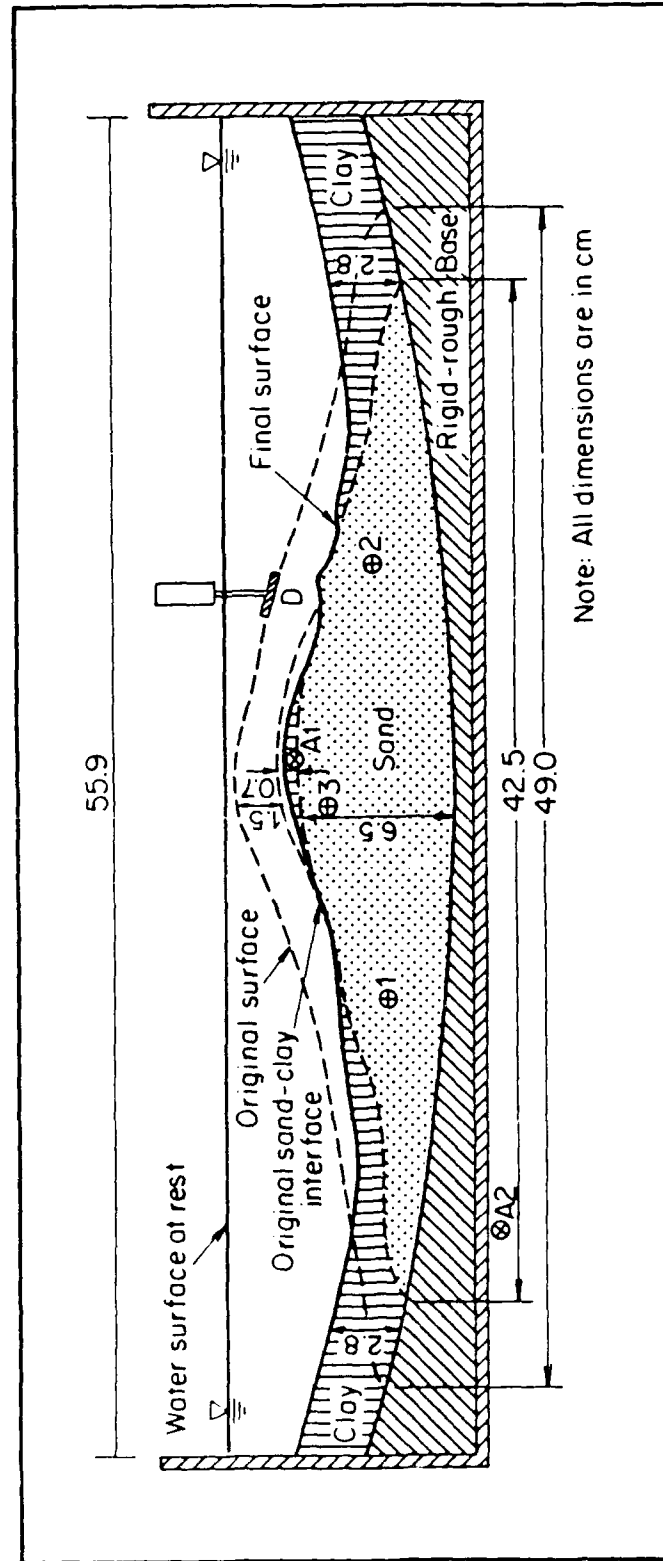


Fig. 8.24. Schematic Representation of a Submerged Sand Embankment Overlaid by a Soft Clay Layer (after Arulanandan et al., 1988)

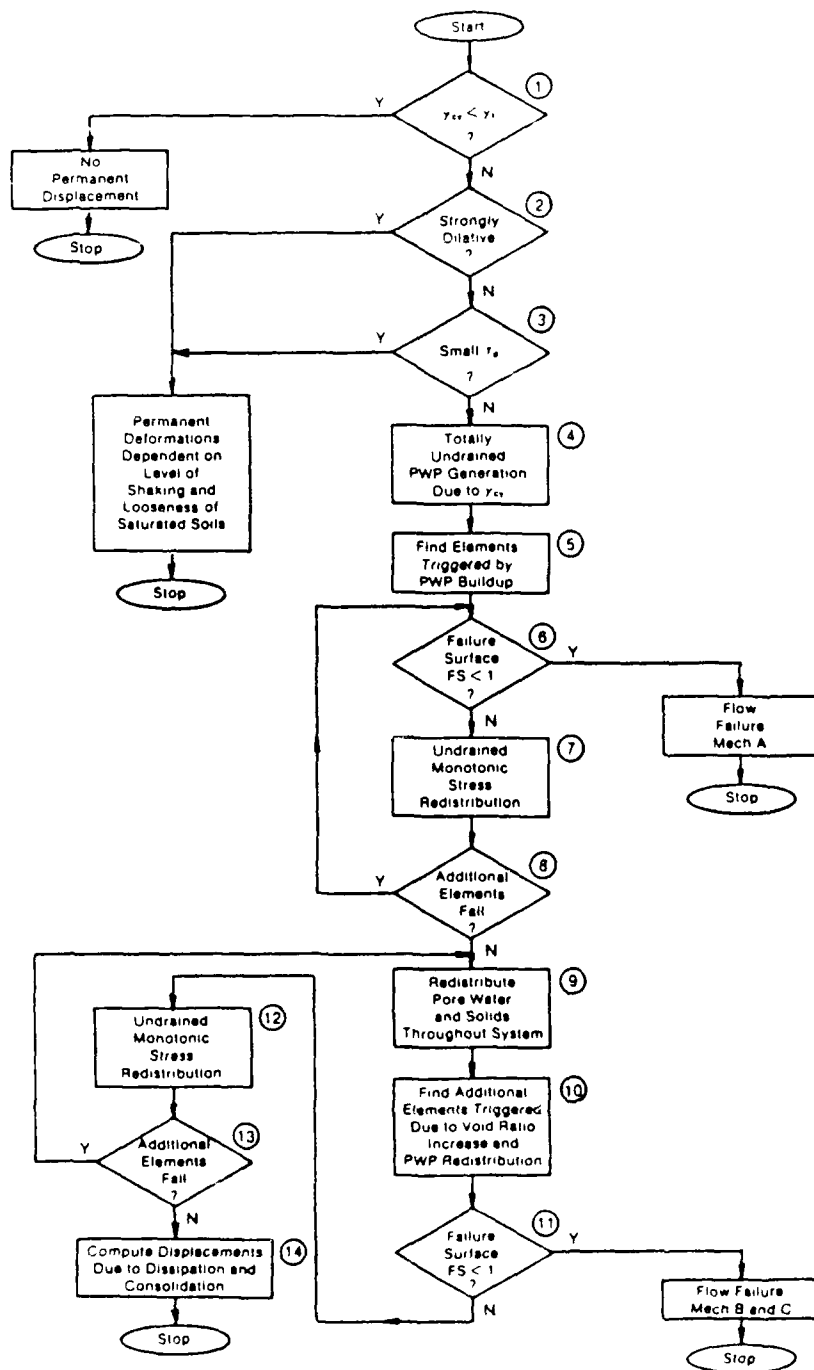


Fig. 8.25. Flowchart of Proposed Conceptual Framework for Analyzing Liquefaction Flow Failures

CHAPTER 9  
A REANALYSIS OF THE LOWER SAN FERNANDO  
DAM SLIDE

9.1 General

On February 9, 1971, shortly after 6.00 AM local time a strong earthquake struck the San Fernando Valley in California. The nearby Van Norman Lake Complex, comprised of the hydraulic fill Upper and Lower San Fernando Dams, was severely shaken and damaged by the earthquake. The Upper San Fernando Dam suffered extensive cracking and some permanent deformations, while the Lower San Fernando Dam experienced a major flow slide which caused most of the upstream shell to slide into the reservoir.

The magnitude 6.6 earthquake caused a 200 square mile area of the San Gabriel Mountains to move southward and permanently rise several feet. The length of the fault slip was about 12 to 15 miles and the propagating earthquake waves awakened between 5 to 10 million habitants of Southern California. At the end of the earthquake, 58 people had lost their lives, 2400 were injured and 1500 buildings were demolished or considered unsafe for use (Seed, 1979).

The slide of the Lower San Fernando Dam was a most serious effect of this earthquake, which almost became a catastrophe. Even though a complete breach of the dam did



not occur, only about 4 to 5 ft. of badly cracked material remained as freeboard. This precarious condition led to the evacuation of 80,000 residents living downstream until the water level in the reservoir was lowered to safe values. Had the dam breached, it would have been the worst natural disaster in the history of the United States.

## 9.2 Upper and Lower San Fernando Dams

The Upper San Fernando Dam was constructed on a 50 to 60 ft. deep alluvium deposit composed of stiff clays and clayey gravels. The material underlying the alluvium are Lower Pleistocene sandstones of the Saugus Formation (Seed et al., 1973). Construction of the Upper Dam was mainly done by the semi-hydraulic fill method, in which material was hauled from the borrow pit to the edge of the embankment by wagons and then dumped into the central pond where it was dispersed by monitors operating from floating barges. The semi-hydraulic fill portion was finished by 1921 when it reached elevation 1200 (all dimensions given are in feet). The dam was raised further the next year by placing a rolled fill up to elevation 1218, for a total dam height of about 70 feet. A cross section of the Upper San Fernando Dam is shown in Fig. 9.1.

The Lower San Fernando Dam rests directly on an approximately 35 ft. deep alluvium deposit consisting of stiff clays with lenses of sand and gravel. The material underlying the alluvium is mainly shales, siltstones and sandstones (Seed et al., 1973).

The Lower San Fernando Dam was built using the hydraulic fill method. In this procedure, the soil is obtained by using high powered water jets on a borrow area, and then transporting the water-soil mixture to the dam where it is deposited on a beach sloping inwards towards a central core pool. In this way, the coarser sand particles settle in the beach itself, near the upstream and downstream blankets, while the finer material goes into the water and settles at the bottom of the central core. The finer material provides water tightness while the coarser material gives stability to the dam. There is no additional compaction, and thus both finer and coarser soils stay loose. Construction started in 1912 by building the broad starter dykes at the edges of the upstream and downstream shells by rolled fill methods. Unfortunately the dimensions of these starter dykes are not well known (Seed et al., 1973). Construction of the hydraulic fill zone continued between years 1912 and 1915 until elevation 1090, at which time the borrow area was changed; and then, construction

proceeded until approximately elevation 1100. Between years 1916 and 1930 two rolled fill sections capped the hydraulic fill zone up to elevation 1145. In 1940 a rolled fill berm was added to the downstream side in order to increase its stability. The water level was kept at elevation 1134.6 but in 1966 it was decided to lower the operating level by about 10 feet. Upon completion, this hydraulic fill dam had a height of about 140 feet and a length of 2080 feet, with an upstream slope of 2.5:1 and downstream slopes of 2.5:1 and 4.5:1 (berm). A cross section of the Lower San Fernando Dam is included in Fig. 9.1.

A general reevaluation of the seismic stability of all earth dams in California was carried out in 1966. For the Lower San Fernando Dam, the consulting board suggested a seismic coefficient of 0.15 for the conventional pseudo-static method, based on the known and expected seismicity of the region. The strength of the soils comprising the embankment were determined using laboratory tests on undisturbed specimens; the data produced by these tests was interpreted conservatively to yield the shear strengths of the soils present. The stability analysis was carried out using this seismic coefficient of 0.15 and considering a 25 ft. partial drawdown; a minimum factor of safety of 1.01 was calculated. Since the strength values

were supposed to be on the conservative side, this factor of safety was accepted and the dam was considered safe against ground motions produced in the area (Seed et al., 1973).

### 9.3 Earthquake Damage to the Upper and Lower San Fernando Dams in 1971

The most relevant set of available instrumental earthquake records in the 1971 earthquake consists of a pair of seismoscopes which had been placed on the Lower San Fernando Dam. One of them was located on the crest while the other was on rock at the east abutment. The seismoscopes were analyzed by Scott (1972) using an ingenious procedure which enabled him to convert the abutment seismoscope trace into an acceleration time history. The computed abutment accelerogram contained a peak acceleration of 0.8 g, but due to the uncertainties involved in this procedure Scott suggested that the peaks were probably closer to 0.55 to 0.6 g near the dam area. This evaluation appears to be consistent with other peak accelerations recorded on rock sites at various epicentral distances during this earthquake, as can be seen in Fig. 9.2. The accelerogram produced by Scott using the abutment seismoscope is shown in Fig. 9.3 (Seed et al., 1973).

The most noticable damage caused by the earthquake to the Upper San Fernando Dam were longitudinal cracks running almost the entire length of the dam. These cracks resulted from permanent deformations of the dam, which moved downstream about 5 feet and settled about 3 feet (see Fig. 9.1). Three piezometers installed in the Upper San Fernando Dam permitted the study of pwp generation inside the embankment; the locations of the piezometers and their readings are shown in Fig. 9.4. About 24 hours after the earthquake they were inspected, revealing that the water levels had increased in piezometers 1 and 2, located near the center of the dam, by at least 17 ft and 8.5 ft of water, respectively (see Fig. 9.4). These excess pore pressures may have been even larger, as there was evidence that the water spilled over the well casings of the piezometers. At piezometer 3, located closer to the downstream slope, the pore pressure reading was about 8 ft of water. From FE calculations by Mohamad (1984),  $\bar{\sigma}_{3c} = 0.6 \text{ kg/cm}^2 = 1,200 \text{ psf}$  for the three piezometers, and thus the measured pore pressure ratios were at least of the order of  $r_u = \frac{(8)(62.4)}{1,200} = 0.4$ . Based on the results of Chapter 6, these pwp were enough to trigger flow failure if the factor of safety of the Upper San Fernando Dam after liquefaction had been less than 1.

The damage suffered by the Lower San Fernando Dam was very significant due to a massive slide in the upstream portion of the dam, which carried a large portion of the upstream blanket into the reservoir. After the earthquake shaking had finished the dam caretaker rushed to the crest within five minutes and noted that the slide had already occurred (Seed, 1979). Further analysis of the crest seismoscope recovered underwater after the slide permitted a reconstruction of the sequence of events during and after the earthquake; this is shown in Table 9.1 (Seed, 1979). This reconstruction showed that the slide started about 30 seconds after the main event shaking had ended and it took about 50 seconds to be completed. Therefore, the flow slide was driven by the static weight of the dam and not by the dynamic loads produced by the earthquake.

After the earthquake had finished and the dam was inspected, it was obvious that a large portion of the dam had slid into the reservoir, leaving only as little as 5 feet of freeboard in some places. This precarious freeboard was formed by a near vertical scarp with numerous longitudinal cracks. As there was a possibility that more material could fail, the 80,000 residents living downstream were evacuated and the water level in the reservoir was lowered. After the water went down, the slide debris became

visible showing that large blocks of soil had moved far into the reservoir. The reinforced concrete facing of the upstream slope, which had been at an angle of 2.5:1, was resting horizontally much below its original position. Two piezometers in the downstream portion of the dam recorded excess values of pwp when a reading was taken six hours after the shaking. Figure 9.5 shows their locations and the water levels recorded. One of the piezometers was located in the alluvium, while the other was in the embankment very close to the rock blanket and starter dyke. Rises in the water level of about 3 to 5 ft were measured. From FE results by Mohamad (1984) reproduced in Fig. 9.6,  $\bar{\sigma}_{3c} = 1.6 \text{ kg/cm}^2 = 3,200 \text{ psf}$  for the piezometer in the embankment, and the measured pore pressure ratio,  $r_u = \frac{(3)(6.24)}{3,200} = 0.06$ . The difference between this low value and the high  $r_u$  recorded in the Upper San Fernando Dam is probably due to the Lower San Fernando Dam piezometer being located so close to a rock blanket (see Fig. 9.1), in a zone that probably dissipated a significant amount of the pwp induced by the earthquake in the first few hours after the shaking. On the other hand, the two Upper San Fernando Dam piezometers, located at the center of the dam, dissipated very little pwp in the first few hours after the shaking. It is reasonable

to assume that values of  $r_u$  comparable to those measured at the Upper Dam were induced near the center of the Lower Dam in both upstream and downstream shells during the 1971 earthquake (see also Seed et al., 1973).

#### 9.4 Field Investigation of the Lower San Fernando Dam

Right after the slide of the Lower San Fernando Dam, an extensive field investigation program was carried out in order to analyze and understand the causes of the failure (Seed et al, 1973). The dam is also being reanalyzed 15 years later on the basis of additional field work carried out by GEI (1988). The main results presented in the 1973 and 1988 reports are summarized in this section.

Extensive field exploration (Seed et al., 1973), consisting of detailed observation, trenching and soil sampling revealed that the failure did not involve the foundation soil, but instead occurred along a zone 15 to 20 feet thick in the upstream hydraulic fill blanket. This can be more easily observed by looking at specific cross-sections of the Lower San Fernando Dam described by Figs. 9.7 to 9.9. The sections are E-E (Fig. 9.8), F-F (Fig. 9.9), and G-G (Fig. 8.11). These figures clearly show that large blocks of intact soil floated on top of a layer of liquefied material. This liquefied zone infiltrated



between the large blocks and was extruded below the toe of the original embankment. When the intact blocks were put together like so many pieces of a puzzle, the original dam cross-sections appeared in all cases with the liquefied zone missing.

This reconstruction of the original position of the slide debris showed that the slide must have been triggered by liquefaction of the upstream blanket near the base of the embankment. The soils overlying the liquefied zone then broke into blocks as they moved downwards and upstream for distances ranging from 30 to 150 feet. The movement of these large blocks removed the support of the upstream side of the clay core which could no longer support the overlying mass, causing a secondary slide movement involving the crest of the dam and the upper part of the downstream slope (Seed et al., 1973).

In the 1973 work (Seed et al., 1973), numerous soil samples were also taken for a comprehensive laboratory testing program involving both monotonic and cyclic triaxial tests on undisturbed samples. However, these tests and the field work involved in obtaining the samples did not have all the necessary elements required for the liquefaction evaluation procedure suggested by Castro and Poulos (Poulos et al, 1985; Castro et al., 1985). For this reason, a new

field exploration program was implemented, sponsored by the U.S. Army Corps of Engineers Waterways Experiment Station (WES) under the direction and supervision of GEI (1988). The field work produced was then used for the reevaluation of the dam using steady state concepts and methodologies.

After the 1971 dam failure, the embankment was reconstructed in 1975 to act as a backup dam for a future dam to be built on the reservoir; however, water has not been impounded since 1971. At the moment of the 1985 exploratory campaign, the cross section of the embankment was as shown in Fig. 9.10. This figure shows that a compacted earthfill replaced a portion of the slide debris and the dam crest was placed lower and further downstream compared with its original position.

The 1985 field exploratory program was conducted in order to characterize and obtain undisturbed samples of the remaining hydraulic fill zone on the downstream side. This zone is the area in the downstream shell which is symmetrically opposite to that of the upstream shell which failed in 1971. The slide occurred along an approximately 15 feet thick layer of soil at the base of the upstream shell, and therefore the soil sampling for liquefaction analysis concentrated along this critical layer in the downstream side. Undisturbed samples were taken in this

area, and in addition, a representative mixture of soil from this critical layer was made with soils recovered from a nearby exploration shaft. This mixture of soils is what was tested and was shown in previous chapters as San Fernando Sand SF7. Construction records indicated that the same borrow areas and construction techniques were used for both the upstream and downstream slopes, and therefore they can both be thought to be similar in composition.

A plan view of the dam during the 1985 campaign is shown in Fig. 9.11, which also includes the locations of the numerous borings. Undisturbed fixed piston sampling was done on borings at locations 103 and 111 in order to obtain undisturbed soil samples for testing from the critical soil layer. During this undisturbed sampling program, careful measurements were made during and after the fixed piston sampling in order to be able to backtrack and obtain the in-situ void ratio, in 1985, and in 1971 at the time of the earthquake. These measurements included locking the position of the piston and then pushing and measuring the stroke of the sampler, measuring the gap between the piston and the top of the soil immediately after withdrawal from the borehole, and measuring the clearing ratio of the Shelby tubes. Additional corrections were made to account for the changes in void ratio caused by the 1971 earthquake and

those which occurred after the shaking. Those corrections took into account the lowering of the piezometric surface through the dam and also the differences between the upstream slope where the failure occurred and the downstream slope where the sampling took place (GEI, 1988; Seed et al., 1988). The sixteen values of in-situ void ratios before the 1971 earthquake estimated by GEI (1988) are listed in Table 9.2. Slightly smaller values were estimated by Seed et al. (1988). It is interesting to notice (see Appendix II) that the void ratios after consolidation to  $\bar{\sigma}_{3c} = 1 \text{ kg/cm}^2$ , obtained in the laboratory in the four contractive remolded sedimented specimens ranged between  $e = 0.695$  and  $e = 0.727$ . This laboratory range includes the average void ratio in situ and almost half of all measurements of  $e$  in Table 9.2.

#### 9.5 Determination of Contractive Zone Within the Dam

A static nonlinear finite element analysis of the Lower San Fernando Dam was performed by Mohamad (1984) and was repeated herein.. The computer code was FEADAM (Duncan et al., 1980a), with most parameters obtained directly from Seed et al., (1973), while others were determined by Mohamad (1984). The technique used for obtaining the soil properties is described in a companion report to the FEADAM manual (Duncan et al, 1980b). The parameters used in this

analysis of the Lower San Fernando Dam are shown in Table 9.3. The most important results produced by this finite element calculation pertain to the distribution of the minor effective consolidation stress,  $\bar{\sigma}_{3c}$ , in the saturated hydraulic fill shells. These calculated contours of  $\bar{\sigma}_{3c}$  within the saturated hydraulic fill sand of the Lower San Fernando Dam, which take into account the seepage line within the embankment corresponding to the water level in the reservoir, are shown in Fig. 9.6. It can be seen that for the liquefied zone that failed in 1971,  $\bar{\sigma}_{3c}$  ranges between 0.6 and 1.6 Kg/cm<sup>2</sup>, and in the main section of the triangular wedge of liquefied material (see Fig. 9.8) it ranges between 1.0 and 1.4 Kg/cm<sup>2</sup>. The undisturbed samples taken from the downstream side would correspond to in-situ confining stresses  $\bar{\sigma}_{3c}$  at the time of the earthquake ranging between 1.3 and 1.6 Kg/cm<sup>2</sup>.

The in-situ void ratio calculated by Seed (1988) and GEI (1988) for all available fixed piston measurements are plotted versus this range of pressures  $\bar{\sigma}_{3c} = 1.3$  to 1.6 kg/cm<sup>2</sup> for the upstream slope in Fig. 9.12. The figure also includes the in-situ SSL generated using sedimented samples: this is the same SSL shown in Fig. 6.20 and it constitutes the "best estimate" of the in-situ SSL obtained from the experimental results of Chapter 6. The comparison in Fig.

9.12 clearly shows that the hydraulic fill soil which liquefied in 1971 was contractive at the time of the earthquake, as all in-situ void ratios plot above the SSL. Furthermore, as most of the data would plot above the in-situ SSL even for  $\bar{\sigma}_{3c} = 0.6 \text{ kg/cm}^2$ , which is the smallest value of  $\bar{\sigma}_{3c}$  present upstream, the whole upstream critical layer of the hydraulic fill between the starter dyke and the core should be considered contractive.

Once the conclusion is reached that the critical layer of the hydraulic fill in the upstream side was contractive in 1971, the flow failure caused by the earthquake can be attributed to mechanism A. This is reinforced by the fact that the failure occurred seconds after the shaking, which did not allow for much pwp redistribution in the large silty sand mass.

This finding herein that the soil was contractive in the Lower San Fernando Dam runs contrary to the opinion of some engineers, who feel that uncompacted hydraulic fills tend to have relative densities of the order of 40 percent, which is certainly higher than that necessary for most clean sands to be contractive. The laboratory results presented herein clearly show that the internal stratigraphy of a silty sand or sandy silt hydraulically deposited can greatly affect its void ratio and degree of contractiveness. Both

the stratification and the large amounts of silts present render the relative density concept useless; and the only way currently available to find if a hydraulic fill deposit is contractive is by testing laboratory specimens having the in-situ layered structure, as done herein.

#### 9.6 Determination of In-Situ $S_{us}$

In the GEI (1988) report of the reanalysis of the Lower San Fernando Dam, the undisturbed soil samples from the dam were tested using  $\bar{C}TU$  tests in order to determine their steady state shear strengths  $S_{us}$ . The slope of the SSL using reconstituted homogenous moist tamped specimens was used to correct the  $S_{us}$  of the undisturbed specimens to that of in-situ conditions, by considering all void ratio changes that occurred between the time of the 1971 earthquake and the time of soil testing. This correction was done by GEI along the slope of the moist tamped SSL, as suggested by Poulos et al. (1985), as already discussed in Chapter 2. The correction for  $S_{us}$  of all tests using undisturbed samples, is shown by their summary plot reproduced here in Fig. 9.13. It is interesting to note that the RPI "best estimate" of in-situ  $q_{us}$  SSL obtained herein from  $CyT-\bar{C}AU$  tests in Fig. 6.21 and reproduced in Fig. 9.14, would plot

in the middle of the GEI undisturbed  $S_{us}$  lines in Fig. 9.13 (of course, the comparison is done after allowing for the difference between  $q_{us}$  and  $S_{us}$ ,  $S_{us} = q_{us} \cos \bar{\phi}_{us} = 0.83 q_{us}$ ). This comparison confirms again the assumption that the line in Fig. 9.14 is a good average representation of the in-situ conditions, and serves as a validation for both the GEI and the RPI procedures.

A wide range of  $S_{us}$  values was obtained by GEI from Fig. 9.13 with their method, between 0.15 and 2.5  $\text{Kg/cm}^2$ . The representative value chosen by GEI (1988) for the hydraulic fill was 0.26  $\text{Kg/cm}^2$ , obtained by following the recommendation of the U.S. Army Corps of Engineers (1970) as the average  $S_{us}$  minus one half of the standard deviation for all samples.

In the present work, the representative in-situ  $q_{us}$  SSL of Fig. 9.14 was used to estimate the in-situ  $S_{us}$ . For that purpose, the in-situ void ratios of Table 9.2 (replotted as arrows in Fig. 9.14) were used. The calculations are summarized in Table 9.2.

The total range of  $q_{us}$  in Table 9.2 is from 0.081 to 1.2  $\text{kg/cm}^2$ , or  $S_{us} = 0.067$  to 1.0  $\text{kg/cm}^2$ . As suggested by the U.S. Army Corps of Engineers (1970) and adopted by GEI (1988), a "best estimate"  $S_{us}$  was obtained by taking the value such that about two-thirds of the strengths in the dam



are greater than this "best estimate". As pointed out by GEI (1988), this can be accomplished by taking the average  $S_{us}$  minus half of its standard deviation. This gives a "best estimate"  $S_{us} = 0.21 \text{ kg/cm}^2$  in Table 9.2, which is not far from  $0.20 \text{ kg/cm}^2$  obtained by GEI (1988). Clearly this "best estimate" has a large uncertainty attached to it. Possible lower and upper bounds for the  $S_{us}$  of the upstream shell of the dam can be obtained by taking the average  $S_{us}$  minus a standard deviation and the average  $S_{us}$ , respectively. This gives bounds of  $0.068 \text{ kg/cm}^2$  and  $0.35 \text{ kg/cm}^2$ , as listed in Table 9.2. Summarizing, at the time of the 1971 earthquake, it is estimated that the upstream shell of the Lower San Fernando Dam had an  $S_{us} = 0.21 \pm 0.14 \text{ kg/cm}^2$ .

#### 9.7 Triggering and Flow Failure Evaluation of the Lower San Fernando Dam

The average driving shear stress on the critical failure surface of the downstream slope was calculated to be  $0.48 \text{ Kg/cm}^2$  (GEI, 1988). This was done by performing a slope stability analysis using the actual observed failure surface and the shear strength values of all soils present along the failure curve. The shear strength values used for the hydraulic fill critical layer was varied until a FS of 1

was obtained for the slope. This shear strength giving  $FS=1$  was then defined as the average driving stress acting on the hydraulic fill, and it was found to be  $0.48 \text{ kg/cm}^2$ .

In order to get the local factor of safety in the liquefied hydraulic fill after flow failure triggers, the same failure surface and shear strength parameters are used as in the step explained above, but now the actual value of  $S_{us}$  of the soil is used for the liquefied hydraulic fill critical layer. GEI (1988), using  $S_{us} = 0.26 \text{ Kg/cm}^2$  for the critical sand layer, computed that the hydraulic fill in the upstream slope had a local  $FS = 0.26/0.48 = 0.54$  against liquefaction flow failure. Therefore, in the event that the earthquake was strong or long enough to make the elements along the failure surface trigger, then liquefaction flow failure is predicted by Mechanism A. The same procedure was applied to the downstream slope where the local factor of safety was found to be about 1.00 if all elements triggered, with  $FS$  increasing to 1.5 once the upstream slide occurred (GEI, 1988). The positions of the critical failure surfaces obtained for upstream and downstream are shown in Figs. 9.15 and 9.16, respectively. The fact that  $FS < 1$  in the upstream slope, whereas for the downstream slope is  $FS \approx 1$ , explains why the flow slide occurred on the upstream side. These results should come as no surprise since it is known

that a flow slide occurred in the upstream part of the dam, with the failure surface corresponding closely to that shown in Fig. 9.15. A similar conclusion is obtained herein for the upstream shell of the Lower San Fernando Dam, using  $S_{us} = 0.21 \pm 0.14 \text{ kg/cm}^2$ . These give a "best estimate" for the local  $FS = 0.21/0.48 = 0.44$  and lower and upper bounds of  $FS = 0.07/0.48 = 0.15$  and  $FS = 0.35/0.48 = 0.73$ . Therefore, for any reasonable value assumed for  $S_{us}$ ,  $FS$  is significantly less than one.

A flow failure triggering evaluation for the upstream slope of the Lower San Fernando Dam was conducted herein by calculating the cyclic shear strains induced in the hydraulic fill critical layer by the 1971 earthquake, and comparing these with the cyclic shear strains needed to trigger liquefaction as determined by CyT-CAU tests on sand SF7 in Chapter 7. These cyclic shear strains induced by the 1971 earthquake, having a peak ground surface acceleration in the free field of 0.60 g, were obtained from dynamic analyses of the Lower San Fernando Dam conducted for this purpose. Two calculations were performed using computer programs QUAD-4 (Idriss et al., 1973) and LISB (Stara-Gazetas, 1986).

QUAD-4 is a plane strain, two dimensional, dynamic finite element program that uses variable damping in the

elements and solves the equations of motion by step-by-step time integration. The non-linearity of the shear modulus and damping with level of strain is taken into account by incorporating the relation proposed by Seed and Idriss (1970). The reduction of shear modulus due to nonlinearity is done by running the accelerogram several times and updating the modulus depending on the level of strain. This iterative procedure continues until the strain assumed for the modulus reduction factor agrees with the actual seismic strain produced by the analysis. This is called an equivalent linear method. During the iterations, a similar procedure is used to adjust the strain-dependent material damping.

LISB is a one dimensional inelastic shear beam analysis that takes into account the non-linearity of the soil by using the hyperbolic soil model. The initial stress-strain backbone curves of all elements in the dam are found by statically loading the embankment with horizontal, inertia-like triangular loading using computer program FEADAM. By using different magnitudes of load for each layer it is possible to obtain the layer mean stress-strain behavior as well as the individual element stress-strain behavior. A procedure to go from the layer stresses and strains to the individual element stresses and strains is

then developed. The layer stress-strain behavior is then used for the dynamic shear beam analyses, and the computed dynamic stresses and strain are then converted back to their individual element values.

Both programs assume no degradation of shear modulus due to pwp buildup, but since torque in the CyT-CAU tests does not decrease in any significant manner prior to triggering, this assumption is justifiable. The same observation of the torque not degrading much before triggering, observed in the CyT-CAU tests conducted herein was also reported by Mohamad (1985), and is probably due to the fact that triggering typically occurs at a small or moderate pwp ratio  $r_u$ .

Figure 9.17 presents the shear strain time histories of a particular element in the critical zone of the dam, calculated by the two different methods: 2D equivalent linear and 1D shear beam inelastic nonlinear. In both cases, the accelerogram of Fig. 9.3 was used as input with  $a_p = 0.6$  g. Figure 9.18 includes the peak shear strain  $\gamma_p$  computed in the same QUAD-4 run for all elements located in the critical layer at the base of the dam, upstream and downstream.

The strains produced by these two programs for the soil element in Fig. 9.19 were compared with the triggering

relation for San Fernando Sand SF7 with  $\bar{\sigma}_{3c} = 1 \text{ kg/cm}^2$  and  $K_c = 2.0$  (an average  $K_c = 2$  was obtained by GEI (1988) from the driving shear stress and for the stability analysis of Fig. 9.15). The corresponding triggering  $n_t$  versus  $\gamma_{cy}$  curve, obtained from Fig. 7.31, is reproduced in Fig. 9.19. The value of  $\gamma_{cy}$  needed to trigger flow failure in  $n_t = 1$  cycle is about 0.1 - 0.2%, and thus either of the two dynamic analysis used in Fig. 9.17 predicts triggering occurring in the first 2 seconds of the shaking. The induced strains are so large that it is unnecessary to perform a more refined modelling of the pwp buildup. The conclusion is the same even if the scatter of the data points in Fig. 7.31 is considered, as done in the band plotted in Fig. 9.19.

The values of  $\gamma_p$  induced by the earthquake for the rest of the elements of the most critical layer in the hydraulic fill shells, upstream and downstream, are shown in Figure 9.18 from the same QUAD-4 calculation with  $a_p = 0.6 \text{ g}$ . It can be clearly seen that larger values of  $\gamma_p$  are induced towards the center of the dam for both the upstream and downstream shells, with  $\gamma_p$  near the slope surface being roughly half of that near the core. However, even those elements near the upstream and downstream toes of the dam experienced substantial amounts of cyclic shear strains, in

excess of  $\gamma_p \approx 0.6\%$ , which would have caused triggering in less than a cycle. Therefore, without any doubt, the 1971 earthquake was strong enough to trigger liquefaction in all elements of the critical layer, both upstream and downstream, and since the static factor of safety was significantly less than one, the 1971 liquefaction flow failure could have been predicted by this method. As liquefaction flow failure also triggered in the downstream slope, the reason why this slope did not fail lies in its larger factor of safety. A similar conclusion is valid for the Upper San Fernando Dam, which also triggered but did not flow due to  $FS > 1$  in both slopes (GEI, 1988). This prediction herein that triggering occurred in both dams in 1971 is consistent with the high pwp recorded after the earthquake in the Upper San Fernando Dam, as previously discussed in Section 9.3.

#### 9.8 Earthquake Shaking Before 1971

Since its completion in 1915, the Lower San Fernando Dam has been subjected to various earthquakes as listed in Table 9.4. The information in the table on earthquake dates, epicentral distances and magnitudes were obtained from GEI (1988). However, the values of peak ground surface

acceleration at the site,  $a_p$ , were estimated herein using the attenuation relation proposed by Joyner and Boore (1981). The accelerations obtained by GEI (1988) using essentially Schnabel et al.'s (1973) attenuation curves are also included in Table 9.4 for comparison. For the magnitude 5.25, August 30, 1930 earthquake, GEI (1988) gives two ranges of  $a_p$ : 0-0.02g corresponding to an epicentral distance of 43.2 km, and 0.02-0.09g for a possible closer location of the event. This 1930 earthquake is important, as it is the only one before 1971 which caused some damage to the dam. Such damage consisted of small transverse cracks near the contact with the left abutment, with a 0.15 to 0.25 ft settlement of the parapet wall located on the upstream side of the crest. According to the caretaker, who had lived at the dam since construction, this was the strongest earthquake he had experienced; this tends to confirm the range of larger  $a_p = 0.02 - 0.09$  g in Table 9.4 for the 1930 event. It is interesting that neither the July 21, 1952, magnitude 7.7 event causing  $a_p = 0.06$  g (0.05-0.12g), nor the August 30, 1967, magnitude 4 earthquake causing  $a_p \approx 0.1$ g, did any damage to the dam (GEI, 1988).

Therefore, it is useful to verify that the triggering procedure proposed herein, previously applied to predict



flow failure in 1971, is consistent with the absence of flow failure triggering observed for all earthquakes in Table 9.4, the beginning of damage for the 1930 event and the absence of any damage for the rest of the earthquakes.

For that purpose, Program QUAD-4 was run several times using the same input accelerogram of Fig. 9.3, but scaled to  $a_p = 0.05g, 0.1g, 0.2g$  and  $0.3g$ , and the seismic strains were calculated for the critical hydraulic fill layer at the base of the Lower San Fernando Dam. In conjunction with the results for  $a_p = 0.6g$  already presented in Figs. 9.17 and 9.18, these runs allowed for a complete parametric study on the influence of  $a_p$  on peak seismic strains in that layer, and an evaluation of the levels of pwp buildup and predicted triggering or nontriggering generated by these levels of ground shaking. The results of this parametric study using QUAD-4 are summarized in Figs. 9.20 to 9.22. It should be recognized, however, that the same input accelerogram recorded in 1971 was used in all runs, with the accelerations scaled down, and this may overestimate or underestimate the response of the dam when subjected to seismic excitation of different frequency contents and durations.

Figures 9.18, 9.20 and 9.21 present the peak values of

shear strain,  $\gamma_p$ , generated in different elements along the critical layer by the various input  $a_p$  used. As expected,  $\gamma_p$  increases as  $a_p$  increases. Also, in all cases  $\gamma_p$  for the upstream shell is largest near the clay core, at the element indicated in Fig. 9.17, and smallest near the upstream slope. A similar trend is also true for  $\gamma_p$  in the downstream shell. Figure 9.22 plots  $\gamma_p$  versus  $a_p$  for both extreme elements in the upstream shell, thus defining a band which encompasses the values of  $\gamma_p$  for all elements between the core and the upstream slope, for a given  $a_p$ .

Figure 9.22 includes the ranges of  $\gamma_p$  associated with  $a_p = 0.05g, 0.1g, 0.2g, 0.3g$  and  $0.6g$ . The figure also includes two ranges of  $\gamma_p$  needed to trigger flow failure liquefaction in  $N = 1$  cycle and  $N = 5$  cycles, respectively, obtained from the triggering relation band of Fig. 9.19. The band for 1 cycle in Fig. 9.22 was obtained by assuming  $\gamma_p = \gamma_{cy}$ , which resulted in  $\gamma_p = 0.15$  to  $0.3\%$ ; on the other hand, the band for 5 cycles were obtained by using  $\gamma_p = 1.5 \gamma_{cy}$ , or  $\gamma_p = 0.03$  to  $0.1\%$ . This arbitrary factor of 1.5 corresponds to  $\gamma_{cy} = (2/3) \gamma_p$ , and is similar to the criterion often used to approximately transform an irregular accelerogram time history to an equivalent number of equal acceleration pulses (Seed, 1979). These ranges of  $\gamma_p$  needed to trigger in 1 cycle and 5 cycles have been superimposed on

Fig. 9.22. In this evaluation,  $N = 1$  cycle was arbitrarily taken as representative of short duration shaking, typical of very low earthquake magnitudes, while  $N=5$  cycles was used for long duration shaking usually associated with larger magnitudes. These estimated  $N$  contain a large degree of uncertainty, as magnitude is not the only parameter controlling duration, with large durations of shaking developing sometimes on soil even for relatively low magnitude earthquakes (see Dobry et al., 1978). The value of  $N$  also depends on other factors, including frequency content of the shaking, fundamental period of the dam, etc. However, these  $N=1$  and 5 cycles selected as representative can be used for a crude evaluation of flow failure triggering of the upstream slope of the Lower San Fernando Dam for different  $a_p$ .

The evaluation is summarized in Fig. 9.22 and Table 9.5. It predicts that for  $a_p \leq 0.05g$  no triggering occurs, not even in the most critical elements of the dam, consistent with the lack of damage reported for all earthquakes in this acceleration range in Table 9.4. For  $a_p \approx 0.06$  to  $0.10g$ , triggering at least in the most critical elements is predicted for 5 cycles but not for 1 cycle, that is, the possibility exists of some damage or even of flow failure in this acceleration range; this is consistent with

the limited damage experienced by the dam in the 1930 event. It is also consistent with the lack of effects reported for the 1952 earthquake with  $a_p \approx 0.1g$ , but it suggests that the dam may have been close to triggering in that earthquake. Finally, for  $a_p \geq 0.20g$ , complete triggering and flow failure of the upstream slope is predicted, except perhaps for  $N=1$  cycle, for which at least some damage is expected. This, of course, is what happened in 1971, with  $a_p \approx 0.60g$  and the actual flow failure of the slope.

The results of this discussion are also consistent with the published performance of hydraulic fill dams during earthquakes, where it has been reported that these dams start experiencing some sort of trouble above about  $0.2 g$  (Seed et al., 1978). During the same Kern County earthquake of 1952 listed in Table 9.4 (Magnitude 7.7), three earth dams were shaken, with two of them showing some type of damage. The Dry Canyon Dam was shaken with an estimated  $a_p = 0.12 g$ , and developed cracks indicative of a potential slide, and the South Haiwee Dam developed slight longitudinal cracking with an estimated  $a_p \approx 0.04 g$ . On the other hand, Fairmont Dam with an estimated  $a_p = 0.18 g$  did not suffer any reported damage (Seed et al., 1978). Three hydraulic fill dams in Russia were also shaken by

earthquakes causing  $a_p$  of 0.1, 0.12 and 0.17 g. Only the Boz'suiskaya Dam suffered any damage in the form of 1 foot settlement with an earthquake of estimated  $a_p \approx 0.17$  g.

Below  $a_p = 0.2$  g a more sophisticated analyses using the pwp model proposed herein in Section 7.5 would be necessary, in order to pinpoint more accurately the exact value of  $a_p$  necessary to trigger various soil elements for a particular earthquake and dam. Other factors beside the peak acceleration of the earthquake which may affect the magnitude of shear strains induced by an earthquake are: frequency content of the accelerogram, shear modulus of the soils, and dam geometry. Further research is still needed to clarify the grey area below 0.2 g that affects triggering.

Table 9.1.1. Sequence of Events in the Flow Slide of the Lower San Fernando Dam (after Seed, 1979)

Time	Event
0	Start of main shock of earthquake
≈ 14s	Strong motion completed—slight tilting of dam crest
≈ 40s	Start of slide movements at crest of dam
≈ 90s	End of main slide movement—instrument tilted about 26°

Table 9.2. Determination of In Situ  $S_{us}$  Using the In Situ Void Ratios of the Undisturbed Specimens. The In-Situ  $e$  Were Estimated by GEI (1988)

Void Ratio e	Porosity n	q <sub>us</sub> (Kg/cm <sup>2</sup> )	
0.780	0.438	0.081	
0.763	0.433	0.125	
0.758	0.431	0.135	
0.755	0.430	0.150	
0.745	0.427	0.190	
0.740	0.425	0.210	
0.730	0.422	0.260	
0.725	0.420	0.300	
0.715	0.417	0.370	
0.713	0.416	0.400	
0.707	0.414	0.460	
0.703	0.413	0.510	
0.698	0.411	0.540	
0.690	0.408	0.660	
0.667	0.400	1.150	
0.665	0.399	1.200	
Average	0.722	0.419	0.421

	<u>Average - 1 St. Dev.</u>	<u>Average - 0.5 St. Dev.</u> ("Best Estimate")	<u>Average</u>
$q_{us}$	0.082 Kg/cm <sup>2</sup>	0.25 Kg/cm <sup>2</sup>	0.421 Kg/cm <sup>2</sup>
$S_{us} = 0.83 q_{us}$	0.068	0.21	0.35

Table 9.3. Parameters Used in the Static Finite Element Analysis of the Lower San Fernando Dam (after Mohamad, 1985)

Soil Parameter	Symbol	Values Used in Analysis			
		Roller Fill	Ground Shale	Clay Core	Foundation Alluvium
Total Unit Weight	$(\rho g)_t$ (pcf)	134	122	122	130
Buoyant Unit Weight	$(\rho g)_b$ (pcf)	72	60	60	60
Cohesion	$c$ (psf)	2600	0	2600	0
Friction Angle	$\phi$	25°	37°	37°	30°
Modulus Number	$k$	300	510	510	330
Modulus Exponent	$n$	0.76	0.54	0.54	0.41
Failure Ratio	$R_f$	0.90	0.72	0.72	0.76
Bulk Modulus Number	$k_b$	360	446	446	398
Bulk Modulus Exponent	$m$	0	0	0	0



Table 9.4. Estimated Peak Ground Accelerations from Historical Earthquakes Prior to 1971

Earthquake Date	Distance from Dam Site to Epicenter	Magnitude	Estimated $a_p$ at Lower San Fernando Dam Joyner and Boore (1981)	Estimated $a_p$ at Lower San Fernando Dam by GEI (1988)
1919, February 16	93	NR	-	-
1920, June 21	35	4.9	0.04	<0.01
1925, June 29	121	6.25	0.01	0-0.03
1926, February 18	98	NR	-	-
1927, November 4	200	[7.5]	0.01	0-0.03
1930, August 30	43.2	5.25	0.03	0-0.09
1931, April 4	13	(4)	0.06	[~0.04]
1933, March 10	88	6.3	0.02	0-0.07
1952, July 21	93	7.7	0.06	0.05-0.12
1952, August 22	118	5.8	0.01	0-0.02
1952, August 23	37	5.0	0.04	0-0.02
1954, January 12	93	5.9	0.02	0.01-0.05
1956, February 7	35	4.6	0.03	[~0.02]
1964, February 8	13	[3.7]	~0.05	[~0.03]
1964, August 30	4	4	~0.1	[~0.05]
1965, July 16	22	4	~0.03	[~0.02]

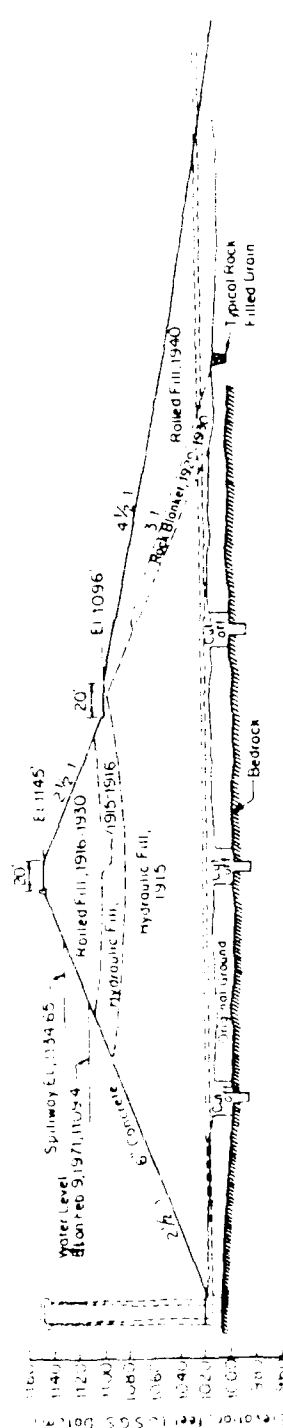
1) Significant pre-1971 earthquakes in the San Fernando earthquake area listed by Richter (1973), starting from the end of dam construction.

2) Data from the National Geophysical Data Center/National Oceanic and Atmospheric Administration earthquake data file. Values in brackets taken from Richter (1973) because information not provided by NGDC/NOAA. NR indicates no record.

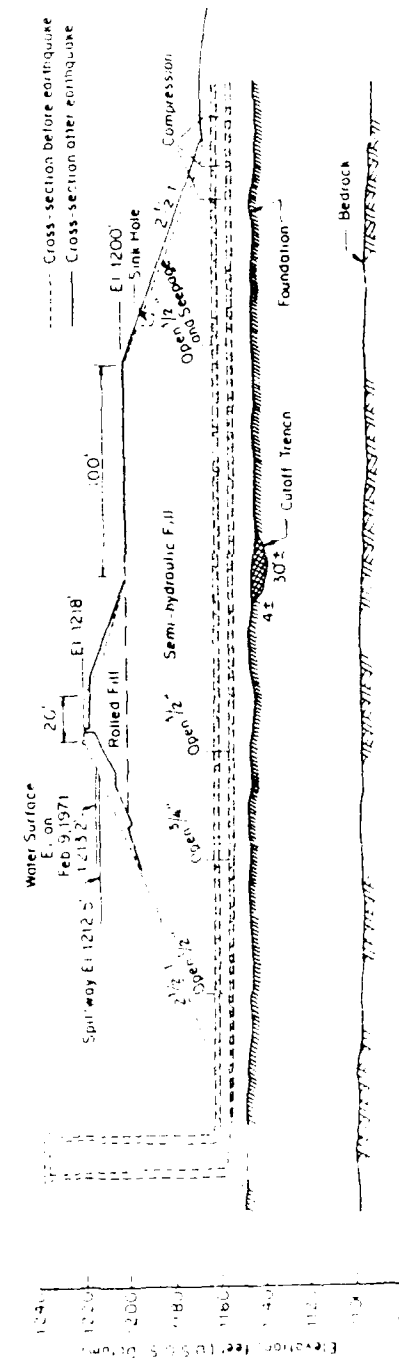
Data from NGDC/NOAA Records and GEI (1988)

Table 9.5. Triggering Evaluation of the Upstream Slope of the Lower San Fernando Dam

$a_v$	N = 5 Cycles (Long Duration Earthquake)		N = 1 Cycles (Short Duration Earthquake)	
	Triggering	Flow Failure	Triggering	Flow Failure
$\geq 0.05$ g	No Triggering	No	No Triggering	No
0.06	Most Critical Elements May Trigger	Probably not Some Damage Possible	No Triggering	No
0.10	Most Critical Elements will Probably Trigger Other Elements May Also Trigger	Possible	No Triggering	No
0.20	All Elements Will Trigger	Predicted	Most Critical Elements will Probably Trigger Other Elements May Also Trigger	Possible
0.30	All Elements Will Trigger	Predicted	All Elements Will Probably Trigger	Predicted
0.60	All Elements Will Trigger	Predicted	All Elements Will Trigger	Predicted



Cross-Section Through Lower San Fernando Dam  
(After L.A. Dept of Water and Power)



Cross-Section Through Upper San Fernando Dam  
(After L.A. Dept of Water and Power)

Fig. 9.1. Cross Section of the Lower and Upper San Fernando Dams

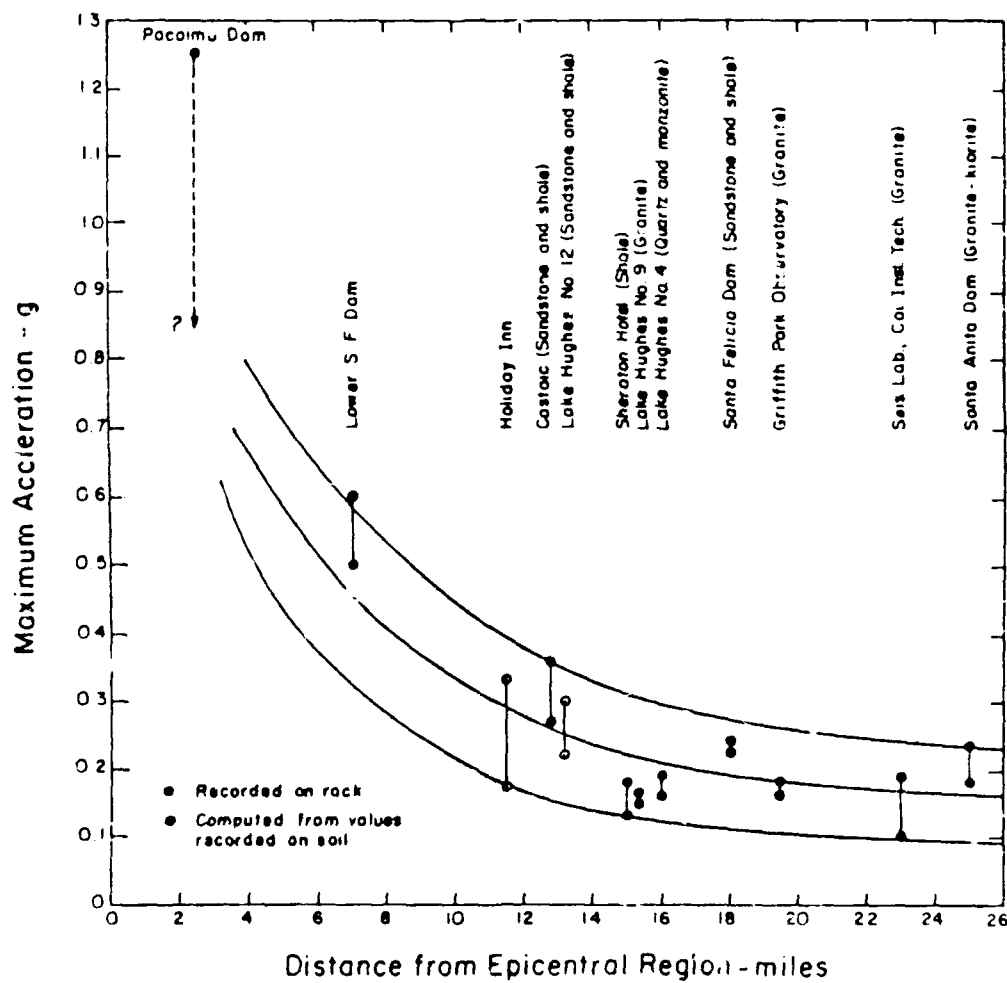


Fig. 9.2. Maximum Accelerations Recorded on Rock in San Fernando Earthquake, 1971 (after Seed et al., 1973)

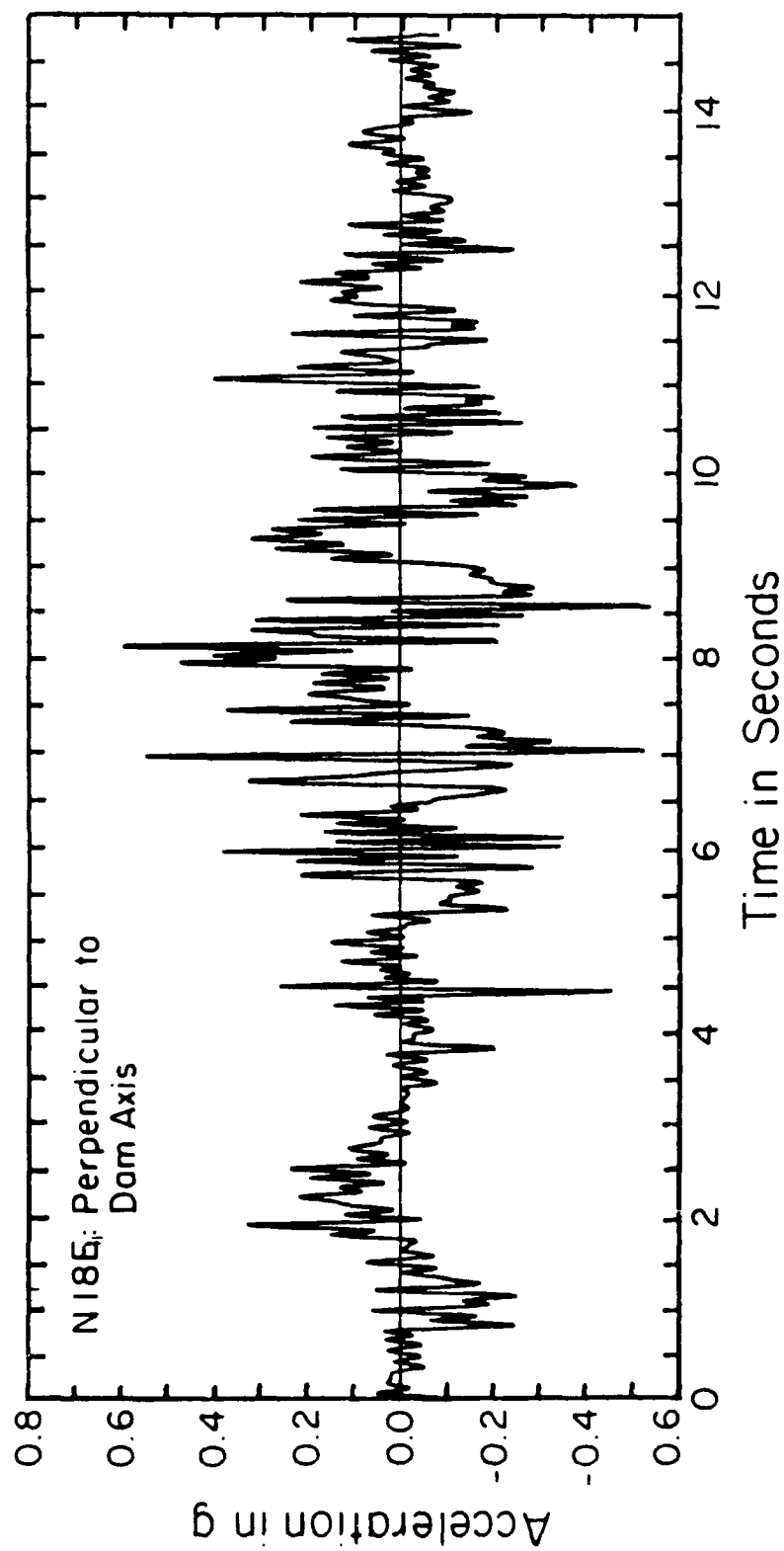


Fig. 9.3. Acceleration Time History Derived from Seismoscope Record on East Abutment of Lower San Fernando Dam, Earthquake of 1971 (after Scott, 1973)

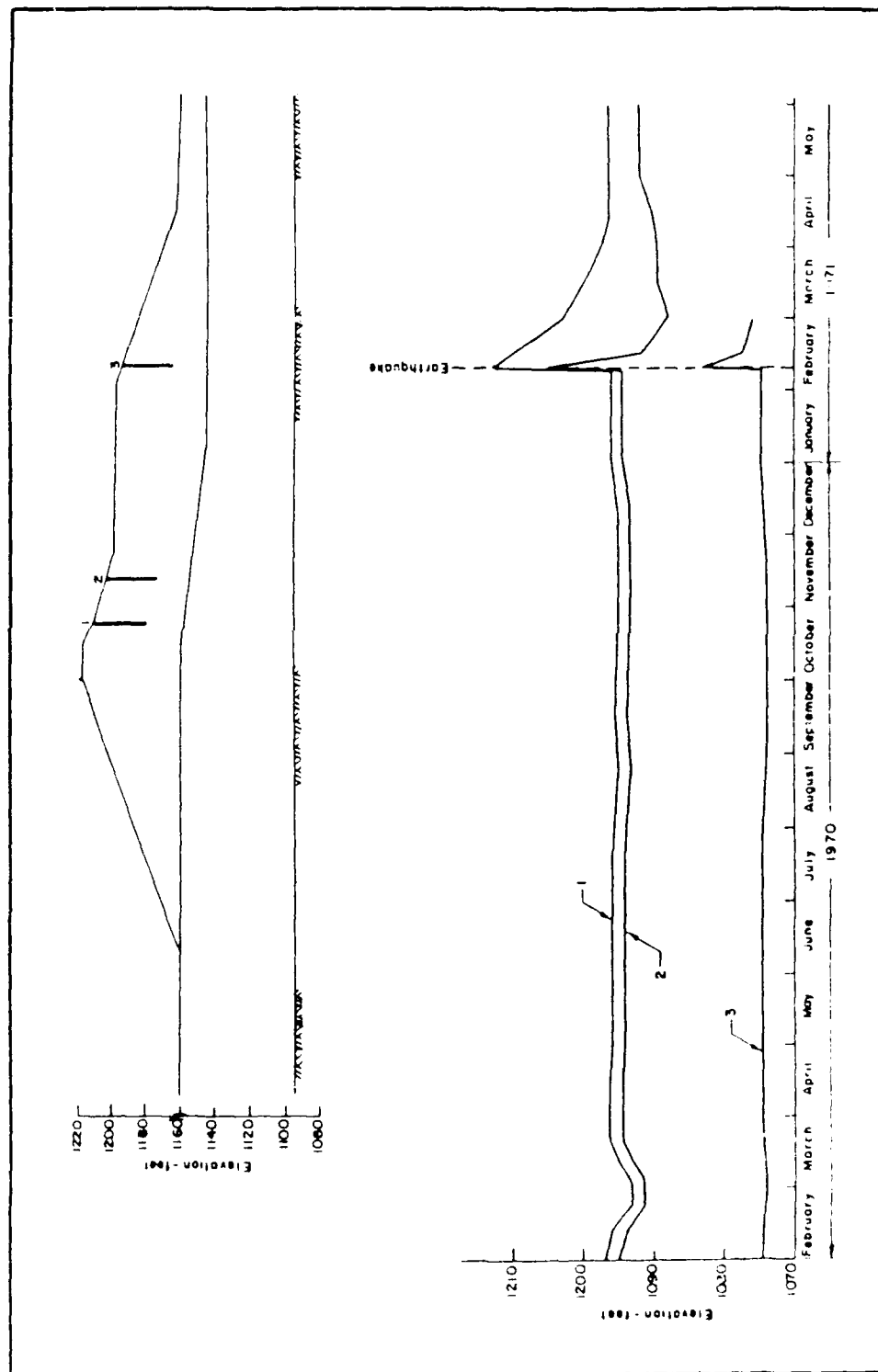


Fig. 9.4. Location and Changes in Water Level in Piezometers Following the Earthquake - Upper San Fernando Dam (after Seed et al., 1973)

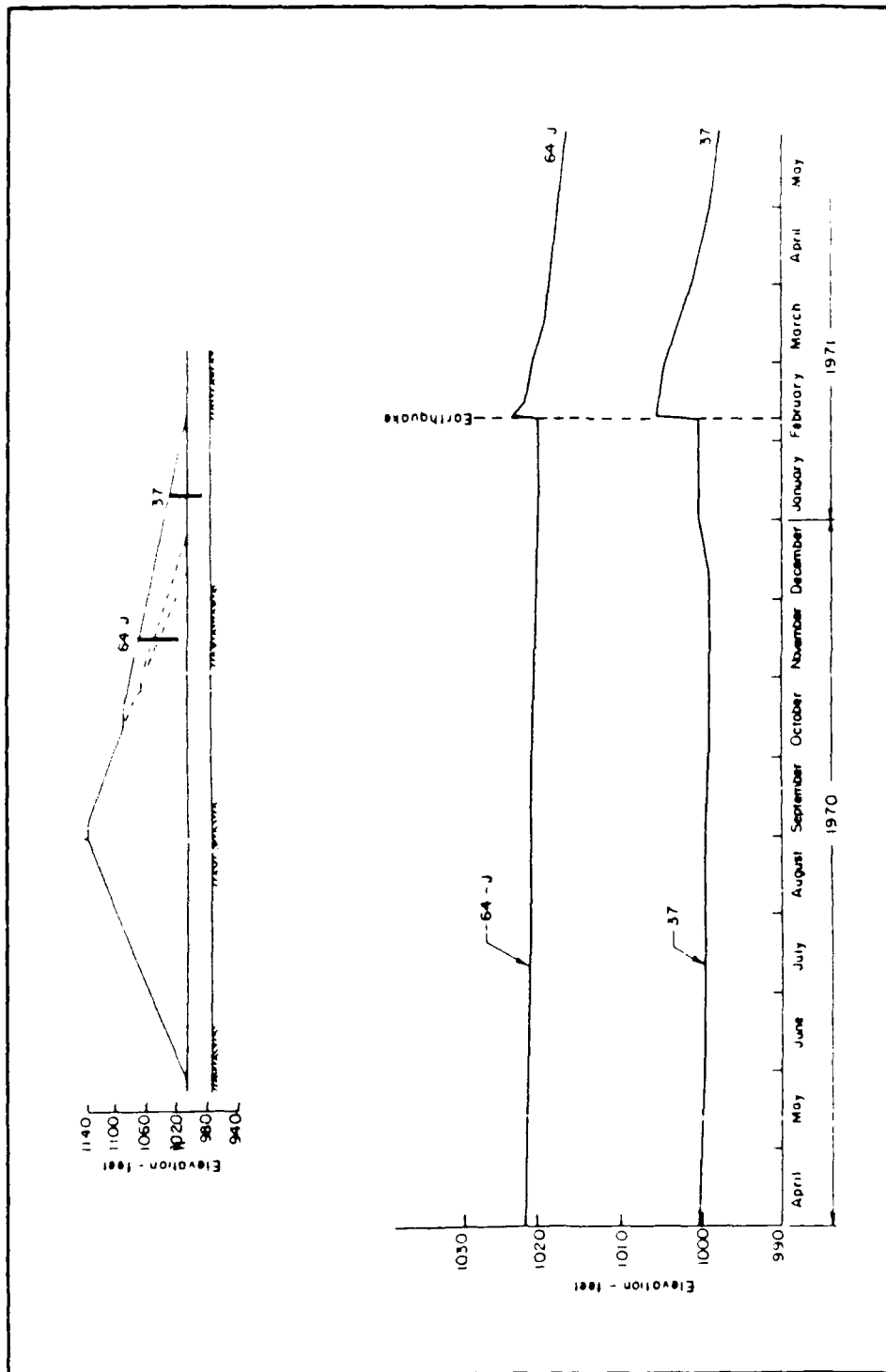


Fig. 9.5. Location and Changes in Water Level in Piezometers Following the Earthquake - Lower San Fernando Dam (after Seed et al., 1973)

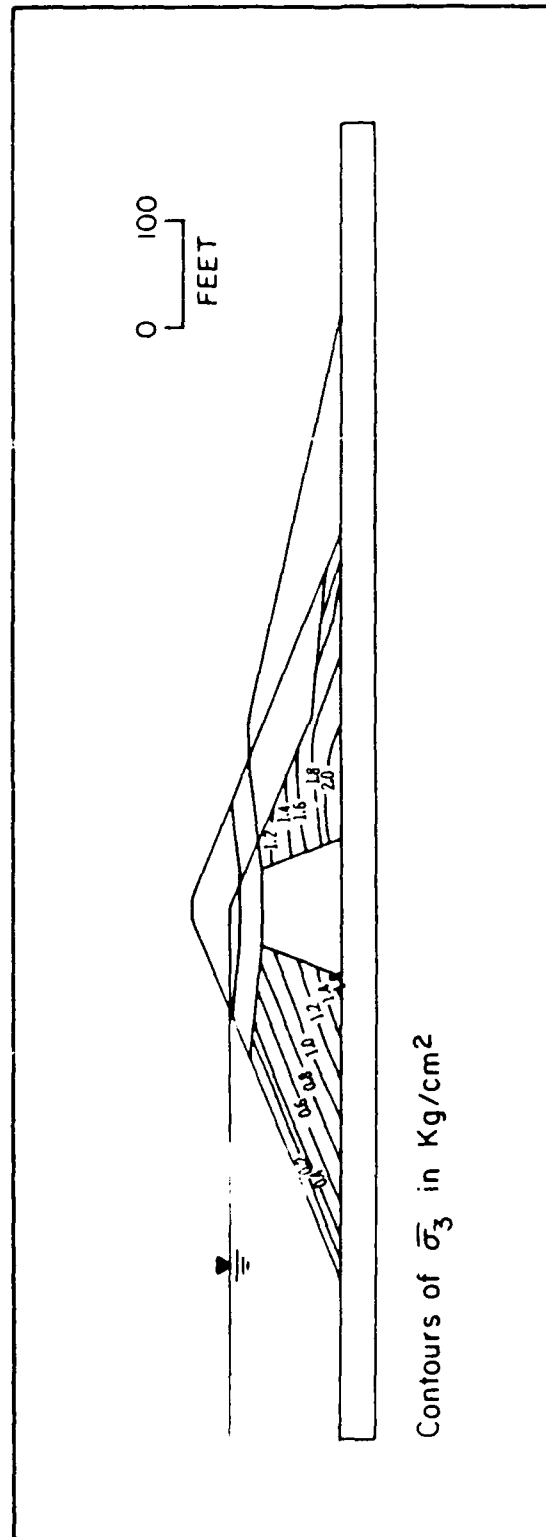


Fig. 9.6. Contours of  $\bar{\sigma}_3$  Within Saturated Hydraulic Fill Sand of Lower San Fernando Dam (after Mohamad, 1985)





**Fig. 9.7.** Plan of the Lower San Fernando Dam Showing the Different Cross Sections Studied (after Seed et al., 1973)

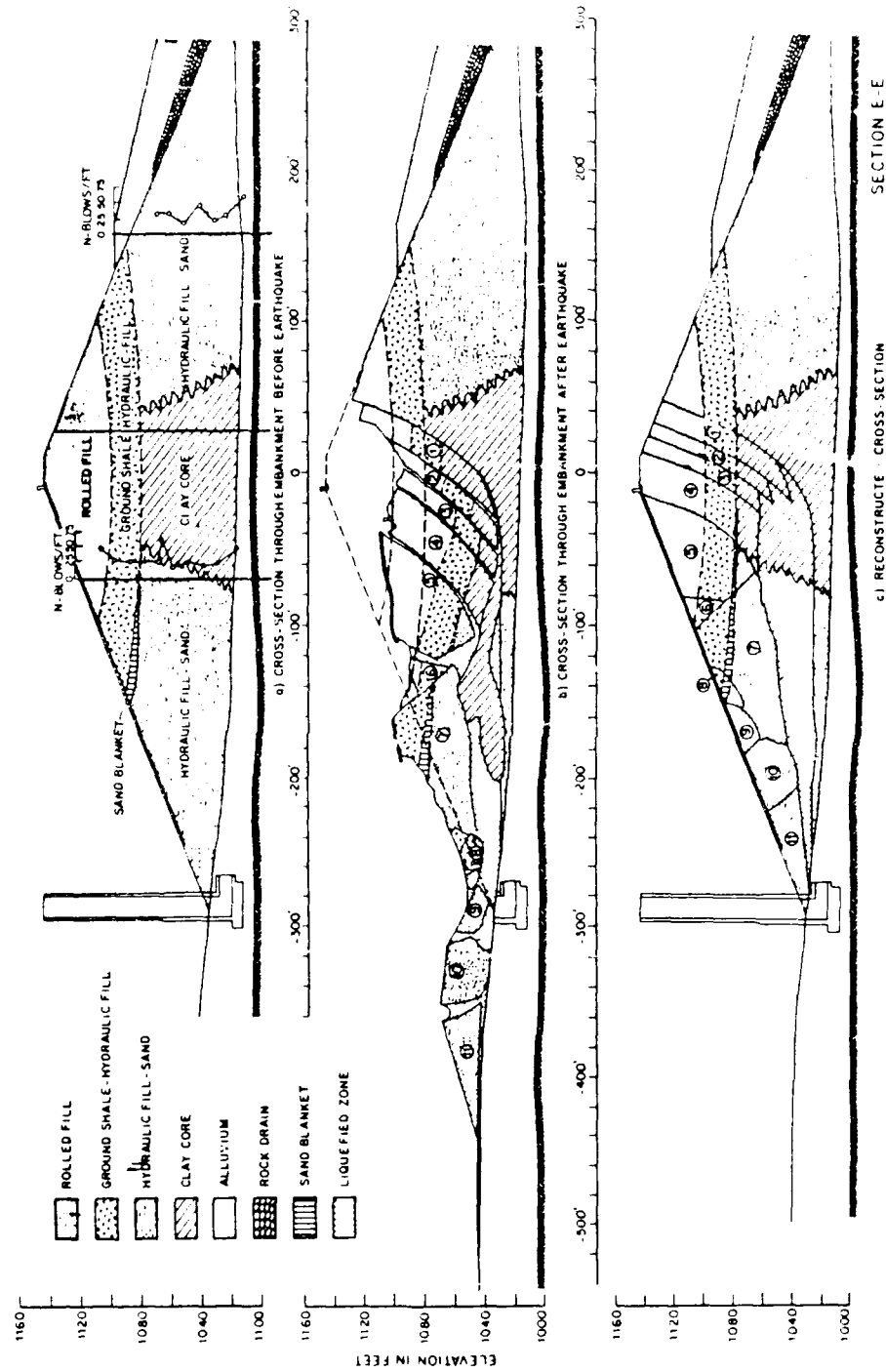


Fig. 9.8. Section E-E of the Lower San Fernando Dam  
(after Seed et al., 1973)

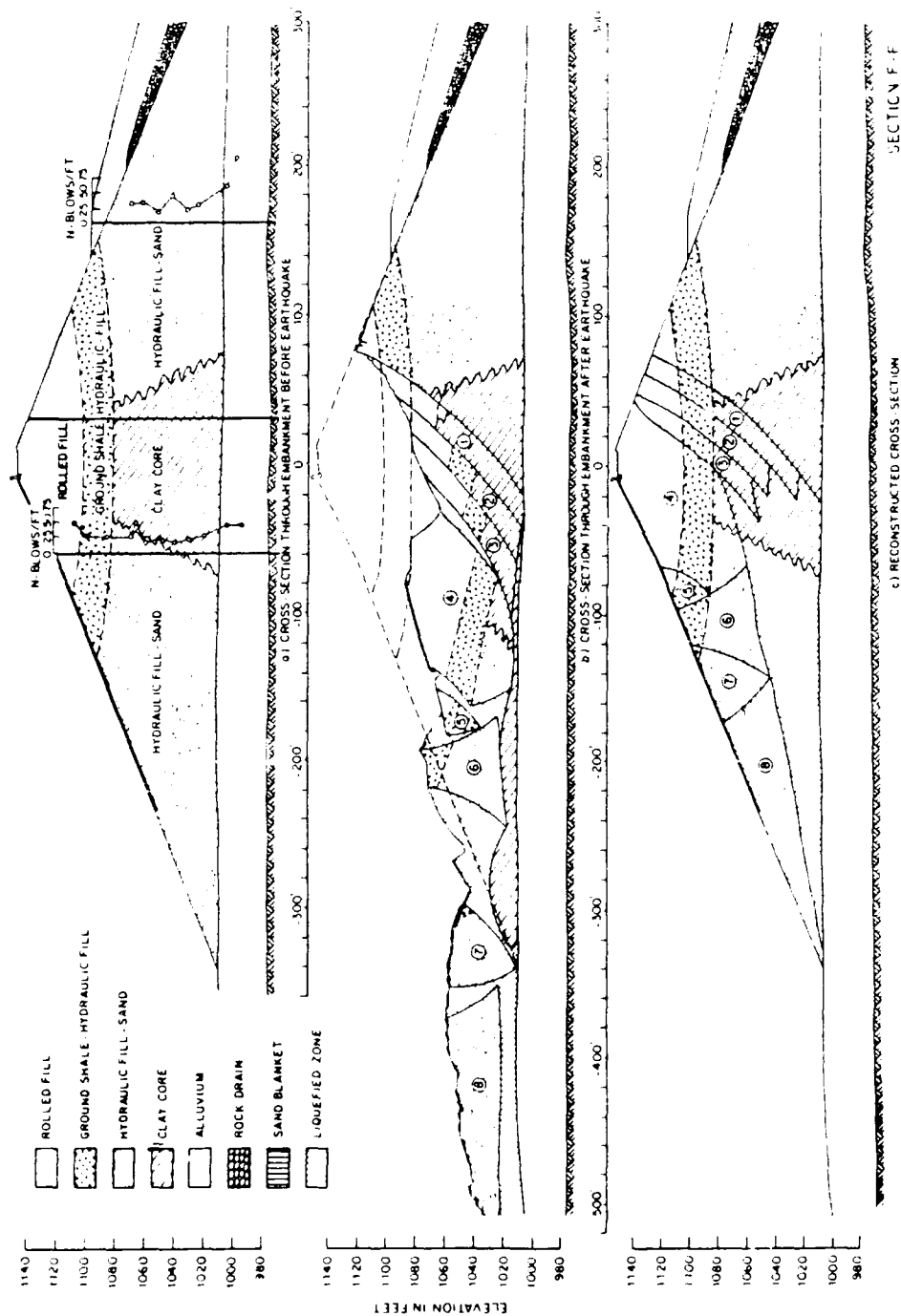


Fig. 9.9. Section F-F of the Lower San Fernando Dam  
(after Seed et al., 1973)

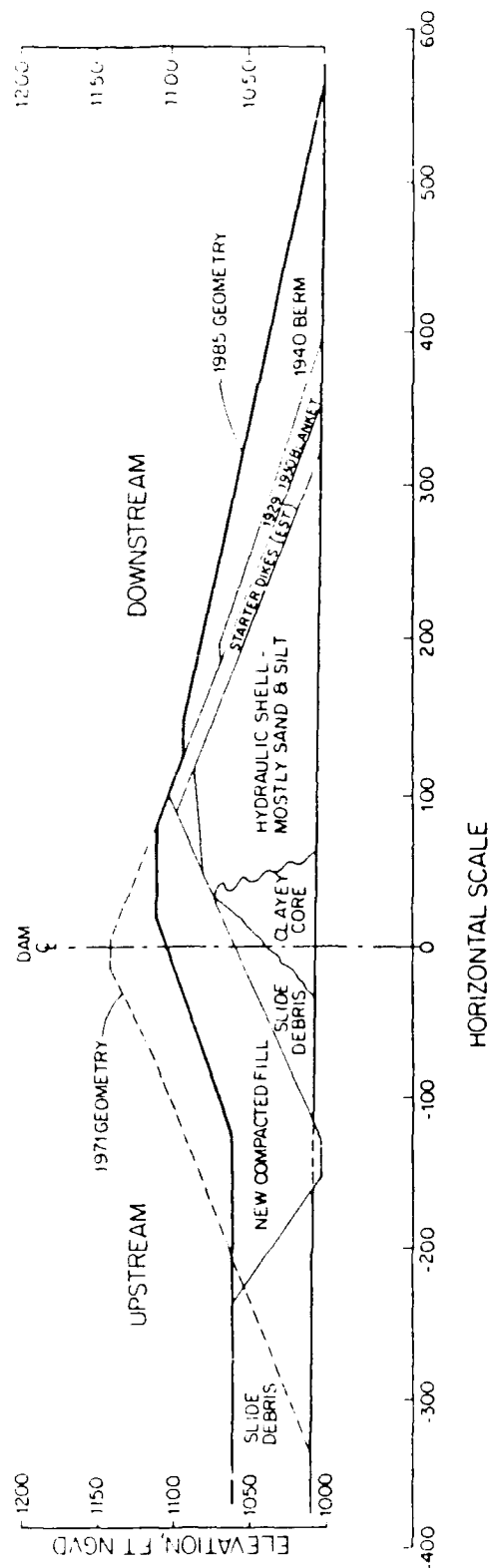


Fig. 9.10. Cross Section of the Lower San Fernando Dam at the Time of the 1985 Exploration (after GEI, 1988)

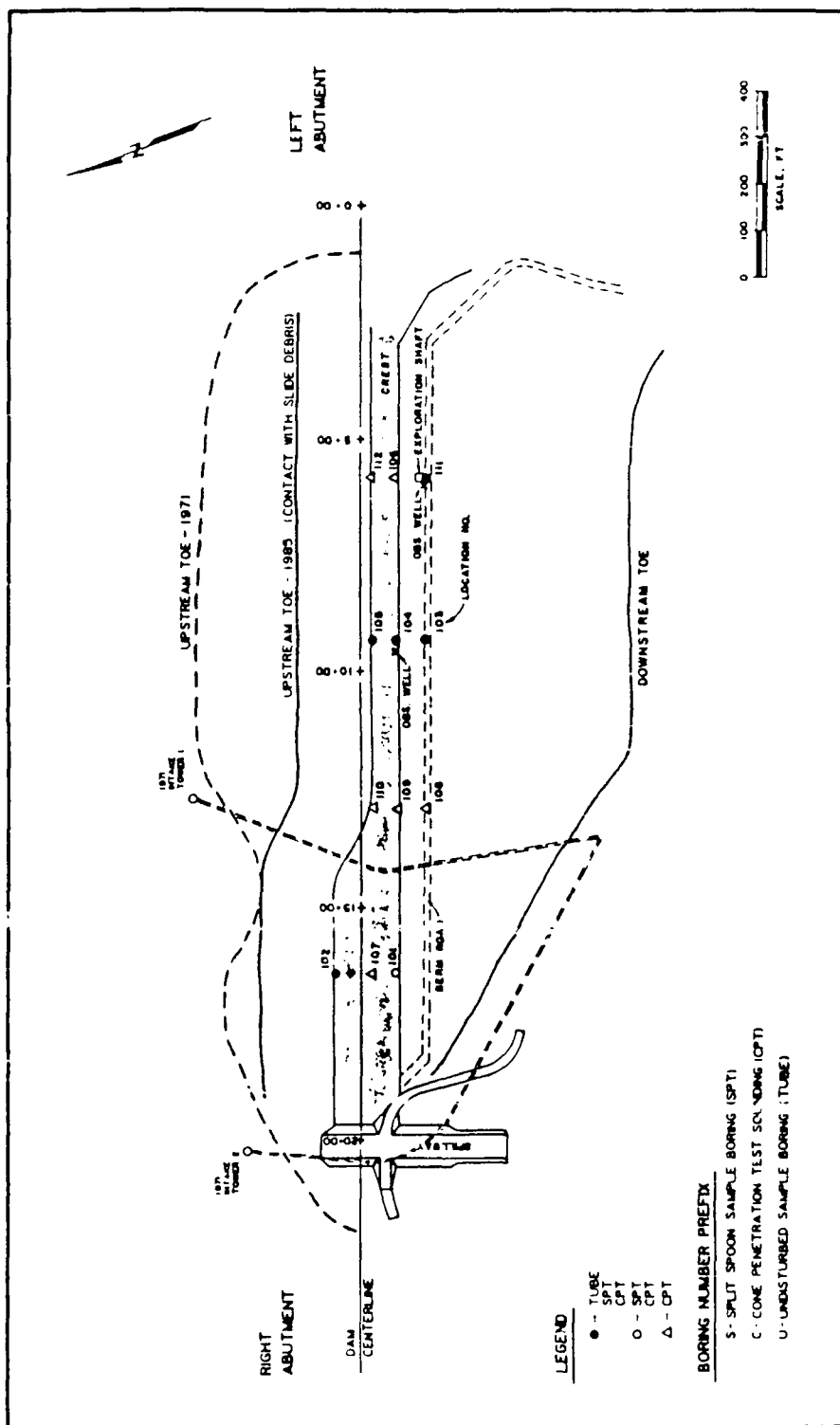


Fig. 9.11. Location of Borings in the 1985 Exploration Study (after GEI, 1988)

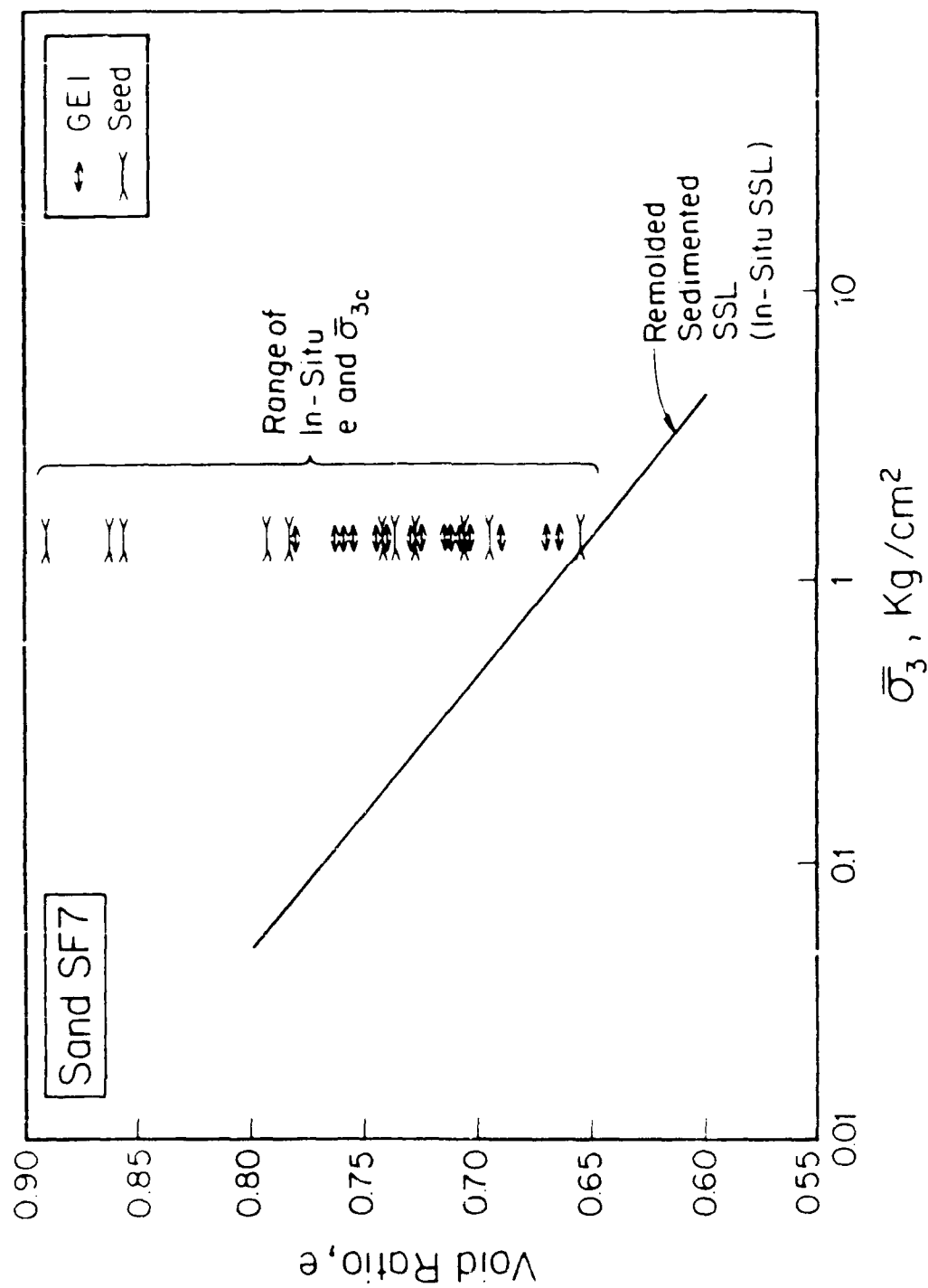


Fig. 9.12. Determination of Contractiveness of the In Situ Materials of the Lower San Fernando Dam

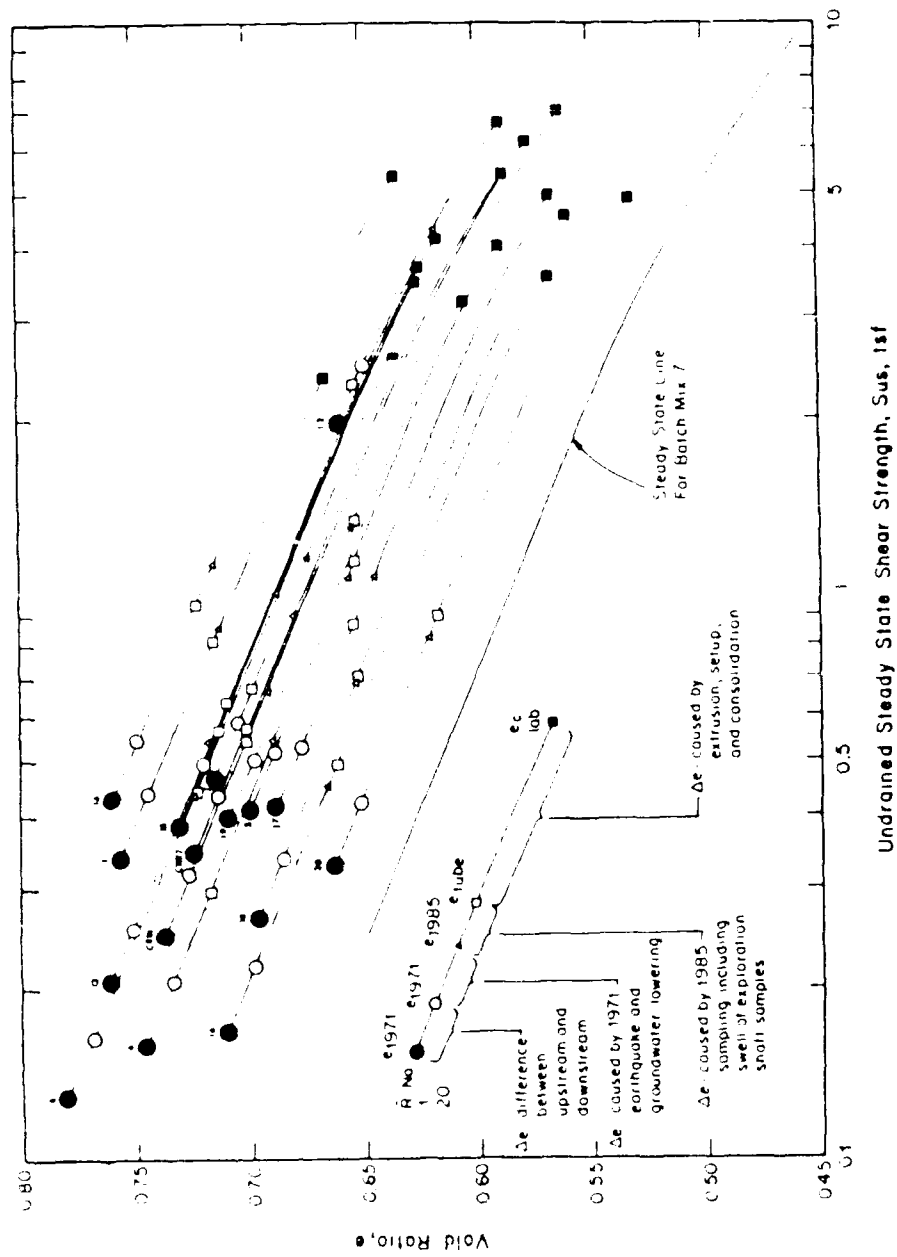


Fig. 9.13. Determination of In Situ  $S_{us}$  Using the GEI Procedure (after GEI, 1988)

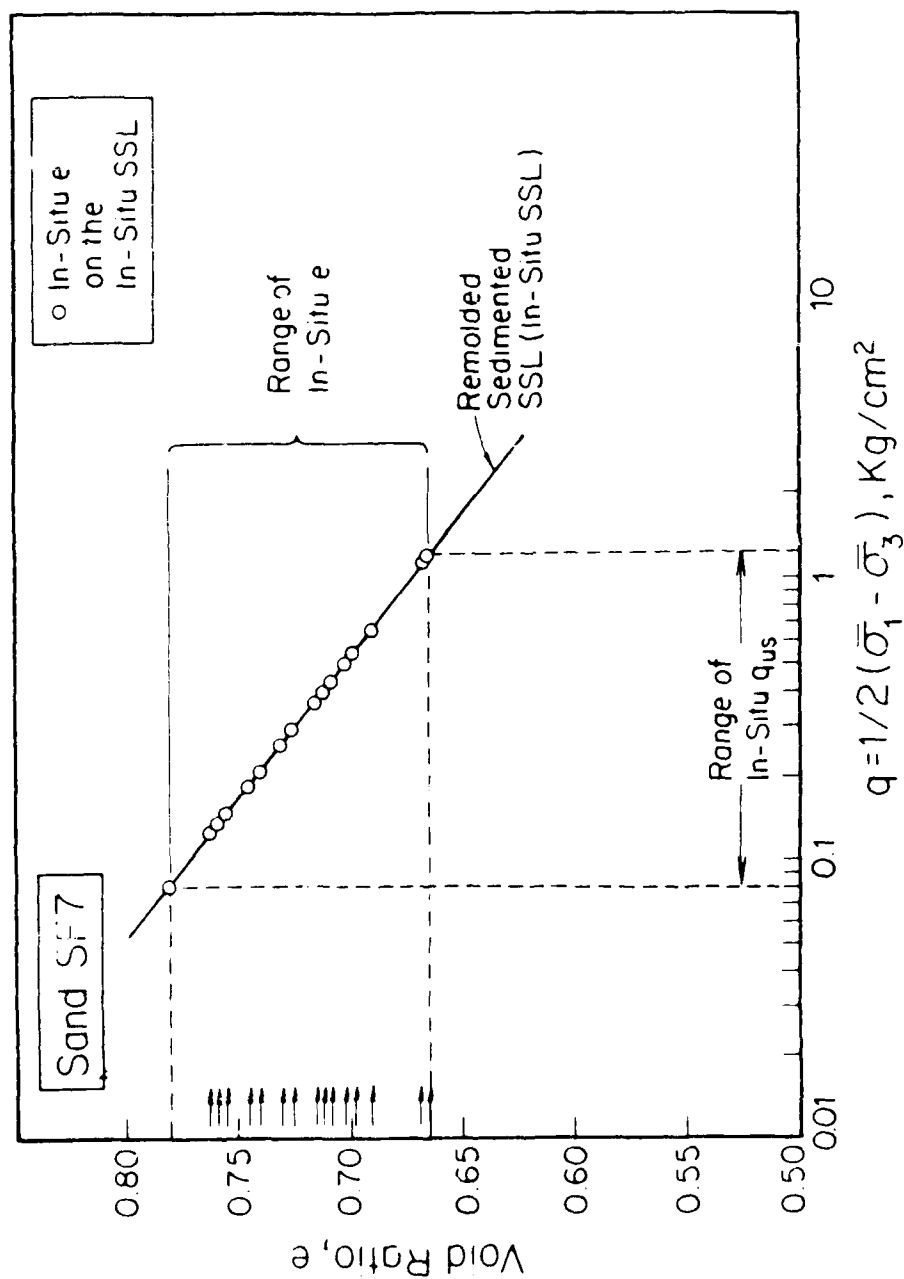


Fig. 9.14. Estimates of the In Situ  $S_{us}$  Using the Average Void Ratio and the In Situ SSL



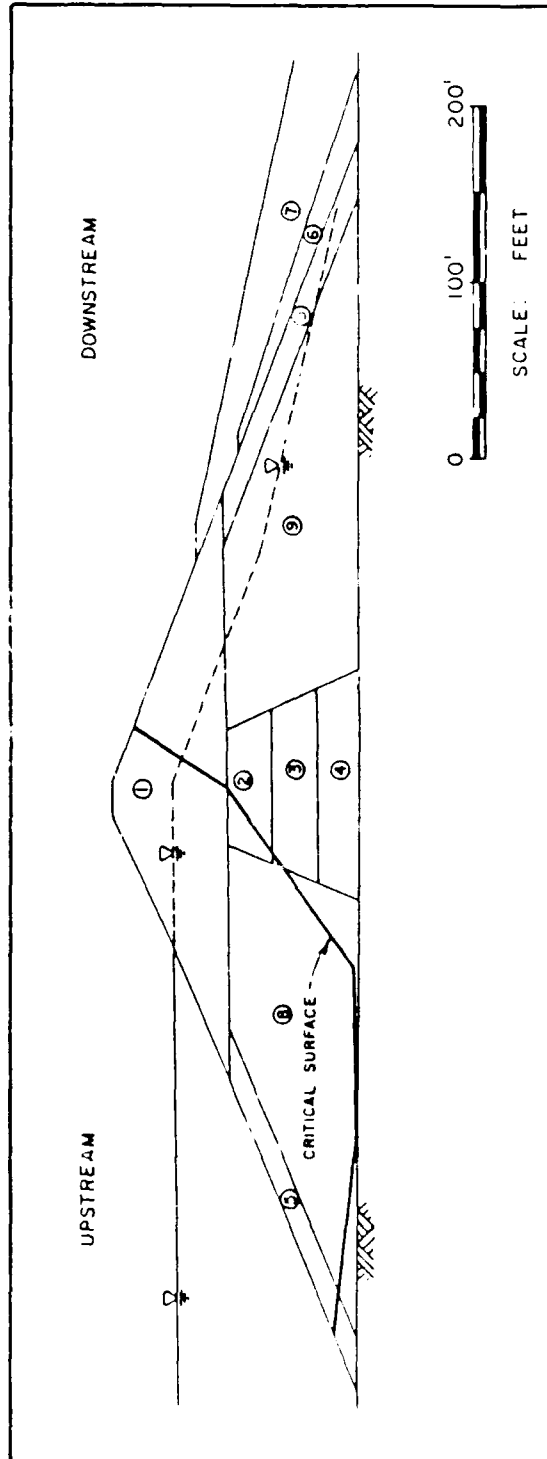


Fig. 9.15. Critical Failure Surface Through Upstream Slope of the Lower San Fernando Dam (after GEI, 1988)

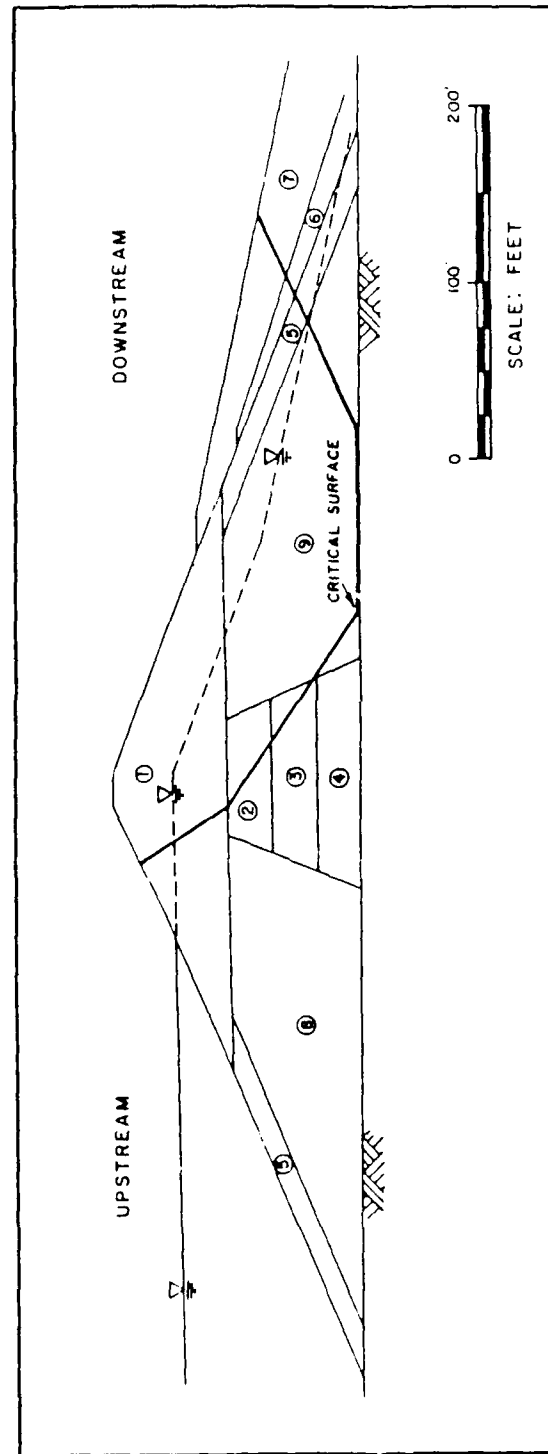


Fig. 9.16. Critical Failure Surface Through Downstream Slope of the Lower San Fernando Dam (after GEI, 1988)

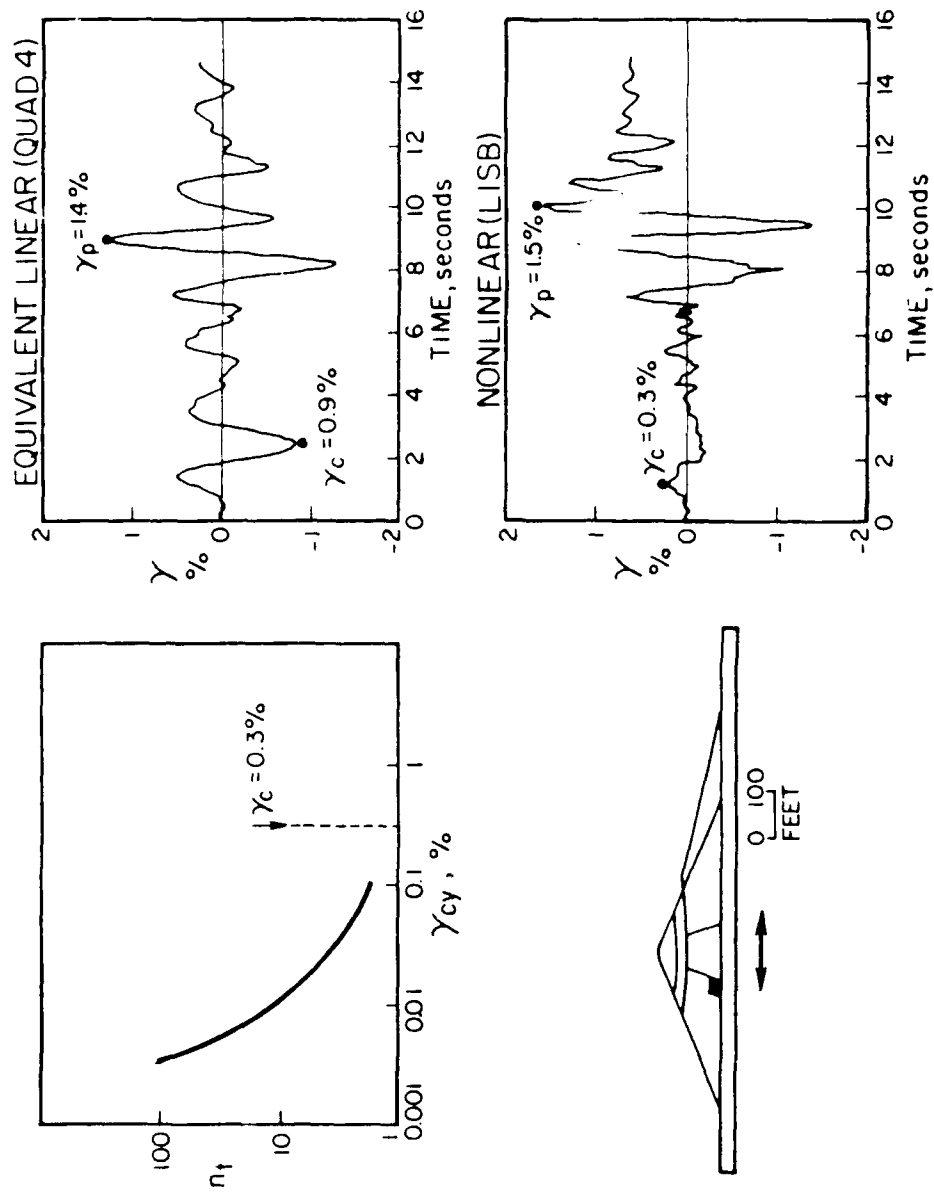


Fig. 9.17. Dynamic Analyses of the Lower San Fernando Dam Showing Magnitude of Cyclic Shear Strains

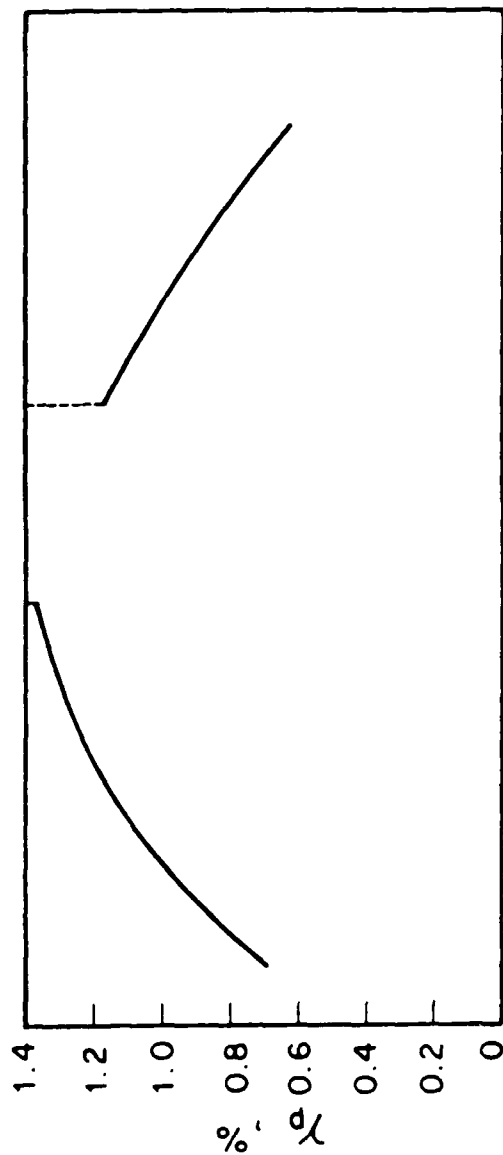
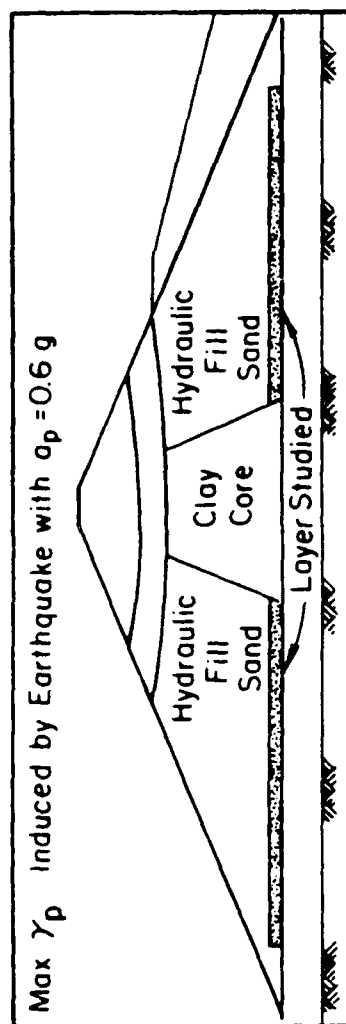


Fig. 9.18. Peak Cyclic Shear Strain Induced by the Earthquake With  $a_p = 0.6g$ , Predicted Using QUAD-4

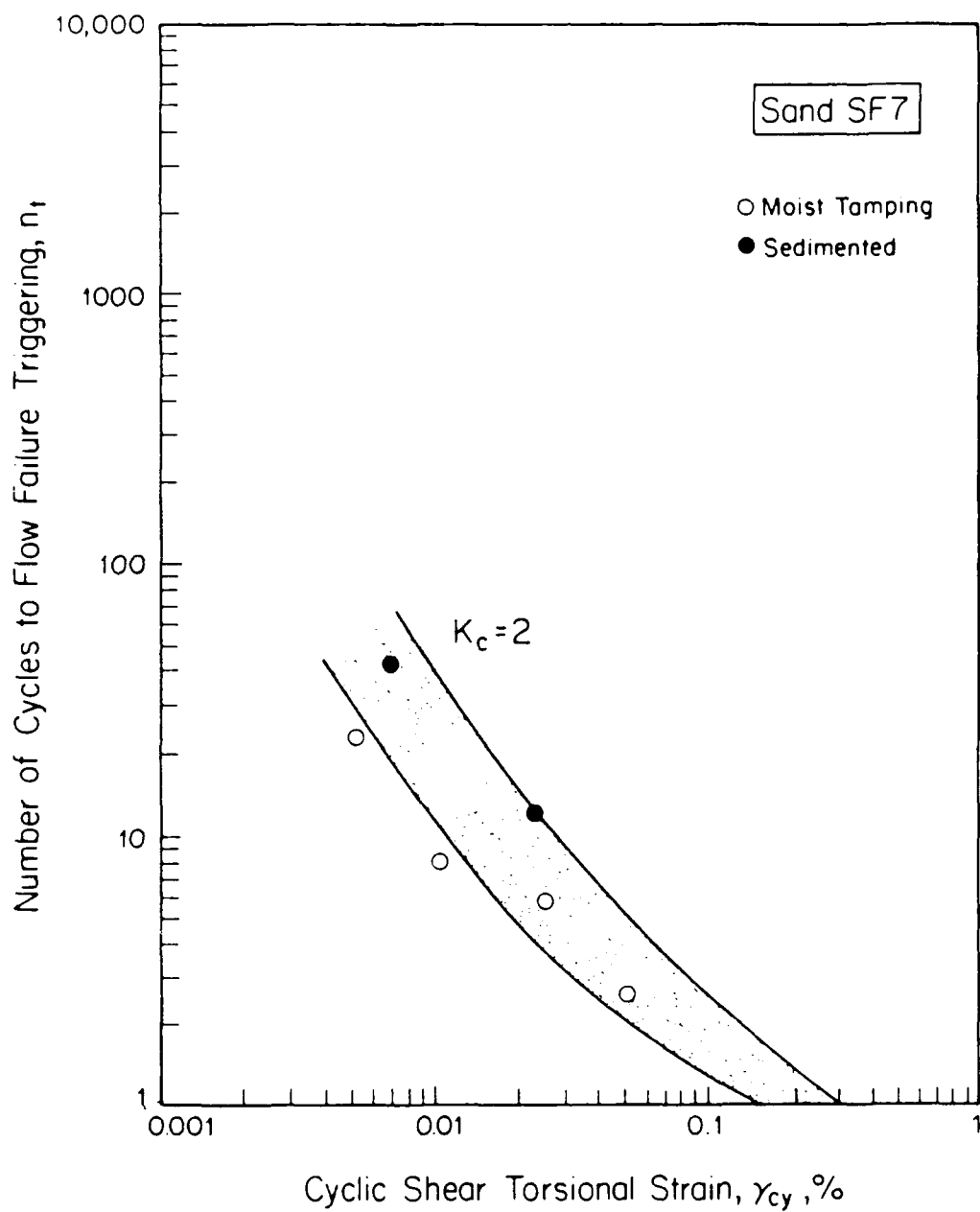


Fig. 9.19. Triggering Band for San Fernando Sand SF7,  $K_c = 2$ ,  $\bar{\sigma}_{3c} = 1 \text{ kg/cm}^2$  (data from Fig. 7.31)

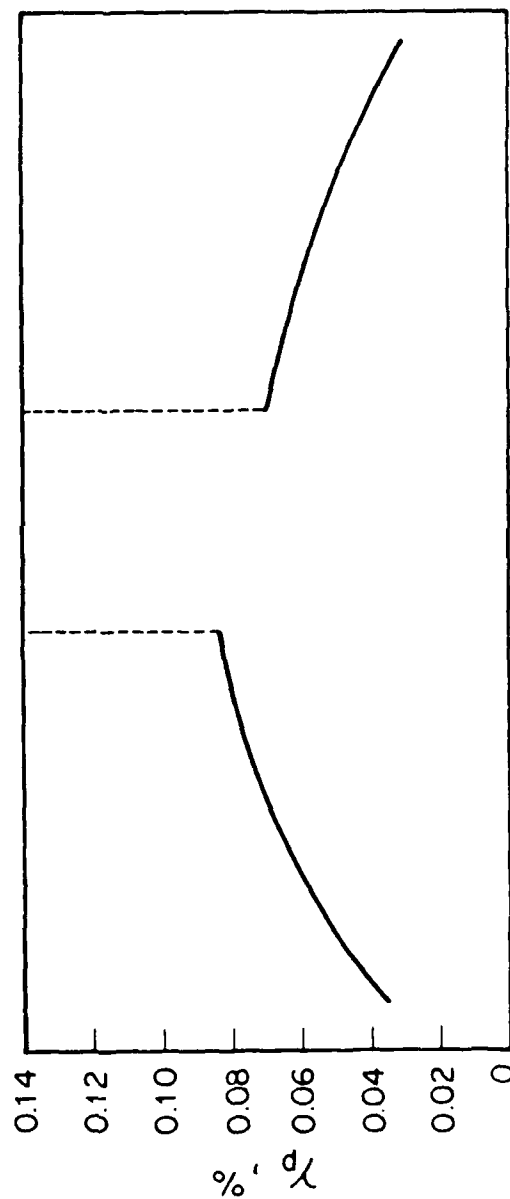
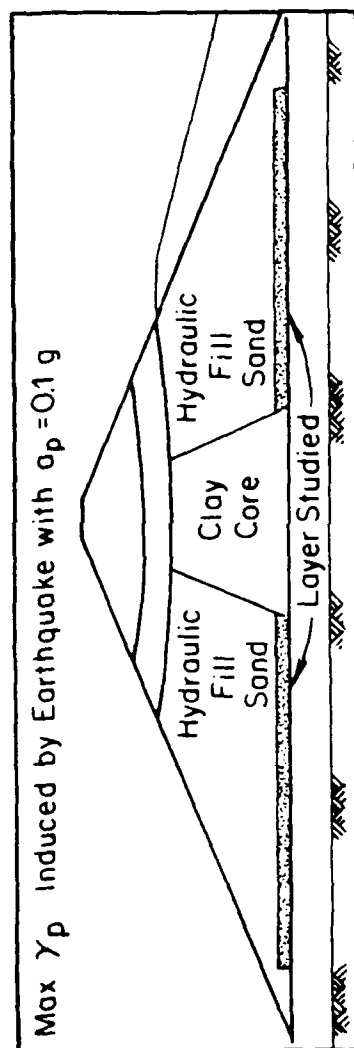


Fig. 9.20. Peak Cyclic Shear Strains Induced by the Earthquake with  $a_p = 0.1g$ , Predicted Using QUAD-4

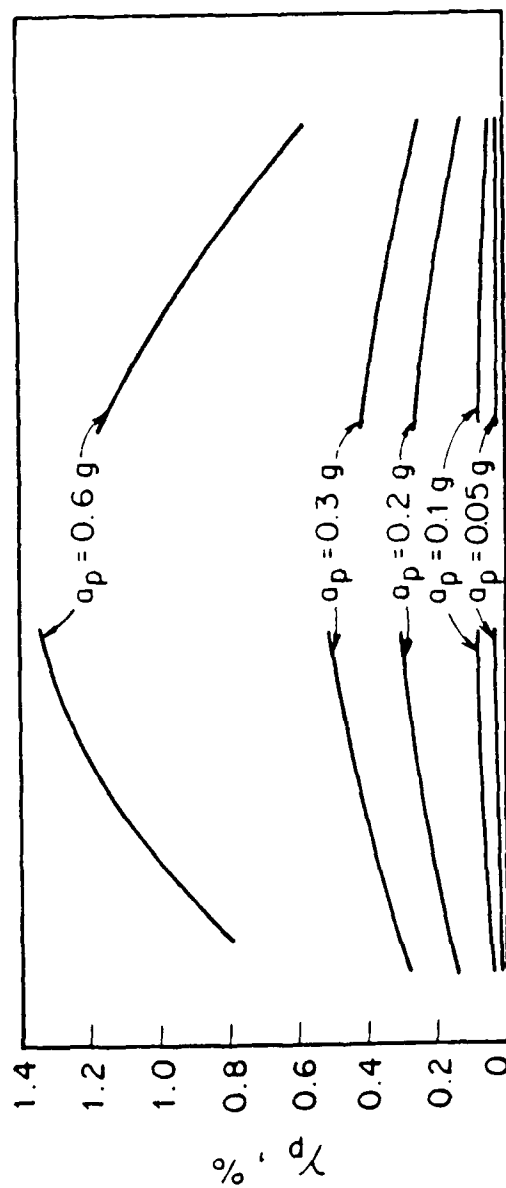
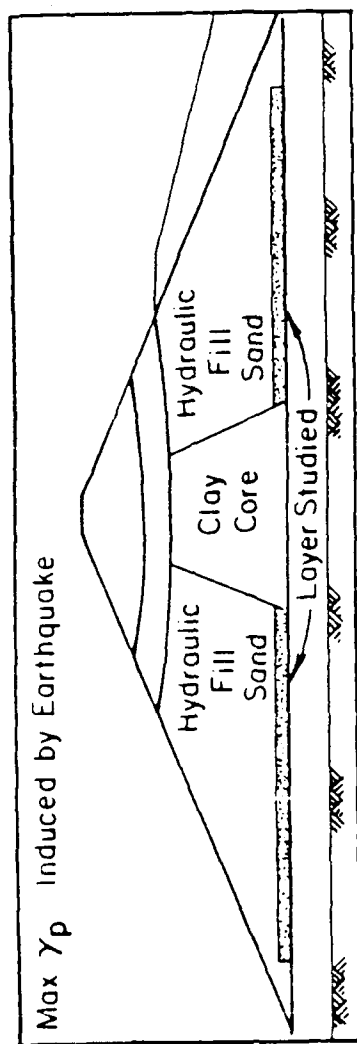


Fig. 9.21. Peak Cyclic Shear Strains Induced by the Earthquake with Different Values of  $a_p$ , Predicted Using QUAD-4

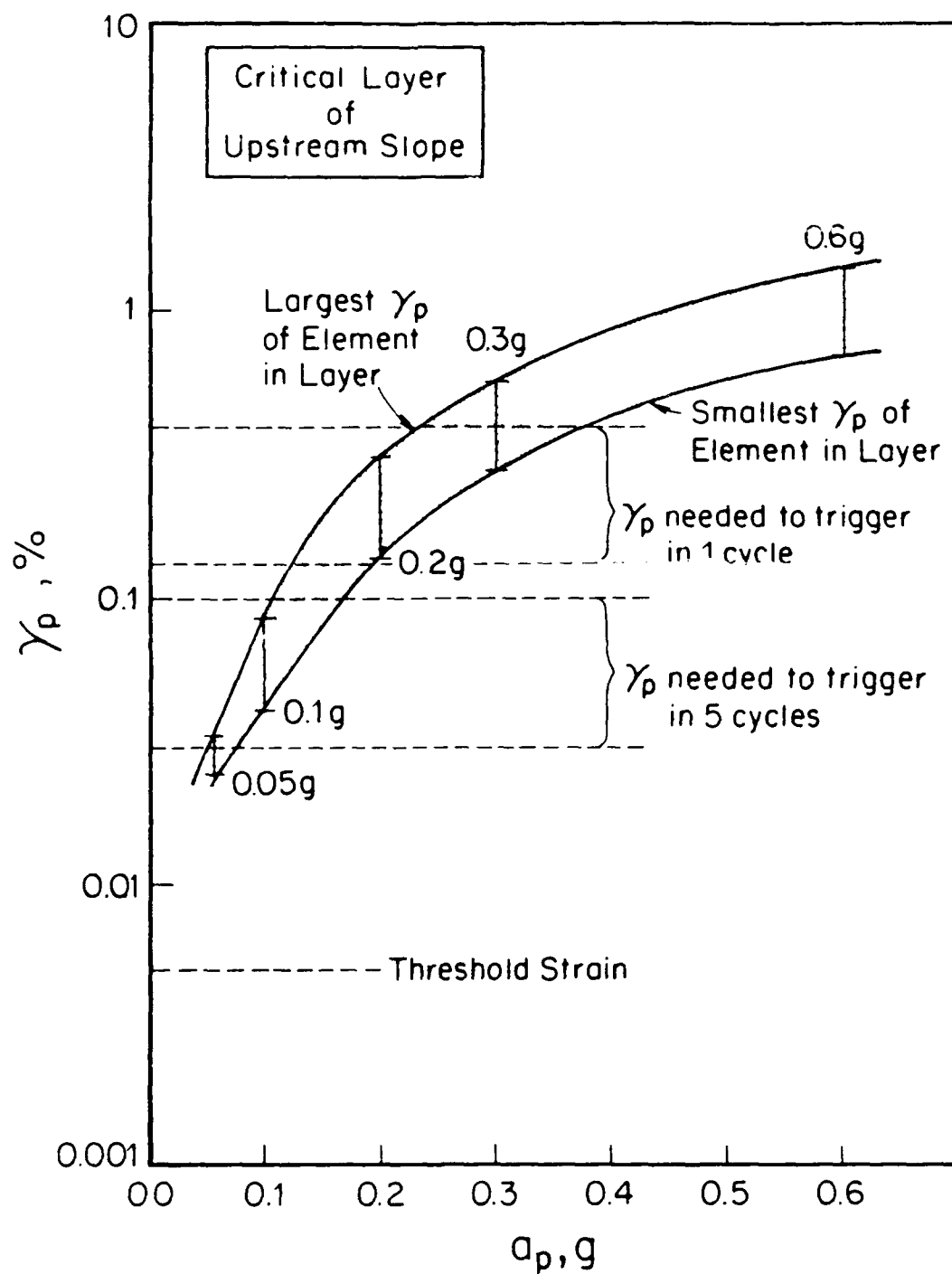


Fig. 9.22. Peak Cyclic Shear Strains Induced by the Earthquake on the Critical Layer of the Upstream Slope Predicted Using QUAD-3 ( $\gamma_p$  from Fig. 9.21)



## CHAPTER 10

### SUMMARY AND CONCLUSIONS

A comprehensive experimental testing program was conducted using several silty sands in a contractive state, in order to better understand the factors influencing seismically induced liquefaction flow failures, with particular emphasis on earth dams and slopes. The results of the tests addressed all three main soil property questions needed to evaluate the possibility of undrained flow failure in the field (Mechanism A). These questions are: a) is the soil contractive? b) if the answer to the previous question is positive, will the expected earthquake produce an intensity and duration of cyclic straining big enough to trigger liquefaction and reduce the shear strength of the soil to its steady-state value  $S_{us}$ ?, and c) what is the value of  $S_{us}$ ?. The test results were analyzed in some depth, and the conclusions were compared with actual flow failure case histories. An eleven-step logical conceptual framework was proposed for the evaluation of a specific slope, earth embankment or foundation subjected to seismic shaking, including the possibility of undrained and partially drained failure mechanisms. Finally, the procedure was applied to the flow failure of the upstream slope of the Lower San Fernando Dam in the 1971 earthquake, using test results on sand retrieved from the dam.

A total of 129 tests were conducted, with nine of the experiments done on undisturbed samples, while the remaining 120 tests were on remolded specimens. Nineteen monotonic  $\overline{CU}$  and  $\overline{CAU}$  tests were conducted on the remolded samples, while the other 101 experiments were cyclic. Most of the tests were done on contractive specimens using a technique developed at RPI, in which a solid-cylinder contractive sand specimen is first anisotropically consolidated in a triaxial cell, and is then cyclically loaded in torsion in strain-controlled undrained condition to flow failure (CyT  $\overline{CAU}$  test). Information relevant to the three questions a), b) and c) listed above are obtained from this test. Although the CyT- $\overline{CAU}$  technique had previously been used, this work constitutes the first time it has been systematically applied to clarify the conditions needed to seismically trigger flow failures.

Five soils were tested using mainly the CyT- $\overline{CAU}$  technique to determine their triggering and flow failure characteristics. Of these, three sands were more systematically studied. They are: Ottawa F125 Sand, Lagunillas Sand A, and Lower San Fernando Dam Sand Batch Mix No. 7 (SF7). Ottawa Sand is an industrially produced, slightly silty sand, while the other two sands are real silty sands obtained from specific engineering projects.

Lagunillas Sand was provided by INTEVEP S.A., and was retrieved from the Eastern Shore of Lake Maracaibo, in Venezuela; while the San Fernando Sand was retrieved from the downstream slope of the Lower San Fernando Dam by Geotechnical Engineers, Inc. (GEI).

Most of the remolded specimens used in the CyT-CAU and other tests were compacted by the moist tamping undercompaction method. However, a few samples of SF7 sand were prepared using a wet raining sedimentation method, in which segregation and layering were present to a greater degree than in any of the other placement methods typically utilized in this kind of study, in an effort to reproduce the soil fabric created in-situ by the hydraulic fill method and by natural water sedimentation processes. Comparisons between moist tamping and sedimentation results, as well as with other laboratory and field data, were illuminating, and the results of the SF7 data from sedimented specimens were applied directly to the evaluation of the Lower San Fernando Dam.

The results of the testing program were analyzed from two complementary viewpoints, treated respectively in Chapters 6 and 7. They are: the shear strength behavior, including the steady-state lines, the effective stress conditions at triggering, and the pore pressure needed for

triggering, for both monotonic and cyclic loading; and the pore pressure buildup and number of straining cycles needed for triggering when cyclic loading is used. The influence of a number of parameters was investigated, including: void ratio, consolidation stress  $\bar{\sigma}_{3c}$ , coefficient of anisotropic consolidation  $K_c = \bar{\sigma}_{1c}/\bar{\sigma}_{3c}$ , cyclic shear strain  $\gamma_{cy}$ , soil fabric, and sand type. Specific conclusions are discussed at the end of the corresponding sections in Chapters 6 and 7, including comparisons with tests on SF7 sand performed in other laboratories (Seed and GEI).

Discussions and conclusions about a number of other issues related to testing techniques, relation between laboratory results and flow failure in the field, and the 1971 San Fernando Dam slope failure, are presented throughout the body of this work. Specifically, the proposed conceptual framework for flow failure evaluation is included in Section 8.7, while Chapter 9 presents the reanalysis of the San Fernando Dam slide based on the results of this investigation. It is useful to repeat some of the main conclusions as follows:

- (1) The two steady-state lines (SSL) and the steady-state strength envelope are in first approximation unique for a given sand and

independent of type of test (monotonic or cyclic),  $K_c$ , and  $\gamma_{cy}$ . The evidence suggests that the steady-state strength envelope is also independent of  $e$  and soil fabric. On the other hand, the SSL's seem to be independent of soil fabric only for relatively homogeneous specimens; if layered specimens are tested such as prepared using the sedimentation method, the SSL's are significantly affected. This is consistent with results found by other researchers.

- (2) The value of pore pressure ratio needed to trigger flow failure due to cyclic loading,  $r_{ut} = u_t/\bar{\sigma}_{3c}$ , is for a given contractive sand a unique function of  $K_c$ . This function is independent of  $\bar{\sigma}_{3c}$ ,  $e$ ,  $\gamma_{cy}$  and sand fabric. The value of  $r_{ut}$  decreases as  $K_c$  increases, and for the typical  $K_c$  encountered in slopes  $r_{ut}$  is significantly less than  $r_u = 1$  applicable to liquefaction of isotropically consolidated sands.
- (3) A unique effective stress condition is necessary to trigger liquefaction flow failure due to cyclic loading for a given contractive sand and  $K_c$ , with this triggering envelope being independent of  $e$ ,

$\bar{\sigma}_{3C}$ ,  $\gamma_{CY}$  and sand fabric.

- (4) The number of cycles needed to trigger flow failure in a given contractive sand,  $n_t$ , is mainly a function of  $\gamma_{CY}$ ,  $\bar{\sigma}_{3C}$  and  $K_C$ . For given consolidation conditions  $\bar{\sigma}_{3C}$  and  $K_C$ ,  $n_t$  decreases as the cyclic shear strain  $\gamma_{CY}$  increases. Other things being equal,  $n_t$  generally decreases as  $K_C$  increases, indicating that the steeper a contractive sand slope is, the more susceptible it will usually be to seismically induced undrained flow failure. Also,  $n_t$  increases linearly with  $\bar{\sigma}_{3C}$  when  $K_C$  and  $\gamma_{CY}$  are constant, indicating that more cycles of a given cyclic strain are needed to fail deeper soil. These relations between  $n_t$ ,  $\gamma_{CY}$ ,  $\bar{\sigma}_{3C}$  and  $K_C$ , labelled here "triggering relationships", are in first approximation independent of soil fabric, and triggering relations determined in the laboratory on homogeneous remolded specimens can be applied to layered soil in-situ. This is another manifestation of the inherent "robustness" of the cyclic shear strain as a loading parameter, also found in other applications of the strain approach to liquefaction. Although these triggering relationships vary from one sand to another, the differences are not

extreme, and the results for many sands are probably contained within bands such as Fig. 7.56, useful for preliminary evaluations.

- (5) The rate and shape of pore pressure buildup curves during strain-controlled cyclic loading of anisotropically consolidated sand are greatly influenced by the value of  $K_c$ , and this effect must be considered in effective stress dynamic analyses of soils and earth structures susceptible to liquefaction flow failure. A pore pressure and flow failure triggering analytical model is proposed for this purpose in Section 7.5.
- (6) In most of the tests with sedimented layered SF7 sand specimens, the sand was contractive after sedimentation through water and subsequent consolidation under  $\bar{\sigma}_{3c} = 1 \text{ Kg/cm}^2$  and  $K_c$  ranging from .8 to 2.1 This is a very important finding which suggests that hydraulically deposited, layered silty sand can be contractive in-situ, either in natural alluvial or lacustrine deposits or in hydraulic fill structures such as the Lower San Fernando Dam. On the other hand, for a homogeneous clean sand to be contractive it must be typically deposited at an extremely low relative density.

This conclusion on the contractiveness of hydraulic fills was confirmed by the fact that the in-situ void ratios measured in 1985 in the Lower San Fernando Dam by GEI, after appropriate corrections to account for the differences between upstream and downstream and between 1985 and 1971, all plot clearly above the  $e-\bar{\sigma}_{3c}$  SSL obtained in the laboratory with the sedimented SF7 specimens (Fig. 9.12). Also, the location of the undrained shear strength line determined with these remolded sedimented SF7 specimens (Fig. 9.14), is consistent with the band obtained at GEI by extrapolation of steady-state results from intact specimens from the dam which preserved their original layering (Fig. 9.13). Therefore, a clear conclusion of this evaluation is that the critical silty sand layer in the upstream slope of the Lower San Fernando Dam was contractive prior to the 1971 earthquake, and that both the in situ density and the in situ shear strength were well modelled by the laboratory tests at RPI on remolded sedimented SF7 specimens.

- (7) The "best estimate" steady-state shear strength of the critical layer of the upstream slope of the Lower San Fernando Dam in 1971, obtained in this



work from CyT-CAU tests on sedimented SF7 sand in conjunction with the in-situ void ratio measurements, is  $S_{us} = 0.21 \pm 0.14 \text{ Kg/cm}^2$ . This gives a local static factor of safety against flow failure for this layer of 0.44, with lower and upper bounds of 0.15 and 0.73. As all these factors of safety are significantly below unity, this predicts that the upper slope was in an unstable condition, with an undrained (Mechanism A) flow failure of the slope waiting to be triggered by earthquake shaking of enough intensity and duration. On the other hand, although the downstream slope of the same dam was also found to be contractive and to have similar values of  $S_{us}$ , its local factor of safety against flow failure was about one, which would explain the difference in performance between the two slopes in 1971. These conclusions and values of  $S_{us}$  are generally consistent with those found by GEI and Seed using other methods.

- (8) Dynamic analyses of the Lower San Fernando Dam subjected to the 1971 recorded ground motion having a peak ground surface acceleration  $a_p = 0.6g$ , performed using equivalent linear (QUAD-4) and nonlinear (LISB) methods, revealed that the critical

layer of hydraulic fill in the dam experienced very large seismic strains of the order of 1%, much larger than  $\gamma_{cy} \approx 0.3\%$  needed to trigger flow failure in one cycle (Figs. 9.17 to 9.19). Therefore, triggering is predicted for both slopes of the dam, with flow failure occurring in the upstream slope due to its low factor of safety. A parametric study on the influence of peak ground surface acceleration on triggering, presented in Figs. 9.21 and 9.22, indicates that if  $a_p \lesssim 0.05g$  no triggering occurs even in the most critical soil elements within the dam, while if  $a_p \gtrsim 0.2g$  triggering occurs in most or all elements, and a seismically induced flow failure is predicted in the upstream slope. For  $a_p$  between about 0.05g and 0.20g, various degrees of partial to complete triggering are predicted depending on the duration of the earthquake (and also presumably on the frequency content of the shaking which was not varied in this study). These conclusions are consistent with the performance of the Lower San Fernando Dam in earthquakes prior to 1971, and it is also consistent with the general findings on the seismic performance of a number of hydraulic fill dams reported by Seed et al. (1978).

## REFERENCES

1. Alarcon A. and Leonards (1988): Discussion to "Liquefaction Evaluation Procedure," JGED, ASCE, Vol. 114, No. 2, Feb., pp. 232-236.
2. Andersen A. and Bjerrum (1968): "Slide in Subaqueous Slopes in Loose Sand and Silt," Norwegian Geotechnical Institute Publication, No. 81, pp. 1-9.
3. Arulanandan, K. and Muraleetharan, K. (1988): Discussion to "Liquefaction Evaluation Procedure," JGED, ASCE, Vol. 114, No. 2, Feb., pp. 236-239.
4. Arulanandan, K., Yogachandran, C., Muraleetharan, K.K., Kutter, B.L. and Chang, G.S. (1988): "Laboratory Flow Slide During Earthquake Simulation," Proceedings International Congress for Geotechnical Modelling on the Centrifuge 88, Paris, April 1988.
5. Atkinson, J.H. and Bransby, P.L. (1978): The Mechanics of Soils: An Introduction to Critical State Soil Mechanics, McGraw-Hill, London.
6. Baldi, G. and Nova, R. (1984): "Membrane Penetration Effects in Triaxial Testing," JGED, ASCE, Vol. 110, No. 3, March, 1984.
7. Baziar, M.H. (1987): "Influence of the Testing Technique on the Steady State Lines of Sand," M.S. Thesis, Rensselaer Polytechnic Institute, Troy, NY, August, 1987.
8. Bjerrum, L. (1974): "Subaqueous Slope Failures in Norwegian Fjords," Norwegian Geotechnical Institute, Publication No. 88.
9. Brawner, C.O. and Campbell, D.B. (1972): "The Tailings

Structure and Its Characteristics: A Soil Engineers Viewpoint," Proceedings of the 1st International Tailing Symposium, Tucson, Arizona.

10. California Department of Water Resources (1971): "Report of Soils Testing of Upper San Fernando Dam," Jan.
11. California Department of Water Resources (1972): "Report of Soils Testing of Lower San Fernando Dam," Nov.
12. Casagrande, A. (1936): "Characteristics of Cohesionless Soils Affecting the Stability of Slopes and Earth Fills," Journal of the Boston Society of Civil Engineering, Jan., 1936.
13. Casagrande, A. (1950): "Notes on the Design of Earth Dams," Journal of the Boston Society of Civil Engineering, Vol. 37, No. 4, Oct. 1950, pp. 231-255.
14. Casagrande, A. (1965): "Role of the 'Calculated Risk' in Earthwork and Foundation Engineering," JSMFD, ASCE, Vol. 91, No. SM4, July, pp. 1-41.
15. Casagrande, A. (1976): "Liquefaction and Cyclic Deformation of Sands - A Critical Review," Harvard Soils Mechanics Series, No. 88, Cambridge, Mass., Jan.
16. Castro, G. (1969): "Liquefaction of Sands," Harvard Soil Mechanics Series, No. 81, Cambridge, Mass., Jan.
17. Castro, G. (1975): "Liquefaction and Cyclic Mobility of Saturated Sands," JGED, ASCE, Vol. 101, No. GT6, June, pp. 551-569.
18. Castro, G. and Poulos, S.J. (1977): "Factors Affecting Liquefaction and Cyclic Mobility," JGED, ASCE, Vol.

103, No. GT6, June, pp. 501-516.

19. Castro G., Poulos, S.J., France, J.W. and Enos, J.L. (1982): "Liquefaction Induced by Cyclic Loading," Geotechnical Engineers, Inc. - Report submitted to National Science Foundation, March.
20. Cleary, A.J. (1914): "The Calaveras Dam, California, the Highest Earth Dam," Engineering News, Vol. 72, No. 14, pp. 692-695.
21. Dakoulas, P., Dobry R., Vasquez-Herrera, A., Ng. P. and Gazetas, G. (1988): "Evaluation of Seismic Liquefaction Flow Failure of Three Coastal Dyke Sections," Phase II Report, INTEVEP.
22. De Alba, P. (1988): Discussion to "Liquefaction Evaluation Procedure," JGED, ASCE, Vol. 114, No. 2, Feb., pp. 239-241.
23. Dean, E.T.R. and Schofield, (1983): "Two Centrifuge Model Tests: Earthquake on Submerged Embankments," Report CUED/D-Soils/TR134, Cambridge University.
24. DeGregorio V.B. (1981): "The Effects of Method of Sample Preparation on the Liquefaction Behavior of Sands Under Statically Applied Loads," M.S. Thesis, Clarkson College of Technology, Potsdam, New York.
25. Dennis, N.P. (1988): Discussion to "Liquefaction Evaluation Procedure," JGED, ASCE, Vol. 114, No. 2, Feb., pp. 241-243.
26. Dobry, R. (1964): "Desarrollo y Estado Actual de las Ideas Sobre el Problema de la Licuacion Espontanea de los Suelos Granulares," M.S. Thesis, National University of Mexico (in Spanish).

27. Dobry, R. (1965): "Effects del Sismo de Marzo de 1965 en los Tranques de Relave de El Cobre," Report IDIEM, Universidad di Chile, Vol. 4, No. 2, October.
28. Dobry, R. (1987): "Some Basic Aspects of Soil Liquefaction During Earthquakes," Proceedings from the Symposium on Seismic Hazards, Ground Motions, Soil-Liquefaction and Engineering Practice in Eastern North America, December.
29. Dobry, R. and Alvarez, L. (1967): "Seismic Failures of Chilean Tailings Dams," JSMFD, ASCE, Vol. 93, No. SM6, Nov., pp. 237-260.
30. Dobry, R., Idriss, I.M., and Ng, E. (1978): "Duration Characteristics of Horizontal Components of Strong-Motion Earthquake Records," Bulletin of the Seismological Society of America, Vol. 68, No. 5, October, pp. 1487-1520.
31. Dobry, R. and Ladd, R.S. (1980): "Discussion of 'Soil Liquefaction and Cyclic Mobility Evaluation for Level Ground During Earthquakes' by H.B. Seed and of 'Liquefaction Potential: Science versus Practice' by R.B. Peck," JGED, ASCE Vol. 106, No. GT6, June, pp. 720-724.
32. Dobry, R., Powell, D.J., Yokel, F.Y. and Ladd, R.S. (1980): "Liquefaction Potential of Saturated Sand - The Stiffness Method," Proc. 7th World Conf. on Earthquake Engr., Istanbul, Turkey, Vol. 3, pp. 25-32.
33. Dobry, R., Stokoe, K.H. II, Ladd, R.S. and Youd, T.L. (1981a): "Liquefaction Susceptibility from S-Wave Velocity," Proc. Session on In Situ Testing to Evaluate Liquefaction Susceptibility, ASCE Nat. Convention, St. Louis, Missouri, Oct.
34. Dobry, R., Yokel, F.Y. and Ladd, R.S. (1981b): "Liquefaction Potential of Overconsolidated Sands in

Moderately Seismic Areas," Pro. Conf. on Earthquakes and Earthquake Engineering in the Eastern United States, Vol. 2, Knoxville, Tennessee, Sept., pp. 643-664.

35. Dobry, R., Ladd, R.S., Yokel, F.Y., Chung, R.M. and Powell, D. (1982): "Prediction of Pore Water Pressure Buildup and Liquefaction of Sands During Earthquakes by the Cyclic Strain Method," National Bureau of Standards, Building Science Series 138, U.S. Dept. of Commerce, July.
36. Dobry, R., Mohamad, R., Dakoulas, P. and Gazetas, G. (1984a): "Liquefaction Evaluation of Earth Dams - A New Approach," Proc. 8th World Conf. on Earthquake Eng., San Francisco, Vol. III, July, pp. 333-340.
37. Dobry, R., Pierce, W.G., Dyvik, R. and Thomas, G.E. (1984b): "Pore Pressure Model for Cyclic Straining of Sand," submitted for publication.
38. Dobry, R., Vasquez-Herrera, A., Mohamad, R. and Vucetic, M. (1985): "Liquefaction Flow Failure of Silty Sand by Torsional Cyclic Tests," Advances in the Art of Testing Soils Under Cyclic Conditions, ASCE, October, 1985.
39. Donnelly, M. (1980): "The Effects of Method of Sample Preparation on the Stress-Strain Behavior of Sands in Undrained Stress-Controlled Triaxial Tests," M.S. Thesis, Clarkson College of Technology, Potsdam, New York.
40. Drnevich, V.P. and Richart, F.E. Jr. (1970): "Dynamic Prestraining of Dry Sand," JSMFD, ASCE, Vol. 96, No. SM2, pp. 453-469.
41. Duncan, J.M., Bryne, P., Wong, K.S. and Mabry, P. (1980a): "Strength, Stress-Strain and Bulk Modulus Parameters for Finite Element Analyses of Stresses and

Movements in Soil Masses," Report No. UCB/GT/80-01, Dept. of Civil Engineering, Univ. of California, Berkeley, Aug.

42. Duncan, J.M., Wong, K.S. and Ozawa, Y. (1980b): "FEADAM: A Computer Program for Finite Element Analysis of Dams," Report No. UCB/GT/80-02, Dept. of Civil Engineering, Univ. of California, Berkeley, Dec.
43. Durham, G.N. and Townsend, F.C. (1973): "Effect of Relative Density on the Liquefaction Susceptibility of a Fine Sand under Controlled-Stress Loading," ASTM, STP 523, pp. 319-331.
44. Dyvik, R., Dobry, R., Thomas, G.E. and Pierce, W.G. (1984): "Influence of Consolidation Shear Stresses and Relative Density on Threshold Strain and Pore Pressure during Cyclic Straining of Saturated Sand," U.S. Army Waterways Experiment Station, Miscellaneous Paper GL-84-15, July.
45. Engineering News-Record (1925): "What Happened to Municipal Utilities of Santa Barbara," Engineering News Record, Vol. 95, No. 4, July.
46. Engineering News-Record (1930): "Break in Downstream Dyke at Saluda Dam Releases Segregation Pool," Engineering News Record, Feb., pp. 364-376.
47. Engineering News-Record (1930): "Hydraulic-Fill Dam of Fine Volcanic Ash Fails Disastrously," Engineering News Record, May, pp. 869-871.
48. Engineering News Record (1938): "Slide at Fort Peck Dam Moves Eight Million Yards of Fill," This Weeks Event, Engineering News Record, Sept., pp. 385.
49. Finn, W.D.L. (1982): "Fundamental Aspects of Response of Tailings Dams to Earthquakes," Proc. Session on



dynamic stability of Tailings Dams, ASCE Nat. Convention, New Orleans, Louisiana, Oct., pp. 46-72.

50. Finn, W.D., Yogendrakumar M., Yoshida, N. and Yoshida, H. (1987): "Analysis of Porewater Pressures in Seismic Centrifuge Tests," Soil Dynamics and Liquefaction ed. A.S. Cakmak, Proceedings 3rd Intl. Conference on Soil Dynamics and Earthquake Engineering, Princeton.
51. Frydman, S. Zeitlen, J.G. and Alpan, I. (1973): "The Membrane Effect in Triaxial Testing of Granular Soils," Journal of Testing and Evaluation, Vol. 1, No. 1, Jan., pp. 37-41.
52. GEI, Geotechnical Engineers Inc. (1988): "Re-evaluation of the Lower San Fernando Dam," Report submitted to the U.S. Army Corps of Engineers, Waterways Experiment Station, February 1988.
53. Habibian A., Steedman, R.S. and Schofield, A.N. (1985): "Earthquake Centrifuge Studies of the Bolivar Coast Dyke Problem," Progress Report No. 2, July 1985, Cambridge University Engineering Department.
54. Hadala, P.J. and Torrey, V.H. (1987): "Mississippi River Bank Flow Slides," The Peck Symposium, University of Illinois at Urbana.
55. Hamada, M., Yosuda, S., Isoyama, R. and Emoto, K. (1986): "Study on Liquefaction Induced Permanent Ground Displacements," Report for the Association for the Development of Earthquake Prediction.
56. Hammer, M. (1985): "Membrane Penetration Effect on Pore Pressures during Cyclic Triaxial Tests on Sands," M.S. Thesis, Rensselaer Polytechnic Institute, Troy, N.Y.
57. Hardin, B.O. and Drnevich, V.P. (1972): "Shear Modulus

and Damping in Soils: Measurements and Parameter Effects," JSMFD, ASCE, Vol. 98, No. SM6, June, pp. 603-624.

58. Hazen, A. (1918): "A Study of the Slip in the Calaveras Dam," Engineering News Record, Sept, Vol. 81, No. 26, pp. 1158-1161.
59. Hazen, A. (1920): "Hydraulic Fill Dams," Transactins, ASCE, Paper 1458, pp. 1713-1745.
60. Hazen A. and Metcalf, L. (1918): "Middle Section of Upstream Side of Calaveras Dam Slips into Reservoir," Engineering News Record, April, Vol. 80, No. 14, pp. 679-681.
61. Horn, H.M. (1979): "North American Experience in Sampling and Laboratory Dynamic Testing," Geotechnical Testing Journal, GTJODJ, Vol. 2, No. 2, June, pp. 84-97.
62. Huishan, L. and Taiping, Q. (1984): "Liquefaction Potential of Saturated Sand Deposits Underlying Foundation of Structure," Proceedings 8th WCEE, San Francisco.
63. Idriss, I.M., Lysmer, J., Hwang, R. and Seed, H.B. (1973): "QUAD-4: A Computer Program for Evaluating the Seismic Response of Soil Structures by Variable Damping Finite Element Procedures," Report No. EERC 73-16, Earthquake Engineering Research Center, College of Engineering, Univ. of California, Berkeley, July.
64. Idriss, I.M., Seed, H.B. and Serff, N. (1974): "Seismic Response by Variable Damping Finite Elements," JGED, ASCE, Vol. 100, No. GT1, Jan., pp. 1-13.
65. Ishihara, K. and Li, S., (1972): "Liquefaction of Saturated Sand in Triaxial Torsion Shear Test," Soils

and Foundations, Vol. 12, No. 2, June, pp. 19-39.

66. Ishihara, K. and Okada, S. (1978): "Effects of Stress History on Cyclic Behavior of Sand," Soils and Foundations, Vol. 18, No. 4, Dec., pp. 31-45.
67. Ishihara, K. and Silver, M.L. (1977): "Large Diameter Sand Sampling to Provide Specimens for Liquefaction Testing," Proc. IX Intl. Conf. on Soil Mech. and Fdn. Eng., Specialty Session 2, Tokyo.
68. Ishihara, K., Tatsuoka, F. and Yasuda, S. (1975): "Undrained Deformation and Liquefaction of Sands Under Cyclic Stresses," Soils and Foundations, Vol. 15, No. 1, March, pp. 29-44.
69. Jennings, J.E. (1979): "The Failure of a Slimes Dam at Bafokeng: Mechanism of Failure and Associated Design Considerations," The Civil Engineer in South Africa, June.
70. Jeyapalan, J.K., Duncan, J.M. and Seed, H.B. (1983): "Investigation of Flow Failures of Tailings Dams," JGED, ASCE, Vol. 109, No. 2, Feb., pp. 172-189.
71. Keikbusch, M. and Schuppener, B. (1977): "Membrane Penetration and Its Effect on Pore Pressures," JGED, ASCE, Vol. 103, No. GT11, Nov., pp. 1267-1279.
72. Kolbuszewski, J.J. (1948a): "An Experimental Study of the Maximum and Minimum Porosities of Sands," Proceedings, II ICSMFE, Rotterdam.
73. Kolbuszewski, J.J. (1948b): "General Investigation of the Fundamental Factors Controlling Loose Packing of Sands," Proceedings, II, ICSMFE, Rotterdam.
74. Koppejan, A.W., van Wamelen, B.M. and Weinberg, L.J.H.

- (1948): "Coastal Flow Slides in the Dutch Provincence of Zeeland," Proceedings II ICSMFE, Rotterdam.
75. Kramer, S.L., Seed, H.B. (1988): "Initiation of Soil Liquefaction under Static Loading Conditions," JGED, ASCE, Vol. 114, No. 4, April.
  76. Kutter, B.L. (1988): Discussion to "Liquefaction Evaluation Procedure," JGED, ASCE, Vol. 114, No. 2, Feb. pp. 243-246.
  77. Ladd, R.S. (1977): "Specimen Preparation and Cyclic Stability of Sands," JGED, ASCE, Vol. 103, No. GT6, June, pp. 535-547.
  78. Ladd, R.S. (1977): "Preparing Test Specimens Using Undercompaction," Geotechnical Testing Journal, Vol. 1, No. 1, March, pp. 16-23.
  79. Lade, P.V. and Hernandez, S.B. (1977): "Membrane Penetration Effects in Undrained Tests," JGED, ASCE, Vol. 103, No. GT2, Feb., pp. 109-125.
  80. Lade, P.V. and Nelson, R.B. and Ito, Y.M. (1987): "Instability of Granular Materials with Non-associated Flow," Submitted for Publication, Journal Engineering Mechanics Div., ASCE.
  81. Lade, P.V. and Nelson, R.B. and Ito, Y.M. (1987): "Non-associated Flow and Stability of Granular Materials," ASCE, Journal Engineering Mechanics, December.
  82. Lambe, T.W. and Whitman, R.V. (1969): *Soil Mechanics*, John Wiley and Sons.
  83. Lee, K.L. and Seed, H.B. (1967): "Dynamic Strength of Anisotropically Consolidated Sand," JSMFD, ASCE, Vol.

93, No. SM5, Sept., pp. 169-190.

84. Lee, K.L., Seed, H.B., Idriss, I.M. and Makdisi, F.I. (1975): "Properties of Soil in the San Fernando Hydraulic Fill Dams," JGED, ASCE, Vol. 101, No. GT8, Aug., pp. 801-821.
85. Lindenberg, J. and Koning, H.L. (1981): "Critical Density of Sand," Geotechnique, Vol. 31, No. 2, pp. 231-245.
86. Lingyao, L., Kuiefen, L. and Dongping, B. (1980): "Earthquake Damage of Baihe Earth Dam and Liquefaction Characteristics of Sand and Gravel Materials," Proc. 7th World Conf. on Earthquake Engineering, Istanbul, Turkey, Sept., pp. 171-178.
87. Luong, M.P. (1980): "Stress-Strain Aspects of Cohesionless Soils under Cyclic and Transient Loading," Proc. Intl. Symp. on Soils under Cyclic and Transient Loading, Vol. 1, Swansea, U.K., Jan., pp. 315-324.
88. Luong, M.P. and Sidaner, J.F. (1981): "Undrained Behavior of Cohesionless Soils under Cyclic and Transient Loading," Proc. Intl. Conf. on Recent Advances in Earthquake Eng. and Soil Dynamics, Vol. 1, St. Louis, Missouri, April-May, pp. 215-220.
89. Lupini, J.F., Skinner, J.E. and Vaughan, P.R. (1981): "The Demand Residual Strength of Cohesive Soils," Geotechnique, Vol. 31, No. 2, pp. 181-213.
90. Makdisi, F.I., Kagawa, T. and Seed, H.B. (1982): "Seismic Response of Earth Dams in Triangular Canyons," JGED, ASCE, Vol. 108, No. GT10, Oct., pp. 1328-1337.
91. Marcuson, W.F. III, Ballard, R.F. Jr. and Ledbetter, R.H. (1979): "Liquefaction Failure of Tailings Dams Resulting from the Near Izu Oshima Earthquake, 14 and

15 January 1978," Proc. 6th Pan American Conf. on Soil Mech. and Fdn. Eng., Lima, Peru, Vol. 2, 1979, pp. 69-80.

92. Marcuson, W.F. III and Franklin, A.G. (1979): "State of the Art of Undisturbed Sampling of Cohesionless Soils," U.S. Army Waterways Experiment Station, Miscellaneous paper GL 79-16, July.
93. Martin, G.R., Finn, W.D.L. and Seed, H.B. (1975): "Fundamentals of Liquefaction Under Cyclic Loading," JGED, ASCE, Vol. 101, No. GT5, May, pp. 423-483.
94. Martin, G.R., Finn, W.D.L. and Seed, H.B. (1978): "Effects of System Compliance on Liquefaction Tests," JGED, ASCE, Vol. 104, No. GT4, April, pp. 463-479.
95. Maslov, N.N. (1958): "Problem of High Earth Density in Conditions of Seismic Activity," Sixth Congress of Large Dams, Question No. 22, R. 115, New York.
96. Middlebrooks, T.A. (1940): "Fort Peck Slide," Transaction, ASCE, paper No. 2144, pp. 723-764.
97. Newmark, N.M. (1965): "Effects on Earthquakes on Dams and Embankments," Geotechnique, Vol. 15, No. 2, pp. 139-160.
98. Mohamad, R. and Dobry, R. (1986): "Undrained Monotonic and Cyclic Triaxial Strength of Sand," JGED, ASCE, Vol. 112, No. 2, Oct., pp. 941-958.
99. Mulilis, J.P., Chan, C.K. and Seed, H.B. (1975): "The Effects of Method of Sample Preparation on the Cyclic Stress-Strain Behavior of Sands," Report No. EERC 75-18, University of California, Berkeley, July.
100. NRC, National Research Council (1985): "Liquefaction of

Soils During Earthquakes," National Academy Press, Washington, DC.

101. Okusa, S. and Anma, S. (1980): "Slope Failures and Tailings Dam Damage in the 1987 Izo-Ohshima-Kinkai Earthquake," Engineering Geology, Vol. 16, pp. 195-224.
102. Okusa, S., Anma, S. and Maikuma, H. (1980): "Liquefaction of Mine Tailings in the 1978 Izu-Ohshima-Kinkai Earthquake, Central Japan, Proceedings 7th World Conference on Earthquake Engineering, Istanbul, Turkey.
103. Okusa, S., Anma, S. and Maikuma, H. (1984): "The Propagation of Liquefaction Pressure and Delayed Failure of a Tailing Dam Dyke in the 1978 Izu-Ohshima-Kinkai Earthquake, Proceedings 8th World Conference on Earthquake Engineering, San Francisco.
104. Padfield, C.J. (1978): "The Stability of River Banks and Flood Embankments," Ph.D. Thesis, Cambridge University.
105. Peck, R.B. (1979): "Liquefaction Potential: Science Versus Practice," JGED, ASCE, Vol. 105, No. GT3, March, pp. 393-398.
106. Peraza, L. (1985): "Undrained Cyclic Torsional Triaxial Tests on Hollow Cylindrical Specimens of Sand," M.S. Thesis, Rensselaer Polytechnic Institute, Troy, N.Y.
107. Pierce, W.G. (1985): "Constitutive Relations for Saturated Sand Under Undrained Cyclic Loading," Ph.D. Thesis, Rensselaer Polytechnic Institute, Troy, N.Y.
108. Pilecki, T.J. (1988): Discussion to "Liquefaction Evaluation Procedure," JGED, ASCE, Vol. 114, No. 2, Feb., pp. 243-246.

109. Poulos, S.J. (1981): "The Steady State of Deformation," JGED, ASCE, Vol. 107, No. GT5, May, pp. 553-562.
110. Poulos, S.J., Castro, G. and France, J.W. (1984): "Procedure for Liquefaction Evaluation," JGED, ASCE, Vol. 111, No. 6 June, pp. 772-792.
111. Poulos, S.J., Castro, G. and France, J.W. (1988): Closure to "Liquefaction Evaluation Procedure," JGED, ASCE, Vol. 114, No. 2, Feb., pp. 251-259.
112. Poulos, S.J., Robinsky, E. and Keller, T.O. (1985): "Liquefaction Resistance of Thickened Tailings," JGED, ASCE, Vol. 111, No. 12, Dec., pp. 1380-1394.
113. Prater, E.G. (1980): "On the Interpretation of Cyclic Triaxial Test Data with Application to the Seismic Behavior of Fill Dams," Proc. Intl. Symp. on Soils under Cyclic and Transient Loading, Vol. 2, Swansea, U.K., Jan., pp. 495-508.
114. Pyke, R. (1988): Discussion to "Liquefaction Evaluation Procedure," JGED, ASCE, Vol. 114, NO. 2, Feb., pp. 246-247.
115. Pyke, R.M., Chan, C.K. and Seed, H.B. (1974): "Settlement and Liquefaction of Sands Under Multi-Directional Shaking," Report No. EERC 74-2, University of California, Berkeley, February.
116. Raines, J.R., Borja, R.I., Anwar, H. and Seed, R.B. (1987): "Numerical Modelling of Membrane Penetration Effects on Undrained Triaxial Tests," in Soil Dynamics and Liquefaction ed. A. Cakmak Proceedings, 3rd Intl. Conf. Soil Dynamics and Earthquake Engineering, Princeton.
117. Raju, V.S. and Sadasivan, S.K. (1974): "Membrane Penetration in Triaxial Tests on Sands," JGED, ASCE,



Vol. 100, No. GT4, April, pp. 482-489.

118. Ramana, K.V. and Raju, V.S. (1982): "Membrane Penetration in Triaxial Tests," JGED, ASCE, Vol. 108, No. GT2, Feb., pp. 305-310.
119. Schofield, A.N. (1980): "Cambridge Geotechnical Centrifuge Operations," Geotechnique, Vol. 30, No. 3, pp. 227-268.
120. Schofield, A.N. (1981): "Dynamic and Earthquake Geotechnical Centrifuge Modelling," State of the Art Review, Intl. Conf. Recent Advances in Geotechnical Earthquake Engineering and Soil Dynamics, St. Louis.
121. Schofield, A.N. and Venter, K. (1984): "Earthquake Induced Pore Pressures in the Foundation of a Sea Dyke," Report CUFD/D-Soils/TR 150, Cambridge University.
122. Schofield, A.N. and Wroth, C.P. (1968): Critical State Soil Mechanics, McGraw-Hill, London.
123. Schuyler, J.D. (1907): "Recent Practice in Hydraulic-Fill Dam Construction," Transactions, ASCE, Vol. 58, No. 1043, pp. 196-259.
124. Schuyler, J.D. (1909): "The Slide in the Necaxa Hydraulic-Fill Dam," Engineering News, Vol. 62, NO. 3, July, pp. 72-74.
125. Scott, R.F. (1973): "The Calculation of Horizontal Accelerations from Seismoscope Records," Bull. Seismological Soc. of America, Vol. 63, No. 5, Oct., pp. 1637-1661.
126. Seed, H.B. (1968): "Landslides during Earthquakes due to Soil Liquefaction," JSMFD, ASCE, Vol. 94, No. SM5,

Sept., pp. 1055-1122.

127. Seed, H.B. (1967): "Soil Stability Problems Caused by Earthquakes," Soil Mechanics and Bituminous Materials, Research Laboratory, Dept. Civil Engr., University of California, Berkeley, January.
128. Seed, H.B. (1979): "Considerations in the Earthquake-Resistant Design of Earth Dams," Geotechnique, Vol. 29, No. 3, pp. 215-263.
129. Seed, H.B. (1979): "Earthquake Resistant Design of Earth Dams," Proc. Symp. on Seismic Design of Embankments and Caverns, ASCE, May, pp. 41-64.
130. Seed, H.B. (1986): "Design Problems in Soil Liquefaction," Report No. UCB/EERC-86-02, Feb., Univ. of California, Berkeley.
131. Seed, H.B. and Idriss, I.M. (1967): "Analysis of Soil Liquefaction: Niigata Earthquake," JSMFD, ASCE, Vol. 93, No. SM3, May, pp. 83-108.
132. Seed, H.B. and Idriss, I.M. (1970): "Soil Moduli and Damping Factors for Dynamic Response Analyses, Report No. EERC 70-10, Earthquake Engineering Research Center, College of Engineering, Univ. of California, Berkeley, Dec.
133. Seed, H.B. and Idriss, I.M. (1971): "Simplified Procedure for Evaluating Soil Liquefaction Potential," JSMFD, ASCE, Vol. 97, No. SM9, September, pp. 1249-1274.
134. Seed, H.B. and Idriss, I.M. (1980): "On the Importance of Dissipation Effects in Evaluating Pore Pressure Changes due to Cyclic Loading," Proc. Intl. Symp. on Soils under Cyclic and Transient Loading, Vol. 2, Swansea, U.K., Jan., pp. 569-580.

135. Seed, H.B. and Lee, K.L. (1966): "Liquefaction of Saturated Sands during Cyclic Loading," JSMFD, ASCE, Vol. 92, No. SM6, Nov. pp. 105-134.
136. Seed, H.B. and Lee, K.L. (1969): "Pore-Water Pressures in Earth Slopes under Seismic Loading Conditions," Proc. 4th World Conf. on Earthquake Engr., Vol. 3, Santiago, Chile, pp. 1-11.
137. Seed, H.B., Lee, K.L. and Idriss, I.M. (1969): "An Analysis of Sheffield Dam Failure," JSMFD, ASCE, Vol. 95, No. SM6, Nov., pp. 1453-1490.
138. Seed, H.B., Lee, K.L., Idriss, I.M. and Makdisi, F.I. (1973): "Analysis of the Slides in the San Fernando Dams during the Earthquake of Feb. 9, 1971," Report No. EERC 73-2, Earthquake Engineering Research Center, College of Engineering, University, of California, Berkeley, June.
139. Seed, H.B., Lee, K.L., Idriss, I.M. and Makdisi, F.I. (1975a): "The Slides in the San Fernando Dams during the Earthquake of February 9, 1971," JGED, ASCE, Vol. 101, No. GT7, July, pp. 651-689.
140. Seed, H.B., Idriss, I.M., Lee, K.L. and Makdisi, F.I. (1975b): "Dynamic Analysis of the Slide in the Lower San Fernando Dam during the Earthquake of February 9, 1971," JGED, ASCE, Vol. 101, No. GT8, Sept., pp. 889-911.
141. Seed, H.B., Makdisi, F.I. and De Alba, P. (1978): "Performance of Earth Dams during Earthquakes," JGED, ASCE, Vol. 104, No. GT7, July, pp. 967-994.
142. Seed, H.B., Seed, R.B. and Harder, L.F. (1987): "Re-evaluation of the Slide in the Lower San Fernando Dam in the Earthquake of Feb. 9, 1971," Report by H. Bolton Seed, Inc., California.

143. Selig, E.T. and Chang, C.S. (1981): "Soil Failure Modes in Undrained Cyclic Loading," JGED, ASCE, Vol. 107, No. GT5, May, pp. 539-551.
144. Siegel, R.A. (1975a): "Computer Analysis of General Slope Stability Problems," Report No. JHRP-75-8, Purdue Univ., West Lafayette, Indiana.
145. Seigel, R.A. (1975b): "STABL User Manual," Report No. JHRP-75-9, Purdue University, West Lafayette, Indiana.
146. Senour, C. and Turnbull, W.J. (1948): "A Study of Foundation Failures at a River Bank Revetment," Proceedings, II ICSMFE, Rotterdam.
147. Silver, M.L. and Seed, H.B. (1971): "Volume Changes in Sands During Cyclic Loading," JSMFD, ASCE, Vol. 97, No. SM9, September.
148. Singh, S., Seed, H.B. and Chan, C.K. (1982): "Undisturbed Sampling of Saturated Sands by Freezing," JGED, ASCE, Vol. 108, No. GT2, Feb., pp. 247-264.
149. Sladen, J.A. and Handford, G. (1987): "A Potential Systematic Error in Laboratory Testing of Very Loose Sands," Canadian Geotechnical Journal, Vol. 24, August, pp. 462-466.
150. Sladen, J.A., Hollander, R.D. and Krahn, J. (1985): "The Liquefaction of Sands, A Collapse Surface Approach," Canadian Geotechnical Journal, Vol. 22, pp. 564-578.
151. Smith, E.S. (1969): "Tailings Disposal and Liquefaction," Transactions, Society of Mining Engineers, AIME, Vol. 244, pp. 179-187.
152. Smith, E.S. (1972): "Tailings Disposal-Failures and

Lessons," Proceedings of the 1st International Tailing Symposium, Tuscon, Arizona.

153. Stokoe, K.H. II and Hoar, R.J. (1978): "Variables Affecting In-Situ Seismic Measurements," Proceeding ASCE Geotechnical Engineering Division Specialty Conference on Earthquake Engineering and Soil Dynamics, New York, NY.
154. Stokoe, K.H. II and Woods, R.D. (1972): "In-Situ Shear Wave Velocity by Crosshole Method," JSMFD, ASCE, Vol. 98, No. SM5, May, pp. 443-460.
155. Succarieh, M., Dakoulas, P., Vasquez, A. and Dobry, R. (1987): "Steady State Behavior of Leighton Buzzard Sand," Report No. CE-87-01 prepared for INTEVEP, Department of Civil Engineering, Rensselaer Polytechnic Institute, March.
156. Terzaghi, K. (1956): "Varieties of Submarine Slope Failures," Proceedings of the Eighth Texas Conference on Soil Mechanics and Foundation Engineering.
157. Thomas, G. and Dobry, R. (1984): "Cyclic Strain-Controlled Tests for Liquefaction Studies of Saturated Debris from Mount St. Helen Volcanic Explosion," Report No. CE-84-4, Dept. of Civil Engineering, Rensselaer Polytechnic Institute, Troy, N.Y.
158. Thorne, S.D. (1983): "Liquefaction Behavior of Dilative Sand during Seismic Loading," M.E. Project, Rensselaer Polytechnic Institute, Troy, N.Y.
159. Torrey, V.H. and Weaver, F.J. (1984): "Flow Failures in Mississippi Riverbanks," IV Int. Symposium on Landslides, Toronto, Canada, Vol. 2, pp. 355-360.
160. U.S. Army Corps of Engineers (1970): "Engineering and

Design Stability of Earth and Rock-Fill Dams," Manual No. 1110-2-1902, Office of The Chief of Engineers, Washington, D.C.

161. U.S. Army Corps of Engineers (1988): "Re-evaluation of the Lower San Fernando Dam," U.S. Army Corps of Engineers, W.E.S., in preparation.
162. Vaid, Y.P. and Chern, J.C. (1983a): "Effect of Static Shear on Resistance to Liquefaction," Soils and Foundations, Vol. 23, No. 1, March, pp. 47-60.
163. Vaid, Y.P. and Chern, J.C. (1983b): "Mechanism of Deformation during Cyclic Undrained Loading of Saturated Sands," Soil Dynamics and Earthquake Eng., Vol. 2, No. 3, pp. 171-177.
164. Vaid, Y.P. and Negussey, D. (1984): "A Critical Assessment of Membrane Penetration in the Triaxial Test," Geotechnical Testing Journal, Vol. 7, No. 2, June, pp. 70-76.
165. Whitman, R.V. (1970): "Hydraulic Fills to Support Structural Loads," JSMFD, ASCE, Vol. 96, No. SM1, January.
166. Willis, B. (1925): "A Study of the Santa Barbara Earthquake of June 1929, 192S, BSSA, Vol. 15, No. 4, Dec., pp. 255-278.
167. Woyzechowski, (1986): Personal Communication.
168. Yamada, Goji (1966): "Damage to Earth Structures and Foundations by the Niigata Earthquake, June, 16, 1964, in JNR", Soils and Foundation, Vol. 6, No. 1.
169. Yoshimi, Y. (1970): "An Outline of Damage During the Tokachioki Earthquake," Soils and Foundations, Vol. 10,

No. 2.

170. Yoshimi, Y., Hatanaka, M. and Oh-Oka, H. (1978): "Undisturbed Sampling of Saturated Sands by Freezing," Soils and Foundations, Vol. 18, No. 3, Sept., pp. 59-73.
171. Youd, T.L. (1972): "Compaction of Sands by Repeated Shear Straining," JSMFD, ASCE, Vol. 98, No. SM7, July, pp. 709-725.
172. Youd, T.L. (1973): "Liquefaction, Flow and Associated Ground Failure," Circular 688, U.S. Geological Survey.

APPENDIX I - INDIVIDUAL TEST RESULTS ON OTTAWA SAND F125



# OTTAWA F125 SAND

Test #	Test Type	e	$\bar{\sigma}_{3c}$	K <sub>c</sub>	$\bar{p}_{us}$	Q <sub>us</sub>	$\bar{p}_{ut}$	Q <sub>ut</sub>	r <sub>ut</sub>	$\gamma_{cy}(\%)$	n <sub>t</sub>	Comment
F125-49	CyT-CAU	0.812	0.984	2.0	0.173	0.103	1.272	0.499	0.214	0.08	15.5	
F125-50	CyT-CAU	0.8195	0.984	2.0	0.156	0.094	1.292	0.483	0.179	0.0424	1	
F125-51	CyT-CAU + CAU	0.8305	0.984	1.50	0.091	0.055	0.944	0.285	0.330	0.0424	N.A.	(8)
F125-52	CIU	0.783	4.077	1.0	0.112	0.077	2.937	0.658	0.441	N.A.	N.A.	(2),(9)
F125-53	CIU	0.799	4.077	1.0	0.398	0.254	2.601	0.957	0.580	N.A.	N.A.	(1),(4)
F125-54	CIU	0.8138	4.077	1.0	N.R.	0.114	N.R.	0.094	N.R.	N.A.	N.A.	(3)
F125-55	CIU	0.826	4.077	1.0	N.R.	0.103	N.R.	0.645	N.R.	N.A.	N.A.	(3)
F125-56	CIU	0.8004	4.077	1.0	N.R.	0.140	N.R.	0.673	N.R.	N.A.	N.A.	(3)

All units in Kg/cm<sup>2</sup>

N.A. - Not Applicable

N.R. - Not Recorded

1) e Measurements not Accurate

2) Old Platens

3) Wrong Pore Pressure Measurement<sup>3</sup>

4) Pore Pressure at Steady State not Measured

5) Variable Strain

6) Cyclic Axial Triaxial Stress Controlled

7) Cyclic Strains too Small to be Recorded

8) CyT-CAU for 10 Cycles followed by CAU

9) Strain Controlled

# OTTAWA F125 SAND

Test #	Test Type	e	$\bar{\sigma}_{1c}$	$K_c$	$\bar{p}_{us}$	$q_{us}$	$\bar{p}_{ut}$	$q_{ut}$	$r_{ut}$	$\gamma_{cy}(\%)$	$n_t$	Comment
F125-33	CyT-CAU	0.8738	0.562	1.49	0.055	0.037	0.411	0.139	0.516	0.0082	26	(1)
F125-34	CyT-CAU	0.8289	0.98	1.51	0.072	0.054	0.786	0.241	0.446	0.013	20	
F125-35	CyT-CAU	0.8366	1.51	1.51	N.A.	0.066	1.038	0.387	0.570	0.02	17	(4)
F125-36	CyT-CAU	0.833	4.08	2.47	1.525	0.918	6.444	2.981	0.151	0.018	19	(1)
F125-37	CyT-CAU	0.7696	4.08	2.46	N.A.	0.928	5.943	2.656	0.194	0.076	3	(4)
F125-38	CyT-CAU	0.7714	4.08	2.47	1.792	1.031	6.452	2.989	0.151	0.0196	89	
F125-39	CyT-CAU	0.7548	4.08	2.9	3.41	1.793	7.461	3.823	0.108	0.015	115	
F125-40	CyT-CAU	0.7508	4.08	2.9	3.190	1.793	7.585	3.859	0.086	0.033	33	
F125-41	CyT-CAU	0.7649	4.08	2.9	3.766	1.929	7.629	3.85	0.073	0.087	4.5	
F125-42	CAU	0.8158	0.984	2.0	0.096	0.078	1.531	0.573	0.027	N.A.	N.A.	
F125-43	CCA	0.825	0.984	2.0	0.132	0.074	1.305	0.496	0.179	0.0058	38	(7)
F125-44	CyT-CAU	0.8223	0.984	2.0	0.149	0.097	1.305	0.497	0.179	N.A.	N.A.	(5)
F125-45	CyT-CAU	0.7863	0.984	2.925	0.744	0.445	1.834	0.941	0.093	0.0123	5.5	
F125-46	CyT-CAU	0.8062	0.0984	2.49	0.299	0.193	1.611	0.732	0.107	0.0116	11	
F125-47	CAD	0.79661	0.984	2.4	1.24	0.688	N.A.	N.A.	N.A.	N.A.	N.A.	
F125-48	CyT-CAU	0.8166	0.984	2.0	0.149	0.097	1.304	0.496	0.179	0.019	4	

All units in Kg cm<sup>2</sup>

# OTTAWA F125 SAND

Test #	Test Type	e	$\bar{\sigma}_{3c}$	$K_c$	$\bar{p}_{us}$	$q_{us}$	$\bar{p}_{ut}$	$q_{ut}$	$r_{ut}$	$\gamma_{cy}(\%)$	$n_t$	Comment
F125-17	CyT-CAU	0.793	4.077	1.52	N.R.	0.131	3.424	1.059	0.42	0.0356	13	(4)
F125-18	CyT-CAU	0.808	4.077	1.52	N.R.	0.116	3.424	1.055	0.425	0.11613	2	(4)
F125-19	CyT-CAU	0.780	4.077	1.52	N.R.	0.102	3.411	1.047	0.42	0.02533	35	(4)
F125-20	CyT-CAU	0.790	4.077	1.5	0.239	0.136	3.295	1.063	0.453	0.0586	7	
F125-21	CIU	0.8057	4.077	1	0.316	0.171	2.621	0.872	0.571		N.A.	(1),(2)
F125-22	CIU	0.885	4.077	1	0.235	0.173	2.184	0.703	0.637		N.A.	(1),(2)
F125-23	CyT-CAU	0.814	4.077	1.2	N.R.	0.058	N.R.	0.398	N.R.	0.251	2	
F125-24	CyT-CAU	0.814	4.077	1.2	0.108	0.073	1.148	0.410	0.819	0.1087	18	
F125-25	CyT-CAU	0.8251	4.077	1.2	N.A.	0.127	1.602	0.425	0.711	0.054	26	(4)
F125-26	CyT-CAU	0.814	4.077	1.2	0.132	0.075	1.150	0.412	0.819	0.0321	332	
F125-27	CAD	0.8644	0.562	2.0	0.500	0.28	N.A.	N.A.	N.A.	N.A.	N.A.	
F125-28	CIU	0.866	4.077	1.0	0.21	0.09	2.613	0.59	0.504	N.A.	N.A.	(1),(2),(9)
F125-29	Threshold	0.810	4.077	1.0	N.A.	N.A.	N.A.	N.A.	N.A.	N.A.	N.A.	
F125-30	Threshold		4.077	1.0	N.A.	N.A.	N.A.	N.A.	N.A.	N.A.	N.A.	
F125-31	CyT-CAU	0.8357	0.98	1.51	N.A.	0.047	0.849	0.251	0.393	0.044	2	(4)
F125-32	CyT-CAU	0.8346	0.98	1.51	N.A.	0.045	0.723	0.249	0.518	0.021	8.5	(4)

All units in Kg/cm<sup>2</sup>

# OTTAWA F125 SAND

Test #	Test Type	e	$\bar{\sigma}_{3c}$	K <sub>c</sub>	$\rho_{us}$	q <sub>us</sub>	$\bar{p}_{ut}$	q <sub>ut</sub>	r <sub>ut</sub>	$\gamma_{cy}(\%)$	n <sub>i</sub>	Comment
F125-1	CyT-CAU	0.813	4.077	2	0.397	0.292	5.305	2.070	0.207	0.0383	8	(1),(2)
F125-2	CyT-CAU	0.820	4.077	1	N.A.	N.A.	N.A.	N.A.	1	0.3873	4	
F125-3	CyT-CAU	0.831	4.077	2	0.441	0.336	5.144	2.051	0.241	0.0374	11	(1),(2)
F125-4	CyT-CAU	0.84	4.077	2	0.462	0.286	5.277	2.043	0.207	0.0338	13	(1),(2)
F125-5	CyT-CAU	0.7627	5.480	2	N.R.	0.800	7.107	2.853	0.224	0.025	14	(3)
F125-6	CyT-CAU	0.777	4.077	1	N.A.	N.A.	N.A.	N.A.	N.A.	0.1956	13	
F125-7	CyT-CAU	0.730	4.077	1	N.A.	N.A.	N.A.	N.A.	N.A.	0.062	115	
F125-8	CyT-CAU	0.798	4.077	1	N.A.	N.A.	N.A.	2.091	N.A.	0.037	2160	
F125-9	CyT-CAU	0.7647	4.077	2	N.A.	0.392	N.R.	2.091	N.R.	0.0885	1	(4)
F125-10	CyT-CAU	0.785	4.077	2	N.A.	0.507	5.422	2.135	0.194	0.022	12	(4)
F125-11	CyT-CAU	0.7737	4.077	2	0.901	0.514	5.44	2.066	0.172	0.044	3	
F125-12	CyT-CAU	0.7991	4.077	2	N.R.	0.164	5.421	2.046	0.172	0.0196	5	
F125-13	CyT-CAU	0.794	4.077	2	N.R.	0.193	5.301	2.058	0.205	0.01293	46	(4)
F125-14	CyT-CAU	0.789	4.077	2	N.R.	0.188	5.47	2.051	0.162	0.0264	17	(4)
F125-15	CyT-CAU	0.788	4.077	2	N.R.	0.171	5.533	2.070	0.151	0.008	27	(4)
F125-16	CyT-CAU	0.772	4.077	2	N.R.	0.296	5.166	2.055	0.237	0.00647	139	(4)

All units in Kg/cm<sup>2</sup>

APPENDIX II - INDIVIDUAL TEST RESULTS ON SANDS A, B AND C

## SAND A

Test #	Test Type	e	$\bar{\sigma}_{3c}$	K <sub>c</sub>	$\bar{p}_{us}$	Q <sub>us</sub>	$\bar{p}_{ut}$	Q <sub>ut</sub>	r <sub>ut</sub>	$\gamma_{cy}(\%)$	n <sub>i</sub>	Comment
LAGA-44	CyT-CAU	0.827	3.73	1.517	0.628	0.365	2.424	0.930	0.599	0.047	37	(1),(2)
LAGA-45	CyT-CAU	0.806	3.73	1.517	0.587	0.323	2.372	0.896	0.504	0.171	3	(1),(2)
LAGA-46	CyT-CAU	0.779	3.73	1.517	0.546	0.290	2.405	0.964	0.612	0.023	1223	(1),(2)
LAGA-47	CyT-CAU	0.806	3.73	1.226	0.310	0.170	1.170	0.417	0.849	0.066	96	(1),(2)
LAGA-48	CyT-CAU	0.827	3.73	1.226	0.271	0.155	1.100	0.415	0.816	0.180	6.5	(1),(2)
LAGA-49	CyT-CAU	0.807	3.73	1.231	0.214	0.165	1.052	0.418	0.830	0.266	3.5	(1),(2)
LAGA-50	CyT-CAU	0.734	3.73	2.252	2.255	1.235	5.059	2.317	0.264	0.080	4	(1),(2)
LAGA-51	CyT-CAU	0.742	3.73	2.244	2.042	1.057	5.041	2.281	0.226	0.113	2	(1),(2)
LAGA-52	CyT-CAU	0.762	3.73	2.234	1.841	0.997	4.965	2.240	0.189	0.153	1	(1),(2)

All units in Kg/cm<sup>2</sup>

1) e Measurements not Accurate N.A. = Not Applicable

2) Old Platens N.R. = Not Recorded

3) Pore Pressure not Recorded

## SAND A

Test #	TestType	e	$\bar{\sigma}_{3c}$	$K_c$	$\bar{p}_{us}$	$q_{us}$	$\bar{p}_{ut}$	$q_{ut}$	$r_{ut}$	$\gamma_{cy}(\%)$	$n_t$	Comment
TJA-1	$\overline{CIU}$	0.8345	4.07	1.0	0.482	0.25	2.364	0.677	0.586	N.A.	N.A.	(1),(2)
TJA-2	$\overline{CIU}$	0.7565	6.538	1.0	0.938	0.516	3.961	1.149	0.570	N.A.	N.A.	(1),(2)
TJA-3	$\overline{CAU}$	0.7713	5.132	2.0	2.695	1.359	7.207	2.856	0.055	N.A.	N.A.	(1),(2)
TJA-4	$\overline{Cyt-CAU}$	0.7478	6.53	2.0	2.599	1.348	8.109	3.286	0.252	0.138	3	(1),(2)
TJA-5	$\overline{Cyt-CAU}$	0.7956	4.07	2.02	1.463	0.787	5.091	2.052	0.255	0.074	6	(1),(2)
TJA-6	$\overline{Cyt-CAU}$	0.8051	4.07	2.0	1.295	0.707	4.903	1.979	0.283	0.0462	7	(1),(2)
LAGA-8	$\overline{Cyt-CAU}$	0.7714	4.07	2.0	1.783	0.933	4.852	2.032	0.309	0.1006	3	(1),(2)
LAGA-9	$\overline{Cyt-CAU}$	0.7859	3.72	2.04	1.700	0.965	4.566	1.924	0.32	0.048	10	(1),(2),(3)
LAGA-10	$\overline{Cyt-CAU}$	0.7874	2.67	1.98	1.084	0.574	3.302	1.302	0.251	0.0545	4	(1),(2)
LAGA-11	$\overline{Cyt-CAU}$	0.7504	4.07	2.05	1.915	0.986	4.876	2.087	0.316	0.0494	11	(1),(2)
LAGA-12	$\overline{Cyt-CAU}$	0.7902	2.67	2.03	1.103	0.595	3.22	1.354	0.301	0.0512	5	(1),(2)
LAGA-13	$\overline{Cyt-CAU}$	0.7624	4.78	2.02	2.204	1.139	5.81	2.425	0.292	0.049	14	(1),(2)
LAGA-16	$\overline{Cyt-CAU}$	0.7766	4.077	2.056	2.221	1.293	4.649	2.118	0.379	0.148	1	(1),(2)
LAGA-22	$\overline{Cyt-CAU}$	0.7332	4.077	2.03	2.102	1.188	4.766	2.095	0.341	0.0447	21	(1),(2)
LAGA-25	$\overline{Cyt-CAU}$	0.7355	4.077	2.03	1.853	1.079	5.033	2.080	0.321	0.019	113	(1),(2)
LAGA-38	$\overline{CIU}$	0.8048	4.077	1.0	1.883	0.507	3.774	1.207	0.371	N.A.	N.A.	(1),(2),(3)

All units in Kg/cm<sup>2</sup>

# SAND B

Test #	Test Type	e	$\bar{\sigma}_{3c}$	K <sub>c</sub>	$\bar{p}_{us}$	q <sub>us</sub>	$\bar{p}_{ut}$	q <sub>ut</sub>	r <sub>ut</sub>	$\gamma_{cy}(\%)$	n <sub>t</sub>	Comment
BACHB-39	CyT-CAU	0.8744	4.07	2.02	2.071	1.382	5.024	2.071	0.226	0.298	1	(1),(2)
BACHB-40	CIU	0.9024	4.07	1.00	0.500	0.307	2.318	0.912	0.655	N.A.	N.A.	(1),(2)
BACHB-42	CyT-CAU	0.8588	6.53	2.02	2.554	1.429	7.333	3.326	0.387	0.148	4	(1),(2)
BACHB-43	CyT-CAU	0.8845	4.077	2.02	1.086	0.664	4.878	2.066	0.310	0.042	26	(1),(2)

All units in Kg/cm<sup>2</sup>

N.R. - Not Recorded

1) e Measurements not Accurate

2) Old Platens



# SAND C

Test #	Test Type	e	$\bar{\sigma}_{3c}$	K <sub>c</sub>	$\bar{p}_{us}$	q <sub>us</sub>	$\bar{p}_{ut}$	q <sub>ut</sub>	r <sub>ut</sub>	$\gamma_{cy}(\%)$	n <sub>t</sub>	Comment
LAGC-23	CyT-CAU	0.818	2.671	2.02	1.687	1.007	2.656	1.323	0.501	0.097	4	(1),(2)
LAGC-24	CyT-CAU	0.8047	5.132	2.01	3.629	2.04	6.255	2.595	0.285	0.084	12	(1),(2)
LAGC-27	CyT-CAU	0.8372	0.9140	2.00	0.303	0.232	0.957	0.464	0.462	0.022	19	(1),(2)
LAGC-28	CIU	0.7892	7.2416	1.00	3.166	1.760	4.762	2.02	2.742	N.A.	N.A.	(1),(2)
LAGC-41	CIU	0.836	4.07	1.00	1.146	0.542	2.323	0.593	1.730	N.A.	N.A.	(1),(2)

All units in Kg/cm<sup>2</sup>

N.A. = Not Applicable

1) e Measurements not Accurate

2) Old Platens

APPENDIX III - INDIVIDUAL TEST RESULTS ON SAN FERNANDO SAND  
SF7

# SAN FERNANDO SF7 SAND

Test #	Test Type	e	$\bar{\sigma}_{3c}$	K <sub>c</sub>	$\bar{p}_{us}$	q <sub>us</sub>	$\bar{p}_{ut}$	q <sub>ut</sub>	r <sub>ut</sub>	$\gamma_{cy}(\%)$	n <sub>t</sub>	Comment
SF7-17	CyT-CAU	0.6206	1.0	2.21	0.909	0.54	1.224	0.591	0.357	0.026	11.5	
SF7-18	CyT-CAU	0.6229	1.0	2.22	0.95	0.539	1.242	0.592	0.339	0.051	4	
SF7-19	Threshold	0.6799	1.0	1.0	N.A.	N.A.	N.A.	N.A.	N.A.	N.A.	N.A.	
SF7-20	CAU	0.6432	1.0	2.0	0.528	0.282	1.05	0.475	0.425		N.A.	(3)
SF7-21	Threshold	0.6249	1.0	2.0	N.A.	N.A.	N.A.	N.A.	N.A.		N.A.	
SF7-22	CyT-CAU	0.7127	1.0	1.8	0.680	0.364	0.946	0.393	0.437	0.0568	6	(2)
SF7-23	CyT-CAU	0.7274	1.0	1.73	0.632	0.332	0.882	0.365	0.464	0.11	2.5	(2)
SF7-24	CyT-CAU	0.6566	1.0	1.79	N.A.	N.A.	N.A.	N.A.	N.A.	0.0518	N.A.	(2),(1)
SF7-25	CyT-CAU	0.7017	1.0	2.1	0.967	0.51	1.149	0.534	0.375	0.0072	39.5	(2)
SF7-26	CyT-CAU	0.6953	1.0	2.09	0.915	0.502	1.119	0.53	0.402	0.024	11.5	(2)
SF7-27	CyT-CAU	0.6305	1.0	1.81	N.A.	N.A.	N.A.	N.A.	N.A.	0.0179	41.5	(1)

All units in Kg/cm<sup>2</sup>

- 1) No Flow Failure, Dilative Specimen  
2) Sedimented Sample  
3) Strain Controlled  
4) Number of Cycles not Recorded
- N.A. = Not Applicable  
N.R. = Not Recorded

SAN FERNANDO SF7 SAND

Test #	Test Type	e	$\bar{\sigma}_{3c}$	$K_c$	$\bar{p}_{us}$	$q_{us}$	$\bar{p}_{ut}$	$q_{ut}$	$r_{ut}$	$\gamma_{cv}(\%)$	$n_t$	Comment
SF7-1	CyT-CAU	0.672	1.0	1.41	0.221	0.151	0.506	0.198	0.683	0.05	23	
SF7-2	CyT-CAU	0.6423	1.0	2.0	0.538	0.327	1.077	0.480	0.393	0.0518	2.5	
SF7-3	CIU	0.6629	2.0	1.0	0.392	0.26	0.961	0.346	0.687	N.A.	N.A.	
SF7-4	CyT-CAU	0.6467	1.0	2.0	0.502	0.317	1.085	0.487	0.393	0.0257	5.5	
SF7-5	CyT-CAU	0.6246	1.0	2.0	0.695	0.392	1.093	0.495	0.393	0.005	21	
SF7-6	CyT-CAU	0.6475	1.0	2.0	0.593	0.329	1.082	0.485	0.393	0.0107	7	
SF7-7	CyT-CAU	0.6595	1.0	1.7	0.427	0.260	1.802	0.345	0.536	0.0493	8	
SF7-8	CyT-CAU	0.6594	1.0	1.7	0.455	0.270	0.821	0.346	0.518	0.0245	20	
SF7-9	CyT-CAU	0.6594	1.0	1.7	0.447	0.271	0.785	0.346	0.554	0.1027	3.5	
SF7-10	CyT-CAU	0.5965	1.0	2.67	N.A.	N.A.	N.A.	N.A.	N.A.	0.0048	N.A.	(1)
SF7-11	CyT-CAU	0.6236	1.0	2.21	0.865	0.496	1.20	0.585	0.375	0.0109	7	
SF7-12	CyT-CAU	0.610	1.0	2.53	N.A.	N.A.	N.A.	N.A.	N.A.	0.0048	N.A.	(1)
SF7-13	CIU	0.6799	1.0	1.0	0.288	0.191	1.590	0.234	0.638	N.A.	N.A.	
SF7-14	CyT-CIU	0.6436	1.0	1.86	0.605	0.368	1.065	0.423	0.348	0.011	N.A.	
SF7-15	CyT-CIU	0.6362	1.0	1.88	0.655	0.374	1.027	0.429	0.393	0.499	6.5	(4)
SF7-16	CyT-CIU	0.6268	1.0	1.87	0.618	0.337	1.024	0.426	0.393	0.0245	12.5	

All units in Kg/cm.<sup>2</sup>

APPENDIX IV - INDIVIDUAL TEST RESULTS ON UNDISTURBED  
SPECIMENS  
OF SANDS A, B OR C

# UNDISTURBED SPECIMENS

Test #	Test Type	e	$\bar{\sigma}_{3c}$	K <sub>c</sub>	$\bar{p}_{us}$	q <sub>us</sub>
17	CIU	0.6534	6.978	1.00	5.178	2.70
18	CIU	0.5877	7.1	1.00	4.596	2.275
19	CIU	0.677	10.757	1.00	7.066	3.48
21	CIU	0.6827	10.757	1.00	7.07	3.55
26	CIU	0.587	16.00	1.00	9.20	4.71
29	CIU	0.8089	7.2416	1.00	N.A.	N.A.
31	CYT CAU + CAU	0.6223	6.8901	2.12	N.A.	N.A.
32	CIU	0.6824	7.24	1.00	N.A.	N.A.
36	CIU	0.628	90.0	1.00	47.77	26.1

All units in Kg/cm<sup>2</sup>

N.A. = Not Applicable